26th Danubia-Adria Symposium on Advances in Experimental Mechanics

September 23rd – 26th, 2009
Montanuniversität Leoben / Austria

MONTAN
UNIVERSITÄT
WWW.UNILEOBEN.AC.AT

Imprint

26th Danubia-Adria Symposium on Advances in Experimental Mechanics

Organized by:
Montanuniversität Leoben, Chair of Mechanical Engineering (AMB)
Austrian Society of Experimental Strain Analysis (ASESA)

Co-organized by:
Croatian Society of Mechanics (HDM)
Hungarian Scientific Society of Mechanical Engineering (GTE)
Italia Association for Stress Analysis (AIAS)
Committee of Mechanics of Polish Academy of Sciences (KMPAM)
Romanian Association for Experimental Stress Analysis (ARTENS)
Serbian Society of Mechanics (SSM)
Slovak Society of Mechanics (SSM)
Czech Technical University in Prague (CVUT)

Scientific Board

Austria:	J. Eberhardsteiner (Vienna)
	W. Eichlseder (Leoben)
Croatia:	I. Alfirevic (Zagreb)
	D. Semenski (Zagreb)
Czech Republic:	F. Plánička (Plzen)
	M. Růžička (Prague)
Hungary:	L. Borbás (Budapest)
Italy:	F. Cosmi (Trieste)
	G. Nicoletto (Parma)
Poland:	R. Bedzinski (Wroclaw)
	L. Dietrich (Warsaw)
Romania:	N. Iliescu (Bucharest)
	I. Pastrav (Cluj-Napoca)
Serbia:	M.Ognjanovic (Belgrade)
	M. Zivkovic (Kragujevac)
Slovakia:	O. Bokůvka (Zilina)
	P. Palček (Zilina)

Honorary Members of International Scientific Board

R.Beer (Vienna), A. Freddi (Bologna), I. Huszár (Gödöllö), S. Jecic (Zagreb), F. Thamm (Budapest), S. Holý (Prague)

Local Organizing Committee

Univ.-Prof. Dr. Wilfried Eichlseder, Univ.-Prof. Dr. Josef Eberhardsteiner, Dipl.-Ing. Thomas Fössl, Dipl.-Ing. Wen Tan, Mag. (FH) Martina Pöll

Thank you for the financial support of the following institutions and companies:

HBM

DANTEC DYNAMICS

MTS®

Prager Elektronik

OLYMPUS

Excellence in Automation and Drives

SIEMENS

Table of Contents

THE IMPACT OF WORN OUT TOOL ON THE CHARACTER AND TYPE OF CHIP FORMATION

Aco Antić [1)], Petar Petrović [2)], Milan Zeljković [1)]

1) University of Novi Sad, Faculty of Technical Sciences, Trg D. Obradovića 6, 21000 Novi Sad, Serbia

2) University of Belgrad, Faculty of Mechanical Engineering, Kraljice Marije 16, 11120 Belgrad, Serbia

Corresponding authors: antica@uns.ac.rs;

1. Introduction

Chip formation in the process of machining includes high strain rates, high temperatures and non-linear plastic flow of material. Plastic flow of material generates local stresses on the tool's cutting edge, distribution of temperature onto the tool through the chip and defines the condition of the tool's processed surface after the removal of the material. The intensity of local and main stresses is determined by the power of the machine tool and the structure itself, which again results from dynamic and static deformations. These stresses determine the intensity of various physical phenomena which characterize the tool wearing, as chemical processes, abrasive and diffusive wearing. This results in warming up and thermal induction and extension of the structure, which directly affects the machining precision [1, 2, 4]. Therefore, due to foresee the adequate behavior of the processing system on global scale, information on plastic deformation and flow of material in the immediate proximity of the tool tip is of vital importance. Researches have shown that careful monitoring of this plastic flow enables observation of several clear dynamic phenomena reflecting through formation of the following chip shapes: discontinuous; continuous; with continuous folds on edges; shear localized and segmented. The ideal approach would describe every type of chip formation as stable dynamic balanced system by means of partial differential equation, describing the elastic and plastic flow. At high speed machining, chip formation occurs mainly through two types, as the continuous and shear localized [4, 5]. When changing the machining speed, in most of materials a transition from continuous to shear localized chip will occur, which happens during the critical machining speed, Figure 1.
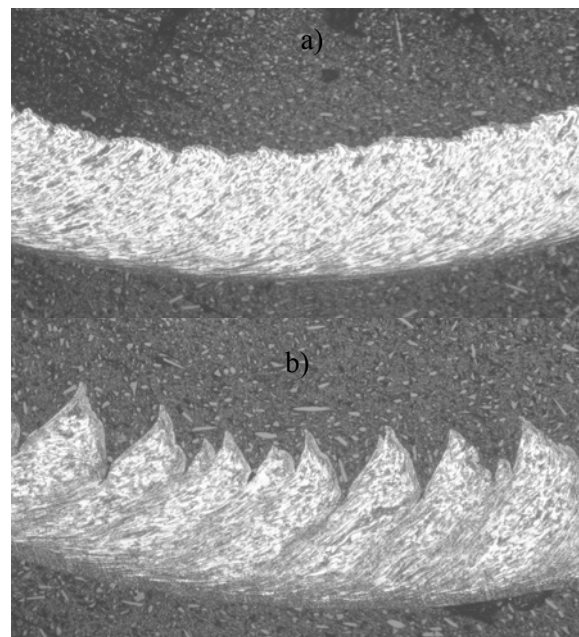
Fig.1: Types of chip formation:
a) new tool insert, b) worn out tool insert

2. Experimental results

Researches have shown that the upper part of spectrum of the vibrations acceleration measured on the turner chisel arm in the area close to the cutting wedge enables the indirect identification of changes in rates of chip formation induced by changes in the rate of the cutting tool weariness, i.e. by degradation of its cutting performances by wearing. Within the range of 5-50 kHz there is a large number of tool's frequencies, which produces resonance under influence of the exciting force which arises by chip fragmentation in the process of lamella formation. During the formation of a chip lamella it is clear that the material in front of the primary shear zone is elastically stressed at times, and the momentary elastic energy of the stress will be proportionate to the integral product of the shear stress in the primary zone and of the elastic dislocation of the shear zone.

Within any segment formation, the cutting localization is sometimes destabilized also by the primary shear zone itself, by changes occurring in its upper part, which results in the release of elastic energy of the stress.

The frequency of segment formation is usually higher than 10 kHz, which is above the level of conventional response of classical sensors. By releasing the shear energy of the lamella, a far more dominant peak source is observed in the signal of vibrations in case of production of saw-tooth chips. This is best illustrated by test data, Figure 2.
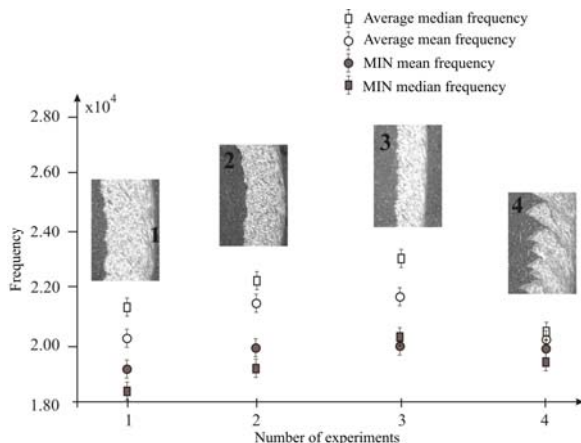
Fig. 2: Parameters of median and frequency changes depending on the chip structure.

By the analysis of test results it could be concluded that the type of chip formed in the cutting process is affected predominantly not only by the material's condition and properties and the cutting speed, but also by the rate of the cutting tool insert's weariness, i.e. the geometry of the tool. The obtained test results show that by maintaining the constant machining regime: cutting speed, feed and depth, as well as material's constant properties, when changing the rate of weariness of the tool in certain moment a transition occurs from one type of chips into another. This is due to the changed cutting geometry which changes depending on the tool's rate of weariness. Change of cutting geometry and consequently of the chip type is detected directly on parameters under observation in analyzed region of the high frequency part of the vibration spectrum. Each of 4 levels of weariness of the tool insert produces a certain type of chip which is reflected by the monitored parameters in the spectrum of vibration. This track could be followed in any vibration signal spectrum chart as the function of weariness of the tool insert based on several parameters, the achieved values which are shown in Table 1.

Frequency Parameters x10^3	tool wear rates			
	1	2	3	4
	VB 0	VB 0,25	VB 0,55	VB 0,95
median	21.59	21.97	22.48	21.40
mean	20.59	21.57	21.59	20.92
min median	17.34	18.81	20.88	19.54
min mean	19.28	19.97	20.19	20.04

Table 1: Values of parameters monitored during the experiment

3. Acknowledgements

4. References

[1] T.J. Burns, M.A. Davies, On repeated adiabatic shear band formation during high-speed machining, International Journal of Plasticity18 (2002) 487–506.

[2] M. Cotterell, G. Byrne, Dynamics of chip formation during orthogonal cutting of titanium alloy Ti–6Al–4V, CIRP Annals - Manufacturing Technology 57 (2008) 93–96.

[3] F.J. Alonso, D.R. Salgado, Analysis of the structure of vibration signals for tool wear detection, Mechanical Systems and Signal Processing 22 (2008) 735–748.

[4] M. Calamaz, D. Coupard, F. Girot, A new material model for 2D numerical simulation of serrated chip formation when machining titanium alloy Ti–6Al–4V, International Journal of Machine Tools & Manufacture 48 (2008) 275–288.

[5] K. Katuku, A. Koursaris, I. Sigalas, Wear, cutting forces and chip characteristics when dry turning ASTM Grade 2 austempered ductile iron with PcBN cutting tools under finishing conditions, Journal of Materials processing technology 209 (2009) 2412–2420.

CASTING PORE CHARACTERIZATION BY X-RAY COMPUTED TOMOGRAPHY AND METALLOGRAPHY

G. Anzelotti [1)], S. Fintová [2)], R. Konečná [2)], G. Nicoletto [1)]

[1)] University of Parma, Dept. of Industrial Engineering, 43100 Parma, Italy.

[2)] University of Žilina, Dept. of Materials Engineering, Žilina, Slovakia.

Corresponding author: g.anzelotti@ied.unipr.it; gianni.nicoletto@unipr.it

1. Introduction

Cast Al-Si alloys are widely used in automotive applications for their excellent combination of mechanical and technological properties. Fatigue properties of aluminum castings are however sensitive to the casting defects, [1]. The maximum defect size has been recognized as the most important parameter in determining the fatigue properties of aluminum castings. The larger the maximum defect size, the lower the fatigue strength, [2].

In this paper a method of statistical pore size characterization by metallography is initially considered. Then, x-ray computed tomography (XCT) is used to reconstruct the 3D distribution of casting pores in AlSi7Mg. Special interest is devoted to shrinkage pores, which are irregular in shape. The XCT results are used to discuss metallographic issues in equivalent pore sizing criteria.

2. Pore sizing by metallography

Metallography can be routinely used to study porosity in AlSi castings.
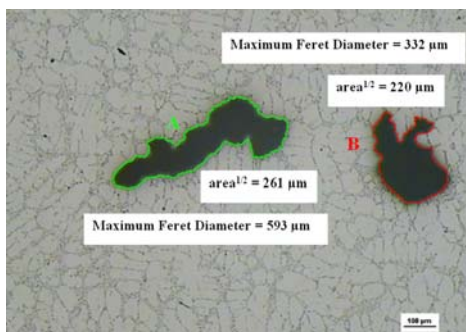
Fig. 1: Casting pores in AlSi7Mg by metallography

Fig. 1 shows two casting pores in AlSi7Mg and two definitions of equivalent pore size, namely the maximum Feret diameter (i.e. maximum distance between two points on the pore surface), [3], and $(area)^{1/2}$, [2], to define pore severity in fatigue. Quite different equivalent sizes are obtained because one pore in Fig. 1 is rounded and the other is elongated.

Measurements of largest pore equivalent sizes found in a significant number of metallographic fields of view can be discussed in the light of the Gumbel's distribution, [2]. An example of largest pore size data sets (i.e. Maximum Feret Diameter) entered into the Gumbel plot is shown in Fig. 2. Since each data set appreciably fulfills the linearity condition, the Gumbel statistical distribution can be used for fitting and extrapolation. The slope of the regression line is an indicator of the scatter in the data. Inspection of Fig. 2 shows that set A (modified with Na and cast in steel mold) has the largest scatter among the three materials while set B (modified with Sr and cast in steel mold) and C (modified with Sr and sand cast) have similar and reduced scatter.
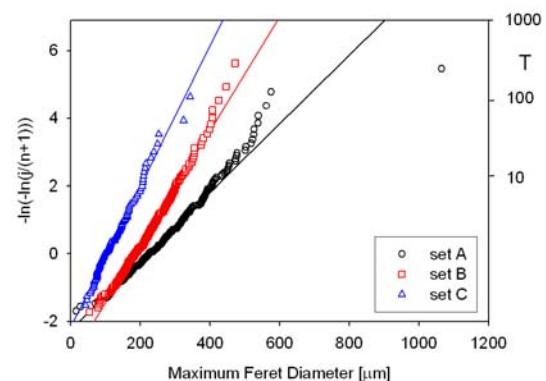
Fig. 2: Largest pore sizes in Al-Si alloy by metallography

3. Pore reconstruction by XCT

X-ray tomography (XCT) is a technology finding applications in material science, [4]. It exploits the penetrating power of a high density focused x-ray beam. A two-step procedure was developed. In the first step, a large number of XCT scans of a material volume are acquired. These scans are "front photos" of the specimen,

representing pixel by pixel the absorption coefficient of the material crossed by X-rays. From these scans, cross-section images (i.e. slices) of the material volume are obtained with a back-projection algorithm. The second step of the procedure is the 3D reconstruction of pores from the series of slices. An original software has been developed to obtain all the pores inside the volume under investigation (i.e. a cylinder 4 mm in diameter and 1 mm in length shown in Fig. 3).
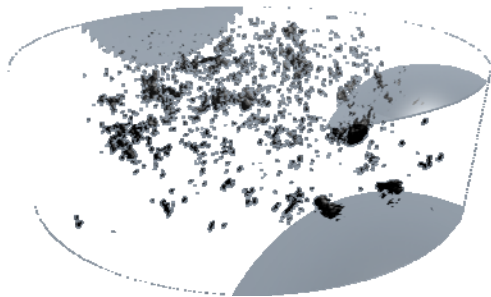
Fig. 3: Reconstruction of the porosity in a cylindrical volume of AlSi7Mg

Only the outer surface of each pore is stored as non-structured triangular surfaces according to the STL standard and finally smoothed. The high spatial resolution allows the reconstruction of the intricate geometry of a shrinkage pore, see Fig. 4.
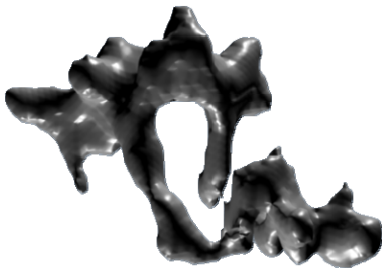
Fig. 4: Typical shrinkage pore

4. Sectioning a shrinkage pore

The branched appearance of shrinkage pores poses a challenge to the metallographic characterization of largest pore sizes for fatigue model development. Methods were originally developed to quantify the role of inclusions, which are typically compact in shape, [2]. Metallography observes a random material section under high magnification. It is unlikely that section a shrinkage pore exposes the maximum pore dimension. An example of a shrinkage pore sectioning is visualized in Fig. 5, where isolated neighboring cavities are found. None of these pseudo-pores, even the largest one, has a size comparable to the size of

the original pore. Therefore guidelines for estimating representative pore sizes based on coalescence conditions of neighboring pores are needed.
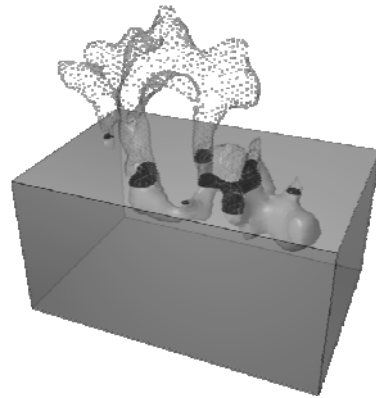
Fig. 5: Cross-section of a shrinkage pore

An on-going FEM investigation of the effective stresses near pores of different kinds, [5], demonstrates that gas and shrinkage pores of similar size in terms of max. Feret diameter give comparable stress concentration with negligible influence of pore morphology.

5. Acknowledgements

6. References

[1] Q.G. Wang, D. Apelian, D.A. Lados (2001) J. of Light Metals, **1,** 73-84

[2] Y. Murakami (2002) Metal Fatigue: Effects of Small Defects and Nonmetallic Inclusions, Elsevier

[3] Q. G. Wang, P. E. Jones, (2007) Metal. Matls Trans B, **38,** 615-621

[4] P. Powazka, et al. (2008) Procs Leoben Fatigue Symp

[5] A. Vincenzi et al. (2009) Procs DAS Leoben.

MECHANICAL PROPERTIES OF CORONARY VEINS AND ITS MODEL MATERIALS

Tibor Balazs [1], Eszter Bognar [1], Janos Dobranszky [2], Laszlo Devenyi [1]

[1] Budapest University of Technology and Economics (BUTE), Department of Material Science and Engineering, 1111 Budapest, Goldmann square 3. Hungary

[2] Research Group for Metals Technology of the HAS and BUTE, Department of Materials Science and Engineering, 1111 Budapest, Goldmann square 3. Hungary

Corresponding author: tibor.balazs@freemail.hu

1. Introduction

The mechanical properties of coronary veins are an exciting question for all the companies who are making special medical devices for the coronary and for those physicians who are performing electrophysiological procedures and resynchronization pacemaker implantations. They have to know the mechanical limits of the coronary veins. Unfortunately the available vein examinations are concentrating on saphenous veins and the most experienced are basically investigating arteries from different parts of the body and basically no test results for the coronary veins.

Not enough to have experimental results for arteries from all over the body because the structural differences between arteries and veins are causing differences in the mechanical properties as well. That means it is not possible to convert the mechanical properties of the arteries to the veins. The aim of this investigation is to develop a technique for evaluate the tensile strength of coronary veins.

2. Experimental

Coronary veins were prepared form pig hearts immediately after receiving from slaughterhouse and kept in a physiologic saline solution (0,9 %) until the test is performed. Four longitudinal sample were prepared from the received coronary. The sizes of the prepared rectangular samples were detailed in Table 1.

For the sample fixation a grip was used with reticulated metal surface and the tensile test was done with Zwick Z020 tensile test machine.

The test was performed in a 37°C physiologic solution in order to ensure similar circumstances like the original surround. The rest of the solution was stored in a furnace and after each and every test the physiologic solution was changed for a new 37°C solution.

No.	Width mm	Thickness mm	Length mm	Area mm^2
1	8,00	0,45	22,53	3,60
2	8,83	0,34	17,87	2,98
3	8,80	0,24	18,53	2,11
4	7,17	0,46	16,10	3,27

Tab. 1: Dimensions of the coronary vein samples

The schematic draw of the testing equipment is shown in Fig. 1.
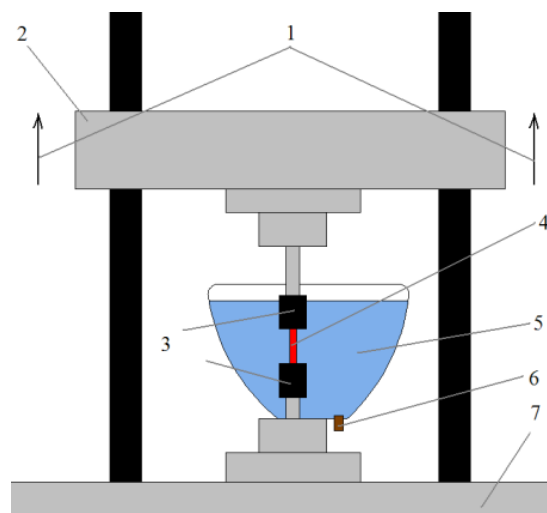
Fig. 1: Testing equipment: 1- tensile force; 2 - upper clamp; 3 – grips; 4 - vein sample; 5 - physiologic solution on 37°C; 6 - plug; 7 - lower clamp)

Because the usual stretching speed is two slow for the veins a 20 mm/min was used for all the tested samples and the distance was always 5 mm (L_0) between the upper and lower clamp at the beginning. During the tests the force was recorded in the function of travel distance.

3. Results

Based on the test results a maximal force could be defined and also the tensile strength, strain and Young's modulus with the equations below:

$$\sigma = \frac{F_{max}}{A_0} \qquad \varepsilon = \frac{\Delta L}{L_0} \cdot 100\% \qquad E = \frac{\sigma}{\varepsilon}$$

Where is σ–stress, ε relative extension, E–Young's modulus, A_0–starting cross-sections, L_0–distance between the two clamp, ΔL–travel distance, F_{max}–maximal force

The maximal force is given by the test results because it was recorded in the function of the travel distance and the cross section is detailed in Table 1.

The maximal force curve in the function of the travel distance is shown in Figure 2.
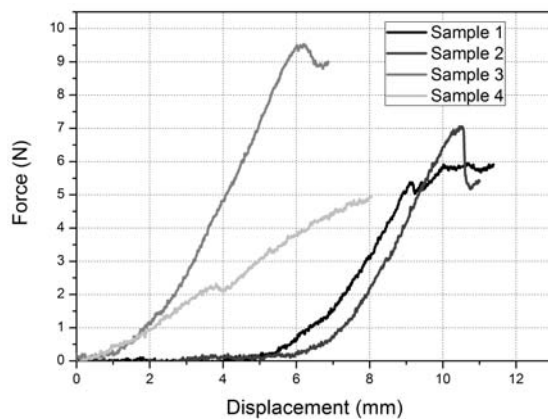
Fig. 1: Maximal force – travel displacement for the tested sample

The trend of the curves is similar in all the four case, after loading they have a faster uploading. In two cases the first 5mm travel distance don't need a considerable force. The prepared samples are not rigid samples and it happens that the length of the sample remains longer after fixation than the 5mm distance between the two grips.

In these two cases the length of the sample until beginning of loading was defined as the beginning distance. The maximal force and the calculated tensile strength, strain and Young's modulus with adequate equations is detailed in Table 2.

The results are similar for three samples, but one is different. It has higher elongation, it needs lower force for tearing and it has a lower Young's modulus. Probably it could be a different orientation of the sample.

No.	Max. force N	Relative extension %	Tensile strength MPa	Young's modulus mm^2
1	5,94	0,74	1,65	2,23
2	7,05	0,72	2,37	3,31
3	9,44	1,20	4,47	3,71
4	4,94	1,61	1,51	0,94

Tab. 2: Results of vein's tensile tests

4. Discussion

The fixation mode should be improved in order to avoid the elongation without force. The results are showing the typical properties of coronary veins, but more samples needs to be tested. The basic idea is appropriate for in vitro testing and it is also good to define the coronary veins properties. The longitudinal and transversal samples should be differentiate and tested in different groups.

5. References

[1] L. Xiao, P. Aditya, K.S. Ghassam, Biaxial incremental homeostatic elastic moduli of coronary artery: two layer model. Am. J. Physiol Heart Circ. Physiol. 2004. 287: H1663 - H1669

[2] Y.C. Fung, S.Q. Liu, Determination of the Mechanical Properties of the Different layers of Blood Vessels in vivo. PNAS 1995. 92:2169 – 2173

[3] F. Molnár, S. Till, G. Halász, Arterial blood flow and blood pressure measurements at a physical model of human arterial system. Embec 2005, 3rd European Medical & Biological Engineering Conference,

[4] S. Till and G. Halász, The effect of different artery wall models on arterial blood flow simulation; Proceedings of the first conference on biomechanics, Budapest, Hungary, 2004, pp. 480-485.

[5] L.E. Boerboom, TA Wooldridge, GN Olinger, NJ Rusch, Effects of storage solutions on contraction and relaxation of isolated saphenous veins. J Cardiovasc Pharmacol. 1992;20 Suppl. 12:S80-4

DETERMINATION OF WIND LOAD ON ANTENNA TOWER

Jani Barle [1), Danko Radica [1), Bernardin Peroš [2),

[1) University of Split, Faculty of Electrical Engineering, Mechanical Engineering and Naval Architecture, R. Boškovića b.b, 21000 Split, CROATIA, email: jani.barle@fesb.hr ; danko.radica@fesb.hr

[2) University of Split, Faculty of Civil Engineering and Architecture, Dept. of Steel and TimberStructures, Matice hrvatske 15, 21000 Split, CROATIA, email: bernardin.peros@gradst.hr

Corresponding author: danko.radica@fesb.hr

1. Introduction

Dominantly wind loaded structures are those where wind created forces in combination with other loads, is the dominant form of load. Wind speed is variable so these, otherwise stationary structures are under variable load.

The region of Dalmatia, is categorized as the most unfavourable region regarding the wind loads, and therefore is a favourable location for real scale field tests. A question of greatest engineering importance is determination of the correct wind load values for two exceptionally strong winds: catabatic, locally conditioned Bora [1], and another strong southerly wind Scirocco, encountered in the coastal belt of Dalmatia.

The reason for determination of these loads is to estimate metal fatigue of antenna tower parts. Actual load components depend on many parameters; wind speed, mounting position of structure and its design, but main influence has the wind speed because doubling the speed increases acting force four-fold [2].

2. Experimental system description

Wind speed and direction data were taken from standard meteorology rotating cup anemometers, mounted on three levels of the antenna tower, with one second sampling frequency. For determination of structure stresses four characteristic levels are chosen, fig. 1. Sensors used for measuring are 1 kΩ, halve and full bridge connected, T-rosette type strain gauges. This strain gauge setup gives good temperature compensation on each measuring spot. All measuring devices were connected to one common recording unit.
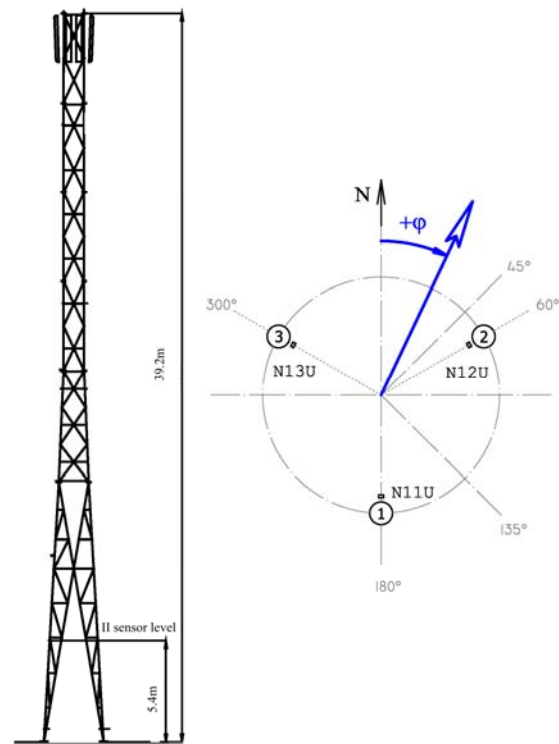
Fig. 1: Tower with positions of measuring cross-sections, second level enumeration of strain gauges.

3. Experimental and numerical analysis

Figs 2 and 3 show representative samples of stress recording for both dominant winds, Bora and Sirocco, respectively, at the second sensor level of the tower. These depict the fact that stress in legs of the tower depend on wind direction.
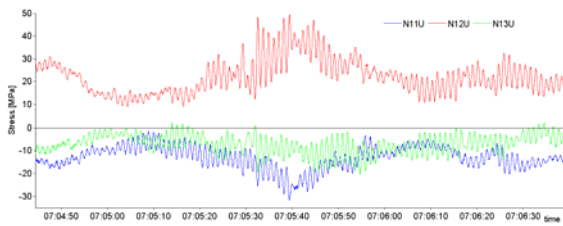
Fig. 2: Characteristic time interval for wind Bora on second sensor level
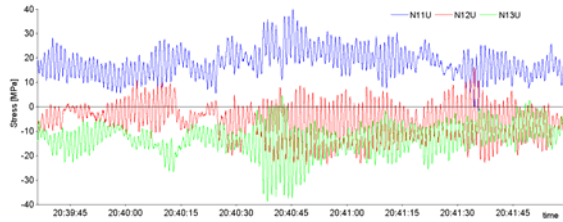
Fig. 3: Characteristic time interval for wind Scirocco on second sensor level

The first representative load history of Bora (fig. 2) wind has duration of 28 hours with average speed measured with cup anemometer of 14 m/s and maximum speed of 24 m/s. Direction of this wind was settled on 45° (ref. to angle φ on fig. 1). Scirocco wind was blowing 9 hours with average speed of 14 m/s and maximum speed of 26 m/s. Direction of this wind was changing from 135° to 180°.

From recorded data it is obvious that tower response on wind load is predominantly in first vibration mode what is agreement with [3]. and the respective frequency is 0.97 Hz.
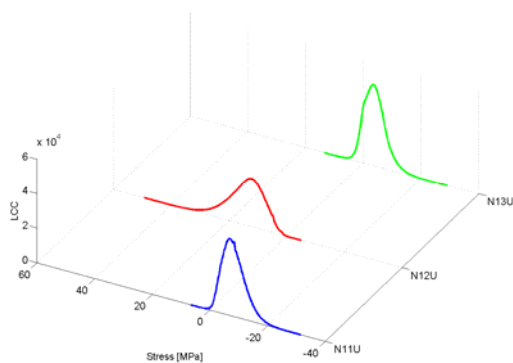
Fig. 4: RLCC of Bora (load case 1)
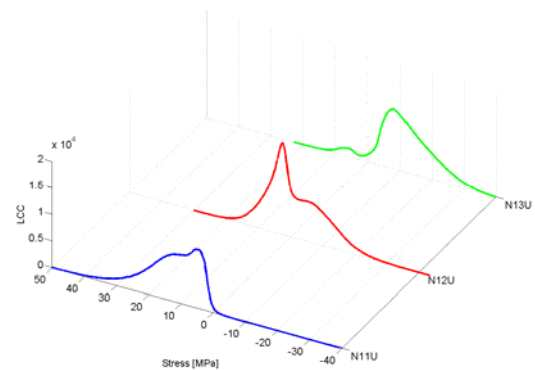
Fig. 5: RLCC of Scirocco (load case 2)

Used counting method in this analysis is **R**estricted-**L**evel-**C**rossing-**C**ounting according to ASTM standard [4]. Figures 4. and 5. present results of RLCC for both load cases.

4. Concluding remarks

Representative wind speed data for a certain location is only relevant load for this class of structures and the known load spectra is a prerequisite for optimal structural design. The results presented here can also be used in extrapolation for other load intensities and finally, for fatigue life evaluations of existing structures.

5. References

[1] Bajić, A., Peroš, B., Meteorological basis for wind loads calculation in Croatia, Wind and Structures, Vol. 8 (2005) 389-406.

[2] Barlow, J.B., Rae, W.H., Pope, A., Low speed wind tunnel testing, John Wiley & Sons, (1999).

[3] Materazzi, A.L., Venanzi, I., A simplified approach for the wind response analysis of cable-stayed masts, Journal of Wind Engineering and Industrial Aerodinamics, Vol. 95 (2007) 1272-1288.

[4] ASTM E-1049, Standard Practices for Cycle Counting in Fatigue Analysis,(1985).

NECK – STEM COUPLING IN MODULAR HIP PROTHESIS MECHANICAL PROBLEMS AND FAILURE ANALYSIS

**Rudolf J.Beer[1], Wolfgang Huber[2], Zvonimir Tomicevic[3],
Janos Kodvanj[3], Roland Reihsner[1]**

[1] Vienna University of Technology (A), [2] Dep. of Orthopaedics Gen. Hospital Wr. Neustadt (A),
[3] University of Zagreb (HR)

Corresponding author: rudolf.beer@tuwien.ac.at

1. Introduction

In modern hip arthroplasty a mechanical reconstruction is demanded which works as close as possible to the anatomical demands. From the mechanical point of view there are four principal points to be obeyed, which are:

1. Problems to due necessary replacement
2. The necessary mobility (degree of freedom and the needed domains for the different movements).
3. Failure analysis with view to there possible influence to lifetime
4. The forces acting on it (gait analysis).

The first necessity of hip replacement are of course given by medical findings. However the lifetime of the artificial replacement by the mechanical properties of the material used and by the design of the couple cone to sleeve which means by the loadtransfer and of course by kind of loading (ad. 4).

2. Method and results

This investigation is therefore divided into two parts.

First: Experimental determining of the stress-strain behaviour for the material used (Ti-6Al-4V) especially by a higher loading velocity.

Second: Numerical studies to investigate the influence of the design parameter to the kind of loadtransfer between the partners of the modular system For this purpose 4 different (Fig. 1) have been designed with 4, 6, 8, 10 and 12 notches All models have been loaded with a press-in-force to obtain practically the same grip between cone and sleeve. For all

models also 4 different distances (gap) were used between the end of the cone and the bottom off the sleeve. Fig. 1.1 shows the model which was used as a reference. Fig 1.2 shows a borehole in the cone.

Fig. 1.3 shows a more realistic design of the sleeve and fig. 1.4 represents a combination model 2 and model 3.

Reference model	bored cone
Fig. 1.1	**Fig. 1.2**
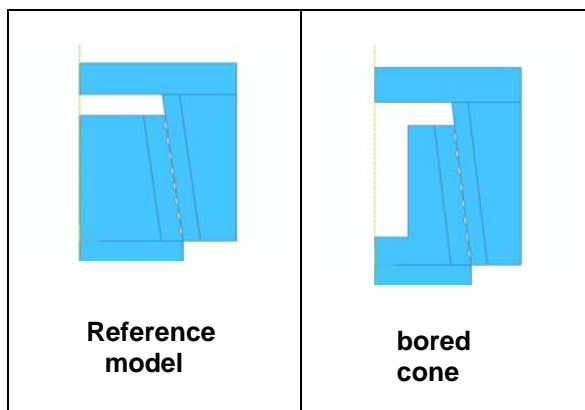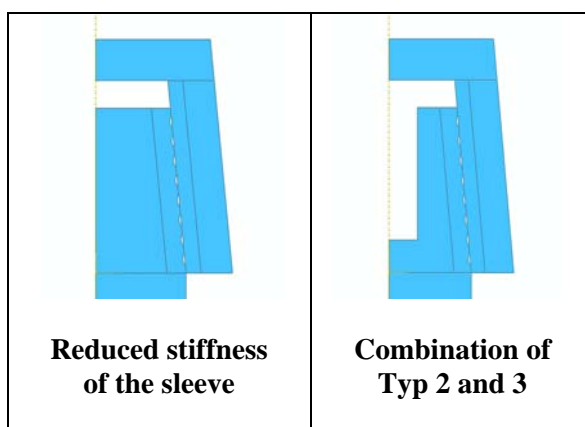
Reduced stiffness of the sleeve	Combination of Typ 2 and 3
Fig. 1.3	**Fig. 1.4**

Fig. 2 shows a sketch of the mounting procedure and the energy input necessary to achieve the same residual state of stress in all cases. The significant difference between the models with 8 and 10 notches in contrast to the model having 12 notches is caused by the smaller real single contact areas between the notches.
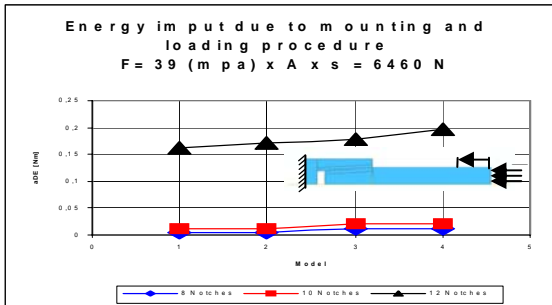
Fig. 2
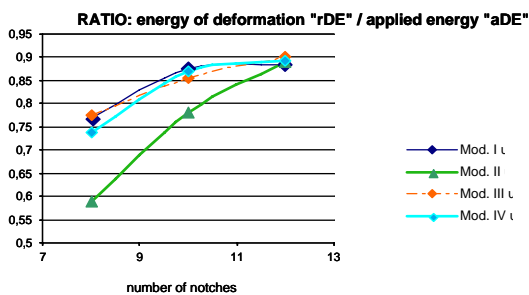
Fig. 3 shows the ratio of a measure of the residual deformation energy to the applied energy input.

Fig. 3

Fig. 4.1 and 4.2 show model 1 and 4 under the same loading conditions. The difference of the measure of the deformation energy is very small (ca. $2^o/_{oo}$). However the difference of the remaining plastification is about $15^o/_o$.
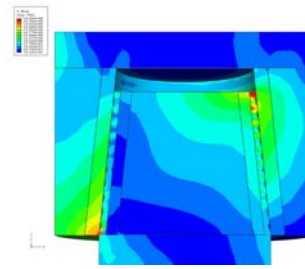
Fig. 4.1
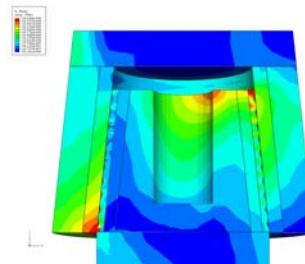
Fig. 4.2

3. Conclusions

Fig. 3 shows that the number of unit length should be as high as possible and the advantage of model 4 shows the way how to proceed.

4. References

[1] Chao, E.Y et al: Stress analysis of conical coupling joint in modular prosthetic system design. Trnasact. -30th Annual Meeting of Orthopaedic Re. Soc. Vol. 103- Atlanta, Georgia

MULTISCALE MODELS DESCRIBING INFLUENCE OF SMALL HYDROGEN CONCENTRATIONS ON STRENGTH AND OTHER MECHANICAL PROPERTIES OF MATERIALS

Alexander Belyaev[1), Dmitry Indeitsev [1), Vladimir Polyanskiy[2), Alexander Sukhanov[2)

[1) Institute of Problems in Mechanical Engineering, Russian Academy of Sciences, 199178 V.O., Bolshoj pr., 61, St.-Petersburg, Russia

[2) State Polytechnic University of St. Petersburg, 195251 Politekhnicheskaya, 29 St.-Petersburg, Russia

Corresponding author Alexander Belyaev: vice.ipme@gmail.com

The influence of small natural concentrations of hydrogen on material properties is very considerable. It becomes observable at the level of about a single atom per 50000 atoms of matrix of the matter.

On one hand, this influence of hydrogen can not be ignored since, in many cases, it is the only explanation of changes in material properties in time and under external loading. On the other hand, this influence is difficult to describe due to smallness of this factor and variety of consequences. For example, under change in the hydrogen concentrations by three-four times at the level of one atom per 10000 matrix atoms the mechanical properties of the material can change from brittleness to superplasticity.

An important role is played by the bonding energy of hydrogen in material. The hydrogen with large bonding energy is passive which means that even considerable changes in concentration of this hydrogen may have no influence on the mechanical properties. Quite the contrary, the hydrogen with low bonding energy tends to zones of tensile stresses (Gorsky's effect) and the effect of this mobile hydrogen on mechanical properties is approximately 10 times stronger than that of bonded hydrogen.

These effects can be described by a two-continuum model of medium. The presentation is concerned with the model itself and the most important properties. The presence of the second continuum allows one to describe simultaneously the hydrogen embrittlement and superplastic transformations on the stress-stain diagram in the form of certain structural instability.

By using two-continuum model we constructed time-dependence of the stress relaxation under increasing natural concentration of hydrogen. As an example we demonstrate the stress distribution for a flange of the gas pipeline. Under the redistribution of hydrogen due to the tensile stresses on the pipeline surface the concentrators of these tensile stresses were shown to lead to increasing accumulation of hydrogen in the concentration zones, appearance of hydrogen embrittlement and destruction.

Application of two-continuum models to describing multiscale materials, e.g. steels with nanostructures and/or nanostructural films allows obtaining adequate results which describe SMART-influence on properties of these structures. In contrast to the homogeneous materials, the nanocrystal materials in the presence of hydrogen demonstrate stabilization of their properties as hydrogen decreases the surface energy of crystals in material and prevent their increasing up to the microsize.

Summarising, we suggest a novel approach to modeling the solids with account for the influence of hydrogen on the properties of free surface on monocrystals of various scales.

DEVELOPMENT OF A FRETTING WEAR PARAMETER FOR IMPLEMENTATION OF WEAR IN A NUMERICAL ANALYSIS

Thomas Christiner [1), István Gódor [1), Paul Kainzinger [1), Wilfried Eichlseder [1)

[1) University of Leoben, Department Product Engineering / Chair of Mechanical Engineering,

Franz-Josef-Str. 18, 8700 Leoben, Austria.

Corresponding author: thomas.christiner@unileoben.ac.at

1. Introduction

In industrial applications machines consist of contact and joint areas e.g.: shaft to hub joints or plate disk fixings in an aeroplane turbine engine. Due to application small movements, often in an oscillatory manner, can be observed. This conditions lead to fretting, a wear process gaining more awareness in modern light weight design driven industry.

Fretting is defined as small oscillatory movement of two or more bodies under contact pressure. Several forms of fretting can be distinguished: fretting fatigue, fretting wear and fretting corrosion. Fretting fatigue is a reduction of the fatigue properties of the material due to the superimposed fretting load. Fretting wear describes a wear process driven by high contact pressures and displacement amplitude. Fretting corrosion is a tribo- chemical wear process [1]. The material degradation process is always a combination of this 3 fretting forms.

2. Experimental Investigations

At the chair of mechanical engineering a damage equivalent fretting testing method was developed [2].

In the presented study this testing method is used to evaluate the complex processes during fretting wear and to enable a fretting characterization of material combinations under laboratory conditions. The experiments were conducted at different load levels and different displacement levels. Besides different material combinations different surface roughness and coating combinations have been tested.

The experiments were analyzed by light and scanning electron microscopy. Besides fractography the worn surfaces were characterized by there energy wear density.

3. Numerical Investigations

The determined material properties are implemented into a numerical simulation. A commercial FE code and a FORTRAN 77 program are combined to tackle the changing surface geometry [3].

An energy like working parameter P is used to simulate the wear evolution during the fretting process. The parameter is a first approach to implement fretting wear in a product development process at an early stage. It is applicable to identify fretting wear threatened contact regions and will undergo further considerations concerning the different influences on the complex wear process.

4. Conclusion

A first approach to implement fretting wear in the product development process is presented. Material properties are identified and implemented into a simulation chain. In a next step the energy like Parameter P will have to undergo further considerations focusing on e.g.: the manufacturing process and COF evolution.

5. References

[1] Vincent L.: "Materials and Fretting", Fretting Fatigue ESIS 18 (Editing by R. B. Waterhouse and T. C. Lindley) 1994, Mechanical Engineering Publications, London, pp. 323-337

[2] Reiser J.: "Entwicklung einer Untersuchungsmethodik zur Evaluierung des Fretting -Widerstandes", Diploma thesis, University of Leoben, Chair of Mechanical Engineering, 2008

[3] McColl I. R., Ding J., Leen S. B.: „Finite element simulation and experimental validation of fretting wear", Wear 256 (2004) 1114-1127.

STUDIES ON BUCKLING BEHAVIOUR OF THE COMPOSITE PLATES WITH DELAMINATIONS

Elena Felicia Beznea [1), Ionel Chirica [1)

[1) University Dunarea de Jos of Galati, Domneasca Str., 47, 800008 Galati, Romania.

elena.beznea@ugal.ro, ionel.chirica@ugal.ro

1. Introduction

The laminated polymer composites used in shipbuilding structures are situated such that they are susceptible to foreign object impacts which can result in barely visible impact damage, often as interlaminar delaminations, that can be quite extensive and can significantly reduce a structure's load bearing capability.

The aim of the work is to analyze the influence of delamination on the changes in the buckling behaviour of ship deck plates made of composite materials. An orthotropic delamination model, describing mixed mode delaminating, by using COSMOS/M soft package, was applied. So, the damaged part of the structures and the undamaged part have been represented by well-known finite elements (layered shell elements). The influence of the position and the ellipse's diameters ratio (having the constant area) of delaminated zone on the critical buckling force was investigated [1].

2. Model characteristics

For the present study, a 3-D model with 4-node SHELL4L composite element of COSMOS/M was used. The panel is divided into two sub-laminates by a hypothetical plane containing the delamination. For this reason, the present finite element model would be referred to as two sub-laminates model (figure 1). The two sub-laminates are separately modeled using 4-node SHELL4L composite element, and then joined face to face with appropriate interfacial constraint conditions for the corresponding nodes on the sub-laminates, depending on whether the nodes lie in the delaminated or undelaminated region.

The square plates (320x320mm, 16 biaxial layers having the layer's thickness of 0.32 mm), clamped on the sides, are made of E-glass/polyester having the material characteristics:

$E_x = 46$ GPa, $E_y = 13$ GPa, $E_z = 13$ GPa,

$G_{xy} = 5$GPa, $G_{xz} = 5$GPa, $G_{yz} = 4.6$GPa,

$\mu_{xy} = 0.3$, $\mu_{yz} = 0.42$, $\mu_{xz} = 0.3$

$R_x^T = 1.062$GPa, $R_x^C = 0.61$GPa, $R_y^T = 0.031$GPa,

$R_y^C = 0.118$GPa, $R_{xy} = 0.72$GPa.

The layers topology is [02/45/902/45/02]s .

For the behaviour model of material, two cases has been considered: linear behaviour and nonlinear behaviour (Tsai-Wu failure criterion).

For perfect plate (without delaminations), the values of the buckling load are: p_{cr}=30.1 MPa (linear calculus), p_{cr}=37.5 MPa (nonlinear calculus).

The in-plane loading was applied as a uniform compressive pressure in the x direction. The ellipse's diameters of the delamination area are considered from the condition of the same area for all cases. In the parametric calculus, the following diameters ratios were considered: dx/dy={0.5; 1; 2}.

The position of the delamination along the thickness is been considered between two neighbors layers i and i+1, (i=1,16). In the paper, all the cases are considered. Taking into account the thickness symmetry of the plates, will be presented only cases of position of delamination on one side of symmetry axis.

In the figure 2, the numerical and experimental results for the case of delamination placed in the symmetry axis is presented. In the figure 3, the test rig is presented.
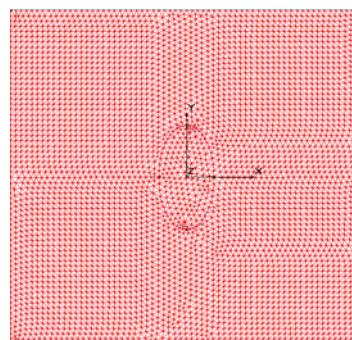
Fig. 1: Mesh model of the delaminated plate
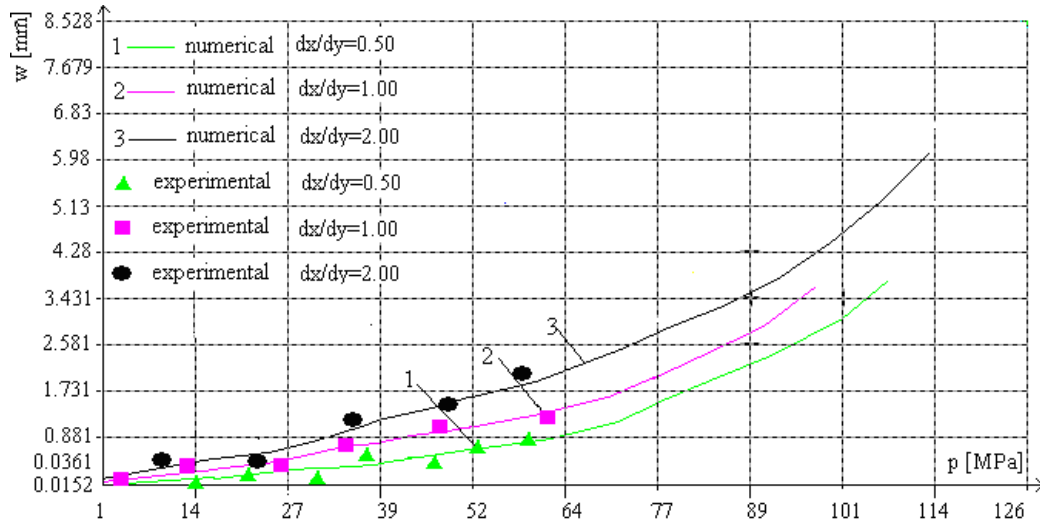
Fig. 2: Variation of maximum transversal displacement versus inplane load.
Case of the delamination placed between layers 8 and 9

Tab. 1 Buckling load range.

Position of delami-nation	Graphical method [MPa]		Tsai-Wu criterion			
			Fail 1 Tension [MPa]		**Fail 2 Compression [MPa]**	
	min pcr	*max pcr*	*min pcr*	*max pcr*	*min pcr*	*max pcr*
Layer 1 Layer 2	80	105	30	63	75	104
Layer 2 Layer 3	105	117	30	63	75	105
Layer 3 Layer 4	102	123	33	68	86	117
Layer 4 Layer 5	102	126	34	68	86	117
Layer 5 Layer 6	102	128	34	68	87	116

Fig. 3: Variation Test rig

3. Acknowledgments

[1] D.F. Adams, L.A. Carlsson, R.B. Pipes, Experimental Characterization of Advanced Composite materials, Ed. Taylor & Francis Group, (2003).

[2] E.F. Beznea, Studies and researches on the buckling behaviour of the composite panels, Doctoral Thesis, University Dunarea de Jos of Galati, (2008).

[3] E.F. Beznea, I. Chirica, R. Chirica, Buckling behaviour of plates with central elliptical delamination, Proceedings of MARSTRUCT 2009, The 2-nd Int. Conf. on Marine Structures, Lisbon, Portugal, March 2009, Analysis and Design of Marine Structures, (2009) 429-434.

APPLICATION OF OPTICAL FIBER BASED MEASURING TECHNIQUES FOR STRAIN FIELD MEASUREMENTS IN COMPOSITE BRAIDED TUBE SPECIMENS

Wojciech Błażejewski [1)], Andrzej Czulak [2)], <u>Paweł Gąsior</u> [1)], Jerzy Kaleta [1)]

[1)]   Institute of Materials Science and Applied Mechanics, Wroclaw University of Technology, Smoluchowskiego 25, 50-370 Wroclaw, Poland.

[2)]   Institut für Leichtbau und Kunststofftechnik, Technische Universität Dresden, Dőrerstraße 26, Dresden D-01062, Germany.

Corresponding author: pawel.gasior@pwr.wroc.pl

1. Introduction

Composite rotation-symmetrical elements (e.g. pressure vessels, pipes, shafts, mast, etc.) are most often fabricated from long fibers by winding technology. That method is completely automated and widespread [1-2]. The composite layers are packed in an ordered and programmed way in compliance with foreseen loadings. The braiding method for composite elements manufacturing is new and alternative technique in comparison with classical winding method [2] and allows realization of reinforcement layer at an any angle in a range from 5º to 86º. Furthermore that technique makes possible embedding additional elements between composite layers. It is possible to create so called "smart materials" with embedded other layers (i.e. with specific magnetic properties) as well as sensors (i.e. optical fiber based ones), which locally measure strain and temperature distributions inside composite material.
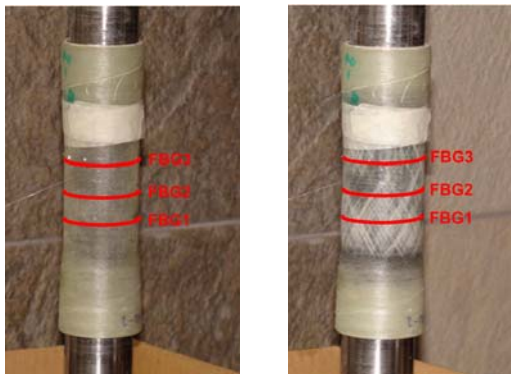
Fig. 1: Views of real specimen with installed FBG before and after the pressure test.

However, because there are not precise strength analysis of finished structures, that new method is not a widespread. A main target of

presented research was to carry out an experiment and prepare FEM analysis to compare obtained results. Three different tube specimens (fig.1) made from glass-epoxy composite were tested: 30º, 45º and 60º. They were differ from each other only by an angle of reinforcement. As a working medium a heap of rubber disks inside a specimen was compressed. It allowed to obtain uniaxial stress distribution (only circumferential strains were registered).

2. Experimental results

During the test a compressive force (pressure), displacement of pistons as well as deformation (strain) in circumferential direction were measured. Because of large deformation on the outer surface of specimens, even few percents, Fiber Bragg Gratings (FBG) for strain measurements were used. It let to perform strain measurement very precisely in a wide range [3,4] which was not possible to obtain by classical method (electric resistance wire strain gauge).
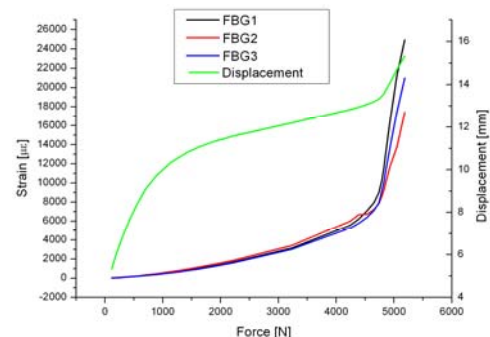
Fig. 2: Exemplary force – strain and force – displacement curves for specimen with reinforcement angle 30º [5].

Exemplary test results for selected specimen are presented in fig. 2. Obtained force –

displacement curves have two characteristic inflexion points. In a range of 0÷1.2 kN an air was pushed out and rubber disks were arranged inside a specimen. Next from 1.2 to about 4.75 kN a proper compression and uniaxial stress occurred. Over 4.75 kN a meaningful increase of registered strains was observed (second inflexion point of force-displacement curve).

It was a result of a matrix failure in composite. So called delamination between two phases (glass fiber and epoxy resin) occurred. It was also o moment when a specimen started to whiten (see fig. 1). Maximal registered strain by FBG sensors reached 2.5% (25000 με).
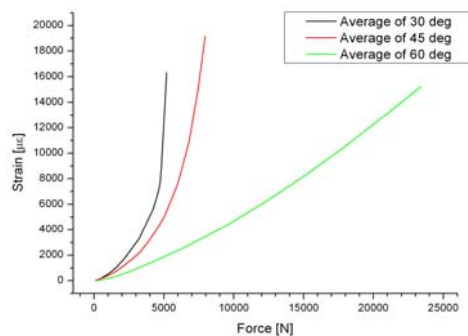
Fig. 3: Average values of circumferential strains for three different tube types: 30º, 45º and 60º in a function of applied load [5].

In figure 3 there is a matching of average values of circumferential strains for three different tube types (30º, 45º, 60º) presented. For 60º-type specimens it is possible to observe for the same applied force (internal pressure) much more smaller values of registered strains than for other ones. It confirms that applied loading is mainly carried by reinforcement than for epoxy matrix and allows for substantially improve strength of composite elements for such type of loading. It also testifies thesis that strength of composite tube-type elements exposed to internal pressure increases together with an angle of reinforcement. An optimal angle for such loaded structures is 90º.

In fig. 4 there is a dependence between circumferential strains measured by FBG3 in comparison with strains from FBG1 and FBG2. It is possible to observe that in a range from 0 to ~6000 με (which responds to applied force 4.3 kN) curves are converged. Above of mentioned value strains registered by FBG2 are not linear any more. It indicates that first defects in composite structure occurred and they are located close to the sensor FBG2.
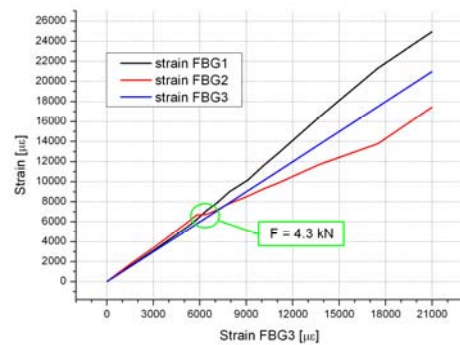
Fig. 4: Comparison of circumferential strain for tube specimen 30° [5].

3. Summary

Obtained test results confirm that optical fiber sensors can be successfully applied for strain measurements of braided composite elements and will be very useful to realize FEM analysis in a nearest future. They allow for local measurements with good sensitivity (~1 με) in a very wide range (±3%). It is also possible to defect detection in composite material (delamination) in its early stage.

4. References

[1] Soden P.D., and others: Influence of winding angle on the strength and deformation of filament-wound composite tubes subjected to uniaxial and biaxial loads. Composites Science and Technology 46, pp 363-378.

[2] Peters S. T.: Handbook of Composites, 2. ed., Chapman & Hall, London.

[3] Yu F., Yin S.: Fiber Optic Sensors, Marcel Dekker, Inc., New York, 2002

[4] Blazejewski W., and others: Optical fiber sensors integrated with composite material based constructions, Proc. SPIE 6608 - Lightguides and Their Applications III, 660802, 2007.

[5] Błażejewski W. and others: Pressure tests of composite braided tube specimens, Polish Society fo Composite Materials - Composites, 2009, in press.

FATIGUE RESISTANCE OF Cr-Ni-Mo STAINLESS STEELS AFTER CORROSION ATACK BY AGGRESSIVE CHLORIDES-CONTAINING ENVIRONMENT

Otakar Bokůvka, František Nový, Viera Zatkalíková and Veronika Valovičová[1]

[1] University of Žilina, Faculty of Mechanical Engineering, Department of Materials Engineering, Univerzitná 1, 010 26 Žilina, Slovakia

Corresponding author: bokuvka@uniza.sk

1. Introduction

Resistance to pitting and crevice corrosion is very important if the steel is to be used in chloride-containing environments. Austenitic stainless steels show a very high corrosion resistance in many aggressive environments, nevertheless they can suffer pitting corrosion in chloride ion rich solutions [1]. Austenitic steels are more or less resistant to general corrosion, crevice corrosion and pitting, depending on the quantity of alloying elements. Resistance to pitting and crevice corrosion increases with increasing contents of chromium, molybdenum and nitrogen [2].

This work deals with the influence of pitting corrosion of two most corrosion resistant Cr-Mo-Ni stainless steels on their fatigue resistance.

2. Experimental procedures, materials and results

The pitting corrosion is a form of local corrosion producing pits those are relatively small compared to the overall exposed surface. It is very serious type of corrosion damage because of the rapidity with which the material can be perforated [3]. It is typical for passivating metals and alloys exposed to aggressive environment (namely Cl⁻, Br⁻, ClO⁻), [4]. The passive film is locally perforated and the aggressive anions reach the uncovered metal surface which is consequently locally dissolved. The local breakdown of passive film is achieved at the critical electrode potential - the pitting potential (E_p) [5].

Although the mechanism of the stable pit growth seems to be well described, the processes leading to breakdown of the passive film are still the subjects of many controversial interpretations. There is general agreement that the first step in localized corrosion is absorption of chloride ions on the metal surface. In different pit's initiation models various phenomena occurring locally on the passive metal preceding a film breakdown are taken into consideration (competitive adsorption between OH⁻ and Cl⁻, formation of surface chloride islands, thinning of the passive film by forming metal chlorides or transitional complexes, etc.) [3]. The phase of the pit growth starts after the local perforation of passive film and by the direct contact of the uncovered metal with the aggressive ions. If the electrode potential is high enough [6, 7], metal M is dissolved and cations M^{n+} are formed.

$$M \rightarrow M^{n+} + ne^- \qquad (1)$$

The attacked locality becomes the anode and the surrounding surface becomes the cathode, which is considerably larger then the anode. Cations M^{n+} hydrolyse and pH in the pit is rapidly decreasing (Fig. 1). The fall of pH inside the pit supports its farther growth.

$$M^{n+} + nH_2O \rightarrow M(OH)_n + nH^+ \qquad (2)$$

Fig. 1 Chemical processes in corrosion pit (example of pitting corrosion of steel) [4]

The last phase of the pit's development is its repassivation, which is achieved by the decrease of potential on the value of the

repassivation potential E_{rp}. The pit's surface is passivated again [3, 5].

The corrosion attack was realized in chloride solution according ASTM G4 standard [7]. This standard is used for evaluation of resistance of stainless steel against pitting corrosion. Immersion tests were carried out in the 5% $FeCl_3$ solution (Cl^- concentration of 0.9624 $mol.dm^{-3}$) at the temperature 50^oC. The duration of the mentioned test was 24 hours. After 24 hour exposure the specimens were carefully brushed, washed by de-mineralized water and freely dried up.

Commercial AISI316L and AISI316Ti stainless steels were used as experimental material. The chemical composition, microstructure and mechanical properties are described properly in [8].
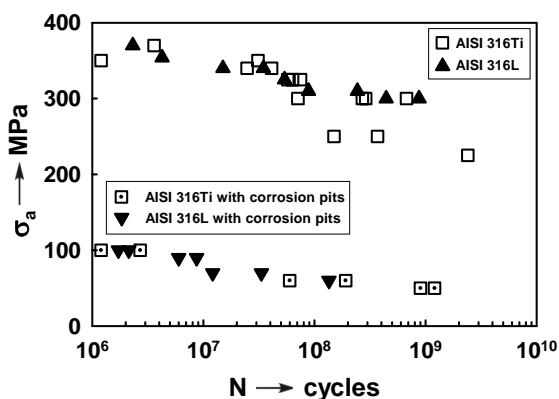
Fig. 2 S-N curves of AISI 316L and AISI 316Ti steels

Fatigue investigations were carried out under fully reversed axial loading in the region from N = 10^6 to N = 10^9 cycles using high-frequency resonant ultrasonic machine. Fatigue tests were conducted under constant amplitude loading at a load ratio R = -1, frequency f ≈ 20 kHz and ambient temperature, using smooth specimens with polished surface.

The results of fatigue tests were plotted as relation of stress amplitude vs. number of cycles to failure in Fig. 2. The fatigue limit σ_c (at N = 10^9 cycles) of AISI 316L steel is σ_c = 280 MPa and in case of AISI 316Ti steel it is σ_c = 300 MPa. The significant effect of corrosion damage was recorded. Due to the corrosion attack was the fatigue limit reduced to the value of 65 MPa. Fatigue cracks initiated naturally at the microstructurally weakest points. Crystallographic oriented initiation of fatigue crack was observed on all of the fatigue failed specimens without corrosion attack.
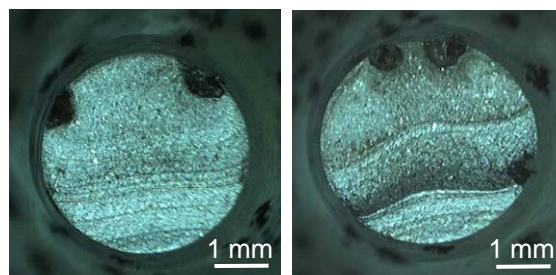
Fig. 3 Fatigue fractures and corrosion pits

Surface crack initiation due to the formation of extrusion and intrusion during fatigue test was typical for the both steels (AISI 316L and AISI 316Ti) without corrosion damage. On the other hand, after corrosion damage, both steels were characteristic by fatigue crack initiation from the corrosion pits on the surface (Fig. 3). In this case the fatigue crack initiation was highly shortened due to the occurrence of corrosion pits and the total number of cycles was very close to the number of cycles of fatigue crack propagation.

3. Acknowledgements

4. References

[1] Teoh, S. H.: Fatigue of biomaterials: a review. International Journal of Fatigue, 22, 10, November 2000, p. 825-837.

[2] Hadzima, B. - Liptáková, T.: Základy elektrochemickej korózie kovov. EDIS ŽU, Žilina 2008. (In Slovak)

[3] Szklarska – Smialowska, Z.: Pitting and crevice corrosion, NACE International, Houston, Texas, 2005.

[4] Číhal, V.: Korozivzdorné oceli a slitiny, Academia Praha, 1999. (In Czech).

[5] ASM Handbook, Vol. 13 Corrosion, ASM International, 4th edition, 1992.

[6] Khatak, H. S. – RAJ, B.: Corrosion of Austenitic Stainless Steels, Mechanism, Mitigation and Monitoring. ASM International, Ohio, 2002.

[7] Baboian, R. et al.: Corrosion Test and Standards: Aplication and Interpretation, ASTM Manual Series, Philadelphia, PA 19103, USA, 1995.

[8] Nový, F. – Bokůvka, O. – Chalupová, M. – Motýľová, E.: Fatigue resistance of AISI 316L and AISI316Ti steels. Materials Engineering, 15, 2a, 2008, p. 79-84.

MEASUREMENT AND LONG-TERM OBSERVATION OF CRACKS IN CONCRETE

Petr Bouška [1), Miroslav Vokáč [1), Vladislav Hrdoušek [2), Petr Klimeš [3)

1) Czech Technical University in Prague, Klokner Institute, Šolínova 7, 166 08 Praha 6 – Dejvice, Czech Republic

2) Czech Technical University in Prague, Faculty of Civil Engineering, Thákurova 7, 166 29 Praha 6 – Dejvice, Czech Republic

3) EUROVIA CS, a.s., Závod Řevnice, Rybní 795, 252 30 Řevnice, Czech Republic

Corresponding author: bouska@klok.cvut.cz

1. Introduction

The initiation and development of cracks can provide an indication of important problems in concrete pavements, floors, bridges and other engineering structures. Crack initiation reduces not only the durability of structures but also their serviceability. There are several limit values of crack widths in standards and codes, and in the conditions set by developers. Widely-used methods provide only subjective crack width values. Until now, cracks in concrete structures have not been adequately documented. A comprehensive concept for a methodology for measuring cracks on concrete structures is presented in paper. This proposal describes a method for documenting crack layout, measuring crack width and for long-term monitoring of cracks. The accuracy of crack width measurement is analysed on the basis of width tests in laboratory conditions.

The aim of crack measurement is to observe the layout of cracks and their long-term propagation. The ambient temperature and the temperature of the structure need to be measured. Crack width is inspected in order to assess the lifetime and the reliability of the structure.

2. Crack in concrete

The limiting value of tensile deformation depends on several factors: the components of the concrete, the age of the concrete, rate of loading, etc. Stimulated deformation is caused by the concrete mixture, the interior elements (armature), and the external conditions.

Several methods are used in laboratory conditions and in real structures to identify the occurrence of cracks. These methods include visual observation, painting a contrasting colour on to the surface of concrete, and wetting the surface. Acoustic analysers, ultrasound instruments and the impulse method can be used.

Many contact methods and contactless methods are available, based on mechanical, optical and electric measurement for crack width changes in time: deformeters, mechanical indicators, enlarging magnifiers, microscopes, inductive potentiometer sensors, string tensometers, and optical sensors with optical fibres.
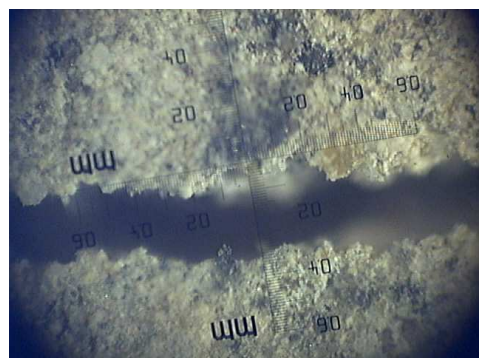
Fig. 1: Crack in concrete, microscopic observation.

3. Crack width

Accurate crack width definition is of fundamental importance. Some simplification of the course of the border is necessary, and

this reduces the accuracy of the measurement. A photographic image of a crack, using a microscope, is shown in Fig. 1. The cracks in a concrete structure are usually measured using a crack scale, an enlarging magnifier or a portable microscope.
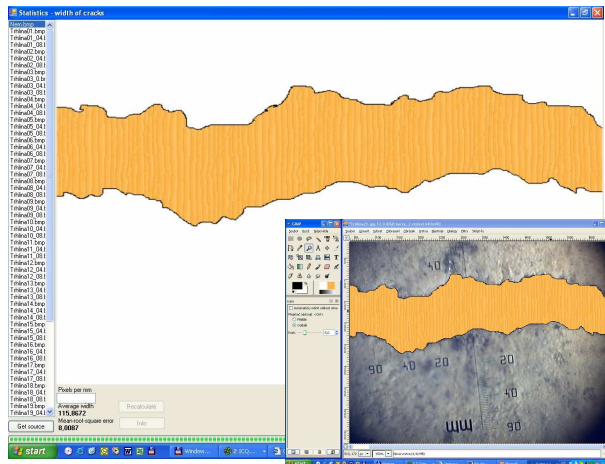
Fig. 2: Crack width evaluation by proper software.

4. Conclusions

A method for estimating crack widths in concrete structures has been proposed, using experiences on measurements on concrete bridges. The objectivity and accuracy of particular methods for measuring cracks in concrete structures was verified in laboratory tests.

5. Acknowledgment.

6. References

[1] Klimeš, P., Bouška, P., Hrdoušek V. Methodology of crack measurement in concrete structures, In: Conference on Testing and Quality in Civil Engineering, 26.-27. September, 2007, CTU Prague (in Czech).

[2] Vokáč M., Novotný T., Bouška, P. Uncertainty of crack measurement in concrete structures. In: Construmat 2007. Brno University of Technology.

THEORETICAL AND EXPERIMENTAL STUDY OF THE PROPELLER HARMONIC TORQUE AND THRUST STRUCTURE

Nicolae Buzbuchi , Liviu Constantin Stan[1]

1) Constanta Maritime University, Marine Engineering Dept., 107 Mircea cel Batran Str., 900663
Constanta, Romania

Corresponding author: nbuzbuchi@hotmail.com, liviustan14@yahoo.com

1. Introduction

The paper is an attempt to the harmonic structure computation of the marine propeller torque and thrust, being predictive methods of propeller excitations induced into the marine engine shafting system in the design stage. Two quasi-steady methods using the lifting line theory, the first being semi-theoretical due to the wake field experimentally determined and based on the direct Prandtl theory, and the second one based on a developed Lerbs induction coefficients, an analytical method using only the propeller series diagrams and general empirical formulae for the wake and suction coefficients, have been presented. The paper shows the simplicity and accuracy of the last method, as a primary information on the propeller excitations, and this procedure takes into account a non-dimensional expression of the circulation, as a two-dimension function of the blade radius and angle of rotation. A validation calculation with experiments of propeller excitations induced into the shafting system is analyzed, showing acceptable agreement between calculated and measured excitations.

2. Theoretical backgrounds

As mentioned above, the main cause of unsteady propeller forces when a ship is running in calm water is the wake non-uniformity. Most theoretical methods, by considering the calm water running condition corresponding to the self-propulsion point, allow the time-average loads to be calculated with reasonable accuracy. At present, several techniques using quasi-steady procedures, stripwise unsteady procedures and methods based on unsteady lifting surface theory have been developed for the estimation of unsteady loadings arising from the circumferential variation in the inflow velocity. All these procedures require the designer to be acquainted with the flow patterns at the propeller disc.

2.1 The semi-analytical method

The quasi-steady method assumes that the characteristics of a propeller in each phase of unsteady motion are approximated by those in uniform flow at the same phase. Thus, if the non-uniform flow field is known around a propeller from experiments, the flow speed and the angle of attack at each phase are easily calculated according to the diagram represented in fig. 1.

Fig. 1. Schedule of the Quasi-Steady Method.

The propeller characteristics at each phase of the unsteady motion are obtained either using the lifting line theory which gives loading distribution along the radius, or considering the total blade loading calculated from the experimental open-water characteristics of the propeller, which is to be distributed along the radius using weight functions as recommended in [1].

2.2 The analytical method

This model is based on the same lifting line theory, but using the propeller vortex model: the j-th blade will be substituted by a line of bounded vortices which interacts with a filament of free vortices (fig. 2).

Fig. 2. Schematic Propeller Vortex Model.

Taking into account the overall dimensions of a concrete 55,000 tdw bulk carrier having a four-bladed propeller with a diameter D = 6.4 m, and using the flow-chart shown in fig. 3, one can obtain the corresponding results for the computed propeller torque and thrust amplitudes and phases.
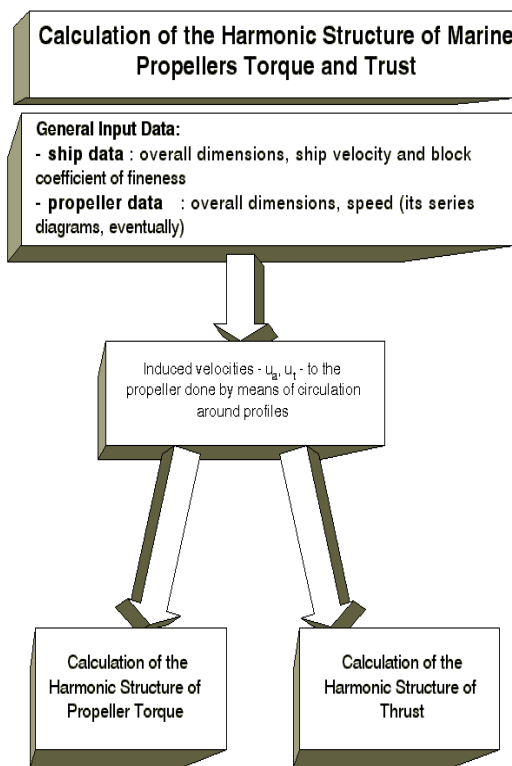
Fig. 3. Flow-chart for the Calculation of the Propeller Harmonic Excitations.

3. Experimental investigations

The prediction capacity of the theoretical models was check on physical model. Experiments have been carried-out at the Romanian Ship Research and Design Institute ICEPRONAV Galatz-Romania on dummy model (scale 1:30) in order to determine in the towing tank the nominal wake, the loading coefficients and the efficiency (fig. 4 and 5). The torque and thrust fluctuations were determinate in a cavitation tunnel with a propeller dynamometer in the measurement section 850x850 mm. The data from this device may be digitally read and automatically recorded by a

printer. Tab. 1 presents the measurements results, transposed at real scale. The differences are included in Bureau Veritas limits [3], according to the 16-th International Towing Tank Conference. The main conclusion carried-out is that this analytical second method is a good predictive one for the marine propeller excitations induced in the engine shafting system, due to the acceptable agreement with experiment performed on scaled models, as shown in Tab. 1.
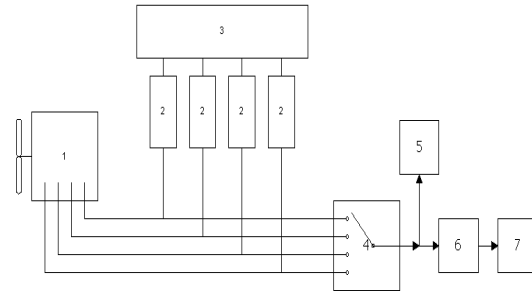
Fig. 4. Measurement Devices: 1-Dynamometer; 2-Amplifier; 3-Printer; 4-Swich; 5-Osciloscop; 6-Dynamic Analyzer; 7-Recorder.
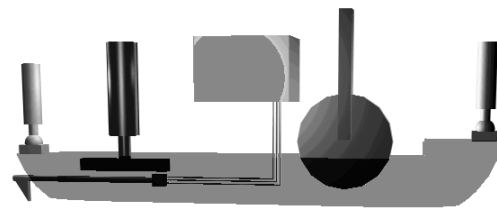
Fig. 5. Towing Tank Schedule.

	Calculated		Measured	
k	Torque	Thrust	Torque	Thrust
1	0.02111	0.02279	0.02373	0.02340
2	0.00392	0.00535	0.0343	0.00435

Tab. 1. Comparison between Computed and Measured Ratio Magnitudes.

4. References

[1] Dumitrescu, H., Georgescu, A., Dumitrache, Al., Ghita, Gh., Ceanga, V., Popovici, J.S., Nicolescu, B. *Propeller Computation* (in Romanian), Romanian Academic Publishing House, Bucharest, 1990.

[2] Taraza, D., Buzbuchi, N., Popovici, J.S. *Calculation of the Harmonic Structure of Marine Propeller Torque and Thrust*, International Off-Highway & Powerplant Congress & Exposition, Milwaukee, Wisconsin, 1994.

[3]]`***Excitation Forces from Cavitating Marine Propeller, NV-570 Computer program, Det Norske Veritas.

NUMERICAL AND EXPERIMENTAL ANALYSIS ON TORSIONAL BEHAVIOUR OF THE SHIP HULL MODEL

Ionel Chirica [1), Doina Boazu [1), Raluca Chirica [1), Elena Felicia Beznea [1)

[1) University Dunarea de Jos of Galati, Domneasca Str., 47, 800008 Galati, Romania.

ionel.chirica@ugal.ro, doina.boazu@ugal.ro, ralucachirica@yahoo.com, elena.beznea@ugal.ro

1. Introduction

In the paper, a new methodology (numerical and experimental) proposed to analyze the ship hull torsion made of composite materials, is treated. The torsion analysis is performed on a scale model (1:50) of a container ship, made of composite materials. The aim of the work is to analyze the influence of the very large open decks on the torsion behaviour of the ship hull made of composite materials.

2. Model characteristics

The model has the main characteristics: length L=2.4m, breadth B=0.4m, depth D=0.2m. The material is E-glass/polyester having the characteristics, determined by experimental tests:
E_x=46 GPa, E_y=13 GPa, E_z=13 GPa,
G_{xy}=5 GPa, G_{xz} = 5 GPa, G_{yz} = 4.6 GPa,
$\mu_{xy} = 0.3$, $\mu_{yz} = 0.42$, $\mu_{xz} = 0.3$

The thicknesses' values of the hull shell are: 2 mm for side shell and 3 mm for deck and bulkheads.

3. Numerical analysis

For the present study, a 3-D model with 4-node SHELL4L composite elements of COSMOS/M was used. The ship hull model was loaded by a torque M_x in the midship. Due to the fact, the real ship has much stiffened structure in the both end, the model is clamped at the ends. In the figure 1, the stress state on the deformed ship hull numerical model, according to the numerical calculus with COSMOS/M is shown.

4. Experimental analysis

In figure 4, the experimental rig for torsion of the ship hull model is presented. The stress state in the ship deck was determined by the strain gauges measurement.

The torsion angle of the ship hull model cross section is determined by taking into account the displacements of the points placed on the outline (fig. 1), according to the rotation of the rigid body (thin-walled beam hypothesis).
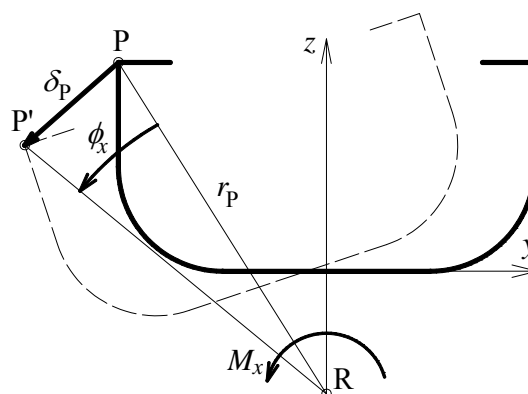
Fig. 1: Torsion angle calculus

The displacements were obtained with test rig (LVDT equipment, as it is seen in the figure 4).

The stress state obtained with the FE analysis was compared with the values of the stresses determined by measurements done in the bulkheads sections.

5. Concluding remarks

In the Fig. 2, the deformed ship hull numerical model, according to the numerical calculus with COSMOS/M is shown. Due to the variation of the cross section shape of the model, a coupled lateral bending occurred (Fig. 2).

The variation of the relative normal stress in the midship open section. The values obtained with FE analysis and according to the strain gauges measurements are presented.
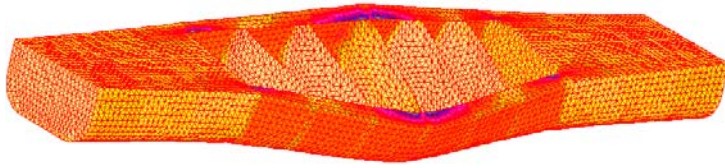
Fig. 2: Deformed FEM model

Fig. 4: Torsion rig for experiments
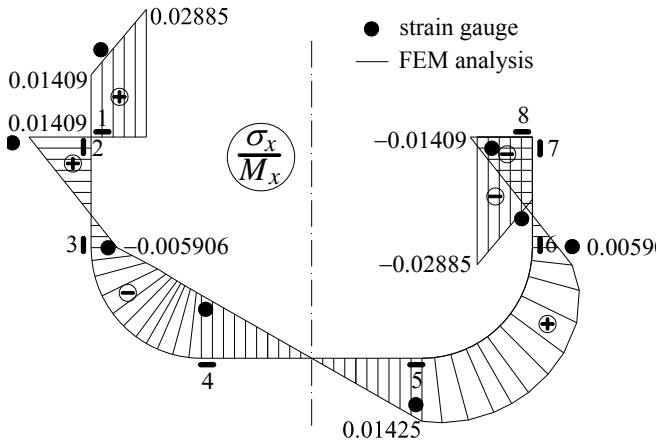
Fig. 3: Variation of the relative normal stress in the midship open section

7. References

[1] D.F. Adams, L.A. Carlsson, R.B. Pipes, Experimental Characterization of Advanced Composite materials, Ed. Taylor & Francis Group, London, (2003).

[2] I. Chirica, R., Chirica, Structuri compozite cu pereti subtiri, Editura Didactica si Pedagogica, Bucuresti, (2005).

In figure 4, the experimental rig for torsion of the ship hull model is presented.

The variation of the relative torsion angle (ϕ_x/M_x) along the ship model obtained so from FEM analysis, thin-walled beam theory and from experimental measurements is presented in figure 5. As it is seen in figure 5, the maximum value of the parameter (ϕ_x/M_x) in the midship (open section type) is almost 2 times more than the maximum torsion angle in the closed area.
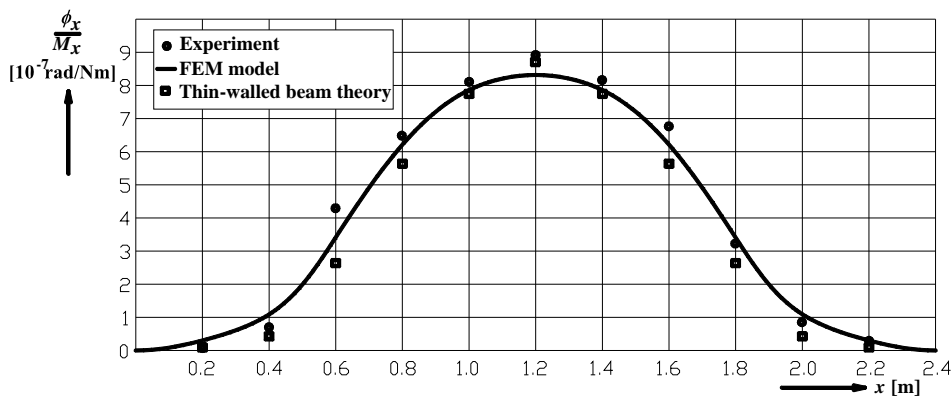
Fig. 5: Variation of the relative torsion angle along the ship model

FATIGUE BEHAVIOR OF THE MAGNESIUM ALLOY ZK60 IN HIGH CYCLE FATIGUE

Dan Mihai Constantinescu [1], Petru Moldovan [1], Wym H. Sillekens [2], Marin Sandu [1], Dragos Alexandru Apostol [1], Matei Constantin Miron [1]

[1] University POLITEHNICA of Bucharest, Department of Strength of Materials, Splaiul Independentei nr. 313, 060042 Bucharest, Romania.

[2] Netherlands Organisation for Applied Scientific Research – TNO Science and Industry, Netherlands.

Corresponding author: dan.constantinescu@upb.ro

1. Introduction

Not too much information is available in the literature for establishing fatigue properties of magnesium alloys. A compilation of existing fatigue and fatigue crack growth data of different Mg-alloys has been published by ASM International [1]. One can underline that fatigue properties of some of the studied Mg-alloys are very good. Fatigue limits (on base of 10^8 cycles) up to approximately 100 MPa (for AZ63, AZ91, AZ92) are reported for cast Mg-alloys after appropriate production and heat treatment and fatigue limits up to 130 MPa (AZ31 and AZ80) for wrought Mg-alloys under cyclic axial loading.

Previous work [2] showed that the frequency of testing has a clear influence on the fatigue response of the AZ80A-F material, especially when the amplitude is not as big as to give a very short fatigue life. At that time not enough data were available to explain better the obtained results and make pertinent observations on the fatigue strength of the magnesium alloy AZ80A by taking into account the influence of the average stress and the frequency of testing. We avoided for the extruded AZ80 the anisotropic deformation behavior in the direction of tension and compression, and we performed axial fatigue tests in tension-tension with a force controlled constant amplitude.

2. Fatigue Testing Procedure

Present research concentrates on the fatigue behavior of the ZK60 extruded magnesium alloy. We follow standards ASTM 466-96: Standard practice for conducting force controlled constant amplitude axial fatigue tests of metallic materials, ASTM 468-96: Standard practice for presentation of constant amplitude fatigue test results for metallic materials.

Fatigue testing is done by using a 5 tf (6.3 tf in static testing) Walter-Bai servo-hydraulic machine at a frequency of 10 Hz. Hour-glass specimens machined according to the standard were tested in force control in reversed loading. The static tension tests followed ASTM E8M-04: Standard Test Method for Tension Testing of Metallic Materials [Metric] and the following average values were obtained: Young's modulus E = 43.6 GPa, ultimate strength R_m = 280.3 MPa, and offset yield limit $R_{p0,2}$ = 136 MPa. The elongation at failure measured with an Epsilon 3542 extensometer as A = 16,82 %.

3. Obtained results

The force amplitude was decreased in consecutive tests from 11 kN to 5.3 kN as to obtain stress amplitudes from about 160 MPa to 75 MPa as shown in Tab. 1.

Test no.	Force ampl. [kN]	Cycles till failure	Max. stress [MPa]	Min. stress [MPa]
1	10.37	20897	157.61	-156.16
3	10.64	20744	149.99	-154.36
11	10.50	22176	148.4	-150.23
12	11.00	28702	147.36	-148.02
10	9.81	28203	140.38	-143.81

18	9.67	40376	140.27	-140.27
19	9.83	23038	143.74	-146.31
2	9.43	22536	134.43	-138.56
6	9.31	59723	130.28	-136.14
21	9.31	54828	130.18	-133.95
13	9.00	84687	124.52	-124.8
14	9.10	60409	125.39	-125.66
22	8.67	35500	120.04	-119.90
25	8.70	137636	122.63	-122.49
15	7.40	811692	100.36	-101.17
16	7.15	1246045	100.58	-100.44
17	5.30	6453095	75.80	-75.37

Tab. 1: Fatigue data obtained for ZK60 alloy.

The corresponding S-N curve is represented in Fig. 1. Although not too many data are available up to now, we may suggest that a reasonable value for the fatigue limit could be 100 MPa.
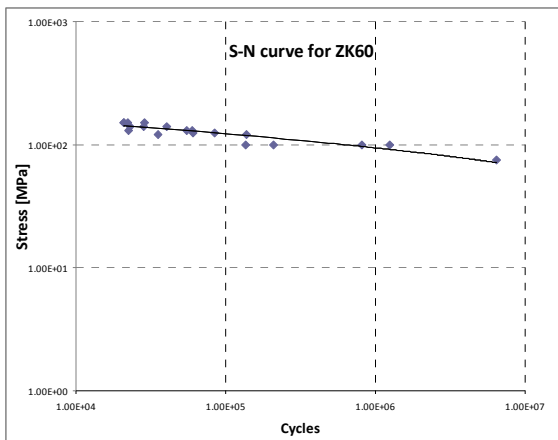
Fig. 1: Plot of data for obtaining the S-N curve of extruded ZK60.

Some SEM analyses revealed that this material contains mangan and titanium, although it should be 98 % magnesium and 2 % zirconium and silicium. As seen in Fig. 2 voids are inevitable.
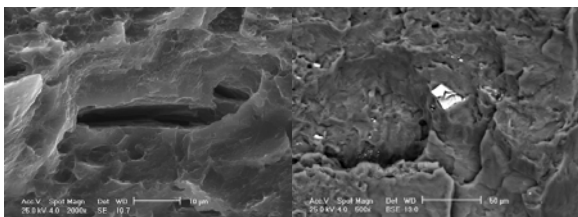
Fig. 2: SEM analyses of ZK60.

However, another test at an amplitude of 75 MPa didn't lead to the failure of the specimen. It is interesting to monitor the histeresis loops during each test. Just as an example, in Fig. 3 the first 100 cycles, the middle ones, and the last 100 cycles are shown.
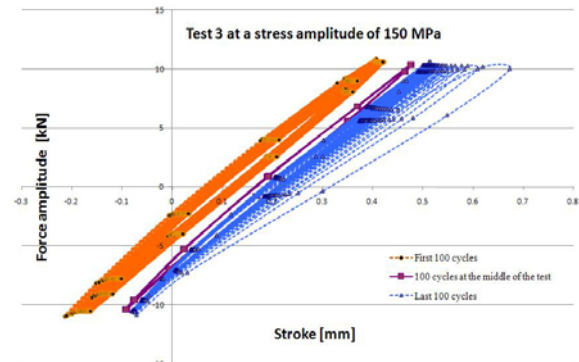
Fig. 3: Histeresis loops obtained during a test at an amplitude of 150 MPa.

So, after about 10000 cycles the behavior of the material becomes stable, and 100 cycles almost superpose the response of the material being mostly linear-elastic. Last 100 cycles are indicating a severe deterioration, and the material creeps considerably.

4. Acknowledgements

5. References

[1] S.D. Henry, G.M. Davidson, S.R. Lampman, F. Reidenbach, R.L. Boring, W.W. Scott, Jr. (editors), Fatigue Data Book: Light Structural Alloys. ASM International, Materials Park – Ohio, USA, (1995)

[2] D.M. Constantinescu, P. Moldovan, W. Sillekens, M. Sandu, G. Popescu, G., F. Baciu, Fatigue life particularities of AZ80 magnesium alloys used in automotive industry, 2nd fatigue Symposium, Leoben, Ed. W. Eichlseder (2008) 117-127

FATIGUE BEHAVIOUR OF SHORT FIBRE REINFORCED POLYAMIDE: MORPHOLOGICAL AND NUMERICAL ANALYSIS OF FIBRE ORIENTATION EFFECTS

Francesca Cosmi [1), Andrea Bernasconi [2)

[1) Università degli Studi di Trieste, Dipartimento di Ingegneria Meccanica, via A. Valerio 10, 34127 Trieste, Italy.

[2) Politecnico di Milano, Dipartimento di Meccanica, via La Masa 34, 20156 Milano, Italy.

Corresponding author: cosmi@units.it

1. Introduction

Different fatigue behaviours can be observed when short fibre reinforced polyamide notched specimens of same geometry are injection moulded through different gates [1]. This appears to be due to the different fibre orientation patterns obtained [2].

Recently, a novel technique based on micro-tomography 3D reconstruction of the fibre structure has been introduced and quantification of fibre orientation principal directions has been shown possible by means of a global parameter, the Mean Intercept Length (MIL) [3].

In this work, we examined the fatigue strength of injection moulded notched flat specimens (fig. 1) of a short glass fibre reinforced polyamide (PA6 GF 30).

The effect of injection point location was analyzed both in light of fibre orientation and of the elastic properties computed by a micro-mechanical model based on the Cell Method, introduced in [4].
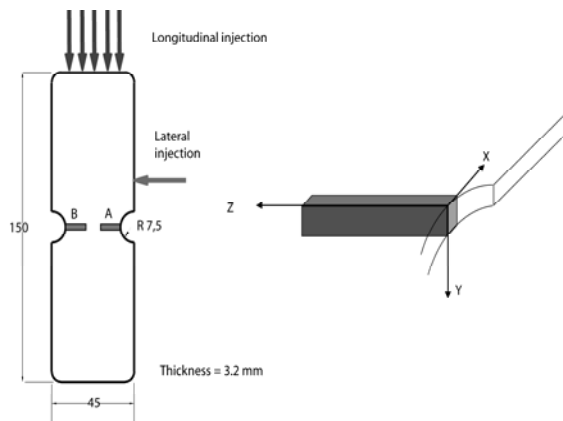
Fig. 1: Specimens type, dimensions and injection gates; position of micro-CT examined samples.

2. Experimental Results

The experimental results of the fatigue tests are shown in fig. 2.
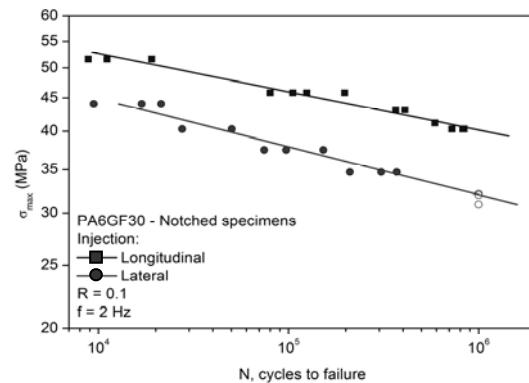
Fig. 2: S-N curves for specimens with lateral notches.

In order to investigate whether the observed variations in fatigue behaviour were related to differences in fibre orientation at notches as a consequence of the different injection points, samples extracted in the location A of fig.1, close to the notches, were analyzed over a 5mm portion of the gauge section. Micro-CTs with a resolution of 9 μm were obtained at the SYRMEP beamline of Elettra synchrotron light source (Trieste, Italy) using Phase Contrast (PHC) imaging techniques. The core layer (mid plane) of each reconstructed sample was divided into a series of cubic Volumes Of Interest, VOI, 80x80x80 voxel^3, that were singularly analyzed (fig.3).

The morphological characterization by MIL (using Quant3D software) is discussed in detail in [3]. Results are shown in fig.4.

The Cell Method model has already been used for this material in [5]. Material properties in each cell of a 812905 cells mesh were scaled

based on the base material (matrix and glass fiber) properties and the apparent elastic moduli along the specimen axis (load direction in the fatigue tests) E_x were computed by simulation. Results are shown in fig.5.
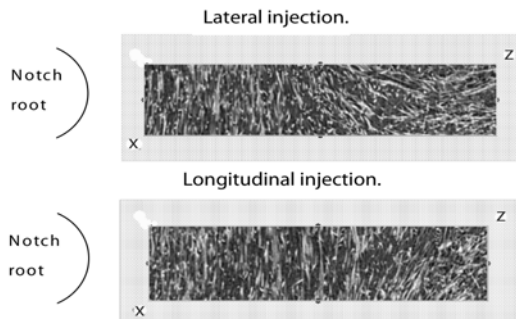
Fig. 3: Lateral and longitudinal injection, point A, core layer: μ-CT reconstruction.
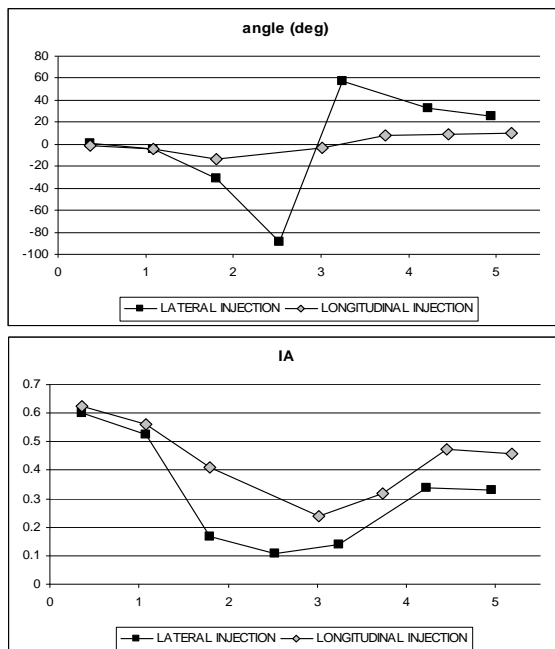
Fig. 4: Preferred fibre orientation with respect to specimen y axis (above), and Index of Anisotropy IA (below), at different z positions (mm), core layer.

3. Conclusions

Differences have been observed in the fatigue behaviour of short fibre reinforced polyamide notched specimens depending on injection point location. These experimental results might be attributed to different strain distributions due to variations of the local apparent elastic properties along the specimen section, which in turn are closely related to changes in fibre orientation occurring during the manufacturing process. In order to precisely quantify these effects, further investigation is needed.
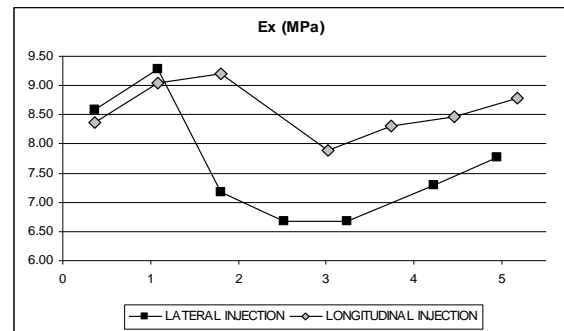
Fig. 5: Apparent elastic modulus (MPa) along specimen x axis, at different z positions (mm), core layer.

4. Acknowledgements

5. References

[1] Bernasconi A. Davoli P., Basile A. and Filippi A. Effect of fibre orientation on the fatigue behaviour of a short glass fibre reinforced polyamide-6. Int J Fatigue, Vol. 29 (2007) 199-208.

[2] Bernasconi A., Cosmi F. Combined effect of notches and fibre orientation on fatigue behaviour of short fibre reinforced polyamide. Submitted to Strain.

[3] Bernasconi A., Cosmi F., Dreossi D. Local anisotropy analysis in injection moulded fibre reinforced polymer composites. Composites Science and Technology, Vol. 68 (2008) 2574-2581.

[4] Cosmi, F., Dreossi, D. Numerical and experimental structural analysis of trabecular architectures. Meccanica, Vol. 42 (2007) 85-93.

[5] Cosmi, F. Morphological and numerical characterization of a PA6-GF 30 sample, 25th Danubia Adria Symposium, Ceske Budejovice, Czech Republic, 24-27.09.2008

NANOINDENTATION TESTING OF BORON CARBIDE THIN FILM AT ELEVATED TEMPERATURE

Radim Ctvrtlik[1,2], Martin Stranyanek[1,2], Petr Bohac[2]

[1] Joint Laboratory of Optics of Palacky University and Institute of Physics of Academy of Sciences of the Czech Republic, v.v.i., 17. listopadu 50, 772 07 Olomouc, Czech Republic.

[2] Institute of Physics, v.v.i., Academy of Sciences of the Czech Republic, Na Slovance 2, 182 21 Prague 8, Czech Republic.

Corresponding author: ctvrtlik@fzu.cz

1. Introduction

Boron carbide (B_4C), is the third hardest material after diamond and cubic boron nitride. In addition it exhibits many other attractive properties, such as high elastic modulus and wear resistance combined with low mass density and high chemical stability [1]. Boron carbide is considered to be a promising candidate for a wide range of applications as a protector or cutting tool.

Because of its high application potential it is of particular interest to investigate its mechanical properties at conditions which are close to those experienced in service, especially at elevated temperatures.

In this paper, mechanical properties (hardness and elastic modulus) of amorphous boron carbide thin film were investigated at ambient and elevated temperatures up to 450 °C using depth sensing nanoindentation technique.

2. Experimental

Amorphous boron carbide film was deposited on the unheated substrate Si(111) by DC-magnetron sputtering of hot-pressed B_4C target using the Leybold-Heraeus Z 550 M sputtering plants.

Load–displacement curves were obtained with a calibrated diamond Berkovich indenter using NanoTest™ NT600 instrument equipped with a computer-control heating stage [2]. Heating was applied to both indenter and the sample. The nanoindentation tests were carried out at temperatures of 25, 100, 200, 300, 400, 450 °C at following experimental conditions: loading to 10 mN, holding maximum load for 5s, and complete unloading. Loading and unloading rates were set to 0.5 mN.s^{-1}. The

indentation hardness and reduced elastic modulus $E_r = E/(1-\nu^2)$, where E and ν are the Young's modulus and the Poisson's ratio, respectively, were determined from indentation curves measured at load of 10 mN by means of Oliver–Pharr method [3].
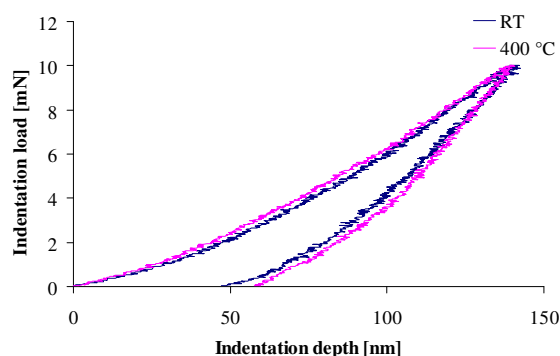
Fig. 1: Indentation curves of a-B_4C thin film measured at room and elevated temperature.

3. Results and discussion

Amorphous character of investigated film was established using Raman spectroscopy and confirmed by reflection electron diffraction. The thickness of the film was measured by ALFA-STEP profilometer with the value of 1.2 µm.

Sufficiently low value of indentation load of 10 mN ensured that the maximum penetration depth did not exceed ~12% of the film thickness. In this case the Si(111) substrate does not have any pronounced influence on the measured hardness though depth of the indenter penetration is large enough to reduce possible errors.

The measured hardness and reduced modulus at ambient temperature are (25.8±0.9)GPa and (288±10)GPa, respectively.

The temperature dependencies of a-B_4C hardness and reduced modulus obtained in our experiments are shown in fig.2. First, the increase of temperature up to 200 °C results in gradual reduction of hardness. Further increase of temperature leads to a small increase of hardness probably due to some film annealing which takes place during measurement. It should be noted that sample is exposed to the final temperature for thermal stabilisation before measurement for approximately two hours.

This is in consistency with reduced modulus dependence. One can see approximately constant values up to 200 °C, whereas at higher temperatures the slow increase is apparent. This increase is probably due to a gradual improvement of the atomic structure.
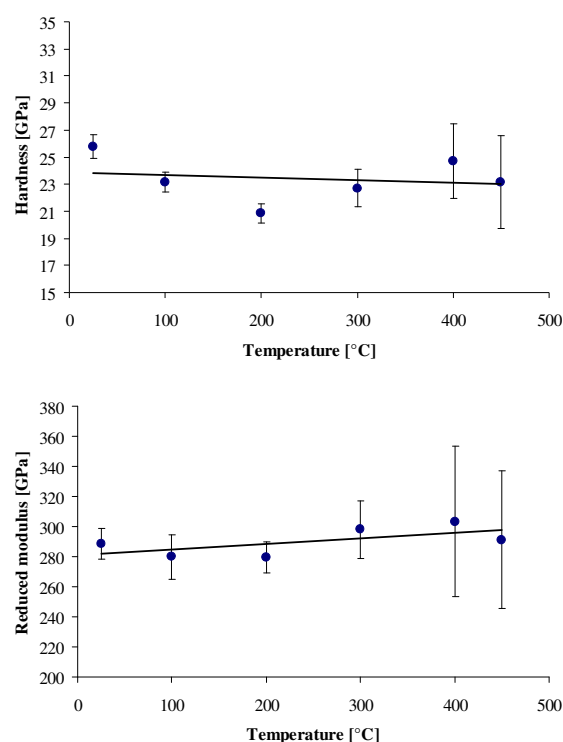
Fig. 2: Indentation hardness and reduced modulus of a-B_4C film versus temperature.

4. Summary

The hardness and elastic modulus of amorphous B_4C film were investigated using a NanoTest NT600 machine equipped with a hot-stage at ambient temperature and at elevated temperatures up to 450 °C. Although presented data show small variations in hardness and reduced modulus with temperature, generally it can be concluded that hardness of B_4C film is quite stable with temperature up to 450 °C. Our results point out that nanoindentation is very powerful method even at elevated temperatures.

Detailed interpretation of hot stage data is generally a complex task and further investigation is needed.

5. Acknowledgements

6. References

[1] V. Kulikovsky, V. Vorlicek, P. Bohac, R. Ctvrtlik, M. Stranyanek, A. Dejneka, L. Jastrabik, Mechanical properties and structure of amorphous and crystalline B_4C films. Diamond & Related Materials, Vol. 18 (2009) 27-33

[2] R. Ctvrtlik, M. Stranyanek, P. Bohac, L. Jastrabik, NanoTest NT600 – A device for analyse of mechanical properties of materials. Materials Structure, Vol. 13, (2006) 90-93.

[3] W.C. Oliver, G.M. Pharr, An improved technique for determining hardness and elastic modulus using load and displacement sensing indentation experiments. Journal of Material Research, Vol. 7 (1992) 1564-1583.

EKSPERIMENTAL – NUMERICAL ANALYSIS OF DYNAMIC EFFECTS IN CHAIN MULTIBUCKET EXCAVATORS

Jerzy Czmochowski, Marcin Kowalczyk, Mariusz Stańco [1]

[1] Wroclaw University of Technology, Faculty of Mechanical Engineering,
ul. Lukasiewicza 7/9, 50-371 Wroclaw, Poland.

Corresponding author: jerzy.czmochowski@pwr.wroc.pl

1. Introduction

There are often applied machines in the mining of the lignite coal about the long operating period frequently reaching 50 years [2]. Therefore the analyses of the state of these machines are being conducted in order to determine the alternative of their exploitation or replacing it by new. One of examinations conducted at this occasion there are measurements of oscillation and dynamic influences during mining [1]. These examinations are aimed at determining real dynamic loading and the scope of changes of stresses which can be a base for determining the fatigue life of elements of the load-carrying system [3]. Linking experimental methods with numerical methods it is possible on the basis of measurements in selected points to appoint the state of stresses and deformations in the entire load-carrying system.

Fig. 1: View of RS-560 chain excavator

2. Experimental Results

In experimental research the measuring system compound of accelerometer sensors, the TEAC LX- 10 recorder and the FlexPro 7.0 analyzer of oscillation was applied. Basic systems of the excavator are mounted on the so-called royal shaft which is subjected to great loads from bending.

Because of great loadings of the central part of the excavator sensors were arranged, as it is showed on fig. 2. The measurements were conducted during the mining in different locations of the bucket chain boom. The instance course of changes of accelerations registered in the middle part in measuring point 6 was shown on fig. 3. On the basis of these courses a amplitude spectrum of accelerations was determined in the form like on fig. 4.
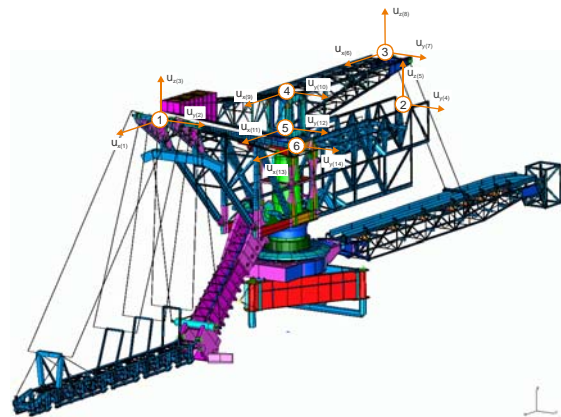
Fig. 2: Measurement points arangement
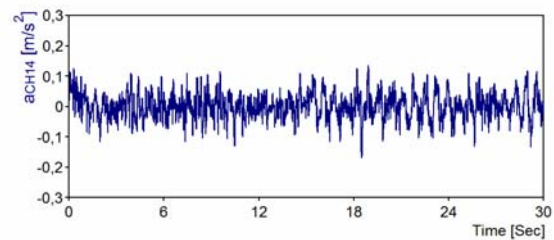
Fig. 3: Course of acceleration changes in point 6.
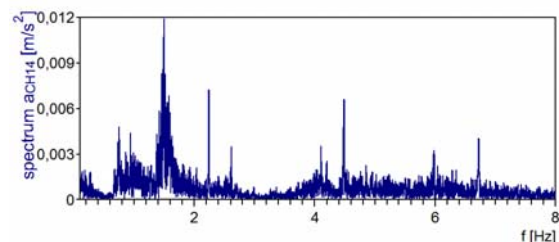
Fig. 4: Widmo amplitudowe przyspieszeń.

On the basis of courses of accelerations a square average value a_{RMS} of accelerations act-

ing in measuring points of the load-carrying system of the excavator was calculated. a_{RMS} values were used for calculating dynamic factors essential as far as the durability of load carrying structure is concerned according to the following relation

$$D = a_{RMS}/g, \text{ where } g = 9,81\text{m/s}^2.$$

Measured values of accelerations and dynamic factors calculated on their base are showing, that in relation to requirements of the DIN22261-2 standard, are much lower. What means, that at such a level of loadings the excavator can work longer than it would result from calculations according to the norm.

Courses of changes of accelerations enable also to determine the number of cycles for determined levels of the value of accelerations e.g. with rainflow counting method. This data was a basis for estimating the fatigue life

3. Numerical Results

The influence of measured dynamic loads on the load-carrying structure of the excavator was determined with the help of computer simulations. A FEM shell-beam model was built [4, 5] in I-DEAS NX software shown on fig. 5.

Fig. 5: FEM model of load-carrying structure of excavator

The strength calculations in accordance to DIN22261-2 standard are conducted for H1b case, for maximal difference of loadings appearing during the exploitation. Values measured on the structure were taken into account in FEM calculations. The instance result in the form of distribution of stresses for the maximal difference of loadings was shown on fig. 6.

According to the standard for the given level of average stresses an acceptable difference of stresses is determined. The determined level of difference of stresses enables to state, that in the majority the load-carrying structure is working

in the unrestricted fatigue strength.
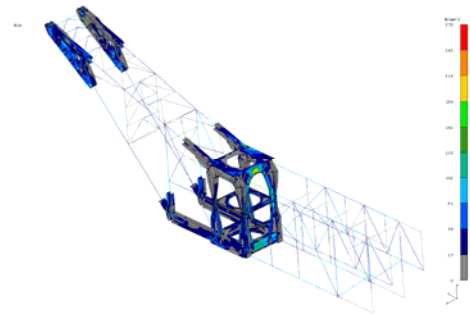
Fig. 6: Huber-Misses stresses distribution comming from dynamic loadings

4. Summary

At the work the results of experimental and numerical research conducted on the chain multi-bucket excavator were placed. On the basis of measurements on the structure a loadings spectrum was determined, which was a basis for estimating the real dynamic factors and calculating the fatigue life. Above analyses allowed to indicate places exposed to fatigue cracking, changes being aimed at prolonging the operating time were drawn up.

5. References

[1] J. Czmochowski, Identification of modal models of the machines working in the mining of the lignite coal (in Polish), Wrocław University of Technology Publishing House, 2008.

[2] R. Jankowiak, E. Rusiński, Stahlkonstruktionen von polnischen Umschlag- und Fördergeraten. Stahlbau 72(2003), Heft 8.

[3] M. Kowalczyk, Method of diagnosing machines in progressing failure states (in Polish), PhD dissertation. Institute of Machines Design and Operation, Wrocław University of Technology, PRE 11/2005, Wrocław 2005.

[4] E. Rusiński, J. Czmochowski, T. Smolnicki, Advanced Finite Element Method for Load-carrying Structures of Machines (in Polish), Wrocław University Publishing House, Wroclaw 2000

[5] E. Rusiński , J. Czmochowski, Die Modalanalyse des Oberbaus eines Baggers vom Typ SchRs-800. Surface Mining Braunkohle 2001 Vol. 53 No. 3, 319-324

MONITORING SYSTEM ON THE CETINA BRIDGE AND RESULTS ACQUIRED DURING TEST LOADING

Domagoj Damjanović [1], Mladenko Rak[1], Joško Krolo[1]

[1]   University of Zagreb, Faculty of Civil Engineering, Kačićeva 26, 10 000 Zagreb, Croatia.

Corresponding author: ddomagoj@grad.hr

1. Introduction

The main superstructure is 140,27 m concrete arch with 21,50 m (f/L=1/6.52) arch rise. The fixed arch is of a box-shaped cross section, B/H=8,00/2,50 m. The flange walls are 40,0 cm thick. Diaphragm walls are planned in the arch imposts and in the connections of piers and the arches. The deck's superstructure is grid shaped with more than 21.60 m ten spans. It consists of five prefabricated prestressed girders in cross section, connected with monolith 20 cm thick deck plate and cross section girders over the supports. Prefabricated girders are of a 120 cm T-profile. Pier sections consist of two piers connected with the head beam. The bridge design involves a permanent observation of the structure in exploitation called „monitoring".

2. Monitoring system

Monitoring includes the periodic measuring of displacements, dynamic characteristics and of reinforcement corrosion, along with continuous measuring of strains, temperature and humidity. Over the abutments and piers permanent bench marks are installed in two lines. Reinforcement corrosion is being observed in six measuring points over Raupach–Schiesssl sensors embedded into the concrete. The readings are supposed to be quarterly conducted. The measuring of strains, temperature and humidity is being performed continuously on 24 locations. All the sensors are being powered continuously over the solar collector installed near the bridge. The recordings are being collected in the monitoring centre located in the arch apex where all the sensors are connected over A/D convector to the „data logger"(Fig. 1). Strains are measured by LVDT sensors in three arch cross sections (impost, quarter of the arch and

apex), and in two deck structure cross sections, in total in 16 measuring points (Fig. 2).
Temperature is also measured in each cross section, while humidity is measured in two sections in the arch and in the deck structure profile (Fig. 3 & 4).

Fig. 1: Monitoring centre
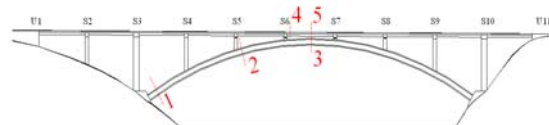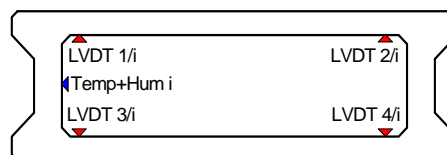
Fig. 2: Cross section markings
Fig. 3: The cross section of the arch (i=1,2,3)
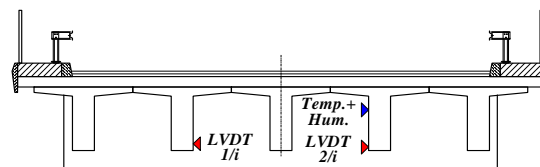
Fig. 4: The cross section of the deck structure (i=4,5)

3. Results acquired during test loading

Test loading was conducted through eight phases using eight heavy trucks of the average mass around 30 tons. The monitoring system was activated in the course of test loading. During the investigation the data were collected from the sensors. Figures 5 and 6

show deformation measuring results in the section 2 and section 5.
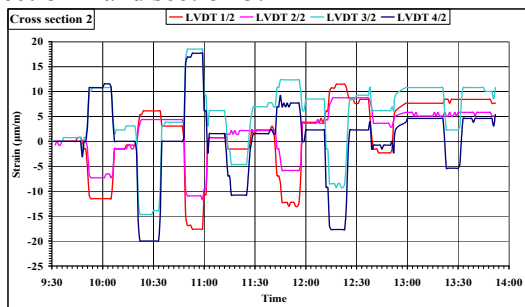
Fig. 5: Records of strains in cross section 2
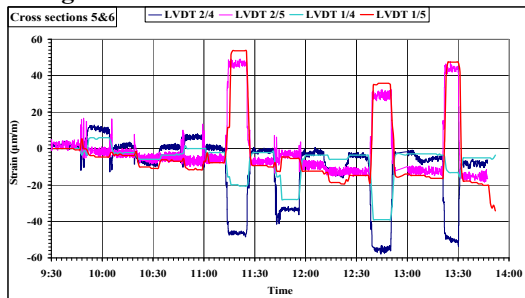
Fig. 6: Records of strains in cross section 4

During the load testing displacements were measured in two lines, above all the supports and in the centres of deck structure span. Figure 7 graphically presents experimentally and numerically determined displacements for the 7th loading phase in which maximal displacements were measured.
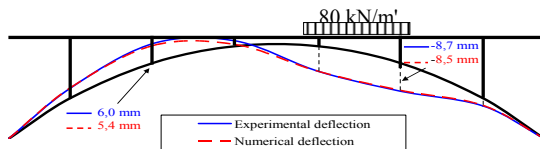
Fig 7. Comparison of experimental and numerical displacements for the 7th loading phase

In order to continuously monitor the bridge structure's condition both dynamic and static parameters of the structure were determined (natural frequencies, dynamic factors, attenuation).
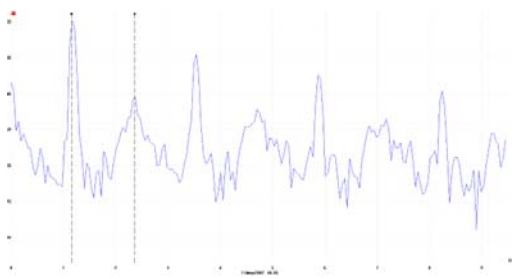
Fig. 8: PSD record (1st and 3rd natural frequency)

Table 1 shows the comparison of the first 10 experimentally and numerically determined natural frequencies. Figure 8 shows the record

of the power spectral density, which leads to identify 1st and 3rd natural frequency. Figure 9 presents several numerical oscillation modes.

Oscillation modes	Experimental frequencies (Hz)	Numerical frequency (Hz)
1. Lateral	1,148	1,084
2. Vertical	1,414	1,343
3. Torsional	2,344	2,302
4. Vertical	2,352	2,303
5. Torsional	3,185	3,123
6. Vertical	3,453	3,426
7. Vertical	4,162	4,128
8. Torsional	4,609	4,654
9. Vertical	5,141	5,072
10. Vertical	5,883	5,788

Tab. 1: Comparison of experimental and numerical natural frequencies
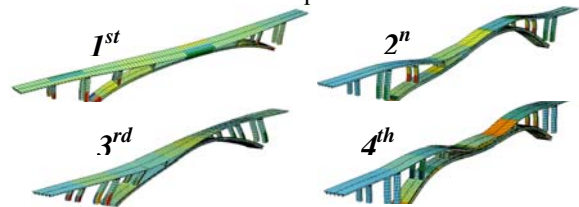
Fig. 9: Numerical oscillation modes

4. Conclusions

The installation of the monitoring system on the infrastructure facilities is of great importance enabling thus early damages or even prediction of damages on the structure. The monitoring costs are relatively low compared to total initial investment and maintenance costs, providing that maintenance works were not conducted on time. The cost benefits of such systems will prove to be highly advantageous in future. The test loading of the Cetina bridge was used for checking the part of the monitor system related to observation of structure's relevant characteristics.

5. References

[1] Rak M., Bjegović D., Mikulić D., Krolo J., Stipanović I. Design of monitoring of the bridge Cetina. 180-304/05. Faculty of civil engineering.

[2] Rak, M., Damjanović D., Čalogović, V. Report: Load testing of the bridge Cetina. 180-136/07. Faculty of civil engineering.

[3] Rak, Mladenko; Bjegović, Dubravka; Kapović, Zdravko; Stipanović, Irina; Damjanović, Domagoj. Durability Monitoring System on the Bridge over Krka River. Bridges International conference proceedings Zagreb:2006. SECON HDGK,. 1137-1146.

DETERMINATION OF THE STRESSES IN A METAL BAND OF A CONVEYOR WITH A SKEWED CYLINDRICAL TAIL PULLEY

K. Decker[1], T. Gabmayer[2], K. Hoffmann[3]

Vienna University of Technology,
Institute for Engineering Design and Logistics Engineering,
Getreidemarkt 9/E307, 1060 Vienna, Austria

[1] decker@ikl.tuwien.ac.at, [2] gabmayer@ikl.tuwien.ac.at, [3] hoffmann@ikl.tuwien.ac.at

Introduction

A wide range of systems has been developed to control the position of running metal bands. This paper deals with the mostly used guiding system, which controls the position of the metal band by changing the skewing angle β of a tail pulley. This system is shown in figure 1.
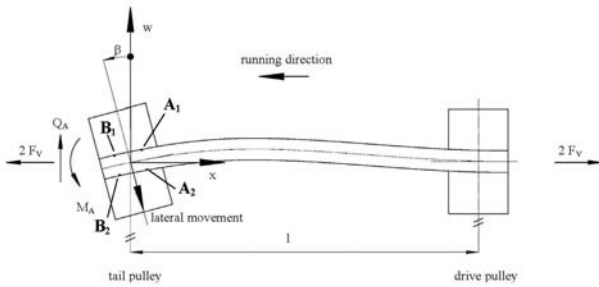
Figure 1: Simple conveyor with cylindrical pulleys

The skewed tail pulley causes higher tensions in the outer band edge and lower tensions in the inner band edge. As mentioned in [1] and [2], the metal band will move in the direction of lower tension.

In order to prevent the metal band from damage it is necessary to limit the skewing angle of the pulley during the control process.

This paper deals with the determination of the stresses in the band edge depending on the skewing angle. The investigations were carried out for the band between the pulleys (point A1 and A2 in figure 1) as well as for the points B1 and B2 when the band is in contact with the tail pulley. The following three methods were used:

a) Analytical approach using the bending theory of first and second order
b) Finite elements method (FEM)
c) Measurements using strain gauges

Analytical approach

I) Bending theory of first order with consideration of the shear deformation - fixed contact between band and pulleys
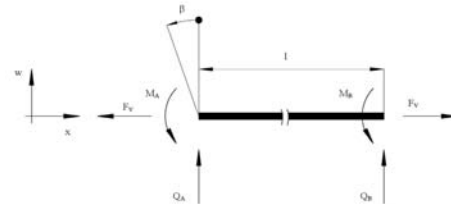
Figure 2: Mechanical model A of the metal band

$$Q_A = \frac{6btG\beta EJ_y}{btGl^2 + 12EJ_y}, \qquad M_A = \frac{\beta EJ_y}{l} + \frac{lQ_A}{2}, \qquad \sigma_v = \frac{F_v}{bt}$$

$$\sigma_{A1,2} = \sigma_v \pm \frac{2M_A}{J_y b}, \qquad \sigma_{B1,2} = \sigma_v \pm \frac{2M_A}{J_y b} + \frac{tE}{D+t}$$

$$\beta_{max} = \frac{\sigma_v}{\dfrac{3Gb^2 tlE}{2Gbtl^2 + 24EJ_y} + \dfrac{bE}{2l}} = 0,225°$$

II) Bending theory of second order with consideration of the shear deformation - friction contact between band and pulleys
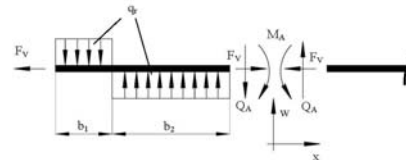
Figure 3: Mechanical model B of the metal band

The values for the stresses can be calculated in a similar way. This approach leads to transcendental equations for Q_A and M_A which were solved by the Levenberg-Marquardt algorithm.

The results for both approaches are shown in figure 6 and figure 7.

Finite elements method (FEM)

The finite elements method was used to verify the calculated results. The stresses for the band between the pulleys are illustrated in figure 4 for a skewing angle of 0.211° and a prestressing of 100 N/mm².
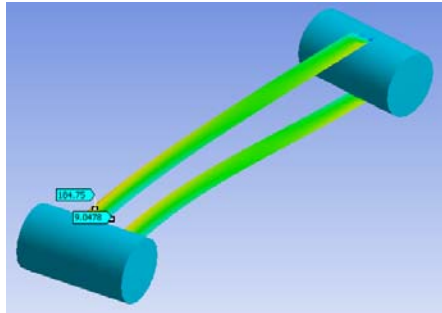
Figure 4: Representative results of FEM

Since a fixed contact was chosen between the band and the pulleys the bending stress, which is caused by the curvature of the band, is not included in the results. The effective stresses for the points B1 and B2 follows as:

$$\sigma_{B1,2} = \sigma_{FEM} + \frac{t \cdot E}{D + t}$$

t...thickness of the band

E...Young's modulus

D...diameter of the pulley

Measurements using strain gauges

The results were verified by measurements as well. Two strain gauges were applied on the metal band with a distance of 11.5 mm to the band edge. The results had to be multiplied by an increase factor to get the effective stresses in the band edge. Because of the small thickness of the band (0.3 mm) the influence of the thickness of the strain gauges and the glue on the effective strain on the surface of the band had to be considered. The results are shown in figure 5 for a skewing angle of 0.211° and a prestressing of 100 N/mm².
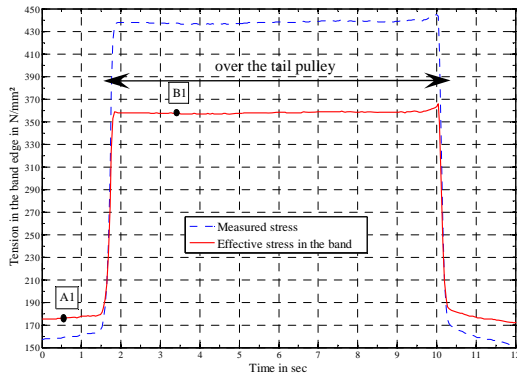
Figure 5: Representative measurement results

Summary of the results

Figure 6 shows the stresses in the two band edges against the skewing angle before the band has

contact with the tail pulley (point A1 and A2). In figure 7 the results are stated for the points B1 and B2, where the band is in contact with the pulley.
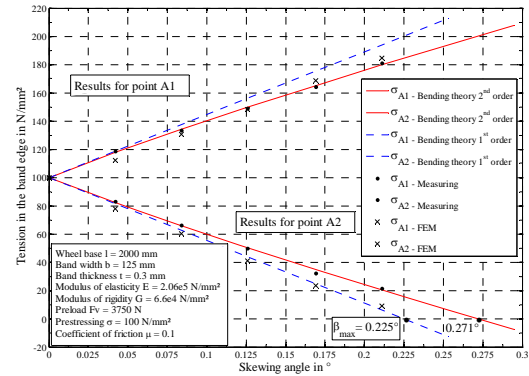
Figure 6: Results for point A1 and A2
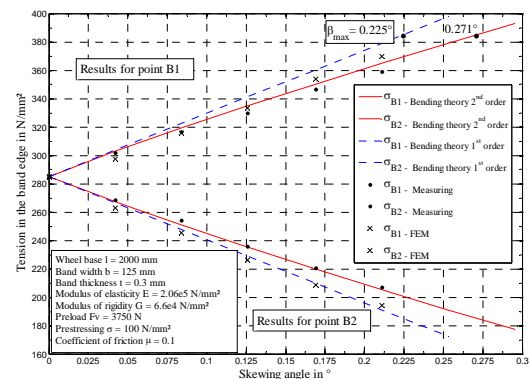
Figure 7: Results for point B1 and B2

Two conditions have to be fulfilled to prevent the band from damage and to ensure a safe band run:

$$\sigma_{B1} \leq \sigma_{permissible} \ldots \text{ to avoid plastic deformation}$$

$$\sigma_{A2} > 0 \ldots\ldots\ldots\ldots \text{ to avoid a slack band edge}$$

Conclusion

The results presented in this paper can be applied to predict the stresses in the band edge of a conveyor. With an analytical approach it is possible to determine the maximum skewing angle β_{max} of the tail pulley to make sure, that the band will not get slack during the control process.

References

[1] P. Ritzinger, *Lateral movement of slowly running metal bands on cylindrical pulleys (Seitlicher Bandverlauf von langsam-laufenden Metallbändern auf zylindrischen Trommeln),* Dissertation, Vienna University of Technology, 1997

[2] M. Egger, *Lateral running behaviour of the band of belt conveyors (Seitliches Laufverhalten des Fördergurtes beim Gurtbandförderer),* Dissertation, Vienna University of Technology, 2000

EXPERIMENTAL AND NUMERICAL SIMULATION OF BOGIE FRAME

Antonio De Iorio [1), Giovanni Pio Pucillo [1), Alessandro Bon [2) Luigi Prone [2)

[1) University of Naples Federico II, p.le V. Tecchio 80, 80125 Naples, Italy, [2) Firema Trasporti Spa, Triboniano-Str. 220, 20156 Milan, Italy.

Corresponding author: antdeior@unina.it

1. Introduction

To assess structural requirements of bogie frames, actual design standard require static and dynamic full scale testing to improve calculation and manufacturing quality. As each bogie frame differ from the others, a very flexible testing facility is necessary. This is the case of V-Test Lab, in Caserta [1].

Some experiences on numerical calculation and experimental data analysis from full-scale tests are shown in this paper, with the focus on the benefits that came from an a priori estimation of sensible zones of bogie frames for each loading condition.

Moreover, evaluation of instrumentation errors, in terms of control variables of structural response of the test article, will be shown in this paper.

2. Experimental vs. Numerical Results

The test rig equipment is shown in fig. 1.
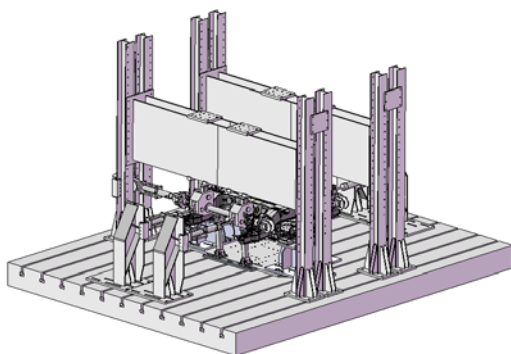
Fig. 1: Isometric view of testing facility.

It is equipped by twenty-one hydraulic actuators. A real time control system guarantee synchronous application of each kind of load history on bogie frame. Here, a set of *ad hoc* fittings and twenty-one actuators guarantee load application, on each direction, on wheels, with the superposition of twist [2]. The same apply

for loads due to components attached to the bogie frame, such as masses, brakes, anti-roll bars and so on.

The geometrical flexibility of the test rig is a necessary requisite to perform a comparison between two *worlds*, the experimental and the numerical one: test rig arrangement must be representative of the numerical idealization! Moreover, for fatigue test, in a previous work the Authors proposed a tool to evaluate and to control the correctness of applied loads on the bogie frame [3].

2.1 Strain gauges data evaluation

Prior to effectuate the required tests on the bogie, a method to evaluate calibration curves of measurement chain and uncertainty has been established. A typical flow chart is shown in tab. 1, where statistical data are calculated from strain gauges data and used to evaluate some commonly accepted parameters. Typically, more than seventy strain gauges are applied on a bogie frame.

Channel label	V_{med}	S_R^2	U_T	U	K_{GF}
Ei	1005	1.5 E-4	9.3 E-2	2.6 E-1	1.005

Tab. 1: Typical calibration and uncertainty parameters.

Moreover, it is very important to choose strain gauge characteristics, such as grid length, temperature compensation capabilities, unidirectional or tri-directional (rosettes) type, and so on. A critical issue is to estimate stress from unidirectional measured strain.

2.2 Numerical analysis

Actually, Finite Element Method (FEM) is the most powerful tool to perform accurate

calculation on complex geometry, such as a bogie frame.

Although actual FEM codes are very user-friendly, discretization techniques and, above all, contact and link simulation are a critical task [4]: a robust tool is necessary to obtain a numerical model easily comparable to experimental data.

Data acquired during test consist of many strain gauge measurements. The mayor difficulty is to understand the correlation between these experimental points and numerical data [5].

The correct way, in our opinion, is to perform an *a priori* numerical estimation of the most sensible strain gauges for the specified load condition. Prior to begin with complex static and dynamic loading condition, it is often very helpful to perform some initial calibration proofs, such as the symmetric ones, and, afterwards, to *complicate* them by introducing, step by step, the remaining loads.

Numerical to experimental correlation is a very useful tool to understanding possible anomalies that can occur through two types of tests. The former are that required from Authority's members designed for approval of the specific kind of test; the latter are those characterizing static and fatigue strength of the bogie.

Also, actions to prevent departures from procedures for performing tests and evaluation methods to validate non-standard methods, such as laboratory-developed can be made by the aid of a efficient bogie finite element model.

3. References

[1] A. De Iorio, G. P. Pucillo et Al, A Full Scale Testing Facility for Transport Security. Centre of Competence for Transport Systems of the Campania Region (2007), ISBN/EAN 978-88-87965-51-3, 177-193.

[2] C. Bianchi, Sicurezza di marcia contro lo svio a bassa velocità. Calcolo delle variazioni di carico di una ruota. Ingegneria Ferroviaria, Vol. 10 (1980) 5-12.

[3] A. De Iorio, G. P. Pucillo et Al, Incertezza di Misura dei Carichi Affaticanti applicati con un Sistema di Attuatori a Strutture Reali. XXXVIIth AIAS National Meeting, Rome, 10-13 September 2008, ISBN/EAN 978-88-87965-51-3.

[4] O. C. Zienkiewicz, R. L. Taylor, The Finite Element Method, Fifth Edition, Vol. 2. Butterworth-Heinemann (2000).

[5] A. J. Durelli, E. A. Phillips, C. H. Tsao, Introduction to the Theoretical and Experimental Analysis of Stress and Strain. McGraw-Hill (1958)

THE COMPARISON RESEARCH OF OPERATOR CABINS OF WORKING MACHINES

Damian Derlukiewicz, Jacek Karliński, Sebastian Koziołek, Mariusz Ptak [1],

[1] Wroclaw University of Technology, Faculty of Mechanical Engineering,
ul. Lukasiewicza 7/9, 50-371 Wroclaw, Poland

Corresponding author: damian.derlukiewicz@pwr.wroc.pl

1. Introduction

All the protective constructions must pass specified tests according to standards to be implement into practise. The modern systems as a computer aided design and engineering enable to conduct these kind of tests without building the structure and the testing facility. All the simulations are performed with the use of CAD system that bases on the Finite Element Method [1]. This study shows a comparison of the computer simulations to the experiment.

All the operator's protective structures must meet the requirements of standard PN-92/G-59001 "Self-propelled mining machines – Rock slide protective structures for operator – Requirements and Tests", that describes the required tests as a dynamic loading of a protective structure by the impact on the upper part of the structure of the research bob that falls on the structure with the potential energy E regard to impact point (presented on figure 1).

E = 60 000J
m = 1500 ÷ 6000 kg
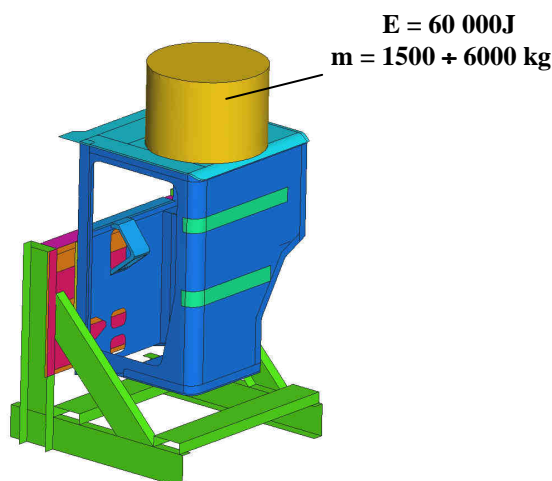
Fig. 1: The RSPS test- geometrical model with boundary conditions

The standard describes the lower area, that the research bob hits in the structure roof should be circular with a diameter at least 0.8 m. According to that the minimal distance of protected area DLV from structure elements should be at least 50mm.

The research results are positively accepted only if the structure does not break down or does not undergo the deformation in the elastic-plastic range in the way that breaks by the protective structure element into the protective area defined by the DLV.

2. Description of the numerical simulations

The nonlinear strength calculations of the protective structure with the use of Finite Element Method (FEM) in the dynamic range were performed for the assumed boundary conditions according the RSPS standard. The strength calculations were conducted with the use of CAE system that bases on the FEM.

The results of the analyses in the form of displacement contours are shown in Figure 2.
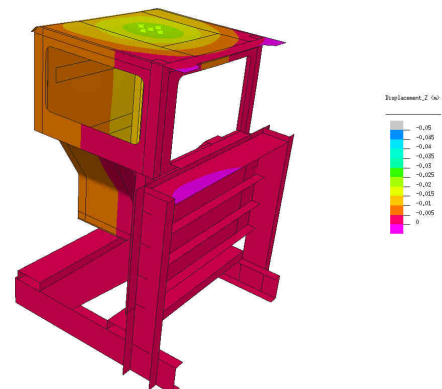
Fig. 2: The RSPS test- displacement contours for the maximal deflection.

In case of performing the strength analyses in the nonlinear range (solving the differential equations progress in the way of iteration) in the geometrical (high displacement) and physical (elastic-plastic material characteristics) respect, the received results error depends on the method of solving the differential equations and the material characteristic description [2], [3].

3. Experimental research

In the range of experimental test (verification test) the destructive strength test was conducted on the prototype of a protective structure. The impact energy of the research bob was 60000J according to the RSPS standard. The view of the test is presented on figure 3 together with the graph of the defection of the selected point measured by the Polytec Laser vibrometer PSV-400-B.

Fig. 4: Experiment - view of the cabin with the loading bob

The measurement results show the good conformity with the results from numerical simulations. The permanent plastic displacement and concerned with that deflection in the impact area amount to 42mm. In the numerical analysis the permanent deflection amounts to 17mm.
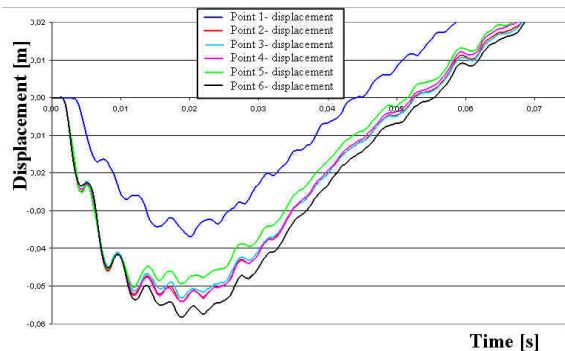
Fig. 5: The graph of vertical displacements for chosen points of the operator cabin
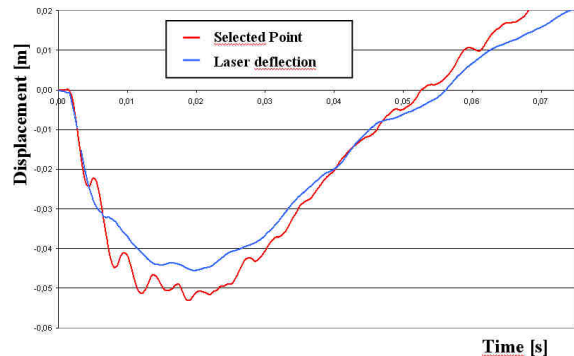
Fig. 6: . Displacement in the selected point – laser vibrometer measurement

Results were interpreted with the help of the DIN 22261 standard. They stated that obtained values were in a safe range.

4. Summary

Resuming, solving problem with the use of Finite Element Method shows that the received results are always raised in the respect of deflection, displacement values as well as the stresses values.

In the case of linear analyses it was found that the simulation results are accurate to the real object state.

5. References

[1] Rusiński E., Czmochowski J., Smolnicki T.: Advanced finite element method (in Polish), Oficyna PWr, Wroclaw 2000.

[2] Rusiński E., Karliński J.: ”Destruction simulations of the operator's cabin of the mining machine according to the aspect of operator's work safety”, Systems 2004 vol. 9 spec. iss. 2

[3] Smolnicki T.: The analysis of loading distribution in large size bearing of the mining machine rotational joint (in polish), 22nd Systems (Wrocław). 2002 vol. 7, spec. iss. nr 1, s. 506-515.

FATIGUE DAMAGE ACCUMULATION FOR ALLOYED STEEL USED FOR RAILWAY WHEELS

Dietrich Lech [1], Kukla Dominik [1],

[1] Institute of Fundamental Technological Research, Department for Strength of Materials, Pawińskiego Str. 5B, 02-106 Warsaw, Poland.

Corresponding author: ldietr@ippt.gov.pl

1. Introduction

Two modes of deformation mechanism due to development of a fatigue damage process can be distinguished depending on a kind of metal and its state defined by manufacture process. In the first one deformations which occur due to cycling loading are governed by cyclic plasticity rule as a result of micro slip and slip band decohesion. The fatigue indicator parameter can be defined in the case based on changes of the strain amplitude for a constant stress amplitude of a cyclic loading as shown on Fig. 1a.
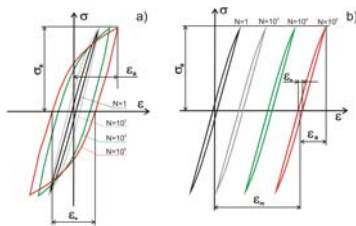
Fig. 1: Two modes of deformation due to fatigue damage: a) cyclic plasticity and b) ratcheting.

The second deformation mechanism arises as a consequences of a local deformation around voids and inclusions and leads to development of ratcheting [1]. The fatigue indicator parameter in the ratcheting mechanism can be defined based on changes of the mean strain for a constant stress amplitude of a cyclic loading as shown on Fig. 1b. The cyclic plasticity deformation mechanism of a high cyclic fatigue damage process occurs for example for alloyed steel used for pressure vessels working at high temperature, such as A336 or A387 steel according to the ASTM [2]. The ratcheting mechanism of a high cyclic fatigue damage process occurs in all alloys of metals with sufficiently large density of voids or other defects such as nonmetallic inclusions. The cast Al-Si-Mg alloys are a good example of metals exhibit the ratchet mechanism during a fatigue damage process [3].

2. Experimental Results

2.1 Material and specimen

The high cycle fatigue (HCF) tests were performed using hourglass specimens shown on Fig.2. Specimens were cut out from a railways wheel made of the P54T alloyed steel with chemical composition as given in Tab.1. Specimens were machining in such a way that all machine traces were along the specimen axis.

Tab. 1.

C	MN	Si	Cr	Ni	Cu
0.55	0.7	0.2	0.3	0.3	0.3
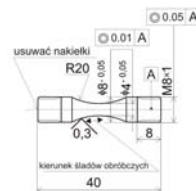
Fig. 2: Specimen on the left side and special griping system used in the HCF tests.

Specimens were mounted in a special griping system which is able to align specimen with the grips of the used load frame and also to eliminate any backlash. The gripping system in a version for a high cycle test is shown on a picture (fig. 2 on the right) with the transverse strain extensometer used for monitoring of the specimen diameter variation during entire test.

All specimens were loaded using the MTS 858 load frame, with nominal axial load of ± 25 kN, a fully digital controller was used for program and control a course of experiments. The high cycle fatigue tests were performed with a frequency 20 Hz under a constant nominal stress amplitude with monitoring during a whole test response of material in the axial strain calculated from diameter changes of

specimen. In this way it is possible not only determines the standard S/N fatigue curve but also observes a development of the fatigue process based on recorded mechanical parameters such as a strain amplitude, a width of a hysteresis loop and a mean strain in a sequent cycles.

2.2 Results

The additional information on strain response of material in sequential cycles of a constant stress amplitude enable us to define: a type of a damage mechanism, a fatigue indicator parameter, a development of damage, and the most important, a range of the applicability of the linear accumulation fatigue rule if exist at all. The information enable us to distinguish subsets of experimental points of the S/N curve which corresponds to different distribution of initial inclusions in the measuring part of specimen.

An exemplary and typical for the tested material behavior is shown on Fig. 3 for specimen under stress amplitude equal to 400 MPa.

Fig. 3: The stress - strain curves of a selected cycles for specimen P1 tested under stress amplitude equal to 400 MPa.

A stress – strain curve in a sequential cycles has the same elastic form and shifts in the direction of tension for increasing number of cycles. Development of damage due to cycle loading leads to ratcheting and in consequence to fracture of specimen. The tested material exhibit increase value of a mean strain ε_m with growing number of cycles in loading under constant stress amplitude and zero value of a mean stress. The inelastic strain ε_{in} equal to a width of the hysteresis loop has a constant value up to the last period of the lifetime when increases rapidly just before fracture of specimen. The ratcheting in a form of a growing value of a mean strain is a main mechanism of damage development in high cycle fatigue for the tested P54T steel. And the mean value of strain in one cycle can be consider as a fatigue indicator parameter and

can be used to define a damage parameter D as shown on fig. 4.

Fig. 4: The axial strain as a function of the normed fatigue on the left and evolution of the damage parameter, on the right.

3. Conclusions

The used procedure of the fatigue testing enable us to monitor development of a damage process during cycling loading to defined a fatigue indicator parameter and to determine the rate of fatigue damage.

The ratcheting in a form of a growing value of a mean strain is a main mechanism of damage development in high cycle fatigue for the tested P54T alloyed steel.

The damage development in the case is dominated by the initiation of the process and what is the most important the linear fatigue accumulation law should not be used for fatigue life prediction in case of this cast aluminum alloy.

4. References

[1] George W. Woodruff, Micromechanical Modeling of High Cycle Fatigue Processes, 2007 ASM/TMS Symposium on Computational Materials Design GE Global Research, August 20-21, 2007

[2] Socha G., "Prediction of the fatigue life on the basis of damage progress rate curves", International Journal of fatigue vol. 26 no 4, 339-347, 2004.

[3] Dietrich L., Radziejewska J., Report IPPT 2009, NADIA – New Automotive components Designed for and manufactured by Intelligent processing of light Alloys, SIXTH EU FRAMEWORK PROGRAMME.

GLULAM BEAM EVALUATION BASED NON- DESTRUCTIVE TECHNOLOGIES

Ferenc Divos [1], Jozsef Szalai [2], Jozsef Garab [3], Arpad Toth [4],

[1] Professor, University of West Hungary, Bajcsy Zs. u.4, H-9400 Sopron, Hungary

[2] Professor, University of West Hungary, Bajcsy Zs. u.4, H-9400 Sopron, Hungary

[3] PhD Student, University of West Hungary, Bajcsy Zs. u.4, H-9400 Sopron, Hungary

[4] PhD Student, University of West Hungary, Bajcsy Zs. u.4, H-9400 Sopron, Hungary

Corresponding author: garabj@fmk.nyme.hu

1. Introduction

The glulam structures in Hungary are typically cover sport, swimming pool, and spa facilities. Unfortunately some of them show degradation and delamination. The first structure has been demolished last Summer, because of severe delamination. University of West Hungary developed an evaluation procedure for in-service glulam beams.

2. Evaluation steps

The evaluation starts with a visual investigation. The investigations are shown in fig.1 Surface cracks, and degradation are important indicators of beam condition.

Fig. 1: Crack depth determination by thin plate penetration

The visual investigation is not enough. As you can see in the fig.2 we used acoustics methods to determinate the crack depths and the MOE of the lamellas. We measured sound velocity in a lamella along the fibers to determinate MOE.

Fig. 2: Crack depth determination by acoustics (stress wave sensors)

Fig. 3: Velocity determination in a lamella

Strength properties are predicted based on the MOE value. We also measure the actual moisture distribution inside the beam. For the evaluation of the test result we need to know the internal stresses.

Detecting internal decay or holes in glulam structure is possible by measuring the transit time of p- waves between the two sides of beam. fig.4

Fig. 4: Red spots shows the defected location

We measured shear strength between the lamellas too. This is critical information but the measuring is difficult so our measures were a laboratory trial. See fig.5.
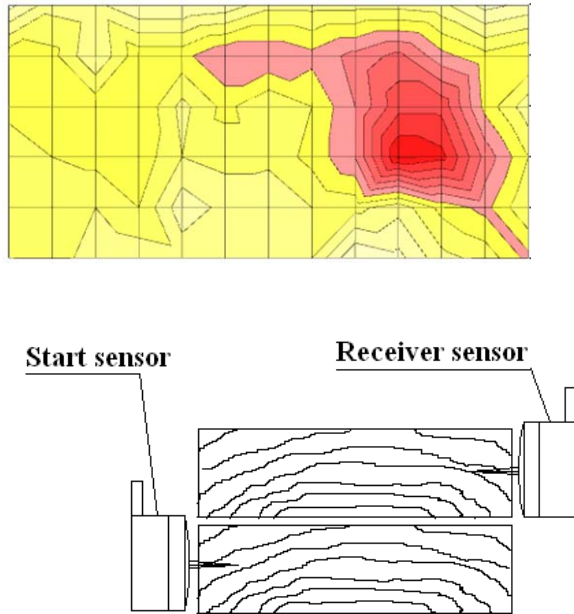
Fig. 5: Measure the shear strength by NDT

3. Results

In straight and curved glued laminated timbers (glulam) residual stresses can be significant due to change of climatic conditions. The stress caused by the manufacturing process, the load and the climatic conditions add together. The resulting stress may cause failure. We can find them in practice when the lamellas break or crack parallel to the fibre direction. Our research team uses a stress evaluation method developed at the University of West Hungary [1]. If we know the geometry of the glulam structure, the properties of the lamellas -the thickness, Young's modulus, the climatic and the manufacturing residual stress can be determined. We also need the initial and final temperature and the moisture content values of the lamellas to calculate the climate residual stresses.

We are presenting an example based on the measurements on a curved glulam beam in a Hungarian Spa. We have calculated the residual stresses caused by the manufacturing process and the residual stresses due to change of climatic conditions. On the fig.6 you can see the residual stresses in the lamellas by the manufacturing process.

The fig.7shows you the residual stresses by the climate conditions.
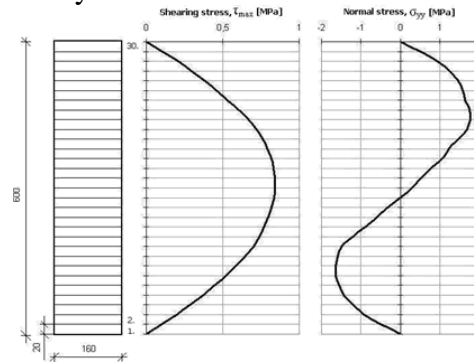
Fig. 7: Residual stresses by the manufacturing process
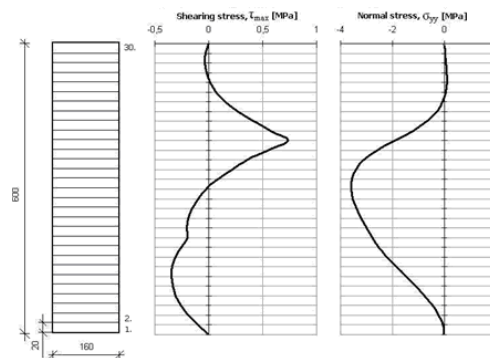
Fig. 8: Residual stresses due to change of climate conditions

4. Conclusion

Based on this investigation we can say that the architects have to take special care when dealing with residual stress especially in spa area, wellness centrums, baths, where the structure is made of wood and the moisture is always changing. Acoustic techniques provides useful data in glulam evaluation, especially in the lamellas MOE and crack depth determination.

5. References

[1] Szalai, J., Theoretische und experimentelle Unterszchung der Herstellungsbedingten Eigenspannungen von gekrümmten Brettschichtträgern. Holz als Roh- und Werkstoff 44. 1986. 69-75

DIGITAL IMAGE CORRELATION METHOD APPLIED TO MATERIAL TESTING

Mircea DUDESCU[1], Adrian BOTEAN[1] and Mihail HĂRDĂU[1],

[1] Technical University of Cluj-Napoca, Faculty of Mechanics, Department of Strength of Materials. Str. Const. Daicoviciu nr. 15, 400020 Cluj-Napoca, ROMANIA. Tel. +40 264 401661

Corresponding author: mircea.dudescu@rezi.utcluj.ro

1. Introduction

The paper presents the application of digital image correlation method to determine materials curves and constants (E-modulus, Poisson ratio). The method was applied for aluminum specimens subjected to tension.

The image correlation technique based on Q400 measuring system developed by Dantec Dynamics [1] has proven to be a useful tool for contour and deformations analysis. For 3-dimensional measurement of the displacements it uses two cameras. If the object is observed by two cameras from different directions, the position of each object point is focused on a specific pixel in the camera plane (Fig.1). If the positions of the two cameras relatively to each other, the magnifications of the lenses and all imaging parameters are known, the absolute 3-dimensional coordinates of any surface point in the space can be calculated. If this calculation is done for every point of the object surface, the 3D surface contour of the object can be determined in all areas, which are observed by both cameras.

Then a digital image correlation process determines the shift and/or rotation and distortion of little facet elements determined in the reference image. Such correlation algorithms can determine the maximum of the displacement with an accuracy of up to 1/100 pixel. This procedure allows the determination of the object deformation in a plane parallel to the image plane of the camera [2].

With the known displacement vectors of each surface point and the reference contour, the strains can be calculated. They can be derived by the analysis of the distortion of each local facet, which has been used for correlation [2].
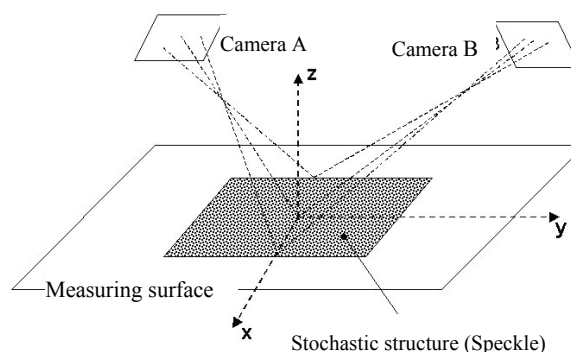
Fig. 1: Image correlation principle [2]

The Q400 measuring system is very easy to handle. Before any measurement the system calibration is necessary to be performed. The Q-400 system has, for a successful measurement, a calibration procedure incorporated in the measurement and analysis software ISTRA-4D. By the calibration procedure are determined the intrinsic and extrinsic parameters of the cameras. A test plate with a chess model on it is moved in front of the cameras.

The software automatically registers the nodal points of the test plate and calculates the intrinsic (focal length, principal point and radial and tangential distortions of the lenses) and extrinsic (translation vector and rotation matrix) parameters.

2. Methods

The experimental set-up, presented in figure 2, consists of the optical measurement system Q400, the aluminum specimen and the tensile test machine type INSTRON 3360.
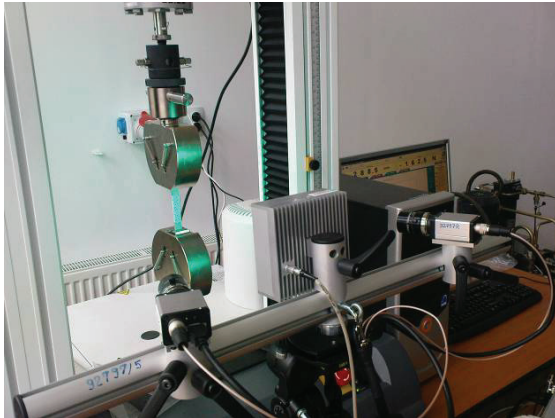
Fig. 2: Experimental set-up

The tensile test was conducted according to the EN 10002-1:1990 European Standard for tensile testing of metallic materials at ambient temperature [4]. Five specimens having the same dimensions were tested in the same conditions to check if the measuring results can be reproduced. Instead of using a classical extensometer during the tensile test many images of the specimen were acquired by both cameras of the optical measurement system. The values of the corresponding force at the acquisition time were recorded.

3. Results

After evaluation procedures the results consisting of 3D displacements of the analyzed specimen were obtained. Strain calculation should take into account also the contour information to get the in-plane strain. In this case the surface was plane and it could be noticed a small rigid body movement of the specimens that were not precisely aligned in the grips of the testing machine. These 2D strain values were automatically computed by the ISTRA-4D software and displays as colour-coded images or discreet values in the selected points or along desired lines. Picking a specific position one can get for example the principal strains in that point or using so called "gauge function" of the ISTRA-4D software the mean values of principal strains over measuring steps.

Calculating the engineering stress one cans gets the strain-stress curve and important information regarding the tested materials.
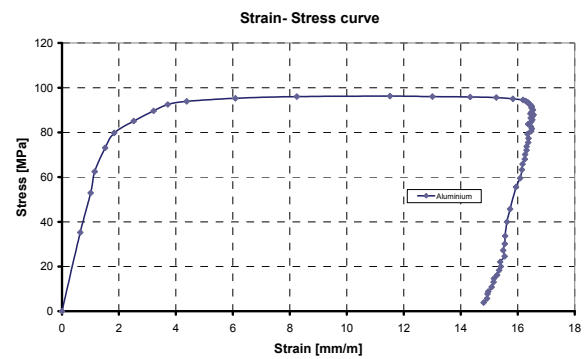
Fig. 3: Engineering stress-strain curve of aluminium

Thus for tested commercial aluminium the material constants were Young modulus about 58 N/mm^2, Poisson ratio 0,35. The yield stress was about 92 N/mm^2 and the ultimate stress about 98 N/mm^2.

The measured values had closer values to those presented in the literature. This validates the experimental method of the 3D image correlation and shows its high potential for material testing, fracture mechanics and component investigation. The measuring system Q-400 from Dantec Dynamics proved to be very accurate and reliable especially in the field of large displacements. Full field information in terms of displacements and strains increase the understanding of the material behaviour under loads.

4. References

[1]***, Digital 3D-Correlation System Q-400, www.dantecdynamics.com.

[2] Becker, T., Splitthof, K., Siebert, T., Kletting, P. (2006). Error Estimations of 3D Digital Image Correlation Measurements, In: *International Conference Speckle06 "Speckles, From Grains to Flowers"* Nimes, France.

[3] Herbst C., Splitthof K. (2006). *Q400 Application Note* - T-Q-400-Basics-3DCORR-002a-EN, Dantec Dynamics GmbH, Ulm, Germany, www. dantec-dynamics.com

[4]***, EN 10002-1:1990, Metallic materials. Tensile testing. Part 1: Method of test at ambient temperature.

INVESTIGATION OF THE "ARENA ZAGREB" MULTIFUNCTIONAL HALL'S ROOF

Ivan Duvnjak[1], Domagoj Damjanović[1], Mladenko Rak[1], Ljudevit Herceg[1], Goran Janjuš[2]

[1]Faculty of Civil Engineering, University of Zagreb, Kačićeva 26, 10000 Zagreb, Croatia
[2]UPI-2M d.o.o.Krajiška 10, 10000 Zagreb, Croatia

Corresponding author: iduvnjak@grad.hr

1. Introduction

The hall roof's structure is almost rectangular in plan. It was built over some 143 x 104 m surface (15000 spectators). The structure consists of curved steel girders (HEB 450) suspended over L=104 m span by means of cables system (Ø66 and Ø 64 mm) and of suspenders. The main cable is suspended from RC prestressed steel flanges in the highest points in the east-west direction, while main steel girders lean against RC hall's structure in the bottom zone. Two parallel spatial stabilizing steel trusses were designed in the direction of secondary girders (north-south) that had to transmit loads uniformly on adjacent complex.

2. Description of investigation and measurement

The investigation of girders was conducted so that hangers (Fig. 1&2) were suspended from the main girder's medium nodes. The platforms for loads amounting from the total of 440 kN (40 kN per node) were fastened to the suspenders.
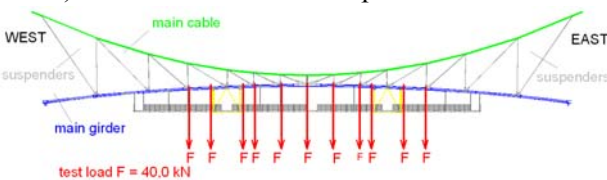
Fig.1: Cross section, load

The investigation was conducted throughout 5 phases (5 girders in a set), and unloading was performed after the completion of each phase. The vertical deflections in each loading phase were measured at 5 characteristic points (Fig. 2) along each girder.
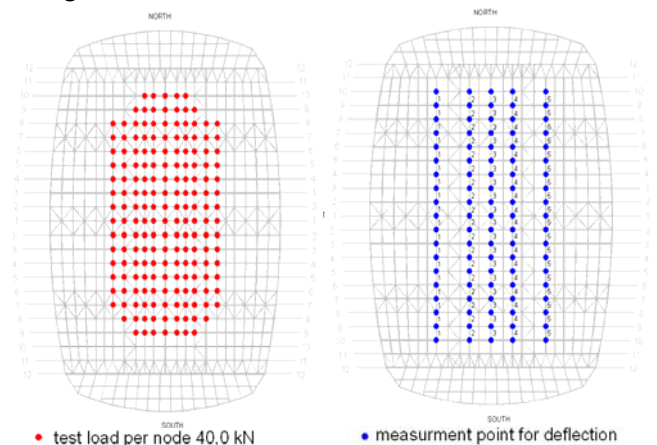
Fig.2: The plan of roof, loads, deflections

Deformations were measured by means of LVDT sensors in the middle of each main cable, and in some vertical and diagonal cables (Fig. 3)
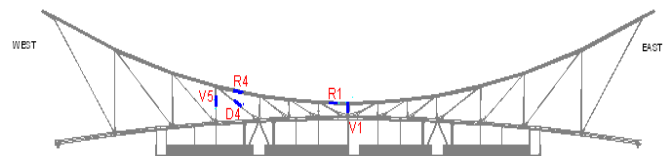
Fig.3: Measuring points for measuring relative deformations of cables and hangers

Both static and dynamic investigations were conducted. Natural frequencies of the roof structure were determined. The structure's excitation was induced through rocking of the mass including 2 men in the centre, and in the quarter of roof's span. During the roof's excitation

certain time series signals were registered along with the functions of power spectral density (PSD) determining relevant dynamic parameters. At the same time, during static investigation, the monitoring installed on two characteristic main roof structure girders was activated (Fig. 4). Monitoring includes continuous measuring of the structure's deformations.
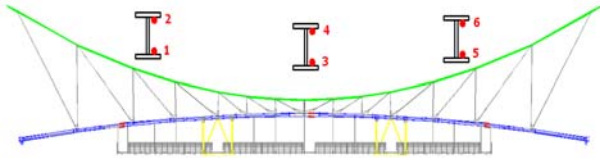
Fig.4: Points for measuring relative deformations during monitoring

3. Results obtained during test loading

Figure 5 graphically presents experimental and numerical deflections determined in the 3rd phase at one of the characteristic girders no.3.

5,5 cm   8,1 cm   9,8 cm   7,8 cm   5,3 cm
7,4 cm   12,5 cm   16,9 cm   12,5 cm   7,4 cm
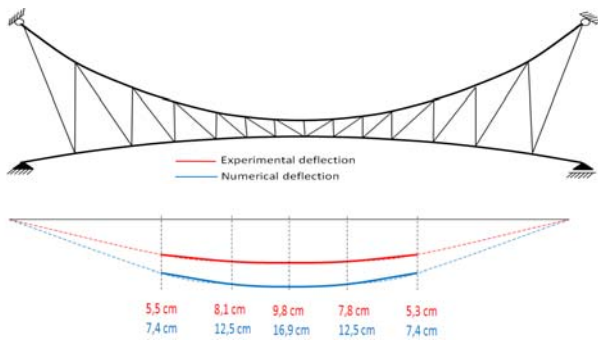
Fig.5: Comparison of experimental and numerical deflections of the girders no.3

The diagram (Fig. 6) shows recordings of relative deformations of cables and suspenders. Figure 7 presents deformations of main steel girder no.3.
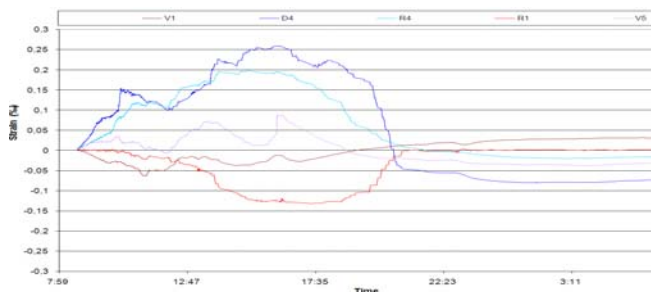
Fig.6: Records of relative deformations of cables and suspenders
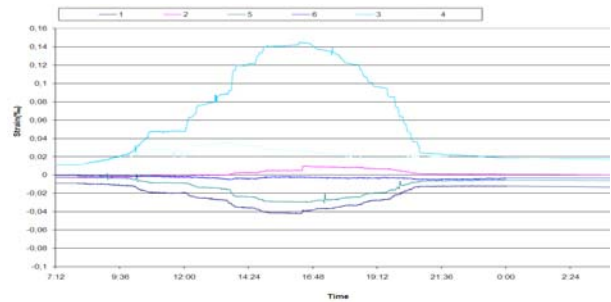
Fig.7: Recordings of main girder's relative deformations (no.3) during monitoring

Figure 8 presents one of the power spectral density recordings (PSD), which served to determine natural frequencies.
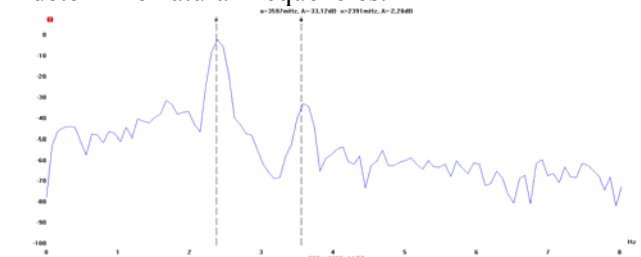
Fig. 8: PSD record (3rd and 5th natu. freq.)

Table 1 shows the comparison of experimental and numerical natural frequencies during roof structure's excitation

Natural frequency	Experimental freq. (Hz)	Numerical freq. (Hz)
1	1,28	1,27
2	1,64	1,75
3	2,39	2.45
4	2,70	2.99
5	3,60	3.50

Tab.1: Comparison of experimental and numerical roof's natural frequencies

4. Conclusions

The results of measured deflections, deformations and natural frequencies are within expected limits and comply with numerical values. The results indicate that the roof structure's performance meets the design requirements.

5. References

[1] Rak M., Damjanović D., Duvnjak I., Čalogović V., Report: Probno ispitivanje krovišta „Arena Zagreb"
[2] Rak M., Damjanović D., Duvnjak I., Report: Dinamičko ispitivanje krovišta „Arena Zagreb"

THE INSPECTION OF THE PEDESTRIAN BRIDGE OVER THE RIVER DRAVA IN OSIJEK CONDUCTED BY DYNAMIC INVESTIGATION

Ivan Duvnjak[1], Domagoj Damjanović[1], Ljudevit Herceg[1],

[1]Faculty of Civil Engineering, University of Zagreb, Kačićeva 26, 10000 Zagreb, Croatia

Corresponding author: iduvnjak@grad.hr

1. Introduction

A suspension bridge with 209,5m span connects left and right banks of the Drava river (Fig. 1). The main bearing system consists of cables anchored on either bank over 30,0m high pylons. The deck is suspended by the suspenders from the cables with 4,0m distances. The cables are connected over suspenders and concrete slabs with tendons running beyond the deck and anchored in the pylon blocks. The usable width is 5,0m, and the overall width 6,0m.

Fig.1: A look at the pedestrian bridge

2. Investigation and measurement

The investigation plans included the testing of the force magnitude in all the suspenders of the downstream and upstream bridge section, then the investigation of the force magnitude in main cables, and dynamic investigation of the bridge at excitation through live load and wind.
The investigation of the force magnitude in suspenders was conducted using resonant dynamic method, and by measuring natural frequencies of suspenders' transversal oscillation. The force magnitude in the suspenders and main cables was determined on the basis of correlation between natural oscillation frequency and the stress.

The recording of the dynamic response in each suspender (total number 2 x 102 = 204) and main cables (total 2) was performed by means of the accelerometer and electronic circuit of A/D converter and frequency analyzer. Natural frequencies were determined from frequent recordings of power spectral density functions (PSD). The bridge's structure dynamic investigation was carried out through the excitation with live load (pedestrians) and horizontal excitation through wind (wind velocity 8–12 m/sec.). The recordings of structure's dynamic response were conducted in time intervals and frequency domain over electro dynamical equipment Hottinger SMU 31, and electronic circuit of A/D converter and frequency analyzer. The force measurements results in the suspenders and main cables, and dynamic investigation were compared with the ones stemming from 1993 - the year of bridge reconstruction and were compared with the results of the structural analysis.

3. Measurement results

Figures 2 and 3 show the comparison of the forces results in cables in downstream and upstream direction.

ordinal number of suspenders
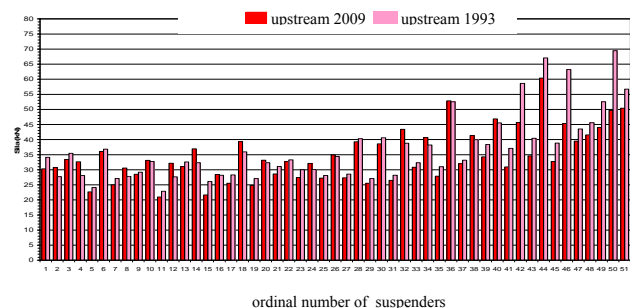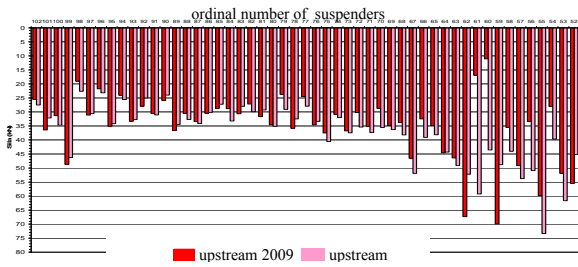
Fig. 2: Forces comparison in suspenders (upstream 2009, upstream 1993)
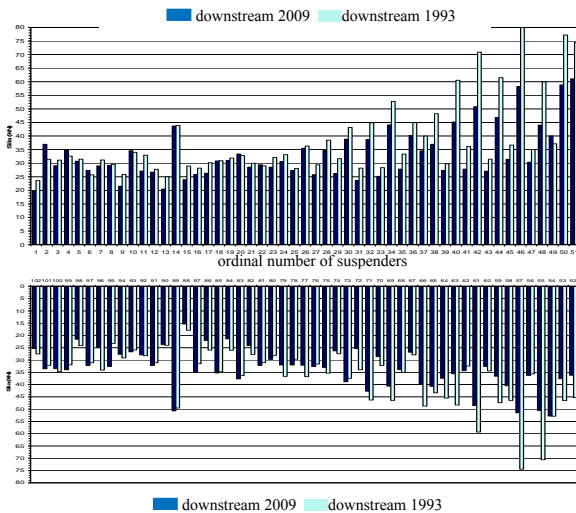
Fig. 3: Forces comparison in suspenders (downstream in 2009, downstream in 1993)

Forces in suspenders fell on average by 8% compared to the situation in 1993. With regard to structural analysis the measured forces in suspenders are on average higher by 6%. Largest deviations of measured forces with regard to forces in suspenders from structural analysis are in upstream suspenders no. 59–62. The connection element to the main cables of upstream suspenders 60 and 61 is damaged. The lowest force was measured in the above mentioned suspenders (11,09 and 16,91 kN), and the highest force was measured in adjacent suspenders no. 59 and 62 (69,94 and 67,35 kN).

Figure 4 presents the recording of power spectral density which served to determine 1 natural frequency of the main cable.
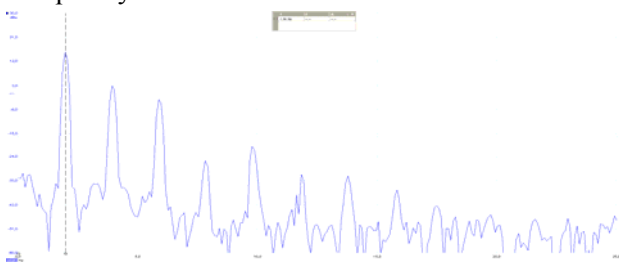
Fig. 4. Main cable on the right bank downstream (1,98 Hz)

Forces results in cables and their comparison with numerical values from the structural analysis are shown in Table 1.

Main cables	Exp.. freq. (Hz)	Exp.horizontal force (kN)	Numer. horz. force(kN)
Right bank downstream	1,98	4492	
Right bank upstream	2,00	4583	4845
Left bank downstream	2,05	4816	
Left bank upstream	2,05	4816	

Tab.1: Comparison of experimental and numerical forces in main cables

Table 2 shows experimental results of natural frequencies for dynamic investigation of the bridge's structure.

Natural frequency	Exp. natural frequency. 2009 (Hz)	Exp. natural frequency 1993 (Hz)
1	0,62	0,68
2	1,15	1,18
3	1,66	1,62
4	1,87	1,81

Tab.2: Comparison of experimental and natural frequencies for the years 2009 and 1993

4. Conclusions

Comparison of results from 2009 and 1993 proved the bridge's satisfying performance during exploitation. The investigation of force magnitude by resonant dynamic method and determination of natural frequencies proved the method of such structures' condition investigation to be efficient and quick. With regard to costs and speed of such investigations the method is to be recommended as regular type of inspection for the above mentioned and similar structures.

5. References

[1] Damjanović D., Herceg Lj., Duvnjak I., Izvještaj: „Stanje konstrukcije pješačkog mosta preko rijeke Drave u Osijeku"

[2] Krolo J., Herceg Lj., Izvještaj: „Ispitivanje sila u užadi na pješačkom mostu preko rijeke Drave nakon korekcije sila"

TENSILE PROPERTIES DETERMINATION OF NI-ALLOY WITH THE USE SMALL PUNCH TEST TECHNIQUE

Jan Džugan [1], Pavel Konopík [1], Michal Zemko [1], Robert Varga [1], Pavel Hosnedl [2]

[1] COMTES FHT a.s., Průmyslová 995, 334 41 Dobřany, The Czech Republic

[2] ŠKODA J.S. a.s., Orlík 266, 316 06 Plzeň, The Czech Republic

Corresponding author: jan.dzugan@comtesfht.cz

1. Introduction

There is increasing demand for operation temperatures increase of power production components nowadays. Therefore, an application of Ni-alloys in this field is increasing. As these components are very expensive and very important from the safety point of view, their service life has to be properly estimated and the material properties deterioration during operation has to be carefully monitored. Material available for properties evaluation of in service components is minimal therefore non-destructive or semi-non-destructive methods are utilized. One of the recently used methods for the materials properties assessment is Small Punch Test (SPT) technique. The method is using miniature discs testing for material properties determination. In the current investigation basic study of SPT method applicability to Ni-alloys properties evaluation is performed. There are performed SPT and tensile test at room temperature, followed by FEM simulation for evaluation of the material properties from SPT tests. Tensile tests are used as a reference for comparison of the results obtained from SPT.

2. Tensile tests

Standard tensile tests according to CSN EN 10002-1 were performed on the material investigated. Samples of diameter 5mm and gauge length 25 mm were tested and basic tensile properties were determined, **Tab. 1**.

Specimen	$R_{p0,2}$ [MPa]	R_m [MPa]	A_5 [%]	Z [%]
A	241,7	639,0	62,1	63,8
B	249,6	634,3	61,4	67,6
C	247,7	641,7	58,3	67,2
average	246,3	638,3	60,6	66,2

Tab. 1: Tensile tests results of Ni-Alloy

3. Small Punch Test

SPT tests were performed in special fixture developed for these tests for testing in servo-hydraulic testing machine. Sample deformation was measured by extensometer attached to the testing fixture. All tests were performed at ambient temperature. Samples dimensions are following: diameter 8mm and thickness 0,5mm. Tests records are shown in **Fig. 1**.
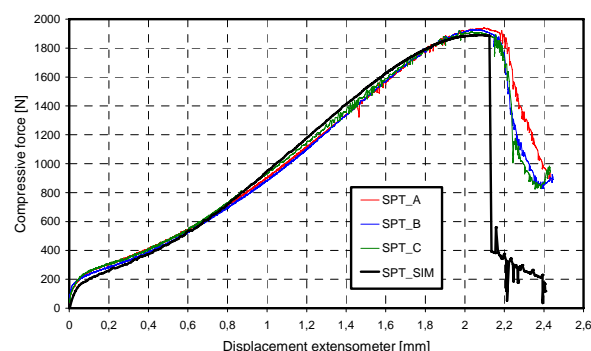
Fig. 1: Comparison of SPT records with FEM based results.

4. FEM simulation

In order to obtain tensile test properties from SPT, an inverse solution was performed. The input data of FEM program package, representing tensile curve, were modified till agreement between simulated SPT test records and real tests was attained, **Fig. 1**.

Subsequently, FEM simulation of tensile test with the use the obtained input data from FEM analysis of SPT was performed and basic tensile test data were evaluated. Comparison of evaluated tensile properties based on SPT and real tensile tests are summarized in **Tab. 2**.

Data	$Rp_{0,2}$ [MPa]	R_m [MPa]	A_5 [%]
Measured	246,3	638,3	60,6
Simulated	244,5	648,9	60,1
Deviation [%]	*0,73*	*1,63*	*0,83*

Tab. 2: Comparison of tensile properties obtained by SPT and tensile test

5. Conclusions

Determination of Ni-alloy tensile properties on the basis of Small Punch Test was performed and compared with results of tensile tests. There was found excellent agreement between data obtained by conventional tensile tests and those based on Small Punch Test technique evaluated with the use of FEM simulation. Further steps of this investigation will be testing at temperatures up to 1000°C and verification of the developed evaluation procedure.

MECHANICAL STIMULATION AS A DETERMINE FACTOR OF BONE REGENERATE BIOMECHANICAL PROPERTIES

Jarosław FILIPIAK(1), Piotr KUROPKA(2), Artur KRAWCZYK(3)

Leszek MORASIEWICZ(3),

(1) Wrocław University of Technology, (2) Wrocław Agrocultural Academy,(3) Medical Academy of Wrocław
Corresponding author: jaroslaw.filipiak@pwr.wroc.pl

1. Introduction

The Ilizarov principle of distraction osteogenesis is used in clinical practice to treat limb shortening. The principle consists in gradually increasing the distance between the fragments of a purposefully broken bone. 5-6 days after the fracture the gap between the fragments is filled mainly with connective tissue with a structure typical for a hyperelastic material. It is thanks to the connective tissue and its mechanical properties that a limb's length can be increased [5] (5-7 cm in one stage). There is no question that the rate with which the tissue structures in the fracture gap differentiate and their biological quality depend on the values and direction of the displacement of the bone fragments. Axial displacements of the bone fragments stimulate regeneration processes in the fissure whereas transverse displacements of the fragments inhibit the processes. The aim of this research was to determine how the displacement of the bone fragments during bone elongation affects the mechanical properties of the bone regenerate and its biological quality. In the literature on the subject one can find researches in which the effect of the size of bone fragments displacements on the formation of a callus structure in the fracture gap is examined [1,3,4]. Whereas the effect of such displacements on the processes taking place within the bone regenerate during bone elongation is still little known. Clinical and biological observations show that during bone elongation the biological quality of the bone regenerate changes at a rate much lower than in the treatment of a fracture.

2. MATERIAL AND METHODS

The aim was achieved through experimental research carried out on 21 Merino sheep. Elongation according to the Ilizarov principle [5] was performed on the metatarsal bone of the left posterior limb. Elongation of 20 mm, which amounts to 15% of the length of the limb subjected to elongation, was adopted. A specially designed fixator equipped with linear actuators whose function was to: i) realize bone elongation at a rate of 1mm/24 h until the intended elongation was reached and ii) apply mechanical stimulation (in the form of cyclic displacements of the bone fragments) to the bone regenerate were used for this purpose. The bone regenerate was stimulated at a frequency of 1 Hz for 1 hour each day. The sheep were divided into three measurement groups. The sheep belonging to group A and B (8 sheep in each group) were subjected simultaneously to bone elongation and the mechanical stimulation of the bone regenerate through the repeated interfragmentary movement (IFM) at an amplitude of 1 mm (group IFM=1) and 2 mm (group IFM=2). The sheep belonging to group R (5 sheep) were subjected to bone elongation without any mechanical stimulation (reference group). Eight weeks after the treatment the preparations taken were subjected to comprehensive examinations including: radiological, histological and biomechanical examinations.

3. RESULTS

The eight-week bone regenerate area of the metatarsal was divided into small regions *M, CM, PM, CB, PB* (fig.1). These match-like
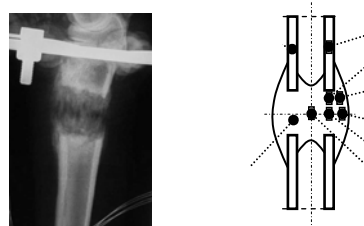
Fig. 1. X – ray of the eight-weeks bone regenerate and location of investigated samples

samples approximately 3mm thick, 3 mm wide and 5 mm long were cut from mentioned above regions. The strength during compression test of the specimens were experimentally determined. Compression strength σ_C was calculated by dividing the maximum compression force by the cross-sectional area of the specimen. In all measurements group the lowest strength were recorded in the central zone of bone regenerate (specimens: *M, CM, PM*) and higher strength in the zone near bone fragment (*CB, PB*) - fig.2.

The lowest compression strength values were calculated for the regenerates produced in the sheep in (reference) group *R*. In comparison with the reference group, the strength values determined in the sheep belonging to group A (*IFM=1mm)* are higher by 23% (regions: *CB, PB*). Analogical in group *B* (*IFM=2mm*) the difference, in comparison with the reference group (*R*), is even larger and amounts to 40%.
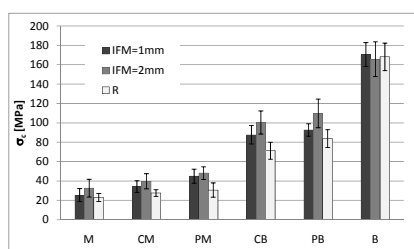
Fig. 2. Compression strength C of specimens in analysed regions

Differences between the particular measurement groups were also revealed by histological examinations of the bone regenerates. The histological examinations were carried out on decalcified and dehydrated preparations dyed in haematoxylin and eosin.

4. DISCUSSION

The results of the experiments have shown a marked effect of the mechanical stimulation (in the form of cyclically repeated axial displacements of the bone fragments) of the bone regenerate on its remodeling rate and biological quality. The biggest improvement in mechanical properties was recorded for measurement group *IFM=2*. This level of mechanical stimulation generates biomechanical conditions ensuring the highest rate of bone tissue formation and differentiation within the regenerate which forms during bone elongation. This is reflected in the histological picture of the regenerates in this test group. The well developed, highly mineralised trabecular bone and the extensive network of blood vessels with numerous branching perpendicular to the bone fragments' axis are the evidence of the fast rate of tissue proliferation and differentiation in the regenerate volume. For comparison, in the case of fracture treatment when the size of the fissure between the bone fragments is constant and below 3 mm, the range of bone fragments displacement generating optimum biomechanical conditions for the growth and differentiation of tissue structures is in a range of 0.4 ÷ 0.6 mm [1,3,4]. Biomechanical conditions are understood as a specific state of strain, pressure and fluid flow rates in the particular tissue structures of the bone regenerate. Such mechanical stimuli are processed at the cellular level into biological stimuli which control the formation and differentiation of tissue structures.

The results of this research attest to the fact that from the clinical point of view, the choice of the mechanical characteristics of the external fixator used for bone elongation is of crucial importance [2,4]. Its characteristics should be so matched that during bone elongation the bone fragments can displace by a value of about 2mm. Then biomechanical conditions assuring the optimal rate of formation and differentiation of bone regenerate tissue structures will prevail in the bone regenerate.

5. REFERENCES

[1] Augat P, Margevicius K., Simon J., Wolf S., Suger G., Claes L.: Influence of size and stability of the osteotomy gap. J. Orthop. Research, 1998, 16, pp. 475-481

[2] Będziński R., Filipiak J.: Experimental analysis of external fixators for femoral bone elongation. Acta Bioeng. and Biomech., Vol.1, No 2, 1999, pp. 93-105

[3] Claes L.E., Eckert-Hubner K., Augat P.: The effect of mechanical stability on local vascularization and tissue differentiation in callus healing. J. Orthop. Research, 20, 2002, pp. 1099-1105

[4] Doblare M., Garcia J.M., Gomez M.J.: Modelling bone tissue fracture and healing: a review. Engineering Fracture Mechanics, 71 (2004), 1809-1840, (4), 2006, 94-99

[5] Ilizarov G.A.: Transosseus Osteosynthesis. Springer Verlag, 1992

EXPERIMENTAL STRESS ANALYSIS OF MACHINE FOR BIO-FUELS PRODUCTION

František Fojtík, Radim Halama, Pavel Macura [1)], Jiří Režnar [2)]

[1)] VŠB-TU Ostrava, Department of Mechanics of Materials, 17. listopadu 15, CZ 708 33 Ostrava – Poruba, Czech Republic.

[2)] Bioenergy group, a.s., Veleslavínova 1, CZ 746 01 Opava, Czech Republic.

Corresponding author: pavel.macura@vsb.cz

1. Introduction

Bio-fuels are one of untraditional and ecological sources for energy generation. They comprise also fuel pellets made of wood saw-dust. They are manufactured by pressing through a disc with round holes with diameter of usually 6 or 8 mm. Due to the fact that machine components are worn very quickly at production and have therefore comparatively short service life, while calculation of force load at pressing of wood saw-dust is rather problematic, extensive measurement of deformations of selected components was made with use of strain gauge method. Results of measurement serve as a basis for subsequent computational stress analysis and service life of the whole equipment, or possibly for its innovation and optimisation.

2. Experimental Results

Design of the pressing machine (granulator) and position of the measured places is shown in the Figure 1.
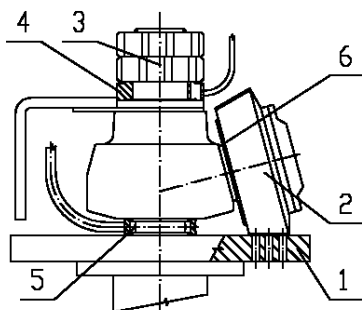
Fig. 1: Schema of granulator.

The engine via gear unit rotates with the pressing disc 1, to which three pressing cones 2 are pressed with pre-stress. Pre-stress is induced by fastening of two nuts on the supporting axis 3, under which a transducer 4 was placed during measurement. Three bending moments were measured on the supporting axis at the place 5. At the third measured place 6 the course of the bending moments on one axis of the pressing cone were recorded.

Two measurements were made. The first one when all machine components of the granulator were new, and the second, when they were already heavily worn out.

The course of development of the axial force in the transducer 4 at manual fastening of the nuts is shown in the Figure. 2.
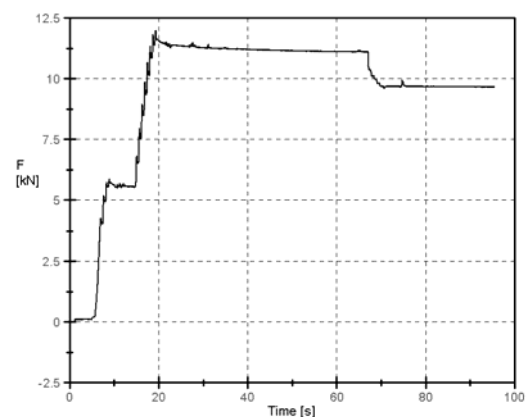
Fig. 2: Course of axial force at manual fastening.
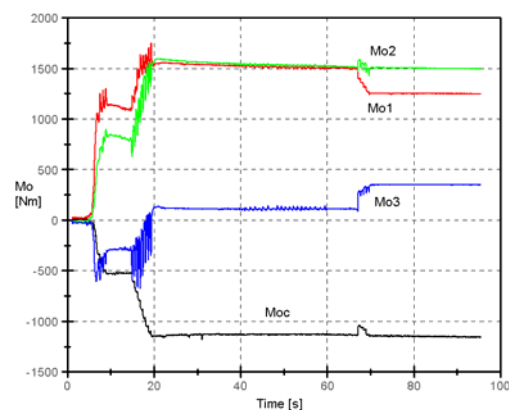
Fig. 3: Course of bending moments during fastening.

This force somewhat decreased at the fastening of the second jam-nut. The courses of bending moments at the places 5 and 6 during fastening of the nuts are shown in the Figure 3.

The granulator is during exploitation sometimes overloaded, when the holes in the pressing disc get clogged. Some courses of the measured values will be shown – at normal full output of the granulator and at its overload.
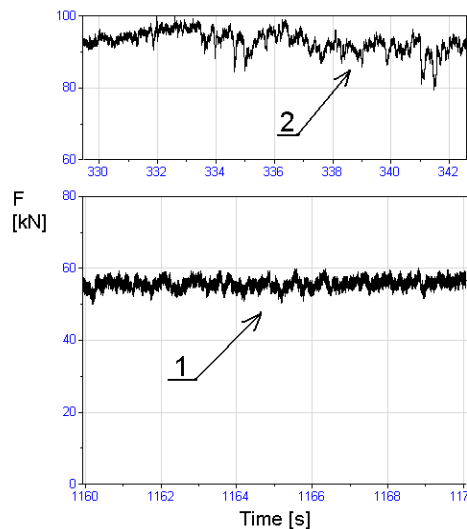
Fig. 4: Course of axial forces during working process.

The Figure 4 shows the courses of the axial forces measured by the transducer 4 at normal full output of the machine and at its overload, when the disc holes get clogged. It is obvious that the resulting force at overload is approximately double.
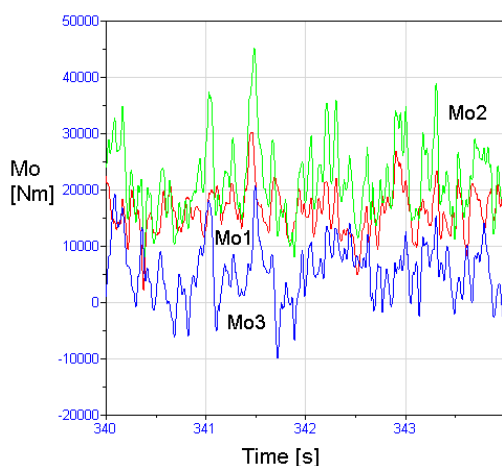
Fig. 5: Course of bending moments at measured places 5.

The course of the bending moments on the supporting axis at the measured place 5 are shown in the Figure 5. Three strain-gauge half-bridges are along the perimeter of the supporting axis glued in the planes, mutually rotated by 120°, similarly as the pressing cones 2 are placed. The resulting bending moments are induced by simultaneous effect of all three pressing forces from individual cones and their magnitudes heavily fluctuate during operation, often even between positive and negative values.

At the measured place 6 a strain-gauge half-bridge was also glued, enabling evaluation of the courses of bending moments on the axis of one of the pressing cones 2. The course of the evaluated bending moment at the granulator overload is plotted in the Figure 6. Their values also fluctuate heavily.
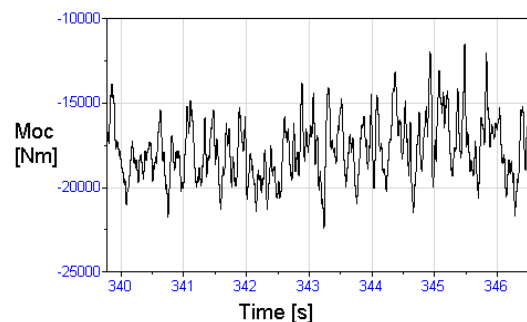
Fig. 6: Course of bending moment at measured place 6.

Detailed results of measurements and following calculations are given in the work [1].

3. Acknowledgements

4. References

[1] Fojtík, F., Macura. P., Halama, R.: Experimental loading analysis of machine for biofuels production. Technical report VŠB-TU Ostrava, February 2009.

DETERMINING THE DAMPING PROPERTIES OF DAMPER FLUIDS

Arpad Forberger [1), Tamas Insperger [1)

[1) Budapest University of Technology and Economics, Muegyetem rkp. 3-5., 1111 Budapest, Hungary.

Corresponding author: aforberger@mm.bme.hu

1. Introduction

Electrorheological fluids are suspensions of polarisable solid particles in a fluid medium of low electrical conductivity. An electric field is applied to increase the resistance to flow and with the field it is totally controllable. Without the control field they readopt their original rheological properties, such low viscosity.

These fluids can be used as fast reacting interfaces between control electronics and mechanical system in actuators, clutches, vibration dampers, motor mounts and valves in hydraulic systems as well. There are several experiments available that discuss the rheological behaviour, properties and adaptability in active control applications of ER fluids. Still there are only a few commercial applications. One is an MR damper developed by GM. Mostly automotive adaptations are the research priorities, in most cases reducing vibration, substituting moving-rotating parts with ER fluid. In the late 1980s GM carried out a study on the application potential of ER fluids, and concluded that a major hurdle was the low yield stress of the ER fluids. Several benefits are known, so let us discuss some. First, after switching off the electric field the fluid shifts very fast, within a few milliseconds, which is essential in active controls. And this process is totally reversible. Today dampers in motor mounts are used always as passive suspension systems, so one cannot change their properties (for example stiffness and damping). And here comes the benefits of ER fluids with their controllable viscosity and damping ratio.

2. Experimental Results

To investigate the effect of the electric field on the dynamic viscosity the flow time of 10 ml ER fluid was measured at different field intensities. Each measurement was continued until the flow of the ER fluid was stopped at certain field intensity. Using the flow time, the specific viscosity was calculated. Fig. 1 shows the effect of the electric field on the specific viscosity of ER fluid at 20 and 50 ^{0}C. The concentration of the ER fluid was 40 w%. The electrode distance was 3 mm. By increasing the electric field intensity, the specific viscosity of the ER fluid increases significantly as seen in the Fig. 1. At 20 ^{0}C the flow of the ER fluid was stopped at 0.833 kV/mm field intensity. At 50 ^{0}C the field intensity that was needed to stop the flow was 0.7 kV/mm. As increasing the temperature causes the viscosity of the ER fluid to decrease, this could be the explanation of the smaller field intensity that is needed to stop the flow.
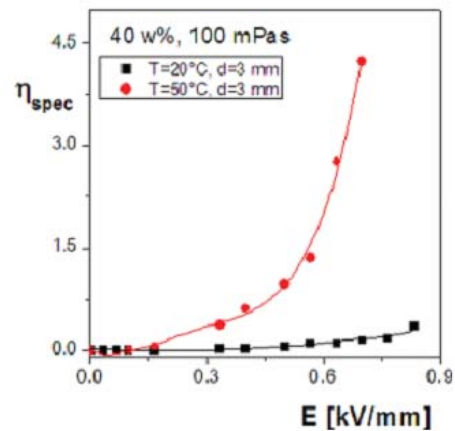
Fig. 1: The effect of the temperature and electric field on the specific viscosity of ER fluid

In Fig. 2 the effect of the electric field on the specific viscosity of the 30 w% ER fluid at different electrode distances can be seen. Each measurement was performed at 50^{0}C. The electrode distance was varied from 3 mm up to 7 mm.
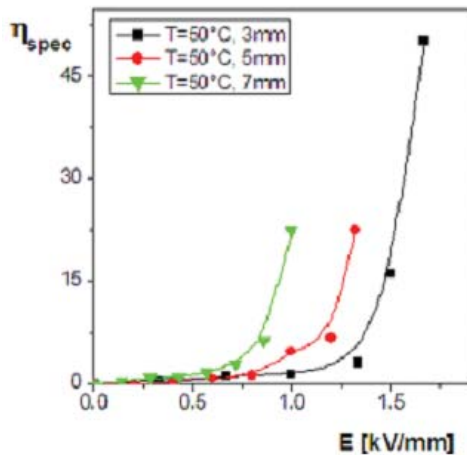
Fig. 2: The effect of the electric field on the specific viscosity of ER fluid at different electrode distances. The temperature and the electrode distances are indicated.

Polymers usually can be characterized using more relaxation constants. The number of the elements to be considered is optional. In this paper a three element Maxwell model is used. The first block J_1 models the inertia of the crankshaft, the second block J_2 models the inertia of the housing, and the J_3 is the inertia of the inertia ring. The stiffness and the damping parameters of the damper oil were determined by measurement. In Fig. 3, the mechanical model of a single Maxwell element can be seen. The two coordinates that govern the motion are x_1 and x_2.
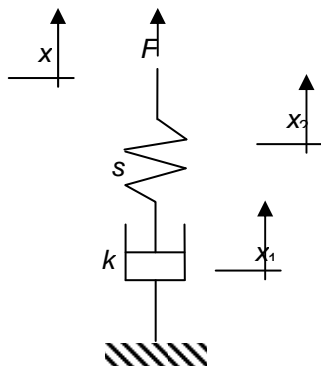
Fig. 3: Single Maxwell element

The equation governing the motion of the dashpot is

$$\dot{x}_1 = \frac{1}{k} F_{(t)} = \frac{1}{k} s\, x_0 e^{-\frac{s}{k}t}$$

3. Acknowledgements

References

[1] Jones TB, Electromechanics of Particles, Cambridge University Press,1995.

[2] Nakano M, Koyama K, Electrorheological Fluids,Magnetorheological Suspensions and their Applications, World Scientific Publishing Co. Pte. Ltd., 1997.

[3] Thao R, Roy GD, Electrorheological fluids,World Scientific Publishing Co. Pte. Ltd., 1994.

[4] Chris A. Papadopoulos. 1998 "Brakes and clutches using ER fluids", Mechatronics Vol. 8, pp. 719-726.

[5] Junjiro Onoda. 1998 "Semi-active vibration suppression of truss structures by electro-rheological fluid", Acta Astronautica, Vol. 40, No. 11, pp. 771-779.

[6] Taro Nakamura. 2004 "Variable viscous control of a homogeneous ER fluid device considering its dynamic characteristics", Mechatronics Vol. 14, pp. 55-68

[7] S.-B. Choi. 2004 "Vibration control of a flexible beam structure using squeeze-mode ER mount", Journal of Sound and Vibration, pp. 185-199

[8] S.-B. Choi. 1998 "Control characteristic of a continuously variable ER damper", Mechatronics, pp. 143-161

[9] S.-B. Choi. 1997 "Feedback control of tension in a moving tape using an ER break actuator", Mechatronics Vol. 7, pp. 53-66

[10] N. D. Sims, D. J. Peel, R. Stanway, A. R. Johnson, W. A. Bullough. 2000 "The electrorheological long stroke damper: a new modeling technique with experimental validation", Journal of Sound and Vibration, pp. 207-227

[11] L. Halász, M. Zrínyi. 1989, Bevezetés a polimerfizikába, Műszaki Könyvkiadó

LINK FROM THE MICROSTRUCTURE TO THE FATIGUE LIFTEIME OF FORGED INCONEL 718 COMPONENTS

H. Maderbacher [1), H. P. Gänser[1), M. Riedler[2), M. Stoschka[1), W. Eichlseder[1)

[1) Chair of Mechanical Engineering, University of Leoben, Franz-Josef-Str. 18, 8700 Leoben, Austria.

[2) Böhler Schmiedetechnik GmbH&Co KG, Mariazellerstraße 25, 8605 Kapfenberg, Austria

Corresponding author: hermann.maderbacher@unileoben.ac.at

1. Introduction

Fatigue behaviour of Inconel 718 aerospace components is strongly influenced by the microstructure. The microstructure itself can be controlled by the forging process and the heat treatment. The result of the work is a model which links the operation temperature and the microstructure out of a microstructure model [1] with the components lifetime.

2. Statistical Interpretation of Experimental Results

There is much data concerning S/N curves and microstructure evaluation for individual grains available from an earlier work [2]. To find out which of these microstructure parameters have an effect on the fatigue behaviour, a statistical interpretation of the parameters is important to find correlations and linear independencies. Figure 1 shows the result of the so called Factor analysis [3], which is a tool to reduce variables to a minimum of linear independent components.

As can be seen, all parameters are reduced to 3 orthogonal components. The first component can be interpreted as a grain size, the second one as grain orientation and the third one as something like the grain shape. It's interesting that the Fatigue stress only correlates with the grain size (=component 1) where also the energy parameter e_M and the parameter of inequality b_M [2] can be found. It was found that the parameters e_M and b_M give the best results to describe the fatigue behaviour of this material.

$$S = \left[\left(F_e \cdot \frac{e_M - 60,116}{31,151}\right) + \left(F_b \cdot \frac{b_M - 81,78}{13,874}\right)\right] \cdot 0,1067 + 0,92$$

(1)
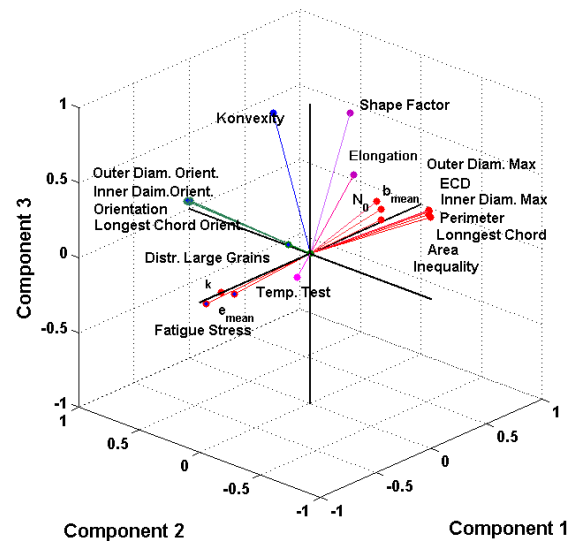
Figure 1: Reduction of all microstructure and S/N-curve parameters to 3 dimensions – Factor Analysis

3. Model to describe the fatigue behaviour out of the microstructure

The linear approach of Eq. 1 shall be used to link the parameters e_M and b_M to the fatigue behaviour. Here F_e and F_b are z-transformed loadings which have to be optimized in this way that the error gets as small as possible. Therefore the standard deviation of the differences of the estimated stress S_{cal} and the experimental stress S_{exp} must get a minimum (Eq. 2). The smallest error was found for $F_e=0.755$ and $F_b=-0.011$ as can be seen in Figure 2.

$$F_e, F_b = \min\left(\sqrt{\mathrm{Var}\left(S_{exp} - S_{cal}\right)}\right)$$

(2)
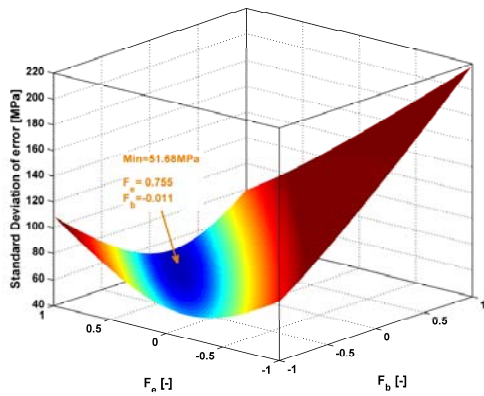
Figure 2: Response surface of the calculation error as a function of the loadings F_e and F_b

Another influence that has to be considered is the operation temperature. Figure 3 shows the dependency of the relative fatigue stress on this operation temperature.
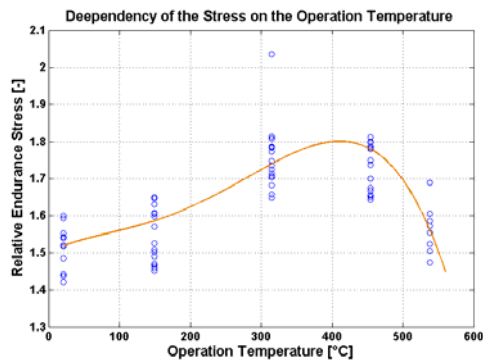
Figure 3: Relative endurance stress as a function of the operation temperature

$$\tau_{Temp} = -1{,}729 \times 10^{-11} \cdot T^4 + 2{,}81 \times 10^{-8} \cdot T^3 + \ldots$$

$$-5{,}397 \times 10^{-6} \cdot T^2 + 8{,}622 \times 10^{-4} \cdot T + 1{,}504 \qquad (3)$$

4. Results

Under consideration of Eq. 1, the temperature influence of Eq. 3 and a material parameter for Inconel 718 $M_{Inconel}$ the fatigue stress can be estimated with Eq. 4. Figure 4 compares the relative estimated stress with the relative experimental stress. The correlation from the estimation to the experiment is 83%, while the correlation for all other parameters is lower. The single parameter which is able to express the experimental fatigue stress best is the grain area with a correlation of 78%.

Correlation of the FatigueStress with different microstructure and SN-curve parameters	Experimental Fatigue Stress
Experimental Fatigue Stress	1,000
e_M	0,751
b_M	-0,701
Area	-0,784
Estimated Fatigue Stress	0,829

Table 1: Comparison of distinct parameters to the experimental fatigue stress

$$S_{cal} = S \cdot \tau_{Temp} \cdot M_{Inconel} \qquad (4)$$
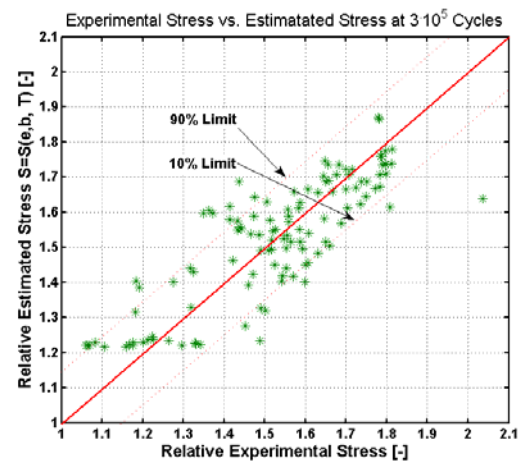
Figure 4: Relative estimated stress versus relative experimental stress

5. References

[1] M. Stockinger, Mikrostrukturelle Simulation des Gesenkschmiedens von Nickelbasis-Legierungen, Dissertation, University of Graz-Austria

[2] M. Stoschka, Assessment of lifetime calculation of forged In718 Aerospace components based on a multi-parametric microstructural evaluation, In: Proceedings of the 11th international symposium superalloy 2008

[3] I. Leyer, Multivariate Statistik in der Ökologie, Eine Einführung, Springer-Verlag Berlin Heidelberg 2007

CORROSION FATIGUE PROPERTIES OF L485MB STEEL

Lubomir Gajdos [1], Martin Sperl [1], Petr Broz [2]

[1] Institute of Theoretical and Applied Mechanics, Academy of Sciences of the Czech Republic, Prosecka 76, 190 00 Prague 9, Czech Republic

[2] Professional Society for Science, Research and Consultancy of the Czech Association of Mechanical Engineers, Cerna 8, 110 00 Prague 1

Corresponding author: gajdos@itam.cas.cz

1. Introduction

The linepipe steel L485MB is used for very high pressure gas pipelines. Gas pressure in a pipeline changes over a day and this is a primary cause of the initiation and growth of fatigue damage in the pipe wall [1]. Damaged or disbonded coating of the pipeline poses potential danger to the pipeline in that the possible aggressive constituents of contaminated soil can come into contact with the bare surface of the metal and cause its corrosion. These two factors can in principle result in the development of corrosion fatigue. It was therefore a matter of interest to investigate the fatigue behaviour of this steel in various corrosive media.

2. Experimental Results

Beside the reference S-N curve, taken for air, three more S-N curves were obtained. They are referred to (i) acidic solution: 50g NaCl + 5g CH_3COOH + 945g H_2O with pH = 2.7 – 3.0; (ii) alkaline solution: 1N water solution Na_2CO_3 and $NaHCO_3$ with the ratio 1:1 according to AGA [2] and pH = 9.3; and (iii) water from water main with pH = 6.5. For fatigue tests flat bars (Fig.1) were used.
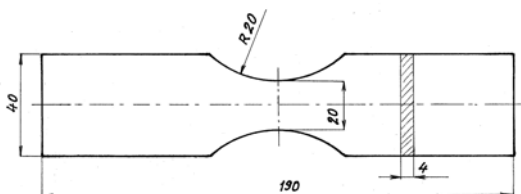
Fig. 1: The fatigue test bar

Static mechanical tests, which preceeded the fatigue tests, yielded the following strength parameters: $R_{p0.2}$ = 490 – 510 MPa and R_m = 620 – 630 MPa. Fatigue tests were carried out in a zero-to-tension cycle using a resonant-frequency fatigue machine with the maximum force capacity 100 kN.
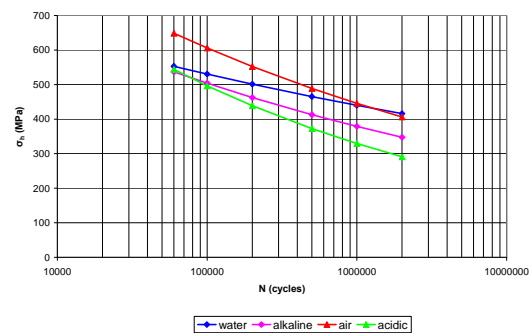
Fig. 2: The S-N curves

The results of fatigue tests are presented on Fig.2 in the form of S-N curves. The S-N curves can be described by power functions of the form

$$\sigma_h = \frac{A}{N^b} \qquad (1)$$

Magnitudes of the constants *A, b,* as resulted from the analysis of the S-N curves, are presented in Tab,1. As far as the fatigue limit is identified with the maximum stress in a cycle for the life N = 2 x 10^6 cycles, the most probable magnitudes of the fatigue limit will be those which are listed in Tab.2.

medium	A	b
air	2811.2	0.1333
water	1352.5	0.0813
alkaline solution	2098.3	0.1239
acidic solution	3856.6	0.1781

Tab. 1: Constants of the S-N curves

medium	air	water	alkaline solution	acidic solution
σ_{hC} (MPa)	406	416	348	291

Tab. 2: Fatigue limits in various media

The S-N curve for water exhibits a small slope. According to expectation this curve lies above the S-N curves for both solutions but below that for air. While for high cyclic loads the fatigue life for water is much shorter than for air, at low cyclic loads their difference decreases and for the life around 10^6 cycles the lives are very close to each other. At the life 2 x 10^6 cycles the corresponding stress (fatigue limit) for water is paradoxically higher than for air. The cause of this behaviour lies in specific properties of water; the course of corrosive actions is predominantly given by admixtures which water always contains.

If we introduce the so called fatigue strength reduction factor k_f [2] as a ratio of the cyclic stress in air and the cyclic stress in a corrosive medium for a given life N we shall obtain dependences $k_f - N$ listed in tab.3.

medium	k_f
air	1
water	$2.0785 \, N^{-0.052}$
alkaline solution	$1.3398 \, N^{-0.0094}$
acidic solution	$0.7289 \, N^{+0.448}$

Tab. 3: The fatigue strength reduction factor

Variations of the fatigue strength reduction factors k_f with life *N* are shown on Fig.3.
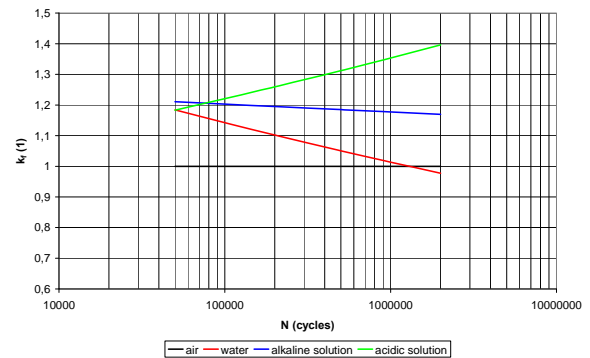
Fig. 3: Variations of the fatigue strength reduction factors on the life

As it follows from the figure, with increasing life the fatigue resistance of the steel L485MB decreases in acidic solution and, on the contrary, it increases in water, and also, to some extent, in alkaline solution, as compared to fatigue resistance in air.

A comparison of fatigue properties in air, water, alkaline and acidic solutions showed that the steel exhibits the best fatigue properties in air. Then it follows: water, alkaline solution, acidic solution.

The highest negative effect on fatigue properties is that of acidic solution for very long lives; e.g. for the life N = 2 x 10^6 the fatigue strength reduction factor is $k_f \approx 1.4$. It means that the fatigue limit of the steel in acidic solution is only about 70% of that found in air.

3. Acknowledgements

4. References

[1] L.Gajdos et al.: Structural Integrity of Pressure Pipelines, Transgas, Prague, 2004
[2] AGA NG-18 Report no.146: Test Method for Defining Susceptibility of Linepipe Steels to Stress Corrosion Cracking, Arlington 1985
[3] L.Krempl: Low-Cycle Fatigue Strength Reduction Factor in Notched Flat Plates, ASME Publication 67-MET-13, New York, 1967

EXPERIMENTAL METHOD TO ESTABLISH THE INDIVIDUAL FIBRES' MECHANICAL PROPERTIES OF THE HARD-WOOD SPECIMENS

Botond-Pál GÁLFI, Ioan SZÁVA[1],

[1] Transilvania University of Braşov,

Corresponding author: bgalfi@yahoo.com, janoska@clicknet.ro

1. Introduction

Usually, all experimental investigations regarding on hard-wood specimens are focused to establish their global mechanical behaviours. In fact, a hard-wood specimen is formed by several annual rings and their connected behaviours establish/determine the specimen's properties.

Taking a specimen which has a cross-section, obtained by a Tangential-Radial sectioning of the hard-wood, one can observe that the earlier and later annual rings are parallel connected, respectively, when the specimen's cross-section is obtained by a Longitudinal-Tangential sectioning, then these fibres are serial connected.

Starting from this fact became useful to establish their individual mechanical behaviours for a better (more accurate) further Finite Element Modelling.

In this sense, after the authors' knowledge, only a few numbers of experimental investigations was focussed up now to establish the individual fibres' mechanical properties, when these fibres (the earlier and the later ones) are working together in a specimen.

If we try to use the experimental results from some individual small specimen's (which are constituted practically from one-two fibres), in our opinion the results cannot be relevant for a high-accuracy FEM calculus.

The authors' idea was to keep these fibres together and to establish in this case their individual mechanical behaviours.
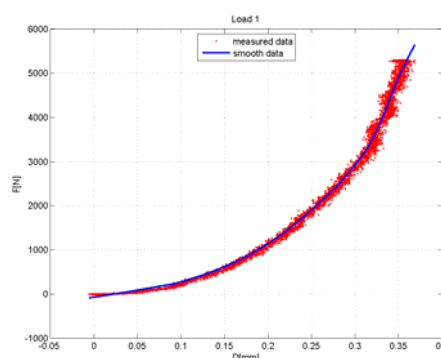
Fig. 1. The force-displacement curve during the loading of the specimen

2. Testing conditions and mathematical background

With a self-conceived stand, presented at YSESM-2008, destined to test under compression parallelipedic hard-wood speci-mens in a normal testing machine, the authors tested specimens having 10 *mm* x 10 *mm* x 50 *mm* sizes. These sizes allow to be observable in specimens a representative number of annual rings (minimum of 5 early rings and also 5 late wood rings). The specimens are worked out having a cross-section, obtained by a Tangential-Radial sectioning of the hard-wood and their compression are realised after their Longitudinal main direction.

Starting from an usual force-constrain curve (fig.1) obtained for a such wood specimen, on can take two, relatively nearly force values F^*, F^{**} and the corresponding constrains $\Delta\ell^*$, $\Delta\ell^{**}$.

For each pair ($F^* - \Delta\ell^*$; $F^{**} - \Delta\ell^{**}$), we can use both the static equations (1), (3), and the Bernoulli-hypothesis described by equations (2a, 2b, 4a, 4b).
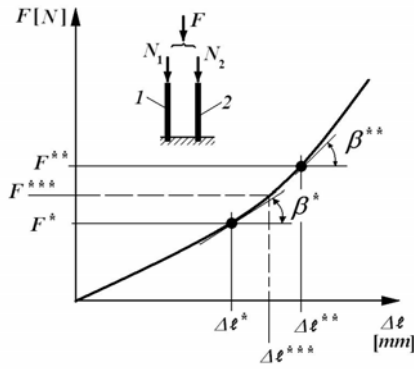
Fig. 2. The calculus scheme

$$\begin{cases} F^* = N_1^* + N_2^* ; & (1) \\ \Delta\ell_1^* = \Delta\ell_2^* = \Delta\ell^* ; & (2) \\ \dfrac{N_1^* \cdot \ell}{E_1^* \cdot A_1} = \Delta\ell^* ; & (2a) \\ \dfrac{N_2^* \cdot \ell}{E_2^* \cdot A_2} = \Delta\ell^* ; & (2b) \end{cases} \begin{cases} F^{**} = N_1^{**} + N_2^{**} ; & (3) \\ \Delta\ell_1^{**} = \Delta\ell_2^{**} = \Delta\ell^{**} ; & (4) \\ \dfrac{N_1^{**} \cdot \ell}{E_1^{**} \cdot A_1} = \Delta\ell^{**} ; & (4a) \\ \dfrac{N_2^{**} \cdot \ell}{E_2^{**} \cdot A_2} = \Delta\ell^{**} , & (4b) \end{cases}$$

where the unknown quantities are $N_1^*, N_1^{**}, N_2^*, N_2^{**}, E_1^*, E_1^{**}, E_2^*, E_2^{**}$, respectively the known ones are $F^*, F^{**}, \Delta\ell^*, \Delta\ell^{**}, A_1, A_2$.

We assume that for $\Delta F = F^{**} - F^*$ relative small, the Young modulus values are practically the same ($E_1^* \cong E_1^{**}; E_2^* \cong E_2^{**}$) and so the above-described system became statically determined.

The obtained values can be verified using one intermediate pair ($F^{***} - \Delta\ell^{***}$) of measured values.

Using this simply procedure, became possible to establish, for each applied load F^*, both the contributions of these two types of annual rings ($N_j^*, j = 1,2$) and the corresponding Young modulus' laws $E_j^* = f\left(N_j^*\right) j = 1,2$.

3. Supplementary considerations

The authors developed in this sense also a digital method to evaluate the magnitudes of the areas from earlier and later annual rings (A_1, A_2) of the tested specimens, which make easier to apply the presented method.

The used data acquisition system assure a good accuracy in obtaining of the force-constrain curve during the loading and unloading phases. In figure 3 is shown a smoothed version of them.
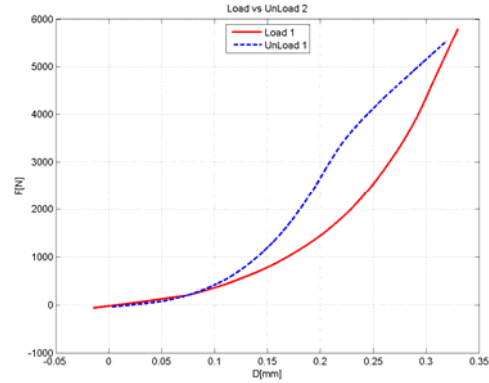
(smooth data)

Fig. 3. The force-displacement curve during the loading and unloading of the specimen

On can observe that during the unloading of the specimen, the effect/the influence of the pre-compressed cells, which have residual deformations, make that the unloading curve is located over the loading one (unusual thing at metallic specimens).

In figure 1 on can observe this influence of the cells' repositioning during the applications of the load (the constrain is little bit changed for the same value of the force).

4. Conclusions

The authors developed/elaborated a new and simply method to establish the annual rings' individual contributions and their mechanical behaviours, when these rings work together in a tested specimen.

The main advantage of this new method consists of in a better approach of the mechanical behaviours of the individual rings, which can be included in a more accuracy Finite Element modelling.

They intend to develop a complete testing system/methodology in this respect.

FATIGUE IMPROVEMENTS OF NITREDED NODULAR CAST IRON CRANCKSHAFT

Radinko Gligorijevic[1], Milosav Ognjanovic[2], Jeremija Jevtic [1],

[1] IMR Institute Belgrade, [2]University of Belgrade

Corresponding author: imrkb@eunet.rs

1. Introduction

The development of engine and vehicle components of ductile cast iron with the object of achieving high fatigue strength and ductility goes a long way towards meeting the requirements for a material suitable for lightweight construction and thus opens up on ever-growing field of applications for cast materials [1-2]. Nodular cast irons combine the favorable characteristics of other ductile materials, such as steel. This paper considers the fatigue strength scatter obtained on a nodular iron crankshaft for a high-speed diesel engine.

2. Testing method and test samples

Bending fatigue testing of crankshafts was performed in a fatigue testing rig (Fig.1).
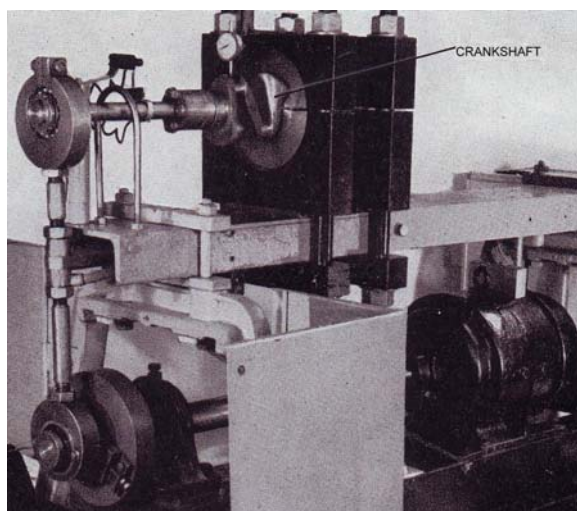
Fig.1: Testing rig of crankshafts at fatigue rotating bending

Testing samples are crankshafts for super high speed diesel engine which were made from nodular cast iron type SNG 800/2 with the following chemical composition: 3,1% C, 2,6% Si, 0,43% Mn, 0,15% Cu. The journal diameter of the crankshaft was 70 mm and crank pin

diameter 57mm, and length 558 mm. They had a tensile strength of 750-850 N/mm^2, yield strength 560-650 N/mm^2, the hardness of 265-300 HB. The microstructure was pearlite with 5-10% ferrite. The nodularity level was 85% and the graphite size 0,030-0,050 μm. One group of crankshafts was submitted to ammonia gas nitriding. The gas nitriding was performed for 25h at 510°C in ammonia gas at the atmospheric pressure using an industrial furnace of Efco type. Before testing all crankshafts were surface crack detected by magnetic flows. In order to determine the region of fatigue strength scatter relative to both nitrided and nonitrided crankshafts the authors performed tests of limited durability and fatigue endurance limit. In the region of limited durability the test was carried out with two load levels i.e. 300 N/mm^2 and 250 N/mm^2 for nonitrided crankshafts. For the nitrided crankshafts load levels in the region of limited durability were 350 N/mm^2 and 300 N/mm^2. Six to ten pieces of crankshaft were tested at each load level to the fracture point (z_Σ). In the region of endurance limit crankshafts were tested to the $N_D=5 \cdot 10^6$, number of load cycles which exceeded the finite number. Tests were carried out by the step by step method (zig-zag meaning that if a crankshaft failed at a number of cycle load which was below $N_D=5 \cdot 10^6$, the next crankshaft would be tested under the first lower load level and vice versa. If a crankshaft did not fail up to $5 \cdot 10^6$ load cycles the test was terminated and the next crankshaft was tested under higher load level 20 N/mm^2.

3. Testing results processing

Tables 1 and 2 show test results obtained with nonitrided crankshafts tested in the region of limited endurance. Numbers of load cycles to failure are given in growing order and for each stress cycle a failure probability $P_R = z_i / (z_\Sigma + 1)$ is calculated. Obtained probabilities are used to approximate tested

z_i	N	$P_R=z_i/(z_\Sigma+1)$	
1	75600	0.090	$P_R(N)=1-$ $e^{-(N/\ 115000)^{4.0}}$ $\eta=115000, \beta=4{,}0$ $P_R=0{,}1; N=68000$ $P_R=0{,}5; N=109000$ $P_R=0{,}9; N=140000$
2	84000	0.181	
3	87000	0.272	
4	90400	0.363	
5	100800	0.454	
6	109200	0.595	
7	112000	0.636	
8	117400	0.727	
9	126000	0.818	
10	158300	0.909	

Tab. 1: Failure probability for nonitrided crankshafts for S_N=300 N/mm^2

Z_i	N	$P_R=Z_i/(Z_\Sigma+1)$	
1	85200	0.111	$P_R(N)=1-$ $e^{-(N/148000)^{3.0}}$ $\eta=148000\quad \beta=3{,}0$ $P_R=0{,}1,\ N=72000$ $P_R=0{,}5,\ N=137000$ $P_R=0{,}9,\ N=200000$
2	92400	0.222	
3	111600	0.333	
4	127600	0.444	
5	142800	0.555	
6	151200	0.666	
7	159600	0.777	
8	220000	0.888	

Tab 2. Failure probability for nonitrided crankshafts for S_N=250 N/mm^2

Fig. 2: *S-N* curve with overall scatter region for nonitrided crankshafts
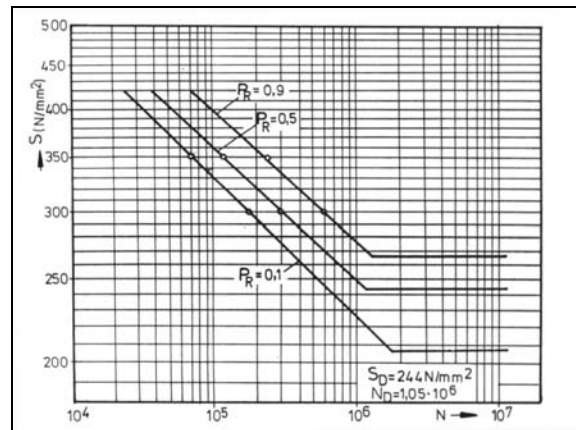
Fig. 3: *S-N* curve with overall scatter region for nitrided crankshafts

results by Weibull function and to determine parameters of this distribution function.

To recognize the amount of fatigue strength scatter within the region of endurance limit 15 pieces of nonitrided crankshafts was tested. The processing of results is analogous to the one relating to the region of limited endurance. On the basis of test results failure probabilities have been calculated following the same procedure as applied to the limited endurance. Finally the Weibull failure probability has been plotted and parameters, functions, and endurance probabilities P_R=0,1; P_R=0,5 and P_R=0,9 determined

Overall scatter region, i.e. full *S-N* curve (Fig. 2), has been plotted on the basis of failure probability distribution within the regions of endurance limit.

The overall scatter region, i.e. full *S-N* curve applicable to gas nitrided crankshafts, is shown in Fig. 3.

4. Conclusion

On the basis of test results it can be concluded:
1. Using Weibull distribution one can easily find failure probabilities, P_R=0,01, P_R=0,1, P_R=0,5 and P_R=0,9, for crankshafts within the region of limited durability and endurance limited.
2. When nodular iron crankshafts are subjected to nitriding their fatigue strength is improved by the factor of 1,3 within region of endurance limited in comparison with nonitrided ones while the scatter of endurance limit is reduced.

5. References

[1] P.Mullinas; Lighter, Higher Performance Crankshafts, High Speed Diesel and Drives, July-August 1990, p.7
[2] T.Sonnenschein, et all., Gegossene Kurbelwelle fur Grfosserien,MTZ 12,1971

A MODE SHAPE-CHANGE CORRELATION APPROACH TO DAMAGE DETECTION

Valentina Golubović-Bugarski [1), **Drago Blagojević**[2), **Đorđe Čiča**[3)

[1,2,3) University of Banja Luka, Faculty of Mechanical Engineering, Stepe Stepanovica 71, 78000 Banja Luka, RS, Bosnia and Herzegovina.

Corresponding author: valentina@urc.bl.ac.yu

1. Introduction

In the most general terms structural damage can be defined as changes introduced into a system that adversely affect the current or future performance of that system. Implicit in this definition is the concept that damage is not meaningful without a comparison between two different states of the system, one of which is assumed to represent the initial and often undamaged state. Damage may also be defined as any deviation in the structure's original geometric or material properties that may cause undesirable stresses, displacements, or vibrations on the structure. These weaknesses and deviations may be due to cracks, loose bolts, broken welds, corrosion, fatigue, etc.

All of them should cause a decrease in the structure's stiffness, and some will also affect its mass and damping properties. Therefore, structural damages should always, at a sufficient level of severity, cause a change in a structure's vibration behaviour, described by modal properties: natural frequencies, damping loss factor and mode shapes. Since the changes on the dynamic characteristics can be measured and studied, it is possible to trace what structural changes have caused the dynamic characteristic to change, thus identifying damage.

The method presented in this paper belongs to the class of methods that use the change in the operational deflection shapes to detect, locate and relatively quantify the damage [1]. The main advantage of the method are that it is not necessary to undertake a modal identification, there is no need for any analytical or numerical model of the structure, and it uses all measured data, in form of frequency response functions, without further treatment.

2. Theoretical description

W. Heylen [2] defined a Response Vector Assurance Criterion (RVAC):

$$RVAC_d(\omega) = \frac{\left| \sum_{i=1}^{N} {}^d\alpha_i(\omega)\overline{\alpha_i(\omega)} \right|^2}{\sum_{i=1}^{N}\left[{}^d\alpha_i(\omega)\overline{{}^d\alpha_i(\omega)} \right]\sum_{i=1}^{N}\left[\alpha_i(\omega)\overline{\alpha_i(\omega)} \right]}$$

where $\alpha_{ij}(\omega)$ is element of the system receptance matrix and corresponds to an individual frequency response function (FRF . For only one applied force, receptance matrix turns to be just a vector, so $\alpha_i(\omega)$ is a single FRF for i-th co-ordinate or measuring point, and N is the total number of measuring points. The element $\alpha_i(\omega)$ corresponds to the undamage structure, while the superscript d stands for damaged structure.

3. Numerical examples

In order to show effectiveness of the proposed method, an FE model of a free-free beam is built in ANSYS package, with 160 beam elements, 161 nodes and two degrees of freedom at each node (u_y, θ_x). The beam dimensions are $400\times10\times10$ mm ($L\times b\times h$), the Young's modulus is $2,1\times10^{10}$ N/m^2, the density is 7820 kg/m^3, Poisson's coefficient 0.3. First four natural frequencies and corresponding mode shapes of the beam are obtained by modal analysis in the frequency range 1-3000 Hz, with frequency resolution of 1 Hz. For harmonic analysis, a random force is applied at node 30, and responses at every 4-th nodes (40 nodes at total) are measured. So, total number of measurement data is 120 000 $\alpha_{ij}(\omega)$ elements of FRF column vector, that is $\alpha_{i30}(\omega)$, $i=1\div40$, $\omega=1\div3000$ Hz. The damage is simulated with a reduction in the second moment of area of element 17. A five damage level of the beam

are simulated: d=1 is undamage beam, and d=2÷5 is beam with 10 %, 20%, 30% and 50%, respectively, reduction of second moment of area of element 17. Procedure of harmonic analysis is repeted for every damage level. The first four natural frequencies for different damage levels are given in Tab.1.

Damage level	Natural frequency (Hz)			
	f_1	f_2	f_3	f_4
1	323.56	887.73	1730	2838
2	322.85	887.5	1730	2837.7
3	322.12	887.01	1729.8	2836.2
4	321.08	886.18	1729	2833
5	317.34	882.74	1726.1	2818

Tab. 1: Natural frequencies for different damage levels, numerically obtained

For every damage level, RVAC is calculated from equation (1). All numerical results are obtained from routines developed in the Matlab package, and shown on Fig.1. It can be seen that RVAC gives information about the relative extend of the damage.
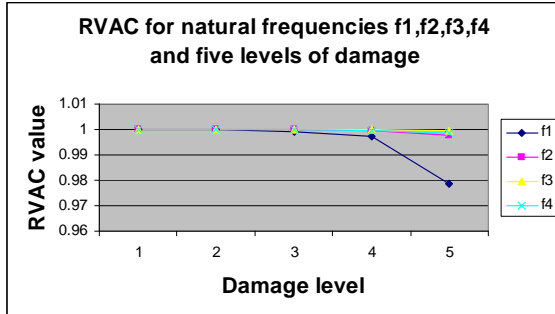
Fig. 1: RVAC value for four natural frequencies of beam and five damage levels

4. Experimental results

For the experimental analysis, the steel beam of dimensions 400×10×10 mm is used. A crack of 0,5 mm width is introduced by wire-cut. The beam is suspended with common strings to simulate free-free conditions. An impact hammer (Endevco type 2302-10) generates excitation on the each of 19 nodes uniformly arranged along the beam. An accelerometer (B&K type 4507) is attached to node 8 to capture the vibration signals. The signals are fed into Multi-channel Data Acquisition Unit Portable PULSE (B&K type 3560 C) and analyzed in the Pulse LabShop 8.0 software, in the frequency range of 0÷3200 Hz. Modal test

is repeated for the four level of damage: d=1 is undamage beam, d=2 coresponds to crack of 1 mm depth, d=3 is crack of 2 mm depth, d=4 is crack of 4 mm depth. The first four natural frequencies for different damage levels are given in Tab.2. Fig.2. shows overlaid FRFs measured at node 8 for four damage levels, and Fig.3. shows RVACs for experimentaly obtained data.

Damage level	Natural frequency (Hz)			
	f_1	f_2	f_3	f_4
1	329	904.5	1776	2850
2	328	902.5	1774	2838
3	325	894.5	1769	2831
4	314.5	874.5	1767	2747

Tab. 2: Natural frequencies for different damage levels, experimentally obtained
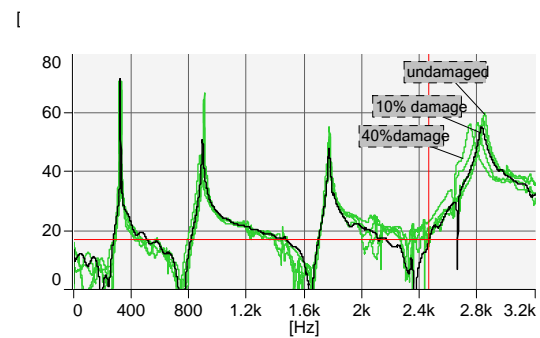
Fig. 2: Overlaid FRFs measured at node 8 for four damage level
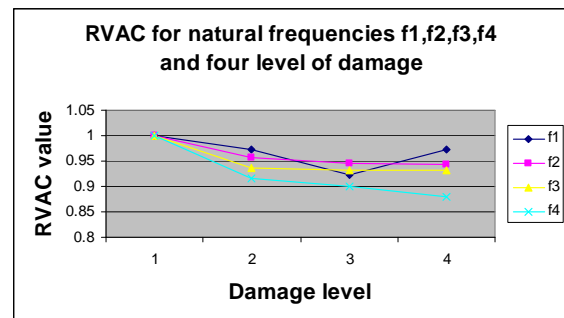
Fig. 3: RVAC value for four natural frequencies of beam and four damage levels

5. References

[1] Sampaio, R.P.C., Maia N.M.M., Strategies for an efficient indicator of structural damage. Mechanical System and Signal Processing, Vol. 22 (2008).

[2] Heylen, W., Lammens, S., Modal Analysis Theory and Testing. K. U. Leuven-PMA (1998), section A6.

ANALYSIS OF FATIGUE DAMAGE IN A PULTRUDED COMPOSITE BY MEANS OF X-RAY MICRO-TOMOGRAPHY

M.Guagliano[1], O. Tizzoni [1] , D. Dreossi[2], F. Cosmi[3]

[1] Politecnico di Milano, via La Masa, 34 - 20156 Milano, Italy, mario.guagliano@polimi.it
[2]Sincrotrone Trieste, SS 14, km 163.5, 34149 Basovizza, Trieste Italy
[3]Università degli Studi di Trieste, via A. Valerio 10 – 34127 Trieste, Italy, cosmi@units.it

Introduction

Pultrusion is one of the most attractive technological process for obtaining polymer matrix composite parts to be manufactured with large production rates and volumes [1-3]. Due to this characteristic and to some peculiar aspect of their physical and mechanical behaviour, pultruded composite are getting more and more used in structural applications in civil infrastructure. This is due to the progress made in pultrusion technology, that allows to manufacture low-cost large-scale load carrying structural profiles. These composites do not need painting, do not conduct electricity (thus, not needing to be insulated) and, thanks to their lightness, they allows to reduce transportation costs and environmental pollution. Bearing these considerations in mind, it seems clear why they are becoming a serious alternative to metal alloys for the construction of shaped beams, pedestrian bridge decks, post for railway noise barriers, floors of bus and other structural parts [4-6].

However, their application in structural engineering is still somewhat limited by the incomplete knowledge about the fatigue strength, so that the behaviour of pultruded composite under time variable loads is not completely investigated and understood. In fact, there are few data that can be found in the references. In [7] a comparative study between the fatigue behaviour of GRP hand lay-up and pultruded phenolic composites is described, but the maximum number of cycle of interest is limited to 1 million, thus preventing the application of these data to longer life-span, typical of civil infrastructures. In [8] the long-term environmental fatigue behaviour of pultruded glass-fiber-reinforced composites under flexural loading is investigated, while [9] describes the tensile fatigue performances of pultruded reinforced polymers profiles, with particular emphasis on the effect of the specimens shape on the fatigue strength and endurance. In the same paper some results obtained from fatigue tests up to 10 million cycles are reported, but the results number is limited and does not allow the determination of a fatigue limit. In [10] the rotating bending fatigue strength of a pultruded glass fiber reinforced composite is investigated.

Most of the studies published until now does not investigate the evolution of fatigue damage during the repetition of the fatigue cycles from a microstructural point of view. This prevents a complete understanding of the fatigue behaviour of pultruded materials. This lacking of knowledge also prevents the definition of fatigue strength assessment criteria based on analytical models defined on the basis of the observed   real damage mechanisms more than on empirical elaborations of the results of fatigue tests.

A deep microstructural analysis of fatigue damage is also important to understand which could be the most appropriate techniques to monitor in real time the status of a pultruded fatigued materials, or which could be the most appropriate non destructive techniques for inspections if the application of a damage tolerant design philosophy is used.

In this paper an experimental investigation aimed to a better understanding of damage evolution of a fatigued pultruded material is described. Fatigue tests were carried out on smooth specimens to obtain the S-N curve of the material. Some tests were interrupted at different stress levels and after a different number of load cycles and were subjected to micro-tomography, with the aim to observe the damage mechanism and the evolution of fatigue damage at different stress levels. X-ray microtomographies were performed with a conventional source at Tomolab (a facility of SYRMEP at Elettra, the synchrotron in Trieste) and allowed to observe the progression of fatigue damage.

The experimental analysis is still being carried on but the results obtained until now are encouraging.

Material

The material is a glass-fiber reinforced composite obtained by pultrusion. The matrix is made of equally distributed polyester not saturated resins commercially called Leguval W 24 GA and Synolite 0175-N-1. The global density of the matrix is about $1,3$ g / cm^3. The glass fibers have a ultimate tensile strength of 1800 MPa, an elastic modulus of 76 GPa and a density of 2.53 g/cm^3. About glass fibers, most of them (84%) are unidirectional (Roving) while the remaining part (Mat and Volumat) (16%) is randomly distributed.
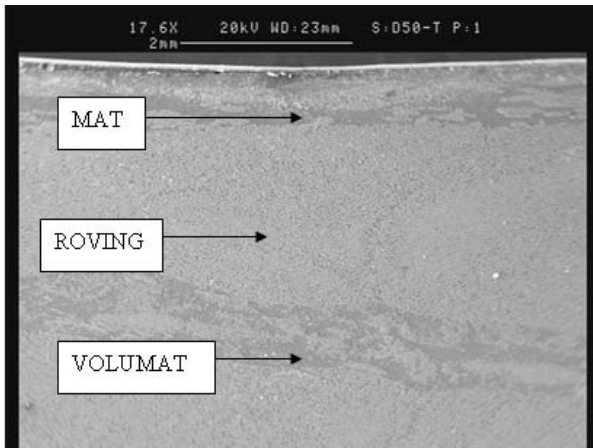
Fig. 1 - SEM micrograph showing Mat, Roving and Volumat layers.

In Fig.1 it is shown a micrograph of the transversal section taken at the SEM showing the main layers of the material.

Computed X-ray microtomography

Computed microtomography (micro-CT) is one of the most advanced techniques in the field of non-destructive evaluation tests. It allows imaging of the internal microstructure of different objects and materials by measuring the 3D X-ray attenuation coefficient map of the sample. The X-rays produced by the source hit the sample, which is placed on a rotary table. The X-rays travelling through structures with different densities and compositions are differently adsorbed and the emerging radiation is then collected on the detector plane, located on the other side of the sample.

This way, a large number of radiographs (projections) of the sample are taken at small angular increments over a 180 degrees rotation; from the projections is then possible to reconstruct the internal 3D microstructure of the sample, using a well known mathematical algorithm based on filtered back-projection method.

The samples were subjected to micro-computed tomography at Tomolab, yielding a series of X-ray based cross sectional images of the samples. A micro focus RX source (focal spot 5-40 micrometers, voltage up to 130 KV and currents up to 130 micro-ampere) was used. The CCD detector had a 12.5 micron pixel size, 12 bit dynamic range and a 50x33 mm field of view and was coupled with a Gadolinium Oxy-sulfide screen for X-rays conversion.

Experimental results

The experimental work is still on course: in Fig. 2 the 2D reconstruction of a damaged specimen is shown: the fatigue cracks can be clearly observed. Other analysis are under development and will allow to understand the dynamic of fatigue damage.
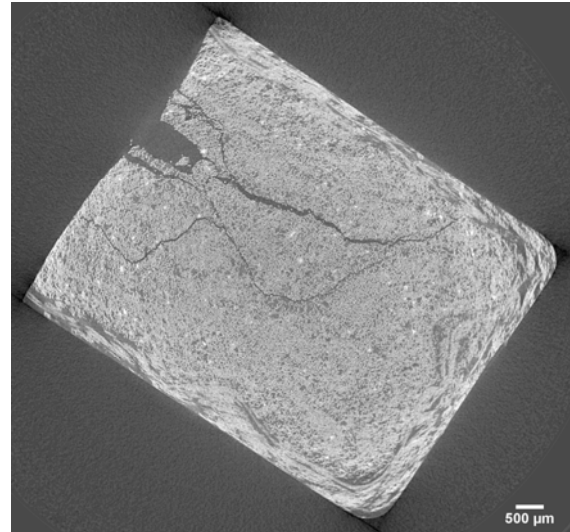
Fig. 2. Reconstruction of a 2D cross-section of a cracked specimen.

References

1. F.S. Trevor, Pultrusion for Engineers", CRC Press, Woodhead Publishing, Ltd, Cambridge, 2000.
2. B.T. Åmström, Manufacturing of Polymer Composites, Chapman & Hall, London, 1997.
3. J.P. Fanucci et al., Pultrusion of Composites, in: T.G. Gutowski (Ed.), Advanced Composites Manufacturing, J. Wiley & Sons, New York, 1997, pp. 259-295.
4. L.-H. Gan, L. Ye, Y.-W. Mai, Optimum design of cross-sectional profiles of pultruded box beams with high ultimate strength, Composite Structures 45 (1999), 279-288.
5. A. Di Tommaso, S. Russo, Shape influence in buckling of gfrp pultruded columns, Mechanics of Composite Materials 39 (4) (2003), 329-340.
6. M. Guagliano, Fatigue behaviour of a pultruded composite box-shaped post for high speed railway application (in Italian), Internal Report 48/2004, Politecnico di Milano.
7. C. Moura Branco et al. , A comparative study of the fatigue behaviour of GRP hand lay-up and pultruded phenolic composites, Int. J. Fatigue 18 (4) (1995), 255-263.
8. K. Liao, C.R. Schultheisz, D.L. Hunston, long-term environmental fatigue of pultruded glass-fiber-reinforced composites under flexural loading, I. J. Fatigue 21 (1999), 485-495.
9. T. Keler, T. Tirelli, A. Zhou, Tensile fatigue performance of pultruded glass fiber reinforced polymer profiles, Composite Structures 68 (2005), 235-245.
10. L. Vergani, Damage mechanisms in pultruded unidirectional fiber reinforced composites under static and fatigue loads, in: M.Guagliano, M.H. Aliabadi (Eds.), Fracture and Damage of Composites, WIT Press, Southampton, 206, pp.49-72.

DEVELOPMENT OF SURFACE DYNAMIC MECHANICAL ANALYSIS TESTS FOR TPU MATERIALS

A. Hausberger [1)], I. Gódor[2)] T. Schwarz[3)] and Z. Major[3)]

[1)] Polymer Competence Center Leoben GmbH, Rosegger Str. 12, 8700 Leoben, Austria.

[2)] Chair of Mechanical Engineering, MUL, Franz Josef Str. 18, 8700 Leoben, Austria.

[3)] SKF Economos Austria GmbH, Gabelhoferstrasse 25, 8750 Judenburg, Austria.

[4)] Institute for Polymer Product Engineering, JKU, Altenberger Str. 69, 4040 Linz, Austria

Corresponding author: andreas.hausberger@pccl.at

1. Introduction

The stick-slip behaviour of elastomers plays an extraordinary important role under service loading conditions in many tribological applications [1].

2. Experimental

The experimental set-up of the ring-on-disc (RoD) test set-up on the dynamic testing machine is shown in fig. 1. The same specimen geometry and the surface quality was used as previously in classical friction and wear tests.

Fig. 1: Test set-up for surface DMA tests.

During these tests a continuous rotational movement of the torsional drive with varying normal load and rotational speed was realized and a representative result of these tests is plotted in fig. 3. However, this type of test does not provide sufficient information about the stick-slip behaviour of the elastomer specimen. Hence, a novel method was developed and implemented on an electrodynamical testing machine. The rotational drive has either a monotonic or an oscillating movement during these tests with varying frequency (f) and angle (φ) and the normal load (F_n) was also varied.
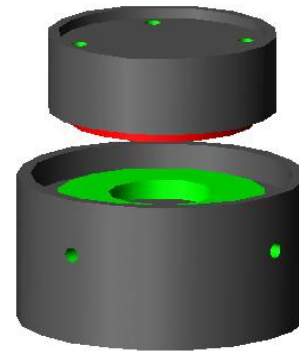
Fig. 2: Test fixture along with the specimen and counterpart for surface DMA tests.
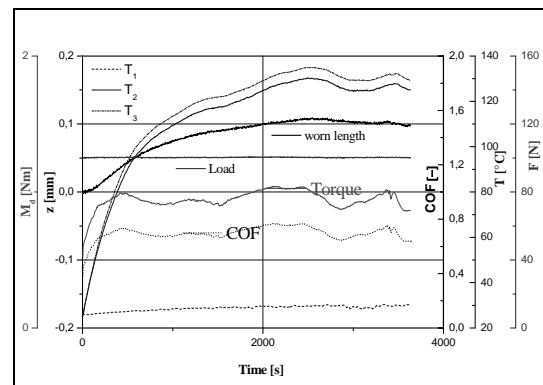
Fig. 3: Results of the friction tests using RoD test set-up.

While the test with monotonic actuator movement can be compared with bulk monotonic monotonic torsion tests, the cyclic loading is very similar to the well-known dynamic mechanical analysis (DMA) tests and called as surface DMA. However, due to the different physical processes, a novel data reduction procedure should also be developed.

3. Results

Torque-rotation (M-φ) curves at various normal loads at low loading rate under monotonic loading are shown in fig. 4a for an unfilled TPU specimen.
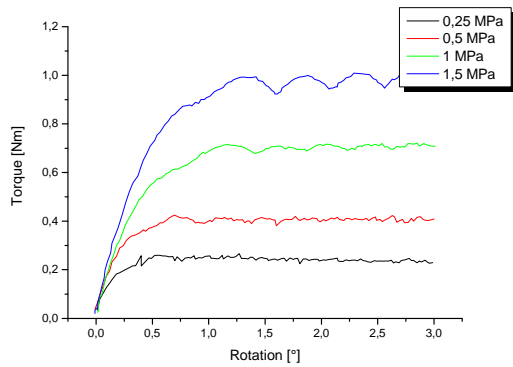
(a)
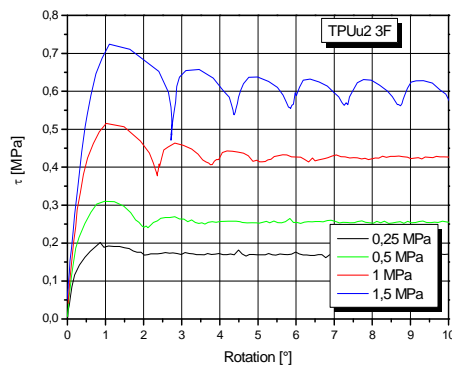
(b)

Fig. 4: Monotonic torque-rotation curves at various normal loads and for various loading rates.

The shear stress was also calculated and curves are shown in fig. 4b. Based on these results the rotation range for the cyclic test was assigned. It is assumed that the first maximum of these curves show the onset of the slip and the first minimum is the onset of the subsequent stick. Hence, cyclic surface DMA experiments were performed over a wide frequency range at various rotations up to about 3° using unfilled TPU materials. The corresponding hysteretic torque-rotation (M-φ) curves are plotted for 1.5 MPa normal stresses in fig. 5a for a low frequency (0.01°/s) and fig. 5b for a higher frequency (1 °/s).
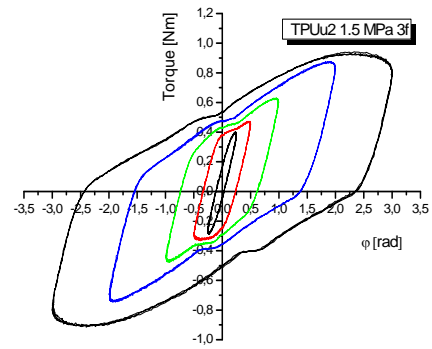
(a)
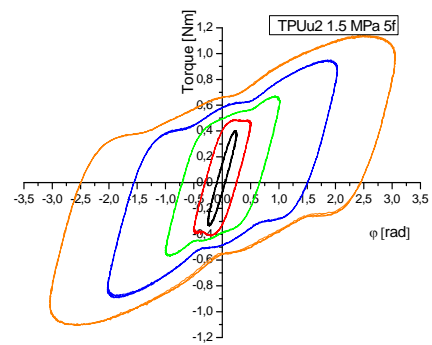
(b)

Fig. 5: Cyclic torque-rotation hysteretic curves at a normal load of 1.5 MPa.

The change between the linear material behaviour through non-linear behaviour to gross-slip are clearly visible on these plots.

4. Acknowledgements

5. References

[1] G. Heinrich, M. Klüppel Wear, 265, Issues 7-8, 20 September 2008, Pages 1052-1060.

COMPARISON OF DIFFERENT MEASURING METHODS FOR POSITIONING OF A RECORDING DEVICE IN LARGE MODELS

Andreas Hrdlicka[1], Friedrich Bleicher[2], Boris Huber[1], Karl Fuchs[1], Christoph Einspieler[2], Johannes Bernreiter[2], Norbert Krouzecky[1]

[1] Vienna University of Technology, Institute of Hydraulic and Water Resources Engineering, Department of Hydraulic Engineering, A-1040 Vienna, Karlsplatz 13, Austria,

[2] Vienna University of Technology, Institute of Production Engieering, A-1040 Vienna, Karlsplatz 13, Austria,

Corresponding author: norbert.krouzecky@tuwien.ac.at

1. Introduction

Within the framework of the Integrated River Engineering Project a hydraulic model with a movable bed was to be constructed for the analysis of the Austrian Danube section east to Vienna. On this occasion different systems and methods for measuring lengths were to be compared, in order to implement an optimised system in the course of the aforementioned project.

The horizontal measures of the simulation model were 50m x 16m. An additional requirement was that a one meter difference in height can vertically be measured at every point of the co-ordinate system.

Fig. 1: Total view of the model of the Danube to the east of Vienna

The geometric ranges of tolerance and the required measuring frequencies were pre-determined. Additionally the basic conditions due to implementation in a continuing test operation and the constructive and economic pre-requisits needed to be taken into account.

Based on the determination of the position of the recording device, the mechanic control should then be coupled with the positioning system in order to be able to control the device automatically and online in the test.

2. Selection Criteria of the Measuring Systems

Within this three-dimensional measuring range accuracy in measuring horizontally needed to be one centimeter maximum, vertically within a millimeter range. Repetition rate while measuring must not exceed 1 Hz, since simultaneous control of the recording device needed to be guaranteed (online measuring).

Additional requirements were consideration of vibrations and potential deflexion of the measuring bridge. Failures such as contamination caused by sand, local fluctuations in humidity, e.g. caused by spray, as well as water reflections also needed to be reflected in the evaluation.

3. Description of Different Systems

The measuring methods analysed for this project can be divided into three main groups:

3.1 Electric measuring of length

Analogue detection of values

The measured values are converted into an electric signal and amplified, i.e. the factor of the

electronic value used in the respective method changes proportionally to the recorded change of length. Depending on the system, the recording of the values can be done mechanically with contact or without contact.

Digital detection of the values

The measured values recorded incrementally or coded are assigned to a signal, which is a reflection of the value. The original value is a digital signal, a sum of counts. The change of the value is recorded through the movement of a recording device.

3.2   Optic measuring of length

Interferometric measuring of length

If two beams of light are superimposed, light interferences in the form of periodic fluctuations in brightness can be monitored, if both waves are moved towards each other. The number of occurring interferences multiplied with the wave length of the light show the length of displacement in relation to the other wave.

3.3   Opto-electronic measuring of length

This method is conducted without contact, the measuring signal is processed either digitally or analoguely.

In contrast to interferometric measuring of lengths, where the reflector for measuring can be moved from the beginning to the end of the length, this method has a distance meter installed on one end and a reflector on the other. The distance meter sends out a visible or infrared light, which is diverted by the reflector or the reflection sheet and is received by the distance meter. The delay of the signal is measured and is the basis for calculating the distance.

Triangulation method

A bundled light beam (e.g. laser beam) is vertically directed to the surface of a testing object. The light is reflected diffusely and directed to a receiver (diode line or photo detector) through a lens system. A different distance between object and receiver causes a change of angle of the reflected light beams. The changed position of the image of the light spot at the diode line corresponds to the allocated change in distance.

4. Choice of the Measuring System

Based on the theoretic approaches of the measuring methods and the economic reasons a system was developed, which combines the advantages of a guide rail construction with an opto-electric length measuring system. The Institute of Production Engineering of the

University of Technology, Vienna was in charge of the realisation.

Several triangulating laser measuring probes (triangulation methods) by Festo are used for length measuring systems [1].

Fig. 2: Measuring bridge with the measuring platform and five mounted laser triangulation sensors

Due to this development it is possible to move the measuring device on every trajectory and to choose almost any velocity. Measuring accuracy horizontally is ±2 mm and vertically ±0,5 mm.

5. References

[1] F. Bleicher et. Al.: "Development of a measuring system for the analysis of hydraulic models of the size of 50x16 m by the use of numerical control technology", Proceedings of the 25th Danubia Adria Symposium, Ceske Budejovice, Czech Republic, September 2008

RESISTANCE OF TELESCOPIC COVER SEALING

Jan Hudec [1), Petr Kolar [1), Pavel Barta [1)

[1) RCMT, Czech Technical University in Prague, Horska 3, 128 00 Prague, Czech Republic.

Corresponding author: j.hudec@rcmt.cvut.cz

1. Introduction

Machine tool manufacturers begin to focus on optimizing peripherals such as telescopic covers [1]. Passive resistance of covers and its sealing wipers in particular becomes more significant factor of drive power dimensioning.
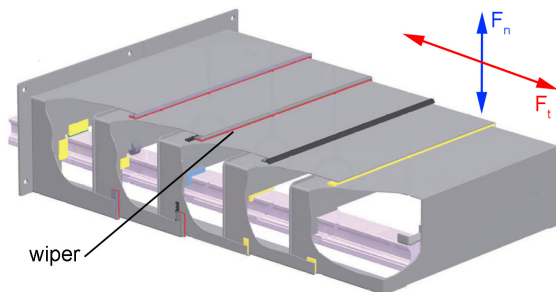
Fig. 1: Telescopic cover - Direction of wiper friction and resistance forces (F_t and F_n)

2. Sealing wiper

Wiper is a polyurethane profile sealing gap between moving metal sheet segments of telescopic cover.

Physical behaviour of sealing wiper has been examined by a mathematical model and it has been verified by an experiment [2]. Its stiffness characteristic is bilinear respecting two contact zones of the wiper (compliant wiper lip and stiffer sealing plane).
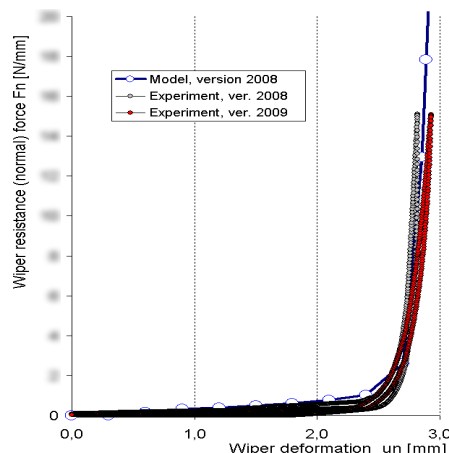
Fig. 2: Comparison of experimental and modelled stiffness characteristics

3. Mathematical model

A mathematical model of cover sealing has been developed. This model predicts behaviour of cover segments deformed by sealant preload during its extension and contraction. These sealing wipers are placed between all top (sloped) segment planes.

This parametrical model (Ansys) allows modification of cover geometry, load and boundary conditions. Result of this model is a set of data ready for postprocessing (Matlab).

3.1 Mesh

A mapped mesh is used for rectangular planes of segments, other planes use free mesh. Metal sheets are represented by SHELL63 elements.

Wipers are substituted by nonlinear COMBIN39 springs due to their bilinear stiffness characteristic (fig. 3).
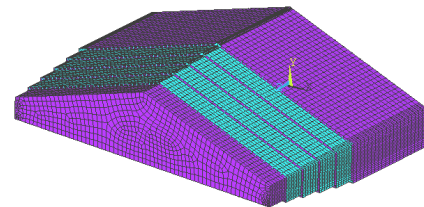
Fig. 3: Resulting mesh of metal sheet segments

3.2 Boundary conditions
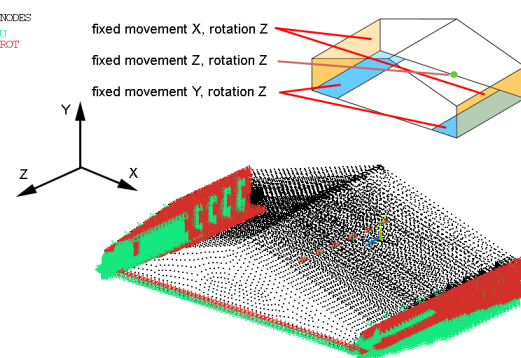
Fig. 4: Applied boundary conditions

Boundary conditions were applied to guiding planes and connection points of scissor mechanism assuring relative movement of segments.

3.3 Computation results
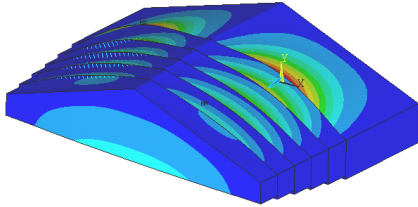
Fig. 5: Nature of cover deformation

Figure 6 shows resistance (normal) forces of all wipers along their length. Wiper deformation and frictional (tangential) force F_t are directly proportional to this resistance force.

It is obvious that the outer cover segment is the most compliant one, because it is not supported by any other segment.

This model also shows whether the wiper is in contact with the segment below to assure sealing functionality. If the normal force of any segment reaches zero, it means that there is no preload of wiper. Zero preload represents gap between wiper and the segment. This can happen in case of large cover and it must be prevented by cover modification [3].
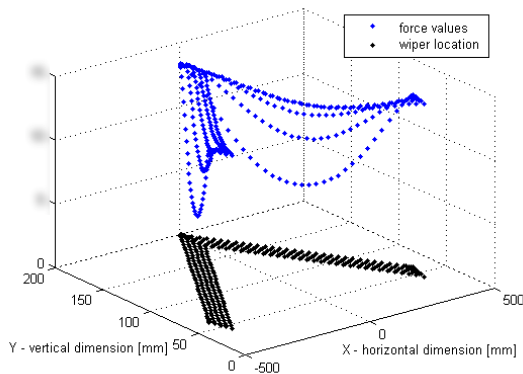
Fig. 6: Normal force curve along wiper length; all wipers in contact with segments

4. Frictional forces

It is possible to make the previous analysis for any extension state of a cover. An overview of frictional forces behaviour during cover extension can be obtained this way (1).

$$F_t = f \cdot F_n , \qquad (1)$$

where f is a friction coefficient of contact materials.
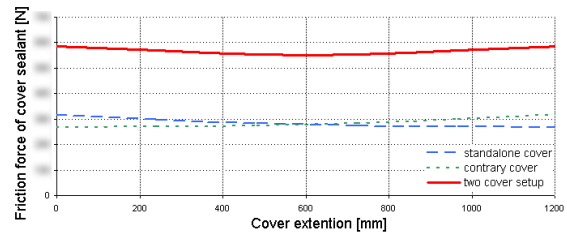
Fig. 7: Frictional force during cover extension

Figure 7 shows 15 % difference of cover sealant frictional force during cover extension. In case of two covers usually mounted onto movable axis of a machine tool, this difference is lower (5 %). This difference is caused by change of relative distance of wipers that provide support of compliant segments.

5. Conclusion

Computational simulation and characteristic of wiper resistance and friction forces presented in this contribution reveals the nature of segment deformation and possible sealing issues caused by wiper preload and segment geometry. It is also possible to predict the friction force curve during the cover extension.

6. Acknowledgements

7. References

[1] J. Smolik, New Emerging Materials and Structures in Field of High Speed Machine Tools. High Speed Machining, Sixth International Conference, San Sebastian 2007

[2] J. Hudec, P. Skacel, P. Kolar, Prediction of Sealing Wiper Resistance Force. 8th Youth Symposium on Experimental Solid Mechanics, Győr 2009 [poster]

[3] J. Hudec, P. Kolar, P. Barta, Complex Model of Two-axis Telescopic Covers: Dimensions and Cover Deflection Avoidance. 3rd International VIDA conference, Poznan 2007, ISBN 978-83-7143-388-7

STRENGTH OF MICRO-BONDED JOINTS WITH CONDUCTIVE ADHESIVES

Kozo Ikegami [1],

[1] Tokyo Denki University, Department of Mechanical Engineering, Kanda-Nishikicho 2-2,

101-8457 Tokyo, Japan.

Corresponding author: kikegami@cck.dendai.ac.jp

1. Introduction

Lead solder is used widely as joining material in many electronic devices and electrical equipment. But the lead is considered to be one factor of environmental pollution and the use of lead is regulated. Joining material free from lead is expected for electronic devices as well as electrical equipments. Conductive adhesive is one substitute joining material for lead solder. There are several papers on the properties of conductive adhesives [1][2][3][4]. But there are few papers on mechanical properties of micro-bonded part with conductive adhesives. This paper presents the experimental results of mechanical properties of micro-bonded joints with conductive adhesives under tensile and torsional loads.

2 Specimens and Testing Equipment

2.1 Conductive adhesives

Conductive adhesive used to the experiment is mixture of adhesive resin and conductive filler. The adhesive resin is epoxy resin and the conductive filler is silver filler with the shape of flake and sphere. The flake and sphere fillers make surface contact and point contacts in the adhesive resin, respectively. Therefore the flake filler is expected to produce higher electrical conductivity than the sphere filler. In the experiment, the effects on the mixture content of the filler on the strength are experimentally investigated for the single filler and the mixed filler. Table 1 shows the filler content used to the conductive adhesive.

2.2 Specimen

The specimen is prepared by overlapping two

Table 1 Content of conductive filler

Specimen	Content (wt%)	Distribution content	
		sphere	flake
A	45	0	10
B	45	3	7
C	65	0	10
D	65	3	7
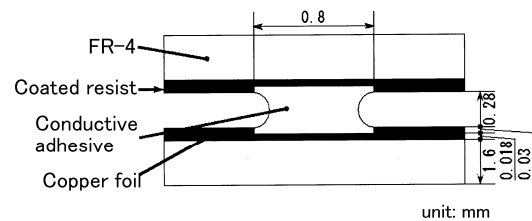
Fig. 1 Cross section of bonding part

printed wire boards with the conductive adhesive resin. The material is FR-4. The copper foil is coated on the board in the diagonal direction of the board. The change of electrical conductivity during loading tests is measured through this copper foil. The conductive adhesive resin is put on the center point circle with diameter 0.8mm of the copper foil. Then the two boards are adhered by overlapping each other. The specimen is cured for one hour at 130 centigrade under pressure 5MPa. The rod with the diameter of 0.28mm is put between two boards to keep the constant distance of the two boards. Figure 1 shows the cross section of the adhesively bonded part.

2.3 Testing equipment

Experiments are conducted by using the testing machine. The machine of consists of vertical moving stage and rotational stage. These stages are able to apply tensile and torsional loads as well as their combined loads to the specimen.

3 Experimental Procedures

The experiments are conducted by subjecting tensile and torsional loads to the specimen at room temperature. The strength are investigated during the loading tests. The tensile stress of the specimen is calculated by dividing the applied load with the cross sectional area on the bonded testing board. The tensile strain is calculated with the change of distance of bonded board by tensile loading. The torsional stress is defined by torsional moment and the diameter of bonded area on the testing board. The torsional strain is calculated by rotational angle of the bonded area.

The tensile loading test is conducting by moving the vertical stage with the speed of 1 micron per second. The torsional loading test is conducting by rotating the rotational stage with the speed 0.1 degree per second.

4 Experimental Results and Discussions

4.1 Tensile and torsional strength for different filler content and distributions

Figures 2 shows the fracture stresses of the micro bonded part with conductive adhesive resin for tension. The conductive adhesives have different filler contents and distributions as shown in Table 1. The tensile fracture stresses for both single and mixed fillers decrease slightly with increase of filler content comparing with specimens A, B, C and D. The strength of specimen A and C is higher than the strength of specimen B and D, respectively. The mixture of flake and spherical fillers reduce the tensile strength.

4.2 Strength for combined tensile torsional loads

Figures 3 shows the strength of joint with mixed fillers under combined tension and torsion. The points are experimental strength and the curve is Mises condition determined by the tensile strength as the reference stress value. The experimental values are slightly larger than Mise conditions. The tensile strength is equal approximately to the torsional strength.
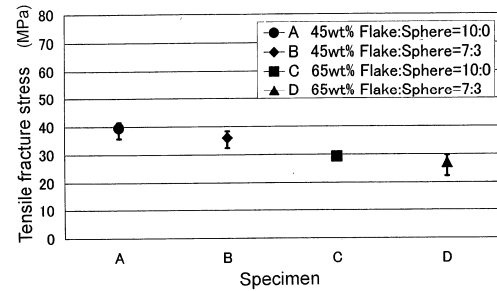
Fig. 2 Tensile strength for different filler contents
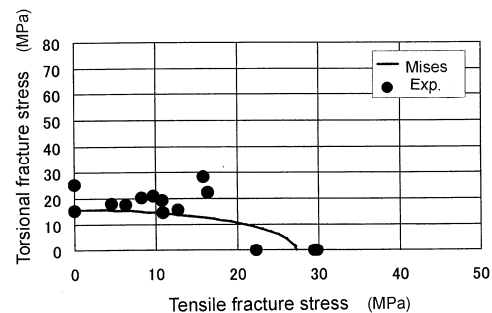
Fig. 3 Combined strength for mixed filler content

5 Conclusions

1. The tensile joint strength for both decreases with increase of the filler content.
2. The mixed sphere and flake fillers reduce the strength comparing with the sphere or flake filler under the same filler content.
3. The joint strength with mixed fillers under combined tension and torsion is approximated by Mises condition.

References

[1] T. Matsumura, R. Takahashi, K. Nagata, M. Ochi, The Journal of Adhesion Society of Japan, **38**: 78-84, 2002.

[2] S. Xu, D. A. Dillard, J. D. Dillard, International Journal of Adhesion and Adhesives, **23**: 235-250, 2003.

[3] T. Tan, X. Qiao, J. Chen, H. Wang, International Journal of Adhesion and Adhesives, **26**: 406-413, 2006.

[4] M. Masuko, S. Takeda, The Journal of Adhesion Society of Japan, **40**: 136-145, 2004.

DEVELOPMENT OF A FUNCTIONAL MODEL FOR A 3D SCANNER

Rajcho Ilarionov [1]

[1]Technical University of Gabrovo, Faculty of Electrical Engineering, Dep. Computer Systems & Technology , H.Dimitar-Str 4, 5300, Gabrovo, Bulgaria

Corresponding author: ilar@tugab.bg

1. Introduction

Modern engineering design is performed using the so-called CAD systems. They include not only software and computing environment, but also input/output devices for 2D and 3D graphic information. This design often requires the input of real three-dimensional objects for the purposes of creating models, measuring parameters or inspection. This is done by means of devices that are commonly referred to as **,,3D scanners"**.

2. Methods

From the consumer point of view, a three-dimensional scanner is any device that automatically collects three-dimensional coordinates from a body surface in a certain sequence. In technological terms, it is a 3D positioning system with 5 degrees of freedom. The mechanical diagram of such a system is shown in Fig. 1. Its purpose is to position the measuring head in the 3D space determined by the scanner shape, take a measurement in each of the desired points and form an output file of the arranged X, Y, Z sequence describing the 3D object.

On the basis of the research done about the features of the commonly used 3D scanners, the following minimum set of basic functions have
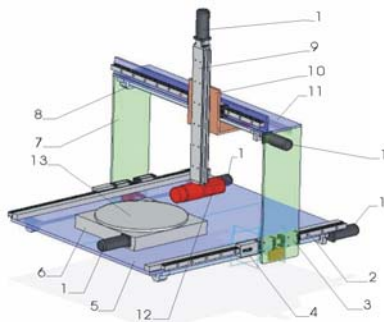
Fig. 1: Positioning system of portal type

been specified:

- positioning system orientation;
- manual movement and positioning;
- ability to scan and record the coordinates for grading purposes;
- setting and storing of scanning programmes;
- automatic scanning according to the set programme;
- automatic tracking and maintaining a position in the measurement range of the laser head.

After a thorough analysis of the above requirements, three basic operation modes can be defined for the scanner:

- Reference mode;
- Manual mode;
- Automatic mode.

On the basis of the considerations presented above, a functional model of a 3D scanner has been assembled, which is shown in Fig. 2.
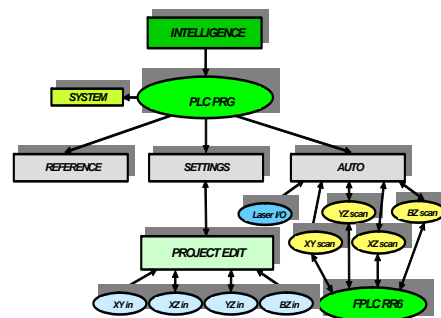
Fig. 2: Functional model

3. Experimental Results

The functional model underlies the structure of the software. It consists of 2 organizational blocks (OB) and 15 functional blocks (FB). It includes three basic operation modes of the scanner:

Referencing mode (FB: Referencing). It is activated whenever the system is switched on. Before the other procedures are performed, the scanner has to be orientated (finding the coordinate system origin), since all other distances are measured relative to these coordinates. Unless it is orientated, operation in another mode is not possible.

Settings mode (FB: Settings/Manual). It is activated for creating or editing projects of the scanned objects. It makes possible manual movement along all axes, as well as visualization of the current position and the distance measured by the laser head. The surfaces used for scanning when creating a new project are XY, XZ, YZ, BZ (B – rotation axis). Each of the objects subject to scanning is described by n surfaces, which determine its complexity. The parameters that are set for each new surface are: start point, end point, measurement range and scanning step.

Automatic mode (FB: Auto). It performs automatic scanning of objects according to projects made in advance, beginning with the surface entered first in the project, monitoring the start and end points and cyclically moving the axes from the scanned surface with the step assigned. The range of the measuring head is controlled and the distance to the scanned object is corrected. The positioning of the axes and the control of the laser head are performed by a synchronously executable organizational block, which defines execution time of 1ms. The operation mode is consecutive and has been divided into two clocks. The first one is positioned to a subsequent point with an assigned step. The second clock is laser head control – start of measurement, validity of the data measured and record of coordinates.

The user interface defines the way in which the interactive dialogue between the user and the computing environment is accomplished during the scanning process. For this purpose dialogue screen pages are created by means of which the software provides certain visualization for each mode, which enables the operator to perform settings, create new programmes and add different programmes for scanning, status visualization, current coordinates, etc. Suitable visualization has to be developed for each of the three operation modes with the respective menus and buttons.

Fig. 3 shows the proposed screen layout of the user interface. When the scanner is started this mode is the first to be displayed. It provides a button menu for selection of all
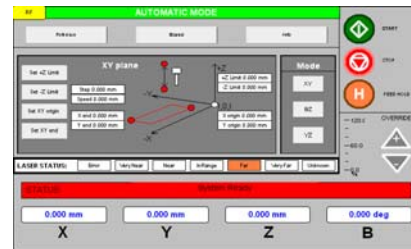
Fig. 3: User interface

menus, buttons for selecting manual or automatic referencing (in sequence Z,X,Y,B), start and stop buttons for referencing, status visualization of the servo-system and the laser head, visualization of the current coordinates and buttons for manual positioning along all axes (the latter are needed in case the system is in a location unsuitable for starting the Referencing mode).

The general view of the 3D scanner is shown in Fig. 4.

Fig. 4: General view of the scanner

4. Conclusion

The proposed functional model underlies the software that has been developed. It allows scanning of arbitrary bodies presented in a cylindrical model or as a set of surfaces. The scan output file is an arranged sequence of X,Y,Z points describing the object. A programme driver has been developed for the scanner for presenting the information in CAD environment.

5. Reference

[1]. Description of CODESYS software product.
[2]. Ilarionov, R. Computer peripherals G, University publishing house "Vassil Aprilov", 2008.

A COMBINED ANALYSIS OF THE STRESS STATE IN THE JAW DEVICE OF AN EQUIPMENT FOR STRETCHING ALUMINUM PLATES

Nicolae Iliescu[1], Costica Atanasiu[1], Stefan Dan Pastrama[1], Gabriel Jiga[1], Radu Canarache[2],

[1] University "Politehnica"of Bucharest, Department of Strength of Materials, Splaiul Independentei, nr. 313, Sector 6, 060042, Bucharest, Romania.
[2] INICAD DESIGN, Str. Popa Tatu, nr. 20, Sector 1, 010805, Bucharest, Romania.

Corresponding author: nviliescu@yahoo.com

1. Introduction

The 50 MPa equipment designed to stretch aluminum plates is made of two jaws in which the ends of the plates are fixed. Each jaw has eight lamellae, drilled and cross-cut at the lower side. The aluminum plate is fixed in the lamellae through a system of clamping dies made of two flattening beams and two wedges (Fig. 1).
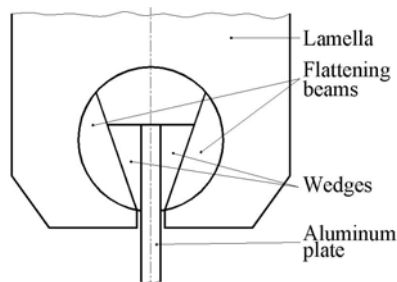
Fig. 1: The fixing system of the aluminum plate

For a correct evaluation of the performances and the technological parameters of the equipment in service, an experimental study was undertaken for the model of a lamella, using the photoelastic technique. The obtained results were compared with numerical results, yielding from Finite Element analyses.

2. Experimental analyses

The stress state that appears during the stretching process of the aluminum plates was experimentally investigated using the two-dimensional photoelastic technique.

The model of a lamella was manufactured at a scale of 1:20 from a cold casted Araldite – D plate having a thickness $b = 6.5$ mm. The flattening beams were modeled as circle segments made of a Plexiglas plate with a thickness of 9.5 mm. The aluminum plate was considered wedged using the wedges and flattening beams. That is why the whole assembly plate – wedges was modeled as a single wedge made also of a 9.5 mm thick Plexiglas plate. The photoelastic measurements were undertaken for three different positions of the wedges, found often in the real process of stretching (Fig. 5).
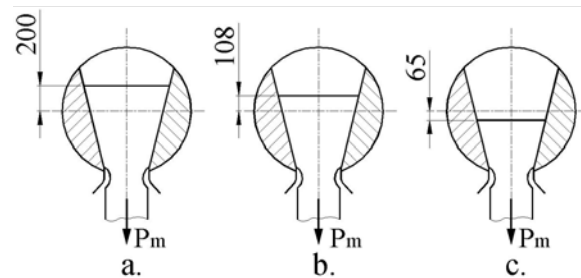
Fig. 2: The considered positions of the wedges

The photoelastic model was loaded in traction with a force $P_m = 362.4$N applied through the wedges and the flattening beams. The traction force was measured with a force cell, mounted on the axis of the screw.

The isoclines and the isochromatic fringes (Fig. 3) were recorded corresponding to the three considered positions of the wedges.
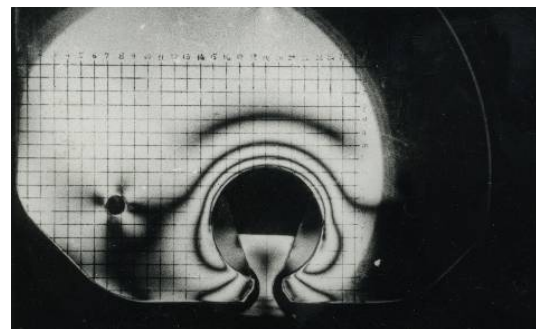
Fig. 3: The isochromatic fringe field (Case 1)

In order to obtain the values of the principal stresses σ_1 and σ_2, a rectangular grid was drawn on the surface of the models. Knowing the values of the fringe order N and the parameter α of the isocline in each node of the grating, the values of the principal stresses σ_1 and σ_2 were determined using the Frocht method [1,2].

For the points situated on the contour of the hole but outside the contact area, only the principal stress σ_1 appears, since the contour is not loaded ($\sigma_2 = 0$). In this case, σ_1 can be obtained directly from the experimental data, using the equation:

$$\sigma_1 = N \cdot f_\sigma \qquad (3)$$

where N is the fringe order experimentally determined and f_σ is the photoelastic constant of the model obtained through a calibration procedure.

In order to obtain the real values of the stresses in the lamella, the results of the photoelastic measurements can be transferred to the real structure, taking into account the scale factors for forces and lengths.

With the data obtained from the above calculations, the variation curves of the principal stresses on the contour of the hole were plotted (Fig. 4).
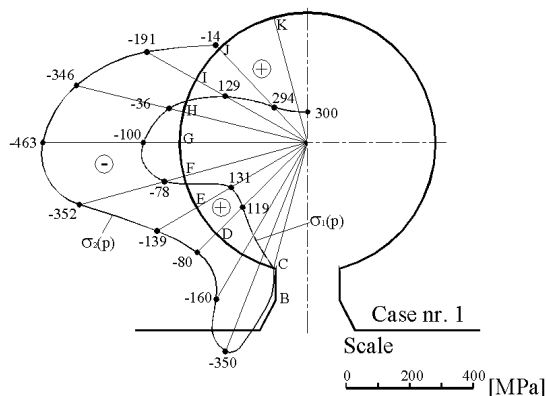
Fig. 4: Principal stresses on the contour of the hole (Case 1)

3. Comparative results

A finite element model was conceived in order to study the behavior of the fixing system in elastic regime. The comparative plot of the principal stresses obtained with the finite element analysis and the photoelastic technique respectively, is shown in Fig. 5 for the first analyzed case.
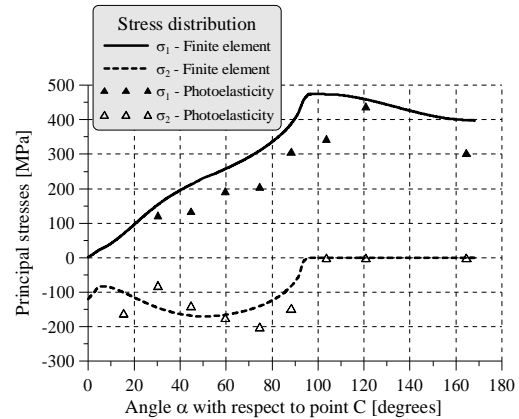
Fig. 5: Comparative plot of the principal stresses (Case 1).

4. Conclusions

A comparative stress analysis was undertaken in order to determine the stress distribution on the contour of a drilled plate. The structure was subjected to traction by a concentrated force, applied in the axis of the hole through a system of wedges. Very refined photoelastic analyses were performed in order to study the behavior of three different positions of the wedge. A finite element model was also conceived in order verify the experimental results. The values of the principal stresses obtained with the two considered methods are in good agreement, showing thus that the numerical model is reliable and can be used for further non-linear analyses.

The stress distributions for the three analyzed cases are similar. The maximum value of the stress σ_1 appears outside the contact zone, while the principal stress σ_2 is maximum near the horizontal diameter. The most unfavorable situation appears in the areas where σ_1 has the maximum positive values.

5. References

[1] Dally, W. J., Riley, F. W. - Experimental Stress Analysis, Mc Graw-Hill, New York (1992).
[2] Holister, G. S. - Experimental Stress Analysis, Cambridge University Press, (1967).

IDENTIFICATION OF ELASTIC PROPERTIES OF WOOD CELL WALLS BY MEANS OF NANOINDENTATION

Andreas Jäger, Thomas Bader, Karin Hofstetter, and Josef Eberhardsteiner[1]

[1] Institute for Mechanics of Materials and Structures, Vienna University of Technology
Karlsplatz 13/202, A-1040 Vienna, Austria.

Corresponding author: andreas.jaeger@tuwien.ac.at

1. Introduction

Wood exhibits a hierarchical structure and is composed of fibers which can be represented as hollow tubes oriented in stem direction (see Fig. 1(a)). The fibers are built up of a cell wall material consisting of stiff cellulose microfibrils which are embedded in a soft polymer matrix. The S2 layer of the cell wall occupies approximately 80 % of the cell wall and mainly contributes to the load bearing capacity of wood. Within the S2 layer, the stiff microfibrils are inclined to the longitudinal cell axis by the so called mircofibril angle, giving an approximately transversely isotropic material.
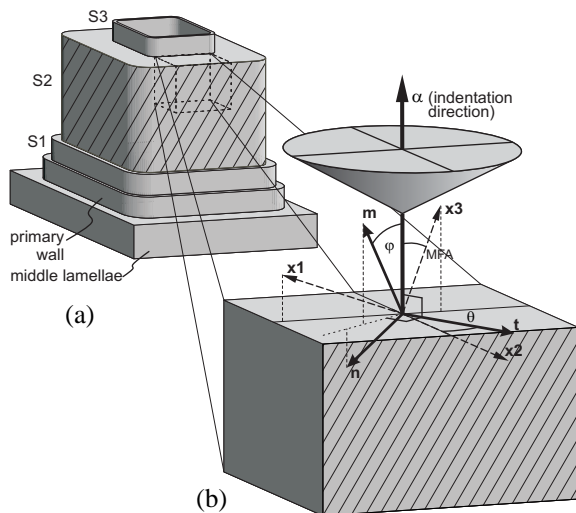
Fig. 1: (a) Wood fiber consisting of different cell wall layers and (b) conical indentation in S2 layer of wood cell wall: orientation of the material axis and indentation direction.

The mechanical properties of the S2 layer can be measured by tension tests on single wood fibers or by means of nanoindentation. As reported by several authors (see, e.g., [1]), the measured indentation modulus in longitudinal direction is considerably smaller than the expected Young's modulus in the same direction. This can be explained by the small transverse modulus of the cell wall which is far below the longitudinal modulus and strongly affects the indentation response. The aim of this paper is to provide a mechanically based relation between the transversely isotropic stiffness tensor of the wood cell wall and the indentation modulus obtained from NI tests.

2. Indentation modulus of transversely isotropic materials

Nanoindentation (NI) is a well known tool for the identification of mechanical properties at the micro- and nanometer scale of materials. In case of isotropic materials, the Young's modulus E can be obtained from the measured indentation modulus $M = E/(1 - \nu^2)$ if the Poisson's ratio ν is known. If NI is employed for testing the S2 layer of wood cell walls (see Figure 1(b)), i.e., an approximately transversely isotropic material, this simple relation is not valid. Applying the theory for indentation of a cone into an elastic anisotropic material developed by Vlassak et al. [2] shows, that the indentation modulus depends on all five independent elastic constants of the stiffness tensor and the microfibril angle (MFA) between the principal material axis $x3$ and the indentation direction α.

3. Validation of micromechanical model

Having at hand the relation between the stiffness tensor and the indentation modulus allows to validate models for the prediction of the stiffness of wood cell walls by comparing measured indentation moduli with indentation moduli predicted by the respective model. In the following, the micromechanical homogenization scheme for the prediction of the wood cell wall stiffness, presented in [3,4], is validated. With this homogenization scheme,

the transversely isotropic elastic behavior is computed based on the chemical composition and the microstructure of the cell wall. Having the elastic parameters at hand, the indentation modulus is determined as a function of the microfibril angle using the theory presented in Section 2. For model validation, experimental results given in [5,6] are used, where the lignin content and the MFA are tested in addition to the indentation modulus. Comparing the predicted indentation moduli with experimental values (see Figure 2), shows a very good agreement between model response and experiment.
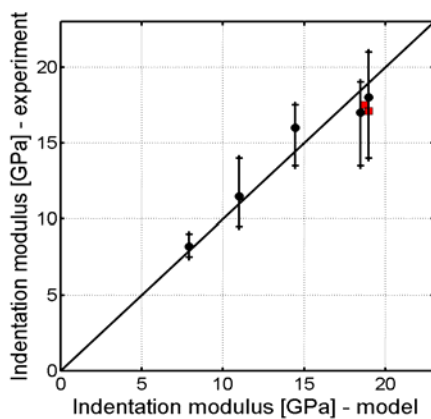
Fig. 2: Comparison of predicted and measured [6] indentation modulus.

Combining the micromechanical model with the model for the indentation modulus allows to study the influence of MFA and moisture content on the indentation modulus of wood cell walls. Figure 2(b) shows the decrease of the predicted indentation modulus with increasing MFA for a typical chemical composition of spruce and varying moisture content.
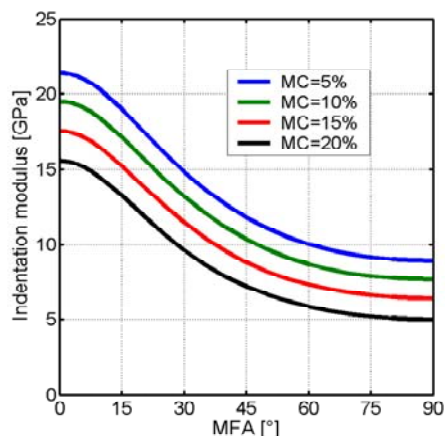
Fig. 3: Predicted variation of indentation modulus as a function of microfibril angle and moisture content.

4. Acknowledgements

5. References

[1] W. Gindl, T. Schöberl, The significance of the elastic modulus of wood cell walls from nanoindentation measurements. Composites A, Vol. 35 (2004) 1345-1349.

[2] J.J. Vlassak, M. Ciavarella, J.R. Barber, X. Wang, The indentation modulus of elastically anisotropic materials for indenters of arbitrary shape. Journal of the Mechanics and Physics of Solids, Vol. 51(9) (2003) 1701-1721.

[3] K. Hofstetter, C. Hellmich, J. Eberhardsteiner, Development and experimental validation of a continuum micromechanics model for the elasticity of wood. European Journal of Mechanics A/Solids, Vol. 24 (2005) 1030-1053.

[4] K. Hofstetter, C. Hellmich, J. Eberhardsteiner, The influence of the microfibril angle on wood stiffness: A continuum micromechanics approach. Computer Assisted Mechanics and Engineering Sciences, Vol. 13(4) (2006) 523-536.

[5] W. Gindl, H.S. Gupta, T. Schöberl, H.C. Lichtenegger, P. Fratzl, Mechanical properties of spruce wood cell walls by nanoindentation. Applied Physics A: Materials Science & Processing, Vol. 79(8) (2004) 2069-2073.

[6] W. Gindl, H.S. Gupta, and C. Grünwald, Lignification of spruce tracheid secondary cell walls related to longitudinal hardness and modulus of elasticity using nanoindentation. Canadian Journal of Botany, Vol. 80 (2002) 1029 – 1033.

DYNAMIC COMPRESSION TESTS OF A POLYURETHANE FLEXIBLE FOAM AS A STEP IN MODELLING IMPACT OF THE HEAD TO THE VEHICLE SEAT HEAD RESTRAINT

[1)], Marcin Jankowski, [2)] Maria Kotełko

[1)] INTAP – Producer of Seats for Automotive, Rokicinska 110/112, 95-006 Bukowiec, Poland.
[2)] Technical University of Lodz, Department of Strength of Materials and Structures, Stefanowskiego 1/15, 90-924 Łódż, Poland.
Corresponding author: m.jankowski@intap.com.pl

1. Introduction

Flexible polyurethane foams are commonly used materials in automotive applications, especially for internal cockpit parts and seats. During accidental impact passenger's head has to be stopped by the headrest (Fig.1). As it is showed in Fig.2, padding material of a headrest has a significant influence on a head deceleration [3]. Mechanical properties of two material systems (polyurethane foam) with a certain range of densities and components proportions have been studied. Dynamic impact tests have been carried out. Results are presented below. Analytical constitutive model of compression has been proposed, which assumes that density, components proportion and strain rate are separable functions [1, 4]. The model has been verified by experimental results of static tests [4]. Impact tests have been conducted due to two objectives: to investigate impact behaviour of examined material and to validate numerical solution based on the method of lump mass [2].

Fig. 1: Impact of a head to a head restraint during vehicle crash test.

2. Experimental Results

Exemplary experimental results of the static tests are shown at Fig.3 [4]. The curves are very sensitive for density and components proportions of the foam.
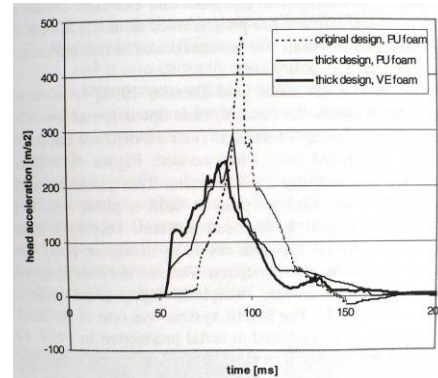
Fig. 2: Head deceleration for three different foam materials of a headrest [3]
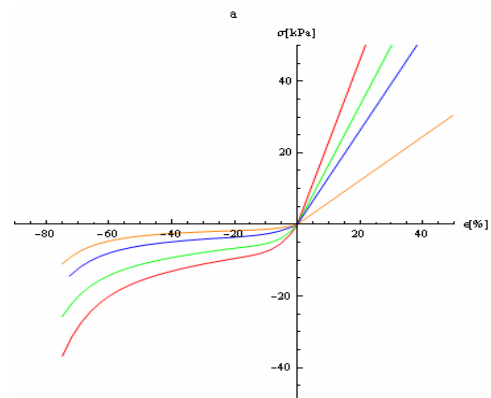
Fig. 3: Static tests results - material system 2, different components proportions [6]

Impact tests were carried out on the special experimental rig shown in Fig.7. Impactor falls from a certain height and hits a specimen. Velocity of impactor is measured by optical device just before contact with a specimen. Deceleration of the impactor during foam deformation is measured by accelerometer and

recorded by a computer. Results of impact tests are presented at Fig. 4,5,6.
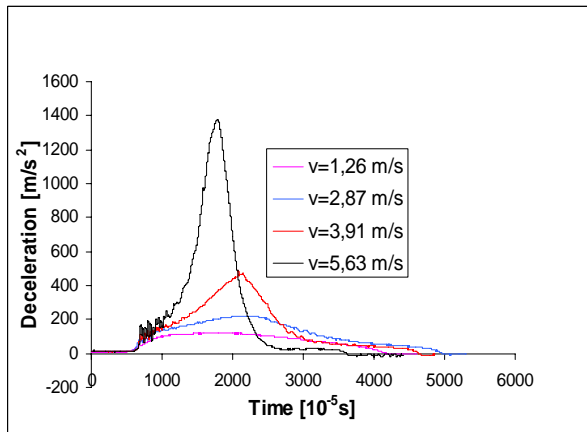
Fig. 4: Sample no.1 - Various impact velocities.
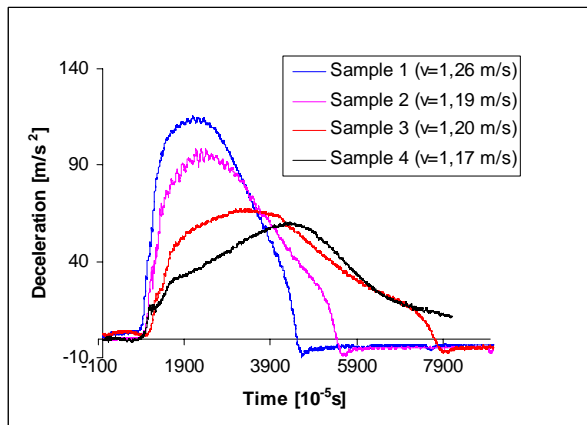
Fig. 5: Samples no.1 – 4 (various components proportions) – Impact velocity ~1,2 m/s.
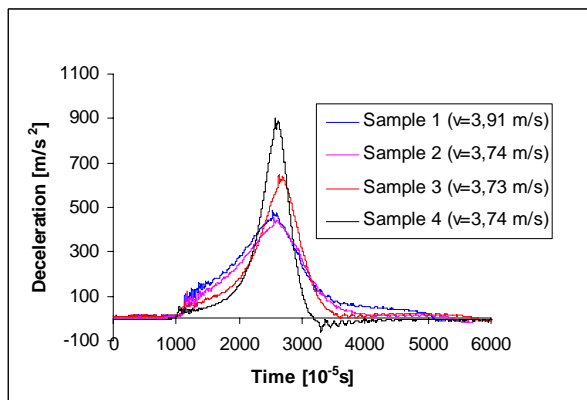
Fig. 6: Samples no.1 – 4 (various components proportions) – Impact velocity ~3,7 m/s

3. Final remarks

As it is shown at Fig. 3 – 6 there is a significant influence of polyurethane flexible foam parameters like density and foam's component proportions upon the deceleration profile during impact. Velocity of the impact is a main parameter which should be known to correctly design foam impact absorber. Maximum peak of deceleration which is of a great importance for a survivability of a passenger during accidental crush of a vehicle depends on the foam parameters, but this influence is stronger or weaker – depending upon the velocity (compare Fig. 5 and Fig. 6).

Results presented here are a part of larger research programme. Results of further research (comparison with numerical solution) will be presented in separate publication.
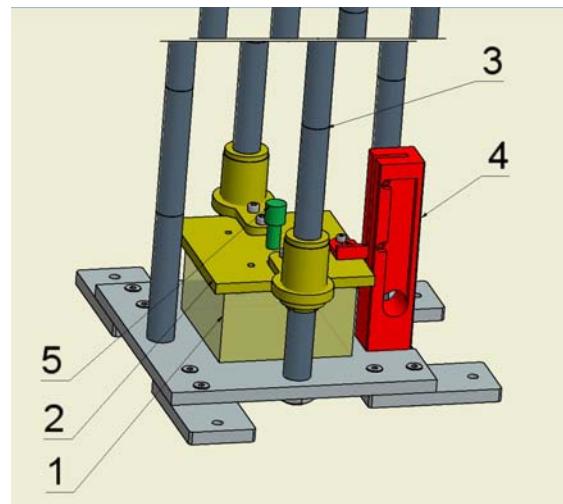
Fig. 7: Impact test device. 1 - foam specimen, 2 - impactor, 3 - impactor guides, 4 - speed measure device, 5 - accelerometer.

4. References

[1] Sherwood J.A., Frost C.C. "Constitutive modeling and simulation of energy absorbing polyurethane foam under impact loading". Polymer Engineering and Science, August 1992,Vol.32,No.16.
[2] Shim V. P. W., Tu Z. H., Lim C. T. „Two – dimensional response of crushable polyurethane foam to low velocity impact". International Journal of Impact Engineering. 703 – 731 (2000)
[3] Schmitt K.U., Niederer P., Muser M., Walz F. "Trauma biomechanics, accidental injury in traffic and sports", Springer 2007.
[4] Jankowski M., Kotełko M. "Experimental identification of constitutive relations in polyurethane flexible foams", Proc. of XXIII Symposium of Experimental Mechanics, Jachranka, Poland, 2008.

ANALYSIS OF LOADING STEEL STRUCTURE OF BUCKET WHEEL EXCAVATOR BY STRESS CONDITION MEASURING

Predrag Jovančić[1], Dragan Ignajtović[1], Taško Maneski[2]

[1]University of Belgrade – Faculty of Mining and Geology, Đušina 7, 11120 Belgrade 35, Serbia
[2]University of Belgrade – Faculty of Mechanical Engineering, Kraljice Marije 16, 11120 Belgrade 35, Serbia
e-mail: pjovancic@rgf.bg.ac.yu

1. Introduction

Bucket wheel excavators are complex systems with large number of functionally important components. Operational life of such machine, as a most important and most complex single system within open cast continuous mining system, is directly related to durability of steel structure. Requirement for long-term monitoring and necessity for data as realistic as possible are lingering establishment of firm relations between steel structure and its durability. Example of stress condition measurement of loading structure at bucket wheel excavator SRs470 located at Drmno open pit of Kostolac coal basin is presented in this paper. This measurement approach provides base for later development of structure's digital model.

2. Experimental Results

Typical measuring locations for determination of stress condition are shown on Fig. 1. These locations are selected according to structural components of the machine, i.e. importance of steel structure for this type of excavator. It should be noted that this excavator was most suitable one, since it is scheduled for revitalization and extension of operational life.

Fig. 1. Selected measuring locations: measuring spot 1 Lamellae of bucket wheel boom; measuring spot 2 – Lower carrier of counter weight structure; measuring spot 3 – Upper carrier of counter weight structure

Proper selection of critical points and limited number of measuring points provides certain results and knowledge on SRs470 excavator steel structure. As already mentioned, strain gauges measuring method was selected regarding type of the structure and loading character.

Force accession measurement was performed at described points at extremely high ambient temperature, in August 2007. Placement of strain gauge at lamellae was done when excavator was under load. First measurement, performed during excavation, provided two signals related to technological operation of excavator. Force accession (stress) diagram in time domain, shown at Fig. 2, for all three measuring spots, represents first signal of stress during block excavation and super-structure slewing to the left.
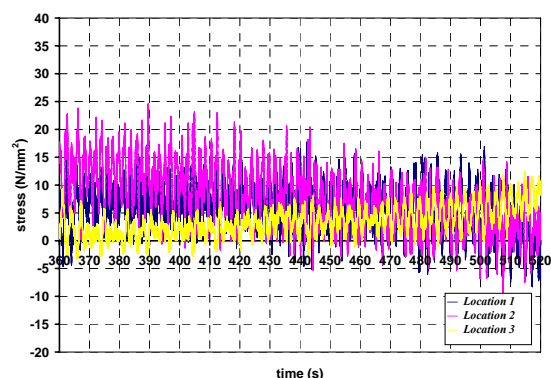
Fig. 2. Stress diagram during excavation, in time domain – first signal (excavation, slewing to the left)

Highest stress accession, of 24.6 N/mm^2, was recorded at lower carrier of counter weight. Stress accession at boom's lamellae is max. 17.8 N/mm^2, while at the stress accession at upper carrier of the counter weight was max. 12.5 N/mm^2. Stress at lamellae is constant throughout the excavation, while the stress at the counter weight carriers varies – it is larger within the lower carrier at the beginning of the process and as the process progress it builds up

within the upper carrier. Lower carrier is certainly exposed to higher loads due to larger impact of counter weight's structure oscillations during excavation to the left.

Force accession (stress) diagram in time domain is shown at Fig. 3, for second signal of stress during block excavation and super-structure slewing to the right.
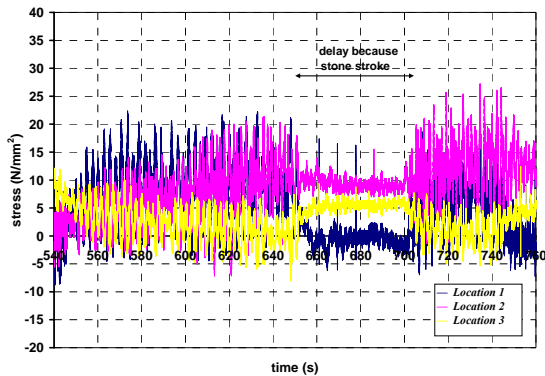
Fig. 3. Stress diagram during excavation, in time domain – second signal (excavation, slewing to the right)

Highest stress accession, of 27.2.N/mm^2, during excavation and slewing to the right was recorded at the lower counter weight carrier. As it can be seen, during right slewing of super-structure stress in lower carrier increases, while it decreases during left slew. Opposing situation is at upper carrier of the counter weight. Stress accession at the bucket wheel lamellae is 21.1 N/mm^2, while at the upper carrier of the counter weight stress accession is 12.4 N/mm^2. Since excavator operated in block which enables maximum performance it can be concluded that stress accession in central pillar is within allowed limit or, in another words, steel structure condition is satisfactory.

Force (stress) accession, for all three measuring spots during transportation of the excavator, but not in excavation, is shown at Fig. 4.
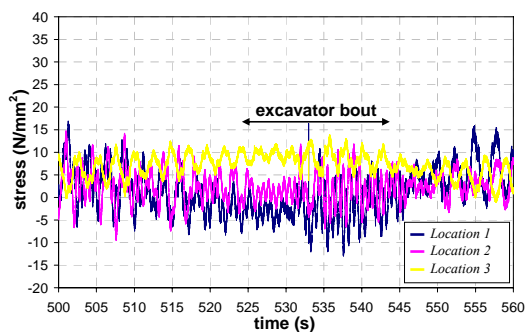
Fig. 4. Stress diagram during transportation of the excavator

During this process highest stress accession, of 16.4 N/mm^2, was measured at the lamellae of the bucket wheel boom. As it can be seen, there is certain correlation of the excavator's structure oscillation, which is manifested in increase and decrease of stress accession at measuring spots. Stress accession at lower counter weight carrier was 11.8 N/mm^2, while stress accession at the upper carrier was 13.8 N/mm^2.

3. Acknowledgements

It can be concluded, according to obtained results, that structures of lamellae and counter weight carriers are behaving well. These structures are exposed to torsion, compression and extension during operation, but also to bending which is manifested in measured stress condition. Opposing to compact excavators, steel structure of this type of excavators behaves better, both during transport and during excavation. This implies proper selection of excavator for operation in harder rocks.

Therefore, according to performed measurements it can be concluded that steel structure of excavator have relatively good behaviour and that stress accession is within technically acceptable limits for this type of bucket wheel excavator.

4. References

[1] IGNJATOVIC, D., JOVANCIC, P., MANESKI, T., *Project on mechanical revitalization of equipment to be relocated from PK Ćirikovac to PK Drmno – Project on mechanical revitalization of bucket wheel excavator SRs470.20/3.0 – internal number 14,* Faculty of Mining and Geology in Belgrade, 2007.

[2] IGNJATOVIC, D., JOVANCIC, P., *Study on Operational life extension of capital equipment at EPS's coal open cast mines – Phase I Bucket wheel excavators*, Faculty of Mining and Geology in Belgrade, 2004.

[3] JOVANCIC, P., *Behaviour diagnostics of drive groups at mining machines*, Journal of Research and Design for Economy, year V, No. 16/2007, p. 27-32, ISSN 1451-4117, UDC 33, COBISS.SR-ID 108368396

ULTRASONIC REFLECTOMETRY IN STUDIUS OF POROUS MATERIALS

Mariusz Kaczmarek[1], Radosław Drelich[1], Bogdan Piwakowski[2], Józef Kubik[1]

[1] Institute of Environmental Mechanics and Applied Computer Science, Kazimierz Wielki University Bydgoszcz, Chodkiewicza 30, 85-064, Poland. Corresponding author: mkk@ukw.edu.pl

[2] Ecole Centrale de Lille, BP 48, Cité Scientifique, 59651 Villeneuve d'Ascq Cedex France

1. Introduction

Studies of reflection of waves from interface between fluid and fluid saturated porous material belong to nondestructive methods used for evaluation of properties of porous materials, [1], [2]. The interpretation of reflection coefficient at different angles, which is the main source of data of reflectometry, requires modelling of inhomogeneous waves for which planes of equal phase and equal amplitude are not parallel, [3]. The description of inhomogeneous waves in fluid saturated porous materials within the framework of Biot's theory was considered e.g. in [4].

The purpose of this paper is to present the elaborated experimental technique and results of experimental and modelling studies of wave reflection from liquid and gas saturated materials. The role of different factors which may influence the reflectometry are discussed.

2. Model

The model of interaction of plane harmonic waves reflected from the interface between free fluid and fluid saturated porous material is considered. The viscosity of free fluid is neglected while viscous interactions between pore fluid and porous material is taken into account. The waves in free fluid are homogeneous and the transmitted waves are inhomogeneous. At the boundary the continuity of normal and tangential components of total stress, the continuity of pressure between free and pore fluid and continuity of mass of fluid are assumed, [4], [6]. In the case of gas saturated porous material the rigid porous medium is assumed with appropriate reduced boundary conditions, [1], [7].

3. Experimental method

The fully computer controlled experimental system of the reflectometer was designed, see Fig. 1. The system includes: pulser (Panametris PR5058), oscilloscope (Tectronix TDS420A) mechanical system of positioning of

transmitting (T) and receiving (R) transducers along with stepper motors (M) and their controllers. The program (in LabView) allows control of kinematics of the reflectometer and automatic data acquisition. The program for signal analysis (in Matlab) performs averaging, spectral analysis, calculation of reflection coefficient and its diffraction correction. The diffraction correction is based on angular spectrum method. The reference signal for calculation of reflection coefficient is taken for face to face position of transducers. The experimental system works both in air (using Ultran transducers) and in water (with Panametrics immersion transducers).
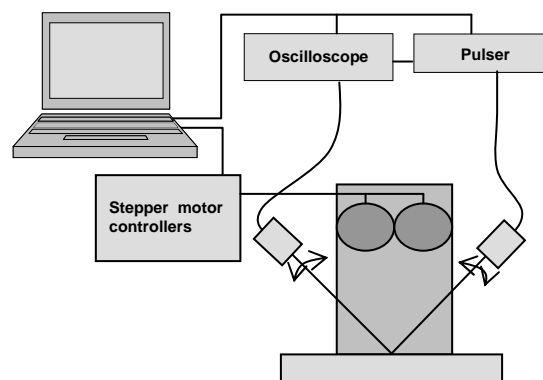
Fig. 1: Setup for reflectometry.

4. Results and discussion

Figure 2 shows the dependence of modulus of reflection coefficient ($|A|$) on incidence angle for sintered glass beads with average grain diameter 260 μm saturated with water (a) and air (b). Results from two tests for opposite surfaces of the same sample are shown while the distance between transducers and sample measured in direction of axes of wave beam amounts about 0.37 m. While the RF signals in water are stable in air significant fluctuations are observed. Thus, a procedure of averaging signals in each position (x10) and for the given number of runs of reflectometer (x10) is applied.

a)

b)
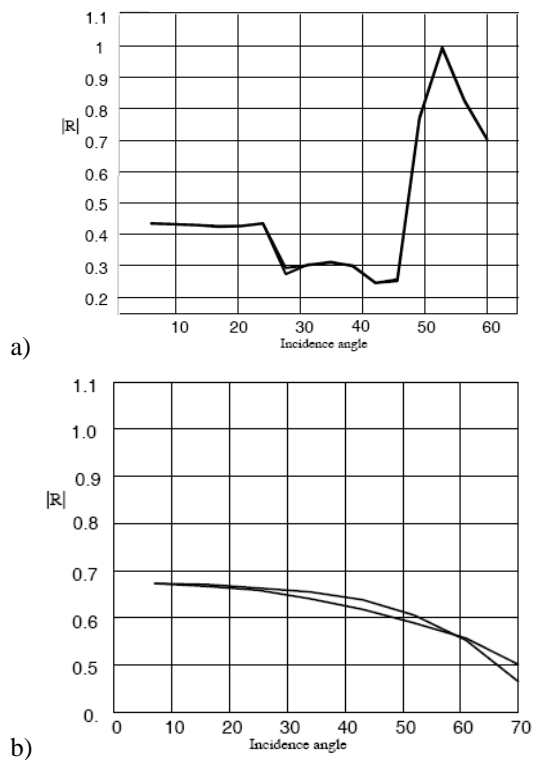
Fig. 2. Reflection coefficient for (a) water/water saturated porous sintered glass, 0.5 MHz, (b) air/air saturated porous glass system, 0.2 MHz. Results of two tests are shown, glass with 260 μm average diameter of grains.

Taking the parameters for sintered glass beads from the paper [8], except for ten times larger permeability, the theoretically determined dependences of reflection coefficient on incidence angle are shown in Fig. 3. For water saturated material the predictions from Biot's model are presented while for gas saturated medium the results for single phase (assuming rigid skeleton) and two phase model are shown. Very good agreement of the models is seen.

Calculations of the diffraction correction using angular spectrum method prove that only for water saturated case the correction is significant. In spite of a quantitative agreement between the experimental and theoretical results more studies dedicated to validation of the model are necessary. First the full set of material and structural parameters must be determined and used in simulations. Then, the role of factors such as precise positioning of samples, quality of the interface or more complex boundary conditions (e.g. including effects of dissipation as proposed in [6] or scattering) should be considered.

a)

b)
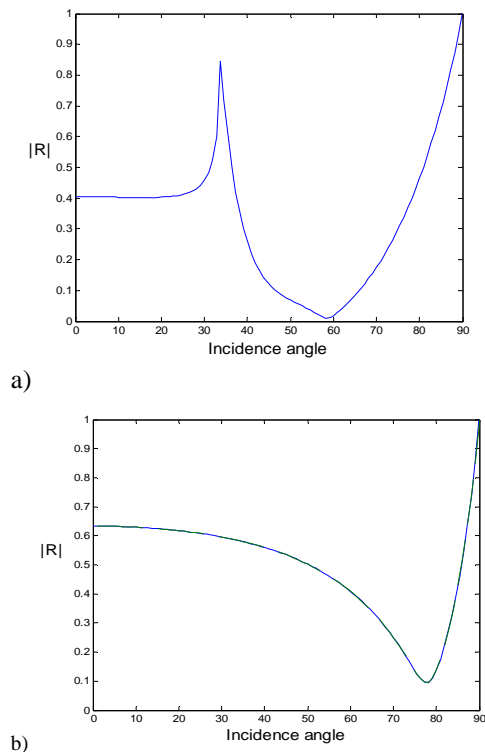
Fig. 3. Calculated reflection coefficients for (a) water/water saturated porous sintered glass, 0.5 MHz, (b) air/air saturated porous glass system, 0.2 MHz. In the second case the predictions of single and two phase models are shown.

The experimental data from ultrasonic reflectometry show qualitative agreement with model both for studies in water and air. In the latter case the model of rigid porous material can be used.

5. References

[1] Fellah Z. E. et al., JASA, 113, 2424, 2003.

[2] Jocker J., and D. Smeulders, Ultrasonics, 319, 2009.

[3] Declercq N. F., IEEE Trans. Ultras. Ferr. Freq. Control, 52, 776, 2005.

[4] Stoll R., T. K. Kan, JASA, 70 (1), 149, 1981.

[5] Biot M. A., JASA, 28, 168, 1956.

[6] Gurevich B., M. Schoenberg, JASA, 105, 2585, 1999.

[7] Allard J. F., Propagation of sound in porous media: modelling sound absorbing materials, Elsevier 1993.

[8] Johnson D. L., T. J. Plona, H. Kojima, 1994. J. Appl. Phys., 76(1) 115, 1994.

VILLARI EFFECT IN EPOXY COMPOSITES WITH TERFENOL-D POWDER

Jerzy KALETA, Daniel LEWANDOWSKI, <u>Rafal MECH</u>

Wroclaw University of Technology, Institute of Material Science and Applied Mechanics

25 Smoluchowskiego Street, 50-370 Wroclaw, Poland

Corresponding author: rafal.mech@pwr.wroc.pl

1. Introduction

The relatively large strain and force output of magnetostrictive Terfenol-D has led many researchers to focus on its uses for actuation. However, a Terfenol-D can also be use as an effective sensor using the reverse nature of the magnetomechanical effect, so called Villari effect [1] which consist in magnetization change of material caused by stress. In this paper the investigations of Villari effect in composites based on Terfenol-D powder were presented. This effect is important because it gives, a possibility to create of new generation sensors like hearing aids, load cells, accelerometers, proximity sensors, torque sensors, magnetometers and many more [2, 3, 4].

2. The Specimens and The Test Set

The specimens were made from one composite with 45% volume fraction of Terfenol-D powder, which was divided in two, and afterward cross section perpendicular and rectangular to polarization lines were made. The specimens are presented in figure 1.
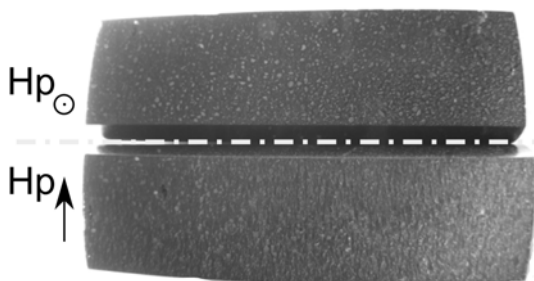
Fig. 1. Composite specimens with 45% volume fraction of Terfenol-D powder cross section perpendicular and rectangular to polarization lines

(Hp – polarization direction).

Procedure of composite production was describe in [5]. The magnetostriction of investigated composite specimen reached 700 ppm in comparison to Terfenol-D 1500 ppm at H=180kA/m (figure 2).
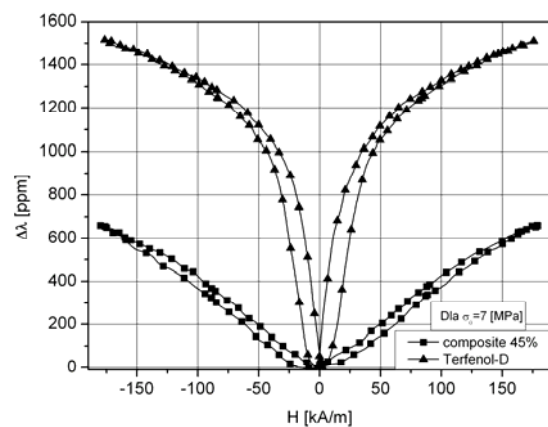
Fig. 1. Comparison of magnetostriction for solid Terfenol-D and composite material.

The MTS hydraulic pulsator was used to control stress in specimens. Moreover to record changes in specimens magnetic field a new test set was design. Its main part was KMZ10A magnetoresistor from Philips. Method enabled recording changes in magnetic signal at different values of stress applied to the specimens. Investigations were made for different positions of sensor regard to specimens.

3. Results of Investigation

Measurement were carried out for cyclic loading force for different amplitude at frequency f=1Hz. Four different points on specimen surface, as it is showed in figure 3 were chosen to measure changes of magnetic field.

Figure 4 presents results of measurement magnetic field changes for different values of applied force in position marked as 1 in figure 3 of the magnetoresistor regard to the investigated specimen. It can be observed that

magnetic response of the specimen rise together with increasing of the force, but shape of the loop did not change.
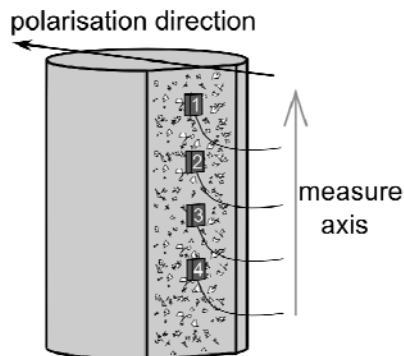
Fig. 1. Sensor position regard to the specimen during investigations of Villari effect.
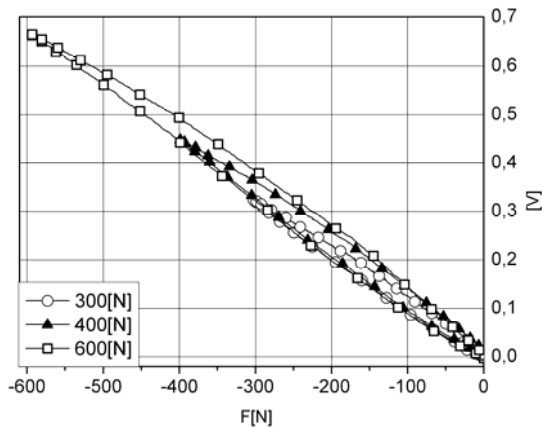
Fig. 1. Comparison of different applied forces on changes in magnetic response of the specimen.
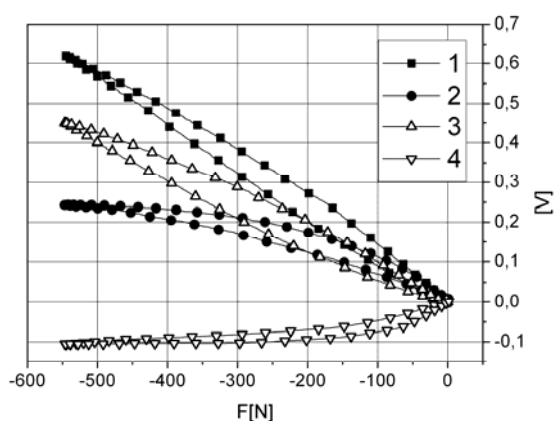
Fig. 1. Comparison of different position of sensor on changes in magnetic response of the specimen at the same value of applied force F=550[N].

Figure 5 shows changes in magnetic response of the investigated specimen depended on different position of sensor along the specimen as it is showed in figure 3.

Changes in shape of the hysteresis loop of investigated specimens, sign of magnetic field, and what is most important change in value of this field can be observed.

Different shapes and values of magnetic response along the specimen length at the same values of applied force, shows that layout of specimen magnetic field is very diversified.

4. Conclusion

1. Produced composite specimens are characterized by the Villari effect.

2. Magnetic field maps of examined specimens are very diversified.

3. Results induce to further investigation in order to use composite materials with Terfenol-D powder as a new type of sensors.

5. References

[1]   E. W. Lee. Magnetostriction and Magnetomechanical Effects. *Rep. Prog. Phys*, 18:184–229, 1955.

[2]   R. Chung and R. Weber. A Terfenol based magnetostrictive diode laser magnetometer. *IEEE TRANSACTIONS ON MAGNETICS*, 27, 1991.

[3]   E. du Tremolet de Lacheisserie.. *Magnetostriction Theory and applications of magnetoelasticity*. CRC Press, 1993.

[4]   R. C. Fenn and M. J. Gerver. Passive damping and velocity sensing using magnetostrictive transduction. *Proc. SPIE Smart Structures and Materials: Smart Structures and Intelligent Systems*, 2190:216–227, 1994.

[5]   J. Kaleta, D. Lewandowski, R. Mech, and P. Gąsior. Solid State Phenomena Vol. 154 pp 35-40. Magnetomechanical properiteis of Terfenol-D powder composites. *Solid State Phenomena*, 154:35–40, 2009.

METHODS OF INVESTIGATING MARTENSITIC TRANSFORMATION INDUCED BY PLASTIC DEFORMATION IN BULK SPECIMENS

Jerzy Kaleta, Przemysław Wiewiórski, <u>Wojciech Wiśniewski</u>,

Wroclaw University of Technology, Institute of Material Science and Applied Mechanics

25 Smoluchowskiego Street, 50-370 Wroclaw, Poland

Corresponding author: wojcich.wisniewski@pwr.wroc.pl

1. Introduction

There are two types of martensite transformation, thermal transformation occurring as a result of the high velocity cooling of austenitic, and deformational transformation, which takes place due to the occurrence of critical plastic deformation. There are several methods of investigation of martensite transformation, among others roentgen diffraction [1], neutron diffraction, microscope measurements [2], density measurements and hardness measurements [1], as well as magnetic measurements [2].

The main objective of the present authors is to elaborate a non-destructive investigative method which is based on measurements of the strength of the magnetic field, induced as a result of the material deformation following the Villari effect.

2. Investigation object

The object of investigation were cylindrical specimens made of austenitic steel AISI 304. Before the investigation the material had undergone thermal treatment, which consisted in exposing specimens to the temperature of $1050^{o}C$ for 35 minutes and then rapid cooling under water. Thermal treatment was conducted to obtain a one-phase material with austenitic structure.

3. Measuring stand and research methodology

In order to perform measurements the experimenters made use of a setup consisting of a material testing machine MTS 810, a computer, an extensometer and an instrument measuring the magnetic field strength (Figure 1). MultiPurpose TestWare software was used to enable registration of mechanical signals (stress $\sigma(t)$ and strain $\varepsilon(t)$) and magnetic (the magnetic field strength $H(t)$). For measurement of the magnetic field strength the experimenters used a unique setup developed at the Institute of Material Science and Applied Mechanics by one of the co-authors of the present work. In this setup four Philips KMZ 10B magnetoresistors were used as sensors. They were placed in line alongside the specimen's section to be measured.
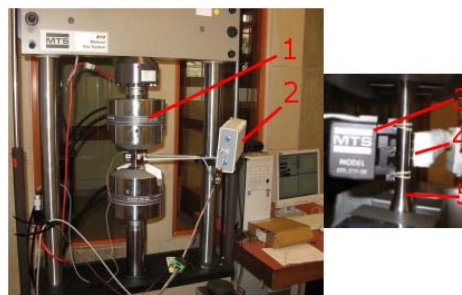
Fig. 1. Measuring stand: 1 – hydraulic pulsator MTS 810, 2 – setup for magnetic field measurement, 3 – extensometer, 4 – magnetoresistors, 5 – specimen.

That measuring stand set up in this way served the purpose of conducting low-cycle fatigue tests. The fatigue process was controlled by means of the amplitude of the total strain. The research was conducted for four thresholds: ε_a = 0.003; 0.0035; 0.004 and 0.005 mm/mm respectively. On each threshold five specimens were tested. The process was realized up to the destruction (complete fracture) of the specimen. The load spectrum was of the sinusoidal character (R=-1), and the frequency equaled 0.2 Hz. The adopted frequency guarded against temperature increase due to the material deformation, which prevented reverse transformation, i.e. α' martensite $\rightarrow \gamma$ austenitic.

4. Findings analysis

Figure 2 presents the spectrum of the stress signal for the deformation threshold $\varepsilon_a = 0.0035$ mm/mm. As we can see the initial stress value equaled $\sigma_a = 250$ MPa and in the course of the fatigue process increased up to the maximum value $\sigma_a = 420$ MPa. Increasing of stress during fatigue process testify to the material strengthening. This strengthening is directly connected with the increase in the α'martensite content in the matrix of γ austenitic.The stress increased up to the moment when first local fractures of the specimen occurred. It was assumed that the specimen fracture took place at the decrease in force value of 1%.
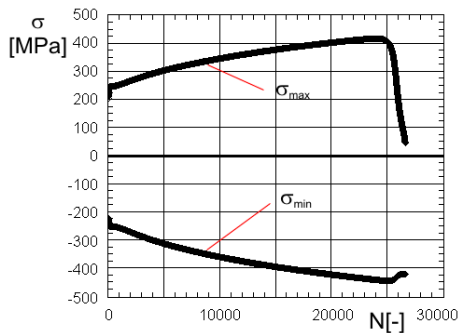
Fig. 2. Spectrum of strain signal.

The tested specimen broke between magnetoresistors 1 and 2, and until the fracture became visible, it was loaded with N number = 24723 cycles. In this area the largest amount of martensite was extruded, which can be ascertained on the basis of the spectrum analysis and analysis of cycles of magnetic mean signals presented in figure 3. Assuming, as in previous works of the present authors, that the number of martensite extrusions is strongly correlated with the absolute value of the magnetic field strength signal H_m, it is easy to observe that the signal value is highest in the case of magnetoresistors 1 and 2. In graphs of magnetic spectrum of the four magnetoresistors (figure 3) one can additionally observe three specific areas. Moving from the left-hand side of the graph, there is the first one made of one-phase material (paramagnetic γ austenitic) – up to N=1000 cycles, then the second one in which due to deformations, α' martensite extrusion takes place and the third area from 24723 cycles, i.e. from the moment the first fractures begin to appear in the specimen until it is pulled apart.
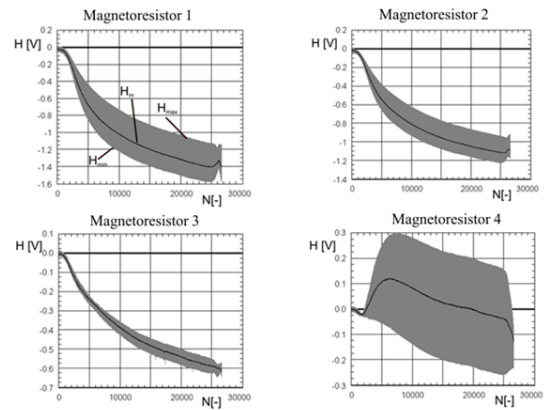
Fig.3. Spectrum of magnetic signals for individual magnetoresistors.

5. Conclusions

- The method of measurement of the magnetic field strength applied in this experiment made it possible both to discover the ferromagnetic phase (α' martenisite) and the fact that it increased locally along the massive specimen as the number of load cycles increased.

- The experiment shows the possibility of discovering inhomogeneous martensite extrusion along the specimen, localization of the process (areas where the first fractures appear) and the moment of the beginning of transformation (allows determining the number of cycles after which the process of phase transition begins).

6. References

[1]   Talonen J., Aspegren P., Hanninen H., Comparison of different methods for measuring strain induced α'-martensite content in austenitic steels, Materials Science and Technology 2004, ss. 1506-1512.

[2]   Kaleta J., Lewandowski D,. Wiśniewski W. Kinetics of cross effects in the process of martensitic transformation induced by cyclic deformation in massive specimens. VIII National Conference on Fracture Mechanics Kielce-Cedzyna, 17-19 September 2001, pp. 391-400.

CONSTRUCTION OF MAGNETIC SCANNER FOR APPLICATION IN EXPERIMENTAL MECHANICS

Jerzy KALETA, Przemyslaw WIEWIORSKI

Wroclaw University of Technology, Institute of Material Science and Applied Mechanics

25 Smoluchowskiego Street, 50-370 Wroclaw, Poland

Corresponding author: przemyslaw.wiewiorski@pwr.wroc.pl

1. Introduction

There is a widespread tendency to introduce new measurement techniques, including experimental mechanics as well, and use cross magneto-mechanical phenomena. One of them is a reverse magnetostriction also known as the Villari effect. In the relevant literature one can encounter individual cases of both construction and application of such equipment that allows creating diagnostic technique which is more and more often referred to as magnetovision. For over a decade, in the team from which the present authors recruit, several generations of cameras and scanners have been developed which ensure a magnetic image of materials subjected to various forms of treatment, mechanical load spectra and phase transformations. The system presented below fully covers examples of applications enumerated above.

2. Magnetic field scanner and research methodology

Our magnetovision system has four independent subsystem for magnetic inspection: Scanner XYZ, Rotational axis analyzer, Tension testing on breakers tool, Fatigue processes on MTS material testing machine.

Sensors are extremely close to tested surface, axially-symmetrical or flat, a special algorithm is applied to correct sensors location to one 3D point. The scheme of the system called the Megscaner was presented in figure 2. The main system devices consists of the following elements:

- advanced system of control ADDI-DATA APC-18001, used mainly in robotics. Equipment regulator contained in the APCI-8001 ensures controlling the whole process of precise positioning of

the scanner and allows attaining its optimal dynamics. (Hp - polarization direction).
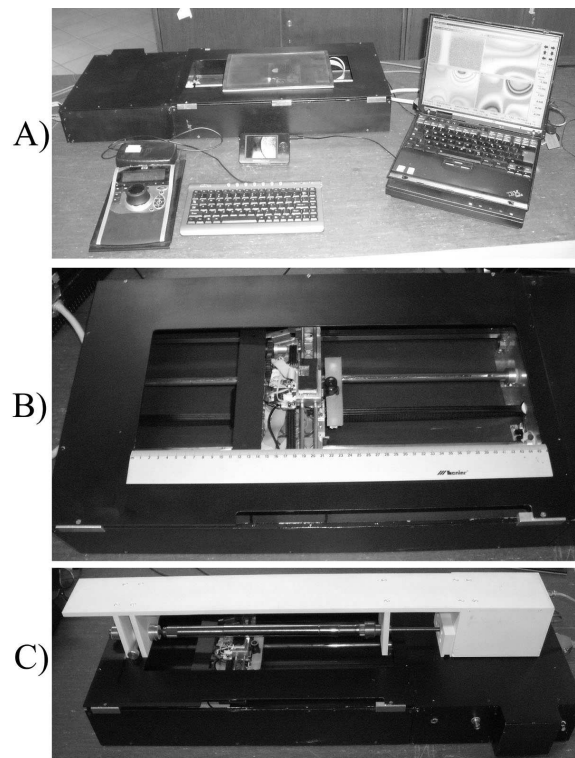
Fig. 2. View of the Magscanner (ver. 2009) system, in which control-measurement part of the XY scanner (A), XY scanner (B) system for scanning axis-symmetrical part (C).

- measurement head in the shape of a three-axis measurement head, basing on Honeywell HMC1053 magnetoresistors, but the whole measurement track is based on the experience gained from previous models. A probe with sensors keeps moving at a constant distance (0.2 mm) from the object examined. The speed at which the head moves can be regulated over a wide range, depending on the quality of measurements (the higher the speed the greater the measurement error).
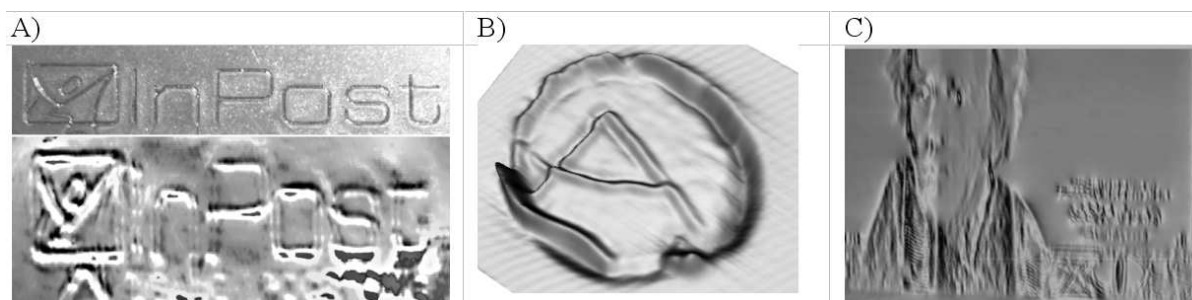
Fig. 1. Examples of the use of the magnetic field stream disturbance for detection of changes on the ferromagnetics surface: laser engraving A), crack on the disc B) magnetopolygraphy C).

- software dedicated to Magscaner/Maglab operating the whole of the system and ensuring visualization of the results. Recently from the Magscaner - software operating experiments the part responsible for further treatment of results has been separated and called Maglab.

3. Maglab – a complete tool for magneto-mechanical evaluation

One of the most important part of Magscaner system is Maglab software. Measurement technique consists of acquiring a cloud of points belonging to equally distant planes, similarly as in tomography, 3D visualisation in CAD under standard IGES. Thanks to the software package Magscanner/Maglab further treatment of the magnetic field distribution maps becomes possible due to measurement as well as its further visualization in programs CAD (ProEngineer) or NURBS (Rhinoceros). Program Maglab (figure 3) allows quick generating of maps of stress distribution, deformation and specific energy for Kirsch problem.

4. Selected applications

Examples of the scanner applications and an earlier version of the magnetovision camera were presented in earlier works by the present authors [1, 2, 3]. New applications of the magnetovision system are connected with determining of the magnetic field around objects exposed to technological procedures so

as to check its correctness (e.g. cutting, laser ablation, electrodischarge drilling, micro-layer plotting, quality of magnetic printing etc.) Figure 1 presents selected examples.
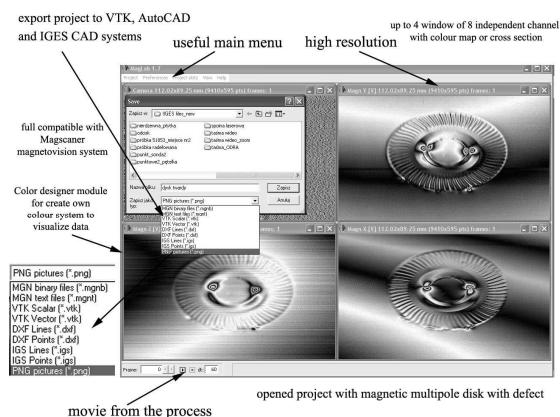
Fig. 2. Window and main features of Maglab software.

5. Conclusion

A new generation scanner (magnetovision camera) as well as a number of its applications have been developed. Due to its compact structure and evolution of the software dedicated to it, this solution can find application in industry as one of methods NDE and in scientific research for identification of cross field models.

6. References

[1] J. Kaleta and P. Wiewiórski. Detekcja defektów magnetycznych prętach kompozytowych z użyciem skanera o dużej rozdzielczości. *Acta Mechanica et Automatica*, 1:39−44, 2007.

[2] J. Kaleta and P. Wiewiórski. Magnetovision as a Tool for Investigation of Fatigue Process of Ferromagnetics. *Proc. of Fatigue 2001*, 2001.

[3] J. Kaleta, P. Wiewiórski and W. Wiśniewski. Magnetyczna pamięć historii odkształcania materiału ferromagnetycznego. *IX Krajowa Konferencja Mechaniki Pękania*, pages 221−228, 2003.

TIME SHORTENING TESTING METHODOLOGY APPLIED ON GEARS WITH NON-STANDARD TOOTH FLANK SURFACE

Jan Kanaval [1]), Pavel Mossóczy [2]), Roman Uhlíř [3]), Karel Petr [4])

[1]) Czech Technical University in Prague, Faculty of Mechanical Engineering, Department of Designing and Machine Components. Technická 4, 166 07 Praha 6, Czech Republic.

[2]) Czech Technical University in Prague, Faculty of Mechanical Engineering, Department of Designing and Machine Components. Technická 4, 166 07 Praha 6, Czech Republic.

[3]) Czech Technical University in Prague, Faculty of Mechanical Engineering, Department of Designing and Machine Components. Technická 4, 166 07 Praha 6, Czech Republic.

[4]) Czech Technical University in Prague, Faculty of Mechanical Engineering, Department of Designing and Machine Components. Technická 4, 166 07 Praha 6, Czech Republic.

Corresponding author: roman.uhlir@fs.cvut.cz

1. Introduction

This work builds on the article from the past conference, where the development of experimental device and time shortening testing methodology proposed in the framework of research on methods of non-standard increasing of operation life depending on flank damage (pitting) of case-hardened gears were described.

2. Experimental Results

Before the date of project's end has been carried out and evaluated runtime tests of three basic groups of gearing with the adjusted pinions. The main supervised output values are total pitting damaged area (see fig. 1). In DIN 3990 standard, the determined value for one tooth is 4% surface failure of tooth area on one tooth and 1% on whole gear.
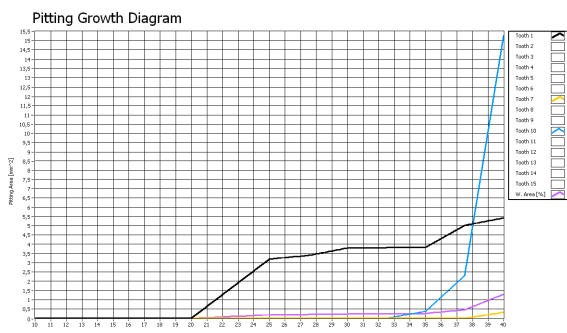
Fig. 1: Pitting Growth Diagram.

The first group, which included a default case-hardened gears produced according to current manufactured practices (reference gearing), verified the accuracy of the methodology of design and strength check of gears. Experimentally was achieved the calculation of gearing lifetime. A characteristic phenomenon was significant variance of values of life among each gearing.
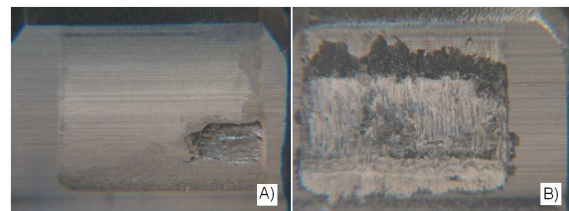
Fig. 2: Flank damane of case-hardened gear (A) and gear with WC layer (B)

In the second group were tested gears with the case-hardened pinion with the ion-implanted CrN and TiN on the teeth flanks (IBAD technology).

In the third group were tested gears with the coated pinion by WC layer (HVOF technology).

In the context of a comprehensive evaluation of the tests was checked hardness (Microhardness and structure) of case-hardened gears. Further there were checked their geometry before and after the runtime test and were also analyzed samples of used oil.

With a respect to the technological problems in the practical mastery of ion-implantation CrN and TiN, manufacturing and regrinding of coated WC layer has not been clearly demonstrated increase of the fatigue resistance of the tooth flank yet. However, there have been mapped limiting factors of the selected promising technologies to strengthen the tooth flank, which represent the ideas for the implementation of other running tests. The experiments currently continue within the

dissertation solved on the Czech Technical University in Prague, Faculty of Mechanical Engineering.

3. Numerical Model

From the tests of gears were created documents for verification of numerical model of the crack propagation in the conditions of contact fatigue.
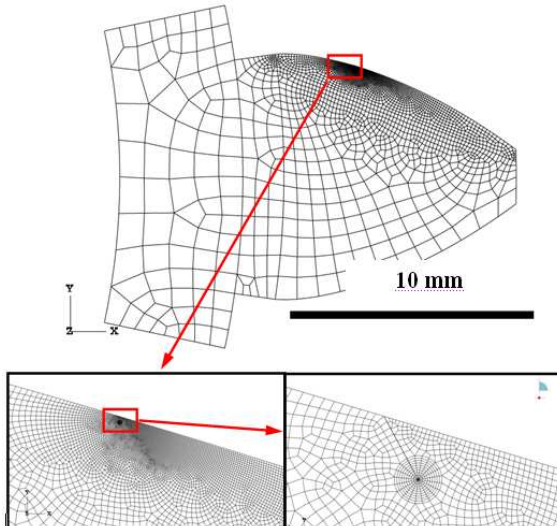
Fig. 3: Numerical model of crack propagation

Unlike the tests of the standards specimens was not possible to continuously monitor the development of the crack leading to the creation of pitting dimple, but to dimple itself, which was created by break off of separate crank of the material. Verification criteria are the geometric parameters of pitting and estimation of the total number of cycles to its creation in the sequence gear mesh condition.

Geometry of dimples and pitting cracks at different stages were studied on metallographic sections and cuts made in the most damaged teeth. Cuts were conducted in order to go through centre of macro-dimple. Acquired images were processed using of programme LuciaNet.
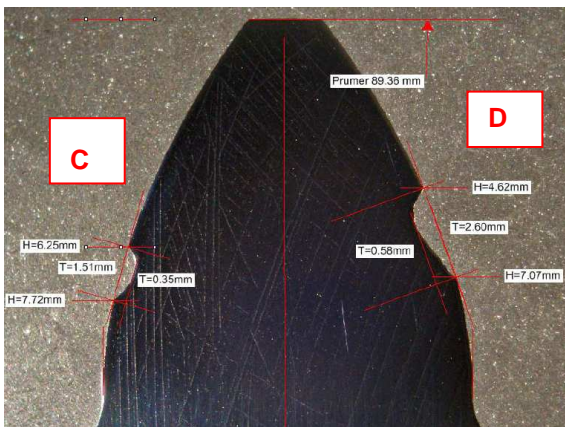
Fig. 4: Metallographic section of tooth

4. Conclusion

The first series of measurement were made. Time shortening testing methodology has been verified. The basic data for verification of numerical model of the spread of cracks in the conditions of contact fatigue have been obtained.

5. Acknowledgements

6. References

[1] Žák, P. - Dynybyl, V., Research of Gearwheels for Industry use - Photographic Method for Pitting Size Evaluation. In: 48th International Conference of Machine Elements and Mechanisms Departments 2007: STU v Bratislave, SjF, s. 94.

[2] Tischler, D.: Optimalizace povlaku CrN vysokoenergetickou modifikací technologie IBAD. Praha: ČVUT. Fakulta strojní. Ústav fyziky, 2005. 98 s. Disertační práce. Školitel Prof. Ing. František Černý DrSc.

[3] M. Španiel, Pitting. Šíření únavových trhlin v podmínkách cyklického zatížení kontaktem. Project reg. number: 101/06/1427

Testing of the fracture nature of wood using acoustic emission technology

Antal Kánnár PhD.[1]

[1]associate professor, University of West Hungary, Institute for Applied Mechanics and Structures, H-9400. Ady E. út. 5. Sopron

Corresponding author: toni@fmk.nyme.hu

Summary

Spruce was investigated by acoustic emission during tensile tests. The examined moisture contents were 0%, 12%, and 26%. The fracture surfaces were photographed using electron-microscopy. The experiments showed, that micro-damage processes start near the ultimate strength, regardless of moisture content. This indicates the brittle behaviour of wood.

The analysis of detected acoustic events at different moisture contents indicated that the number and properties of events supposedly resulting from breaking do not change with increasing moisture content. Decrease occurs in the total number of events at higher moisture contents as a consequence of the increasing acoustic attenuation of wood and the elimination of friction type events. Electron microscopic analysis of fracture surfaces supports the result of acoustic emission experiments. The fracture surfaces showed characteristic brittle tension and shear across the cell wall of different cells. Based on both investigations we can say that wood has brittle fracture characteristics in the 0-30% moisture content range.

Experiment

Spruce species (*Picea abies*) were tested in tension parallel-to-grain in RL plain, at three moisture contents (*Fig.1*). The weakening of the specimens' middle section caused the fracture to occur there or start from that location. The measurement setup allowed events that originated from locations other than the tension mid-region (the mid 30 mm) to be filtered out, based on time delay differences between the two transducers. This is important, because many events originated at the grips because of the combined stress state and events originated in the 8mm thick section too. Each series contained 25 specimen. The moisture content levels used were 0%, 12%, 26%. The applied acoustic emission (AE) apparatus was a Defectophone (KFKI Hungary) with two logarithmic amplifiers and two wideband piezoelectric-transducers type SE1000-H. The examined frequency domain was 20-250 kHz. The applied threshold was 22 µV. The examination of 20-100 kHz range seemed to be essential due to the preliminary analysis, which showed ca. 30% of the total events are in this range (Kánnár 2004). The coupling material was silicon grease. The characteristic fracture

Fig.1. Specimen detail (units: in [mm])
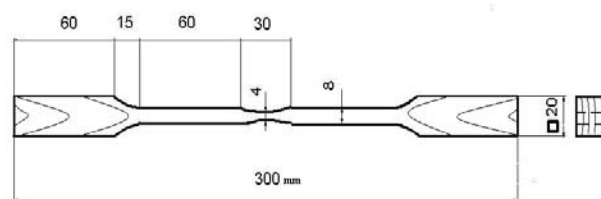
surfaces were captured via electron microscopy (EM)

Results

The experiments showed that the AE processes start at stress levels near the ultimate strength in most cases (*Fig.2*). Because the sources of AE are breaks, cracks and the friction of fracture surfaces, this implies brittle behaviour in wood. This behaviour did not change with increasing moisture content. At higher moisture content levels fewer events were detected, but the starting point of the micro-damage process did not vary. Drawing further conclusions concerning the relationship between AE processes and moisture content was difficult, because the investigation of AE processes of several specimens - made of the same wood species - did not give an unequivocal picture about the AE behaviour of wood. Some specimens broke producing a few events while in other cases several hundred events could be detected. The reason for this anomaly is that failures may be initiated at various points within

the full volume of the stressed specimen, which progress randomly towards one another (Bariska 1985). Additionally, the advancement of micro-damage processes is a function of the particular specimen's biological and anatomical structure.
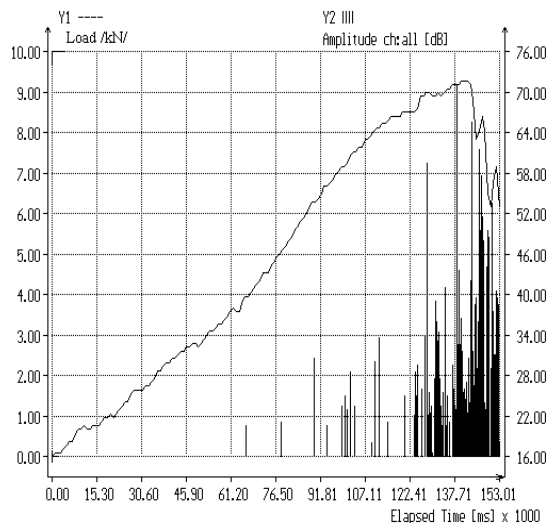
Fig2. Acoustic activity of spruce specimen no. 10 at 12% MC

Based on the above considerations, the data resulting from specimens with equal moisture content were pooled and examined in clusters. These clusters consist of 3000-6000 acoustic events each, which are representative in terms of the AE properties of wood. Valuable conclusions can be drawn from the examination of the distribution of AE events concerning the fracture behaviour of wood.

It was examined the amplitude of events, the energy of events and the rise time.
In summary, we can say that increasing the MC causes decrease in the number of friction type events. The number of fracture type events does not change considerably with changing MC.

To verify the conclusions of AE experiments, SEM images were taken of the fracture surfaces at each MC level. The characteristic fracture modes were tension and shear at all MC content levels, so these two types were analysed in all cases. Fig. 3 shows the fracture surface of spruce at 0% MC. The picture shows a view of the fracture surface. It demonstrates that most tracheids showed brittle transwall failure, but at certain points, bundles of tracheids were pulled out. The picture shows one of the extracted tracheids packets, along with brittle shear fracture on their lateral surfaces.

Shear failure is actuated along ray parenchyma cells, that constitute critical cross-sections in terms of shear. This brittle behaviour does not change at higher MC. (Fig.4.)
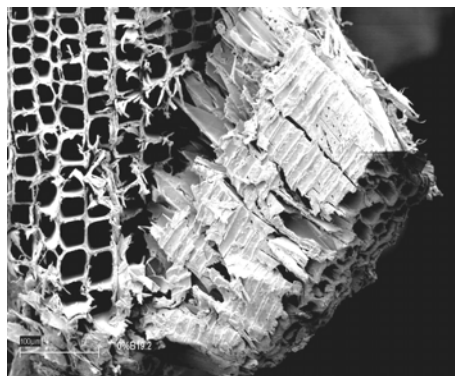
Fig.3. Tension fracture surface of spruce at 0% MC after tensile test
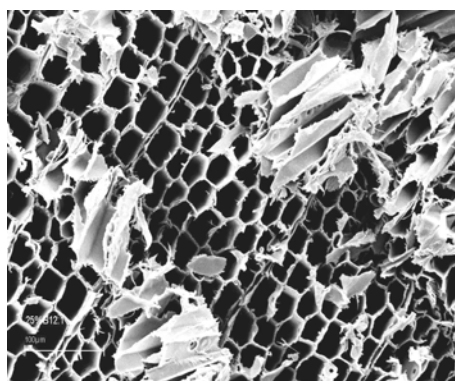
Fig 4. Tensile fracture surface of spruce at 26% MC after tensile test

Summarizing the experiences of fracture surface analysis at different MC's, we can state that the characteristic fracture mode of wood is brittle tension and shear.
The brittle character does not change considerably with increasing MC.

References

Bariska, M.- Kucera, L.J. (1985): On the fracture morphology in wood. Part II.   Macroscopical deformations upon ultimate axial compression in wood.   Wood Sci. Technol.19: 19-34.

Kánnár, A. (2004): The investigation of applicability of acoustic emission technology for the assessment of mechanical properties of wood ; Doctoral dissertation, University of West Hungary, Sopron Hungary

Determination of shear moduli of wood using normal stress

Zsolt Karácsonyi [1],

[1] University of West Hungary, Sopron, Faculty of Wood Technology, Institute for Applied Mechanics and Structures, Bajcsy-Zs.-Str. 4, 9400 Sopron, Hungary.

Corresponding author: kzsolt@fmk.nyme.hu

1. Introduction

Shear modulus of wood is one of the most important elastic material constant. The stiffness tensor and the ductility tensor is known/given in system of anatomical main orientation. Three components of these tensors are depend on shear modul coming under anatomical main flats. If we know the elastic constant, we can determine previous tensors. If we know the previous tensors, we can numerate the deformation state by stress state and the stress state by deformation state. However there isn't an easy work to determine, to measure the exact value of shear modul. The reason for this is that there is difficult to generate clear shearing stress in a selected cross-section in the course experiment circumstance. In addition to determine measure of angle's change is one of the most difficult deflection-measuring work.

These difficulties result in many technologies have been worked out to measure the shear modulus for our days. Plurality of these methods contain still something theoretical and/or measurement technological question. An opportunity presents to determine the shear modulus by indirect measure in case anisotropic materials like wood. During this method at first: accordingly directed beam specimen has to be formed (the angle of the fiber direction and the load direction is 45°). Second: expose this specimen to clear tension or clear pressure. Third: have to measure the specific strains parallel and perpendicular to the load direction.

$$G_{ij} = \frac{\sigma^{i'i'}}{2 \cdot \left(\varepsilon_{i'i'} - \varepsilon_{j'j'} \right)},$$

where

$i', j' = 1', 2', 3'$

$i, j = L, R, T,$

G_{ij} – shear modulus,

$\varepsilon_{i'i'}$ - specific strains parallel to the load direction,

$\varepsilon_{j'j'}$ - specific strains perpendicular to the load direction,

$\sigma^{i'i'}$ - tension (or compression) stress.

This indirect technology is simple and exact. Even so only a few similar measuring has been found in the bibliography. This method usually was referred like theoretical possibility. To make the test we need for a prime mover to material search and for a machine to determine the deflection. We can use a new instrument to determine the deflection. It is the videoextensometer, which give the deflection through optically and computationally way. The experimental arrangement of the simple tension tests are shown in fig. 1.
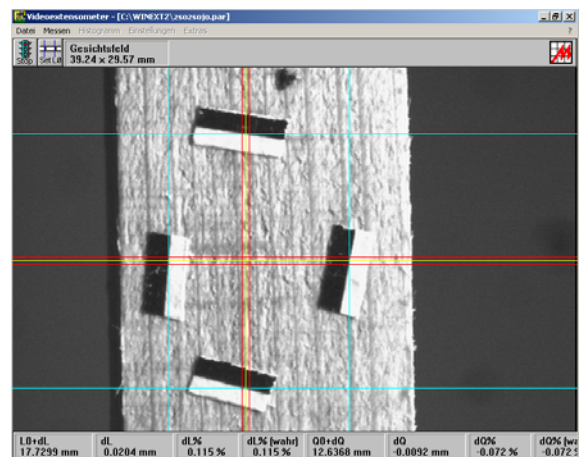
Fig. 1: Picture of videoextensometer during measure

2. Experimental Results

The experimental results of the simple tension tests are shown in fig. 2.
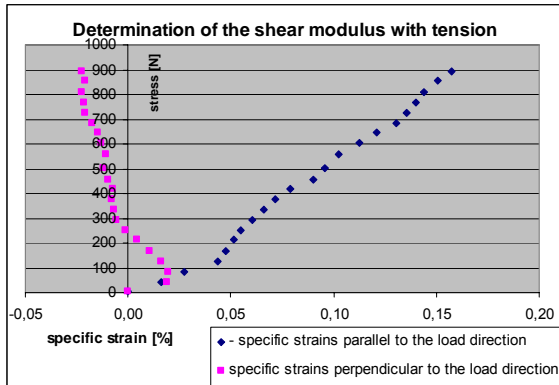
Fig. 2: Specific strains by simple tension

Tab. 1. The experimental results of the simple tension

Num.: LR1	A [mm^2]=	410,8
Stress [N]	Strains parallel to the load d.[mm]	Strains perpendicular to the load d.[mm]
2,9297	17,827799	13,187456
↓	↓	↓
893,6904	17,855822	13,184515
	$\varepsilon_{parallel}$[%]	$\varepsilon_{perpendicular}$[%]
	0,00000	0,00000
	↓	↓
	0,15719	-0,02230
	σ [MPa]	
	0,007131694	
	↓	
	2,175487829	
	$\nu_{L'R'}$[MPa]	G_{LR}[MPa]
	-0,141879	606,02

3. References

[1]   Szalai, J. (1994): Anizotropic elasticity and strength of wood and wooden structures

[2]   Zhang, W., Sliker, A. (1991): Measuring shear moduli in wood with small tension and compression samples. Wood and Fiber Science, 23(1), 1991, pp. 58-68

[3]   Ebrahimi, G., Sliker, A. (1981): Measurement of shear modulus in wood by a tension test. Wood Science 13(3)171-176

EDUCATIONS-DEVELOPMENT INNOVATION OF PROGRAM "NANO- MICROSYSTEMS AND ELECTRONICS TECHNIQUE"

Prof. Dr-Ing. Stefan Kartunov, Dr-Ing. Desislava Petrova [1),]

[1)]   Technical University, Hadji Dimitar Str. 4, 5300 Gabrovo, Bulgaria.

Corresponding author: skartunov@abv.bg

1. Introduction

Components, subsystems and systems for various applications as automotive electronics, information systems, measurement and automation systems, medical and life science are tending to be fabricated by microtechnology [1]. The variety of components fabricated by Microtechnologies can be divided into different classes by their basic function [2-10].

2. Experimental Results

2.1. Fabrication Technologies

Corresponding to the basic function different fabrication technologies for microcomponents have been established where components of similar function also have been demonstrated by different technologies [2-3]. Besides monolithic integration on silicon microcomponents can be fabricated on different substrate materials which are suited for their specific applications. Shows some basic properties and the price range for 150 mm wafers [4].

2.2.   Integration Concepts

Depending on the function of the microcomponent different substrate materials must be processed independently, joined or bonded together. Thus we may distinguish different concepts of integration: *Hybrid integration* and *Multilevel wafer-stack*. Subject to market penetration of the product and the fabrication volume the best integration concept suited can be selected.

area (defined by function), μm^2; C_p – packaging costs per pin (ca. 0,01€ per pin); n_p – number of pins; C_h – housing or case costs. Thus the costs for a multilevel wafer-stack or hybrid integrated device with N substrate levels are calculating by [6]:

$$C_{total} = \sum_{i=1}^{N} (C_{mi} + C_{wi}) \times \frac{A_{ci}}{A_{wi}} + n_p \times C_p + C_h, i \in \{1 \dots N\}$$

The influence of various cost elements can be studied by a micromechanical silicon sensor with integrated electronic circuits. In the first case two separate chips are interconnected by n_p wire bonds where a standard CMOS process for the electronic chip and a bulk micromachined sensor chip with 8 mask levels have been assumed. The monolithic integration can be performed either by a subsequent process where firstly 16 mask levels of CMOS are processed followed by 8 additional mask levels for micromachining or a CMOS compatible process where only two additional mask levels for surface are assumed. For a representative sensor system some cost values are summarized with [6].

2.3.   Fabrication Costs

The fabrication costs of microstructure components can be calculated using different cost factors where certain factors depending on process complexity and production volume are dominant [4-5]. These cost factors can be evaluated and assigned to the fabrication process blocks listed above. A rough calculation for complete components is determined by the following parameters: C_{mi} – substrate material costs; C_{wi} – wafer processing costs (200 - 1000 € depending on technology); A_{wi} – wafer area (usable part), μm^2; A_{ci} – chip

Using these costs data the component costs are calculated versus the relative chip area of microelectronics. On Fig. 1 and Fig. 2 costs per chip versus relative microelectronic chip area; wafer costs assumed: monolith, integration one

(24 mask levels) 750 €, integration two (18 mask levels) 600€. When we consider different substrate materials and fabrication technologies of microstructured components the costs of processed wafers costs per chip area are very

different: CMOS 5 - 10, 12 - 18 mask levels [€cent/mm^2]; Thinfilm on glass max, 6 mask levels 3 – 5 [€cent/mm^2]; Surfacemicro-machining electroplatethinfilm, max 6 mask levels 2 – 4 [€ cent/mm^2]; LIGA (master), One synchrotron exposure > 1004 [€ cent/mm^2].
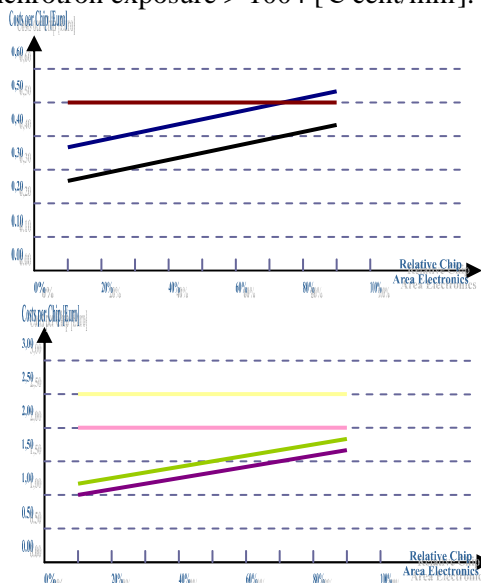
Fig. 1. Different mmC with total chip area A_c=10mm^2
Fig. 2. Different mmC with total chip area A_c=50mm^2

2.4. Educations-development innovation

In frame of education program "Nano and microelectronics and micro system technique" we propose the scientific investigation in the field nanotechnology of functional materials, modeling of constructions and systems MST and nano-devices and creation of sensors on the base of oxide functional materials. Such scientific works are carried out in Siberian Federal University (SFU) and in TU Gabrovo-BG [6]. Professional training consist in the perfect possess of specific technologies in the concrete field of science and technique. The successful bunch of specialist with wide fundamental training and narrow specialist can realize only at the complex approach to education. For that demands the introduction of fundamental knowledge's fragments in special courses. At the same time needs the logical organization of obtained knowledge's [7]. Education program "Nano- and microelectronics and micro system technique" should include row of disciplines. The teaching should build around system. The structure of education can be present as creative algorithms for all stage of learning in [8-9] in detail. During action of TEMPUS- and MON-BG-project will be prepare 3 course of educated students. Purpose and Tasks–Sumary. The applied scientific aspect is connected with modeling module usage for simulating of the component behaviour, without necessety of their real manufacturing [10].

3. Acknowledgements

The variety of Microtechnologies can be divided by device function and fabrication technology. The fabrication costs strongly depend on chip area and investment costs. Due to the device function the technology suited is determined and from that the wafer fabrication costs follow. Therefore the chip area required and the costs of processed wafers are the determinants of microcomponent costs. New methodology of education based on the providing of creative thinking experience, found and solve the manufactory tasks will allow to prepare the claimed high quality specialist.

4. References

[1] S. Kartunov, D. Petrova, Database management system for automated design of micromechanical components for products in microsystem engineering, RaDMI – 2003, 19-23. September 2003, Herceg Novi, Serbia and Montenegro.

[2] D. Petrova, Database management system for automated design of micromechanical components for products in microsystem engineering and CAD system "MICROSYS" by product innovation, ADP–2007, 18 – 20.10.2005, Semkovo, Bulgaria.

[3] D. Petrova, Economic aspects for effectiveness by produce micromechanical components based on Microtechnologies and effectiveness from application CAD system "MICROSYS", ADP – 2007, 18 – 20.10.2005, Semkovo, Bulgaria.

[4] D. Petrova, Actual concepts for realization of investment projects, Current problems in socio-economics by 21st century, Moskva (2008).

[5] E. Gongalova, D. Petrova, Investment and investigations projects, Express (2008).

[6] D. Petrova, Database management system for automated design of micromechanical components for products in microsystem, Dissertation (2008)

[7] S. Kartunov, T. Patrusheva, Development of education program "Nano and microelectronics and microsystem technique", RADMI – 2008, 14 - 17. September 2008, Užice, Serbia

[8-9]. Т. Патрушева, Учебная программа дисциплины, „Технология производства электронных средств", (In rushan language), Красноярск, СФУ, (2007); S. Kartunov, Учебна програма „Микротехника" (In bulgarian language), ТУ Габрово, (2003)

[10] S. Kartunov, CAD/CAM/CAE-System "MIKRISYS" (In bulgarian language), TU Gabrovo, Habilitation, 2008

INTERNAL DAMPING CAPACITY OF AZ31 ALLOY

Martin Kasenčák[1], Rastislav Mintách [1], Peter Palček[1]

1) University of Žilina, Faculty of Mechanical Engineering, Department of Materials Engineering,
Univerzitna 2, 01026 Žilina, Slovakia

Corresponding author: martin.kasencak@fstroj.uniza.sk

1. Introduction

Magnesium alloys are intensively investigated because of their potential applications in automotive and aerospace industry, when saving of weight and fuel is very important criteria. Magnesium alloy is one of the lightest (density 1.74 gm/cm^3) and prolific metallic material that has excellent mechanical properties such as workability, castability, weldability, creep resistance, specific strength and damping capacity. Simultaneously fine grain magnesium alloys have superior mechanical properties, especially strength then coarse grain alloy [1, 2].

The magnesium alloys belong to metals with excellent damping properties. Damping capacity is the result of interaction between vacancies, impurities, secondary phases and dislocations. The damping is also depended on many others factors as e.g. temperature, grain size, material purity, heat treatment etc. Current knowledge about internal damping behavior of Mg alloys is predominantly related to investigation in the region of low frequency loading (from 0.5 to 300 Hz) [3, 4]. Results of high frequency damping are practically messing in open literature.

The aim of this paper is to present results of a study of internal damping measurement of Mg alloy AZ31 in dependence of temperature at load frequency 20 kHz. The method of resonant system quality determination was used for the internal dumping measurement [5].

2. Experimental Results

Experimental results of damping tests for Mg alloy AZ31 obtain at the continuously heating of the specimen are presented in Fig. 1 and 2. The internal dumping was measured in dependence of the temperature in temperature interval from 35 to 250°C for alloy without heat treatment (Fig. 1) and for alloy after heat treatment (Fig. 2). The heat treatment comprise of homogenization annealing at temperature T = 415 °C, holding time at this temperature for 3 hours and consequential slowly cooling in the furnace. The goal of the heat treatment was removing the original dendritic structure and achieve of polyhedral grains. In Fig. 1 two damping curves marked as the 1th and the 2th measurement are compared. The measurements were performed only in one test bar. It can be seen that the damping does not considerably depend on the temperature up to 200 ^{o}C for both measurements. However significant damping maximum was detected at 150 ^{o}C with other considerable smaller damping peaks in this temperature interval. Concretely the damping value at the temperature 150 ^{o}C was 1.75x10^{-4} for the 1th measurement and 1.8x10^{-4} for the 2th measurement. As can be seen from both damping curves the damping further increases from 200 ^{o}C with increasing of the temperature. It can be further seen from Fig. 1 that the 2th measurement has damping phone (i.e. zone without phase transformation) moved to higher value than for the 1th measurement. Higher damping value for 2th measurement can be probably explained by partial annealing of test bar during 1th damping measurement
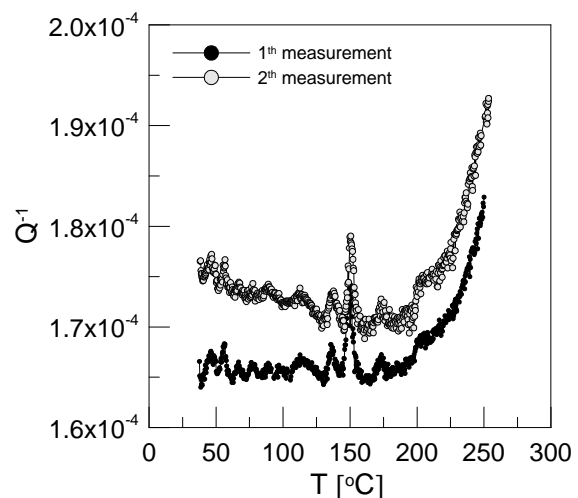
Fig. 1 Damping curves for non-heat treated AZ31

performed to 250 ^{o}C.

The damping curves for annealed alloy are shown in Fig. 2. A couple of damping measurements after heat treatment was performed in same test bar as in the case of original state of Mg alloy (without heat treatment) and is marked as the 3th and 4th measurement. These results are compared together with damping curves for original state (1th and 2th measurement). It can be seen that the heat treatment considerably influenced the character of damping curves, namely by occurrence of two damping maximums at the temperatures 173 ^{o}C and 230 ^{o}C. The damping value was 2.8×10^{-4} for the 3th measurement, and 3.1×10^{-4} for the 4th measurement at 173 ^{o}C and approximately 4.5×10^{-4} for both measurements at 230 ^{o}C. From Fig. 2 can be seen that maximum damping values measured for heat treated alloy are almost three times higher than that for non-heat treated alloy. That is why the maximum peaks for original state of alloy nearly disappeared.
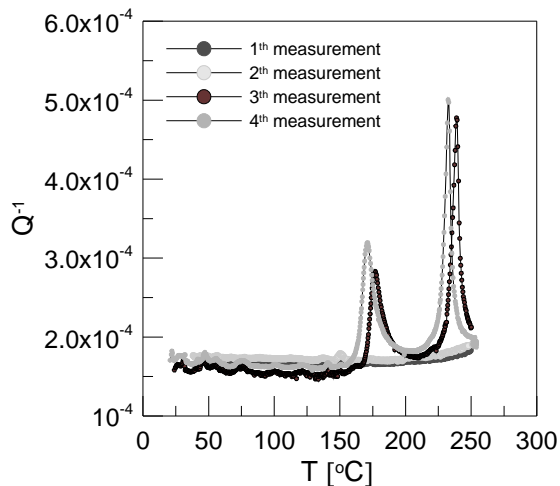
Fig. 2 Damping curves for heat treated AZ31 alloy.

Measured damping maximums can be explained by relaxation processes took place in material for both original and heat treated state of AZ31 alloy. The relaxation processes can be connected with dislocation motion and their interaction with vacancies, impurities, secondary phases or grain boundaries [6]. For lower temperatures (to 120 ^{o}C) the internal damping process is probably a result of dislocation motion in basal planes whereas at higher temperatures grain boundary sliding plays dominant role.

Internal damping measurement of AZ31 magnesium alloy provided these results:

- The dependence of internal damping on temperature was measured for original and heat treated magnesium alloy AZ31 in the temperature range from 35 to 250 ^{o}C.
- In both cases the damping maximums were measured that can be explained by relaxation processes taking place in material.
- The damping values for heat treated alloy were three times higher than that for original state.

3. Acknowledgements

4. References

[1] Ashis Mallick, Srikanth Vedantam, Li Lu: Materials Science and Engineering A 515 (2009) 14–18.

[2] Manuel Marya, Louis G. Hector, Ravi Verma, Wei Tong: Materials Science and Engineering A 418 (2006) 341–356.

[3] Wu S.K, Chang S.H., Chou T.Y., Tong S.: Journal of Alloys and Compounds 465 (2008) p. 210.

[4] Trojanová Z., Weidenfeller B., Riehemann W.: Thermal stresses in Mg–Ag–Nd alloy reinforced by short Saffil fibers studied by internal friction, Mat. Sci. Eng. A 442 (2006) p. 480.

[5] Nishiyama K., et.al.: In: Journal of Alloys and Compounds 355 (2003) p. 22.

[6] Hu X. S., et. al: Scripta Materialia 54 (2006) p. 1639.

EXPERIMENTAL VERIFICATIONS OF CONTROL OF ASYMMETRIC BUILDINGS VIBRATIONS BY TUNED LIQUID COLUMN GAS DAMPERS

Basit Khalid [1],

[1] Vienna University of Technology, Center of Mechanics and Structural Dynamics, Karlsplatz 13/E2063
1040 Vienna, Austria.

Corresponding author: e0628013@student.tuwien.ac.at

1. Introduction

The gas-spring effect of Tuned Liquid Column Gas Dampers (TLCGDs) makes it more practical and robust when compared to typical "classically designed" Tuned Liquid Column Dampers (TLCD), the cost-effective passive energy dissipating devices, to increase the effective structural damping of vibration-prone buildings when subjected to dynamic loads like earthquakes or wind gusts. The main objective of this paper is to examine the influence of a prototype TLCGD both, experimentally (under laboratory conditions) and analytically, on the dynamic response of such a multi-purpose building model. The state-of-the-art designed TLCGD consists of a U- or V-shaped rigid piping system sealed at both ends, partially filled with water along with a gas (e.g., air) enclosed in a chamber above the water, allowing the water column to oscillate and hence, in addition to gravity, a restoring force develops due to the gas-spring effect. The parameters of the gas-spring, the chamber-volume above the water and the equilibrium gas pressure, play a key role for frequency optimisation of the TLCGD. A series of experiments are performed (possibly first time even worldwide) to determine the dynamic response of a coupled asymmetric structure-TLCGD system. The experimental setup consists of a laboratory scaled single-storey mass- and stiffness- asymmetric 3-DOF light-weight space frame model equipped with a TLCGD properly tuned to the first natural frequency of the main structure. The base plate of the model is mounted on rails and connected to the shaker, hence capable of moving forth and back so as to simulate the base excitation for the whole model under various angles of attack. Since the centre of mass and the centre of stiffness do not coincide for an asymmetric structure, even the uni-directional seismic base excitation causes a three dimensional in-plane motion (including rotation about the vertical axis) of the floor [9]. The (optimal) position of the TLCGD on the structure is decided to keep the normal distance of its mid-plane to the modal centre of velocity maximum within the design limits [7,9]. The response of the model equipped with the TLCGD is measured for both cases: the TLCGD piping system added but without water and the properly tuned TLCGD. The modal analysis of asymmetric 3-DOF-space frame depicts three eigen frequencies and corresponding mode shapes of the model. Modelling the TLCGD as a single degree of freedom oscillator (the piston theory was applied to the relative fluid flow), a substructure-synthesis is also performed. Since the modes of the main structure seem to be sufficiently well separated, modal tuning of the TLCGD is performed in a first step by a transformation of the classical Den Hartog formulas by means of a worked analogy between TMD (tuned mechanical damper) and TLCGD[7,9]. Optimal TMD design parameters, frequency ratio and damping ratio, are determined subjected to the harmonic excitation rendering the absolute acceleration minimum. Assigning the equilibrium gas pressure and adjusting the size of the gas volume, the novel pair of control parameters resulting from such a sealed design, easily tune the absorber frequency to its optimal value. The results by numerical simulations are found to be in good agreement with those of the experimental output when substituting the experimentally measured damping parameters of the main structure and of the absorber (the latter differs only slightly from its optimal value, consequently no attempt was made to adjust a

properly designed orifice plate in the relative fluid flow).

2. Experimental Results

Fig.1 shows the experimental configuration of laboratory model whose base is attached with a shaker at angle of attack of 120° along with accelerometers and properly tuned and position TLCGD.
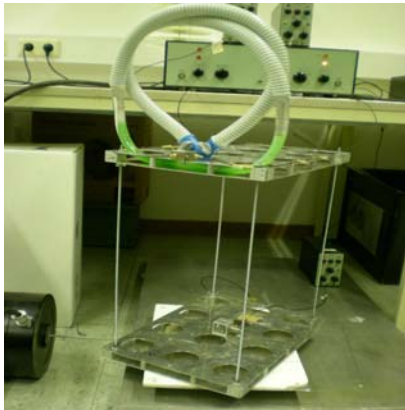
Fig. 1: Experimental configuration of laboratory model; green colour of water is due to dye for better visibility of its surface strokes.

The response in the form of ratio of absolute value of acceleration at top plate and base plate of the model over the ratio of excitation frequency to its first natural frequency both for TLCGD installed but without water and tuned TLCGD are shown in Figs. 2 and 3.
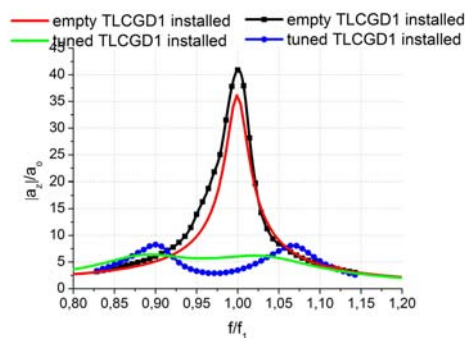
Fig. 2: The line with square and circles show the experimental results while the plane lines represent the simulated results with Den Hartog's optimal value of damping of TLCGD.
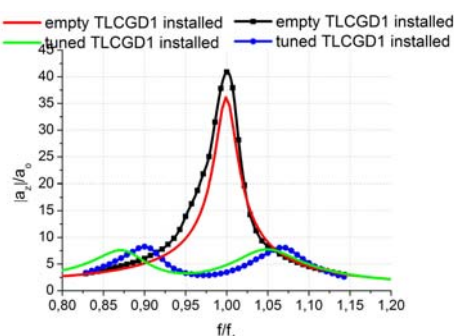
Fig. 3: The line with square and circles show the experimental results while the plane lines represent the simulated results with experimentally measured damping of TLCGD.

3. Acknowledgements

4. References

[1] Hochrainer MJ. Control of vibrations of civil engineering structures with special emphasis on tall buildings. Dissertation, Vienna University of Technology, Austria, 2001.

[2] Hochrainer MJ. Tuned liquid column damper for structural control, Acta Mechanica, 175(2005)57-76.

[3] F. Ziegler, Der fluessigkeitstilger daempft schwingungen im hoch- und brueckenbau. bauingenieur 81(2006), 259-270

[4] Hochrainer MJ, Ziegler F. Control of tall building vibrations by sealed tuned liquid column dampers, Structural Control and Health Monitoring, 13(2006) 980-1002.

[5] Ziegler F. Mechanics of solids and fluids, corr. Repr. 2nd ed. Springer, New York, 1998.

[6] F. Ziegler, Special design of tuned liquid column-gas dampers for the control of spatial structural vibrations. Acta Mechanica 201 (2008), 249–267.

[7] Chuan Fu and F. Ziegler, Vibration prone multi-purpose buildings and towers effectively damped by tuned liquid column-gas dampers. Asian J. Civil Engrg. (Building and Housing) 10/1 (2009), 21-56.

[8] Ziegler F. The tuned liquid column damper as the cost-effective alternative of the mechanical damper in civil engineering structures. International Journal of Acoustics and Vibration, No. 1, 12 (2007) 25-39

[9] Fu Chuan, Effective damping of vibrations of plan-asymmetric buildings, Dissertation, Vienna University of Technology, Austria.

[10] Yalla SK, Kareem A. Semiactive tuned liquid column dampers: experimental study ASCE Journal of Structural Engineering 2003, 129:960-971.

VARIABILITY OF GAIT CHARACTERIZED BY NORMALIZED DEVIATION OF PARAMETERS

Kiss Rita [1],

[1] Budapest University of Technology and Economics, Dept of Structures and Research Centre of Biomechanics, Bertalan L. 2, 1111 Budapest, Hungary.

Corresponding author: kissrit@t-online.hu

1. Introduction

Dynamic perception is the reiterative accuracy of well-known movement. The high number of gait cycles (minimum 25 cycles) analyzed provides an opportunity to calculate the average and standard deviation of different temporal and spatial parameters of each subject. The standard deviation of parameters characterizes the variability of gait.

The study included 45 healthy, young subjects, 11 professional hand ball players, 24 patients after medial meniscectomy, 20 elderly, healthy subjects, and 20 patients with hip osteoarthritis. The gait parameters were determined during a treadmill walking (Fig.1) and the temporal and spatial parameters are calculated from the vertical-reaction force vs time graph. The details of measuring method are in [1].The average, standard deviation and normalized deviation of parameters were calculated for each individual.

Fig. 1: Instruments of simplified gait analysis

2. Experimental Results

For the sake of clarity, the results are summarized in Table 1 in average±SD form.

All subjects were able to walk 50 gait cycles on the treadmill at a speed of 3.6 km/h.

The high number of gait cycles analyzed gives us the opportunity to calculate the average and standard deviation of different temporal and spatial parameters of each subject investigated.

The normalized deviation of parameters enables the modelling of dynamic perception, because it is independent from the value of parameters due to normalization. Our tests show that the size of the parameter is independent from lateral dominance at healthy subjects (Table 1).

The normalized deviation of parameters does not depend on the type of parameters, because dynamic perception is independent from the type of modelling parameters. It means that the analysis of one or few parameters is enough for modelling dynamic perception.

The value of normalized deviation of professional athletes is significantly smaller, than that of healthy age-matched non-professional athletes (Table 1). This confirms the assumption that sports develop static and dynamic perception.

The value of normalized deviation of healthy, elderly subjects is significantly higher, than that of healthy young persons (Table 1). This confirms the assumption that propriocepcion declines with age.

The value of normalized deviation of patients after mensicectomy at both sides is higher than that of healthy age-matched persons (Table 1). This means that the dynamic

perception of the non-affected side declines after the surgery. The value of normalized deviation of the affected side is higher than that of the non-affected, healthy side (Table 1). This finding correlates with the fact that the injury of anterior cruciate ligaments reduce proproception.

The value of normalized deviation of patients with coxarthrosis at both sides is higher than that of healthy age-matched persons (Table 1). This means that the dynamic perception of the non-affected side declines. The value of normalized deviation of the affected side is higher than that of the non-affected, healthy side (Table 1). This finding correlates with the fact that coxarthirtis reduces static proproception.

In conclusion, the simplified gait analysis method can be used for describing the spatial and temporal parameters of a number of gait cycles. The average and standard deviation of parameters of each subject investigated can be calculated. The normalized deviation of parameters enables the modeling of dynamic perception, because it is independent from the value of parameters due to normalization. Our tests show that the size of the parameter is independent from lateral dominance at healthy subjects. The size of the normalized deviation of parameters depends on age, on the intensity

of sports activities, and on orthopeadical diseases. The deviation of spatial and temporal parameters during gait cycles provide a useful, simple quantitative evaluation of the effect of age, movement deficits or sport activities on dynamic perception and movement stability.

3. Acknowledgements

4. References

[1] R.M. Kiss, L. Kocsis, Verification of simplified gait analysis. Periodica Polytechnica, Vol. Online First (2009)

Group	Length of swing phase		Length of double support phase	Cadence	Step length	
	% of cycle		*% of cycle*	*step/minutes*	*mm*	
	Dominant/ Healthy	*Non-dominant/ Affected*			*Dominant/ Healthy*	*Non-dominant/ Affected*
Healthy young	0.183 ± 0.004	0.182 ± 0.005	0.184 ± 0.003	0.181 ± 0.007	0.183 ± 0.002	0.182 ± 0.003
Hand ball players	0.144 ± 0.001	0.143 ± 0.003	0.142 ± 0.002	0.139 ± 0.003	0.142 ± 0.001	0.142 ± 0.004
Healthy elderly	0.234 ± 0.003	0.233 ± 0.002	0.233 ± 0.004	0.232 ± 0.005	0.232 ± 0.004	0.238 ± 0.002
Subjects after meninscectomy	0.201 ± 0.005	0.263 ± 0.006	0.261 ± 0.003	0.263 ± 0.006	0.204 ± 0.003	0.264 ± 0.005
Elderly with hip osteoarthritis	0.273 ± 0.002	0.347 ± 0.003	0.346 ± 0.005	0.349 ± 0.004	0.271 ± 0.005	0.351 ± 0.006

Tab. 1: Average ± SD of normalized deviation of individuals' spatial-temporal parameters

INCOMPRESSIBILITY AND ISOTROPY OF ABDOMINAL AORTIC ANEURYSMS WALLS

Magdalena Kobielarz[1], Romuald Będziński[1]

[1]Wrocław University of Technology, Faculty of Mechanical Engineering, Institute of Machine Design and Operation, Division of Biomedical Engineering and Experimental Mechanics, Łukasiewicza Str. 7/9, 50-371 Wrocław, Poland

Corresponding author: magdalena.kobielarz@pwr.wroc.pl

1. Introduction

Soft tissues in general have a water content of more than 70% and have negligible permeability [1,2]. Therefore, they hardly change their volume even if load is applied. The conservation of constant volume in period of duration of material deformation is invoked the incompressibility assumption [3]. The incompressibility assumption leads to many theoretical simplifications in constitutive model formulations and simple stress analyses because insertion incompressibility constraint (J) into material equation defined as $J \equiv detF = \lambda_1\lambda_2\lambda_3 = 1$ gives thereby $I_3 = 1$.

The walls of blood vessels can sustain finite strains without any noticeable their volume changes, they can be regarded as incompressible materials [1]. The incompressibility assumption of arterial walls has been confirmed experimentally in unique papers [4,5].

In recent years, the experimental mechanical studies of abdominal aortic aneurysms (AAAs), which is the area of a localized and irreversible dilation of a normal abdominal aorta (NAA) have been developed. Although many workers have made the assumption that the AAA wall behaves as an incompressible and isotropic material, the experimental evidence for it is insufficient [6,7].

2. Experimental Results

The uniaxial tensile tests were performed on specimens cut out walls of abdominal aortic aneurysms (n=96) and normal abdominal aorta (n=67) with the use of *MTS Synergie 100* loading system (Fig. 1). Specimens were cut from biological materials in two orthogonal directions: longitudinal (l) and circumferential (c).

Fig. 1. MTS Synergie 100 loading system and videoextensometer system.

The incompressibility and isotropy assumption was verified on the basis of an analysis of the changes in the geometric dimensions of the scrutinized specimen during tests. The geometric dimensions were recorded by the videoextensometer system (*ME 46-350, Messphysik),* employed in such tests for the first time. Stretch ratios were defined on the basis of changes in the geometrical dimensions:

$$\lambda_1 = \lambda_l = \frac{\partial l}{\partial l_0}$$

$$\lambda_2 = \lambda_s = \frac{\partial s}{\partial s_0}$$

$$\lambda_3 = \lambda_g = \frac{\partial g}{\partial g_0}$$

The incompressibility (Tab. 1) and isotropy assumption (Tab. 2) for each analyzed specimen were collected.

Tab. 1. Values of the incompressibility constraint for abdominal aortic aneurysms and normal abdominal aorta cut in two directions: longitudinal and circumferential.

$\lambda_1\lambda_2\lambda_3$			
AAAc	**AAAl**	**NAAc**	**NAAl**
0,98±0,21	0,99±0,25	0,98±0,08	0,99±0,03

Tab. 2. Values of the stretch ration λ_2 and λ_3 for abdominal aortic aneurysms and normal abdominal aorta.

λ_2		λ_3	
AAAc	**AAAl**	**NAAc**	**NAAl**
0,95±0,04	1,0±0,06	0,94±0,04	0,97±0,04

Obtained results indicate that incompressibility and isotropy is a reasonable assumption in that AAA tissues under uniaxial tensile tests and can be straightforward applicable to compute the constitutive modeling.

The assumption of the incompressibility and isotropy of the aortic aneurysms walls allows describing a stress-strain characteristic, which is a highly non-linear curve (Fig.2) by a hyperelastic model, founded on the neo-Hookean generalized model:

$$\Psi = c(\lambda_1^2 + \lambda_2^2 + \lambda_3^2 - 3) = c(I_1 - 3)$$
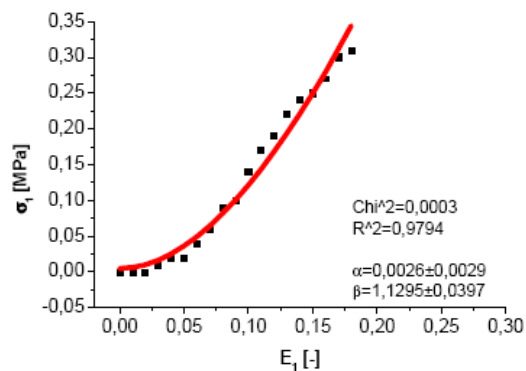
Fig. 2. Stress-strain relationship for abdominal aortic aneurysm cut in circumferential direction (AAAc).

They were described fairly precisely by an essential equation derived from used model ( ). The model applied is a phenomenological model and may be called quasi-structural because of its conformity to the Holzapfel's and Weizsacker's postulate [8], which talks about the additive split of the isochoric strain-energy function into parts connected with the different deformation of a structure; it's mean connected with elastin and collagen fibres (Fig. 3). It's very important mathematical describe behavior of AAAs' walls under deformation to take into consideration influence of complex structure.
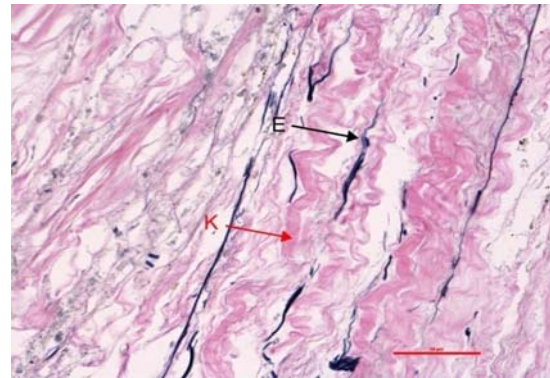
Fig. 3. Collagen and elastin fibres in aortic abdominal aortic aneurysm walls.

3. References

[1] G. Holzapfel, R. Ogden, Biomechanics of soft tissue in cardiovascular systems. SpringerWien NewYork (2003).

[2] J. Vande Geest, M. Sacks, D. Vorp, The effects of aneurysm on the biaxial mechanical behavior of human abdominal aorta. Journal of Biomechanics Vol. 39 (2006) 1324–1334.

[3] R. Vito, S. Dixon, Blood vessel constitutive models—1995–2002. Annual Review of Biomedical Engineering Vol. 5 (2003) 413– 39

[4] T. Carew, R. Vaishnav, D. Patel. Compressibility of the arterial wall. Circulation Research, Vol. 23 (1968) 61– 68

[5] C. Chuong, Y. Fung. Compressibility and constitutive equation of arterial wall in radial compression experiments. Journal of Biomechanics, Vol. 17 (1984) 35–40.

[6] B. Tóth, G. Raffai, I. Bojtár. Analysis of the mechanical parameters of human brain aneurysm. Acta of Bioengineering and Biomechanics, Vol. 7 (2005) 3–23

[7] M. Kobielarz, S. Szotek, P. Kuropka, K. Kaleta. Mechanical and structural properties of abdominal aortic aneurysms. Engineering of Biomaterials, Vol. 11 (2008) 98–100.

[8] G. Holzapfel, H. Weizsacker. Biomechanical behavior of the arterial wall and its numerical characterization. Computers in Biology & Medicine, Vol. 28 (1998) 377–392.

SURFACE PROPERTIES OF TOOL STEEL DEFORMED BY THERMAL FIELDS ORIGINATED MACHINING

Kamil Kolařík [1], Nikolaj Ganev [1], Jan Drahokoupil [1], Zdenek Pala [1],

Petr Haušild [2] and Alena Michalcová [3]

[1] Czech Technical University in Prague, Faculty of Nuclear Sciences and Physical Engineering, Department of Solid State Engineering, Laboratory of X-ray diffraction, Trojanova 13, 120 00 Praha 2, Czech Republic,

[2] Czech Technical University in Prague, Faculty of Nuclear Sciences and Physical Engineering, Department of Materials, Trojanova 13, 120 00 Praha 2, Czech Republic.

[3] Institute of Chemical Technology in Prague, Faculty of Chemical Technology, Department of Metals and Corrosion Engineering, Technická 5, 166 28 Praha 6, Czech Republic.

Corresponding author: kamil.kolarik@email.cz

1. Introduction

Electric discharge machining (EDM) is a process for eroding and removing material from electrically conductive materials by use of consecutive electric sparks. The process is carried out in a dielectric liquid with a small gap between the workpiece and electrode. Each electrical discharge generates heat energy in a narrow area that locally melts, evaporates and is flushed away by dielectric liquid and the remaining melt is recast on the finished surface. The recast layer is referred as white layer. This layer is the result of the solidification of melted zone and known to exhibit high hardness, good adherence to bulk and good resistance to corrosion. However, it contains microcracks as seen in Fig. 1 which may constitute a problem for some applications. Beneath recast layer, a heat affected zone (HAZ) is formed due to the rapid heating and quenching cycles during EDM [1, 2].
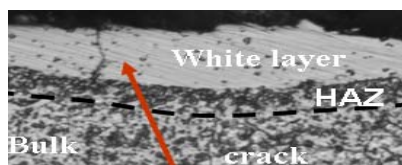
Fig. 1: White layer after EDM in roughing mode. The heat affected zone between white layer and workpiece is also shown.

2. Sample under Investigation

The experimental samples were made from Böhler W300 ferritic-perlitic steel which is widely used in die-sinking industries. One half of the samples was left in basic state, the other was tempered onto hardness of 53 – 54 HRC.

The process of EDM was done by a generator with indirect polarity (tool +, workpiece -). This technology was carried out on the commercial machine *WALTER Exeron S 204* with pulse generator. Two modes of machining were used; *finishing* and *roughing* were done by graphite and copper electrode.

3. Experimental Techniques

The state of residual stresses (RS) was determined by X-ray diffraction (XRD), Barkhausen noise (BN) and layer removal methods (LRM). Phase composition of cut area was evaluated by Rietveld line profile analysis from XRD data [3]. Microstructure and chemical composition of white layer and heat affected zone was investigated using optical microscope and electron microprobe with EDX analysis. The samples were also examined for microhardness HV 0.2.
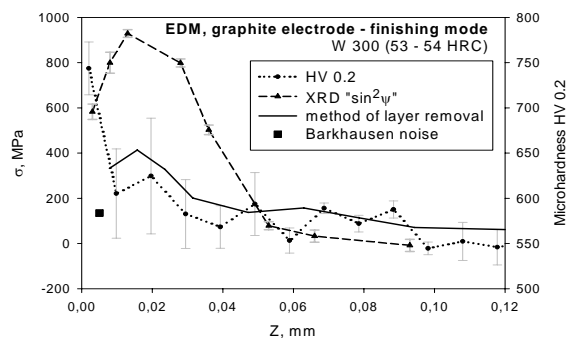
Fig. 2: Results of microhardness and RS for the tempered steel *W 300* machined by graphite electrode in finishing mode.
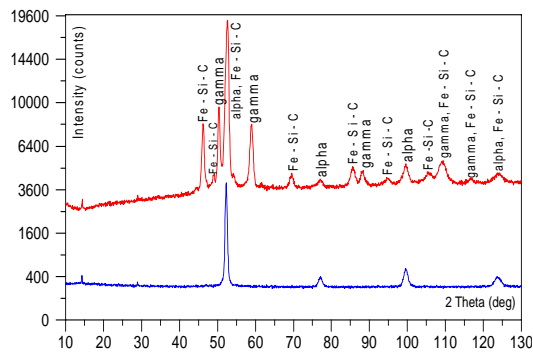
Fig. 3. X-ray patterns of the surface – white layer (upper) and bulk (lower) after EDM.

4. Discussion

Phase analyses of samples machined by roughing mode exhibit similar phase composition in surface layer of 2 μm in thickness and are distinguished by higher content of gamma iron in comparison to finishing mode. Heat treatment does not influence phase composition, but plays an important role in the formation of HAZ. The white layer appears consistent after etching and dendritic structure can be seen. These dendrites are mostly oriented in the same direction, i.e. perpendicular to the surface which is the direction of the maximum cooling gradient. In contrast to the high energy roughing mode (thickness: 20 – 30μm), the finishing mode produces a much thinner white layer (≈ 3 – 6 μm). Heat treatment did not have an impact on the white layer thickness. Due to oil dielectric, large enrichment in carbon content in the white layer with respect to the base material can be seen from EDX analysis. Level of carbon enrichment varies according to the electrode material. The carbon content in the white layer is two and three times as much as in the bulk for copper and graphite electrode respectively.

According to XRD residual stress analysis, EDM generates tensile residual stresses (RS), which increase in value from the surface till the depth where they reach a maximum. This maximum value is around the ultimate tensile strength of the material. Lower values of RS on the surface compared to the maximum in the depth distribution are caused by crack formation since the RS exceed the fracture strength of the material. The further decrease of RS from the point of maximum is due to the condition of mechanical balance between plastically deformed surface and elastically deformed bulk. Maximum values of RS are higher for tempered materials in comparison

with untempered ones. Explanation for such the observed behaviour may rest in the effect of volume changes induced by metallurgical and phase transformations which cannot be omitted for case of hardened material. However, the RS are principally induced by heterogeneous thermal plastic deformations that are the consequences of volume expansions due to surface heating. The transformational processes introduce compressive stress at the surface, yet the initial effect of thermal expansion remains much important and final RS are tensile at the surface.

Samples machined by graphite electrode are distinguished by higher maximal RS in the depth distributions. Surface RS for the case of roughing mode are systematically lower in comparison to finishing mode.

Results of LRM indicate surface values of RS in the rage of 250 to 350 MPa and 550 to 800 MPa for tempered and untempered samples, respectively. Stress distributions are again declining functions of depth. No significant differences between roughing and finishing modes or between the electrode type are observed. RS determination utilizing BN did not reveal any information which would contribute to the analysis of EDM processing parameters.

Microhardness was approx. 580 and 220 HV 0.2 for tempered and untempered samples, respectively. No pronounced surface hardening was recorded except for tempered samples machined by roughing.

5. Acknowledgements

6. References

[1] G. Cusanelli et al.: Microstructure at submicron scale of the white layer produced by EDM technique. J. Mater. Proc. Tech. 149 (2004) 289-295.
[2] B. Ekmenci: Residual stresses and white layer in EDM. Appl. Surf. Sci. 253 (2007) 9234-9240.
[3] Guinebretière, R.: X-ray Diffraction by Polycrystalline Materials. ISTE 2007.

ON THE COPPER BEHAVIOUR SUBJECTED TO TORSION CYCLES AND MONOTONIC TENSION

Zbigniew L. Kowalewski [1), 2)], Tadeusz Szymczak [1), 3)]

[1)] Motor Transport Institute, 80 Jagiellońska St., 03-301 Warsaw, Poland

[2)] Institute of Fundamental Technological Research, Department for Strength of Materials,
21 Świętkorzyska St., 00-049 Warsaw, Poland

[3)] Bialystok University of Technology, Department of Applied Mechanics,
45C Wiejska St., 15-351 Bialystok, Poland

Corresponding author: tadeusz.szymczak@its.waw.pl

1. Introduction

Rapid progress in production of commercial and novel engineering materials creates a necessity for elaboration of more efficient forming technologies. The main research aspect related to this problem frequently leads to reduction of the fabrication costs and elaboration of a new more effective material forming technologies, [1]÷[3]. Just cited papers present an influence of twisting moment on variations of technological parameters during such processes as forging [1] or extrusion [2]. Unfortunately, they do not show stress or strain components variations during the whole loading history. Such knowledge is important from mechanical point of view since provides info allowing constitutive modelling of new technological processes related to different combinations of cyclic and monotonic loading.

This paper puts forward a bit our understanding in this matter since it delivers a new data identifying an influence of torsion cycles on uni-axial monotonic tension.

2. Experimental Details

All tests were carried out under biaxial stress state being combination of monotonic tension and torsion–reverse–torsion cycles. All specimens were manufactured form rods of the M1E pure cooper commonly used in different branches of industry. The specimens were mounted in the gripping system of the computer controlled servo-hydraulic biaxial testing machine. An application of the thin walled tubular specimens allowed the homogeneous biaxial stress conditions to be achieved in the material tested.
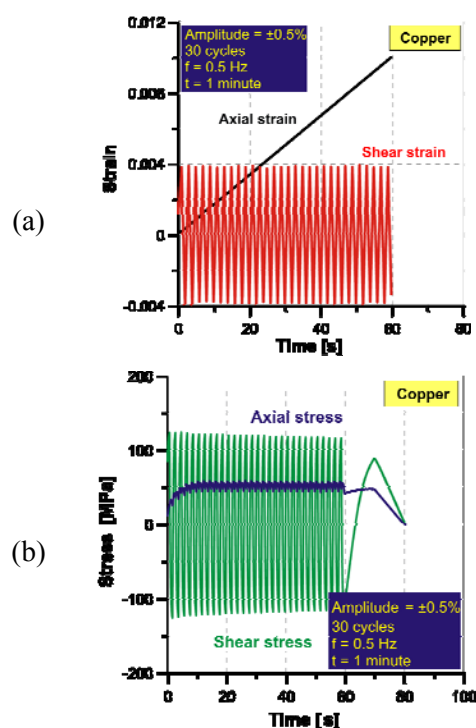
Fig. 1: Loading programme: (a) strain control signals; (b) stress responses.

All tests were strain controlled and the total value of deformation was lower than ±1%. Typical strain controlled loading paths and stress responses in to them are presented in Fig. 1. Four values of cyclic strain amplitude were applied: ±0.3%, ±0.5%, ±0.7% and ±0.9%.

3. Experimental results and disscusion

The experimental results exhibit a force reduction and lowering of the typical material parameters such as the proportional limit and

yield point, Fig. 2. The effects are very strong and depend on the amplitude of the torsion cycles. An increase of the cyclic shear strain amplitude leads to the further decrease of the stress-strain characteristic and the ductility improvement.

(a)
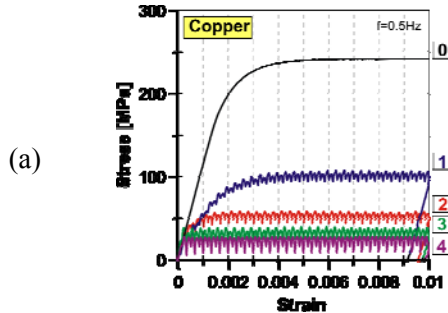
Fig. 2: Comparison of the stress–strain characteristic for the M1E copper; (0 – monotonic tension, 1, 2, 3, 4 – tension assisted by torsion–reverse–torsion cycles for the strain amplitudes equal to ±0.3%, ±0.5%, ±0.7%, ±0.9%, respectively).
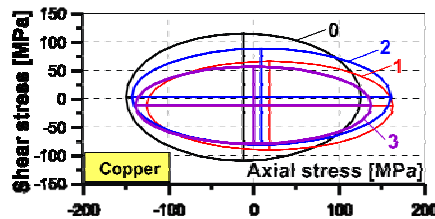
Fig. 3: Comparison of the initial yield surface (0) and subsequent yield loci determined after monotonic tension and torsion cycles for the strain amplitudes equal to ±0.3% (1), ±0.5% (2), ±0.7% (3).

Mechanical parameters variations observed during the main loading programme were checked after unloading process using the yield surface concept, Fig. 3. As it clearly seen, the subsequent yield loci confirm that the reduction of the typical material parameters is only related to torsion–reverse–torsion cycles during monotonic tension. In the tension direction instead of softening the hardening effect of material is visible (Fig. 3). The axial force reduction effect during monotonic tension assisted by torsion cycles (Fig.2) just disappeared. Such behaviour of the material identifies a transient character of the effect in tension direction during an acting of the torsion–reverse–torsion cycles. An additional interesting feature of the copper tested can be easily noticed looking on the torsion direction, Fig. 3. The material softening takes place as an effect of prior torsion cycles. The initial yield surface evolution well reflects it.

4. Remarks

- The torsion–reverse–torsion cycles conducted in the perpendicular direction with respect to the simultaneous monotonic tension leads to an essential axial force reduction.
- An increase of cyclic strain amplitude of the torsion–reverse–torsion cycles increases this effect.
- For the highest strain amplitude of the torsion cycles (±0.9%) considered in the experimental programme a decrease of the mechanical parameters attains the level of 90%.
- The axial force reduction observed during the monotonic tension assisted by torsion–reverse–torsion cycles has a transient character, and it vanishes after interruption of the torsion cycles.
- Such a great force reduction can be treated as an important factor for modification of any technological processes being combination of monotonic and cyclic loading since it gives promising tool for energy demand reduction, and moreover, it ensures more beneficial working conditions leading to the lifetime prolongation of working tools applied.

Acknowledgement

References

[1] W. Bochniak, A. Korbel, R. Szyndler, R. Hanarz, F. Stalony-Dobrzański, L. Błaż, P. Snarski, New forging method of bevel gears from structural steel, J. Mat. Proc. Tech., Vol. 173 (2006), 75–83.

[2] L. X. Kong, P. D. Hodgson, Constitutive modeling of extrusion of lead with cyclic torsion, Mat. Sci. Eng., Vol. A 276 (2006), 32-38.

[3] W. Bochniak, A. Korbel, R. Szyndler, Innovative solutions for metal forming, Proc. Inter. Conf. MEFORM 2001 – Herstellung von Rohren und Profilen, Institut für Metallformung Tagungsband, 239, Freiberg/Riesa, 2001.

STRAIN AND STRESS ANALYSIS IN THE ELASTIC-PLASTIC STATE BY PHOTOELASTIC COATING METHOD

Barbara Kozłowska

Warsaw University of Technology, Faculty of Mechatronical Engineering, ul. Św. Andrzeja Boboli 8, 02-525 Warsaw, Poland.

Corresponding author: B.Kozlowska@mchtr.pw.edu.pl

1. Introduction

The quantitative strain and stress analysis in the elastic-plastic state is of great importance, since the partial material plastifying in the constructional elements during exploitation is acceptable. Because of the difficulties in modelling non-linear problems, theoretical and numerical design always contains some inaccuracy and still needs a final experimental verification. One of the experimental methods which enable the investigation of the constructional elements at working conditions is photoelastic coating method.

In photoelastic coating method, based on the effect of the optical birefringence which occurs in some transparent materials under loading, the thin layer of birefringent material is bonded integrally to the surface of the analyzed object. When the object is loaded and viewed through a reflection polariscope, the surface strains are transmitted to the coating, which exhibits two families of fringe patterns: isoclinic fringes supplying information about directions of principal strains and isochromatic fringes supplying information about the difference of principal strains. The method of photoelastic coating may be applied to the elastic-plastic states analysis due to the assumption of the linear relation between the photoelastic effect and strain in the birefringent material in a wide range. The advantage of photoelastic coating method is its good visualisation of the material plastifying process.

2. Experimental Results

The investigation of elastic-plastic states by means of photoelastic coating method was performed on the models of constructional elements with different stress concentrators made of duralumin sheet 3 mm thick (fig.1) covered with the photoelastic coating.
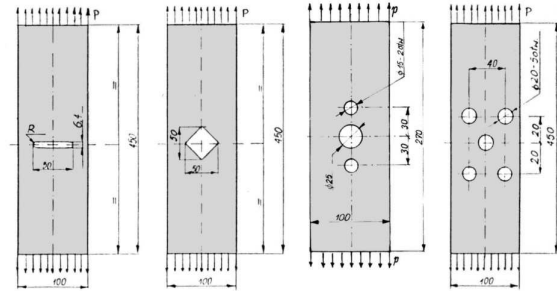
Fig.1. Models of the constructional elements.

The models were loaded at their ends by the uniformly distributed tensile stresses within the over-elastic range of material. As the measure of the intensity of loading the 'loading factor' (s) was accepted (tensile stresses (p) in relation to yield point $R_{0.2} = 182$ MPa).

The photographs of isochromatic pattern were taken for the models (fig.1) under various levels of loading in elastic-plastic range. The isochromatic fringes taken for the model III (with three holes) for a dark-field polariscope at chosen loading levels are shown on fig.2.

a)   b)
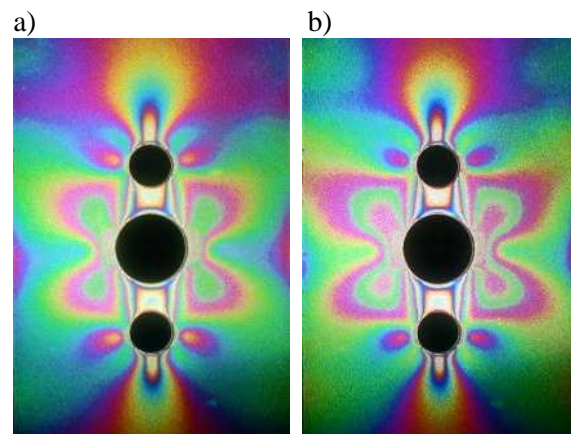
Fig.2. Isochromatic fringes at loading levels: a) s = 0.879, b) s = 0.928

The strain components separation on the basis of the isochromatic fringes was held using the analytical method of characteristic. This method makes use of the relations between the

strain and stress tensor components (Hooke's law) and its extension for over-elastic range of the material required creating of the analogous relations for nonlinear part of the characteristic. For derivation of formulas describing the mentioned relations, the geometrical model of real σ–ε curve was considered [1]. In this model experimentally obtained material characteristic is replaced by n line segments (fig.3). The obtained relations were also used to calculate stress components for non-elastic range of material in analyzed model.

For strain separation and determination of the stress components in the elastic-plastic zones of the models, the 6-sectional model of material characteristic was accepted (fig.3).
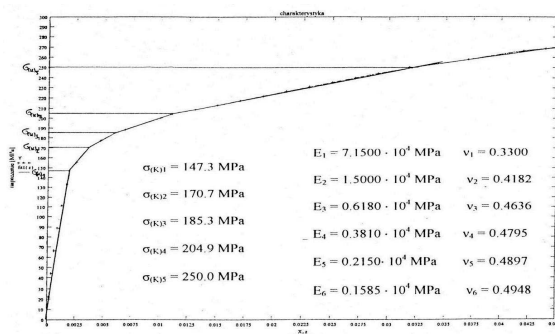
Fig. 3. Model of the material characteristic

The analyzed area for one of the models (model with three holes) for the chosen loading level $s = 0.928$ is shown on fig.4. Because of the double symmetry of the model and loading, only one quarter was considered.
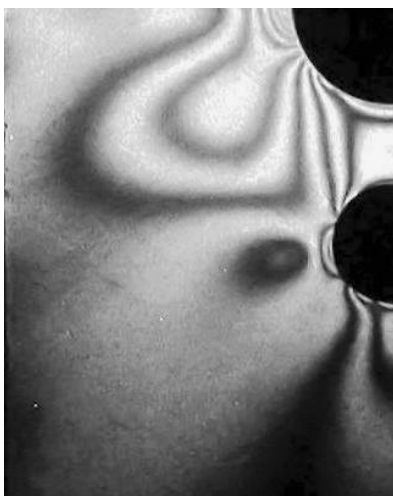
Fig. 4. Analyzed area of model with three holes for loading level s = 0.928

The exemplary results of the calculation of stress components for the model are shown on fig.5 and fig.6.
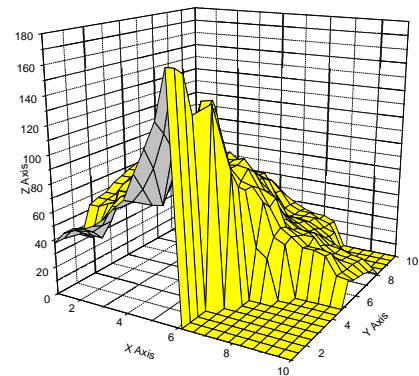
Fig. 5. Stress distribution σ_x (x, y) for $s = 0.928$
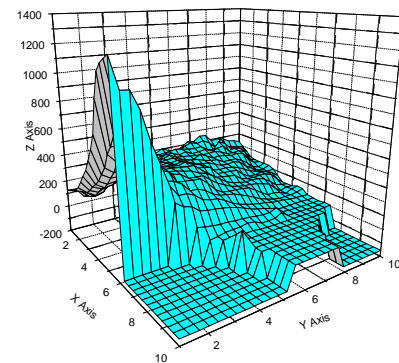
Fig.6. Stress distribution σ_y (x, y) for $s = 0.928$

3. Conclusions

On the basis of the obtained results it can be observed that photoelastic coating method applied to the elastic-plastic analysis of stretched elements with different stress concentrators enables to determine the values of strain components with satisfying accuracy. The accepted 6-sectional model of the material characteristic is sufficient to calculate stress values in the tested area properly. Effects of the calculations were compared with those obtained from the moirė method and the divergence between the results was less then 6%.

4. References

[1] Kapkowski J. Kozłowska B. Elastic-plastic strain analysis by photoelastic coating method. Journal of Theoretical and Applied Mechanics, No.3, Vol.31, Warszawa 1993;

[2] Kozłowska B.: "The investigation of elastic-plastic states by photoelastic coating method". Proc. of the 25th DANUBIA-ADRIA SYMPOSIUM on Advances in Experimental Mechanics, České Budějovice, Czech Republic 2008

DEVELOPMENT OF A METHODOLOGY FOR THE TRIBOLOGICAL ASSESSMENT OF THE SURFACE TOPOGRAPHY WITH MATLAB

Herbert Krampl [1)]

[1)] University of Leoben, Chair of Mechanical Engineering, Franz-Josef-Str. 18, 8700 Leoben, Austria.

Corresponding author: herbert.krampl@stud.unileoben.ac.at

1. Introduction

The surfaces of mechanical construction parts have to resist a multitude of loadings. Many of them come along with surface to surface contacts. Amongst others these are adhesive and abrasive wear, surface fatigue, chemical wear, shear stresses, third body abrasion but also hydrodynamic stresses by lubricant flow. Additionally these loadings can also be accompanied by high temperatures. Hence, they are to be analyzed for tribological purposes. To ensure a long life time of the parts and the functionality of their surfaces, the surfaces have to possess special properties. These properties include the topography, which is till date often evaluated using the arithmetical mean deviation of the roughness profile R_a and the average surface roughness R_z. For tribological applications, however, these values are not of the same significance as the Abbott parameters, which can be derived from an Abbott curve. The Abbott curve shows the material distribution of a surface profile by plotting the height over the material fraction.

2. Experimental Results

2.1 Abbott curve

For establishing the Abbott curve of a measured profile, a surface profile is intersected with a number of horizontal lines using a certain step width (see Fig. 1). Where the chosen step width is used to determine the number of steps by dividing the maximum bandwith of the surface profile through the step width. In Fig. 1, j=1 defines a line at the maximum of the surface profile, j=k stands for a line inside the bandwith and j=m defines a line at the minimum of the surface profile. The sections of the horizontal line produced through overlapping with the profile are summed up and divided by the length of the surface profile (the

scan length). This results in the material fraction in a certain profile height. The Abbott curve is then created by plotting the height steps over the corresponding material fraction (see Fig. 2 and Fig. 5).
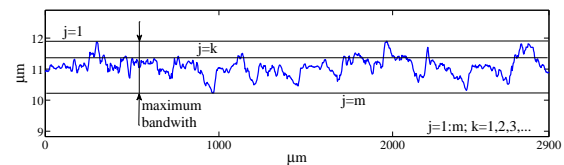
Fig. 1: Creating the Abbott curve

The approach to determine the tribologically relevant Abbott parameters is shown in Fig. 2.
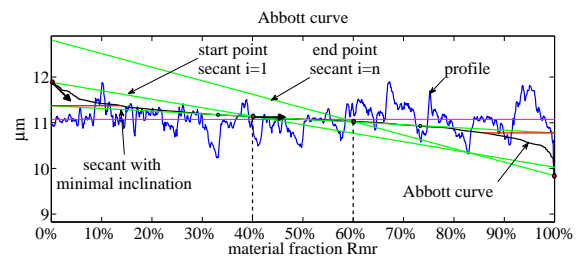
Fig. 2: Evaluation of the secant with minimal inclination

Before calculating the parameters, a secant which connects two points of the Abbott curve with a distance of 40% material fraction has to be shifted along the curve. This procedure creates n secants of which the one with minimal inclination is used in the following procedure to determine the Abbott parameters.

2.2 Calculation of R_{pk} and R_{vk}

Once the secant with minimal inclination is found, the reduced height peak amplitude R_{pk} and the reduced height mark amplitude R_{vk} can be determined. For this a horizontal line is drawn from the intersection of the secant with the ordinate towards the Abbott curve (see Fig. 3). Subsequently a triangle is created which is coextensive with the area between the horizontal line and the section of the Abbott

curve above. The length of the vertical cathetus of this triangle corresponds to R_{pk}.
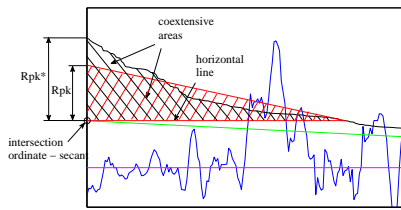
Fig. 3: Calculation of R_{pk}

The reduced height mark amplitude R_{vk} can be obtained in a similar way shown in Fig. 4.
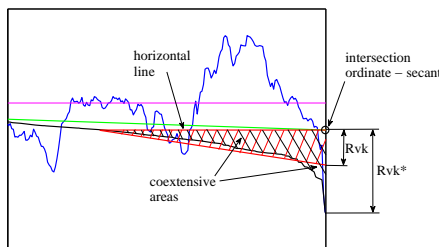
Fig. 4: Calculation of R_{vk}

The core roughness depth R_k, which represents the load capability of a surface's topography, is the distance between the upper and the lower horizontal lines (see fig. 5). The values of Mr1 and Mr2 give the material fraction of the core roughness depth and the height peak amplitudes respectively.
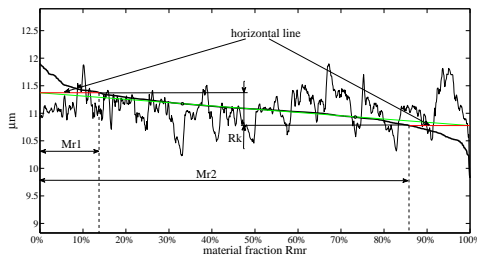
Fig. 5: R_k and material fractions Mr1 and Mr2

2.3 Methodology for the simulation of 2D envelopes

The Abbott parameters for surface profiles investigated with stylus instruments and with confocal laser scanning microscopes show a significant difference. To find out the reason for this phenomenon, a method for simulating the movement of the stylus edge over the surface profile was developed (see fig. 5). Through the motion of the stylus over the profile, the edge produces an envelope which was taken to be responsible for the difference between the Abbott parameters. The stylus edge was formed with a radius of 5 μm and an opening angle of 90°.
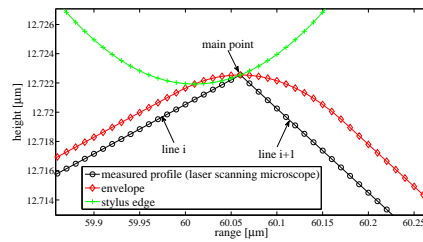
Fig. 6: Stylus edge touching the surface profile

From the new surface profile which is given by the envelope the Abbott parameters were calculated again.

Parameters without simulation:	
R_k:0.60μm	R_{vk}:0.36μm
M_{r2}:85.83%	R_{pk}:0.35μm
Parameters with simulation:	
R_k:0.60μm	R_{vk}:0.36μm
M_{r2}:86.29%	R_{pk}:0.34μm

Tab. 1: Abbott parameters for a cylinder liner without and with simulation, scan length 2.5mm

As shown in Tab. 1, there is no significant difference between the results for the Abbott parameters for a stylus edge with a radius of 5 μm and an opening angle of 90°, no matter if any envelope was simulated or not.

3. Conclusion

The developed method for the calculation of the Abbott parameters can be used to compare different types of surface topographies. The results of the envelope simulation strongly depend on the geometry of the stylus edge. The bigger the stylus is, the bigger the differences between the Abbott parameters will be.

4. References

[1] H. Krampl, Influence of the surface topography on the tribological system piston ring – cylinder liner, Project thesis 2008, University of Leoben

[2] M. Bigerellea, A. Iost, A numerical method to calculate the Abbott parameters: A wear application, Tribology International 40 (2007) 1319–1334

EXPERIMENTAL STUDY OF STEEL CORD BELT PLY OF TIRE

Jan Krmela [1)], Vladimíra Tomanová [2)], Františka Pešlová [3)]

[1)] University of Pardubice, Jan Perner Transport Faculty, Department of Transport Means and Diagnostics, Studentská 95, 53210 Pardubice, Czech Republic.

[2)] Trenčín University of Alexander Dubček, Faculty of Industrial Technologies in Púchov, I. Krasku 491/30, 02001 Púchov, Slovak Republic.

[3)] Czech Technical University in Prague, Faculty of Mechanical Engineering, Department of Materials Engineering, Karlovo nám. 13, 12135 Prague 2, Czech Republic.

Corresponding author: jan.krmela@upce.cz jan2.krmela@post.cz

1. Introduction

The authors deal with composites which structure and geometry matches complex materials into tire for road vehicle. The tires consist of textile and steel cords into tread [1].

The tires are during the operation exposed to combine loading as from a mechanical (statical, dynamic) as a temperature point of view (local heating in subzones, global heating in the tire-tread area permeating into the tire during breaking).

Therefore tire steel-cords are exposed to various chemical and thermal influences (fig. 1) during cyclic loading states by tensile-compression in tire loading processes.
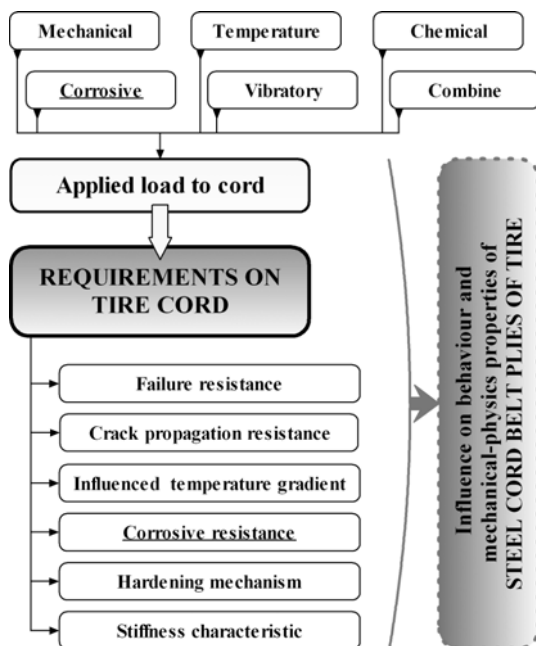
Fig. 1: Requirements on reinforcing tire cords.

The aggressive environment (e.g. action of salts in winter) activates the corroding process on steel-cord surfaces [2]. If cords are with corrosion then adhesive bonds between cord-elastomer are damaged (fig. 2) and safety of steel-cord belt plies and also tire is decreased.
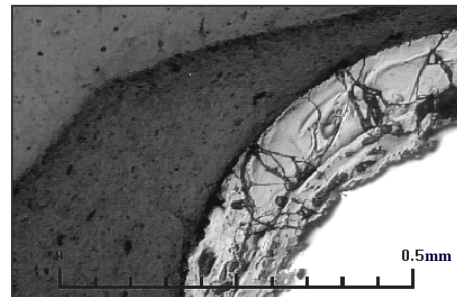
Fig. 2: Damage adhesive bond "steel-cord surfaces-elastomer drift".

2. Experimental Results

The experimental study of macro and microstructures of tire e.g. belt plies is also important for computational modelling of tire.
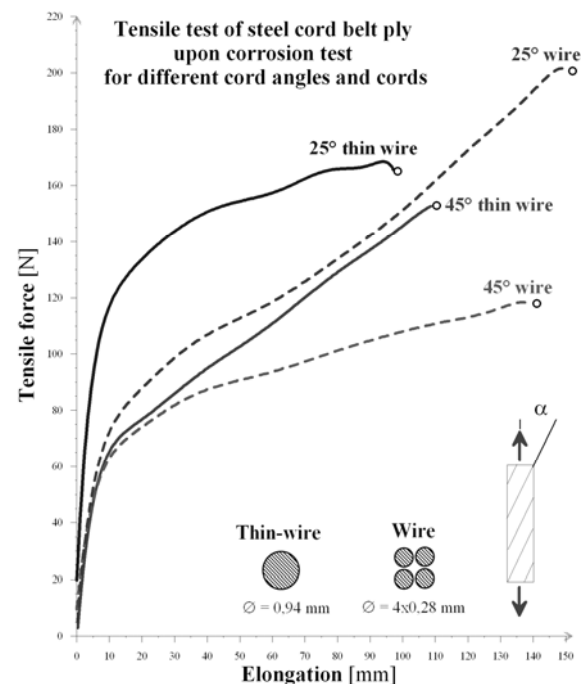
Fig. 3: Tensile test of steel belt ply with corrosion.

It is necessary also knowledge about tensile stiffness of belt ply with corrosion for different cord angles and cord form, fig. 3. The fracture character of test specimen with 25° angle and thin wire cord after tensile and corrosion test in a corrosion chamber is on fig. 4 as an example.
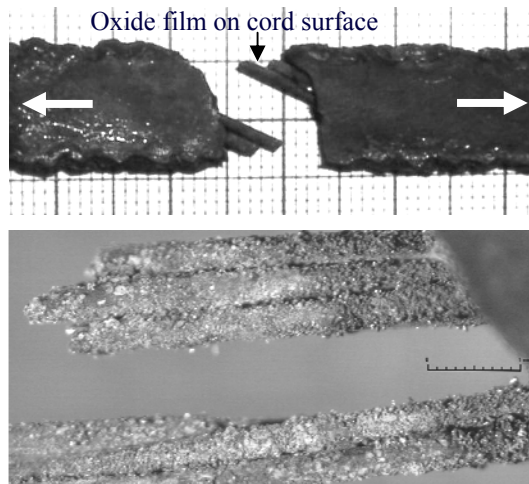
Fig. 4: Sample of fracture character of test specimen with corrosion and detail corrosion on cord surfaces.

The experimental results of tensile tests of undamaged (non-corrosion) steel-cord belt ply for comparison analyses with belt ply upon corrosion tests are shown in fig. 5.
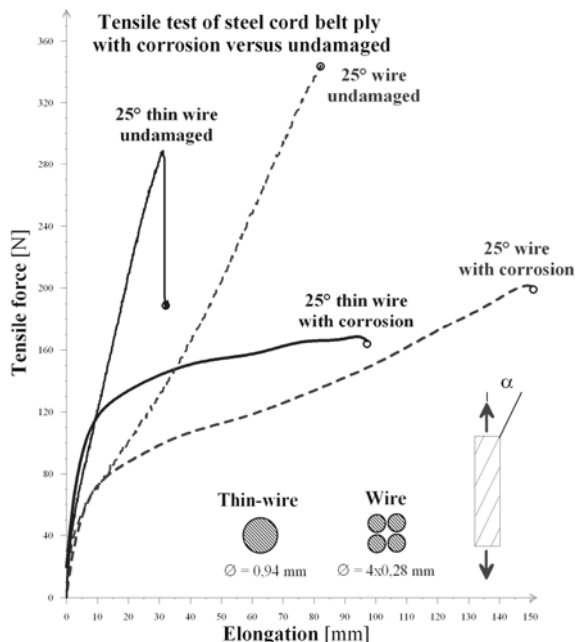
Fig. 5: Comparison of corrosion degradation and undamaged of steel belt ply.

On the experimental results the corrosion attacks on cords are markedly decreased tensile stiffness of steel-cord belt ply (fig. 5) and whole tire.

It is necessary note that the corrosion tests were provided on extreme condition, if they cannot arise on current tire operation.

Corrosion processes on cord surfaces is very dangerous.

3. Remarks

- Any damage in the area of tire crown, namely into steel-cord belt plies, is perilous.

- If extreme corrosion on cords then cord surface treatment lost function of corrosive protection.

- For predication of damaged belt ply is possible used combination of computational with experimental modeling.

- Corrosive attacks on reinforcing cords in whatever form can reduce the quality and operating safety of the whole tire.

4. References

[1] J. Krmela, Systems Approach to the Computational Modelling of Tyres - I. Part. Brno, Czech Rep., ISBN 978-80-7399-365-8. (2008).

[2] J. Krmela, F. Pešlová, S. Kuśmierczak, The Corrosion Process Impact on Stiffness Characteristics of Polycomponent Materials. Key Material Engineering, Vol. 14 (No. 3) (2007) 122-127.

[3] J. Krmela, F. Pešlová, Ľ. Hajduchová, Corrosion Influence on Strain-stress Characteristics of Tire Steel-cords. Key Opotřebení, spolehlivost, diagnostika. Brno, Czech Rep. (2007) 363-370.

[4] J. Krmela et al., Experimental study of Adhesive bond between Steel-cord and Non-linear matrix upon Failure. Key 25th Danubia-Adria Symposium on Experimental Methods in Solid Mechanics. Prague, Czech Rep. (2008) 131-132.

EXPERIMENTAL ANALYSIS OF THE STEEL ROOF TRUSS IN VARAŽDIN NEW SPORT HALL

Joško Krolo[1], Ivan Paska[2], Vlado Šardi[2]

[1]Faculty of Civil Engineering, Univercity of Zagreb, Kačićeva 26, 10 000 Zagreb, Croatia

[2]Coning Inženjering d.d., Augusta Šenoe 4-6, 42 000 Varaždin, Croatia

Corresponding autor: ivan.paska@coning.hr

1. Introduction

This paper deals with parallel overview of numerical calculations and static testing results for a typical truss as a primary structural element of the steel roof construction in new Varaždin Sport Hall. This Sport Hall is one among other few sport auditoriums that had been designed and built during 2008. for the purpose of World handball championship held in Croatia in January 2009. Sport building codes and regulations were not the only and crucial requirements for construction type selection and design for this 5000 audience, but also awarded architectural solution, construction technology, and the most important short time for building erection. Therefore, for this 63 x 84 m plan, simple triangular braced girder was selected as the primary structural element for steel roof construction (Figure 1). So, all long term roof counterfort works, needed surely for more attractive space structures, were avoided.
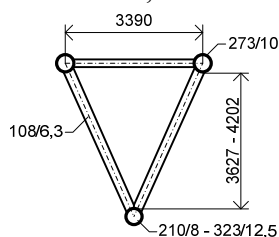
Figure 1: Roof truss cross section (A-A)

Roof trusses are 4,20 m axes high in the middle of 62,8 m span, 3,63 m high at its ends, with one end slide bearing, and 7 m raster between every truss.

All trusses were erected by auto crane with a lifting capacity of 500 t (Figure 2).

Choice of steel roof subcontractor from Slavonia, distant for transportation, increased significantly number of prefabricated sequences in one truss. Instead of only three parts along the span, each of this girder parts had to be cut in upper and lower segment, transported like this, and assembled together at the site with bolted connections.

Numerical analysis of such subsequently softened girders had to be checked by static load testing.

Figure 2: Lifting of complete roof truss by 500 t auto crane

2. Description of testing

The static test procedure was carried out when the whole building was finished, included completed floors, and that complicated testing a lot.

Complete dead load elastic deformations of all roof elements was already realized, so only the substitute ballast for snow loading was conducted in this testing. Investigated truss was additionally loaded with equivalent continuous ballast of 10,9 kN/m only in the middle 35 m of its span (all together 381 kN), and that was instead of continuous snow loading 8,75 kN/m across the complete 62,8 m span. (Figure 3). .That was implemented through the concentrated loads on lower bend nodes.

Arranged steel frames and euro palette was built up with concrete sheets and sand bags as a ballast (Figure 4 and 5).

Girder displacements in the middle and quarters of the span (measuring places 6, 7 and 8) were measured during loading application. Strains were measured on five measuring places, in the middle and quarter of diagonal and vertical elements span (measuring places 1 to 5).

Displacements and strains were measured by means of linear variable differential transformer (LVDT) with the 10^{-3} mm accuracy for displacement and 10^{-6} mm accuracy for strains. Measuring places for deflections and strains can be

seen in Figure 2. The same loading scheme is analysed with numerical model of the whole roof construction in order to analyse secondary roof elements influence.
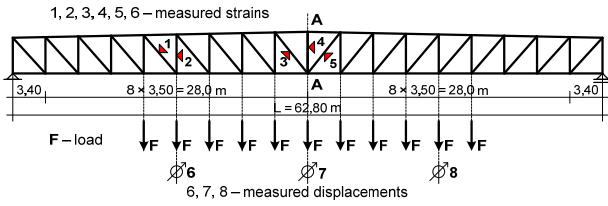
Figure 3: Longitudinal truss disposition with measuring places for strain and deflections

Figure 4

Figure 5

3. Experimental results and comparison with numerical results of testing

The results of measured deflections on measuring places No. 6, 7 and 8 can be seen in Figure 5 and compared with computational values in Figure 6 and Table 1. The results of measured strains on measuring places No.1 and 2 are shown in Figure 7.
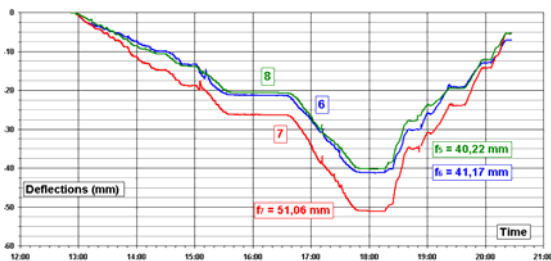
Figure 6: Deflections during the test procedure

Measuring place	Experimental deflection (mm)	Numerical deflection (mm)
6	41,27	51,0
7	51,14	66,3
8	40,25	51,0

Table 1: Comparison of experimental and numerical deflections
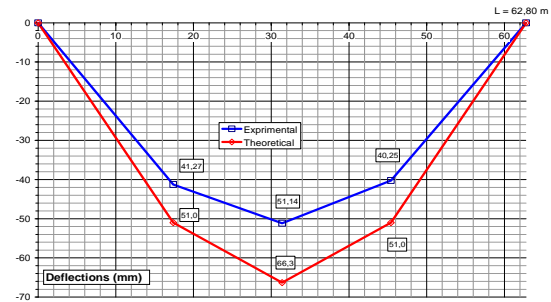
Figure 7: Comparison of experimental and numerical deflections

Figure 8: Strains during the test procedure

From the measured strains stresses are calculated and compared with computational values in Table 2.

Measuring place	Experimental stress (MPa)	Numerical stress (MPa)
1	+34,86	+34,86
2	-13,60	-12,31

Table 2: Comparison of experimental and numerical stresses

4. Conclusions

The paper shows parallel results of the numerical calculations and testing the steel roof truss of 62,8 m span for the same additional loading. The comparison shows that the measured values correspond to the computational ones and confirmed that even such girders subsequently softened with a great number of bolted connections behaves according to design's requirements.

References:

[1] Report: *Experimental testing of the roof steel truss of the 'Sports city hall Varaždin'*, Faculty of Civil Engineering, University of Zagreb, Department for tehnical mechanics, December, No. 180-249/2008.
[2] *Main civil engineering design with static analysis of 'Sports city hall Varaždin'*, Coning d.d., A.Šenoe 4-6, Varaždin, No. 236/2007.
[3] Regulation HRN U.M1.047: *High - rise structures testing by experimental loading and failure testing*, Official Journal No. 4/1987.

THE EVALUATION OF LOADING CAPACITY OF A GLASS CARRIER STRUCTURE BASED ON EXPERIMENTAL AND NUMERICAL APPROACH

Lovre Krstulović-Opara[1a], Željko Domazet[1b]

[1]   University of Split, Faculty of Electrical Engineering, Mechanical Engineering and Naval Architecture, R. Boškovića b.b, HR-21000 Split, CROATIA.

Corresponding author:www.fesb.hr/kk,

1. Introduction

Glass carrier structure, called "spider", is used in construction industry to carry glass facades. Our task was to approve the producer's loading capacity data. The lading capacity is reported in two directions, axial and radial. To test the spider fitting together with spherical joint attachments (glass connector) in axial direction is not an issue. The pair of spider fitting and the pair of spherical joint attachments is positioned in the load-frame and axially loaded, resulting in force-displacement response data.

Figure 1 Axial loading of pairs of spider fittings and spherical joint attachments

Due to the time and budged restriction it was not possible to build testing loading equipment capable to perform a radial loading evaluation. The decision was to rely on numerical model of radially loaded spider fitting and spherical joint attachment. It is not the problem to build such a numerical model based on CAD geometry, but problem is to rely on such a model. Numerical methods, such as FEM, are always giving logical results, but question is how accurate is the numerical model.

2. Numerical model evaluation

The numerical model evaluation was based on the axial loading. To compare the experimental results with the numerical model, a unidirectional strain gage is applied on the spider surface. As additional control of spider deformation, digital comparators

have been used to detect the deformations of laded pair of spiders (Fig.1). When comparing the results, it is important to apply the unidirectional strain gage in the region where principal strain direction can easily be selected. As a strain gage averages deformations on whole region of application, the region of application has to be free from stress concentrations. Therefore a numerical model, based on the CAD geometry, is the first step needed to locate such a region.
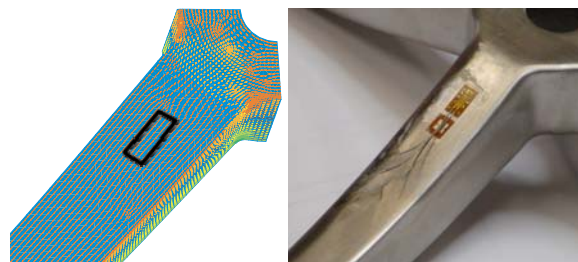
Figure 2 FEM model and the strain gage located in the region free from stress concetrations

For the case of spherical joint attachment, the frictional contact problem has to be considered. Thus a numerical model of spherical joint attachment is modeled and compared with experimental data for axial loading test. The load-displacement data, deformed shape and rupture scenario have been compared. From the numerical model it can be concluded that collapse occurs due to the plastic deformation of cylindrical body and plastic yielding due to the Hertzian stresses few microns under the sphere's surface (Fig. 3 and 4).
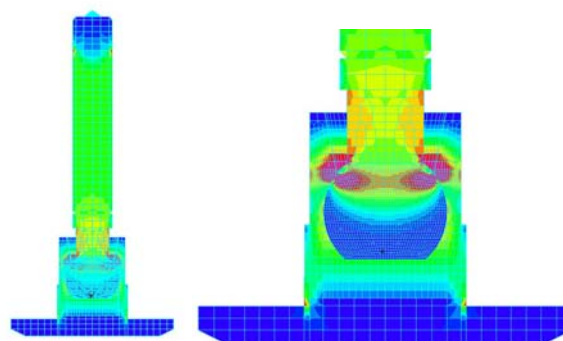
Figure 3 FEM model of the spherical joint wiht stress concetration due to the Hertzian stresses

Figure 4 Yealding of the sphereical joint due to the Hertzian stresses and deformation of cylindrical body

From the compared data it is concluded that the numerical model is reliable for describing the axial and radial loading of the spider fitting and spherical joint attachment.

3. Numerical model of radially loaded spider and spherical joint attachments

Radial loading capacity of the spider fitting was evaluated from the numerical model only. Due to the symmetry conditions, the quarter of spider was modeled with 20306 eight-noded elements. For the radial loading simulation, due to the reduced symmetry conditions, the half of spider was modeled with 40612 elements.

While for the axial loading case the slipping of the spherical joint causes the collapse, the numerical model of radial loading showed that the collapse occurs due to the bending of the bolt.

4. Estimated loading capacity

From the experimental and numerical data of the axially loaded spider fitting and spherical joint attachment, the axial loading capacity was evaluated and numerical model is considered reliable. In table 1 the data for spider fitting made of the AISI304 stainless steel material is displayed. The evaluated data differed from the producer's data (Table 1). The evaluated radial loading capacity of the spider fitting is higher than producer reported, while radial is lower. For the spherical joint attachment evaluated axial loading capacity is significantly higher, while radial is lower than reported in producer's data.
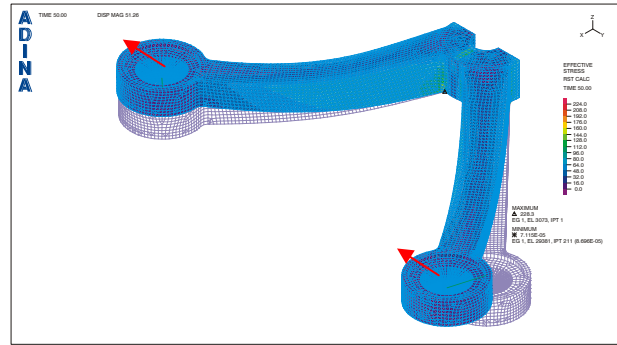
Figure 5 The simulation of radial loading
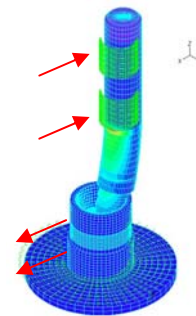
Figure 6 The simulation of radial loading

Table 1 Loading capacity, evaluated and declared

	Axial [N]	Radial [N]
spider-evaluated	2900	4500
spider acc. to producer	4600	2650
spherical j.- evaluated	8500	658
sph.j. acc. to producer	2160	1860

5. Concluding remarks

Very often the experiment cannot be performed for all loading cases. The numerical model data can be used as reliable when evaluating the structure, but this data has to be partly approved with the experiment.

Often it is good to check the producer data because it can significantly differ from reality, what was the case in presented evaluation.

References

[1] http://www.adina.com

[2] http://www.3ds.com/products/catia/

ON THE TOTAL EXPLOITATION OF THE POTENTIALS IN EXPERIMENTAL STRUCTURAL ANALYSIS

Karl-Hans Laermann

Bergische Universität Wuppertal, FB D, Dept. of Civil-Engineering ,

Pauluskirchstr. 7, 42285 Wuppertal, Germany.

Corresponding author: laermann@uni-wuppertal.de

1. Introduction

It is a proven fact that the modern methods and techniques in experimental solid mechanics are inalienable to obtain reliable information on the state of displacements and strains of any kind of structures in the micro- as well as in the macro-scale, no matter whether the structures consist of any kind of material. To make use of the advantages of the results of measurements to fully exploitation their informative potentials, care must be taken of many influences and relations, the effects of which are inherently included in the metered data and which normally are not considered.

2. Influences and effects on results

In this concern it must be kept in mind, that in modern measurement techniques (e.g. electrical, optical, fibre-optical- methods) the respective signals like changes in resistance, voltage, intensities and frequencies etc. are measured. These analogue signals are to transform according to the inherent features of the respective technique and the relation between the metered signals and the displacements and strain (fig. 1).

$$\varepsilon = k \frac{\Delta R}{R}; \qquad \text{strain gauges}$$

$$\varepsilon = k^* \frac{\Delta \lambda}{\lambda_0}; \qquad \text{BRAGG-fibres}$$

$$\varepsilon_1 - \varepsilon_2 = \frac{\hat{S}}{t} N; \qquad \text{photo-elasticity} \qquad (1)$$

$$u, u' = \lambda \cdot C \cdot N \qquad \text{holo-, shearography}$$

Fig. 1: Relation metered signals to strain and displacements.

In order to get reliable data the sensitivity of the methods against method immanent internal as well as external thermal effects are to take into account beside probably other causes which might have influence on the metered signals.

In setting up the stress-strain relations it must be differentiated between linear elasticity, geometrical and physical non-linear elasticity, visco-elasticity, regarding the apparent fact of possible transition between different states. And moreover the effects of plasticity, isotropy, anisotropy etc. are to pursue.

With concern to structural analysis and condition monitoring of structures, the question must be raised, whether it is sufficient to measure displacements and strains to assess the actual state of structures comprehensively [1]. The answer is no! Because for comprehensive assessment the real loading and boundary conditions as well as the state of temperature and its changes are to take into consideration as they have remarkable influence on the results of measurements. Furthermore the actual material parameters are unknown or probably different from presupposed values. In consequence it must be proved, whether the current response of materials corresponds to the presupposed, which might be obtained by separate material testing processes, probably under different premises. And with regard to time-depending effects on the material response like fatigue, ageing as well as physical/chemical deteriorations especially on already existing structures [2], [3], obviously the task of total exploiting the inherent potentials of knowledge included in the metered signals becomes evident. This means to obtain reliable information on the actual material parameters and simultaneously the actual stress state. For solving this task one must fall upon the theoretical relations between all the quantities relevant for description of the problem considered. The kinematic equations describe the connection between measured

127

displacements and the strains, whereas the constitutive equations correlate the stress-strain relations (eq.s (2)).

Kinematic equations: $\varepsilon_{ij} = \psi(u_i, u_{i,j}, ...)$ (2)

Constitutive equations: $\varepsilon_{ij} = \phi(E, \nu, \sigma_{ij}, \Theta, ...)$

Both these sets of equations are depending on the state of elasticity (linear-, non-linear-, visco-elasticity) or whether isotropy, anisotropy etc. is on hand. Depending on the kind of object equilibrium conditions have been proved also as advantageous.

3. Procedure of solution

Generally inverse problems are set up immediately as the equations are ill-posed. For solution therefore proper mathematical algorithms are requested [4]. The quantities to be determined are implicit included in the equations as demonstrated for a plane stress state (eq. (3)).

$$\varepsilon_{ij} = C(1+\nu) \cdot \sigma_{ij} + \nu \cdot C \cdot \sigma_{kk} \cdot \delta_{ij}; \quad C = 1/E$$
(3)

In component formulation eq. (3) holds

$$\begin{Bmatrix} \varepsilon_{11} \\ \varepsilon_{22} \\ \varepsilon_{12} \end{Bmatrix} = \begin{bmatrix} C & -\nu C & 0 \\ -\nu C & C & 0 \\ 0 & 0 & (1+\nu)C \end{bmatrix} \cdot \begin{Bmatrix} \sigma_{11} \\ \sigma_{22} \\ \sigma_{12} \end{Bmatrix}$$

The strains ε_{ij} have been obtained by evaluation of metered signals.

The quantities C, ν, σ_{ij} are unknown, thus a mixed inverse problem is on hand. A separation of the unknown quantities becomes necessary and will be carried out by means of the sensitivity matrix based method (eq.(4)).

$$\begin{Bmatrix} \Delta\varepsilon_{11} \\ \Delta\varepsilon_{22} \\ \Delta\varepsilon_{12} \end{Bmatrix} = \begin{bmatrix} (\sigma_{11}-\nu\sigma_{22}) & -C\sigma_{22} & C & -\nu C & 0 \\ (-\nu\sigma_{11}+\sigma_{22}) & -C\sigma_{11} & -\nu C & C & 0 \\ (1+\nu)\sigma_{12} & C\sigma_{12} & 0 & 0 & (1+\nu)C \end{bmatrix} \cdot \begin{Bmatrix} \Delta C \\ \Delta\nu \\ \Delta\sigma_{11} \\ \Delta\sigma_{22} \\ \Delta\sigma_{12} \end{Bmatrix}$$

$$\Delta\boldsymbol{\varepsilon} = \mathbf{S} \cdot \Delta\mathbf{q} \qquad (4)$$

The set of equations is ill-posed and underdetermined. For estimated values of the unknown quantities

$$\{q^{(0)}\} = (C^{(0)}, \nu^{(0)}, \sigma_{ij}^{(0)})^T$$

the strains $\varepsilon_{ij}^{(0)}$ are calculated. The difference to the metered values holds

$$\Delta\varepsilon_{ij}^{(0)} = \varepsilon_{ij}^{meas.} - \varepsilon_{ij}^{(0)}$$

These differences are inserted into eq.(4), which then will be solved for instance by the minimum-length-method. With the results $\{\Delta q^{(0)}\}$ the unknowns are .improved acc. to

$$\{q^{(1)}\} = \{q^{(0)}\} + \{\Delta q^{(0)}\}.$$

This procedure is to continue until $\{\Delta\varepsilon^{(\mu)}\} \approx 0$.

The method described above yields the comprehensive information on the actual value of any of the unknown quantities like the material properties and the stress state as well as on the temperature- and the load-conditions and solves the task to total exploit the results of measurements. This will be demonstrated by some comprehensible examples.

3. References

[1] Laermann, K.-H., Structural parameter identification, Proc.12th ICEM, Advances in Experimental Mechanics (ed. C. Pappalettere), McGraw-Hill, Milano (2004), 292-293.

[2] Harte, R., Krätzig, W. B., Laermann, K.-H., Integriertes Sicherheitsmanagement durch Computersimulation und Zustands-monitoring, VDI-Jahrbuch 2006/7- Bautechnik, VDI-Verlag, Düsseldorf, (2006), 13-29.

[3] Laermann, K.-H., Assessment of structural integrity and durability – a task of experimental mechanics. Proc. 24th Danubia-Adria-Symposium, Sibiu (2007).

[4] Laermann, K.-H., Inverse Problems in Experimental Structural Mechanics. Shaker-Verlag, Aachen (2008)

THE IMPACT OF BALLAST THICKNESS ON VERTICAL TRACK STABILITY

Stjepan Lakusic [1), Tino Medvidovic [2), Ivica Kozar [2)

[1) University of Zagreb, Faculty of Civil Engineering, Kaciceva 26, 1000 Zagreb, Croatia.

[2) University of Rijeka, Faculty of Civil Engineering, V. Cara Emina 5, 51000 Rijeka, Croatia

Stjepan Lakusic: laki@grad.hr

1. Introduction

The main elements of the upper structure of the classical rail track constructions are the rails, sleepers and the track screen (the ballast). The connection of the rails and the sleepers is achieved by an appropriate method of fastening. The Fig. 1 shows the longitudinal cross-section of the classical rail track construction, [1]. If the rail track ballast is observed, its main purpose is to elastically and equally transfer the loads caused by the rail vehicles to the plane of the lower structure, to secure the direction and height of the rail track and to dampen the vibrations in the rail track. For the ballast to fulfil the said requirements, it must have sufficient dimensions (width and thickness) and must be constructed of a good quality material. The best material for the ballast is crushed stone produced by eruptive origin. The optimal thickness of the ballast is 25 to 30 cm measured from the lower par of the sleeper (Fig. 1).
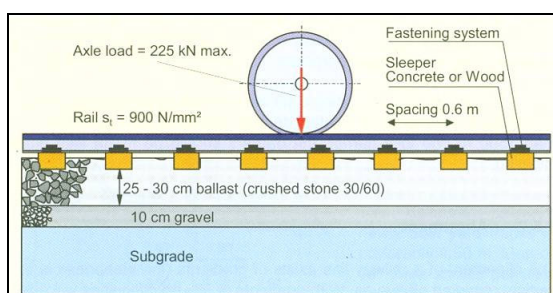
Fig. 1: Principle of track structure.

This paper considers impact of the thickness of the ballast on the vertical stability of the rail track. The measurements were performed on the rail grid of the Croatian Railways (location: Skrljevo - Meja - Pecine). The said section is in a cut and has longitudinal slope of 22 ‰, thickness of the ballast amounts to 15 to 20 cm. During the year 2005 the wooden sleepers were replaced with the concrete sleepers. But, after two years from the replacement, the new sleepers sunk due to further crushing of the ballast (Fig. 2). Due to subsequent crushing, the crushed stones lost their sharp edged form, which in turn lead to reduction of mutual wedging of the granules, which finally lead to settlement of the sleepers.

Fig. 2: Settlement of the concrete sleepers.

2. Experimental Testing and Results

The equipment used to determine the dynamic parameters for this research represents a significant factor upon which depend the basic approach for data collection and their processing. This is one of the basic prerequisites for analysis of the experimental research, to ensure recording and transmission of the data, as an analogue or a digital recording, to the computer that will be "free" of the noise and errors. During the experimental research a lot of effort was made to customise the standard instruments to meet the set requirements. Quite often, original solutions were used both for the data collection phase and for the data processing phase (e.g. the code for transformation of the analogue signals into digital ones, for filtering of the data, for the FFT analysis and etc.).

For this research used was the measuring equipment produced by the Finnish company NOPTEL as follows the laser measuring of the dynamic shift – NOPTEL PSM90. The PSM90 is a device for measuring of small dynamic

transversal shifts or vibrations of the constructions simultaneously in two orthogonal directions. The device is based on a laser transmitter and optic-electronic receiver that are mounted on the object where the measurements are being made. The Fig. 3 show the measuring equipment PSM90 fitted on the rail track.

Fig. 3: Measuring device on the rail track.

The measurements data collected in the field require detailed analysis before they can be correctly interpreted and finally compared to the numerical analysis. Further processing of the measurement data is performed by using the program packages for post-process analysis of the measured data. For this research used was the own program package, [2, 3, 4].

The results of the experimental testing of deformations of the concrete sleepers are shown as the function of deflection over time. Three measurements were made, depending on the axle loads present at the moment on the track: operational train, freight train and passenger train. The representation of the results of the measured deflections for above listed loads is shown in the Fig. 4 to 6.
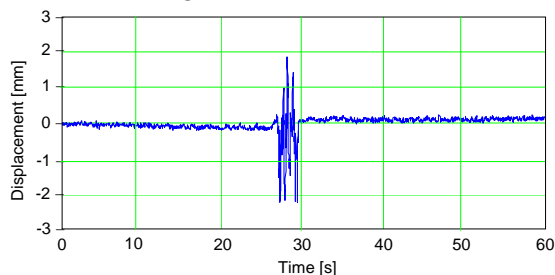
Fig. 4: Deflection of the sleeper (operational train).
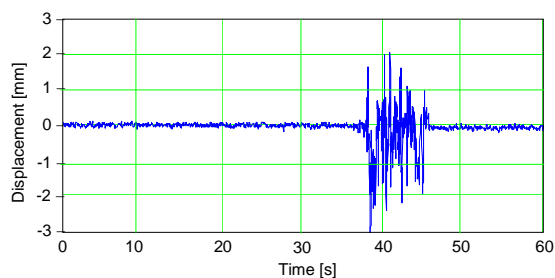
Fig. 5: Deflection of the sleeper (freight train).
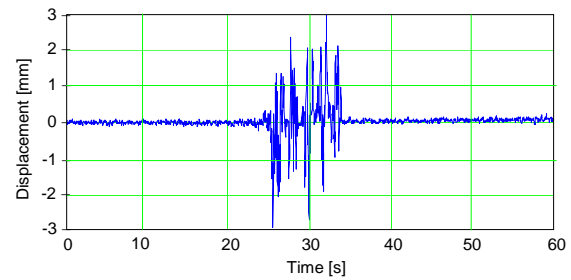
Fig. 6: Deflection of the sleeper (passenger train).

The deflection diagrams show that the range of deformations of the concrete sleepers is from 4.07 mm up to 5.94 mm, observing the total deflection (sagging) and rising of the sleepers. The said phenomenon reflects very unfavourably on the comfort and safety of the ride, and for that reason the driving speed along that section of the rail had to be reduced. The selected testing point can be characterised as a point of a "median" level of damage, in the sense of the quantity of additionally crushed stone ballast and the surface of the covered ballast.

3. Conclusions

Fitting of the concrete sleepers to the ballast of small thickness, resulted in additional crushing of the material. If the concrete sleepers were to be kept on the rail track and crushing of the material avoided, the solution might be rising of the height level for approximately 10 cm or fitting of the concrete sleepers with an elastomeric pad. The Croatian Railways decided to replace the concrete sleepers with the wooden ones, without enlarging the height of the ballast. The solution with the wooden sleepers was shown as the correct one since the wood is softer material that does not act as the "upper jaw" of a crusher on the thin (shallow) ballast, lay on the solid rock bed.

4. References

[1] C. Esveld, *Modern Railway track*, Second edition, MRT-Production, 2001.

[2] T. Medvidović, *Comparison of the measured and calculated dynamic parameters for long flexible constructions*, Univ. of Rijeka, 2007.

[3] I. Kozar, T. Medvidovic, *Some remarks on displacement based dynamic measurements*, 5th ICCSM, Trogir, 2006. Str. 99 – 100,

[4] I. Kozar, T. Medvidovic, *Comparison of the measured and calculated dynamic parameters on constructions*, 1st Conf. of Croatian Society of Mechanical Engineering, Rijeka 2007.

LASER SCANNING CONFOCAL MICROSCOPY FOR SURFACE STRUCTURES AND DEFECTS EVALUATION

Hana Lapšanská [1)], Petr Schovánek [1)]

[1)] Joint Laboratory of Optics of Palacký University and Institute of Physics of the Academy of Sciences of the Czech Republic, 17. listopadu 50a, 772 07 Olomouc, Czech Republic.

Corresponding author: hana.lapsanska@upol.cz

1. Introduction

Precise measurements of fine details on bigger components are often required. Samples like this can cause problems when using traditional light microscopy and we almost never get sufficient and complete information about height parameters of the specimen. Using modern microscopic methods is necessary. Laser scanning confocal microscopy (LSCM) is one of the most suitable one. It is undemanding on specimen preparation. Scanning itself takes usually only few minutes. High resolution images can be analyzed using software functions to get interesting information about specimen surface.

This contribution introduces a modern microscopic method and shows possible measurements and analysis of the component with intentionally fabricated defects. The objective of realized measurements is to find the depth of each defect, detect the deepest one and show its profile.

2. Laser scanning confocal microscopy

LSCM is a modern method of non-contact and non-destructive imaging and measuring of even sub-microns surface structures. It is often used when classic light microscopy is insufficient and scanning electron microscopy (SEM) is not available or usable for example because of sample constitution or its size. In contrast to SEM, investigated specimens do not have to be conductive and usually no special preparation is necessary.

The basic principle of three dimensional measuring with LSCM lies in successive scanning of set of planes and pooling together measured data. Laser beam is focused with an objective lens to a very small spot and scans over the specimen in X-Y directions. Then, implemented detector captures a light from the specimen and outputs the image on the monitor. In confocal optics, pinhole is placed at the position that is optically conjugated with the focusing position (confocal plane) to repel light coming from place other than focusing position. As the result, the part where light was repelled is truly darkened in the image and only focused parts are displayed [1]. Then, objective lens shifts in Z direction and another X-Y plane is scanned. Number of scanned planes is equal to the specimen height desired to be imaged and to the chosen step size of the lens shift. Finally, topographical map (surface reconstruction) is constructed by setting purchased images of separate planes together. Consequent image is bright with high resolution and depth of focus. Contrary to it, in ordinary microscope, the light that comes from the place other than focusing position is overlapped with the image forming light at focusing position and whole image turns blurry [2].

2.1 Microscope LEXT OLS 3100

Microscope LEXT OLS 3100 is a modern device based on upper mentioned technology. It disposes of magnification in range 120x to 14,400x and high resolution, which is 120 nm laterally and 40 nm vertically. Two dimensional measuring as well as three dimensional scan in real colours with subsequent software data assembling and the topographical map construction is possible. Acquired data can be filtered and analysed using various software functions. Many important characteristics of measured specimen can be obtained. For example dimensions, distances and area measurements can be realized. Three dimensional surface reconstruction enables us to get information about height characteristics of measured profile, depth of depressions or dimensions of present defects. We can do surface, area, volume and also roughness measurements.

3. Experiment

The scheme of the part of stainless steel sealing component for air condition system is shown in fig. 1.
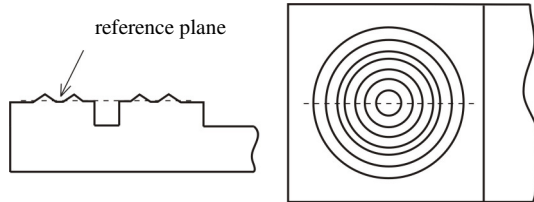
Fig. 1: The scheme of the part of measured component (side and top view).

There are two circular conical teeth on the top side of the component. Because of this shape, it would be hard to get valuable results using conventional light microscope. LEXT OLS 3100 was used. Highly reflective surface and excessive vertical distance required gradual changes of brightness.

First, height of each tooth was measured according to the reference plane (fig. 2, 3). Average height was computed to be 217 µm for the outer circle and 242 µm for the inner one with 2 µm standard deviation.
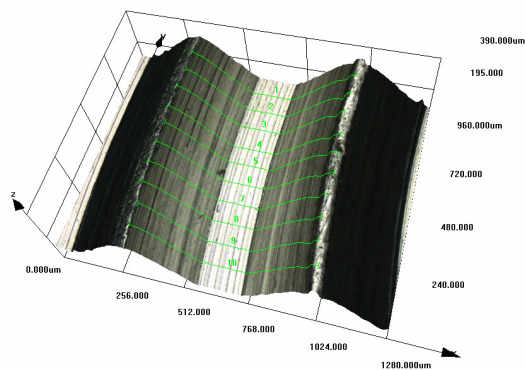
Fig. 2: Image of parts of circular teeth with height measurement.

Fig. 3: X-Z profile 10 from the previous image.

Then, defects present on the top of each tooth were imaged and analyzed. Fig. 4 presents one of them.
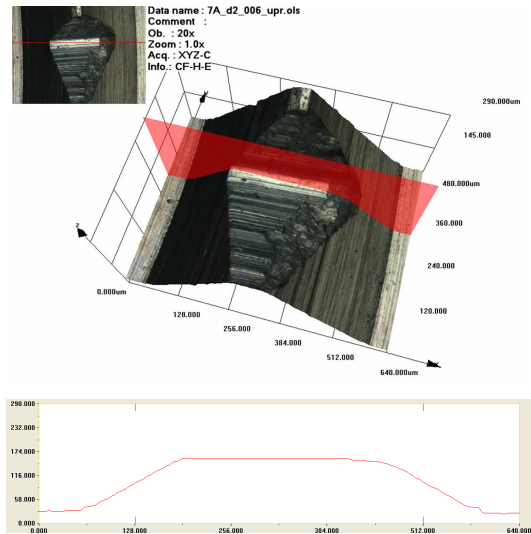
Fig. 4: Defect on the top of outer circle and its profile in chosen position.

4. Conclusion

Many measurements were realized and various defects with different depth were detected. Some defects were too large and had to be imaged in successive steps. Laser scanning confocal microscope seems to be a useful tool for measurements like these.

The aim of these measurements was to identify maximally deep defect and, in connection with another experiments, find out how large and deep can defect be not to affect sealing function of this component. Companion part of this component is going to be measured. Detailed results of all performed measurements will be presented on poster section of the conference.

5. Acknowledgements

6. References

[1] Clarke, A. R., Eberhardt, C. N. Microscopy techniques for materials science. Woodhead Publishing, 2002. ISBN 1855735873.

[2] Confocal Scanning Laser Microscope OLS3100/OLS3000 – User's Manual. Version 5. Olympus Corporation, Japan, 2007.

SIZE EFFECT IN COMPUTATIONAL SIMULATIONS OF EXPERIMENTS WITH COMPOSITE MATERIALS

Tomáš Lasota [1]), Jiří Burša [1]),

[1]) Brno University of Technology, Institute of Solid Mechanics, Mechatronics and Biomechanics, Technická 2896/2, 616 69 Brno, Czech Republic.

Corresponding author: TLasota@seznam.cz

1. Introduction

This paper deals with computational simulations of a composite material with rubber matrix and steel fibres. Typical application of this composite material is for example in construction of car tires. The computational simulations can be realized at various levels of computational models.

First, a computational model with modelled fibres (denoted as bimaterial model below) can be used. It means that 3D models of both rubber matrix and steel fibres must be created. Main disadvantages of this computational model consist in a very complicated creation of fibres (especially if they are not parallel to the specimen edges) and in a rather complex creation of mesh. Due to declination of fibres it is impossible to create a mapped mesh all over the model. Therefore a free mesh with great numbers of elements must be used and herewith the computational time increases substantially.

Second, a computational model without modelled fibres (denoted as unimaterial model below) can be used. It means that only geometric model of the matrix is created and fibres are not modelled. The fibre reinforcement effect is then included in the strain energy density function. Constitutive model with strain energy density function, which includes both rubber matrix and fibres, is specified in Spencer [1, 2]. An advantage of this computational model is that fibres are not modelled; the specimen is created of one homogeneous anisotropic material so that a mapped mesh with low number of elements can be used and the computational time is low order in comparison with the bimaterial model. Nevertheless, this model assumes that the fibres are infinitesimally thin, and thus infinitely flexible with zero bending stiffness of an individual fibre.

Finally the unimaterial model can be used with bending stiffness of fibres incorporated. In this model a strain energy density function depends on Cauchy – Green deformation tensor, fibre direction and newly on the gradients of the deformed fibre vectors. Dependence on the gradient of the deformed fibre vectors incorporate bending stiffness into the constitutive model mentioned in [1, 2]. Constitutive equations for this last computational model are introduced in [3], where it is shown that incorporating the bending stiffness by gradients leads to Cosserat theory of elasticity. This theory was formulated by Cosserat brothers in 1909 [4]. So the last computational model completed by bending stiffness of fibres and based on Cosserat theory of elasticity removes all disadvantages of the foregoing computational models. In addition, this model should be in better agreement with experiment because it can account for any size effects, such as those due to fibre diameter or fibre spacing. Presently, the constitutive model used here is not implemented in any FEM software and there are no publications about using this model in the practical applications.

2. Computational simulations of tension and bending tests

In order to compare the first two (i.e. the bimaterial and unimaterial) models mentioned in introduction, simulations of tension and bending tests were carried out. These simulations were realized with specimens (dimensions 100 x 15 x 2.25 mm) under different declinations of fibres (0°, 30°, 45°, 60°, 90°).

Some results of these simulations are in fig.1 and fig. 2. Both figures show simulations on the specimens with declinations of fibres 30° and 45°; fig. 1 shows results of bending test simulations and fig. 2 is related to the tension

test. Complete results for all declinations of fibres were published in [5].
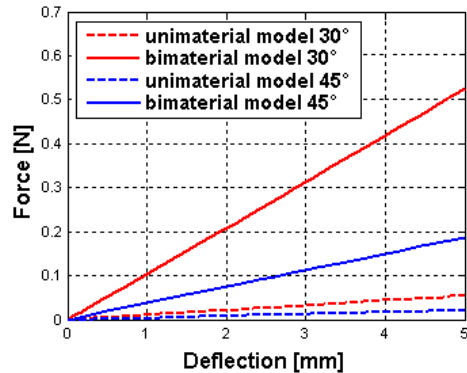
Fig. 1: Bending test – fibres angle 30° and 45°.
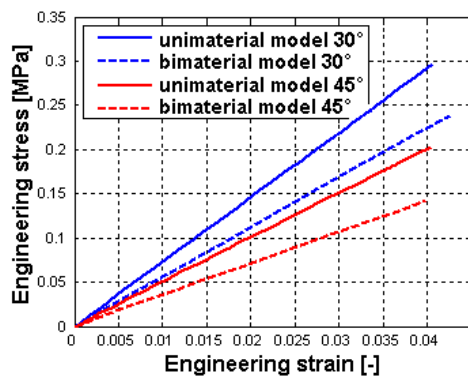
Fig. 2: Tension test – fibres angle 30° and 45°.

Fig. 1 shows that both computational models give contradictory results. Results obtained by the bimaterial model show always a higher stiffness than results obtained by the unimaterial model. A causation of the difference between results is obviously due to the zero bending stiffness in the unimaterial model as mentioned in introduction.

In the tension test (fig. 2) the results show a better agreement. However, there are still some differences (in the models with inclined fibres); they can be caused by the zero bending stiffness again. As the transversal displacements of specimen ends were constraint and only the displacement in loading direction was non-zero, the fibres inside these specimens were bended.

To confirm the above hypotheses, we prepare experiments (bending and tension tests) in near future and will then repeat all simulations for real specimens used in the experiments. Then we will be able to compare the simulations (by using bimaterial and unimaterial models) with the experimental data. We suppose a disagreement between the experiment and both of the computational models. This disagreement can be caused due to the size effect. If we investigate the response of the body to an external physical effect, in which the length scale is comparable to the average size of the constituents in the body, then the constituents of the body are excited individually [6]. In this case, the intrinsic motions of the constituents must be taken into account and therefore the classical theory of elasticity should be substituted by the Cosserat (or micropolar) theory of elasticity [6]). This situation prevails in practical applications when the material is a composite containing macromolecules, fibres or grains. In future works, therefore, we want to create a computational model based on the Cosserat theory of elasticity (the last model mentioned in introduction), to repeat the simulations, and to compare them with the experiment. We expect that the results obtained by this computational model will be in much better agreement with the experiment than the computational models used till now.

3. Acknowledgements

4. References

[1] A. J. M. Spencer, Deformations of Fibre-reinforced Materials, Oxford University Press, London, 1970.

[2] A. J. M. Spencer (Ed.), Continuum Theory of the Mechanics of Fibre-reinforced Composites, CISM Courses and Lectures, vol. 282, Springer, Wien, 1984.

[3] A. J. M. Spencer, K.P. Soldatos, Finite deformations of fibre-reinforced elastic solids with fibre bending stiffness, International Journal of Non-linear Mechanics, vol. 48, Issue 2, 2007, 355-368.

[4] E. et F. Cosserat, Théorie des corps déformables, A. Hermann et Fils, Paris, 1909.

[5] T. Lasota, Porovnani ruznych urovni vypoctovych modelu kompozitu s hyperelastickou matrici, FSI Junior konference 2008, Brno, 2009.

[6] A. C. Eringen, Theory of micropolar elasticity, in: H. Leibowitz, ed., Fracture, An Advanced Treatise (Academic Press, New York, 1968) 621-729.

COMPARISON OF SURFACE TEMPERATURES OF ACRYLIC BONE CEMENTS DURING POLYMERIZATION AFTER DIFFERENT TECHNIQUES OF MIXING

Henrietta Lelovics[1)], Tatiana Liptáková [1)]

[1)] University of Žilina, Department of Materials Engineering, Univerzitná 1, 010 26 Žilina, Slovakia.

Corresponding author: henrietta.lelovics@fstroj.uniza.sk

1. Introduction

Acrylic bone cements are widely used in today's orthopaedic surgery. They main role is to fix the components of the prostheses and to distribute the loads to the surrounding bone and tissues [1-2]. The cement consists of two compounds (powder and liquid) which are mixed together. After mixing the exothermal radical polymerization begins. Free radicals break the covalent C=C bonds of the monomer, allowing them to bind to the lengthening polymer chains. The amount of the heat generated by chemical reaction depends on the thickness of the cement mantle and in some cases cause tissue and bone necrosis [2-4].

This paper deals with monitoring the surface temperature of SmartSet HV acrylic bone cement samples with different thickness prepared by hand and vacuum mixing.

2. Experimental

The cement samples were prepared by hand and vacuum mixing technique, both with exact timing. The quantitative composition of the used bone cement is presented in Tab. 1.

Powder	Methyl Methacrylate/ Methyl Acrylate Copolymer	84 (%w/w)
	Di-Benzoyl Peroxide	1 (%w/w)
	Zirconium Dioxide	15 (%w/w)
Liquid	Methyl Methacrylate	97,5 (%w/w)
	N,N-Dimethyl-p-toluidine	≤ 2,5 (%w/w)
	Hydroquinone	0,0075 (%w/w)

Tab. 1: Quantitative composition of bone cement SmartSet HV

2.1 Sample preparation

The powdered component was poured into a suitable, clean, dry mixing ceramic bowl and then the liquid component was added. The dough was mixed carefully to minimize the air entrapment then the dough was taken into hands and kneaded for a few seconds. For vacuum mixing CEMVAC mixing system was used. After mixing together the components the dough was put into the rotational rheometer with parallel plates about 25mm diameter preheated to 37°C to simulate the in vivo conditions. The samples were trimmed to 2 and 5mm high (the optimal cement mantle thickness in vivo is 2-5mm) [2]. Straining and heating options were turned off during the measurements, only the surface temperatures of the trimmed samples were monitored.

3. Results

Before the measurement the measuring system was preheated to 37°C but opening the chamber, positioning and trimming the samples caused drop of the default temperature of the system to 35,5 – 36,1 °C at the beginning of the measurements.

The measured surface temperature courses are represented in Fig. 1 - 4. The averaged values of peak temperatures and times required to obtain the peak temperatures are represented in Tab. 2 - 3.
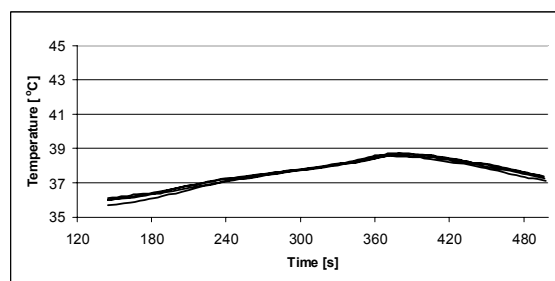
Fig. 1: Surface temperature courses of the hand-mixed samples with 2mm thickness

It was clearly shown, that the amount of produced heat during the cement polymerization depends on the sample thickness. The time required to obtain the peak

temperature on the sample surface from the beginning of mixing procedure is also different and it rises by the sample thickness.
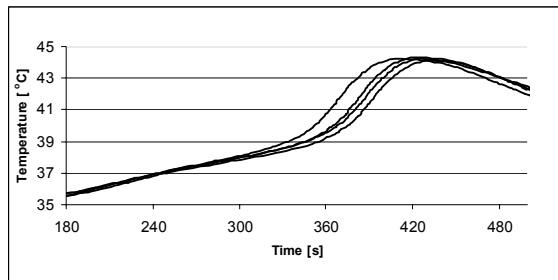
Fig. 2: Surface temperature courses of the hand-mixed samples with 5mm thickness

Thickness [mm]	Peak temperature [^{o}C]	Time [s]
2	39,60 ± 0,12	380,5 ± 6,3
5	44,20 ± 0,04	420,5 ± 4,4

Tab. 2: Averaged values of peak temperatures and times required to obtain the peak temperatures of differently thick hand-mixed cement samples
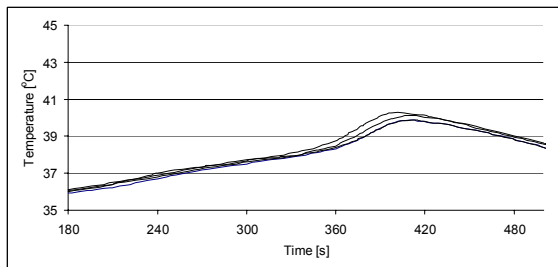
Fig. 3: Surface temperature courses of the vacuum-mixed samples with 2mm thickness
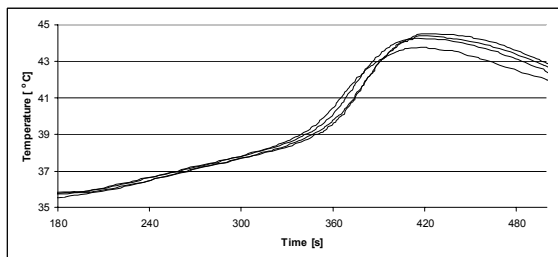
Fig. 4: Surface temperature courses of the vacuum-mixed samples with 5mm thickness

Thickness [mm]	Peak temperature [^{o}C]	Time [s]
2	40,05 ± 0,1	409,5 ± 2,6
5	44,25 ± 0,16	417 ± 1,7

Tab. 2: Averaged values of peak temperatures and times required to obtain the peak temperatures of differently thick hand-mixed cement samples

The measured highest peak temperature under the selected conditions was 44,25 ± 0,16 ^{o}C which cannot cause bone tissue destruction, because the collagens denature with prolonged exposure to temperatures in excess of 56°C [3]. The required time to obtain the peak temperatures was different for the selected mixing techniques and there was no distinct correlation observed between these times and the sample thicknesses.

4. Conclusions

In this paper the temperature courses of polymerizing acrylic bone cement were monitored on the surfaces of the samples. The peak temperature rose with increasing sample thickness but the obtained highest temperature during the selected conditions still can not cause bone tissue necrosis. It was also determined, that the coarser the cement sample, the longer the time required to obtain the peak temperature due to the low thermal conductivity of the cement mass.

5. Acknowledgements

6. References

[1] Lelovics H, Seewald R, Nečas L, Mechanical properties of bone cements. TRANSCOM 2009, in press.

[2] Lelovics H, Seewald R, Nečas L, Observation of surface temperature of acrylic bone cements during polymerization. TRANSCOM 2009, in press.

[3] Dipisa J, Sih G, Berman A, The temperature problem at the bone-acrylic cement interface of the total hip replacement. Clin. Orthop. Vol. 121 (1976) 95–8.

[4] Lelovics H, Liptáková T. Comparison of some mechanical and rheological properties of bone cements. 25th Danubia-Adria symposium on experimental methods in solid mechanics, 2008, Czech Republic, 157-158.

EXPERIMENTAL ANALYSIS OF WEAR AND RESIDUAL STRESSES AT CONTACT FATIGUE

Pavel Macura [1]**, Nikolaj Ganev** [2]**, Radim Halama** [1]**, František Fojtík** [1]**, Kamil Kolařík** [2]**,
Totka Bakalova** [3]

[1] VŠB-TU Ostrava, Department of Mechanics of Materials, 17. listopadu 15, CZ 708 33 Ostrava – Poruba, Czech Republic.

[2] Czech Technical University in Prague, Faculty of Nuclear Sciences and Physical Engineering, Department of Materials, Trojanova 13, 120 00 Praha 2, Czech Republic.

[3] Technical University in Liberec, Faculty of Mechanical Engineering, Department of Machining and Assembly, Hálkova 6, 461 17 Liberec 1, Czech Republic.

Corresponding author: pavel.macura@vsb.cz

1. Introduction

The classical and contact fatigue of materials is reason of many defects. The contact fatigue rises in many cases of process loading of different parts. The gear wheel engagement, contact of working rolls of rolling mill with rolling stock or back-up roll and contact of railway wheel with rail are some examples of contact loading and contact fatigue. Great attention should be paid to those issues from both theoretical and experimental point of view.

2. Testing machine and experimental results

A unique test machine has been developed at the VŠB – TU Ostrava. The device was designed for simulation of various wheel/rail contact cases. The experimental equipment is characterized by the fact that the normal loading force is applied statically by a weight on a lever mechanism, see Fig. 1.
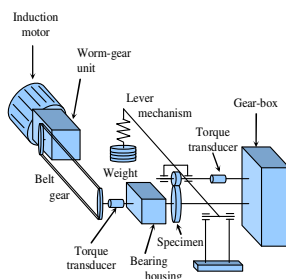
Fig. 1: Scheme of the rolling/sliding test machine.

The driver and follower are powered by a 2,2kW induction motor through several gear stages. A change of gears or appropriate choice of specimen diameters gives a slipping motion

on the contact surface. The test machine enables the simple pulley generating only by means of friction or generating by the pulley braking by means of an electromagnetic brake, followed by the parallel or skew axis of pulley and drum by the dry or lubricated contact and other.

The coefficient of traction was monitored during each test and mainly disc weight loss, disc diameter loss, hardness and surface roughness were investigated at the end of every test. After specimen sectioning the surface layer was prepared for metallographic observation in order to gain a conception about maximal defects and shear strain accumulation. Some results of the contact fatigue with fixed slipping can be seen in Fig. 2.
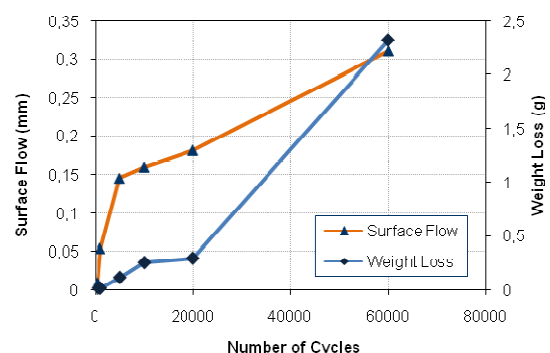
Fig. 2: Results of wear measurements.

At the same time, measurements of residual stresses are provided before and after contact loading. Three methods of experimental stress analysis were used for measurements – hole drilling strain gage method, X-ray diffraction method and magnetoelastic method. The residual stresses before contact loading are relatively small and tensile (~50 MPa). The

courses of principal residual stresses after 2 000 000 cycles of loading can be seen in Fig. 3. Under the contact surface are comparatively high compressive residual stresses. Integral method was used for the residual stress evaluation in case of hole drilling [1].
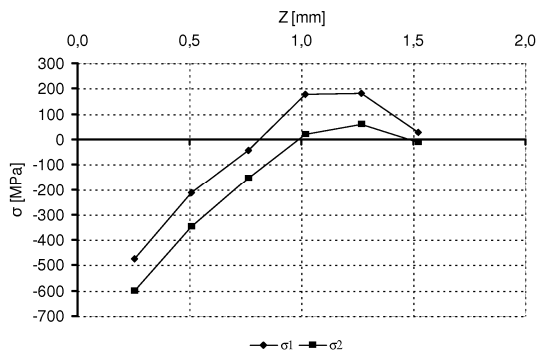
Fig. 3: Courses of principal stresses in pulley after 2 000 000 cycles by hole drilling method.
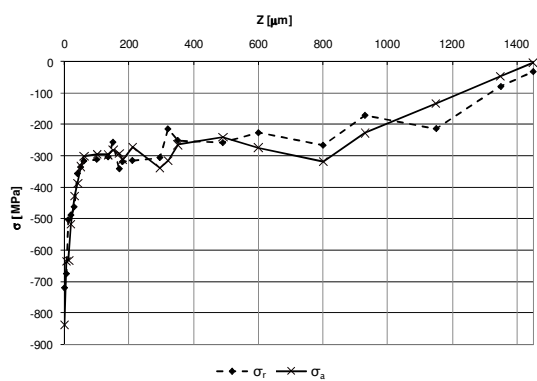
Fig. 4: Residual stresses by X-ray diffraction measurement.

The results of residual stresses obtained by means of X-ray diffraction method after 2 000 000 cycles is shown in Fig. 4.
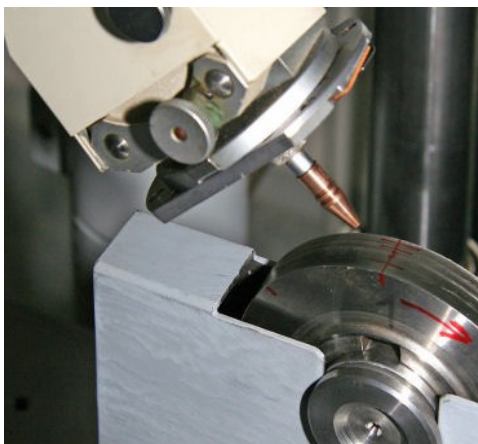
Fig. 5: X-ray measurement equipment.

The measurement equipment can be seen in the Fig. 5, the method of residual stress evaluation is presented in [2]. The residual stresses on the pulley surface were measured by means of X-ray diffraction and magnetoelastic method [3]. The measurement results of a pulley are shown in Tab. 1.

Place	X-ray		Magnetoelastic method	
	σ_A [MPa]	σ_T [MPa]	σ_A [MPa]	σ_T [MPa]
A	-374	-303	-361	-234
B	-341	-178	-342	-168
C	-347	-170	-345	-175
D	-368	-122	-334	-111

Tab. 1: Residual stresses measured by X-ray diffraction and magnetoelastic method.

3. Conclusion

Assessment of contact fatigue on pulley was carried out in the laboratories VŠB-TU Ostrava and CTU in Prague; residual stress depth distributions were obtained by hole-drilling strain gage method and by X-ray diffraction. Results of surface residual stresses measurement by means of X-ray diffraction and magnetoelastic methods are in perfect agreement. The research is of great importance to the producers of wheel sets, rolls for rolling mills and rails.

4. Acknowledgements

5. References

[1] G. S. Schajer, Measurement of non-uniform residual stress using the hole-drilling method, Journal of Engineering materials and technology 110 (1988) No. 4, Part I: pp 339-343, Part II: pp 334-349.

[2] I. Kraus, N. Ganev, Technical Applications of diffraction analysis. Praha, ČVUT Publishing, 2004.

[3] S. Titto, Barkhausen noise method for determining biaxial stresses in feromagnetic materials. US Patent 4977373, 1990.

STABILITY BEHAVIOR OF LAYERED COMPOSITE PANELS: EXPERIMENTAL AND NUMERICAL RESULTS

Steven Maksimović [1), Nataša Trišović [2)

[1) Military Technical Institute, Ratka Resanovića 1, 11000 Belgrade, Serbia

e-mail: s.maksimovic@nadlanu.com

[2) Faculty of Mechanical Engineering, University of Belgrade, Kraljice Marije 16, 11000 Belgrade,

e-mail: ntrisovic@mas.bg.ac.yu

Corresponding author: ntrisovic@mas.bg.ac.yu

1. Introduction

Attention in this work is focused on buckling load and post-buckling behaviour of an axially compressed the carbon epoxy composite (CFC) layered panel. A description of test specimens, testing equipment and instrumentation is given. The problem of deriving the buckling load from the test data is discussed. A comparison between experimental and computation results is made for buckling load and post-buckling behaviour of the layered composite panel. Test results are compared with computation results using Finite Element Method (FEM).

2. Buckling Load From Test Data

To determine buckling load of axially compressed composite panel here strain gauges are used. Strain gauges were applied on both sides of the layered composite plate in loading direction, Fig. 1.
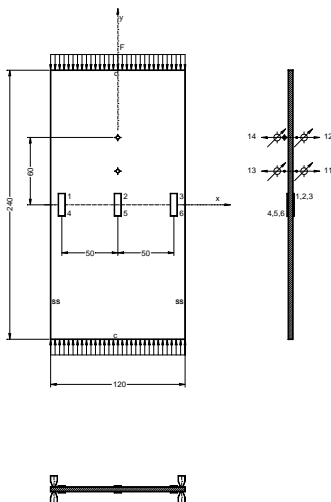
Fig. 1: Positions of Strain Gages and Transducers on Testing Specimen

Results of one buckling test are given in Fig 2. Figures 2a and 2b show the output of three strain gauge pairs as well as the membrane strains.
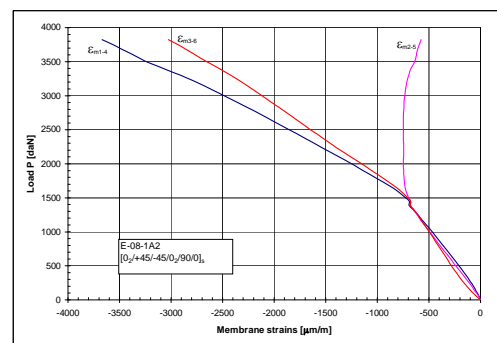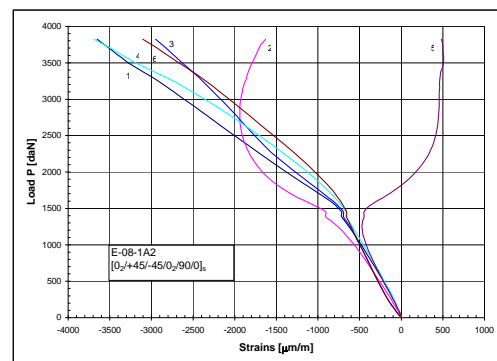
Fig. 2: Load (P) versus membrane strains (ε_m)

The load versus strain plots, Figs 2a and 2b, show the strain reversal behaviour near the buckling load. The test data show a large transition area between the pre- and post-buckling situation so a well defined buckling point cannot be given as one value. The membrane strains were plotted versus end load, Fig 2b. From Figure 2b (Diagrams P-ε_m: loads versus membrane strains) buckling load of this composite panel is in range **(1380 -1450)** daN. The composite plates were tested in a special tool that was attached to an «SCHRENK» test

machine. To achieve clamped (c) and simply supported (ss) boundary conditions during loading of panel, as shown in Fig. 1, in this testing special tool is adopted.

3. Buckling Load From FEM

Much research has been conducted on buckling composite plates. A review of the subject by Leissa[1] quotes more than 90 references. Most of this work is theoretical in nature, and very little, if any, attention is given to post-buckling behaviour. To determine stability behaviour of composite panel here non-linear finite element analysis is used to determine buckling load and post-buckling behaviour[2-4].
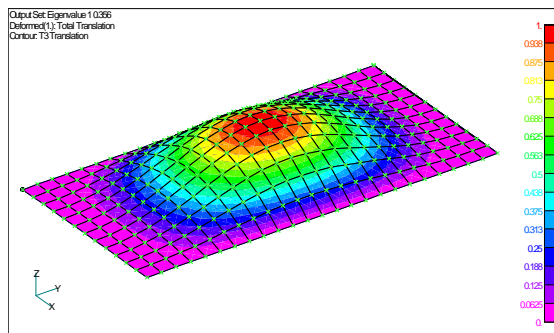
Fig. 3 The First Buckling Mode by FEM
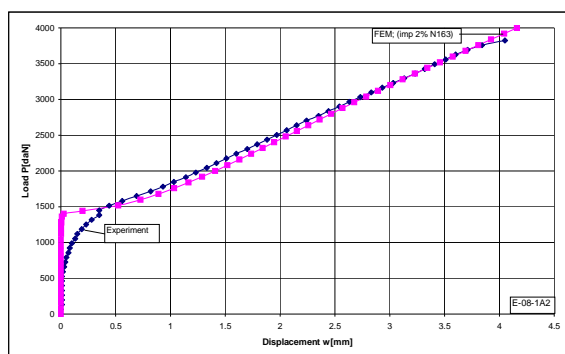
Fig. 4 Relations between load (P) and displacement - (w), with 2% imperfection

Finite element model and first buckling mode is shown in Fig. 3. In Figure 4 are given experimental and computation results of buckling and post-buckling behaviour using relation between load **P** and out of plane displacements (**W**).

Figure 4 present maximum out of plane displacements (w) measured for panels as defined in Figure 1. The load versus out of

plane displacement plot, Fig. 4, shows a change of slope close to the buckling load. The pre-buckling part of this line is straight and if the post-buckling part of this line forms a straight line too, point of intersection can be taken as the buckling load. Buckling load using non-linear finite element analysis is **P_{cr}=1405 daN**, Fig. 4. In Figure 4 finite element predictions is shown for initial imperfection of 2% panel thickness.

4. Conclusion

In this investigation the complete methodology for buckling and post-buckling behaviour of the axially compressed composite panel is illustrated. Methodology is based on using strain gauges for strains detection or transducers for displacements detection. Experimental results are compared with experiments. Good agreement between experimental and non-linear finite element results is obtained.

5. References

[1] A. W. Leissa, Advances in vibration, buckling and postbuckling studies on composite plates, Composite Structures, London, Applied Science Publishers, 1981, p. 312.

[2] S. Maksimović, Instability Analysis of Layered Composite Structures Using Shell Finite Elements Based on the Third Order Theory, J. Applied Composite Materials, Vol.3 (1996) 301-309.

[3] S. Maksimović, Postbuckling and Failure Analysis of Axially Compressed Composite Panels Using FEM, Scientific Technical Review, Vol. LVII, No. 3-4, 2007.

[4] N. Buskell, G.A.O. Davies and K. A. Stevens, Postbuckling Failure of Composite Panels, Proc. 3rd Int. Conference on Composite Structures, Paisley College of Technology, 9 to 11 September 1985.

WITH PHOENIX ON RAILS

Tiberiu Ştefan MĂNESCU
Nicuşor Laurenţiu ZAHARIA
Cristian FĂNICĂ
Dorica Mihaela STROIA

Eftimie Murgu University, 320085 Reşiţa, 1-4 Traian Vuia Square
Romanian Railway Authority - AFER, 010719 Bucharest, 393 Calea Grivitei, e-mail: rentizaharia@yahoo.com
Eftimie Murgu University, 320085 Reşiţa, 1-4 Traian Vuia Square
Eftimie Murgu University, 320085 Reşiţa, 1-4 Traian Vuia Square

1. Introduction

This abstract present the experimental stress analysis at a electrical locomotive's frame bogie. The electrical locomotive are used at passenger and freight trains on Romanian main electrified railways. The designers search for new solution to improve the railway products. Because the locomotive was widely modified, this project was named by his designers "Phoenix" (figure 1). One of the improvements was at locomotive's bogie.

After such modification, tests are made in purpose to obtain a new certification from a Railway Commission. The tests were carried out according to ERRI B12/RP 17 (ERRI – European Railway Research Institute).

Fig. 1: Phoenix electrical locomotive

2. Measurement points

The measurement points were located in the relevant areas of bogie's frame.

The measurements were performed in 16 points (figure 2). Hottinger LY11-10/120 strain gages were glued on the elements of the bogie with Hottinger Z70 adhesive.

The strain gages were connected at measuring devices with cables.

The measurements were performed with Hottinger Centipede 100 Multipoint Measuring Unit (for the static tests) and Hottinger MGCplus (for the dynamic tests).

The measuring devices Centipede 100 and MGCplus were connected to a laptop computer.

The acquisition software used was Catman 4.5 (an Hottinger product).
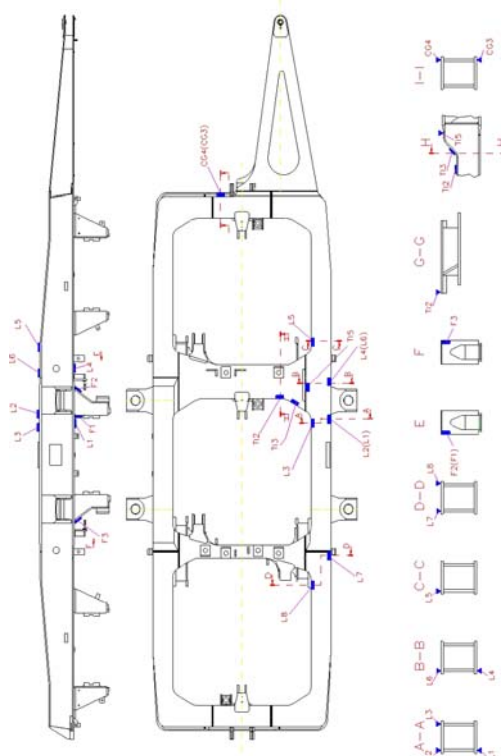
Fig. 2: Measurement points on locomotive's bogie

3. Tests

The tests were performed in two steps:

- static tests,
- dynamic tests.

During the static test, were recorded the static stress σ_{st} due the locomotive's body action on the bogies.

Recording of the stress variation (dynamic components of the stress) $\Delta\sigma_+$ and $\Delta\sigma_-$ were made during locomotive's circulation on maximum speed. Based on values of $\Delta\sigma_+$ and $\Delta\sigma_-$ were calculated outmost values of the stress with the equations:

$$\sigma_{max} = \sigma_{st} + \Delta\sigma_+ \qquad (1)$$

$$\sigma_{min} = \sigma_{st} + \Delta\sigma_- \qquad (2)$$

The medium value of the stress result from the equation:

$$\sigma_m = \frac{\sigma_{max} + \sigma_{min}}{2} \qquad (3)$$

The amplitude of the stress result from the equation:

$$\sigma_v = \frac{\sigma_{max} - \sigma_{min}}{2} \qquad (4)$$

The σ_v values were comparative with the values from Goodman – Smith diagrams presented in annex F.3 of the report ERRI B12/RP17. The allowable condition is:

$$\sigma_v \leq \sigma_{vadm} \qquad (5)$$

In the figure 3 is presented graphically how the tests were done.
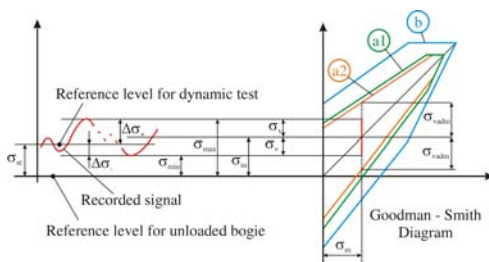
Fig. 3: Test diagram

4. Results

The dynamic diagrams of the highest stresses recorded by measurement points are shown in figures 4÷5 (there are presented only the diagrams for the most stressed points static and dynamic).

The recorded data were made at 200 samples/second for each measuring point. No filter was used for the tests (device settings).

Regarding to Goodman – Smith diagram, al measured stresses were on "a2" curve (figure 3).
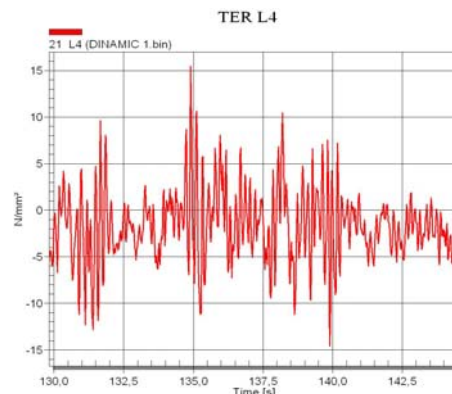
Fig. 4: Dynamic stress for L4
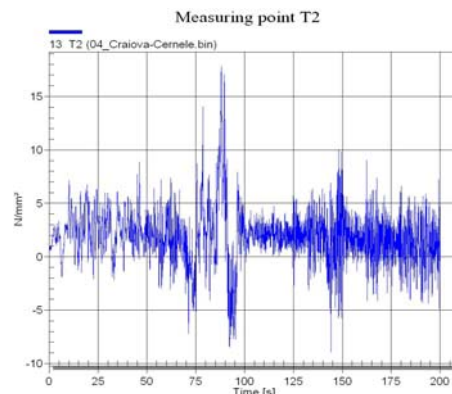
Fig. 5: Dynamic stress for T4

5. Conclusions

The results, was smaller than permissible stress, so we can concluded that the design solution used by manufacturer was good.

Based on test results, the designer can improve his design to increase the quality of the final product.

After the tests the new certification from the Railway Commission was obtain.

6. References

[1] T. Ş. Mănescu, I. Copaci, S. Olaru, F. Creangă, *Tensometria electrică în cercetarea experimentală*, Editura Mirton, Timişoara, 2006

[2] I. Copaci, T. Ş. Mănescu, S. Olaru, F. Creangă, *Rezistenţa la solicitari variabile care apar în exploatarea vehiculelor feroviare*, Editura Mirton, Timişoara, 2005

[3] *****ERRI B12/RP 17 *Programe des essais à faire subir aux wagons à châssis et superstructure en acier (aptes à recevoir l'attelage automatique de choc et traction) et à leurs bogie à châssis en acier,* Utrecht, 1997

EXPERIMENTAL STATIC AND DYNAMIC TESTING OF THE DABAR BRIDGE NEAR ŠIBENIK

Pavao Marović [1), Marko Bertolino [1), Ivan Marović [2)

[1) University of Split, Faculty of Civil Engineering and Architecture, Matice hrvatske 15, HR-21000 Split, Croatia.

[2) University of Rijeka, Faculty of Civil Engineering, Viktora Cara Emina 5, HR-52000 Rijeka, Croatia.

Corresponding author: pavao.marovic@gradst.hr

1. Introduction

Generally, testing of the structures is the only way of proving and evaluating the hypotheses and the assumptions taken into the mathematical and/or numerical models during the design processes.

This paper presents the experimental static and dynamic testing of the Dabar Bridge on the highway Zagreb-Split near the city of Šibenik [1]. Also, this paper presents the comparison of the obtained experimental results with the calculated theoretical i.e. numerical results.

Dabar Bridge, fig. 1, is 330 meters long double bridge (separate longitudinal structures for every traffic direction), over seven spans of 40 + 5 x 50 + 40 meters. It was designed as classical reinforced concrete plane frame system with longitudinal I-girders (fig. 2) connected only with continuous 20 centimetres thick reinforced concrete deck.

Fig. 1: Dabar Bridge – overall view.

Fig. 2: Dabar Bridge – structural system.

Spanning I-girders are 240 centimetres high and were prefabricated while piers and abutments were built monolithically.

2. Description of the Testing

The experimental static and dynamic testing was performed on site. The testing load was determined to obtain design values of the internal cross-section forces. The whole testing was performed according to the Croatian rules [2].

2.1 Static testing

Static load was performed with six trucks weighting approximately 35 metric tonnes each, see fig. 3, placed in the mid-spans. Vertical displacements were measured by geodetic method of levelling in every span along four lines (A, B, C and D), over the supports (1, 3, 5, 7, etc.) and in the mid-spans (2, 4, 6, 8, etc.), altogether at 12 points on each span.

Fig. 3: Dabar Bridge – static loading.

2.2 Dynamic testing

Dynamic load was performed with two heavy trucks of 35,6 and 48,7 metric tonnes each moving along separate bridge structures at the speeds of 20 to 50 km/h. Dynamic response of the structures was registered in the time domain. The data acquisition was performed with uniaxial accelerometers and DEWETRON 2010 system. The FTT analysis was performed from the recorded accelerograms to obtain frequency responses. The natural frequencies were determined from the peaks of the FTT graphs using DEWESoft computer package [3].

3. Experimental Results

Considering space restrictions, only a part of the obtained experimental results [1] will be shown here.

3.1 Static testing

The experimental results of the static testing i.e. vertical displacements in some mid-spans for some loading schemes are shown in Tab. 1.

Point	Load in 1st span	Load in 2nd span	Load in 3rd span
A2	**7.27**	-2.46	-
B2	**7.05**	-2.71	-
C2	**7.26**	-2.61	
D2	**6.95**	-2.42	-
A4	-3.45	**8.08**	-1.20
B4	-3.34	**8.31**	-1.21
C4	-3.62	**8.59**	-1.49
D4	-3.64	**8.28**	-1.39
A6	-	-5.32	**4.50**
B6	-	-5.42	**4.28**
C6	-	-5.57	**4.43**
D6	-	-5.29	**4.44**

Tab. 1: Vertical displacements (mm).

3.2 Dynamic testing

The experimental results of the dynamic testing i.e. natural frequencies and corresponding FTT diagrams for one passage of heavy trucks are shown in figs. 4 and 5, respectively.
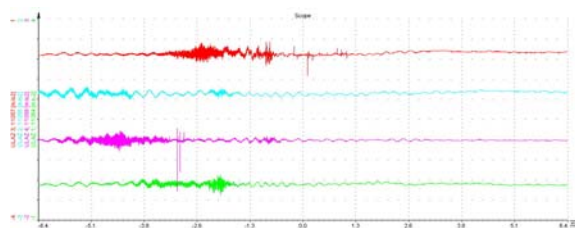
Fig. 4: Natural frequencies.
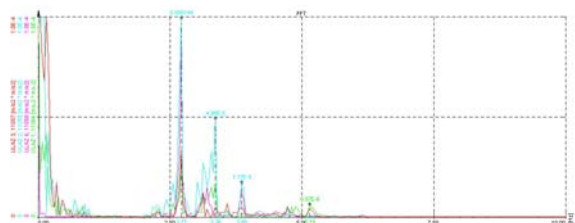
Fig. 5: Power spectral density functions.

4. Numerical Analyses

The numerical analyses, both static and dynamic, were performed on PC with the model, fig. 6, based on the finite element method with the software programme FEAT2000 [4].
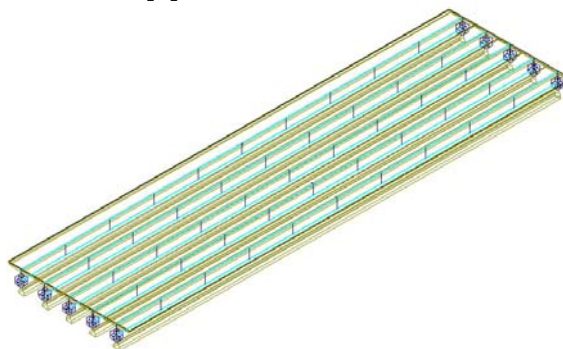
Fig. 6: Dabar Bridge – numerical model.

5. Comparison of Results

The comparisons of maximal vertical displacements are shown in Tab. 2.

Point	Exp. value	Num. value
A4	8.14	13.28
B4	8.34	17.39
C4	8.76	17.96
D4	8.48	13.47

Tab. 2: Comparison of vertical displacements (mm).

The comparisons of averaged natural frequencies are shown in Tab. 3.

	1st mode	2nd mode	3rd mode	4th mode
Exp.	2.73	3.17	3.73	5.13
Num.	2.65	2.79	4.45	6.38

Tab. 3: Comparison of natural frequencies.

6. Conclusions

The obtained experimental results, maximal vertical displacements and dynamic responses, correspond well to the theoretical values. The testing confirmed static and dynamic design hypotheses.

7. References

[1] P. Marović, M. Bertolino, I. Marović, Report on load testing of the bridge Dabar on the highway Zagreb-Split near Šibenik, University of Split, Faculty of Civil Engineering and Architecture, Split, Report No. 1-133609/05-DAB, June 2005.

[2] Croatian Standard HRN U.M1.046: Testing of bridges with test load, 1984.

[3] DEWESoft for Windows 95/98/ME/NT and 2000 ver. 6.1, DEWETRON, 2004.

[4] FEAT2000 for Windows 95/98/NT4.0 ver. 3.00, SCIA CZ

EXPERIMENTAL TESTING OF GRANDSTAND RC GIRDERS OF THE SPALADIUM ARENA IN SPLIT

Pavao Marović, Mirela Galić, Marko Bertolino [1)]

[1)] University of Split, Faculty of Civil Engineering and Architecture, Matice hrvatske 15, HR-21000 Split, Croatia.

Corresponding author: pavao.marovic@gradst.hr

1. Introduction

This paper presents the experimental static and dynamic testing of the grandstand reinforced concrete (RC) girders both as single elements and as monolithically assembled into grandstand structure of the Spaladium Arena in the city of Split [1].

The RC girder is a simple supported beam over the span of 9.0 meters. Total length of the girder is 9.99 meters and is supported in six points, three on each end. Assembled girders are additionally connected in the thirds of the span. Dimensions of the cross-section can be seen in the fig. 1.
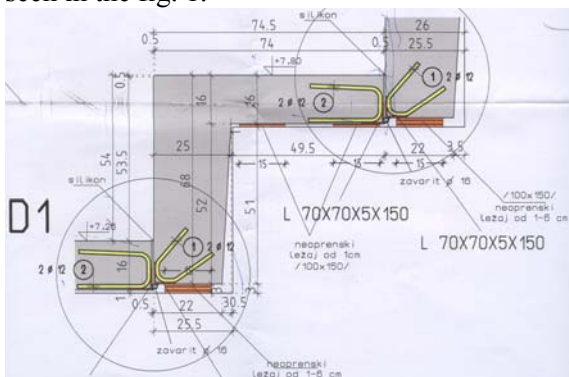
Fig. 1: Grandstand RC girder cross-section.

2. Single Girder Testing

The experimental static and dynamic single girder testing was performed on site of the production in the Konstruktor Concrete Factory. The testing load was determined to obtain design values of the internal cross-section forces. The whole testing was performed according to the Croatian rules [2, 3].

2.1 Static testing

The static load was performed with concrete blocks weighting approximately 500 kilos each placed in the mid-third of the girder over steel frame, see later fig. 6. Vertical and horizontal displacements were measured by dial gages positioned at the supports and in the mid-span, see fig. 2.
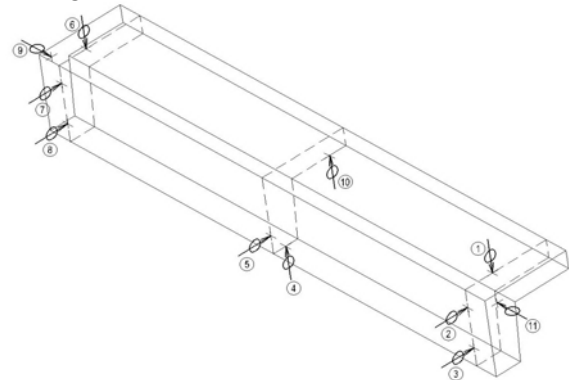
Fig. 2: Positions of dial gages.

Strains of concrete were measured by Barry movable extensometer positioned at the supports and in the mid-span, see fig. 3.
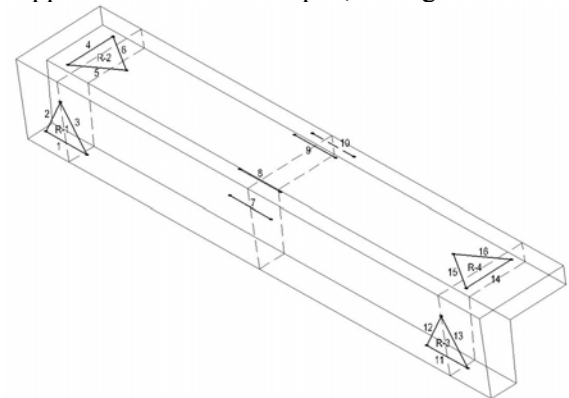
Fig. 3: Positions of strain gages.

2.2 Dynamic testing

The dynamic responses were induced by jumping groups of different number of humans. Dynamic response of the girder was registered in the time domain. The data acquisition was performed with uniaxial accelerometers (whose positions can be seen in fig. 4) and DEWETRON 2010 system. The FTT analysis was performed from the recorded accelograms to obtain frequency responses. The natural frequencies were determined from the peaks of the FTT graphs using DEWESoft computer package [4].
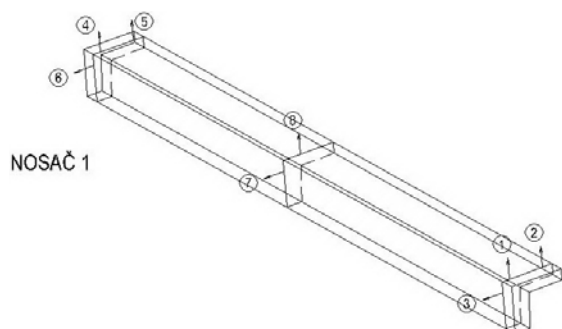
Fig. 4: Positions of accelerometers.

3. Assembled Girder Testing

Assembled girders were connected in the thirds of the spans creating monolithical grandstand structure, fig 5. Only dynamic testing was performed by jumping of humans.

Fig. 5: Assembled grandstand structure.

4. Experimental Results

Considering space restrictions, only a part of the obtained experimental results [1] will be shown here.

4.1 Static testing

Maximal designed bending moment i.e. corresponding testing load is presented in fig. 6.

Fig. 6: Static loading performance.

4.2 Dynamic testing

The experimental results of the dynamic testing i.e. natural frequencies and corresponding FTT diagrams for one jumping are shown in figs. 7 and 8, respectively, for single girder testing. Natural frequencies of the assembled girders i.e. monolithical grandstand is shown in fig. 9.
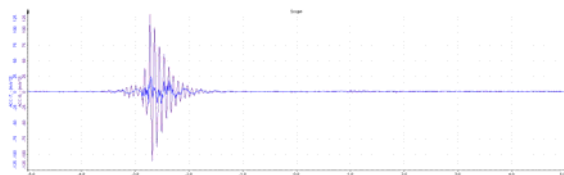
Fig. 7: Natural frequencies – single girder.

Fig. 8: Power spectral density functions.
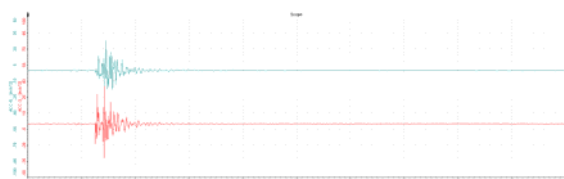
Fig. 9: Natural frequencies – assembled girders.

Single	Assembled girders		
1st mode	1st mode	2nd mode	3rd mode
11.74	8.94	9.55	13.07

Tab. 1: Comparison of natural frequencies.

5. Numerical Analyses

The numerical analyses were performed on PC with the model based on the finite element method with the software program FEAT2000 [5].

6. Conclusions

The obtained experimental results, maximal vertical displacements, strains i.e. stresses and dynamic responses, correspond well to the theoretical values. The testing confirmed static and dynamic design hypotheses.

7. References

[1] P. Marović, M. Galić, M. Bertolino, Report on load testing of the grandstand structure of the Spaladium Arena in Split, University of Split, Faculty of Civil Engineering and Architecture, Split, Report No. 1-133609/08-TDL, November 2008.

[2] Croatian Standard HRN U.M1.047: Load test and break test for the building constructions, 1987.

[3] Croatian Standard HRN EN 13369:2003 - Common rules for precast concrete products (EN 13369:2001), DZNM, Zagreb, 2003.

[4] DEWESoft for Windows 95/98/ME/NT and 2000 ver. 6.1, DEWETRON, 2004.

[5] FEAT2000 for Windows 95/98/NT4.0 ver. 3.00, SCIA CZ

RELATIONS BETWEEN BMD DENSITY AND VOLUMETRIC AND FRACTAL INDICATORS OF HUMAN TRABECULAR BONE

Adam Mazurkiewicz, Tomasz Topoliński [1)]

[1)] University of Technology and Life Sciences, Mechanical Faculty, Kaliskiego 7 Street, 85-789 Bydgoszcz, Poland.

Corresponding author: adam.mazurkiewicz@utp.edu.pl

1. Introduction

To the estimation bone quality and risk of fracture are used commonly densitometric techniques such as quantitative computed tomography (QCT) or dual energy x-ray absorptiometry (DEXA). Result of the measurement is value of density selected part of bone. Limitation this methods is lack posibilities explanation individual differences in trabecular bone architecture [1-2]. Obtained density is mean value which isn't allowed for local differences in subvolume of trabecular bone.

Fractal dimension is one of indicators used to description complex porous structure, in medicine e.g. cancer tissue or trabecular bone architecture [3-5].

The aim of this study is estimation relations between DEXA density, fractal dimension and local subvolume of trabecular bone.

2. Experimental Results

Material to the investigation were samples of human trabecular bone. Samples were collected from 21 osteoporotic (Ost) and 21 coxarthrotic (Cox) femoral heads gained in result of hip arthroplasty. Coxarthrosis is one of bone diseases. A result the one is hyperthrophy articular cartilage in volume and surface femoral head. Because authors didn't have possibilities used as reference group similar number of samples collected with bones without any bone diseases, they assumed as reference group set of coxarthrosis samples. Because coxarthrotic bones similarly as healthy bones are subject to fracutre very seldom assumed that mechanical strength of the bones are not less than bone without any bone diseaes.

The samples used to investigation have cylindrical shape about diameter 10 and height 8,5mm. Manner of collecting sample is presented in fig. 1.
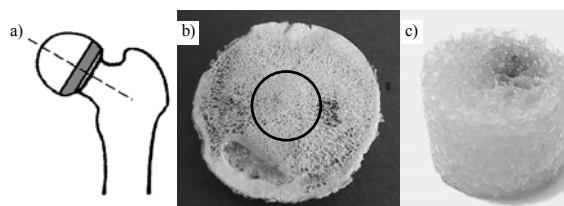
Fig. 1: Manner of collecting sample: cutting slice a), cutting sample b), sample c)

Samples were examined at microCT device (μCT80) with resolution 36μm. In result the investigation were obtained sequential images slices perpendicular to axis of sample.

DEXA density (BMD) was performed with scanner Lunar Expert, General Electric Company.

On the base the images geometical models of sample were created. The ones were divided at subvolumes in shape of layer about height 36μm. The layers were created as following: compared images two neighbouring slices. When on the same coordinate in both images color of pixels represented bone, voxels of layer of bone between the images were created. Size of voxels was the same as pixels at images size i.e. 36μm.

Volume (V) all layers for every sample was examined. On the base were finded mean (V_m), minimal (V_{min}) and maximal (V_{max}) volume of layer for every sample.

For the same layers, the fractal dimension (D_f) was calculated and then the mean (Df_m), minimal (Df_{min}), maximal (Df_{max}) value of this dimension for every sample was determined. For the purpose of defining fractal dimension, the definition of 'box' dimension (Minikowski – Bouligand) was used.

3. Experimental Results

In tab. 1 presented values of detemination coefficient (R^2) obtained for relations between BMD and mean, minimal and maximal volume layers of sample. In tab. 2 presented values of detemination coefficient obtained for relations

between BMD and fractal dimensions. In the tables, maximal values of R^2 are presented for the study of the description of power, logarithmic and numerical functions.

Samples	Ref		V_m	V_{min}	V_{max}
		1	2	3	4
Together	1	BMD	0.5125	0.5713	0.4014
Cox	2	BMD	0.3504	0.4761	0.1962
Ost	3	BMD	0.4035	0.4025	0.3442

Tab. 1: Value of determination coefficient R^2 for the relationship of BMD with volume of layer

Sample	Ref		Df_m	Df_{min}	Df_{max}
		1	3	4	5
Together	1	BMD	0.558	0.582	0.414
Cox	2	BMD	0.439	0.558	0.235
Ost	3	BMD	0.416	0.373	0.341

Tab. 2: Value of determination coefficient R^2 for the relationship of BMD with fractal dimension

Analysis both table is pointed, that generally obtained values R^2 for this relations weren't to high and contained in range $(0,19 \div 0,59)$. Values R^2 were higher for relations between BMD and fractal dimension (7 cases per 9 considered) and always for mean values V_m and Df_m. The highest values R^2 were achieved however for Df_{min} and insignificant lower for V_{min} in both groups of samples together and group of coxarthrosis samples.

Related achived results to study [6] where were demostratet that the strongest relations were finded between deforming force (compression test, axis strain of sample 0,8%) and Df_m, ought to raise doubts unequivocal relations between strength of bones and BMD, used widely in clinical practice.

Therefore combination BMD and any indicator of trabecular archtitecture e.g. fractal dimension probably would get better results than predicted strength of bone using only BMD density.

4. Acknowledgements

5. References

[1] J.S. Bauer, S. Kohlmann, F. Eckstein, D. Mueller, E.M. Lochmüller and T.M. Link, Structural analysis of trabecular bone of the proximal femur using multislice computed tomography: a comparison with dual X-ray absorptiometry for predicting biomechanical strength in vitro. Calcif Tissue Int., Vol. 78 (2006) 78-89.

[2] E.M. Lochmüller, D. Bürklein, V. Kuhn, C. Glaser, R. Müller, C. C. Glüer, F. Eckstein, Mechanical strength of the thoracolumbar spine in the elderly: prediction from in situ dual-energy X-ray absorptiometry, quantitative computed tomography (QCT), upper and lower limb peripheral QCT, and quantitative ultrasound. Bone, Vol. 31 (2002) 77-84.

[3] G.P. Feltrin, V. Macchi, C Saccavini, E. Tosi, C. Dus, A. Fassina, A. Parenti and R. De Caro, Fractal analysis of lumbar vertebral cancellous bone architecture. Clin Anat., Vol. 14 (2001) 414-417.

[4] C.L. Benhamou, S. Poupon, E. Lespessailles, S. Loiseau, R. Jennane, V. Siroux, W. Ohley and L. Pothuaud, Fractal analysis of radiographic trabecular bone texture and bone mineral density: two complementary parameters related to osteoporotic fractures. J Bone Miner Res., Vol. 16 (2001) 697-704.

[5] S. Majumdar, T.M. Link, J. Millard, J.C. Lin, P. Augat, D.Newitt, N. Lane and H.K. Genant, In vivo assessment of trabecular bone structure using fractal analysis of distal radius radiographs. Med Phys., Vol. 27 (2000) 2594-2599.

[6] A. Cichański, A. Mazurkiewicz, K. Nowicki, T. Topoliński, Selected indicators of bone architecture and its behaviour under loading, (Bone – paper in editorial process).

Test System Development for Characterizing of Timing Belts

S. Meister[1], S. Hölbfer[2], I. Gódor[2] and Z. Major[3],

(1) Polymer Competence Center Leoben GmbH, A-8700 Leoben, Austia

(2) Chair of Mechanical Engineering, University of Leoben, A-8700 Leoben, Austria

(3) Institute for Polymer Product Engineering, University of Linz, A-4040 Linz, Austria

Corresponding author: zoltan.major@jku.at

Timing belts are frequently applied as torque transmission devices in various engineering applications (i.e., automotive and agricultural machines) and are exposed to a very complex combination of short-term dynamic and long-term static loads. These loads leads to time dependent local and global deformations of the parts of the timing belts and may results in various failure behaviour. Hence, it is of prime practical interest to characterize the deformation and failure behaviour of timing belts under service relevant loading conditions both on laboratory specimen level and on component level.

The objective of this study was to develop and implement a modular test set-up and methodology for characterizing timing belts. The set-up consists of the three parts; (1) The global deformation behaviour of the timing belt was characterized using a gripping device mounted on a servohydraulic test system, (2) The local deformation behaviour of the teeth was characterized applying another device and using non-contact full-field strain analysis device and (3) for the belt tests a novel component test system was developed.

The device designed and manufactured is shown in Fig. 1. A test specimen was cut form a belt, gripped in the device and subsequently loaded by the testing machine. Both simple monotonic and cyclic loading as well as complex loading can be applied at room temperature and at elevated temperatures.
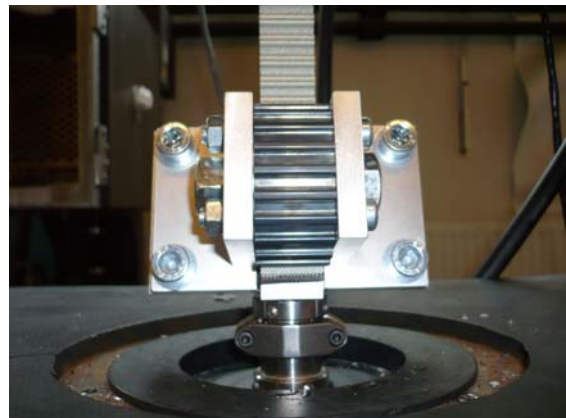
Fig. 1: The device designed fort the belt deformation test.

To characterize the deformation behaviour of timing belt tooth during the contact with a steel counterpart a novel testing device was developed and implemented on a servohydraulic testing machine and the set-up is shown Fig 2.

Fig. 2: Test set-up for the belt tooth tests.

The belt was preloaded in the test equipment and the belt tooth was loaded by the movement of a steel counterpart pulley**.** The local strains in the contact area and in the entire tooth were measured by digital image correlation technique. The development of the major strain during the loading stages is shown in Fig. 3 for a specific belt type and tooth profile. The highly

loaded local area (above 30 % local strain) is clearly recognized in the images above the curve.
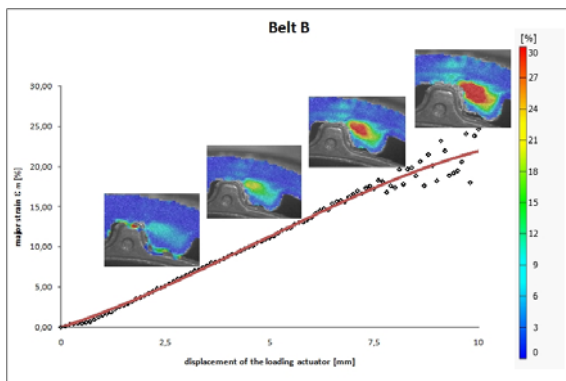
Fig. 3: Major strain vs. displacement curves along with the corresponding deformation images for a belt.

While above tests were carried out on laboratory tests specimen level a further test system for real component tests was also developed. In opposite to the laboratory tests this system is not manufactured yet but it could be easily realized in a short time. The overall view of the belt test system is shown in Fig. 4.

Fig. 4: The view of the belt test system

(P_M=8,3 kW; n_M=10.000/min; F_V= 8 kN)

The loading unit of this test system is shown in Fig. 5. The length of the belt tested and the pre-load can precisely be defined and adjusted using this device.
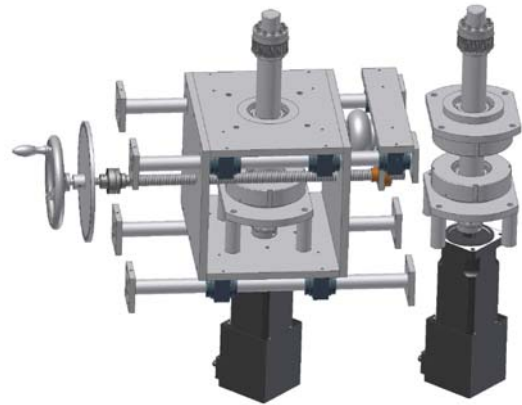
Fig. 5: The loading unit

The loading unit could be combined with a novel non-contact torque measurement system and this integration is shown in Fig. 6. High temperature tests could be performed using the NCTE device.

Fig. 6: The loading unit with the NCTE (Non-Contact- Torque- Engineering) device integrated.

1. Acknowledgments

CREEP COMPLIANCE OF A TIME-DEPENDENT MATERIAL DERIVED FROM INSTRUMENTED MICROINDENTATION

Minster, J. [1), Blahova, O. [2), Lukes, J. [3), Nemecek, J. [3),

1)   Institute of Theoretical and Applied Mechanics AS CR, Prosecka 76, 19000 Prague, Czech Republic

2)   University of West Bohemia Plzen, Czech Republic

3)   CTU in Prague, Faculty of Civil Engineering, Czech Republic

Corresponding author: minster@itam.cas.cz

1. Introduction

The application of instrumented microindentation quasi-static tests enables us to receive quantitative data on Young´s modulus, conventional microhardness, contact depth, stiffness and area during loading-unloading, and also histories of rheological functions such as creep compliance $D(t)$ and its complement relaxation modulus $E(t)$. In response to rheological problems, the solution of the load-displacement relation of a rigid, axisymmetric indenter pressed into a homogeneous, linearly elastic and isotropic half space is taken as fundamental, with its upgrade to a linearly viscoelastic half space [1].

This paper compares the short-term histories of viscoelastic compliance derived for two conditions of a common viscoelastic material (aged and rejuvenated), with the application of three different types of monotonic loading during microindentation. The goal of the study is to assess the potential of this approach.

2. Tested material and test conditions

The tested material was a quasi-homogeneous and quasi-isotropic Comflor 122 epoxy resin mix used for surfacing a range of building substrates, and blended with fillers also used for producing trowelled polymer mortars or polymer concrete mixes. To remove any residual stress, some of tested specimens were annealed at a temperature of 95ºC for 4 hours and cooled slowly to room, i.e. test temperature. The samples are referred to as rejuvenated (R) or (REJ). To assess the effect of ageing, the physical ageing time - five years storage in a black box under laboratory conditions - was identical for each series of measurements. The tests were performed on parts of the same sample in laboratory conditions, with constant relative humidity and temperature control. Two nano/microindenters, each equipped with a Berkovich indenter, were used at two different laboratories - Hysitron Triboscan at CTU in Prague and the Nano XP Indenter at UWB in Plzen.

3. Viscoelastic compliance

The analogy of Sneddon's relation between applied indentation load P and penetration depth h for a linearly viscoelastic material has the form [1]   (1)

$$h^2(t) = \frac{\pi(1-v^2)\tan\alpha}{2} \int_0^t D(t-\tau)\left(\frac{dP(\tau)}{d\tau}\right)d\tau$$

where $D(t)$ is the creep compliance, v is Poisson's ratio, and α the effective face angle of the used indenter. Poisson's ratio can be assumed to be constant for short-time loading histories, so the creep compliance $D(t)$ for the most frequently applied monotonic load history - a step load $P(t)=P_oH(t)$ ($H(t)$ is the Heaviside unit step function) - can be directly deduced from (1)

$$D(t) = \frac{2h^2(t)}{\pi(1-v^2)P_0\tan\alpha} \qquad (2)$$

An ideal step load history cannot ordinarily be generated in laboratory tests. Instead, ramp loading is used with a short rise time t_0 and a constant load thereafter. Due to these conditions, we reject from the analysis a certain time interval after the constant load is reached. This period of time is in general chosen as five to ten times the rise time t_0. To minimize the loss of data, the creep compliance at the beginning of the test can be defined using the indentation under a constant load rate $P(t)=\dot{P}_0H(t)$, which leads to

$$D(t) = \frac{4h(t)}{\pi(1-v^2)\dot{P}_0 \tan\alpha}\left(\frac{dh}{dP}(t)\right) \quad (3)$$

or using the indentation under a constant rate of penetration $h(t)=v_0 t$, with the relation to $D(t)$ in the form

$$D(t) \leq \frac{4v_0^2}{\pi(1-v^2)\tan\alpha}\left(\frac{d^2P}{dt^2}\right)^{-1} \quad (4)$$
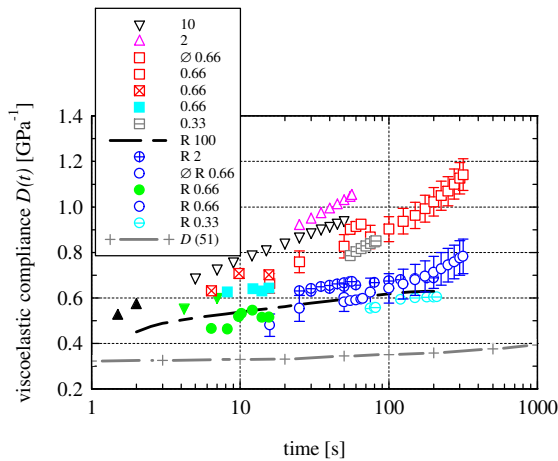
Fig. 1: Comparison of short-term histories of viscoelastic creep compliance measured by a standard macro test ($D(51)$) with data derived from instrumented indentation tests
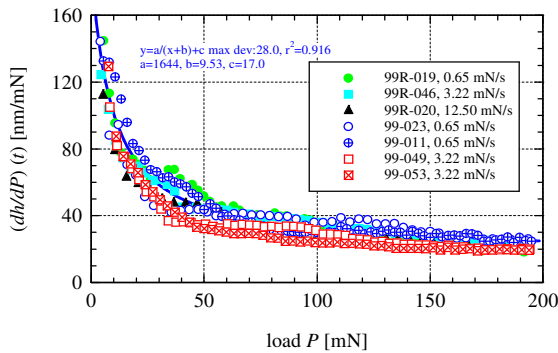
Fig. 2: Comparison of average values of $dh/dP(t)$ versus P for rejuvenated material (full marks) and aged material, for three different rates of loading

Fig.1 shows the results of application of the three monotonic loadings. Five different loading rates ($0.33 \leq dP/dt$ [mN/s] ≤ 100) were used. All marks represent average values of $D(t)$. For reasons of clarity, only some of them are supplemented with characteristic error bars. Circular marks indicate the rejuvenated material with less dispersion of data and lower compliances. The full circular and square marks are derived using Eq. (3), and the full triangular marks at the very beginning correspond with Eq. (4) for v_0= 340 nm/s and v_0=1690 nm/s. Fig.2 proves that there is no difference among

the *dh/dP* values for various loading rates and materials. What differs is the history of indentation depth *h(t)* in the individual tests. Fig.3 presents an example of a risk connected with the application of Eq. (4) with a second derivation in the analysis.
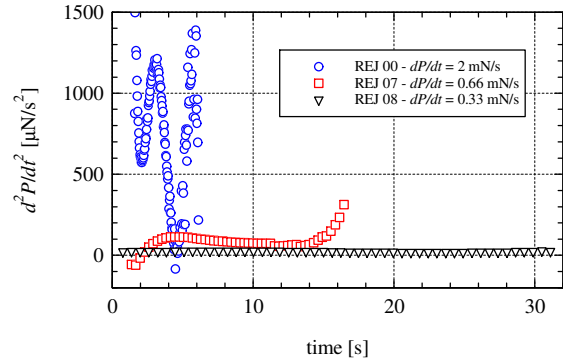
Fig. 3: Comparison of d^2P/dt^2 of rejuvenated material defined for three different rates of penetration

4. Conclusions

Except for a certain dispersion of data, the values of the creep compliance derived under the different test conditions correlate well. Prudent application of the three monotonic loadings extends the time interval for receiving reasonable data to shorter times and enables us to make a qualitative assessment of the creep compliance history. However, for common time dependent quasi-homogeneous and quasi-isotropic material the derived data is at least twice as high as the standard macro values.

5. Acknowledgements

6. Reference

[1] Knauss, W.G., Emri, I., Lu, H., Mechanics of Polymers: Viscoelasticity. Springer Handbook of Experimental Solid Mechanics, Ed. W.N. Sharpe, Springer, Chapter 3, (2008) 49-96

STRENGTH EVALUATION OF THE BEHAVIOUR OF CERAMIC TILES UNDER STATIC LOADING

Matei Constantin Miron [1], Dragos Alexandru Apostol [1],
Dan Mihai Constantinescu [1], Marin Sandu [1], Eniko Volceanov [2]

[1]   University POLITEHNICA of Bucharest, Department of Strength of Materials,
Splaiul Independentei nr. 313, 060042 Bucharest, Romania.

[2]   Institure for Metallurgical Researches, str. Mehadia nr. 39, 060543 Bucharest, Romania.

Corresponding author: dan.constantinescu@upb.ro

1. Introduction

In general, the strength of ceramics may be comparable to most of the construction steels, accompanied by a brittle behaviour and high capacity of absorbing impact energy which gives a huge potential for specific applications. Unfortunately, flaws and other defects usually appear during the manufacturing process, and influence the quality of the product. A probabilistic approach in the reliability evaluation based on the Weibull distribution has been accepted in ceramic design [1].

Static and low velocity impact tests have been performed experimentally, followed by numerical simulation [2]. Up to reaching the sophisticated level of the modelling and simulation of impact at high velocities, one needs to account for a clear description of the static mechanical behaviour of the ceramic alumina tiles. The chemical composition (grain size, processing, material form, added material components) of alumina ceramics plays an important role and looks to influence their behaviour, strength response, displacement and strain fields. The digital image correlation method proves to be very effective in analyzing the response and failure of ceramics and is used in obtaining the results presented in this paper.

2. Static Testing Procedure

Testing in three-point bending is done by using a 6.3 tf Walter-Bai servo-hydraulic machine with a speed of loading of 0.1 mm/min. Force is applied by a cylinder of 10 mm diameter, and the tile is supported on the same steel cylinders each 5 mm appart from the edge of the tile. Ceramic tiles of different grades have sizes of about 50 x 50 mm or 40 x 40 mm. The force analogue signal from the testing machine feeds the experimental set-up.

Each tile is loaded till failure. One needs to account for standard recommendations, but the testing of tiles with the mentioned dimensions was preferred as to obtain more reliable results by having in mind the future impact testing at low and high velocity.

The testing procedure uses the digital image correlation method and the ARAMIS system [3] as a main experimental setup. The digital image correlation method offers a precise optical solution for deformation measurements. ARAMIS is a non-contact optical deformation measuring system which analyzes, calculates and documents material deformations, being particularly suitable for three-dimensional deformation measurements under static and dynamic loading in order to analyze deformations and strains of real components. If the measuring object has only a few object characteristics, like it is the case with homogeneous surfaces, one needs to prepare such surfaces by applying a stochastic spray pattern. The experimental set-up is shown in Fig. 1, with the force applied from the top.

Fig. 1: Experimental testing of ceramic tiles in three-point bending.

We have to underline that some geometry imperfections were probably the cause for some

of the unforeseen events which took place during our tests. Although the supports can rotate in a plane parallel to the line of loading, the top and bottom faces were not always planar; this made possible a non-uniform contact along the support lines and the line of loading and led to unreasonable failures. Such test results were disregarded. In fact some characteristics of a cleavage fracture are noticed and these are going to be discussed later.

An initial calibration before loading is needed in order to define a zero position; for this type of experiment a caliber of 35x28 mm is used. The chosen facet size is 26x26 with a facet step of 13x13, and thus results a facet field of 87x17 facets. As the deformations are very small the averaging has size 5 and 4 runs are considered.

A second type of tests consideres the application of the force directly through a steel bullet in the middle of the ceramic tile. A specially designed device allows the transmision of the force from vertical to horizontal direction. The opposite face to the one on which the bullet acts can be viewed directly by the cameras of the ARAMIS system. In this way one can notice better what happens on most of the surface of the tile; the tile is supported on its edges for about 3-4 mm along the perimeter. In Fig.2 can be observed a lateral view of the device fixed in the lower hydraulic grip of the testing machine and a front view of the tile with the two cameras of the ARAMIS system prepared for acquiring data during testing.
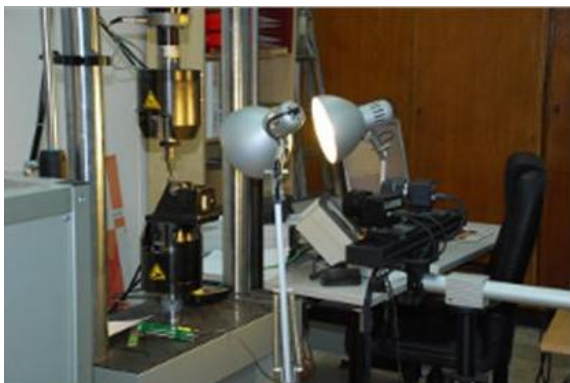
Fig. 2: Device used for the experimental testing of ceramic tiles by applying the force through a bullet.

3. Obtained Results

When applying the force through a bullet, with the ceramic tile in vertical position (fixed in the device – Fig. 2) and viewing the tile on the back surface we can analyze the displacements fields on the three directions and the major, minor or equivalent (Mises) strain fields. As an example, for the specimen denoted CM 15-1 (zirconia toughened alumina mixed with calcium-magnesium), we show just before failure at a force of 11470 N the Mises strain field and the out of plane displacement field (Fig. 3); the strain field is localized quite in the middle of the specimen with a maximum value of about 0.22 %, but the displacement field show some noise and that the tile rests in fact more on two diagonal corners due to a non-flat surface – with a maximum value of about $17 \cdot 10^{-3}$ mm (for such small values the observed noise is expected).
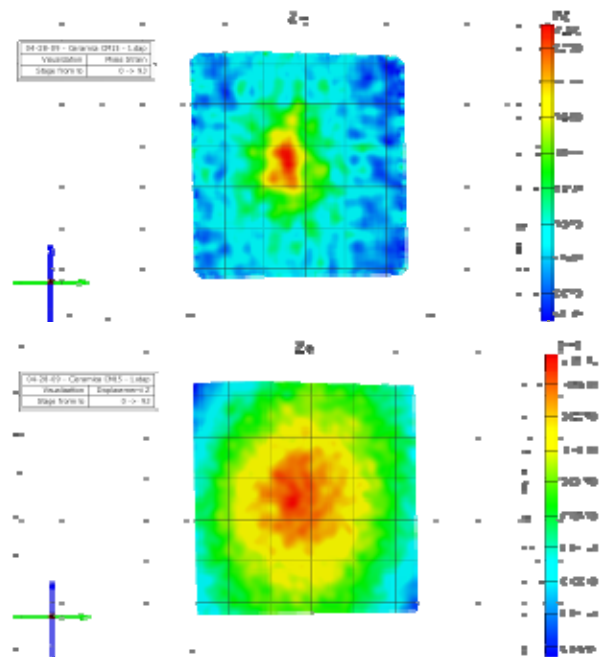
Fig. 3: Mises strains and displacements at failure for a CM 15-1 ceramic tile

4. Acknowledgements

5. References

[1] F. Aldinger, J.F. Baumard, *Materials: Science and Engineering*, Max-Planck Institut für Metallforschung, Stuttgart, (2003) 26-27

[2] D.M. Constantinescu, M. Sandu, E. Volceanov, M. Gavan, St. Sorohan, Experimental and numerical analysis of the behaviour of ceramic tiles under impact. Key Engineering Materials, Vol. 399 (2009) 161-168.

[3] Information on http://www.gom.com

VIBRATION ANALYSIS WITH HIGH SPEED CORRELATION

Eberhard Moser [1],

[1] Dantec Dynamics GmbH, Kaessbohrerstr. 18, 89077 Ulm, Germany.

Eberhard.Moser@dantecdynamics.com

1. Abstract

Digital image correlation techniques have already been successfully proven for accurate displacement analysis. With the use of two cameras, three dimensional measurements of contours and displacements can be carried out. The principle of this technique is pretty easy to understood and realized, opening a nearly unlimited range of applications.

Rapid new developments in the field of digital imaging and computer technology, especially for very much dynamic applications, opens further applications for these measurement method up to high speed deformation and strain analysis, e.g. in the fields of, material testing, fracture mechanics, high speed testing, advanced materials and component testing. The dynamic range is combined with the capability to measure very large strains (up to more than 100%). The absolute resolution depends on the field of view and is scalable. Calibration of the optical setup is a crucial point which will be discussed in detail.

Examples of the analysis of high speed harmonic and transient events out of material research and industrial applications are presented.

1.1 Shock Excitation fig. 1
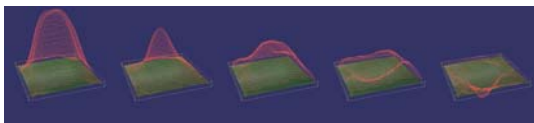
Fig. 1:Full field displacement (scaled by a factor of 300) of the plate

fig. 2
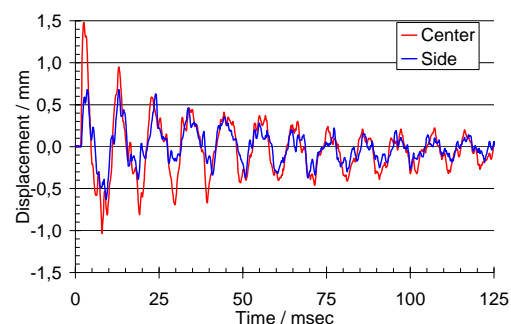
fig. 3
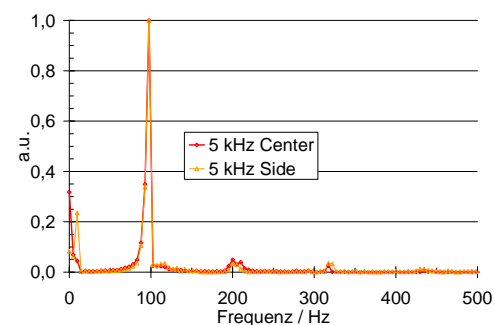
Out-of plane displacement of two points up to 125 msec after firing the explosive charge (**Fig. 2**) and the spectrum (**Fig. 3**)

1.2 Excitation of a Membrane fig. 4

Fig. 4 Experimental setup with High Speed cameras, calibration target, loudspeaker and frequency generator for vibration measurements.

fig. 5
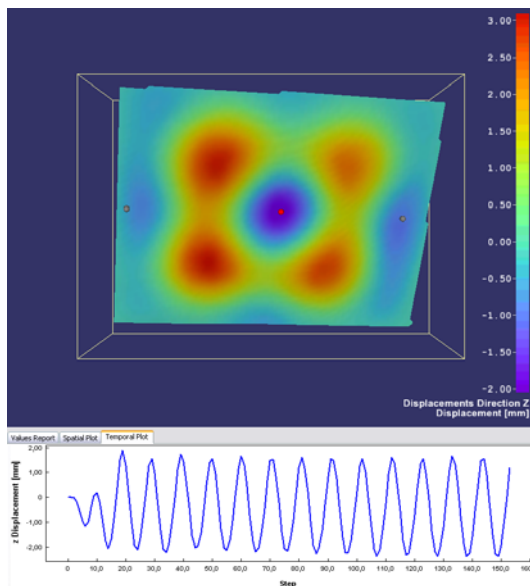
Fig. 5 Full field out- of plane deformation of the membrane at minimum deflection in the center (top) and temporal plot of the displacement of the center point (bottom).

2. References

[1] Sutton M.A., McNeil S.R., Helm J.D., Chao Y.J, "Advances in 2-D and 3-D computer vision for shape and deformation measurements", in Photomechanics, P.K. Rastogi, Ed. Topics in Applied Physics, 77, 323-372, Springer Verlag, New York (2000).

[2] Mguil-Touchal S., Morestin F., Brunet M., "Various Experimental Applications of Digital Image Correlation Method", CMEM 97, Rhodes, May, 45-58

[3] Winter D., "Optische Verschiebungs-messungen nach dem Objektrasterprinzip mit Hilfe eines flächenorientierten Ansatzes", Dissertation in der Fakultät Maschinenbau und Elektronik an der Universität Braunschweig, 1993

[4] Tsai R.Y., "An efficient and accurate camera calibration technique for 3-D machine vision", Proc. IEEE Intl. Conf. Comp. Vision and Patt. Recog., 364-374 (1986)

[5] Neumann, I., „Schwingungsmessungen in der Umweltsimulation mit einem Bildkorrelationsmesssystem", Diploma Thesis, Hochschule Ravensburg-Weingarten, Germany, 2006.

NON-LINEARITY OF FLEXION-EXTENSION CHARACTERISTICS IN LUMBAR SEGMENTS

Nägerl Hans [1]**, Hawallek Theolonius**[1]**, Mansour Michael**[1]**, Hubert Jan**[1]**, Kubein-Meesenburg Dietmar**[1]**, Fanghänel Jochen**[3]**, Martin Wachowski**[2]

University of Göttingen, [1]Dept. of Orthodontics, [2]Dept. of Trauma Surgery, Plastic and Reconstructive Surgery, D-37075 Göttingen Germany, [3]University of Greifswald, Dept. of Oralanatomy.

Corresponding author: hnaeger1@gwdg.de

1. Introduction

Rotational angle-torque characteristics of human lumbar segments generally show distinctive nonlinearity. In flexion/extension of L3/L4- and L4/L5-segments the characteristics looks like "diode characteristics" in electronics. In extension the differential stiffness of the segments is increasing rapidly. This eye-catching *asymmetric* nonlinearity is most likely not caused by the material of the intervertebral disc but by the guidance of the vertebral joints (VJ) whose articulating surfaces are compressed in extension. Segments with removed VJs therefore show *symmetric* S-shaped characteristics when the nonlinearity of the disc material becomes more important.

Linear characteristics following Hook's law should be kinematically accompanied by a stationary instantaneous rotational (helical) axis (IHA). In flexion/extension, when the IHA is migrating parallel to the plates of the disc, the IHA should alter the instantaneous flexional stiffness D according to the Theorem of Steiner:

$$D = D(a) = D_{min} + a^2 \cdot D_N \qquad (1)$$

$D(a)$ = actual, D_{min} = minimal flexional stiffness, D_N = normal stiffness of the intervertebral disc. a = distance between IHA-position in minimal stiffness (D_{min}) and in actual stiffness $D(a)$.

Goal of this investigation presented was to substantiate that the nonlinearity of the characteristics in flexion/extension was actually caused by the IHA migration.

2. Material and method

Analyzed human segments: 2 L_3/L_4, 3 L_4/L_5 segments without pathological signs. Their spatial motions were measured following force systems consisting of laterally directed torque $T_y(t)$ following triangular time functions (periodic time ≥1min) and static axial preloads F_z with precisely adjusted force lines (±0.5mm) which served as parameter. The spatial resolution of position of the moved co-ordinate system was 0.5µm for the translation of its origin and 0.5mdeg for flexion/extension. Thus, IHA-position could a. be determined as function of the flexional angle α in close approximation since small rotational angle intervals (Δα ≤ ROM/400) were used for calculating the IHA-position, b. be related to the varying differential stiffness of the flexional angle-torque characteristics, and c. also to anatomical structures. See also: [1], [2].

3. Results
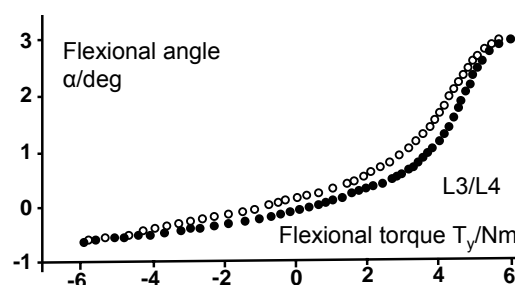
Fig. 1: Characteristic of segment L3/L4A corresponding to IHA-migration in Fig. 2. The minimum differential stiffness is close to 2°-flexion.
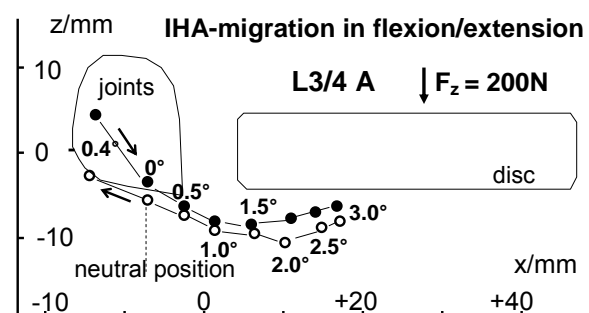
Fig. 2: Traces of radiograph of L3/L4A segment transformed onto the z-x plane and intersections of

IHA in flexion/extension. Parameter: Angle of flexion. ●●●/○○○: Wide IHA-centrodes over more than 30 mm in flexing/extending motion.
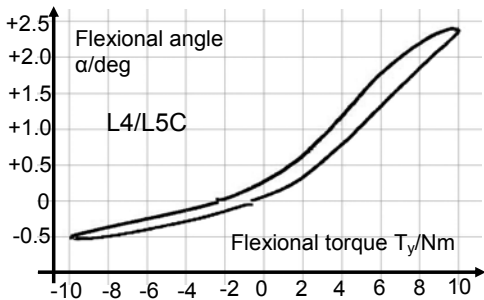
Fig. 3: Characteristic of segment L4/L5C corresponding to IHA-migration in Fig. 4.
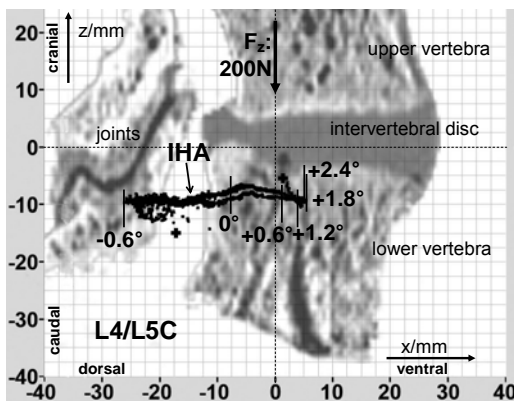
Fig. 4: Radiograph of L4/L5C segment transformed onto the z-x plane and intersections of IHA in flexion/extension. Parameter: Angle of flexion. Preload F_z = 200N. Wide IHA-centrode over more than 30 mm parallel to the intervertebral disc in flexing/extending motion.

The characteristics of all five lumbar segments showed distinct non-linearity. In extension the segments the differential stiffness $dTy/d\alpha = D(\alpha)$ increased rapidly. Accordingly, the IHA migrated to the dorsal. We related segment stiffness $D(\alpha)$ to IHA position via the Theorem of Steiner (figs. 5,6).
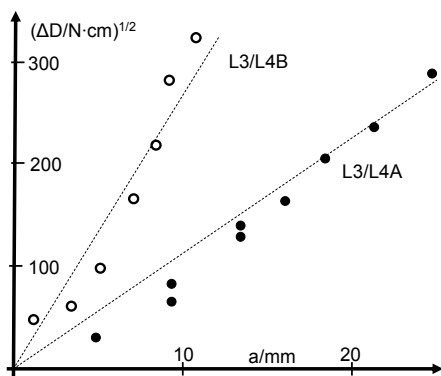
Fig. 5: Segments L3/L4: Steiner analysis of the characteristics. The relation between actual stiffness

D(a) and IHA-position a followed the Steiner Theorem. $\Delta D = D(a) - D_{min}$.
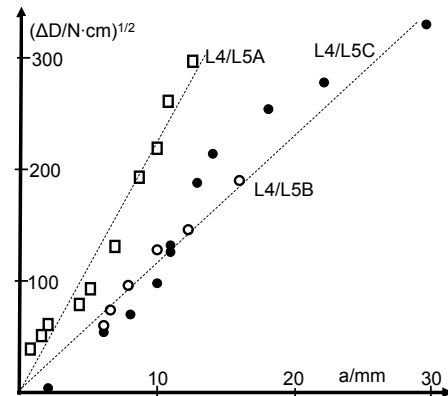
Fig. 6: The non-linearity of the three L4/L5 segments was also produced by the IHA-migration to the dorsal.

4. Discussion

Non-linearity of segment characteristics can be caused by non-linearity of the soft tissues, by swiveling of the IHA, by varying screw pitch of the IHA and/or by IHA-migration. Since a. the unit vector of the IHA-line remained parallel to varying torque T_y, b. the screw pitch of the IHA was small, and c. a considerable non-linearity of the material could be excluded by analogous measurements after removing the joints. Only the considerable migration of the IHA could be related to the non-linearity of the characteristics. The IHA-position is mainly determined by the actual contacts of the articulating surfaces in the joints. The IHA-migration is therefore an artifact of the guidance of the joints.

Our results revealed a general functioning principle in joint mechanics in the human body: By shifting of the IHA via the guidance of diarthroses, the stiffness of synarthroses like intervertebral disc is parametrically controlled.

5. References

[1] Nägerl. H., M. Mansour., Ch. Lee, Kubein-Meesenburg D., J. Fanghänel: Mechanical properties of lumbar and thoracal motion segments. DAS 2003 Györ.

[2] Nägerl H., M. Mansour, Th. Hawallek, D. Kubein-Meesenburg, J. Hubert, M.M. Wachowski: Parametric control of the stiffness of lumbar segments. DAS 2008 Budweis.

EXPERIMENTAL INVESTIGATION OF MODIFIED ROAD BARRIERS WITH FOAMED ALUMINIUM PANELS

Tadeusz Niezgoda, Andrzej Kiczko, Wiesław Barnat, Paweł Dziewulski, and Jacek Nowak

Military University of Technology, Department of Mechanics and Applied Computer Science
2 Kaliskiego Street, 00-908 Warsaw, Poland.

Corresponding author: andrzej.kiczko@wat.edu.pl

1. Introduction

The Department of Mechanics & Applied Computer Science of the Military University of Technology carries out the most advanced experimental investigations and numerical simulations connected with percussive influences on constructions, putting the special emphasis on protective structures which are to ensure safety of people and devices [1-3]. The correlation between an experiment and a numerical simulation is the essential factor which influences the correctness and efficiency of computations.

The aim of the carried out investigations is the choice of the construction which is to be tested in the experimental collision and the validation of the numerical model of the road barrier, modified by the implementation of energy absorbing panels.

The agreement on access to VII Outline Programme on "SST-2007-4.1.6: Intelligent Road Restraint System (RRS)" was declared by the Department of Mechanics & Applied Computer Science of the Military University of Technology.

2. Experiment

The element of the W-Beam protective barrier, complemented with the energy absorbing panel from steel sheet with the thickness of 0.5 mm, joined with rivets, filled in with ALPORAS foamed aluminum plate of 5 x 24 cm and 2 m length, was the subject of investigation (fig. 1). The tests were carried out on the machine for static tests (INSTRON KN1200) completing three-point bending (figs 2, 3). The loading force was transferred through the half-cylinder of 273 mm diameter.

The numerical analysis was performed with the LS Dyna software.
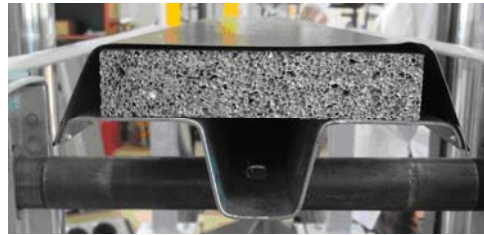
Fig. 1: W beam with riveted energy absorbing panel, filled in with foamed aluminum
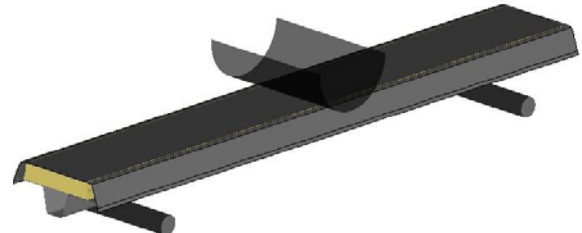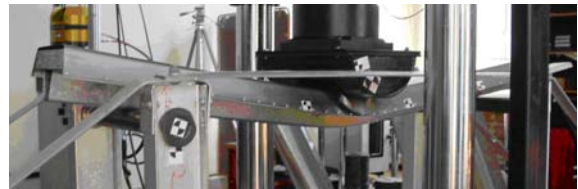
Fig. 2: Bending at the approach angle of 90°, experimental stand and numerical methods

Fig. 3: Bending at the approach angle of 20°, test and numerical simulation

3. Experimental Results

The determination of Displacement-Load curves for the both variants of bending is the result of the experiment. In figs 4 and 5 bending at the approach angle of 90° is presented. In fig. 4 the function of W-beam bending with the protective panel (two upper functions) is compared with the function of bending without panel (the down function). In fig. 5 the comparison between experimental results and FEM calculations for W-beam with the protective panel with foamed aluminum plate is presented.
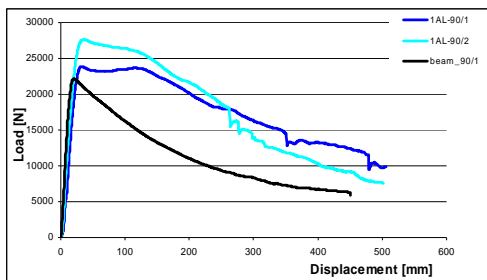
Fig. 4: Diagram of Displacement-Load received in two subsequent tests for W-beam with and without the panel
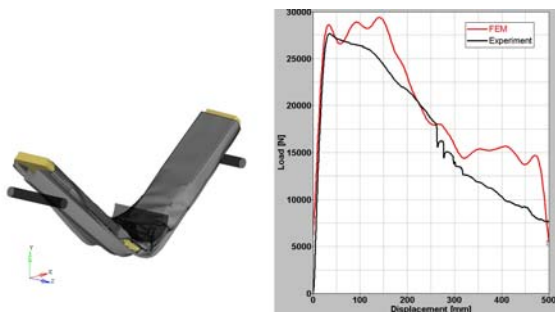
Fig. 5. Comparison between experimental results and results of numerical simulation

In figs 6 and 7 the analogical functions for bending at the approach angle of 20° are shown.
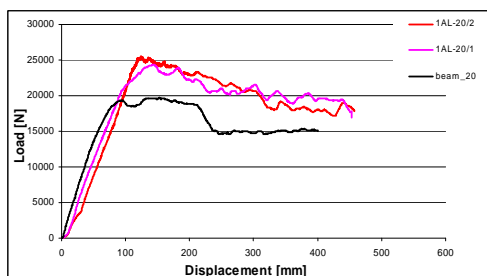
Fig. 6: Function of Displacement-Load Load received in two subsequent tests for W-beam with and without the panel
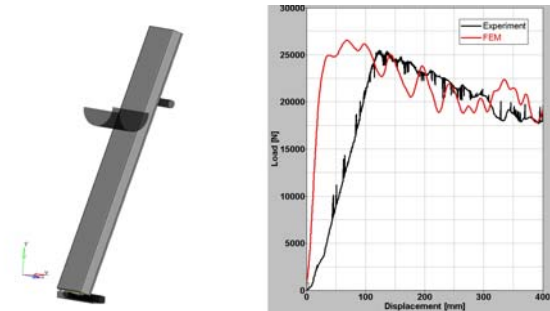
Fig. 7: Comparison between experimental results and results of numerical simulation

The good compatibility of results for experiment and numerical simulation was received during bending at the approach angle of 90°. At the approach angle of 20° appeared the curiosity - too big initial rigidness of the numerical model. One of the reasons of it may be neglecting the susceptibility of supports and the head susceptibility of the KN1200 machine working in unusual conditions. The maximal horizontal displacement of the upper support, measured during the test, was equal to 8 mm, whereas the maximal horizontal displacement of the head was equal to 4 mm.

4. Acknowledgements

5. References

[1] T. Niezgoda and W. Barnat, Analysis of protective structures made of various composite materials subjected to impact. Materials Science & Engineering A, Vol. 483-484 (2008) 705-707.

[2] J. Włodarczyk, T. Niezgoda, W. Barnat, and P. Dziewulski, Validation of numerical models of metallic foams from the aspect of energy absorption. Journal of KONES Powertrain and Transport, Vol. 14 (2007) 561-570.

[3] T. Niezgoda, A. Kiczko, A. Barnat, and P. Dziewulski, Experimental verification of road barriers on their abilities to absorb energy. 25th Danubia-Adria Symposium on Developments in Experimental Mechanics (2008) 187-186.

ENERGY ABSORPTION INVESTIGATION OF FILLING TUBES

Tadeusz Niezgoda, Wiesław Barnat, Stanisław Ochelski

Military University of Technology, Department of Mechanics and Applied Computer Science
2 Kaliskiego Street, 00-908 Warsaw, Poland.

Corresponding author: tadeusz.niezgoda@wat.edu.pl

1. Introduction

The particular elements of energy-absorbing structures should be made from thin-walled elements, because they are to destroy themselves with comparatively small strength in order not to overload the construction. The thin-walled elements are subjected to buckling and violent destruction. The light porous materials are located among the plates or they are formed in the shape of the tube, wavy plates and cross section-shaped elements in order to protect the thin plates (compressed in the plane of the plate) from buckling, [1,2].

The objects of the research were the samples made of epoxy composites (E-53) reinforced with glass fibres formed in roving (STR-012-350-110) with weight $350 g/m^2$, roving stripes (ES-10-400-0-60) and glass mat with the weight 316 g/m^2 .

The investigation on the capability of hitting energy absorption of the sample in the shape of tubes (with internal diameter $D_i = 49,3$ mm) with bevelling angle 45° (on one edge), which play the role of the initiator of progressive destruction process, was carried out.

On the basis of the results, obtained from our own experimental investigations of energy-absorbing elements, the influence of the kind of the matrix, and the kind of reinforcement (the fibres), structure of the polymer composite, the shape and the thickness, foams of filling of tubes on the specific energy absorption (SEA) was determined.

2. Experimental Results

The samples in the shape of Glass/Epoxy (G/E) tubes with the internal diameter ø40mm and ø20mm, and the length 50mm were considered during the investigation. In order to examine the influence of the thickness on the destructive mechanism and the SEA value, the following thicknesses of the tubes walls were

taken into account: 1.0; 1.5; 2.0; 2.5; 3.0, and 4.0 mm, described in the work [3]. Two materials were used to fill in the tubes: foamed polyvinyl chloride (PCW) (PCHW-1-115) and foamed aluminium (ALPORAS) containing: ~97% Al, ~1,5% Ca, ~1,5% Ti.
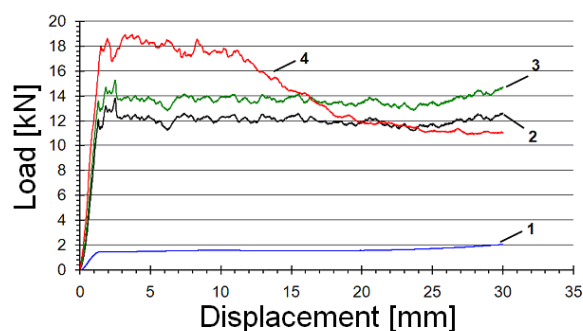
Fig. 1: Relation $P_{destr} - \Delta l$ of G/E sample with the diameter ø40mm and the wall thickness 1,0mm: 1) foamed PCW, 2) G/E sample without filling, 3) the algebraic sum of the ordinates from graphs 1 and 2, 4) G/E sample foamed PCW
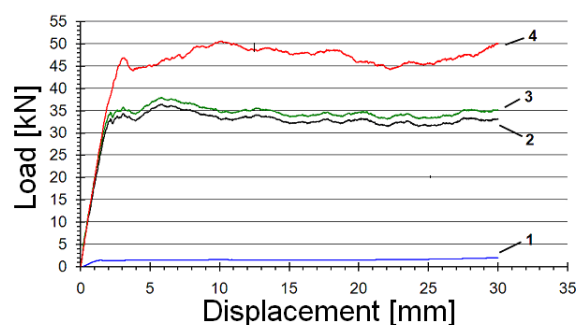
Fig. 2: Relation $P_{destr} - \Delta l$ of G/E sample with the diameter ø40mm and the wall thickness 3,0mm: 1) foamed PCW, 2) G/E sample without filling, 3) the algebraic sum of the ordinates from graphs 1 and 2, 4) G/E sample foamed PCW

On the basis of the experimental results we can conclude two mechanisms of the samples destruction. The first occurs at a small wall thickness (the thickness equal or smaller than 1mm), the second occurs at t>2mm. During the compressing of the tubes filled with foamed materials their upsetting occurs, producing the pressure on the inner surface of the tubes. It results in arising of circumferential stress on the

surface of the external tube. They have greater influence on the tube destruction than stresses caused by the compressing force and they contribute to the early samples destruction. It is confirmed by the falls of destruction force in the relation $P_{destr} - \Delta l$ shown in fig. 1, however there is no fall of the force in the case of the tube of 1mm thickness without filling. For the tube wall thickness larger then 2mm, the tubes filling causes the significant SEA growth, which is greater then SEA sum of the foamed material and the tube without filling. This effect can be seen in fig. 2.

a)

b)

c)
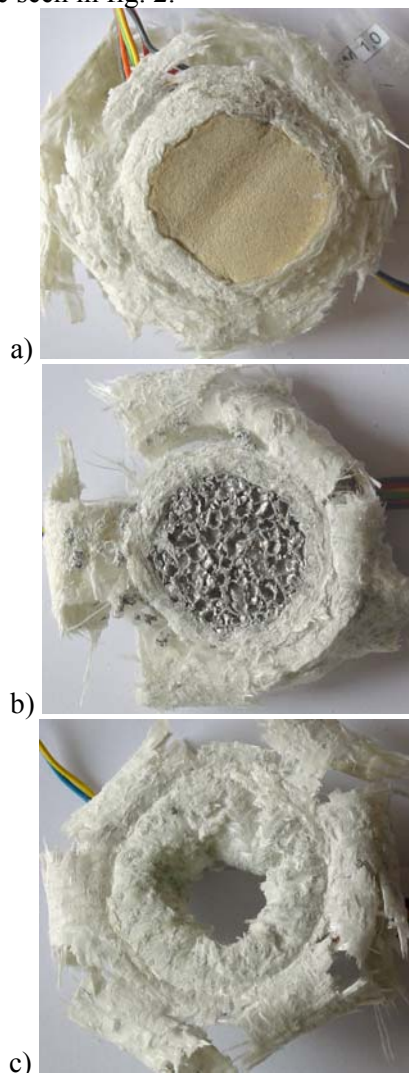
Fig. 3: The pictures of destroyed G/E samples with the wall thickness 1,0mm: a) filled with foamed PCW, b) filled with foamed Al, c) without filling

The filling of the tubes made from G/E composite causes greater SEA increase than in the case of those made from C/E (carbon/epoxy) composite, which is caused by greater destructive deformations of glass fibre reinforced epoxy composites [4].

In the energy absorbing investigations the filling of the tubes with the foamed materials increases SEA when the wall thickness is larger than approximately 1mm. In such case the additional tube loading produced by the pressure of the foamed material is absorbed by the enlarged tube section. However, the tubes with the thickness smaller than 1mm, destroy themselves by the additional circumferential stresses. The mechanism of the wall destruction influences the filled tubes caused SEA increase. During the destruction the wall is curved onto the external edge of the tube. However, in the case of the tube without filling a part of the wall thickness is curved outside –fig. 3

The foamed material, used as filling of the sample, increases absorption energy, however because of the higher element mass it decreases SEA.

3. Acknowledgements

4. References

[1] P.H. Thornton, J.J. Harwood, P. Beardmore, Fiber - reinforced plastic composites for energy absorption purposes. Composite Science and Technology, Vol. 24 (1985) 275-298.

[2] G.L. Farley, R.M. Jones, Prediction of the energy absorption capability of composite tubes. Journal of Composite Materials, Vol. 26 (1992) 388-404.

[3] W. Barnat, P. Bogusz, S. Ochelski, Influence of tubes filling hitting energy absorption. Bull. WAT (in printing)

[4] S. Ochelski, P. Gotowicki - Experimental assessment of energy absorption capability of carbon - epoxy and glass - epoxy composites. Composite Structures, Vol. 87 (2008) 215-224.

INVESTIGATIONS OF 3D STRUCTURAL AND MECHANICAL PROPERTIES OF HUMAN TRBECULAR FERMUR BONE

Anna NIKODEM[1], Romuald BĘDZIŃSKI[1], Szymon DRAGAN[2]

[1]Division of Biomedical Engineering and Experimental Mechanics, Wrocław University of Technology, Poland
ul.Łukasiewicza 7, 50-371 Wrocław
[2]Department of Orthopaedics and Traumatology at the Wrocław Medical University, ul.Borowska 213, 50-556 Wrocław, Poland.

Corresponding author: anna.nikodem@pwr.wroc.pl

1. Introduction

Bone is one of the most incredible biological material, which react during lifetime to any changes in loading conditions by modelling and remodelling processes. This functional adaptation of "healthy" bone is dues to equilibrium in resorption/formation/mineralisation processes. This equilibrium is governed by many different factors like hormones, bone morphogenetic proteins BMP-2, BMP-7, calcium homeostasis and others which influence those processes [1]. In case of any imbalance some metabolic diseases may occur. The most frequent indicators for operative treatment are osteoporosis and osteoarthritis. According to WHO's clinical definition osteoporosis is a skeletal disorder characterised by compromised bone strength predisposing a person to an increased risk of fracture. Osteoarthritis is defined as progressive disorder of the joints caused by gradual loss of cartilage and resulting in the development of bony spurs and cysts at the margins of the joint [2]. These two diseases lead to alterations in structure of cancellous bone. These alterations are characterized by changes in bone mass which is the main determinant measured to assess mechanical resistance, however it explains only 30-60% of variability of the characteristic.

For this reason several microarchitectural parameters like: Tb.Th, Tb.Sp or SMI have been developed [3,4]. Using different combinations of those parameters people still try to find and better understand relationships which can give the best strength explanation. Models may help to improve the understanding mechanism of disease-related changes as well as the effects of different treatment on trabecular bone microstructure and mechanical behaviour. Finally, such information could be used to derive the mechanical quality of bone from available structural indices.

2. Materials and Methods

The analysed data set encompasses 89 cubic samples (10x10x10mm) harvested from 23 human femoral heads (12 from patients with osteoarthritis OA, 7 with osteoporosis OP and 4 obtained *postmortem* classified as healthy bone, control group). All samples were scanned using a microcomputed tomography system (μCT-80 Scanco Medical Switzerland®) providing a spatial resolution of 20 μm.
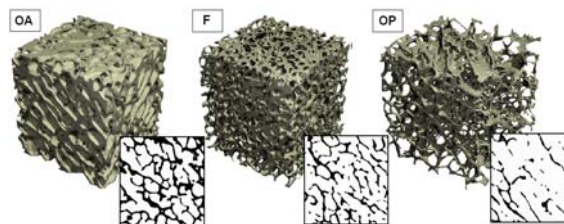
Fig. 1: 3D reconstructions of OA, F and OP samples obtained from μCT-80, Scanco Medical**®**.

Standard 3D algorithms were used to compute volume density BV/TV, bone surface density BS/TV and Tb.Sp, Tb.Th, Tb.N [3]. We also computed SMI, DA (degree of anisotropy), mineral density and Connectivity. To obtain mechanical directional properties (E1, E2, E3) in uniaxial compression test, we used MTS Synergie 100 test machine.

3. Results and Conclusion

The experimental results of 3D structural and directional mechanical properties (table 1, table 2), show significant differences between all three groups (OA,F,OP) of samples.

In comparison to control group (F), osteoporotic samples are characterised by bone loss which is presented by decrease in BV/TV value (by 25%). This bone loss results from reduction in trabecular number, trabecular thickness and also number of trabecular interconnection (ConnD, Tb.N, Tb.Th), especially in horizontal direction.

Furthermore, high decrease in mineral density value, (Mean Density by 45%) confirm problems in bone mineralisation processes. All of mentioned symptoms provides to reduction in elasticity of bone (50%) and growth in anisotropy (DA and DM).

Table 1 Mean 3D-structural properties for OA, F and OP groups, obtained from µCT .

INDEX	OA (n=47)		F (n=15)		OP (n=27)	
	value	±SD	value	±SD	value	±SD
BV/TV [%]	26,71	6,83	25,32	5,67	18,86	5,00
ConnD [1/mm3]	6,49	2,25	5,29	1,38	5,08	2,28
SMI	0,41	0,69	0,25	0,50	1,10	0,43
Tb.N [1/mm]	1,47	0,21	1,42	0,15	1,32	0,18
Tb.Th [mm]	0,20	0,04	0,18	0,02	0,17	0,03
Tb.Sp [mm]	0,64	0,09	0,67	0,08	0,72	0,11
Mean/Density [mgHA/ccm]	209,60	75,31	211,99	73,43	116,72	62,96
DA	1,59	0,20	1,62	0,15	1,71	0,26

BV/TV bone volume density, *Conn.D* connectivity, *SMI* structure model index, *Tb.N* trabecular number, *Tb.Th* trabecular thickness, *Tb.Sp* trabecular separation, *Mean/Density* mineral density, *DA* degree of structural anisotropy.

Table 2 Mean mechanical properties E_1, E_2, E_3 for OA, F and OP groups, obtained in compression test .

INDEX	OA (n=47)		F (n=15)		OP (n=27)	
	value	±SD	value	±SD	value	±SD
E_1 [MPa]	103,15	81,38	147,41	67,66	72,33	68,68
E_2 [MPa]	59,32	47,15	157,36	118,81	45,28	38,71
E_3 [MPa]	85,48	82,63	174,26	131,96	50,32	32,31
DM	1,94	0,52	2,02	0,48	2,19	0,86

DM degree of mechanical anisotropy E_{max}/E_{min}

Table 3 Coefficient of linear regression R between structural indices and Young's modulus E_1 .

Correlation: with E_1	OA (n=47)	F (n=15)	OP (n=27)
BV/TV	0,48	0,75	0,65
MeanDensity	0,55	0,74	0,61
BV/TV*ConnD	0,40	0,78	0,69
MeanDensity*ConnD	0,57	0,68	0,54
DA/DM	0,40	0,32	0,36

Osteoarthritis has several phases: formation of osteophytes or joint space narrowing, appearance of subchondral cysts and bone deterioration in this region (which indicates the erosive phase of disease progression) and bone repair and remodelling. The results of our investigations show, that OA samples with osteoarthritis are characterised by higher BV/TV (5,5%), which caused by more complex and thickened structure (Tb.N, Tb.Th, ConnD). This bone concentration (especially in subchondral region) is relevant to gradual loss of cartilage and change in load bearing

conditions. Despite of higher bone volume, lower value of mechanical properties (30%) were observed. In this case we didn't notice any increase in mineral density proportional to increase in BV/TV value (the average value was even smaller than in control group). According to the obtained data we can suppose, that changes in BV/TV (especially in the second phase) are mainly correlated with deterioration of trabeculae not directly with metabolism of mineral components.

Analysis show that, depending on sample group, different kind of density should be taken into account in order to find the strongest correlation between mechanical and structural properties. For OP and F samples the best correlation was found with BV/TV, for OA with mineral density. Because density can not fully explain bone mechanical properties, we used Multiple Linear Regression Analysis to obtain more accurate correlations number of trabecular intersection (ConnD). We didn't find strong correlation between mechanical and structural anisotropy (DA/DM).However, even in this case we can observe some trends: decrease for OA bone (1,7%) and increase (6%) for OP samples.

4. References

[1] M.Stauber, R.Muller, Age-related changes in trabecular bone microstructures: global and local morphometry. Osteoporos Int, Vol 17 (2006) 616-626.

[2] B.Cornet, X.Marchandise, Bone microstructure and mechanical resistance. Joint Bone Spine Vol.68 (2001) 297-305.

[3] T.Hildebrand, Laib A, Muller R, Dequeker J, Ruegsegger P, Direct three-dimentional morhometric analysis of human cancellous bone: microstructural data from spine, femur, iliac crest, and calcaneus. J Bone Miner Res Vol. 14 (1999), 1167-1174.

[4] RW.Goulet, SA.Goldstein, MJ.Ciarelli, JL.Kuhn, MB.Brown, LA.Feldkamp, The relationship between the structural and orthogonal compressive properties of trabecular bone. J Biomechanics Vol.27 (1994), 375–389.

FRACTURE MORPHOLOGY OF AW-6082 ALLOY AT VARIOUS LOADING CONDITIONS

František Nový, Mária Chalupová, Peter Palček [1)]

[1)] University of Žilina, Faculty of Mechanical Engineering, Department of Materials Engineering, Univerzitná 1, 010 26 Žilina, Slovakia

Corresponding author: frantisek.novy@fstroj.uniza.sk

1. Introduction

Considerable industrial and scientific interest exists on the aluminium alloys of 6xxx series because nearly two-third of all extrusions are made from aluminium alloys, and 90% of these are 6xxx series alloys [1]. The 6xxx aluminium series alloys are very frequently used in mechanical design, mainly due to the fact of allying a relatively high strength, good corrosion resistance and high toughness to a good formability and weldability. For many failure-critical parts of structures, vehicles and machines, impact and fatigue failures in this series of aluminium alloys are not as well understood as for the 7xxx and 2xxx series [2].

This work deals with the study of impact failure resistance at increased temperatures and fatigue resistance at ambient air temperature of AW-6082 alloy.

2. Experimental material, procedures and results

Commercial wrought AW-6082 (AlMgSi1) aluminium alloy was used as an experimental material. The AW-6082 alloy was produced by Alcan (Czech Republic) in the form of extruded bars (20 mm in diameter). The chemical composition of AW-6082, as defined in the standard EN 573-3, as well as the chemical composition of the studied alloy is indicated in Tab. 1.

Si	Fe	Cu	Mn	Mg	Cr	Zn	Ti	Al
0.88	0.35	0.04	0.45	0.76	0.44	0.04	0.03	balance
0.7-1.3	0.5	0.1	0.4-1	0.6-1.2	0.25	0.2	0.1	balance

Tab. 1 Chemical composition of AW6082 alloy (weight %)

The microstructure of AW6082 after extrusion consists of deformed polyedric grains of substitute solid solution of alloying elements in aluminium that are elongated in the extrusion direction. Due to the extrusion the intermetallic phases in the microstructure have a line alignment in the extrusion direction [3].

Artificial ageing following solution treatment is a universally accepted method to strengthen this series of alloys. According to the quasi-binary Al–Mg$_2$Si phase diagram, specimens were solutioned at 530°C with 2 hours holding time and aged at 160°C with 16 hours holding time, for T6 (artificial aging after solution treatment) temper. The parameters of ageing were chosen according to previous experiments, see Fig. 1.
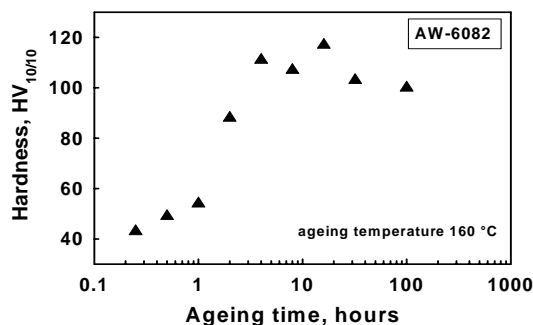
Fig. 1 Ageing curve of AW-6082

Mechanical properties of the peak-aged alloy at room temperature were assessed from the strain–stress curves. The alloy has ultimate tensile strength R_m of 307 MPa with an elongation of 10%. The conditions of the impact tests are given by the STN EN 10045-1 standard. The amount of absorbed energy at the breaking of the test bar and the character of the fracture surface are evaluated. The impact tests were performed at the temperatures of 20°C, 100°C, 200°C and 300°C. Two test bars were broken at each temperature. It has been found only negligible influence of the temperature on the amount of absorbed energy during the impact test. The difference in absorbed energy was $\Delta KV \approx 9$ Joule. On the other hand the significant dependence between temperature and fracture morphology has been found. After impact tests investigated alloy showed

transcrystalline ductile failure with dimple morphology. Two categories of dimples on the fracture surfaces of the specimens broken at the temperature of 20°C were observed. There were present large dimples formed by coarse intermetallic particles (Fig. 2a) and small dimples formed by submicroscopic particles. The increasing size and decreasing amount of dimples with increasing temperature was recorded. For specimen broken at the temperature of 300°C the large dimples with patterning on the surface are characteristic, see Fig. 2b. The results have been explained in terms of slip distribution.
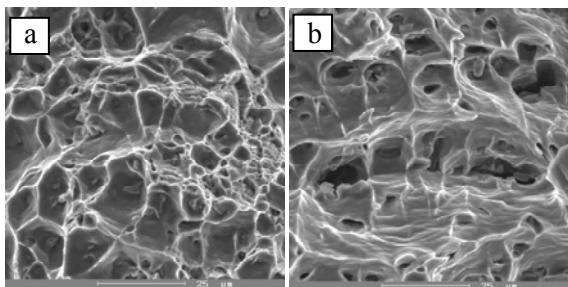
Fig. 2 Ductile fracture after impact tests

Fatigue investigations were carried out under fully reversed axial loading in the region from $N = 10^6$ to $N = 10^9$ cycles using high-frequency resonant ultrasonic machine. Fatigue tests were conducted under constant amplitude loading at a load ratio R = -1, frequency f ≈ 20 kHz and ambient temperature, using unnotched specimens. The results of fatigue tests were plotted as relation of stress amplitude vs. number of cycles to failure in Fig. 3.
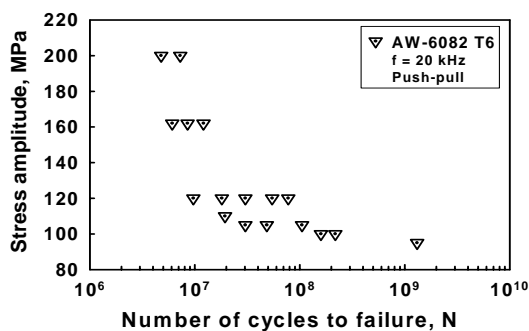
Fig. 3 S-N curve of AW-6082 T6

Fatigue fractures are different from the tensile and impact fractures. Fatigue cracks initiated naturally at the microstructurally weakest points. Non-crystallographic oriented initiation of fatigue crack was observed on all of the fatigue failured specimens (Fig. 4a). At the detailed projection of initiation places of fatigue cracks is documented that after its initiation the crack was non-crystallographic

propagated transversally to the direction of external loading approximately 0.2-0.4 mm deep and after reaching this dimension it changed the direction as well as the way of propagation suddenly. The macroscopic propagation direction of magistral crack and the direction of active loading formed an angle of 30-35° whereby the crack was propagated in a crystallographic way on the first stage mode and the fracture surface is therefore faceted. The fracture behaviour affects fatigue properties of the alloys. Fatigue fracture mode is controlled by deformation behaviour and the deformation behaviour is controlled by the interaction of dislocations and second phase particles. Due to the heterogeneous deformation with planar slip bands the fatigue cracks in the peak aged alloy propagated predominantly on the first stage mode and the fractures were faceted (Fig. 4b). Indicia of striations were observed also.
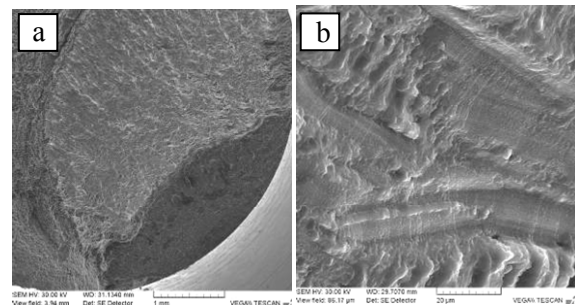
Fig. 4 Fatigue fracture

3. Acknowledgements

4. References

[1] Bidulská, J. - Kvačkaj, T. - Bidulský, R. - Actis Grande, M.: Influence of processing conditions on EN AW2014 material properties and fracture behaviour. Kovove Mater., 46, 2008, p. 339-344, ISSN 0023-432X.

[2] Bolibruchová, D. - Tillová, E.: Zlievarenské zliatiny Al-Si. EDIS, ŽU, 2005, s. 180, ISBN 80-8070-485-6. (In Slovak)

[3] Poliak, R. - Palček, P. - Chalupová, M.: Al-Mg-Si alloy crack properties after various mechanical processing, In: Materials Engineering, 15/4, 2008, s. 33-36, ISSN 1335-0803.

[4] Nový, F. - Palček, P. - Chalupová, M. - Török, P.: Fatigue resistance of extruded AW-7075 aluminium alloy, In.: Proc. 23rd Danubia - Adria Symposium, Podbanské, Slovak republic, 2006, p. 219-220, - ISBN 80-8070-589-5.

EXPERIMENTAL RESEARCH FOR ROBUST DESIGN OF POWER TRANSMISSION COMPONENTS

Milosav Ognjanovic [1],

1)   University of Belgrade, Faculty of Mechanical Engineering,
Kraljice Marije 16, 11120 Belgrade, Serbia.

Corresponding author: mognjanovic@mas.bg.ac.rs

1. Introduction

Robust design understands technical products insensitive to variation of operating conditions and also products which are successfully designed in the first attempt. Power transmission components operate in extreme random conditions. Operating regimes (loads, speeds,…), production conditions and failure processes are random. It is known that it is possible to identify, present and analyze the random process only by using experimental approach supported by statistical indicators. Power transmission operating regime for certain machine system (vehicle, dredge, etc.) is possible to identify by systematic measurements in operating conditions. Possibility of power transmission components failure (gears, bearings, sealing sets, etc.) can be identified failure by probabilistic approach which needs extensive laboratory tests of listed components. Relation between operating regime and failure probability leads to component reliability. By using these elementary reliabilities as design limitations (constraints) for design parameters definition, the robustness of power transmission unit is fulfilled. Similar situation is for the vibrations and noise of power transmission components. The level and frequency structure of vibration and noise produced by these components can be used as design constraint for design parameters definition. Relations between operating conditions, component parameters and responses have to be harmonised by using experimental approach.

2. R-DPD method

This method is based on experimental identification or on estimated operating conditions, then on the results of failure probability testing of gear drive components. The main objective of this method is to design parameter definition of gear drive components for chosen reliability. Also the method provides calculation of load capacity for limited reliability and limited service life. Design parameters of components provide equal service life for all components in the system. The stages of the application of this method are the following.

Stage 1, contains extensive measurements of loads and data processing in order to obtain load spectrum which can represent operating conditions through all service life of machine system. The spectrum shows participation of stress level in the total stress cycles number during service life of the component. In Fig.1a possible load (stress) spectrum of dredge gear drive is shown. This spectrum is transformed to the level of one gear pair in the gear drive unit. Also, load and stress spectrum can be estimated by calculation and observation. Participation of certain stress level σ_{Hi} in the total stress cycles number n_Σ is $p_i = n_{\Sigma i}/n_\Sigma$, where $n_{\Sigma i}$ number of cycles for stress σ_{Hi}.
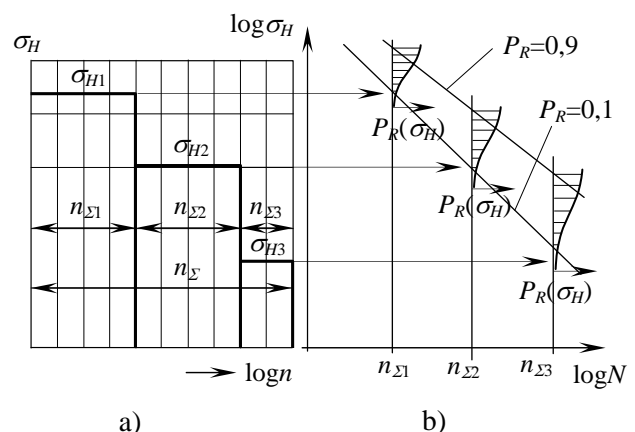
Fig. 1: Relation between operating stress spectrum and failure probability distribution

Stage 2, contains extensive laboratory testing of failure probability of all gear unit components. It requires testing rigs for testing to failure a few sets of gear drive components.

By statistical processing the failure distribution range is obtained. In Fig.1b this failure probability range for gear teeth wear is presented. Using this range for every stress cycles number failure distribution funcion can be defined.

Stage 3, contains elementary reliability calculation for every gear drive component. Unreliability is complex probability which contains probability of operating stress p_i and failure probability under this stress $P_R(\sigma_{Hi})$, i.e.

$$F_p = \sum_{i=1}^{k} p_i(\sigma_{Hi}) P_{Ri}(\sigma_{Hi})$$

where i is the number of operating stress levels. Then elementary reliability is $R=1-F_p$.

Stage 4 is Limitation Analytic Hierarchy Processing – LAHP which understands transformation of chosen level of reliability to the level of gear drive component.

Stage 5 contains design parameters calculation according to reliability level of gear drive component. For elementary reliability, design stress is defined and then dimensions of gear drive component are calculated. Also for chosen reliability, the load capacity can be calculated.

3. VN-DPD method

Design parameters definition according to limited level of gear drive vibration and noise understand harmonisation of parameter in order to reduce vibration and noise. It is based on experimental results and on a few next stages.

Stage 1 is experimental analysis of disturbances in gear transmission components. This is disturbances in gear meshing and in bearings which it is necessary to correlate with design parameters of those components. Effects of transmission errors, misalignments, wear etc. at intensity of disturbances are parameters of disturbance research.

Stage 2 is experimental analysis of response characteristics of gear drive unit. This analysis can be carried out using FE method in order to obtain modal shapes and frequencies of natural vibrations caused by disturbances produced by gear and bearing operation.

Stage 3 contains search of relation between disturbance spectrums and natural frequencies. Campbell's diagram (Fig.2) illustrates this

relation between natural frequencies f_{ni} and disturbance spectrum of gear pair in mesh with mesh frequency $f=zn/60$, and harmonics $2f$ and $3f$. Special software gives possibility to analyse of this relation using measured vibrations and calculated natural frequencies obtained by FME.
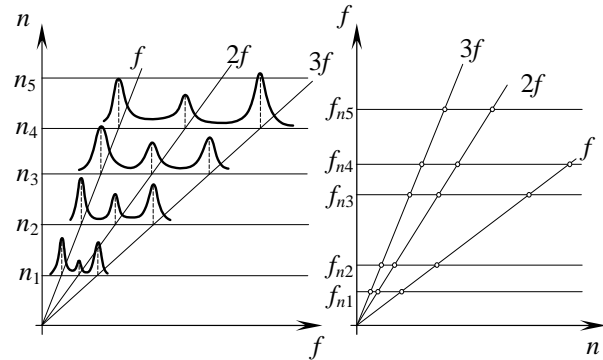
Fig. 2: Relation between desturbance and natural frequencies – Campbell's diagram

Stage 4 continues to make corrections of design parameters in order to avoid coincidence between disturbance and natural frequencies (Fig.2).

4. Conclusion

Robust design of power transmission components using this approach contains application of R-DPD method and VN-DPD method. For the purpose of applying these methods, extensive experimental research of operating conditions, failure probability, vibration and noise of gears and bearings are indispensable.

5. References

[1] Tsai, Y.T., Teng, H.Y., Chen, Y.J., Optimizing reliability design for mechanical systems using geometric approach, Journal of Engineering Design, 3, (2006) 235-249

[2] Verdmar, L., Andersson, A., A method to determine dynamic loads on spur gear teeth and on bearings, Journal of Sound and Vibration, 267, (2003) 1065-1084.

COMPARISON OF EXPERIMENTAL AND THEORETICAL RESULTS FOR WAVE PROPAGATION IN CANCELLOUS BONE

Michał Pakuła, Mariusz Kaczmarek, <u>Józef Kubik</u>,

Kazimierz Wielki University in Bydgoszcz, Institute of Environmental Mechanics and Applied Computer Science, Chodkiewicza 30, 85-064 Bydgoszcz, Poland, Corresponding author: michalp@ukw.edu.pl

1. Introduction

Biot's theory for poroelastic media has attracted the attention with regard to modelling ultrasonic wave propagation in cancellous bone. The theory in the isotropic case predicts existence of two longitudinal waves (known as fast and slow waves), which are observed experimentally. The Biot model gives reasonably good predictions of wave velocity, while predicted values for attenuation are much less than measured data, [1, 2, 6, 7]. This has been attributed to the fact that the Biot model is inappropriate to model highly heterogeneous and anisotropic porous media. Recently, Fellah et al., [2], reported agreement of Biot's model with the experimentally observed behaviour of amplitudes of fast and slow longitudinal wave signals.

The goal of this study was twofold: *(i)* to apply the Biot model to human cancellous bones specimens using both structural and mechanical input parameters that were measured individually for each specimen and *(ii)* to compare these predictions to the experimental values of velocity and frequency-dependent attenuation obtained on the same set of specimens.

2. Material and Method

Measurements were performed on 31 slices of trabecular bone with parallel faces and thicknesses about 1 cm. Specimens were obtained from human proximal femurs. Ultrasonic measurements were performed in immersion using a pair of focused broadband transducers (1 MHz centre frequency). Both transducers were mounted coaxially, separated by twice the focal length, in a through-transmission normal incidence configuration. Transmitted and backscattered radiofrequency (rf) signals were recorded along 2-D scans in steps of 1 mm and were computed to obtain the frequency dependent phase velocity and slope of the frequency-dependent attenuation coefficient so called normalized BUA (nBUA,

dB/MHz/cm), using the procedure widely described in [5]. Biot modelling of ultrasonic wave propagation in cancellous bone requires the a priori knowledge of a large number of material and structural properties. The set of macroscopic structural and mechanical parameters for human cancellous bones, obtained in the previous studies, [3], was used as input data for calculations frequency dependent attenuation coefficient and phase velocity.

3. Results and Discussion

In the Table 1 there are compared the most important input parameters required by Biot model, obtained within the present studies with the parameters measured by the other authors, [2, 5, 7]. Analyzing the data it is worth noticing significant difference in the tortuosity used by the other authors (about 1) and in our studies 1.5±0.4, (measured min value was 1.1 maximum 2.8).

Parameter	[5]	[2]	[7]	Our Studies mean (SD)
Porosity [%]	79	77	79	88 (6)
Permeability [E-6cm^2]	-	-	-	3.6 (2.3)
Tortuosity [-]	1.06	1.01	1.06	1.5 (0.4)
Λ [μm]	-	2.7	-	55.6 (20.1)
K_b [GPa]	2.08	4	0.33	0.53 (0.36)
N [GPa]	0.85	1.7	0.22	0.34(0.22)
K_s [GPa]	20.37	20	6.9	10.8
V@0.8 MHz [m/s]	2689	3219	1603	1776
α@0.8 MHz [dB/cm]	17.4	37.1	1.1	2.7
nBUA [dB/cm/MHz]	-	16.9	-	0.2

Tab. 1: Comparison of input parameters for Biot's model and model predictions reported in the previous studies with own results

High organization of the bone network measured/optimized by Fellah et al., [2], is reflected in higher values of bulk modulus of solid skeleton (K_b) and as a consequence in much higher velocity of fast wave. In contrast, Hosokawa and Otani, [1], and Wear et al., [7], calculated tortuosity and K_b assuming their independence on the other parameters as for example porosity and permeability, therefore it seems that the values are overestimated. Speed of Sound (SOS) values (at 0.8 MHz) measured in our studies (1776 m.s^{-1}) are situated between the values obtained by Fellah et al., [2], for highly oriented structure (3219 and 2414 m.s^{-1}) and Wear et al. ,[8], for calcaneus specimens (1603 m.s^{-1}) having more randomly oriented trabeculaes. Since attenuation coefficient (α @ 0.8 MHz) or nBUA are concerned it is visible strong discrepancy between our results (α =2.7 dB.cm^{-1}, nBUA=0.2 dB.(cm.MHz)$^{-1}$) and the results presented by Fellah et al., [2], (α=37.1 dB.cm^{-1}, nBUA=16.9 dB.(cm.MHz)$^{-1}$).

Fig. 1 shows comparison of the SOS and nBUA obtained form the experiments and theoretical predictions of Biot's model. There was found good correlation for the velocities (R^2=0.49), while the normalized attenuations do not exhibit such behavior (R^2=0.04).
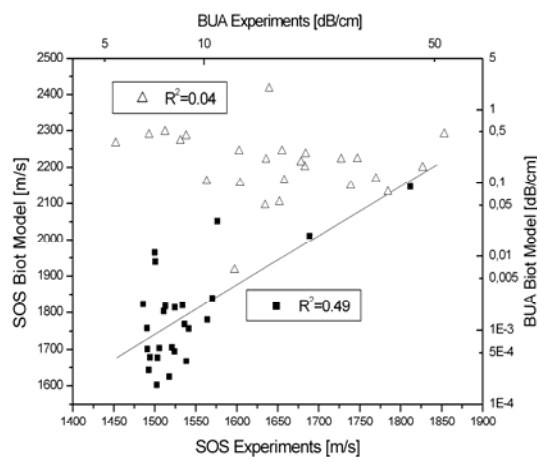
Fig. 1: Comparison of SOS and nBUA from Biot's Model and from experiments.

4. Conclusions

In the work, we performed a comparative study between theoretical predictions of Biot's theory and ultrasonic data. The originality of our study comes from the fact that each bone specimen could be modelled using as the input parameters the individually measured set of mechanical and structural properties. The main

conclusion is that the theoretical predictions do not correlate with ultrasonic experimental data. As possible sources of discrepancy one can distinguish methodological measurement errors that could contribute to the lack of correlation and inappropriate assumptions or shortages of the Biot model. It is conceivable that the differences for phase velocity can be explained partly with experimental uncertainties, but the two order of magnitude difference in attenuation needs more fundamental reasons. One contribution may arise from the anisotropy of bone architecture which was not taken into account by the model and will be the subject of the future studies. However, in our opinion scattering, which is not included in the model, is probably the most important source of discrepancy between Biot's theory and experiments.

5. References

[1] Hosokawa, A. and T. Otani, *Acoustic anisotropy in bovine cancellous bone.* JASA, 1998. 103(5 Pt 1): p. 2718-22.

[2] Fellah, Z.E., et al., *Ultrasonic wave propagation in human cancellous bone: application of Biot theory.* JASA, 2004. 116(1): p. 61-73.

[3] Pakula, M., et al., *Application of Biot's theory to ultrasonic characterization of human cancellous bones: determination of structural, material, and mechanical properties.* JASA, 2008. 123(4): p. 2415-23.

[4].Hosokawa, A. and T. Otani, *Ultrasonic wave propagation in bovine cancellous bone.* JASA, 1997. 101(1): p. 558-62.

[5].Pakula, M. et al., *Characterization of human cancellous bone specimens in terms of Biot's theory.* in *2006 IEEE Ultrasonics Symposium.* 2006.

[6].Williams, J.L., *Ultrasonic wave propagation in cancellous and cortical bone: Prediction of some experimental results by Biot's theory.* JASA, 1992. 91 p.1106-12.

[7]. Wear, K.A., *Comparison of measurements of phase velocity in human calcaneus to Biot theory.* JAcoust Soc Am, 2005. 117(5): p. 3319-24

EFFECT OF MATERIAL INHOMOGENEITY ON OUTPUT OF ULTRASONIC SPECTROSCOPY IN TRANSMISSION MODE

Radosław Drelich, **Michał Pakuła, Mariusz Kaczmarek, Józef Kubik**

Institute of Environmental Mechanics and Applied Computer Science, Kazimierz Wielki University
Bydgoszcz, Chodkiewicza 30, 85-064, Poland. Corresponding author: radeko@ukw.edu.pl

1. Introduction

Fast development of ultrasonic devices and advanced signal processing techniques yielded their common utility not only in scientific but also in industrial and medical applications. Most of the studied materials (e.g. concrete, steel, rocks, wood as well as bones and soft tissues) are heterogeneous, anisotropic and highly attenuating, and therefore their characterization requires specific experimental techniques such as through transmission method, where waves travel only once through a sample. One of the important issues in non-contact ultrasonic material characterization is appropriate evaluation of reflection coefficient at the interfaces between surrounding fluid and sample and/or sample and fluid. Usually it is done by simultaneous recording of the transmitted and reflected signals given that the reflection coefficient can be calculated and accounted in the derivation of attenuation coefficient, [1]. In order to avoid the necessity of evaluation of the reflection coefficient, the method with two samples of the same material having different thicknesses is applied, [2, 3]. However, the technique is often useless due to the strict requirement that the two samples must have identical material properties.

The paper is concentrated on determination of the role of inhomogeneity of material based on the studies of wave parameters in water saturated porous materials using ultrasonic transmission mode. The comparison is done applying two methods. In the first method the wave attenuation and phase velocity are calculated based on signals transmitted through a single sample along with the reference signal. In the second method the wave parameters are determined from the transmission tests for two specimens of different thickness.

2. Materials and experimental method

The model porous materials - sintered glass beads, saturated with water are tested. The average diameter of glass beads constituting skeleton of the material is about 260 μm, while the porosity amounts 30%. Ultrasonic measurements were performed in immersion following the insertion method, [1]. The wave parameters (phase velocity and attenuation coefficient) were computed from spectrum of the broadband pulses transmitted through specimens and spectrum of the reference pulse recorded when there is no specimen between the transmitter and receiver. Experiments were done using three pairs of custom-made 10 mm-diameter unfocused ultrasonic transducers with center frequencies 0.5, 1, and 2 MHz. Transmitted signals were recorded along 2-D scans in steps of 2 mm. The radio-frequency signals were generated and acquired with 60 MHz sampling frequency, by an 8-bits ultrasonic programmable PC board. The scheme of the experimental setup is presented in Fig1.
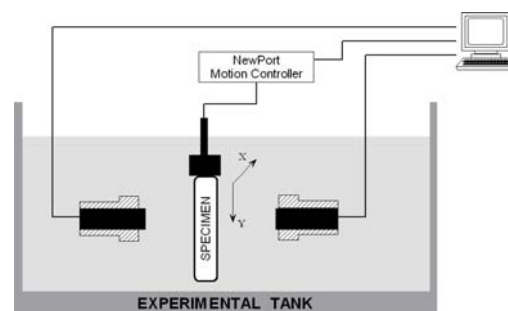
Fig. 1: Sketch of experimental setup.

First the acquisition of the transmitted signals through sample of different thickness and water path was performed. Then given the transmitted signals through the two samples and reference signal through water it is possible to calculate the wave parameters (phase velocity and attenuation coefficient) using two techniques: the first where the transmitted and reference signals are used and the second where the signals transmitted through the two samples having different thicknesses are used.

3. Results and discussion

Figures 2a-2c present ultrasonic images obtained as the result of scan of one of the studied specimens. The images represent the ratio of magnitude of the signal transmitted through the sample to the magnitude of the reference signal transmitted through water. The images were generated for water-saturated samples at three different central frequencies of transducers (0.5, 1 and 2 MHz) and were used to define region of interest (ROI) for further studies.

a   b   c
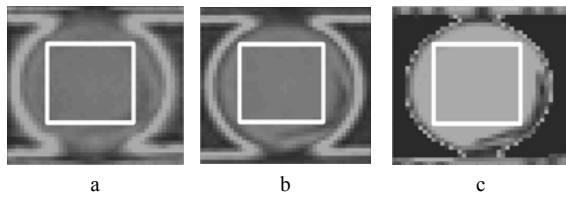
Fig. 2: Ultrasonic images with marked ROI (square in the centre part of each image) including 441 transmitted signals for water saturated specimen at 0.5 MHz (a), 1 MHz (b) and 2 MHz (c).

Subsequently, the transmitted signals in ROI were used to obtain the frequency-dependent phase velocity and attenuation coefficient applying method with two samples, [3]. The ratio of the Fourier transforms of the signals transmitted through the sample to that of a reference signal transmitted through water was computed. The log-magnitude of the spectral ratio normalized to the specimen thickness give the frequency-dependent attenuation coefficient while the phase differences determined for the signals yielded the phase velocity. Figures 3 gathers phase velocity and attenuation along with error bars found according to the above two methods and three pairs of transducers (0.5, 1 and 2 MHz). The wave parameters determined from signals transmitted through the single samples and reference line are marked by empty symbols (○ and □) while the results determined from the signals transmitted through the two samples are represented by filled markers (♦). One can notice essential difference of the obtained results both for velocity and attenuation. It means that the tested samples have different material properties (results from single samples) and the difference has a pronounce influence on parameters found from the method using two samples. The wave velocity in thinner and thicker sample oscillates around 4200 m/s and 3900 m/s, respectively. The attenuation in thinner and thicker samples for lower frequency range is around 9 dB/cm

and 5.8 dB/cm, respectively, and increases with frequency within the upper frequency range. When the wave parameters are found based on the method using two samples the velocity amounts around 3400 m/s and attenuation starts from about 1 dB/cm and then increases faster than the attenuations found for single samples.
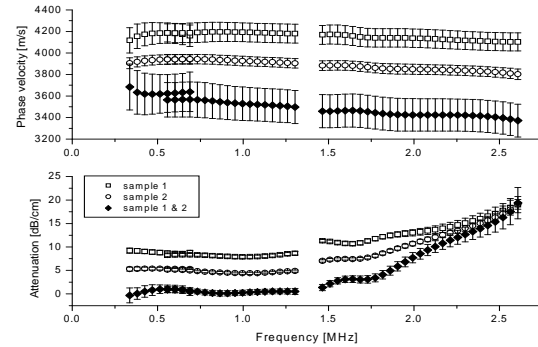
Fig. 3. Phase velocity and attenuation of longitudinal waves in water saturated sintered glass with the average diameter of glass beads 260 μm. Transducers – 0.5, 1 and 2 MHz.

For the highest frequencies the attenuations meet at the same level, probably due to dominating effect of scattering, independent of other mechanisms, [2]. The significant difference of wave velocities and attenuations found from the technique based on single and two samples result from the fact that the latter one assumes homogeneity of material of samples. The condition is not yet satisfied as it is proved by the tests from single samples. It can be noticed that both velocity, attenuation found from the method using two samples are lower than the true values of parameters for the tested materials. Moreover, the measurements errors in this method are almost twice higher.

4. References

[1] S. Chaffai, F. Padilla, G. Berger, and P. Laugier, J Acoust Soc Am 108(3 Pt 1), 1281-1289 (2000).

[2] Drelich R. M. Kaczmarek, J. Kubik, Proceedings 21 Danubia Adria Symposium On Experimental Methods in Solid Mechanics, 2004.

[3] M. Pakula, M. Kaczmarek, and J. Kubik, Ultrasonics 40(1-8), 95-100 (2002).

[4] W. Sachse and Y. H. Pao,, J App Phys 49, 4320-4327 (1978).

[5] Yew E. H. and C. S. Chen, J. Appl.Mech. 45, 1978, 940-442.

ANALYSIS OF MECHANICAL PROPERTIES OF PIA MATER AND DUR A MATER IN CERVIVAL PART OF SPINAL CORD

Anna Paleczny[1], Krzysztof Ścigała[1], Romuald Będziński[1], Marcin Czyż[2], Włodzimierz Jarmundowicz[2]

1) Division of Biomedical Engineering and Experimental Mechanics, Wrocław University of Technology, ul. Lukasiewicza 7/9, 50-371 Wrocław , Poland

2) Department of Neurosurgery, Wrocław Medical University, ul. Traugutta 116, 50-420 Wrocław, Poland

Corresponding author: krzysztof.scigala@pwr.wroc.pl

1. Introduction

Traumatological damages or pathological changes of spinal cord are one of the most dangerous clinical cases and leads to the most permanent and most dangerous decrease in patient condition. Every year research of results of spinal cord damage and research of treatment methods takes enormous financial costs. Only in United State it takes 10 billion dollars every year and still more that 10 000 cases of paralysis coming from spinal cord diseases are recorded every year. For better understanding mechanics of spinal cord injuries it is necessary to analyze mechanical properties of tissues forming spinal cord in order to create adequate models [1]. Nowadays results of many investigations shows that the most essential for spinal cord mechanical behavior are mechanical properties of dura mater and pia mater [2], [3]. However, mostly they are assumed to be homogenous materials [4], [5]. Looking at differences in geometry and properties of vertebras it is hard to believe that spinal cord is not adapted to mechanical environment. Looking into microstructure of that kind of tissues such pia mater and dura mater it is also hard to believe, so complex network of collagen fibers which are main elements of structure leads to homogenous and isotropic mechanical behavior of tissue. From the other hand precise and complex knowledge of spinal cord mechanical behavior can't be overestimated from the point of view of clinical practice. Because of that, the main aim of presented work is to investigated anisotropy and non-homogeneity of mechanical properties of pia mater and dura mater by mean of experimental investigations.

2. Material and method

Material used for investigations were samples of animal spinal cord dissected form young pigs. Healthy spinal cord was dissected from cervical part of spine and cut into samples corresponding to each cervical vertebra (fig. 1).
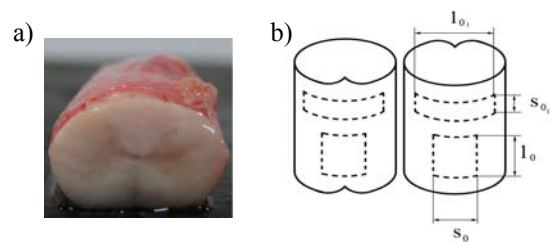
Fig. 1: Sample of spinal cord (a) and placement of pia mater and dura mater specimens (b)

From each sample of spinal cord samples of pia mater and dura mater were dissected. It was investigated over 140 samples dissected form 4 spinal cords – around 70 samples of dura mater and around 70 samples of pia mater. Samples were dissected both in longitudinal and perpendicular direction for each vertebra from C2 to C7. Samples were dissected also from the anterior and posterior side of spinal cord (fig. 1). All samples were mounted in special clamps with rubber inserts, which avoid over compression of samples.
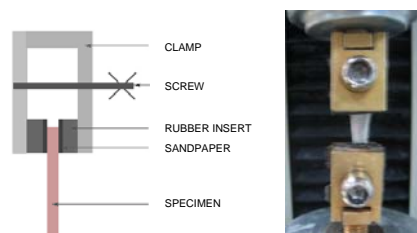
Fig. 2: Mounting of pia mater and dura mater specimens in testing machine

Between rubber inserts and samples small pieces of sandpaper were embedded to avoid sample sliding in the clamps. For each sample tension test was performed with elongation velocity 2mm/min (fig. 2).

3. Results

For each specimen of pia mater and dura mater stress – strain characteristics were estimated. Exemplary results for pia mater are show at fig. 3.
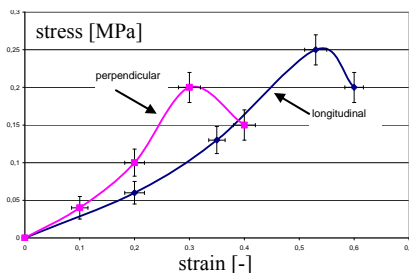
Fig. 3: Exemplary stress-strain characteristics of pia matter

Each characteristic can be described by three segments: first – non-linear, second – linear, third – also non-linear. Values of stress and strain for end of each characteristics segment were estimated. Each of those values was analysed for all samples and the maps of those values distribution on the surface of cervical spinal cord were prepared. Exemplary map is presented on the fig. 4.
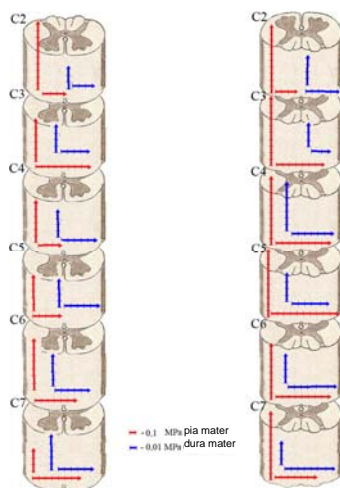
Fig. 4: Exemplary distribution of value of stress at end point of third segment of stress - strain characteristics

Analysis of mentioned above stress and strain values show clearly that they are various on various levels (C2-C7 samples). Specially, results shows that in the samples taken from the

level of C4 and C5 stress values for each end point are significantly higher than in rest of samples. Also higher values are recorded on anterior side of spinal cord than on the posterior side. Significant differences in values for longitudinal and perpendicular specimens shows high anisotropy ratio for mechanical properties for pia mater as well as dura mater.

4. Recapitulation

Presented results of analysis, specially maps of non-homogeneity in pia mater and dura mater mechanical properties allows extension of mathematical models of spinal cord tissues as non linear, orthotropic and non-homogenous material. Application of that kind of models will allow attempt of estimation of correlation between type of injury, medical diagnostics data and range of mechanical damage of spinal cord.

5. References

[1] M. Czyż, K. Ścigała, W. Jarmundowicz, R. Będziński: The biomechanical analysis of the traumatic cervical spinal cord injury using finite element approach, Acta of Bioengineering and Biomechanics, vol. 10 (2008)

[2] R. J. Fiford, L. E. Bilston: The mechanical properties of rat spinal cord in vitro, Journal of Biomech., vol. 38 (2005)

[3] B. Galle, H. Ouyang, R. Shi, E. Nauman: Correlations between tissue-level stress and strain and cellular damage within the guinea pig spinal cord white matter, Journal of Biomech., vol. 40 (2007)

[4] Z. Liangu, S. Dongle, D. Zurong: Biomechanical study of human dura and its substitutes, Chin Med J, vol. 115, (2002)

[5] H. Ozawa, T. Matsumoto, T. Ohash: Mechanical properties and function of spinal pia mater, Journal Neurosurg., (2004)

EXPERIMENTAL INVESTIGATIONS ON THE MECHANICAL BEHAVIOR OF A TOTAL KNEE PROSTHESIS DURING WALKING

Stefan Dan Pastrama[1)], Nicolae Iliescu[1)], Florin Baciu[1)], Lucian Gruionu[2)]

[1)] University "Politehnica" of Bucharest, Department of Strength of Materials, Splaiul Independentei, nr. 313, Sector 6, 060042, Bucharest, Romania.

[2)] University of Craiova, Faculty of Engineering and Management of Technological Systems, Str. Calugareni, nr. 1, 220037, Drobeta Turnu Severin, Romania.

Corresponding author: spastrama@resist.pub.ro

1. Introduction

The paper presents the results of some experimental investigations undertaken in order to study the mechanical behaviour of a total knee prosthesis during walking. A complex dynamic simulator, conceived and manufactured by the authors was used [1]. The study was done on a total knee replacement (TKR) prosthesis fixed on an artificial model of the knee bones, made of polyester. The behaviour was studied through the analysis of strains recorded using strain gauges, glued in some areas with high stresses, previously determined by three-dimensional numerical analyses. A special data acquisition system was used to record and process the response of the strain gauges.

2. Experimental tests

A condylar TKR prosthesis was used in this analysis. The two parts of the prosthesis (cam and tibial part, made of metal backing and polyethylene plate) were fixed using a special cement both on the femoral condyles and in the medullar canal of the tibial bone. The bone fragments of the knee joint (femoral condyls and tibial bone) were manufactured from polyester, using a special 3D printer and previously recorded three-dimensional images of the knee joint bones. The knee-prosthesis set is shown in Fig. 1.

Starting from previously obtained three-dimensional finite element results for such a prosthesis [2], strain gauges were glued on five measuring points, established in areas with high stresses (Fig. 2). Two measuring points were considered on the anterior surface of the cam, at the lower part of the condyles.

Fig. 1: Knee-prosthesis set.

Other two gauges were positioned anterior and posterior respectively, on the metal backing near the intercondylar notch. The fifth gauge was placed in the external proximal metaphysis area of the tibia.
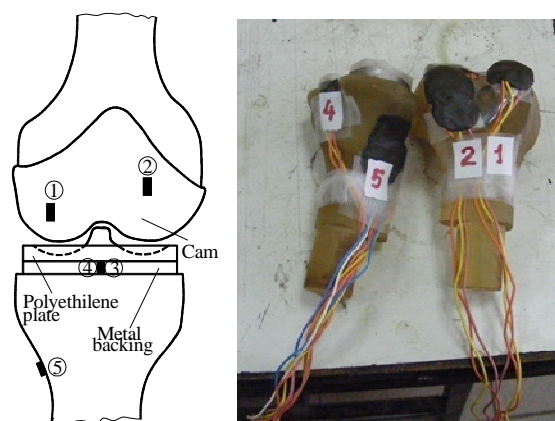
Fig. 2: Placement of the strain gauges.

The load of the prosthetic set during walking sequences was obtained using a complex dynamic simulator. Several pneumatic cylinders are used to simulate the loading with the weight of the trunk and the loadings due to different movements (flexion-extension, anterior-posterior translation internal-external rotation).

Three modes of loading of the prosthetic knee joint were considered as follows:

Mode I: the weight of the trunk, applied in steps from 116 to 400 N, applied through the main cylinder of the simulator;

Mode II: Mode I plus a constant force of 600 N representing the force developed by the quadriceps femoris, and applied through a secondary pneumatic cylinder;

Mode III: Mode II (with a quadriceps femoris force of 120 N) plus a rotation couple that simulates a movement of internal rotation of the tibia.

For each loading step, the flexion angle between the femur and tibia is modified.

The signals obtained from the strain gauges were simultaneously recorded on different channels of an amplifier. Using these recordings, two different types of curves were drawn for each loading mode: strains as a function of the flexion angle (Fig. 3) and strains as a function of the weight of the torso (Fig. 4).
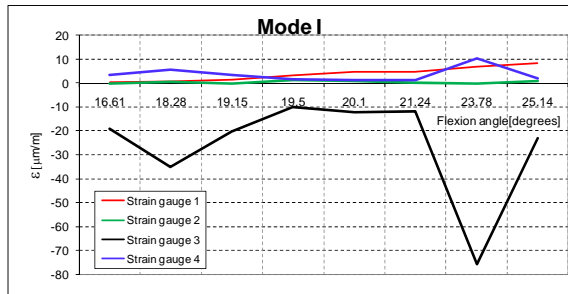
Fig. 3: Strain variation as a function of the flexion angle for loading mode I.
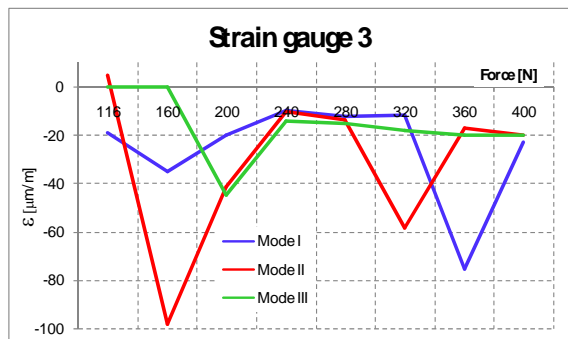
Fig. 4: Strain variation as a function of the weight of the torso (Strain gauge nr. 3)

3. Conclusions

The recorded data shown that the strains recorded by the gauges have a very small

variation with the flexion angle (Fig. 3) with the exception of strain gauge nr. 4. The relatively great variations of the strains recorded by gauge nr. 4 can be explained by the position of this strain gauge: it records the effect produced by the rotation of the cam, which allows the backwards displacement of the tibia through flexion.

Modes II and III produce the most important stresses (Fig. 4), due to the fact that the forces due to quadriceps femoris and tibia rotation appear besides the weight of the torso.

The simulations made for modes II and III with flexion angles up to 25°, showed that, for the considered prosthesis, the guidance surfaces ensure the movement with the same ease for different flexion angle values.

4. Acknowledgements

5. References

[1] L. G. Gruionu, N. Iliescu, S.D. Pastrama, Experimental investigations concerning the biomechanical behavior of the knee joint in some pathological cases. Proceedings of the 24th symposium on Developments in Experimental Mechanics DANUBIA – ADRIA, 19 - 22 Sept., Sibiu, Romania, pp. 31-32 (2007).

[2] L. G. Gruionu, S. D. Pastrama, V. Georgeanu, P. Rinderu, Numerical modeling and simulation of mechanical phenomena in total knee arthroplasty during walking, Proceedings of the 24th symposium on Developments in Experimental Mechanics DANUBIA – ADRIA, 19 - 22 Sept., Sibiu, Romania, pp. 199-200 (2007).

FATIGUE TESTING OF BONDED CONNECTION BETWEEN ALUMINIUM SPAR AND PLASTIC COMPOSITE POCKET OF TRANSPORT HELICOPTER MAIN ROTOR BLADE

Ognjen Peković [1], Ivan Kostić [1], Aleksandar Simonović [1]

[1] University of Belgrade, Faculty of Mechanical Engineering, Kraljice Marije 16, 11000 Beograd, Serbia.

Corresponding author: opekovic@mas.bg.ac.rs

1. Introduction

This paper presents results from fatigue testing of bonded connection between aluminium spar and plastic composite pocket of transport helicopter main rotor blade. Originally main rotor blade is made as full metal blade with dural spar and 21 pocket with additional blade tip pocket made of aluminium honeycomb core and aluminium alloy skins. In order to modernize and revitalize blades of helicopter and extend operational life cycle aluminium blade pockets are replaced with plastic composite pockets with identical geometry because of their light weight and higher fatigue resistance. International aircraft building requirements prescribe strict rules for homologation of new aircraft parts. For helicopter blades and its components fatigue life is one of the most important factors in stress analysis and fatigue testing is required in order to gain blade approval.
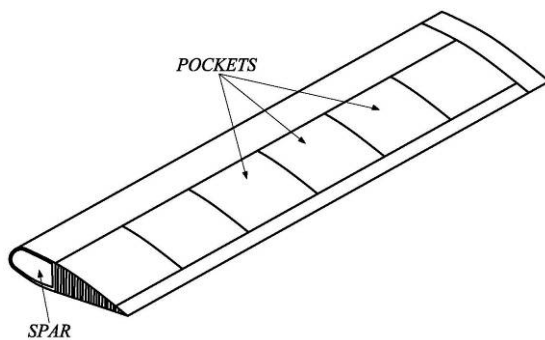
Fig. 1: Multiple pocket blade construction

2. Testing procedure

Testing of bonded connection between old dural spar and new composite pocket is done on test table specially designed for this occasion. Loads on outmost 21st pocket of blade are chosen for relevant loads since this part of the blade has highest local aerodynamic force. Projected operational life of blade is 2000 plus 10% hours at nominal operating mode of 207 rpm. Tests are carried on the new composite part right after production and are composed of three phases:

1. First phase of testing included measurement of static deformations of pocket near trailing edge prior to dynamic simulation of blade operational life cycle. The measurement was performed for three load cases: a) aerodynamic load; b) centrifugal load and c) combined load as simultaneous action of loads in a) and b). These preliminary static tests are used as benchmark for the verification of the state of the blades after simulated 2000 hours of exploitation.

2. The second phase includes applying loads that simulate relevant work regime during the exploitation of 21st composite segment of the blades, defined in the previous phase, but in the dynamic sense. Blade is tested for 28.420.800. cycles with accelerated aging plan.

Fig. 2: Blade on the test table

3. Third phase of testing consists of the static verification measurement identical to those that are made in the first stage.

3. Testing equipment

Beside supporting frame and blade segment with spar and composite pocket, testing

installation consisted of metal plates glued to the surface area of bonded connection (faying surface) for appliance of calculated loads, drive motor with eccentric hub and calibrated spring for generation of transverse force, system for generation of simulated centrifugal force, digital cycle counter and power supply.

Measurements are carried out with two indicators positioned at the middle of pocket trailing edge for measuring of vertical deflection and at trailing edge of pocket rib for measuring of tangential deflection.
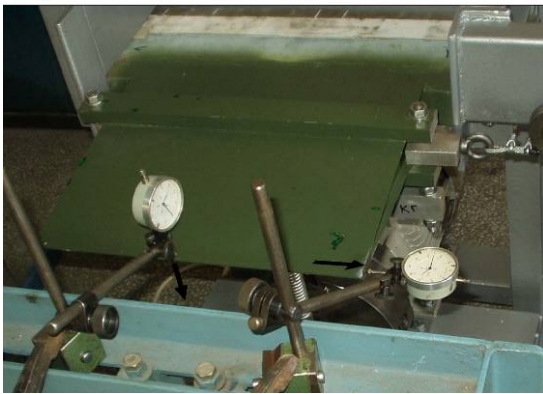
Fig. 3: Measurement of transverse and tangential deflections

4. Results

Experiment results in figures 4.-6. represent vertical deflection of blade pocket trailing edge for load case without initial load. Full line shows deflection in the first phase of experiment while dotted line represents deflection in third phase after 28.420.800 cycles.
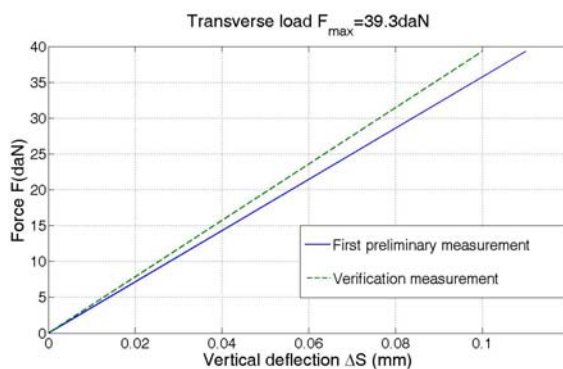
Fig. 16
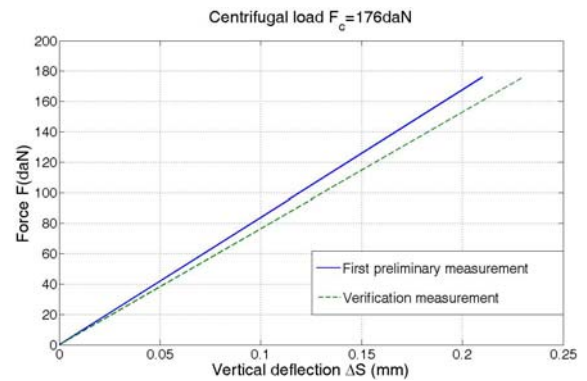
Fig. 18
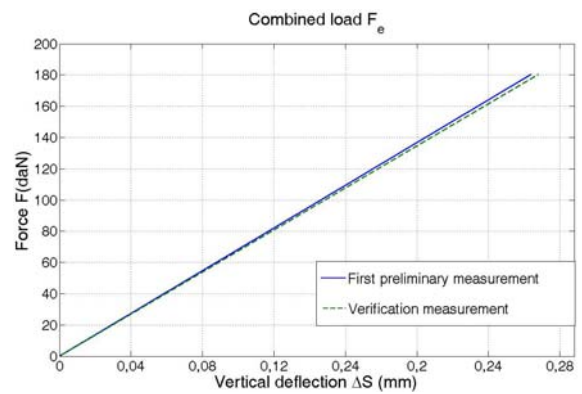
Fig. 20

After testing and comparison of measurements it was concluded that there was no damage to any part of the pocket-spar assembly, all variations of static deformation lie within the tolerance of measurement error, and that after completion of the fatigue testing there was no occurrence of residual deformations.

5. References

[1] M. Nenadović, Osnovi Projektovanja i Konstruisanja Helikoptera. Soko-RO Vazduhoplovstvo-Mostar, 1982
[2] J. Watkinson, The Art of the Helicopter. Elsevier, 2004
[3] M. Balasko, G. Endroczi, J. Veres and F. Korosi, Research of Extension of the Life Cycle of Helicopter Rotor Blade in Hungary. RTO-MP-079 (II), 2001

HYDROGEN DIAGNOSTICS OF MICRODEFECTS AND NANOSTRUCTURES IN MATERIALS

Anatoly Polyanskiy[1] Vladimir Polyanskiy[2], Elena Chernyaeva[3], Yury Yakovlev[2]

[1] ”NPK Electron & beam technology” Ltd, 195220 p.b.162 St.-Petersburg, Russia

[2] State Polytechnic University of St. Petersburg, 195251 Politekhnicheskaya, 29 St.-Petersburg, Russia

[3] St. Petersburg State University, 199034 Universitetskaya nab. 7-9. St. Petersburg, Russia

Corresponding author Vladimir Polyanskiy: vapol@electronbeamtech.com

Hydrogen in small concentrations is containing in all materials and its influence on materials' properties is of crucial importance. Even for concentrations of about 1 hydrogen atom per 10000 atoms of the matrix one can observe the hydrogen embrittlement.

This influence can not be explained by means of the hypothesis of the uniform distribution of hydrogen in the matter. Only the localization of hydrogen in microdefects, on the grains' boundaries and on the surface of nanostructures in the material can explain the considerable change in mechanical properties.

The presentation provides some experimental proof of this localization on example of high-temperature extraction of hydrogen from aluminum alloys.

When microdefects and nanostructures are present, hydrogen is localized on free surface and decreases the free surface energy. This decrease results in termination of growth of micro- and nanocrystals and, on the other hand, leads to reduction of crack resistance and, in turn, to brittle destruction of the material.

The highly sensitive hydrogen analyzer AV-1 allows one to observe the hydrogen emission from microcracks and dislocations on the surface of specimen. The emission occurs during the specimen heating in vacuum and is fixed in the form of small peaks on the extraction curve.

The results of experimental investigations of aluminum alloys and steels, including zinc coated steels are shown. The size of defects determined by means of optical and probe microscopy is in a good agreement with the volume of hydrogen extracted under the atmospheric pressure. This allows us to assume that the microcracks and defects are filled by hydrogen.

These assumptions were proved on monocrystals of silicon. The microdefects on the surface having the characteristic size of 30 micron were produced by using the infrared pulse laser. Small peaks on the curve of high-temperature hydrogen extraction curve were observed when these specimens were tested.

It became clear that for the materials which have no stable chemical link with hydrogen, nearly whole hydrogen is concentrated in microdefects and on the surface of micro- and nanograins. Aluminum alloys, some steels, ceramic and semiconductors eject hydrogen. Thus, the general amount of hydrogen can be used for estimation of the volume concentration of microcracks and dislocations.

The diagnostics in terms of the amount of extracted hydrogen turns out to be efficient and less effort-consuming than other methods of investigations. For instance, in order to determine an average concentration of microdefects by means of microtomography one needs to conduct measurements of about 12 hours whereas the hydrogen analysis takes 45-60 min.

Summarising we can say that we suggest a new approach to experimental investigation and diagnostics of microdefects and nanostructure in materials.

NEW METHODS FOR DURABILITY SIMULATION OF COMPONENTS UNDERGOING DYNAMIC LOADINGS

Helmut Dannbauer, Harald Riener, Markus Kaltenböck [1],

[1] MAGNA POWERTRAIN, Engineering Center Steyr, Steyrerstrasse 32, 4300 St. Valentin, Austria.

Corresponding author: helmut.dannbauer@ecs.steyr.com

1. Introduction

Because of fuel consumption and cost consideration lightweight design is of utmost importance in all vehicle industries. To reach a higher degree of optimization, all input for durability simulation (loads, dynamic response, material properties, manufacturing influences) have to be determined with higher precision in the future.

2. Load Data

Traditionally, load data for vehicles is acquired with wheel force transducers or with sensors at interface points between components. Then those load signals are applied to multi-body models to determine inner forces. If the parameters of the model - especially of flexible elements like bushings - are not accurately known the resulting forces acting on the components are often inaccurate. To avoid that problem an iteration process can be used that make sure that the inner forces are correct. The method can also be applied with tire models so that load data acquired for a specific vehicle can be transferred to similar vehicles.

3. Nonlinear Dynamic Simulation

To determine transient stresses in components, dynamic simulation has reached a high level both with finite element analysis and multi-body simulation. As long as component behavior is linear the major critical issue is modal damping values which determine vibration amplitudes for resonance states. However, many components or assemblies of components also show nonlinear behavior from contact, dry friction or nonlinear stiffness. Whereas these effects can be simulated in principal, the simulation of longer time histories cannot be performed because analysis time is too large for practical application. A new method to consider nonlinearities between flexible parts in multi-body simulation will be presented that allows computation with much lower effort. It will be demonstrated how much gain in accuracy is reached both from considering those nonlinearities and from using local damping instead of modal.

4. Durability Analysis

To assess the strength and operational safety of components, different input data need to be processed together. Stresses from finite element analysis, load data from dynamic simulation and material data from specimen tests are the basic input. Both quasi-static and modal based load definition are common, but in vibration effected parts like body in white, suspension sub-frames or power-train components higher accuracy can be expected from the modal approach – as will be demonstrated.

But to reach a high level of correlation to test bench results and field tests more attention needs to be paid to effects from manufacturing. Results from process simulations like casting, forming and injection molding can already be accounted for in a simplified manner. In the near future significant progresses are feasible for casting influence because porosity models are able to determine local material properties which are subsequently used for durability analysis. Another relevant field is surface effects from processes like hardening and local plastic deformation. Those surface treatments create residual stresses that shift the local stress history but also affect the cyclic material properties. Application examples will demonstrate the strong effect from manufacturing processes.

5. Conclusion

New methods from different fields of numerical simulation are discussed with examples how they can benefit to durability assessment results with improved correlation to test results.

ONE APPROACH TO LOW CYCLE FATIGUE LIFE COMPUTATION OF AERO ENGINE DISKS

Strain Posavljak

"ORAO" a.d., Sabackih djaka bb, 76300 Bijeljina, Republic of Srpska, Bosnia and Herzegovina

Corresponding author: strain.posavljak@orao.aero

1. Introduction

Service life (SL) of aero engine disks is mainly limited by the low cycle fatigue (LCF). Variable centrifugal forces of blades and own centrifugal forces, with or without temperature, provoke this kind of fatigue. Because of that the term of SL can be replaced by the term of LCF life. For LCF life computation of aero engine disks it is need to know: engine start-stop cycles and simple cycles inside of their, cyclic properties of material used or nominated for workmanship, stress-strain response at critical point for all simple cycles. One approach to LCF life computation of aero engine disk dominantly exposed to centrifugal forces of blades and own centrifugal forces is described in this paper.

2. LCF life computation of concrete disk

2.1 The basic information

The first stage low pressure compressor (LPC) rotor disk of R25-300 aero engine here is chosen as representative of aero engine disks, dominantly exposed to centrifugal forces of blades and own centrifugal forces. The mentioned disk has made of steel 13H11N2V2MF. Because of premature cracks which have appeared in area of dovetail joints with blades, proscribe SL of 1200 flight hours was not reached.

2.2 Probability of crack initiation

By data processing about ultrasonically discovered cracks for sample of 79 disks, Waibull's expression of crack initiation probability, P(t), was obtained. On the base of that expression characteristic values of crack initiation life or LCF life: $27.6_{P(t)=0.001}$, $294.3_{P(t)=0.5}$ and $676.1_{P(t)=0.999}$ flight hours were calculated [1].

2.3 Engine start-stop cycles

Start-stop cycles of R25-300 aero engine here are defined as blocks of rotation frequency of LPC rotor. These blocks are marked with A, B, C, D and E. Regulated blocks from A to D simulate engine ground control. One registered flight of aeroplane with R25-300 aero engine was simulated by block of rotation frequency marked with E. Using the method of reservoir, all blocks were decomposed on simple cycles [1].

2.4 Cyclic material properties

For the purpose of LCF life computation of discussed disk, experimentally obtained cyclic properties of fine grain martensite steel 13H11N2V2MF, in delivered state were used. Those properties are contained in Tab. 1 [1].

Property	Value
Modulus of elasticity, E [MPa]	206682
Cyclicstrength coefficient, K' [MPa]	1103
Cyclic strain hardening exponent, n'	0.118
Fatigue strength coefficient, σ'_f [MPa]	1818.8
Fatigue strength exponent, b	-0.144
Fatigue ductility coefficient, ε'_f	0.5351
Fatigue ductility exponent, c	-0.6619

Tab. 1: Cyclic properties of steel 13H11N2V2MF in delivered state

2.5 Stress-strain response

At the first, the blade and critical disk part were observed as separated ideal elastic bodies. Linear stress response and nodal reactions at blade root contact surfaces, in conditions of maximal rotation frequency $n = 186$ s^{-1}, were obtained using the finite element method (FEM). Using FEM in conditions of the same

rotation frequency, mentioned reactions in transformed form used as nodal forces for obtaining of linear stress response of critical disk part. Axysimmetric linear stress response of concrete disk when it observed as blisk, was obtained also (Fig. 1).
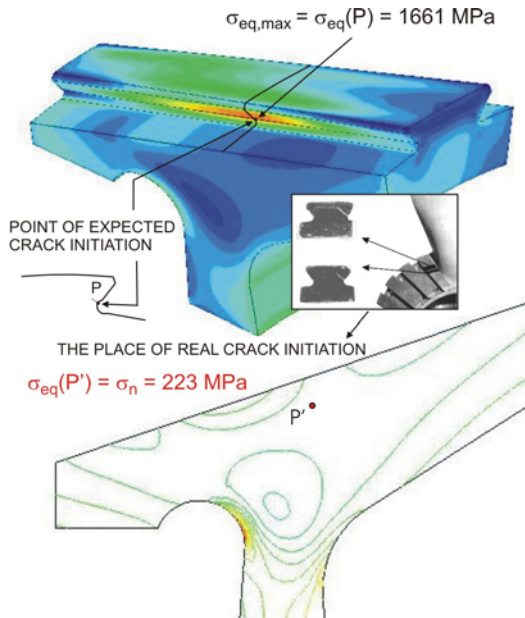
Fig. 1: Linear stress response of critical disk part (above) with axysimmetric linear stress response of disk when it observed as blisk (down).

According to Fig. 1 maximal equivalent stress $\sigma_{eq,max}$ at point of expected crack initiation P (critical point) and belonging strain are unreal. It can see that critical point P corresponds to point of real crack initiation. Equivalent stress at point P' of blisk which corresponds to critical point P of disk, taken as nominal stress σ_n, was served for calculation of so cold equivalent stress concentration factor K_{eq} ($K_{eq}=\sigma_{eq}(P)/\sigma_n$). Respecting memory of metals, real stress-strain response at critical point of disk was described by stabilized hystersis loops assigned to all simple cycles inside of engine start-stop cycles. Example of stress-strain response at critical point of the first stage LPC rotor disk of R25-300 aero engine, for one engine start-stop cycle is shown in Fig. 2. In that figure it can see that for stress-strain response determining, cyclic stress-strain curve, Masing's curve [2] and approximate Sonsino's curve [1] were used. Masing's curve was served for modelling of stabilized hysteresis loops. Equivalent stress concentration factor was used for defining of all approximate Sonsino's curves.
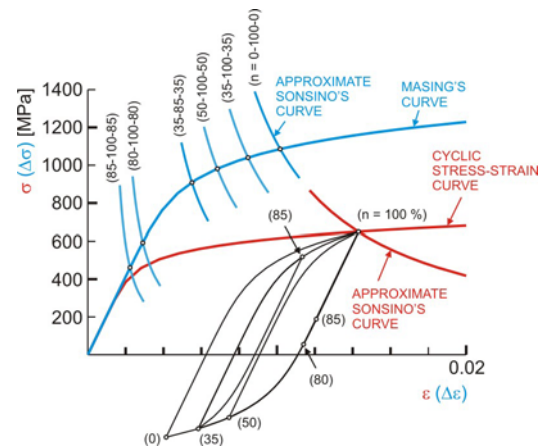
Fig. 2: Stress-strain response at critical point of the first stage LPC rotor disk of R25-300 aero engine for one start-stop cycle.

2.6 Damages and LCF life computation

Damages provoked by simple cycles inside of start-stop cycles and by all start-stop cycles, in this paper determined using Palmgreen-Miner's rule. Spectrums of strain amplitudes were brought in relation with Morrow's curves of LCF [1,2]. LCF life of our disk expressed in flight hours was computed as reciprocal value of one flight hour damage. Computed or estimated LCF life amounts 701 flight hours. On the base of this value it was concluded that real disk with rough machining and rough grain martensite structure can not reached proscribed SL of 1200 flight hours

3. Acknowledgements

4. References

[1] S. Posavljak, Fatigue Life investigation of Aero Engine Rotating Disks, Doctoral dissertation (in Serbian), Belgrade University, Mechanical Faculty (2008).

[2] J. A. Banantine, J. J. Comer, J. L. Handrock, Fundamentals of Material Fatigue Analysis, Prentice-Hall, Englewood Clifs, New Jersy (1990).

ULTRASONIC MEASURED PARAMETERS OF GRANULAR MEDIA

Mihai Valentin PREDOI [1], Cristian Cătălin PETRE[2], Daniela PREDOI[3], Marian SOARE[4]

1) Politehnica University of Bucharest, Department of Mechanics, Splaiul Independenței 313, 060042, Bucharest, Romania.

2) Politehnica University of Bucharest, Department of Strength of Materials, Splaiul Independenței 313, 060042, Bucharest, Romania

3) National Institute of Materials Physics, P.O. Box. MG 07, 077125, Magurele, Romania

4) S.C. Nuclear NDT Research & Services, Șoseaua Berceni, Nr.104, Sector 4, Bucharest , Romania.

Corresponding author: predoi@cat.mec.pub.ro

1. Introduction

Granular materials are widely used in many domains, from civil engineering (concrete, etc.) to medical applications (Hydroxyapatite, etc.). Their elastic properties are among other parameters which are requested for a complete characterisation of these materials. This relatively old problem was confronted from the beginning with the difficulty of being non-homogeneous materials. Only recently, new methods have been developed, based on modern techniques, such as ultrasonic waves.

The Hydroxyapatite is chemically similar to the mineral component of bones and hard tissues. It is one of few materials that are classed as bioactive, meaning that it will support bone ingrowths (it is bioactive) and osseointegration when used in orthopaedic or dental applications.

Coatings of hydroxyapatite are often applied to metallic implants (most commonly titanium/titanium alloys and stainless steels) to alter the surface properties. Without the coating, the body would see a foreign body and work in such a way as to isolate it from surrounding tissues. To date, the only commercially accepted method of applying hydroxyapatite coatings to metallic implants is plasma spraying.

In [1] is presented the application of a simple model for the prediction of the acoustic properties of porous granular media with some assumed pore geometry and pore size distribution close to log-normal. One of the first biomedical studies of the bone as a porous medium is presented in [2] with the objective of proving if scattering alone may cause such a high attenuation as that observed in calcaneus. A temporal model of the direct and inverse scattering problem for the propagation of transient ultrasonic waves in a homogeneous isotropic slab of porous material having a rigid frame is investigated in [3]. The porous medium is modelled via Biot's theory and the scattering by a single pore is characterized from the definition of a scattering matrix.

2. Numerical simulation

The experiment has also been numerically tested using finite elements (FEM) [4] in order to estimate the optimum dimensions of the fluid container. At 2 MHz central frequency of the transducer, the ultrasonic beam has small variations of diameter, so that a depth of 50 mm and a diameter of 40mm for the container are sufficient.
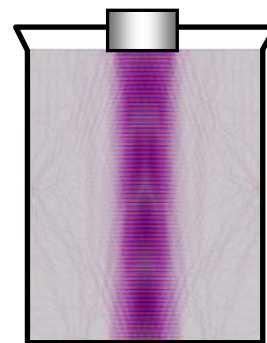
Fig. 1: Fluid particle displacements (FEM)

The wavelength in water at this frequency is 0.7 mm. Numerical results are presented as

displacements in fig.1, in which the wavelength can be easily remarked.

3. Experimental setup

The experimental setup is presented in fig.2
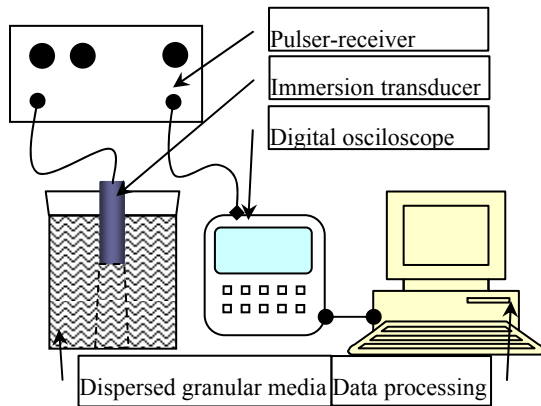
Fig. 2: Experimental setup

The particles of hydroxyapatite are dispersed in pure water. The concentration and particle size are two of the parameters. A 300V pulser-receiver sends ultrasonic pulses to an immersion transducer (2 MHz resonance frequency) which is introduced in the heterogeneous fluid.
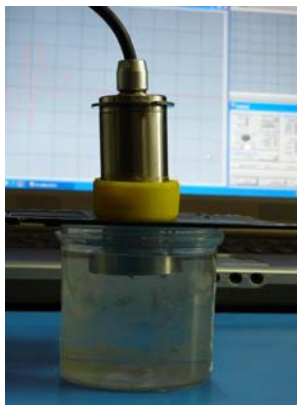
Fig. 3: 2MHz transducer immersed in water

The acquired signals are presented in fig. 4 and indicate a dispersed signal due to the presence of small particles in the fluid. There are many parameters influencing the phenomenon, so that numerous experiments are required for a direct indication of the dispersed particles properties such as mean size and relative particle density.
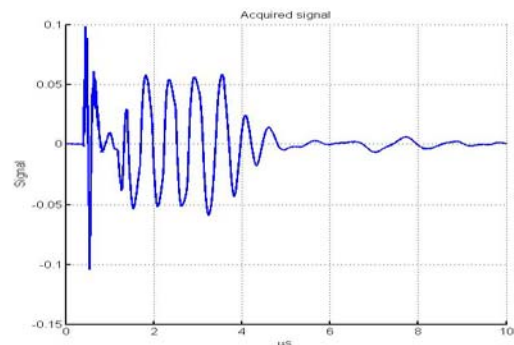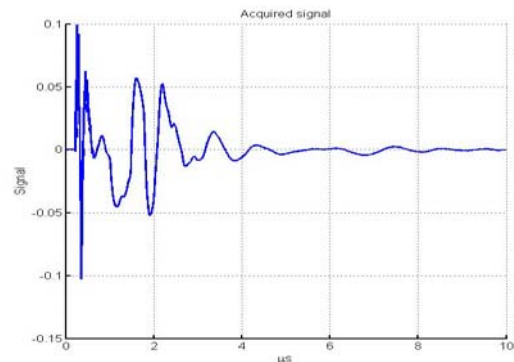
Fig. 4: Acquired signals in water (top) and particles in water (bottom)

4. Conclusion

The main results, very important for future developments is the high sensitivity of the method to the presence of dispersed particles in the fluid.

5. References

[1] K. V. Horoshenkov, M. J. Swift, The acoustic properties of granular materials with pore size distribution close to log-normal, J. Acoust. Soc. Am. 110 (5), Pt. 1, (2001) 2371-2378.

[2] F. Luppé, J.–M. Conoir, H. Franklin, Scattering by a fluid cylinder in a porous medium: Application to trabecular bone, J. Acoust. Soc. Am. 111 (6), (2002), 2573-2582.

[3] Z. E. A. Fellah, M. Fellah, W. Lauriks, C. Depollier, Direct and inverse scattering of transient acoustic waves by a slab of rigid porous material, J. Acoust. Soc. Am. 113 (1), (2003), 61-72.

[4] COMSOL A.B. – Users' Manual, 2008.

INVESTIGATION OF RIVET JOIN IN COMPOSITE LAMINATES

Paweł Pyrzanowski [1)], Agnieszka Jarzębińska-Dziegciar [1)]

[1)] Warsaw University of Technology, Institute of Aeronautics and Applied Mechanics, Nowowiejska 24, 00-665 Warsaw, Poland.

Corresponding author: pyrzan@meil.pw.edu.pl

1. Introduction

Composite materials are more and more widely applied in industry, especially in modern industrial branches such as transportation. They are used not only to produce elements subjected to moderate load, but also in the whole high-strength structures. The best example could be aviation industry, in which application of composites have increased from approx. 2% (in nineteen eighties, airplanes like MD-80, Boeing 757) up to 47% in Boeing 787 *Dreamliner* (in the year 2007). The participation of composites is even greater in lighter airships and sailplanes, and in the so-called light airplanes.

One of the most difficult problems in composites if joining and introduction of concentrated force. One of the methods is using of rivets. In this work influence of layers direction on the destructive force for 5 plies glass-epoxy laminate was investigated.

2. Specimens and Experimental Stand

Experiments were made for 8 specimens shown in fig. 1. Configuration of fibres directions in 5 plies is described in Tab. 1.
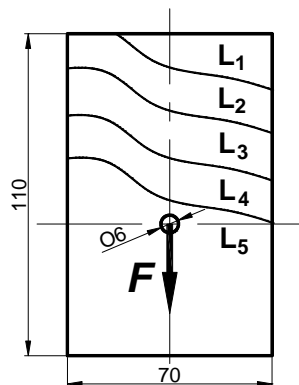
Fig. 1: General view of specimen.

Every specimens were made from glass woven roving fabric STR028-150 (nominal density 150 g/m^2) and epoxy resin EP53. The thickness of the specimens was 0.9 mm.

specimen number	number of the ply				
	L_1	L_2	L_3	L_4	L_5
1	+	+	×	+	+
2	+	×	×	×	+
3	+	×	+	×	+
4	+	+	+	+	+
5	×	×	+	×	×
6	×	+	+	+	×
7	×	+	×	+	×
8	×	×	×	×	×

Tab. 1: Direction of fibres in plies of laminate

In the hole Ø6 mm steel tubular rivet was inserted. From both sides of laminate steel cover plate was applied. Compression force between them was 40 N.

For investigations special experimental stand shown in fig. 2 was made.
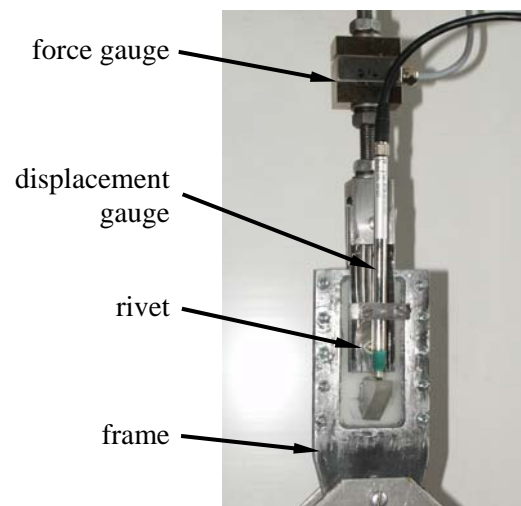
Fig. 2: Specimen in the stand

Load was applied in displacement-controlled mode. The speed of displacement varied from about 1 mm/min at the beginning of loading to about 15 mm/min at the end of loading. During experiment loading force and displacement of rivet were measured.

3. Experimental Results

In fig. 3 relationship between displacement and load force for 1st and 7th specimen are presented. In the figure the force in which rivet starts destroying the laminate (F_o), the force of the end of the second linear part of line (F_1), and the maximal value of load force (F_{max}) are shown.

a)

b)
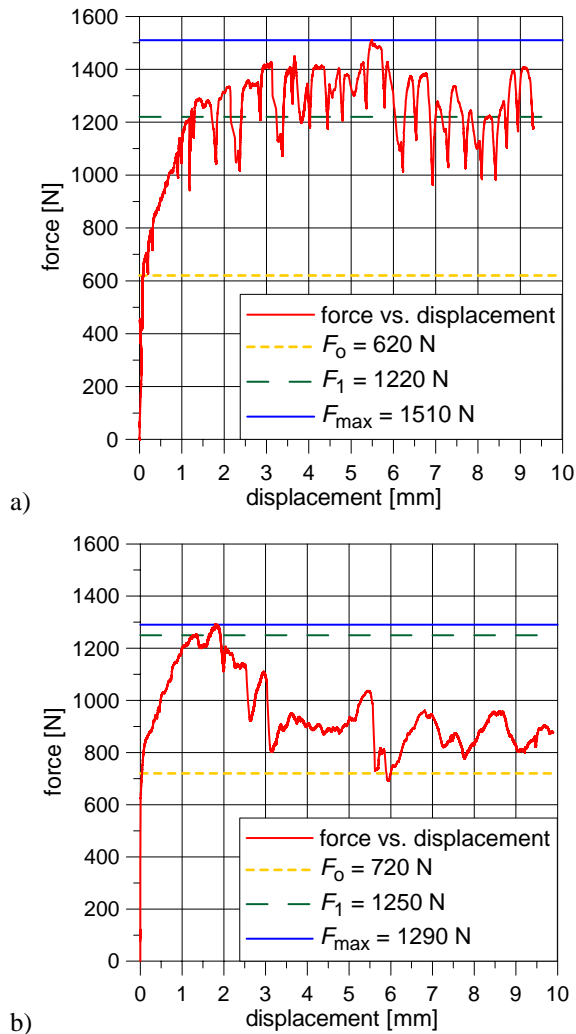
Fig. 3: Load force vs. displacement for:
a) 1st and b) 7th specimen.

For one group of specimens the maximal value of load force is observed for big value of displacement and the load is nearly constant, increase and decrease when fibres are ripped (spec. 1st, 3rd and 5th). For the second group of specimens the load force decrease when displacement increase (spec. 2nd, 4th, 6th, 7th and 8th).

Fig 4. shows the most interesting values – maximal forces F_{max} for every specimens. It is visible, that the maximal force depends to the little extent on the direction of fibres in plies.
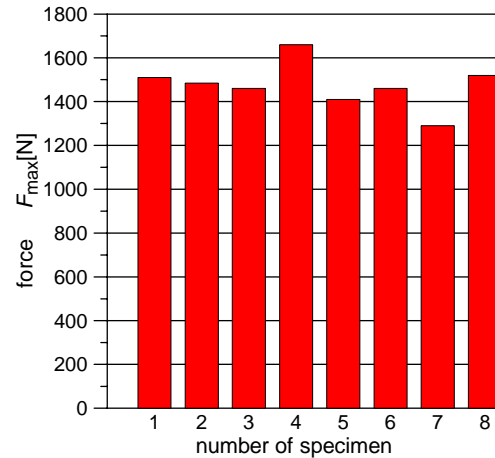
Fig. 4: Load force vs. displacement for 1st specimen.

In fig. 5 views of destroyed holes are shown. It is visible, that the process of destruction for specimens is different. Laminate is most destroyed for plies with fibres parallel and perpendicular to the load direction (spec. 4th – fig. 5d; spec. 1st – fig. 5a and spec. 3rd – fig. 5c). The least destruction is visible for specimens with fibres lying at the angle of 45º to the load direction (spec. 8th – fig. 5h; spec. 7th – fig. 5g and spec. 5th – fig. 5e). For similar number of fibres oblique and parallel/perpendicular to the load direction destruction is dependent on the direction of outer plies (spec. 2nd – fig. 5b and spec. 6th – fig. 5f).
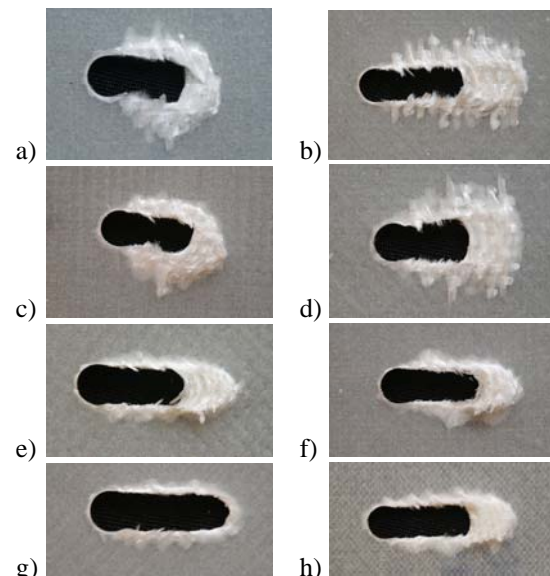
Fig. 5: Destroyed holes for 1st to 8th spec. (a to h)

4. Conclusions

Investigations shows, that instead of different mechanism of destruction, maximal destroyed force for laminates very little depend on the directions of fibres.

KINEMATIC SIMULATIONS USING CATIA SOFTWARE

Klara Rafa [1],

[1] University of Novi Sad, Faculty of Technical Sciences, Dositej Obradović sqr. 6, 21000 Novi Sad, Serbia.

Corresponding author: klara@iis.ns.ac.yu

1. Introduction

On subject Mechanics our students are solving various problems referred to mechanisms which are usually presented by a schema as shown on figure 1. To ensure better understanding of the material and to be able to answer questions such as, "what is moving and how?", we tried to make this mechanisms "alive". Current CAD systems include modules for simulation analyses so in this research the author tried to find out how mechanisms and their behavior can be simulated.
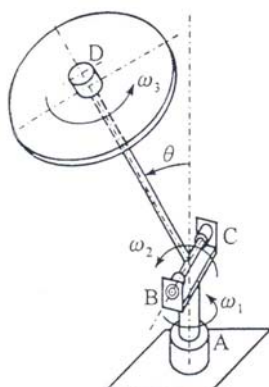
Fig. 1: The schema of the mechanism.

2. Simulation of mechanisms

For this research the powerful 3D CAD system, software CATIA has been used. CATIA mechanical design automation software is a feature – based, parametric solid modeling design tool which represents the current state of the art.

The first step in solving this problem was creating a 3D model of the mechanism shown on Figure 1. The mechanism consists of several individual piece parts and the designer has to create a model for each of them in the *Part Design* module. Parts are made up of a number of individual constituent elements called features and these are: bosses, cuts, holes, ribs, fillets, chamfers and drafts.

The assembly is created using the same method as new parts in a special module of this software, in the *Assembly Design*. The assembly is created by adding and orienting existing parts in an assembly. Component parts are oriented and positioned in the assembly using constraints. Constraints remove degrees of freedom from the components [1].

To make a preliminary assembly it is allowed to insert parts into the assembly without constraints. In the *Assembly Design*, parts can "jump" from one position to another and they can be dragged and dropped using different tools for translation and rotation.
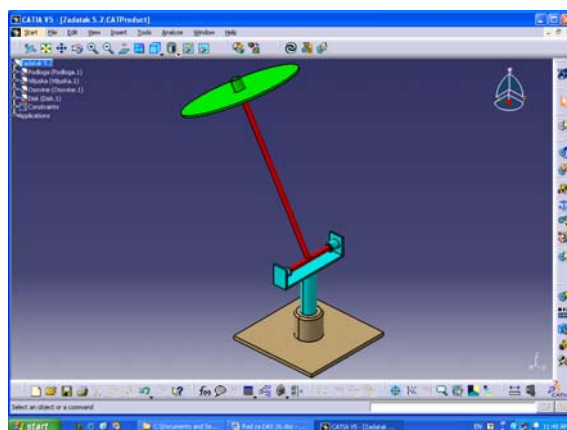
Fig. 2: The assembly created in CATIA.

The next step in reaching the final goal was to insert the created assembly (Fig. 2) into the *DMU Kinematics Simulator*.

DMU Kinematics Simulator makes it possible to put assemblies in motion. The *DMU Kinematics* workbench allows to add kinematic mechanisms to assemblies and to use these mechanisms to simulate assembly's motion. Using simulations helps the designer to evaluate the design. *DMU Kinematics Simulator* gives the tools to get assembly designs moving [2].

DMU Kinematics Simulator defines mechanisms for digital mock-ups of all sizes using a wide variety of joint types, or by generating them automatically from mechanical

assembly constraints. *DMU Kinematics Simulator* also simulates mechanism motion easily with mouse-based manipulation in order to validate mechanisms. *DMU Kinematics Simulator* analyzes mechanism motion by checking interferences and computing minimal distances.

In this module, the first step is to define the fixed part of the mechanism. Then the joints have to be defined. 16 different types of joints are available in CATIA. Furthermore, it is necessary to assign commands to joints: mutually rotation or translation of the elements in the joint, which will move according to defined limits. The user can ask the software to analyze the mechanism (Fig. 3).
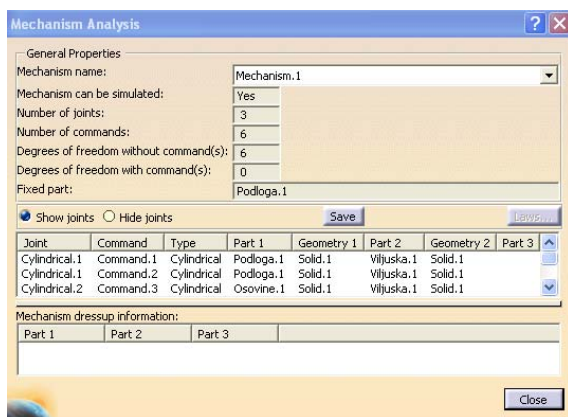
Fig. 3: Mechanism Analysis.

In case, everything is correctly defined, CATIA sends a message to a user, that the created mechanism can be simulated – the designer can run the simulation. The user can easily simulate motion using the mouse.
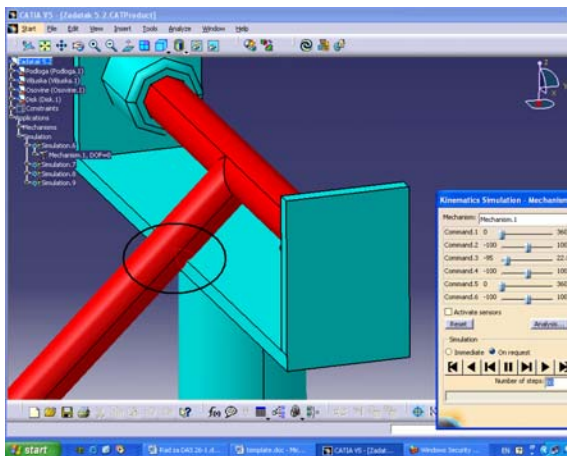
Fig. 4: Detected collision.

During mock-up design review, users do not only need to view simulated kinematics but also analyze the mechanism's consistency with the functional specifications. *DMU Kinematics*

Simulator performs interference and clearance checking as well as computing the minimum distance. A 'stop on collision' option freezes the motion for detailed analysis (Fig. 4).

Finally, the user can replay a motion simulation, or save it as a video file.

Kinematic simulation of the presented mechanism in Virtual Reality is given in the addition (presentation) of this paper.

3. Conclusions

After this research, it can be concluded that CATIA software makes it possible to define, create, analyze and simulate mechanisms. A CATIA model is fully associative to the assemblies that reference it: changes to the model are automatically reflected in the associated assemblies. Mechanisms can be generated automatically from mechanical assembly constraints defined in *Assembly Design* allowing quick and easy definition of mechanisms. CATIA analyzes mechanism motion dynamically with visual feedback by checking limits and interferences. It is possible to simulate the motion of only one selected joint as well as to simulate the overall motion of the mechanism at the same time.

The final goal of this research has been reached: the author succeeded to simulate the mechanism. Simulations are saved as an AVI files and they are presented to students on Mechanics lessons. This way of teaching students certainly has great effects and makes students more motivated in solving their tasks on this subject.

4. References

[1] F. Karam, C. Kleismit, Catia V5. Thomson Learning, CopyRight 2004.
[2] G. N. Zamani, M. J. Weaver, Catia V5, Dizajn mehanizama i njihova animacija. Kompjuter biblioteka, Beograd 2007.

DEVELOPMENT OF A FRETTING TESTING AND EVALUATION METHOD

Johannes Reiser [1], István Gòdor[1], Wilfried Eichlseder[1]

[1] University of Leoben, Chair of mechanical engineering , Franz-Josef-Str. 18, 8700 Leoben, Austria.

Corresponding author: johannes.reiser@unileoben.ac.at

1. Introduction

Stronger, faster, and lighter, are the goals engineers have to achieve simultaneously. These guidelines are realized by optimizing the structure of components to weight considerations which eventually might lead to compliance in microscopic scale. Due to microscopic relative motion at the interfaces of components, fretting starts to damage the surface and could further lead to their failure. Fretting could be prevented by use of appropriate material combinations. To test the fretting resistance of different material combinations a testing and evaluation method has been developed.

2. Experimental Setup

Fretting wear tests have been performed on fretting testing rig developed at the chair of mechanical engineering shown in Fig. 1
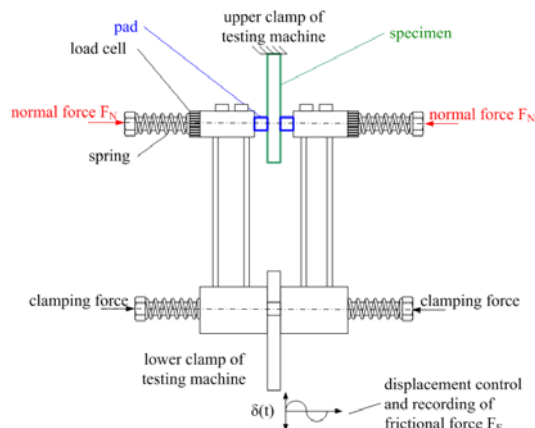
Fig.1: Schema of Fretting Testing Rig.

FE-Simulation of the rig has been performed to understand the behaviour of the rig during testing and for damage analysis of specimen. Tests have been carried out with different test configurations and as reference, steel pads in combination with grinded steel specimen have been considered. For comparison of the results, specimens have been coated with a metallic coating. The tests have been performed on a servohydraulic test bench in displacement controlled mode with an amplitude δ of 70μm. The pads have been pressed against the specimen with a constant normal force of 1,05kN which results in contact pressure of 15MPa between pad and specimen. The force was controlled by using load cells. The force needed by the test bench for applying the amplitude of motion was recorded for later analysis.

3. Experimental Results

Each fretting test got a special type of damage on the surface of the specimen which, in combination with analysis of the recorded test data, gives the characteristic behaviour of the different test configurations. For further interpretation of the fretting behaviour, the recorded data was used, to draw the evolution of the coefficient of friction μ. The evolution of coefficient of friction μ is shown in Fig. 2.
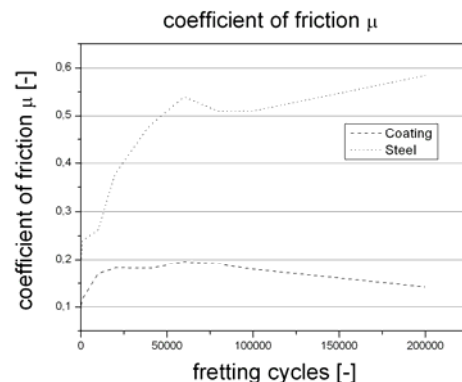
Fig.2: Evolution of Coefficient of Friction

The evolution of COF shows that in steel-steel contact of the reference, the curve begins at a higher value than on coated contacts and then starts to increase, while coated contacts show a low coefficient of friction over the whole testing cycle. For investigation of dissipated energy during fretting testing, the

friction force was plotted over the displacement as shown in Fig.3.
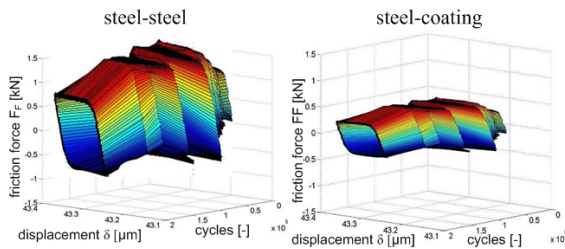
Fig.3: Fretting hysteresis of steel and coating

The size of the curves represents the dissipated energy so it is clear that more energy was dissipated in steel-steel contact, than in contact of steel-coating. As fretting not only depends on dissipated energy but also in combination with surface damage, the degraded surface volume was evaluated by using laser confocal microscopy. In Fig.4 the 3D view of the surfaces is shown.
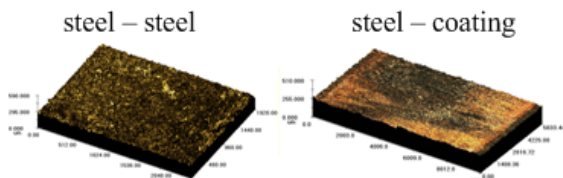
Fig.4: 3D plot of specimen surface

To distinguish the types of damage, the surfaces of the specimen have been examined by using scanning electron microscope. The difference can clearly be seen in Fig.5. The steel surface shows a degraded and damaged wavy structure in contrast to the coated surface, which shows nearly no damage and just a slight degradation of the coating.
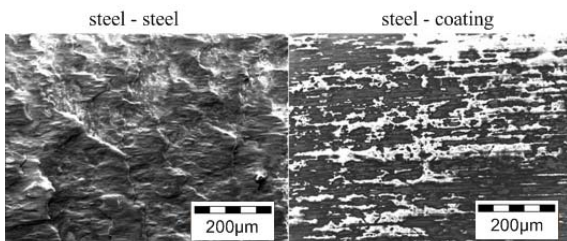
Fig.5: SEM micrography of steel and coated surface

So the main task is to combine the results of coefficient of friction, dissipated energy, worn volume and further, the SEM analysis of the damaged surfaces to create a guideline for fretting resistance. Therefore the wear energy density e_V [kJ/mm3] was calculated for both contact configurations. The result is depicted in Fig.6. It can be seen that the coated surface shows a higher value of wear energy density than the steel surface. So at first sight, it seems

clear, that the higher the wear energy density, the higher is the resistance against fretting.
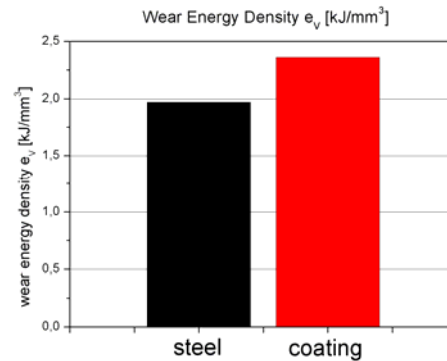
Fig.6: Wear energy density e_V

But taking a closer look, the difference in wear energy density is not that big, so it is very important to also have a closer look at the SEM micrographs, which confirm the higher fretting resistance of the coated surface relative to the steel surface.

4. Conclusion

The presented method allows the evaluation of fretting resistance of different surface conditions. This is done by combining the results of recorded test data with visual inspection of the corresponding SEM micrographs to ensure that the calculated wear energy density gives a reliable ranking of fretting resistance.

5. Acknowledgements

6. References

[1] Reiser J., Diploma Thesis, Development of a fretting testing and evaluation method, Chair of mechanical Engineering, University of Leoben, 2008

ASSESSMENT OF BRIDGE CRANES RESIDUAL LIFE

Eugeniusz Rusiński[1], Marcin Kowalczyk[1], Przemysław Moczko[1], Zaklina Stamboliska[2]

[1]Wroclaw University of Technology, Faculty of Mechanical Engineering; ul. Lukasiewicza 7/9, 50-371 Wroclaw, Poland

[2] CEMENTARNICA "USJE" A.D – SKOPJE, Macedonia

Corresponding author: przemyslaw.moczko@pwr.wroc.pl

1. Object characteristic

Many different types of cranes are widely used in industry. Lifetime of each crane is limited by standards and by designing requirements as well. However old cranes not always have to be replaced by new structures. In order to estimate residual life of load carrying structures of worn cranes it is necessary to obtain information about stress level, exploitation loads and overall condition (non destructive tests). Comparison of design and exploitation loads can give useful information about condition of the crane. Based on such approach measurements of exploitation loads of bridge cranes were performed to estimate condition of their load carrying structures. Figure 1 presents one of investigations objects. It is bridge crane 30 m span and 9 t capacity.

Fig. 1. The bridge crane - 30 m bridge, 9 t capacity

2. Measuring system

Measuring system was installed on the trolleys structures. The system consists of the following items:

a) Strain gauges – located on the trolley main beam, which transfer the loads coming from the basket through trolley wheels to the bridge of the crane; this location has advantage in comparison with bottom flange of bridge location, that is independent from differ locations of the trolley on the bridge.

b) Accelerometers – PCB PIEZOTRONICS type M393B04, range 0,06 – 450 Hz – located on the trolley to measure operational accelerations in directions: X – along crane rail, Y – along trolley rail, Z – vertical;

c) Spectrum analyser - LMS SCADAS MOBILE VB8, 102.4 kHz sampling rate per channel, 24 bit resolution, 105 dB signal-to-noise ratio – for data acquisition and signal conditioning.

d) Computer – for measuring system control.

The system is capable to measure following data: strain, which represents load (after calibration) of the crane,

acceleration – measured in 3 directions: X – along crane rail, Y – along trolley rail, Z – vertical.

After installation the system (figure 2) was calibrated with loads applied to basket. The calibration was done to record answer of the strain gauges to particular loads (2, 4 or 8 tons) and evaluates calibration factors for cranes operation measurements.

Fig. 2. Measuring system - strain gauges fixed to trolley structure

3. Results of measurements

Results of measurements are time signals of vertical loads and accelerations in three orthogonal directions. Figure 3 presents three cycles of crane operation (loading of basket, travel of the crane, discharge of basket). Figure

4 presents time signal of accelerations during normal operation of the crane. Acceleration presented on the graph concerns acceleration loads of the crane along rails. The following results from measurements are obtained:

static loads do not exceeds design values-9t,

dynamic loads are within standards [1-3] coefficients,

operation accelerations do not exceeds design values – 0.5 m/s2,

no static or dynamic overloads were observed during measurements.
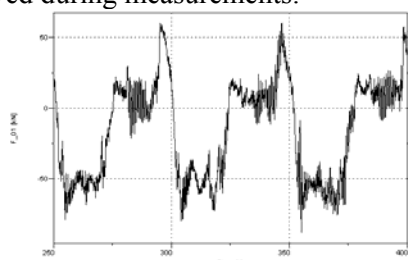
Fig. 3. Time signal of operation load in [kN]
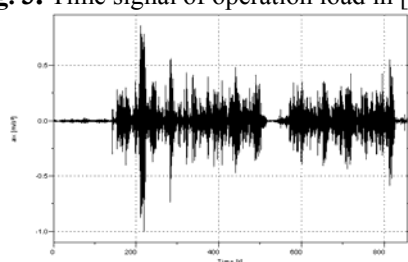
Fig. 4. Time signal of acceleration, ax [m/s2]

4. Strength analysis

Based on the measurements results the finite element method [1,3] has been used to estimate stress level in the crane to perform strength and fatigue calculations. Schell elements were used for discretisation of the crane model. Loads and restraints of the shaft were applied in consideration of measurements results and standards [4-6]. The following loads combinations were considered in the strength calculations:

A1.1 – unsteady crane travel with full basket – trolley in the middle and side end position

A1.2 – unsteady trolley travel with full basket

A3 – unsteady bucket with material lifting - trolley in the middle and side end position

A4.1 – unsteady crane travel with full basket, additional vertical rail joints loads – trolley in the middle and side end position

B5.1 – bridge travel diagonal loads - trolley in the side end position

B5.2 – trolley travel diagonal loads - trolley in the middle and side end position

C1 – lifting of the full basket with maximum speed - trolley in the middle position

The maximum stress level according tu Huber-Mises theory equals σ_{red} = 150 MPa (fig. 5) for A1.1 load combination.
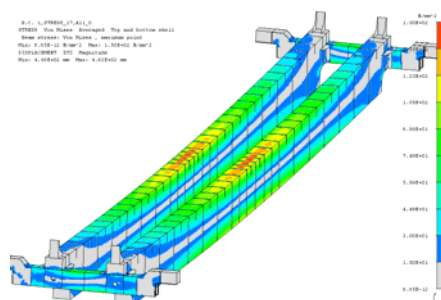
Fig. 5. Huber-Misses stress in the crane – load combination – A1.1

5. Acknowledgements

Based on loads measurements, finite element method calculations and non-destructive tests, final assessment of the cranes load carrying structures can be given. Such complete approach is the best way to estimate residual life of old structures and to optimise maintenance costs. Considering results of investigation in the presented example, there is no need to stop operation of the cranes. In order to assure safety of operation periodical checks (visual and NDT) have to be carried out.

6. References

[1] Zienkiewicz O.C., Taylor R.L.: The finite element method. Vol. 1, Vol. 2. McGraw-Hill Bool Company, London 1991.

[2] Rusiński E., "Finite Element Method; System COSMOS/M" (in Polish), WKŁ, Warsaw 1994

[3] Rusiński E., Czmochowski J., Smolnicki T.: Advanced Finite Element Method for Load-carrying Structures of Machines (in Polish), Oficyna Wydawnicza PWr., Wroclaw 2000

[4] PN-EN 13001-1:2007 – Crane safety. General design. General principles and requirements

[5] PN-EN 13001-2:2004 - Crane safety. General design. Load effect

[6] PN-79/M-06515 - Cranes. Design rules.

MULTIAXIAL FATIGUE TESTING AND PREDICTION

Milan Růžička[1], Miroslav Balda[2], Jan Papuga[1], Zbyněk Hrubý[1], Aleš Hodr[1]

[1]Czech Technical University (CTU) in Prague, Faculty of Mechanical Engineering,
Technicka 4, 166 07 Prague, Czech Republic

[2]Centre of Material Diagnostics (CMD), Institute of Thermomechanics, Academy of Sciences of the
Czech Republic
Veleslavínova 11, 301 14 Pilsen, Czech Republic

Corresponding author: milan.ruzicka@fs.cvut.cz

1. Introduction

Multiaxial loading is quite a complicated teaser, if its effect on fatigue life or a fatigue limit has to be evaluated. If the individual load channels act non-proportionally a further hardening caused by a rotation of principal axes is induced. Methods for multiaxial high-cycle fatigue calculations have one very pleasing attribute - they do not require so much computational effort as low-cycle methods burdened by plasticity effects. This seems to be one of the reasons, why every year several new methods are published in this category.

A long-term mapping of predictive capability of a set of calculation methods was started at the CTU in Prague [1]. During our research practice, the software called PragTic was build to help us in performing all those complicated calculations accompanying the multiaxial solution. In addition to this development, the use of PragTic allowed to test a lot of criteria on large amount of the multiaxial high-cycle fatigue data published abroad. That way was born the FatLim database. FatLim currently sums up results of computations by 18 different calculation methods over 428 experimental points. Both PragTic as well as FatLim are freely available on the website [2]. Thanks to the structure of PragTic's code it is relatively easy to implement new criteria there and to test their adequacy on experimental results according FatLim database.

Any multiaxial fatigue calculation in the region of finite life is a complicated matter, because some cycles exceed the cyclic yield stress. The induced plasticity corresponds to a form of energy accumulation, release of which is at last accompanied by a formation of micro-cracks. Nevertheless, the necessity to involve the plasticity into the FE-solution presents a very unfavourable obstacle for any engineering application. First, the use of elastic-plastic model in the FE-calculation slowdowns it's processing. Second, use of such a solution for cases with applied random or very long load history is not realistic due to very long computational time. Therefore, methods applied Power Spectral Density (PSD) are used recently.

Experimental investigation, fatigue life prediction methodology and results will be described in the poster contribution.

2. Two channel loading tests by constant amplitude and their evaluation

The material used in our experimental program was CSN 411523 carbon steel of the Czech provenience. The specimens had shapes of a smooth and notched tube of the outer diameter 30 mm and the wall thickness 2 mm in the critical cross-section. The notch for crack initiation was created by a hole of 3 mm in diameter.

Tests were performed on the electro-hydraulic two channels loading machine by combined push-pull and torsion loading. Within years 2006-2008 eight different types of the load paths with constant amplitudes of normal and shear stress was experimentally and computationally investigated. Shapes of load paths in the coordinates normal and shear stress are visible from Fig. 1.

The results were described in [3] in detail. The new own multiaxial approaches, Papuga
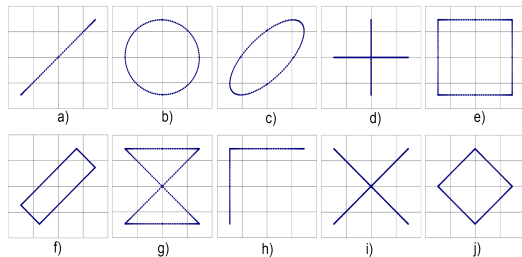
Fig. 1 *Shape of the load paths*

Critical Plane (PCr) and Papuga Integral (PI) methods developed for unlimited fatigue life were investigated and published in [1], and further tested in [4]. These procedures were later enlarged also for high cycle fatigue region, as the PCF criteria.

Many uniaxial and multiaxial fatigue criteria were compared by an evaluation of all load paths (for example Papuga's PCr and PI methods, Feltner and Morrow energetic criteria, SWT parameter, Watson&Topper and Socie methods, Wang&Brown method). Further, the Papuga Critical Plane (PCr) method was enlarged for a use in the finite life region. Its implementation was tested on the same experimental data. Results showed that PCF procedure is usable for high cycle fatigue region. The evaluation was published in [5].

3. Two channel loading tests by stochastic loading and their evaluation

Nowadays research is focused on utilization of PSD for generating of the fatigue loading sequences and fatigue life prediction. Computed programs used for generating of Gaussian processes with prescribed PSD and their implementation on electro-hydraulic testing machines for combined loading were developed. Notched tube specimens were loaded by random tensile forces and in torque with different PSD shapes. One type of the four next potential combinations is described in Fig. 2. Since the machine does not interpret input processes precisely, the actual processes were measured, iterated and processed into a complex damaging stress and its spectral properties. These results will be presented on the symposium.
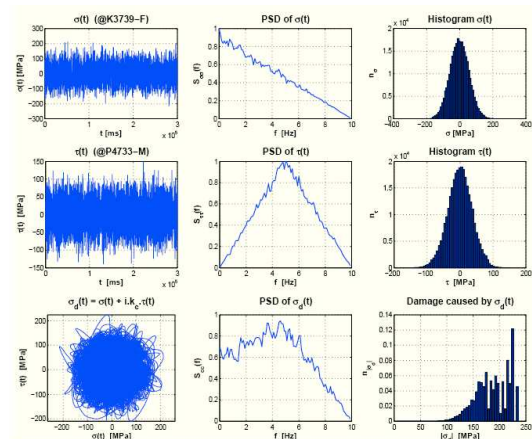
Fig. 2 *Stochastic loadings and their*

4. Conclusion

The use of the original PCr method (for a fatigue limit region) as well as FCF criteria (for high cycle fatigue) was proved to give good results for number of two channel loading paths (in the tension and torsion with constant amplitudes).

A rule of combination of standard deviations was proposed for evaluation of two channel loading tests by stochastic loading with prescribed PSD. This criterion showed very good accordance with experimental results.

5. Acknowledgements

6. References

[1] Papuga, J.: Mapping of Fatigue Damages - Program Shell of FE-Calculation. [PhD Thesis], CTU in Prague 2005.

[2] http://www.pragtic.com

[3] Papuga, J., Hrubý, Z., Růžička: Load Path Effect under Multiaxial Load Conditions. The Sixth International Conference on Low Cycle Fatigue, Berlin (Germany), 8th to 12th September 2008, pp. 312-318.

[4] Papuga, J, Růžička, M.: Two new multiaxial criteria for high cycle fatigue computation. International Journal of Fatigue, 30, 2008. pp. 58 – 66

[5] Růžička, M., Papuga, J., Hrubý, Z., Doubrava, K: Use of elastic stresses for a multiaxial fatigue prediction. J. Applied and Computational Mechanics, 1, 2007. pp. 631 – 640.

POSSIBILITIES TO REDUCE THE STRESS CONCENTRATION IN ADHESIVE BONDED JOINTS

**Marin Sandu [1], Adriana Sandu [1], Dan Mihai Constantinescu [1],
Matei Miron [1], Dragoş Apostol [1]**

[1] University POLITEHNICA of Bucharest, Department of Strength of Materials,
Splaiul Independentei nr. 313, 060042 Bucharest, Romania.

Corresponding author: marin_sandu@yahoo.com

1. Introduction

Adhesive bonding is a particularly effective method of assembling complex structures, especially those made from dissimilar materials.

In order to ensure efficiency, safety and reliability of bonded joints, an adequate understanding of their behaviour is necessary. A lot of work concerning the stress analysis, mathematical modelling and experimental study of adhesive bonded joints has been done. In almost all published researches only two stress components (shear stress and transverse peel stress) have been considered, but the deformation field near the edge of a joint is three-dimensional. Consequently the Finite Element Analysis (FEA) is the most adequate in order to study the influence of various geometric modifications on the stress state in the joints. Papers [1]-[5] show the beneficial effect of different configurations of tapering the ends of the adherends in the overlap area.

This work focuses on the evaluation of the stress concentration in some geometrical configurations of adhesively bonded single-strapped joints based on finite element analyses. Earlier studies have shown that the single strap joint configuration is less efficient than the single lap joint. However, in paper [6] it was demonstrated that strapped joints (Fig. 1,a) can be as efficient as lap joints as long as they are properly designed and an analytical model for determining the deformations in balanced and unbalanced single-strap joints was presented. In the case of single-strapped joints the differential equations that govern the distribution of peel and shear stresses in the adhesive are coupled and only a numerical solution can be obtained.

The single-strapped joint is currently used in aircraft repairs where a good solution as the double-strapped joint is not applicable because the external surface of the structure needs to be smooth. The simpler method to increase the strength of a single-strapped joint (Fig. 1,a) is to use a strap thicker than the assembled sheets [1].

2. Results of FEAs

In order to emphasize the strong influence of the design on the joints stress states, many FEAs were done. In all cases the adherends were made of aluminium 2024 T3 with the ultimate strength R_m = 480 MPa, the modulus of elasticity E = 73000 MPa and the Poisson's ratio v = 0.33. The adhesive was AV 119 (also known as Araldite® 2007), which have modulus of elasticity E_a = 3000 MPa, the Poisson's ratio v_a = 0.34, the tensile strength σ_r = 70 MPa and the shear strength τ_r = 47 MPa.
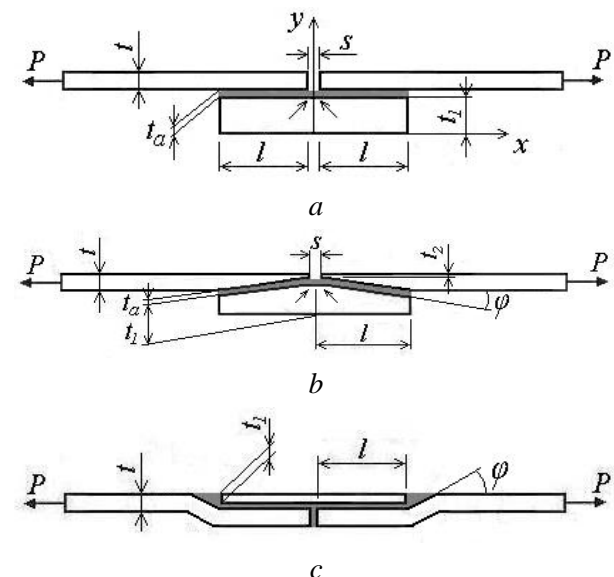
Fig. 1: Three variants of single strapped joint that will be compared

Single-strapped joints having various overlap lengths and different ratios between the thicknesses t and t_1 were analyzed. The adhesive layer thickness and the joint width were the same in all cases, t_a = 0.25 mm and b = 25 mm.

Due to the symmetry, a finite element model will contain only half of the analyzed joint. Fig. 2 presents the variation of the stresses from the middle to the right end of a single lap joint (Fig. 1,a) that have $t = 2$ mm, $t_1 = 5$ mm and $l = 19$ mm. For inter-comparative purposes, the equivalent stresses (σ_{eq}), the peel, shear an tensile stresses (σ_y, τ_{xy}, σ_x) were normalized with respect to the nominal tensile stress induced into the adherends $\sigma_n = P/(b\,t)$. In the case of configurations a and b (Fig. 1), the key factor in the reduction of stress peaks in the adherends and adhesive was to increase the ratio t_1/t, while for the variant c beneficial effects were obtained by decreasing this ratio.
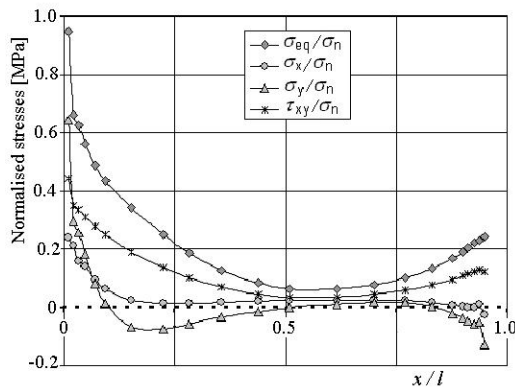
Fig. 2: Normalised stresses into the adhesive layer of single lap joint

Plastic zones can occur at relatively low loading levels due to the presence of high peel and shear stresses in the middle of the joint. Shear and peel stress concentrations reduce the load capacity of the joint and are controlled by geometric and material parameters (e.g. adherends thickness, overlap length, adhesive layer thickness, adhesive fillet geometry, adherend tensile modulus, adherend and adhesive Poisson's ratio, adhesive shear modulus).

In the cases a and b, the highest values of stresses in the adhesive appear in the points indicated by arrows in Fig. 1. In Tab. 1 the values of the stresses in these points are presented. Practically there are no bending stresses in the adherends, but the maximum bending stresses into the straps were in between $1.8\sigma_n$ and $2.8\sigma_n$.

The normalised stresses in case of the joint variant c, with strap and adherends from aluminium, having $t = 2$ mm, $t_1 = 0.75$ mm and $l = 25$ mm, are indicated in Tab. 2.

Thicknesses [mm]	$\dfrac{\sigma_{eq}}{\sigma_n}$	$\dfrac{\sigma_x}{\sigma_n}$	$\dfrac{\sigma_y}{\sigma_n}$	$\dfrac{\tau_{xy}}{\sigma_n}$
$t=2$; $t_1=5$	0.49	0.15	0.19	0.27
$t=2$; $t_1=4$	0.58	0.18	0.22	0.31
$t=2$; $t_1=3$	0.69	0.22	0.27	0.37
$t=2$; $t_1=2$	0.71	0.23	0.31	0.39

Tab. 1: Maximum normalised stresses in adhesive in case of joint variant b (Fig. 1)

Component of the joint	$\dfrac{\sigma_{eq}}{\sigma_n}$	$\dfrac{\sigma_x}{\sigma_n}$	$\dfrac{\sigma_y}{\sigma_n}$	$\dfrac{\tau_{xy}}{\sigma_n}$
Strap	1.28	1.45	0	0
Adherends	2.11	2.70	0.42	0.31
Adhesive	0.51	0.39	0.13	0.26

Tab. 2: Maximum normalised stresses in adhesive in case of joint variant c (Fig. 1)

The maximum lateral deflection at the middle of a specimen with the total length of 200 mm was of 0.775 mm. If the strap is made of steel, this deflection decreases at 0.322 mm, while the maximum stresses will be modified a little comparing with those from Tab. 2.

3. References

[1] M. Sandu, A. Sandu, D.M. Constantinescu, St. Sorohan, The effect of geometry and material properties on the load capacity of single-strapped adhesive bonded joints. Key Engineering Materials, Vol. 399 (2009) 89-96

[2] M. Davies, D. Bond, Principles and practices of adhesive bonded structural joints and repairs. International Journal of Adhesion and Adhesives (IJAA), 19 (1999) 91-105

[3] A. Rispler, L. Tong, G. Steven, M. Wisnom, Shape optimization of adhesive fillet. IJAA, Vol. 20 (2000) 221-231

[4] Min You et al., A numerical study of adhesively bonded aluminum single lap joints with an inner chamfer on the adherends. IJAA, Vol. 28 (2007) 71-76

[5] G. Belingardi, L. Goglio, A. Tarditi, Investigating the effect of spew and chamfer size on the stresses in metal/plastic adhesive joints. IJAA, Vol. 22 (2002) 273-282

[6] K. Shahin, F. Taheri, Analysis of deformations and stresses in balanced and unbalanced adhesively bonded single-strap joints. Composite structures, Vol. 81 (2007) 511-524

EXPERIMENTAL VERIFICATION OF THE STRESS DISTRIBUTION IN THE CRANE MAST

Momir Šarenac[1], Miroslav Milutinović[2], Hotimir Ličen[3]

[1),2)] University in East Sarajevo, Faculty of Mechanical Engeneering, Vuka Karadžića Str. 30, 71123 East Sarajevo, BiH

[3)] University in Novi Sad, Faculty of Tehnical Sciences, trg Dositeja Obradovića 6, 21000 Novi Sad, Serbia

Corresponding author: m.milutinovic82@gmail.com

1. Introduction

Crane (Figure 1) has been repaired after damage and htan analysis of stress conditions and arow deformation was carried out. Figure 1 shows area of a variation slope by applying experimental measuring and numerical calculation angles, the length of arrows and crane loads.
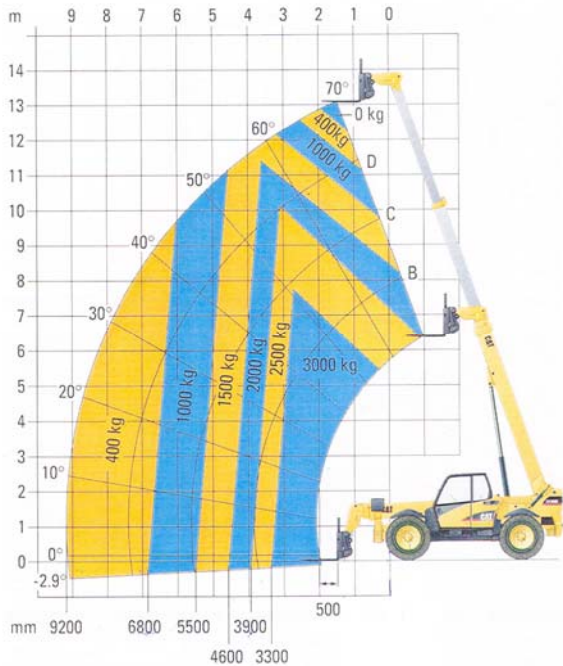
Fig. 1 Area of slope angles variations, the length of arrows and crane loads

2. Measurement of stress and deformation

Measurement is performed by applying the strain gauges at a distance of 1150 mm from the point of force action which burdens console. Cross section of console with the measuring tapes arrangement is given on Figure 3.
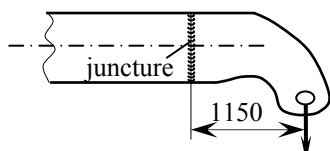
Fig. 2 Position of juncture in relation to the external load
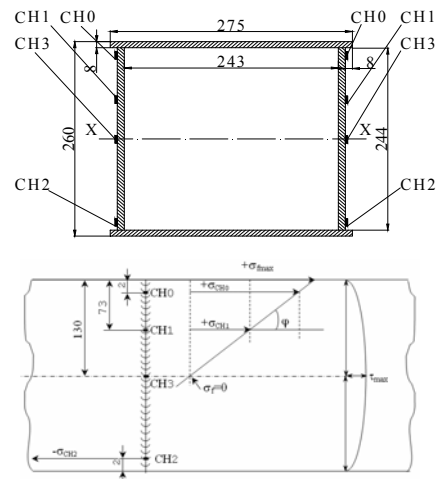
Fig. 3 Dimensions of cross section

On the basis of the cross section and length of arrows, stress calculation and deformations results were obtained. In order to make a review of calculated values of stress in the junction zone experimental measurement has been performed.

For this purpose method with measurement tapes – tensometry was used. Figure 2 shows arrangement of regarding to console edge.

In Figure 4 is shown a diagram with measured values for the following data:

$$m=430kg, \quad l=2650mm, \quad \alpha=10^o$$
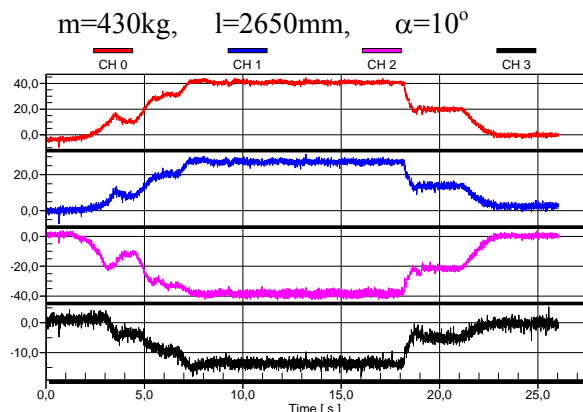
Fig. 4 Measured deformation values

In the diagram on the Figure 4 we can see the values of the deformation given in Table 1.

Tab. 1

	CH0	CH1	CH2	CH3
max	41μm/m	27μm/m	-40μm/m	-14μm/m

Measuring results are obtained for other variations of parameters,to in the identical way so stress can be calculated at all locations where the are settled. In tables 2 and 3 are shown values for the same angle $\alpha=10^o$, and for two different values only of load and length.

Tab. 2 (m=430kg, l=8600mm, $\alpha=10^o$)

	CH0	CH1	CH2	CH3
max	45μm/m	28μm/m	-42μm/m	-15μm/m

Tab. 3 (m=2090kg, l=3400mm, $\alpha=10^o$)

	CH0	CH1	CH2	CH3
max	237μm/m	138μm/m	-236μm/m	-75μm/m

3. Analysis of measurement results

Measurement results were obtained on the basis of symmetrically arranged in relation to axis x of arow. CH0 make the first measurement position, on the identical manner measurement tapes CH1 make the second measurement place, CH2 and CH3 third and fourth measurement place. CH0 is set for measuring the highest stress in the arrows, while the CH1 set for measuring stress and checking linear stress distribution in the arrow. CH2 is glued symmetrically regarding to the axis x with measurement tape CH0 to check if the stress is the same as CH0 but with a different sign. CH3 is the rose-shaped, placed on the neutral bending axis and it is measuring the maximum stress to the shearing caused by bending moment. Results obtained by using of are completely consistent with the results obtained by calculations. Figure 3 shows one of a number of diagrams that are obtained by experiment. This diagram considering variations of angles (10°, 35° and 55°), the length of arrows (2650, 3400, 4450 and 8600mm) and mass load 430kg and 2090kg.

4. Numerical verification

In order to have correct results obtained from measurements and calculation there is numerical verification by method of finite elements. On the following figure 5 the finite element for angle of 10°, the length of 1650mm and loads of 4218.3 N is given. Identically, analysis for other angles, length and load is done. This method shows that there aren`t critical palces where the arrows lead to fracture in the working conditions, during raising the load.
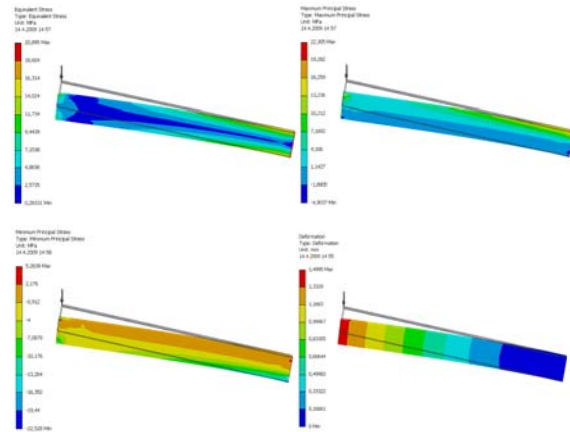
Fig. 5. Results of numerical analysis

5.Conclusion

Deductive analysis of the state of stress and deformation in the crane arrows show that changing angles and load of arrows do not affect on the variation of stress intensity and deformation. Damages are obviously consequences of incorrect handling crane. The effect of pressure stress is very low giving the overall size of stress compared to the bending stress. Bending stress intensity does not significantly depend of the arrow angle because specific form of its and its working bodies.

6. REFERENCES

[1] Ernest O. Debelin, Measurement Systems, Application and Design, Department of Mechanical Engineering, the Ohio State University, 1990, PP.220-233.

[2] A.Ajovalasit, L.D`Acquisto, S. Fragapane, B. Zuccarello, On the Stiffness and the Reinforcement Effect of Electrical Resistance Strain Gauges, Applied Mechanics and Materials, vol.3-4, page 349-354, 2005.

DEVELOPMENT OF A TEST METHODOLOGY FOR THE SYSTEM PISTON RING – CYLINDER LINER

Jürgen Schiffer [1), István Gódor [1), Florian Grün [1), Wilfried Eichlseder [1)

[1) University of Leoben, Department Product Engineering / Chair of Mechanical Engineering,

Franz-Josef-Str. 18, 8700 Leoben, Austria.

Corresponding author: juergen.schiffer@unileoben.ac.at

1. Introduction

Stringent legal requirements, rising demands of reliability and growing technical standards lead to an increase in the thermal, mechanical and tribological loads on the components of combustion engines. Hence, the tribological system of piston ring – cylinder liner is of particular interest. The optimization process has to consider the complete tribosystem which is shown in Fig. 1.
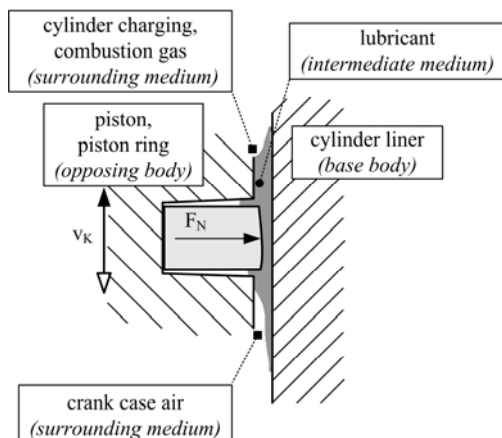
Fig. 1: Tribological system piston ring – cylinder liner

It is necessary to investigate the effects of materials, surface conditions and lubricants on the complete tribological system [1]. It is indeed possible to analyse the system using engine tests, but they are very cost intensive and the test results are, sometimes, difficult to interpret. Therefore, we designed a new test method, which is based on an analogous model [2]. The base material of the cylinder liner is cast iron (GG25). The piston rings are coated with a chrome-ceramic-layer.

2. Experimental Setup

The test rig TE77 (high frequency friction machine) of Phoenix Tribology was used for the tribological investigation of the described system. Fig. 2 shows the test configuration with the analogous test model ring-on-liner. The two specimen were cut out from a real component of a gas engine from GE Jenbacher GmbH & Co OHG. An important point of all investigations is the conformity between the two specimens. To guarantee the conformity, a light-gap-methodology is applied [3].
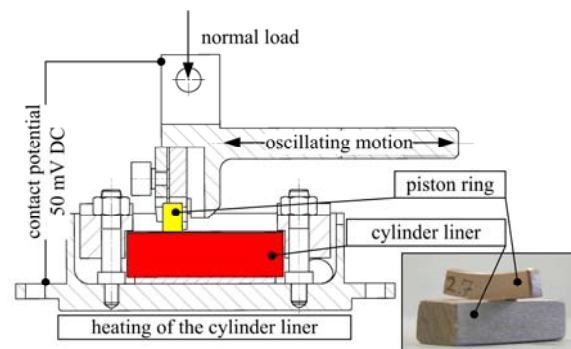
Fig. 2: Test configuration ring-on-liner

The cylinder liner is installed in a case. This case is mounted and is linearly adjustable on the heating plate. The piston ring is installed with an adapter on the driving rod. This rod applies the reciprocating movement and the normal load. On the right side of the cylinder liner the lubricant (gas engine oil) is applied via drip-feed. To ensure equivalent conditions of temperature in combustion engines, the cylinder liner is heated by four heating cartridges, located beneath the case.

Test data was continuously recorded. A typical plot of measured data is shown in Fig. 3. Coefficient of friction, frequency, normal load, contact potential and temperature are plotted over test time. The specimen temperature is measured in the middle of the cylinder liner, while the contact-near-temperature is measured at a hole drilled in the piston ring close to the contact surface. The contact potential represents the electrical resistance between piston ring and cylinder liner and is further used for qualitative

determination of the boundary layer and the tribofilms formed.
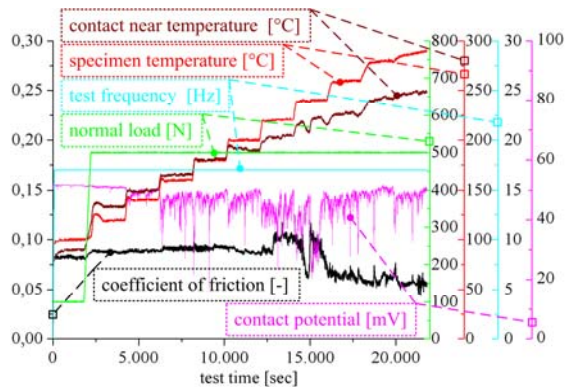
Fig. 3: Typical plot of measured data

3. Experimental Strategies and Results

The described component scale test configuration allows conducting damage-equivalent investigations of the system piston ring – cylinder liner. After reference tests have been performed, different test strategies were developed:

- *Seizure test:* Investigation of the thermal stability of the system.

- *Test with stepped parameters:* Analysis of dependence between coefficient of friction, frequency and normal load.

- *Long-time test with constant parameters:* Investigation of running-in- and long term sliding and wear characteristics.

Further we designed an Arizona-Dust test methodology to replicate the operating condition with oil of insufficient purity.

Fig. 4 shows a characteristic light micrograph of a cylinder liner and piston ring after a long-time test with the following test parameters:

- Normal load: 1000 N (~40 MPa)

- Frequency: 20 Hz

- Contact near temperature: approx. 230 °C

- Test time: 100 h

The plateau hone micro topography of the cylinder liner fulfilled its function. The large plateaus bear the load, whereas, the deep primary-hone-scores store the lubricant. Due to the running-in and wear process of the cylinder liner, base material is degraded and hard phases (called Steadit) remain in the contact zone. The piston ring shows an acceptable damage.
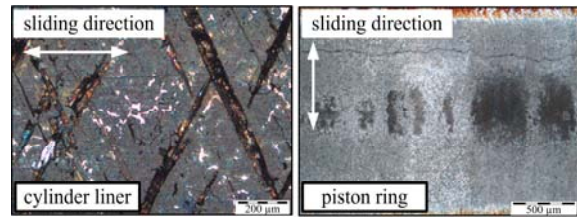
Fig. 4: Cylinder liner and piston ring after a long-time test

Generally at higher loads and temperatures, partial wear-protection layers (so called tribofilms) start to build up.

4. Conclusion

With the shown test methodology it is possible to accomplish damage-equivalent tests with high quality measurement results. The results with base material GG25 are our benchmark. Further optimization of the system concerning topography, base material and optional thermal treatment is possible.

5. Acknowledgements

6. References

[1] Andersson P., Tamminen J., Sandström C.-E.: "Piston ring tribology – A literature survey", VTT Research notes 2178, ESPOO 2002

[2] Schiffer J.: "Development of a damage equivalent test methodology for the system piston ring-cylinder liner", Diploma thesis, University of Leoben, Chair of Mechanical Engineering, 2009

[3] Krampl H.: „Influence of the surface topography on the tribological system piston ring – cylinder liner", Project thesis, University of Leoben, Chair of Mechanical Engineering, 2009

THERMOMECHANICAL CHARACTERISATION OF POLYMERS AND THEIR COMPOSITES

M. Schoenfeld [a], J. Saupe [b], H.J. Feige [a], J. Grimm [b], J. Vogel [a]

[a] Dept. of Applied Mechanics, [b] Dept. of MEMS, University of Applied Sciences Zwickau, Dr.-Friedrichs-Ring 2A, D-08056 Zwickau, Germany,

Corresponding author: maik.schoenfeld@fh-zwickau.de

1. Introduction

Polymers are increasingly used in different industries starting from automotive and aeronautical engineering up to medicine or micro electromechanical systems (MEMS). To ensure product functionality and reliability the materials as well as the components are mechanically and/or thermally tested in a wide range. Different measuring techniques are applied to determine their material properties like stress-strain-curves, YOUNG's modulus or tensile strength. In the following, dynamic mechanical analysis (DMA), digital image correlation (DIC) and nanoindentation have been used to characterise polymer materials and their fibre-reinforced composites.

2. Experimental techniques

Polymers have distinct temperature depending material properties. Characteristic material parameters are the storage modulus E′, the loss modulus E′′ and the loss factor tan δ. The **Dynamic Mechanical Analyser** (DMA 242 C/1/G from Netzsch GmbH Selb) is a powerful system to analyse these parameters. Different load modes are available, for example three-point-bending (3PB), tension, compression or linear shearing. In the following 3PB is used, Fig. 1.
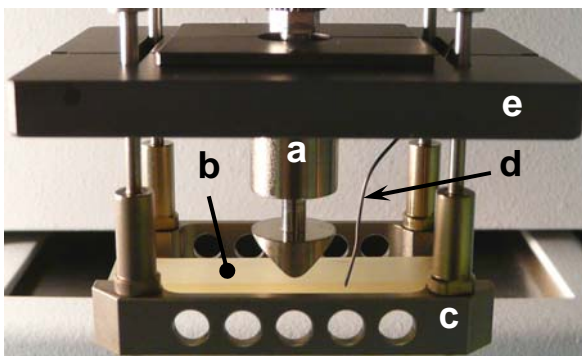
Fig. 1   3PB load module with Araldite B specimen
a) pushing rod b) specimen c) support (l_{Sup} = 40 mm)
d) thermocouple e) radiation shield

Measurements are performed on Araldite B specimens (50 mm x 8 mm x 3 mm), Fig 2. Storage modulus E′ and loss factor tan δ are measured for a temperature range from 22 °C up to 150 °C under sinusoidal loading at two discrete frequencies 1 Hz and 50 Hz.
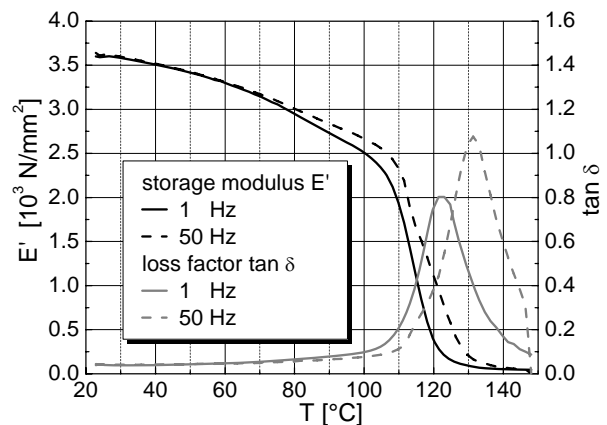
Fig. 2   Temperature and frequency dependent storage modulus and loss factor of Araldite B
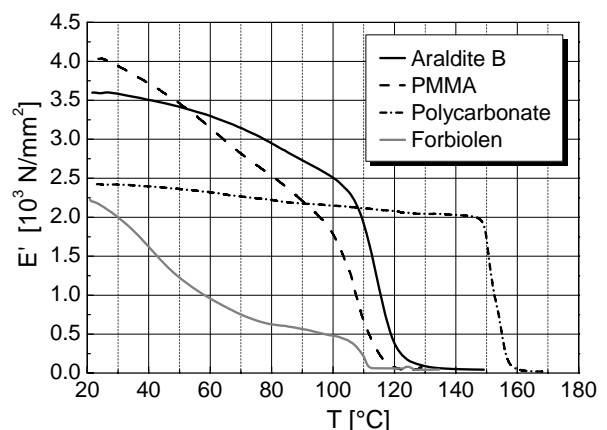
Fig. 3   Storage modulus of different polymers and composites as function of temperature

To analyse frequency and temperature dependent differences in storage modulus DMA is a powerful tool to compare different polymers and their fibre-reinforced composites. Fig. 3 shows the temperature dependent E' of epoxy resign Araldite B, PMMA and Polycarbonate. In addition to the

polymers, an innovative natural fibre composite, called Forbiolen, has been tested. Furthermore, the glass transition temperature T_g can be determined. Its critical value occurs approx. at the maximum of loss factor tan δ.

To analyse the deformation behaviour of thin polymer foils non-destructive **tensile test** and **digital image correlation** (**DIC**) are combined, Fig. 4. The sample is displacement-controlled loaded in a universal testing machine Z005/TN2A from Zwick GmbH & Co. Ulm up to a predefined load. This load is set to a value at which the specimen is not damaged irreversible. The deformation analysis is carried out by the DIC-system ARAMIS from GOMmbH Braunschweig. To get a good correlation between load and recorded deformation field, the image acquisition of the DIC-system is triggered by the load signal of the testing machine using an external triggerbox.
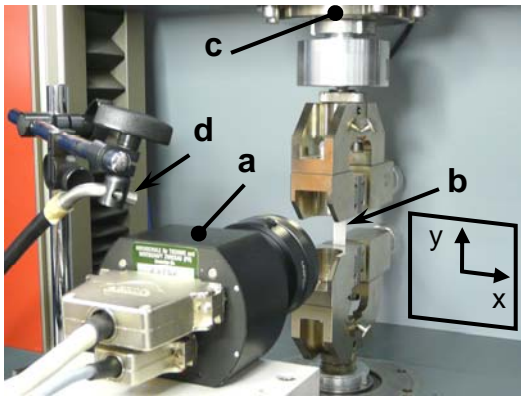
Fig. 4 Experimental set-up; a) sample coated with random pattern (50 mm x 10 mm x 0.35 mm), b) testing machine, c) cold-light source, d) CDD-Camera (1280 x 1024 pixel) of the DIC system

Whereas strain gauges or clip-on extensometer allow only the measurement of discrete strain values, the in-plane displacement field can be determined by DIC. The components of strain tensor are derived from the displacement components numerically. Fig. 5 shows the strain field $\varepsilon_y(x, y)$ of a photosensitive SU-8 sample processed on wafer level for MEMS applications. The mean value ε_y over nine discrete points is $\varepsilon_y \approx 3440$ μm/m. Using the determined strain value ε_y, the YOUNG's modulus E_{DIC} can be estimated by

$$E_{DIC} = F / (A \, \varepsilon_y)$$

with F as applied load and A as cross-sectional area. The mean E_{DIC} (here: 3730 N/mm^2) can be analysed as a function of the technological process of the SU-8 specimens.
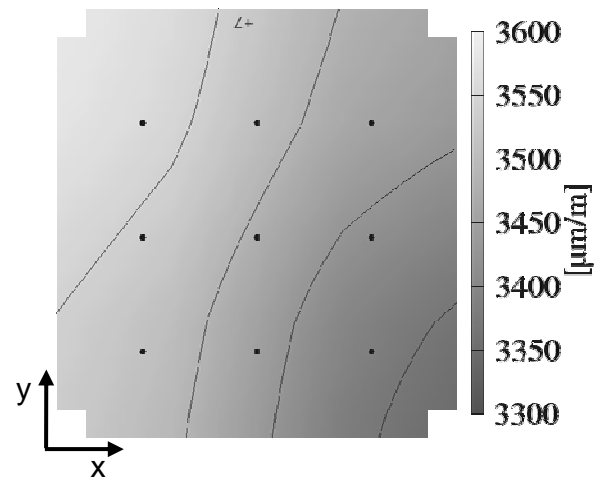
Fig. 5 $\varepsilon_y(x, y)$ strain field on the surface of a 350 μm thick SU-8 sample under tensile load F = 45 N; area of interest approx. 8 mm x 8 mm

Furthermore, **Ultra Nanoindentation** (UNHT) is a very efficient method to determine the hardness and YOUNG's modulus E_{IT} values on precise positions on sample surface. The CSM system used allows extreme accuracy and extremely low thermal drift. The OLIVER/PHARR method based on a BERKOVICH indenter has been applied to determine E_{IT} from normal force versus penetration depth, Fig. 6. The mechanical properties of microstructures can be described with a high local resolution by analysing YOUNG's modulus and hardness distribution.
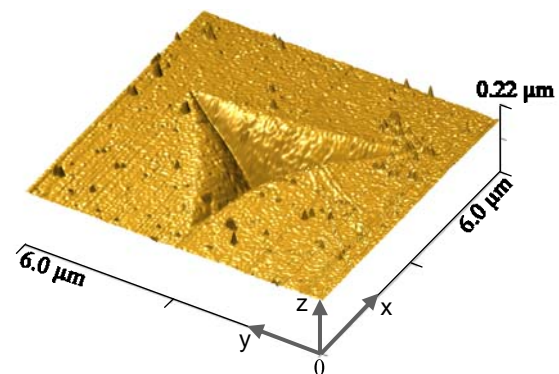
Fig. 6 AFM image of a indent left by a BERKOVICH tip in a photosensitive polymer specimen mr-l5050; E_{IT} up to 4600 N/mm^2 (measured with CSM Ultranano-indenter from CSM Instruments Peseux)

3. Acknowledgement

EXPERIMENTAL EVALUATION OF ORTHOPAEDICS SUITABILITY OF DIFFERENT BIOMATERIALS COMBINATIONS

Radek Sedlacek [1]

[1] Czech Technical University in Prague, Faculty of Mechanical Engineering, Laboratory of Biomechanics, Technicka 4, 166 07 Prague, Czech Republic

Corresponding author: radek.sedlacek@fs.cvut.cz

1. Introduction

This article deals with experimental evaluation of bio-compatible and bio-stable materials used in orthopaedics for joint replacement. The evaluation is based on very specific wear resistance testing of biomaterials. This type of testing is very important for comparison of different biomaterials and their modifications and for appreciation of new directions at the joint replacement design (for example in total knee or hip joint replacement). The special experiments were carried out in collaboration with company MEDIN ORTHOPAEDICS Inc. - developing and producing bone-substitute biomaterials and implants.

2. Methods

The special wear resistance tests, called "Ring On Disc", were completely carried out with a lot of pairs of different biomaterials. The experiments were executed according to ISO 6474:1994. This International Standard deals with evaluation of properties of biomaterials used for production of bone replacement. The standard requires a long-time mechanical testing at which a complete volume of worn material is evaluated. The test conditions, requirements on the testing system and specimens' preparation are closely determined. For the specimens treatment and their evaluation, a procedure is assessed which ensures the testing objectivity.

The method is based on loading and rotating two pieces from biomaterials. The Fig. 1 shows the schematic diagram of the test. A ring is loaded onto a flat plate from different material. The axial load that is applied on the ring is all the time constant and equal 1500±10 N. The ring is rotated through an arc of ±25° at a frequency of (1 ± 0.1) Hz for a given period of time (100 ± 1) hours. There is distilled water using as the surrounding medium.
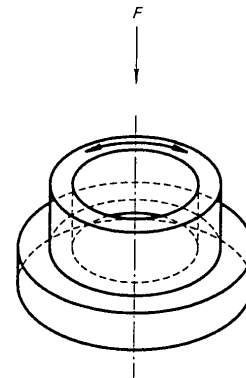
Fig. 1: Schematic diagram

The outer diameter of the ring is 20 mm, inner diameter is 14 mm. Thickness of the ring is 6 mm. The diameter of the disc is 25 mm and thickness is 6 mm. There is the geometry of ring and disc test pieces with definition of necessary dimensions in the standard [5].

As a measure of wear resistance is determined and used volume of the wear track on the disc. The wear track cross-sectional area is analyzed from measured profile for each disc alone. The volume is calculated from this area. After that the average volume is calculated for one group of specimens. The profile measurements of the tested specimens were carried out using a specially adapted assembly.

The Experiments were executed on the top quality testing system MTS 858 MINI BIONIX placed in "Laboratory of Biomechanics" at the Czech Technical University in Prague, Faculty of Mechanical Engineering, Department of Mechanics, Biomechanics and Mechatronics.

3. Experimental Results

The evaluation of the wear resistance was addict on the suitability of different type of biomaterials and their modification. Totally the tests were executed with 5 groups o specimens from different materials. There were 5 tested pairs in each group (means 5x5x100 hours of testing). The final parameters obtained in these tests - the wear volumes - were calculated (see Tab. 1, UHMWPE = Ultra High Molecular Weight Polyethylene). The comparison of different combinations of biomaterials used for implants can be implemented from this analysis.

Material of RING	Material of DISC	Wear volume [mm^3]
Vitalium alloy (Co-Cr-Mo)	Irradiated UHMWPE (crosslink) – 100 kGy	4.78
Vitalium alloy (Co-Cr-Mo)	UHMWPE (no crosslink)	5.51
Alumina ceramics (Al$_2$O$_3$)	Pressed UHMWPE	5.62
Titanium alloy (Ti$_6$Al$_4$V) with DLC	UHMWPE	6.61
Zirconia ceramics (Y-TZP)	PEEK (PolyEther-EtherKetone)	7.59

Tab. 1: Final parameters of mechanical testing

4. Conclusion

We obtained the objective data about wear resistance for 5 combinations of different biomaterials and their modifications. The resulting wear volume indicates the amount of elements that are loosening during loading of the bone substitute implant in human body and describes one from very important mechanical properties. The suitability for orthopaedics can be evaluated from these data.

We found out the worn volume on the UHMWPE modified by crosslink is less than on the UHMWPE without modification and less than other combinations of biomaterials too. The results show the modification by crosslink is for UHMWPE material useful. For next development it is purposeful to finish tests with other bone-substitute materials. Experiments with PEEK and titanium alloy covered by DLC are executing now.

5. Acknowledgements

6. References

[1] Saikko V., Keränen J.: Wear simulation of Alumina-on-alumina prosthetic hip joints using a multidirectional motion Pin-on-disk device, Journal of American Ceramic Society, 2002, vol. 85, p. 2785-2791

[2] Lappalainen R., Santavirta S.: Potential of coatings in total hip replacement, Clinical Orthopaedics and Related Research, 2005, vol. 430, p. 72-79

[3] Sedlacek R., Tuzarova Z.: The Analysis of the Influence of Implant Surface Roughness on the Wear of UHMWPE Cup. In: ESBME 2008, Chania 2008, p. 85-86

[4] EN 12010 Non-active surgical implants - Joint replacement implants - Particular requirements. CERN 1998

[5] ISO 6474 (E) Implants for surgery – Ceramic materials based on high purity alumina. CERN 1994

APPLICATION OF CONDUCTIVE AFM TECHNIQUE TO MEASURE ELECTRICAL CONDUCTANCE OF TRIBOFILMS

Kartik Pondicherry [1], Igor Beinik [2], Florian Grün [3], István Gódor [3], Christian Teichert [2]

1) Materials Center Leoben, Roseggerstr. 12, 8700 Leoben, Austria.

2) University of Leoben, Institute of Physics, Franz-Josef-Str. 18, 8700 Leoben, Austria.

3) University of Leoben, Chair of Mechanical Engineering, Franz-Josef-Str. 18, 8700 Leoben, Austria.

Corresponding author: kartik.pondicherry@mcl.at

1. Introduction

Lubricants for mechanical applications possess a layer forming ability besides their rheological properties. Electrical contact potential (ECP) measurements can be used to visualize in-situ, the formation of so-called tribofilms during tribometric tests, with test configurations such as ring on disc and pin on plate [1, 2]. The present work deals with a steel specimen (plate) which was used in a pin on plate tribometric test using fully formulated engine oil. The pin consisted of a Cu-based sliding material. An observed increase in the contact potential during the test is ascribed to the formation of tribological layers, also known as tribofilms, which are inherently insulating in nature [3]. In an attempt to validate the ECP measurements, conductive atomic force microscopy (C-AFM) has been used to measure the electrical conductivity of the tribofilms formed on the steel surface.

2. Experimental Setup

C-AFM is an AFM technique used for characterizing conductivity variations in samples with high resistance. A voltage is applied between the tip and the sample and the resulting current is monitored as a function of the position. The measurements were carried out under ambient conditions with a Nanoscope III multimode AFM in contact mode. The spring constant of the cantilever was 10 N/m and radius of curvature of the tip was ≥ 35 nm. An applied voltage of 7 V and a scan frequency of 0.4 Hz were used for the measurements over areas of 40 x 40 µm and 25 x 25 µm. The images were processed using Gwyddion software [http://gwyddion.net].

3. Experimental Results

An optical micrograph of an area showing characteristic layer formation is shown in Fig. 1. An indent was made in order to facilitate relocation of the same area for other analysis.
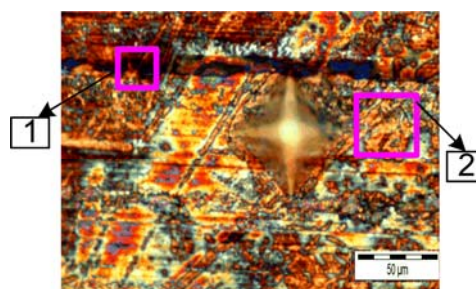
Fig. 1: Optical micrograph of a characteristic region showing a paddy structure. Areas marked 1 and 2 were investigated for their electrical conductivity.

In order to verify if an increase in the contact potential is indeed mediated by the formation of these tribofilms, representative areas with and without the films, marked as *1* and *2* respectively in Fig. 1 were mapped for their topography and electrical conductivity. Fig. 2 (a) and (b) depict the topography and electrical conductivity images of the region without the boundary layer.
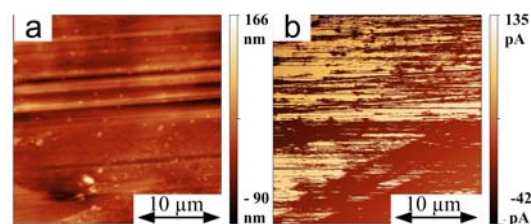
Fig. 2: The topography (a) and electrical conductivity (b) images of area 1 in Fig. 1.

From the topography image, the surface appears to be relatively smooth whereas the electrical

conductivity is quite inhomogeneous. Although, it could be argued that in the upper half of the area analysed, that the conductivity might have been influenced by the topography, the unevenness in the lower half of Fig. 2 (b) can not be attributed to the same. In the conductivity image, areas appearing brighter are more conductive than those appearing dark. Similar measurements were carried out in other areas without layers and from the results it is concluded that these surfaces showed electrical conductivity.

Whereas, from Fig. 3, which depicts the electrical conductivity of the region with the paddy structure, it is clear that the surface in this region is electrically insulating. It is seen from the image that the conductivity is almost uniform and the magnitude being almost zero. Here as well, several measurements were carried out in the similar regions with the pads and it has been observed that these regions were absolutely insulating in nature. Although from Fig. 3 (a), we see that there the topography is not as smooth as that in Fig. 2 (a), the corresponding electrical conductivity image shows us that the conductivity is not influenced by the topography.
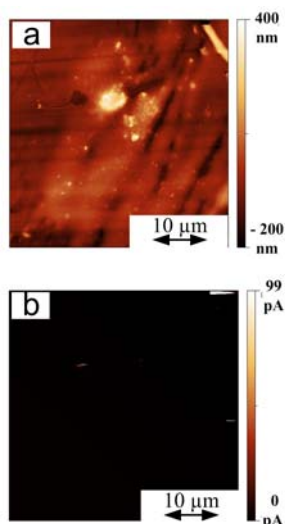
Fig. 3: Image of topography (a) and electrical conductivity (b) of paddy region marked as 2 in Fig. 1

4. Summary and Conclusions

From the results of the analysis it has been observed that the regions without the layers are conductive in nature whereas those with the layers are totally insulating. Furthermore, we see that there is a very negligible influence of the topography on the conductivity of the

sample. Hence, it can be stated that C-AFM technique is a very helpful tool in order to substantiate the results obtained from the in-situ contact potential measurements during a tribometric test.

5. Acknowledgements

6. References

[1] Tung, S. et. al., Tribological Investigation of the Polymer-Based Lubrication System Using a Laboratory Reciprocating Bench Test, Tribology Transactions 50 (2007) 4 458-465.

[2] Grün, F., Gódor, I., Javidi, A., "Methodik zur in-situ-Messung der Interaktionen zwischen Werkstoff, Schmierstoff und Beanspruchungskollektiv", Symposium der Österreichischen Tribologischen Gesellschaft – ÖTG, Wr. Neustadt, 2008, pp. 53-60.

[3] Gauvin, M., Dassenoy, F., Belin, M., Minfray, C., Guerret-Piecourt, C., Bec, S., Martin, J.M., Montagnac, G., Reynard, B. Boundary Lubrication by Pure Crystalline Zinc Orthophosphate Powder in Oil, Tribology Letters (2008) 31, 139-148.

BONE CEMENTS MIXING TECHNIQUE INFLUENCE ON THEIR IMPACT AND BENDING PROPERTIES

R. Seewald, P. Palček, T. Liptáková

University of Žilina, Fakulty of Mechanical Engineering, Department of Materials Engineering,
Univerzitná 1, 01026 , Žilina, Slovakia
Corresponding author: tatiana.liptakova@fstroj.uniza.sk

1. Introduction

Bone cement is used in orthopedic surgery for fixation of total endoprostheses of hip, knee and elbow joints. Since the 60's of the last century, when first experiments were done on bone cements, they went under different modifications in they structure and quality. They consist of two basic components (powder and liquid) which are mixed together under the conditions recommended by manufacturer which vary for each type of cement. After mixing the components the exothermal polymerization reaction and hardening begins [1]. The endoprosthesis is inserted into the bone canal which is filled with polymerizing bone cement. Bone cements have much less modulus of elasticity like the metal endoprosthesis, but they are stiff enough and are fully biocompatible. The main role of bone cements is to distribute the loads from the metal endoprosthesis into the surrounding bone and tissues [2].

In this paper the influence of bone cements mixing technique on results of impact strength tests and bending tests performed are presented.

2. Experimental materials, methods and conditions

To determine the impact and bending properties of small polymer samples made mainly with cutting from final products the device Dynstat was used.

The aim of the impact strength test is to determine the energy required to break the samples, which is a measure of the material resistance to impact straining.

During the bending test the bending moment M_o and the diffraction angle α are measured.

Three kinds of bone cements for the experiments were used: SMARTSETTMHV, OSTEOBOND® and Palacos®R. The components of the cements were mixed together at room temperature and atmospheric pressure using 2 techniques of mixing: a) liquid into the powder, b) powder into the liquid [3].

To simulate the real in vivo hardening conditions to design special mould, where the required pressure for cement hardening (more then 16kPa) was provided by weights, was necessary. The scheme of the muddle is presented on Fig. 1. The samples obtained from the muddle had 4x4mm cross section and were cut into 15mm length [4].

Fig. 1: Scheme of the muddle for sample preparation

3. Results and discussion

The aim of this paper was to establish possibly connections between the mixing techniques and mechanical properties of the prepared samples. The values measured for samples prepared by recommended mixing technique are marked with symbol ($^\bullet$).

The averaged energies measured during the impact tests on Fig. 3 are presented. After the impact strength tests the porosity of the fracture surfaces was established, the results are presented on Fig. 4. and some of the fracture surfaces on Fig. 2 a,b,c.

On the all fracture surfaces, pores with diameter up to 0,5mm are visible, vary in shape and size. These pores cause stress concentration and can initiate fractures in cement mantle. It was shown, that in term of impact stress, it is necessary to reduce cement porosity, for example by vacuum mixing, to prevent the entrapment of air into the viscous cement mass during mixing.

Fig. 2: Fracture surfaces of the bone cements prepared by mixing technique powder to liquid. a) SMARTSETTMHV, b) OSTEOBOND®, c) PALACOS®R
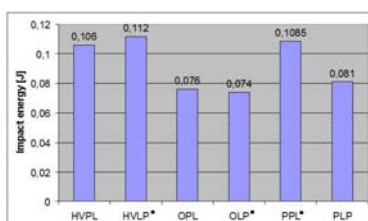
Fig. 3: Averaged impact energies of the cements prepared by different techniques
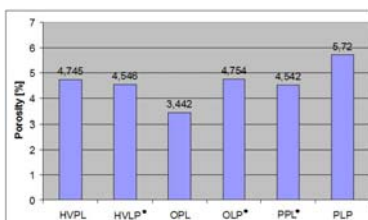
Fig. 4: Averaged porosities of the fracture surfaces after impact strength tests
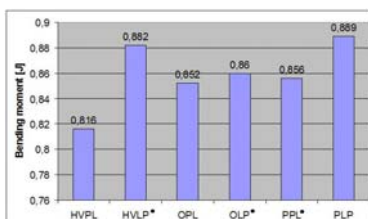
Fig. 5: Averaged bending moments of the samples prepared by different techniques
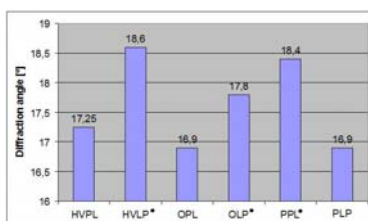
Fig. 6: Averaged diffraction angles of the samples prepared by different techniques

The results of bending tests are presented on Fig. 5 and on Fig. 6. The vice-versa technique of mixing much more affected the diffraction angles but caused higher bending moments at bone cement PALACOS®R contrary of the other two cements.

The influence of the room temperature on the hardening time was also observed. The higher was the temperature the shorter was the setting time of the cement [5].

4. Acknowledgements

5. References

[1] Constantz, BR., Ison Ira, C., Fulmer, MT., Poser, RD., Smith, ST., VanWagoner, M., Ross, J., Goldstein, St. A., Jupiter, JB., Rosenthal, DI.: Skeletal Repair by in Situ Formation of the Mineral Phase of the Bone. (1995) Science page: 267ff.

[2] Deb, S., Di Silvio, L., Vasquez, B., San Roman, J.: Water Absorption Characteristics and Cytotoxic and Biological Evaluation of Bone Cements Formulated with a Noval Aktivator, Biomaterials, 1999, No. 48, pp. 719-725.

[3] Lelovics, H., Liptáková, T.: Comparison of Some Mechanical and Rheological Properties of Bone Cements, 25th Danubia-Adria symposium on Advances in Experimental Mechanics, 2008, Czech Republic, pp. 157-158.

[4] Seewald, R., Lelovics, H., Nečas, L.: Mechanical properties of bone cements, TRANSCOM 2009, Žilina, In press.

[5] Lelovics, H., Seewald, R., Nečas, L.: Observation of Surface Temperature of Acrylic Bone Cement During Polymerization, TRANSCOM 2009, Žilina, In press.

SHOCK AND VIBRATION OF TRANSFORMER FOR EMU TRAINS

Damir Semenski[1], Ivan Sitar[2], Gino Pucci[3], Mislav Ilijašević[2], Stjepan Baršun[2], Hinko Wolf[1]

[1]   University of Zagreb, Faculty of Mechanical Engineering and Naval Architecture, Ivana Lučića 5, HR-10000 Zagreb, CROATIA. Phone: +385 1 61 68 211

[2]   Končar Distribution and Special Transformers Inc., Josipa Mokrovića 8, HR-10090 Zagreb, CROATIA. Phone: +385 1 37 83 719

[3]   CESI, Via Pastrengo 9, 24068 Seriate (BG), ITALY. Phone: +39 35 55 77 606

Corresponding author: damir.semenski@fsb.hr

1. Introduction

Traction transformers are used for a power supply of EMU (electric multiple unit) or electrical locomotive from the catenary system. They are installed on a vehicle and must be placed in an area defined by the requirements of designers due to customer specifications. Due to 100% low-flow access on the vehicle (new KONČAR's low floor EMU), transformer shown at Fig. 1 is placed on the roof of the train. Transformer consists of active part (magnetic core and windings) and transformer tank (including accessories and cooling unit). The tank holds all transformer mass and through its structure the transformer is fixed to the vehicle.
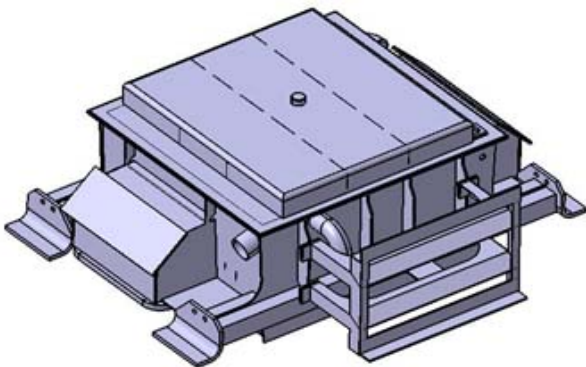
Fig. 1: CAD model of transformer for EMU trains.

Main transformer is the heaviest single component of the vehicle, therefore its optimization has the utmost importance for designers. Transformer dimensions (volume and weight) must meet severe mechanical constraints of train overall without impairing vehicle's performance and reliability. This particular unit has total mass of 3460kg and dimensions of 0.8 (H), 2.1 (W) and 2.3 (L) meters. According to the last edition of IEC standard for traction transformers [1], shock and vibration withstand test is classified as a type test and should be performed on every new transformer design.

2. Numerical Analysis

Numerical analysis was performed by finite element method using parabolic elements with intermediate nodes. Dynamic analysis [2] was performed by using 14 different loading models. Von Mises stresses (Fig. 2) at the region where maximum values occur are presented for simulated condition that corresponds for the 3*g* half-time shock directed to the driving direction.
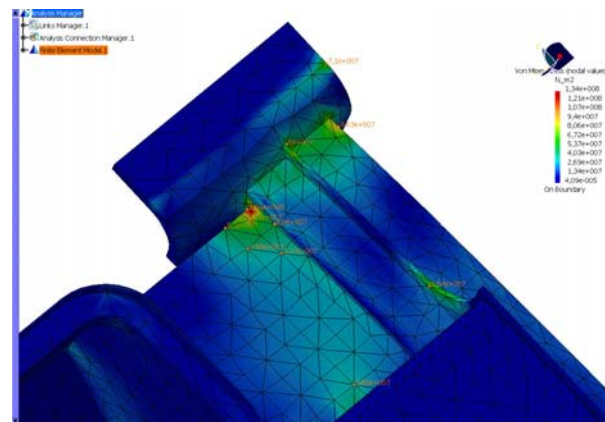
Fig. 2: Max. stresses for 3*g* shock in driving direction.

Experimental control of numerical results is done by measuring strains during simple pressure probe. At the bottom panel, where maximum displacements occur, the differences were less than 3%.

3. Testing

The shaking table of six degrees freedom MASTER (<u>M</u>ulti<u>A</u>xes <u>S</u>haking <u>T</u>able for <u>E</u>arthquake <u>R</u>eproduction) was used as the excitation and processing equipment (Fig. 3).
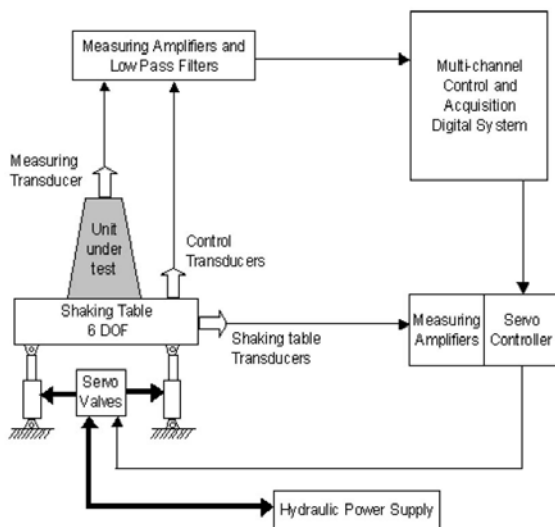
Fig. 3: Testing equipment MASTER.

During the tests the unit was fixed to the steel platform of the shaking table by means of two plate supports. Every accelerometer was identified for each measuring position by a number (Fig. 4). During the tests the unit was in non-operating conditions.
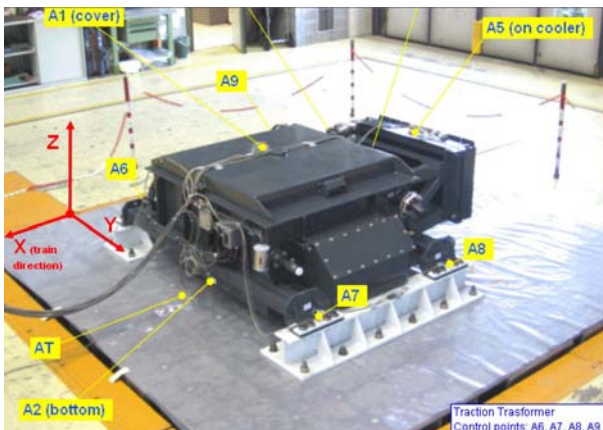
Fig. 4: Position of accelerometers during testing.

Test objective was to analyse the dynamic behaviour of the unit, which was subjected separately along three perpendicular axes (X longitudinal driving direction, Y lateral and Z vertical) to the 15 different dynamic types of loading. Mono-directional excitation tests consisted in resonance search test, simulated long life random test and half shine shock test [3].

4. Results

Results of the half shine test by 3*g* pulse excitation during 50ms sre shown in control diagram (Fig. 5).
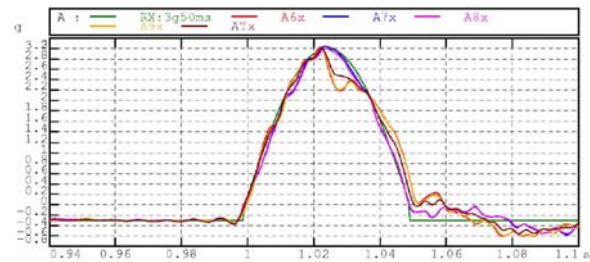
Fig. 5: Acceleration time histories at 4 positions.

Time histories of measurements channels 1 and 2 are shown in diagrams (Fig. 6).
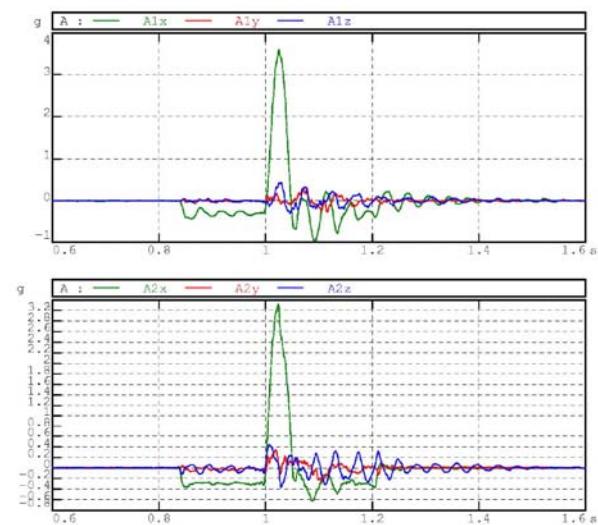
Fig. 6: Half shine shock response at positions 1 and 2.

5. Conclusion Remark

Experimental measurements verified the design numerical simulations and proofed the reliability of the product, important for customer.

References

[1] *IEC 60310* Railway applications – Traction transformers and inductors on board rolling stock, 3rd ed., 2004-02.

[2] D. Semenski, B. Jerbić, Mehanički proračun transformatora za vlak, *Elab. of Fac. of Mech. Eng. and Naval Arch. for KONČAR D&ST*, Zagreb, 2008.

[3] Shock and vibration tests of transformer MOZ 1510-27.5, *CESI test report for KONČAR D&ST*, Seriate (BG), 2009.

EXPERIMENTAL INVESTIGATION FOR MECHANICAL BOND FOR COMPOSITE FLOORS

Noémi Seres [1), László Dunai [1)

[1) Budapest University of Technology and Economics, Department of Structural Engineering, Bertalan Lajos 2, 1111 Budapest, Hungary.

Corresponding author: nseres@vbt.bme.hu

1. Introduction

The lightweight composite floor is basically composed of three system components: steel beam, profile deck as permanent formwork and reinforced concrete slab. The interlock between the steel deck and the concrete slab is created (i) by friction and/or (ii) by mechanical bond, which is typically created by rolled embossments on the steel deck. The efficiency of the composite slabs depends on the composite action of steel and concrete structural members.

The design methods for strength checking proposed by Eurocode 4 [1] consider the mechanical bond as it is smeared all over the interlock surface. The aim of the ongoing research work is to determine the design characteristics of the mechanical bond on the basis of the local behaviour of an individual embossment and the interaction between them. The paper shows a novel experimental analysis of an individual embossed mechanical bond.

2. Experimental Program

The test specimens are made on the basis of traditional pull–out tests, with the difference that the steel plate is not a half wave of an open through profile, but such a plate which has one enlarged embossment, as shown in fig. 1. The scope of the enlargement of the embossment is to be able to create the specimen and to follow the phenomenon by strain gauge measurement. In order to keep the original geometric ratio of the embossment, the steel plate thickness is chosen to be thicker (1,5 mm and 2 mm) than the plate thickness in a regular composite floor. Two plates are placed back-to-back in the middle of one concrete cube. A 6 mm thick spacer plate is installed between the embossed plates. An 80 mm diameter hole is cut on the spacer plate, which leave the area of the

embossment without restraint and insures the free deformation of the embossment.

During the design of the specimen the global failure of the concrete block has to be avoided, hence frequently (30 mm) distributed stirrups are put in the concrete block along the plate.
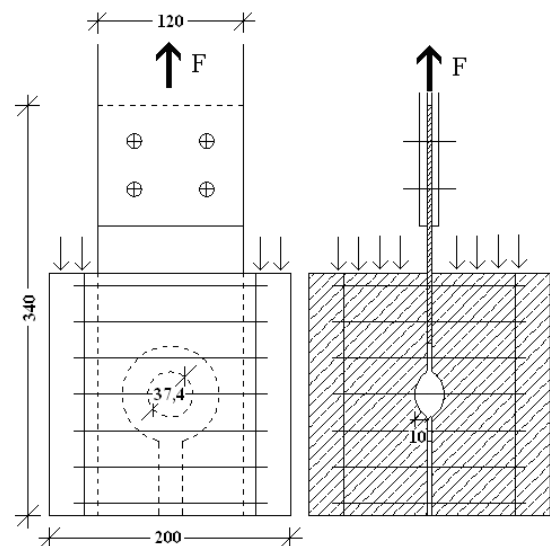
Fig. 1: Test specimens.

The embossment's height is 10 mm, its diameter is 37,4 mm.

The strain gauges (1,5 mm base length) are placed in two arrangements, as shown in fig. 2. Five base gauges are put on all of the embossed plate pairs, and on two of them ten supplementary gauges are put besides.
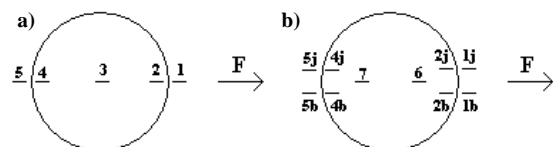
Fig. 2: Strain gauges (a) basic and (b) supplementary.

Besides the strains, the relative displacement between the steel plate and the concrete cube is also measured with inductive transducers.

3. Test Results

3.1 The phenomenon

As the load is introduced, the first mark of the failure appears on the concrete block. By increasing the load, the first crack appears in line with the steel plate at the exterior surface of the concrete block. After, the crack propagates all over the height of the cube and the steel plate slips out of the concrete block.

Two kinds of crack can be identified from the full crack pattern. The first one is parallel with the steel plate and propagates from top to bottom in the concrete cube, and arises also on the supported and the side surfaces. The second one is representative on the supported surface and its near area, and the crack propagates from the edge of the steel plate to the corner of the concrete cube.

3.2 Force – displacement relationship

Fig. 3 shows two typical force – displacement curves. The response of the specimen is almost rigid for the initial loading (2 – 3 kN). After, the behaviour changes and considered as linear. The short linear phase is followed by a nonlinear part, with gradually decreasing slope. By experimental observation, the end of the linear phase can be identified by a micro crack propagation, which leads to the appearance of the first crack on the concrete surface. After the steel plate slips, a small amount of load increase can be observed till failure.
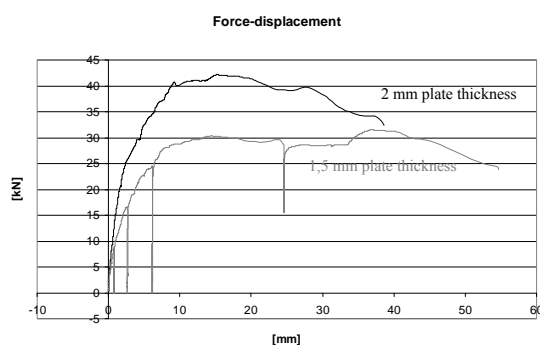
Fig. 3: Force - displacement curves.

On the basis of the force – displacement relationship the connection can be called ductile, because it has a significant deformation capacity.

3.3 Strains

The strain gauges show same behaviour by position and by specimen type. By the evaluation of the strain results it is found, that the yielding on the steel plate appears at very low load level (5–10 kN) at #2 gauge position (fig. 2). A typical result of the strain measurement at gauge #3 can be seen in fig. 4. In fig. 5 the typical crack pattern and the failure mechanism of the embossment can be seen.
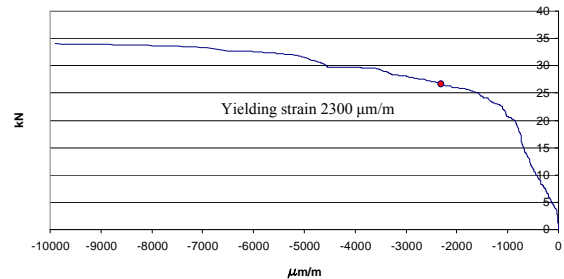
Fig. 4: Strains at gauge position #3 on specimen 2.2.
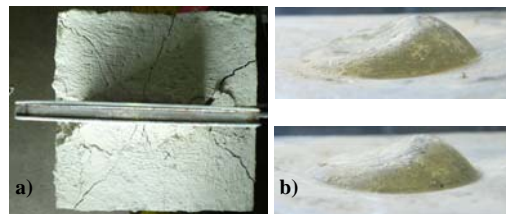
Fig. 5: Crack pattern (a) and failure mechanism (b).

4. Concluding Remarks

In the paper an experimental investigation of an individual embossed mechanical bond is detailed. A new test specimen is introduced to analyze the local behaviour of embossments. The basic behaviour modes are observed from the tests and the results are evaluated quantitatively. The results are used for the validation of the developed advanced numerical model for the embossment's behaviour. The model is to be applied for the analysis of embossments interaction, too.

5. Acknowledgements

6. References

[1] EN 1994-1-1 (2004), Design of composite steel and concrete structures – Part 1.1

INFLUENCE OF CROSS SECTION POSITION ON THE BEARING CAPACITY OF TRAPEZOIDAL PROFILED THIN SHEETS

Diana Šimić [1]

[1] University of Zagreb, Faculty of Civil Engineering, Department of Mechanics. Kačićeva 26, 10 000 Zagreb, Croatia.

Corresponding author: dianas@grad.hr

1. Introduction

The load bearing mechanism of trapezoidal profiled thin sheets subjected to transverse load is manifested through the occurrence of local buckling in the flat unstiffened part of cross section subject to compression, once a certain intensity of pressure is reached. After occurrence of local buckling in the compression zone, the distribution of stress along the width of the compression zone is no longer uniform. The stresses are reduced at the point of local cross-section buckling, while stress concentration occurs at the portion of cross section next to the edge bracing.

2. Experimental Results

Experimental investigations of the trapezoidal profiled sheets behavior under transverse load were conducted on two trapezoidal sheets marked T 39/250/0.7; Č.0147, as shown in Figure 1. The testing was performed for the negative position of sheet, marked Sheet 1, and for the positive sheet position, marked Sheet 2, cf. Figure 2. During testing, the load was gradually applied on trapezoidal sheets by increasing to 5 cm the level of water in the container situated above the trapezoidal sheet, cf. Figure. 3.
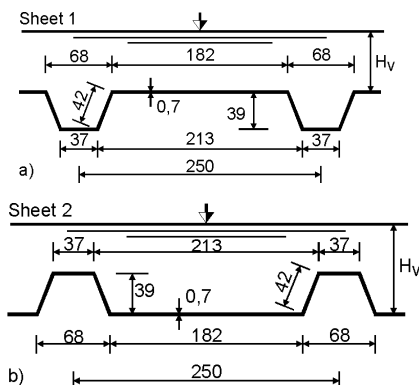
Fig. 2: Position of trapezoidal sheets during testing: a) negative position, b) positive position.
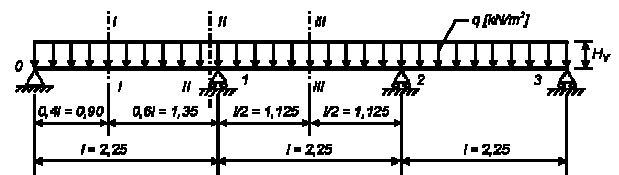
Fig. 1: Loaded continuous beam and typical cross sections

Fig. 3: Testing of the trapezoidal Sheet 1

The deflection diagrams for Sheets 1 and 2 are presented in Figures 4 and 5, respectively.

For the trapezoidal Sheet 1, the failure of load-bearing capacity occurred at the load value of q = 2.35 kN/m2, cf. Figure 6, while for the Sheet 2 this failure occurred at q = 3.0 kN/m2, cf. Figure 7.

For both trapezoidal sheets the failure occurred because of the local buckling of trapezoidal sheet compression zone at the point of maximum bending moment in the first span. The limit load of trapezoidal sheet is 28 % greater for positive position when compared to the negative position.
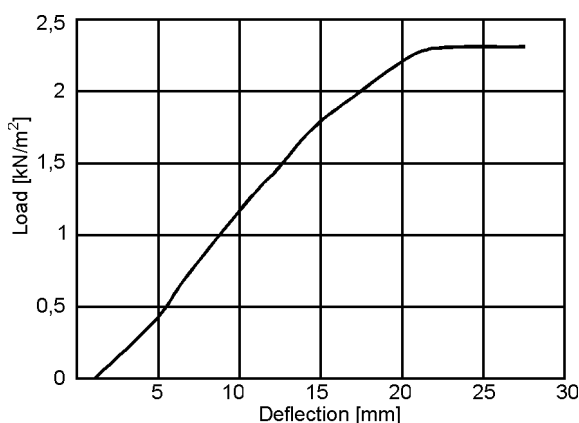
Fig. 4: Load-deflection failure diagram for Sheet 1.
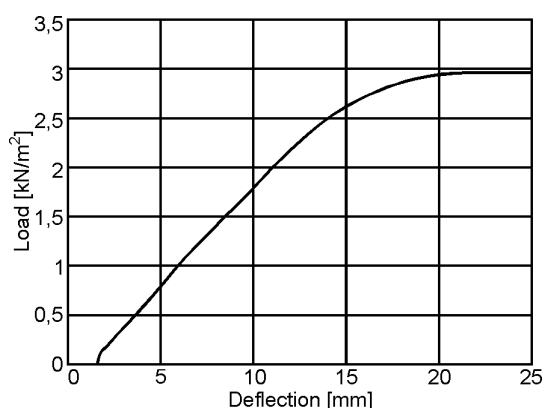
Fig. 5: Load- deflection failure diagram for Sheet 2

Fig. 6: Trapezoidal Sheet 1 after testing.

For the load q = 1.5 kN/m^2 the trapezoidal sheet deflection is 35 % greater in negative position when compared to trapezoidal sheet deflection in positive position. Differences obtained in the trapezoidal sheet limit load and deflection values may be explained by the fact that in case of negative trapezoidal sheet position a wider zone is in compression in the area of maximum bending moment on the span. In case of positive trapezoidal sheet position, the wider zone is in compression above the bearing which would otherwise make it more stable.

Fig. 7: Trapetoidal Sheet 2 in first span after testing

This analysis shows that the stability of the zone in compression plays a principal role in the bearing capacity of trapezoidal sheets.

3. Remarks

The above investigations have shown that the bearing capacity and deflections of trapezoidal sheets do not depend on the shape and size only, but also on the position of the trapezoidal-sheet cross section subjected to loading. The bearing capacity of the trapezoidal sheet increases with the favorable position of the trapezoidal sheet which makes it more stable.

4. Acknowledgements

5. References

[1] Androić, B; Dujmović, D.; Džeba, I.: Beispiele nach EC3, Bemesung und Konstruktion von Stahl bauten, Werner Verlag, Düsseldorf, 1996.

[2] Eurocode 3: Design of steel structures - Part 1-3; European Committee for Standardization, October 1997.

[3] Schwarze, K.: Bemessung von Stahltrapezprofilen nach DIN 18807 unter Beachtung der Anpassungs-richtlinie Stahlbau. Bauingenieur Bd. 73 (1998), Nr. 7/8 - Juli/August.

FAILURE ANALYSIS OF BLOCK BRAKE UNIT SUPPORT OF EMU

Goran Simić [1), Dragan Milković [1),

[1) University of Belgrade - Faculty of Mechanical Engineering, Railway Engineering Department,
Kraljice Marije 16, 11000 Belgrade, Serbia.

Corresponding author: dmilkovic@mas.bg.ac.rs

1. Introduction

Frequent occurrence of failures of Block brake unit (BBU) support of Electric multiple unit (EMU) of Serbian Railways induced investigation of the failure causes. Since these failures started to appear after some modifications made on the braking system, the first task was to establish the importance and effect of these changes on braking system.

In the original design brake force was developed between composite block brake shoe with nearly constant friction coefficient, and wheel tread. Since composite block brake shoe has low heat transfer ability, most of the heat produced during braking was transferred to wheel. This resulted in high thermal stresses and serious wheel tread damages. Often failures jeopardised reliability of the train. After some analyses, an expert team has decided to replace composite shoes with cast iron shoes (P10). This type of shoe is commonly used on freight wagons.
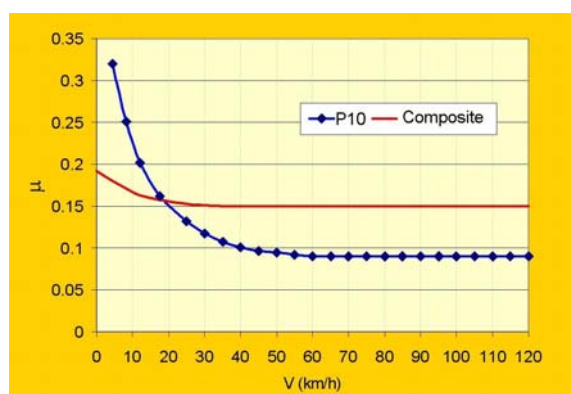
Fig. 1: Friction coefficient for P10 and composite shoe

This change improved heat transfer and solved initial running surface damage problem. Lower average friction coefficient of P10 shoes (fig. 1), enlarged stopping distances of the train. It was necessary to increase air pressure in brake cylinder by acceptable 10%, and in that way to achieve higher friction force. This change was not

suficient, and decrease of the maximum speed from 120 to 100 km/h was necessary, too.

After several months, a new problem appeared - breaking of the connecting plate of BBU support, often combined or preceeded by breaking of the screw connection (Fig. 2), even with dangerous drop away of the BBU.
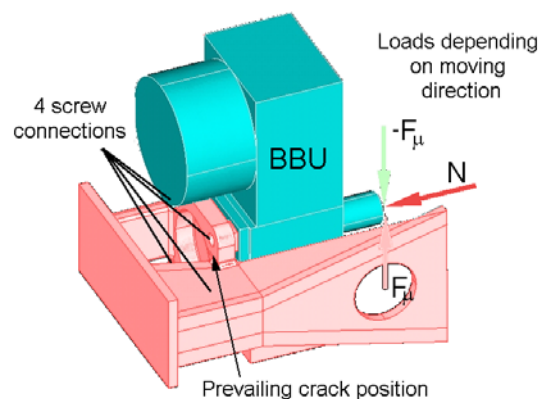
Fig. 2: Scheme of the BBU support

2. Analysis and Experimental Results [1]

Despite the normal force augmentation by only 10%, friction force of the P10 shoes, can at low speeds rise more than 50% compared to composite shoes. This is caused by friction coefficient vs. sliding speed dependence (Fig. 1). The results of Finite Element Analysis show that this is not enough for the crack occurrences in BBU support.

To clarify in-service conditions, especially dynamic influences during braking process, several brake tests were performed, using air brake only, or combining electro-dynamic (ED) and pneumatic braking. Measurement of the air cylinder pressure, determines the normal force applied to brake shoe. Speed measurement helps to follow the behaviour of the friction during braking. Vertical vibrations ($\ddot{z}$) measurement of BBUs gives estimation of inertial forces applied to support and screw connection along with friction force. Displacement measurement between BBU and shoes (z) defines

the influence of existing gaps in vertical link connection (Fig. 3) on vibrations. Second derivative of this quantity is relative acceleration, that can be used for determining dominant vibrations source.
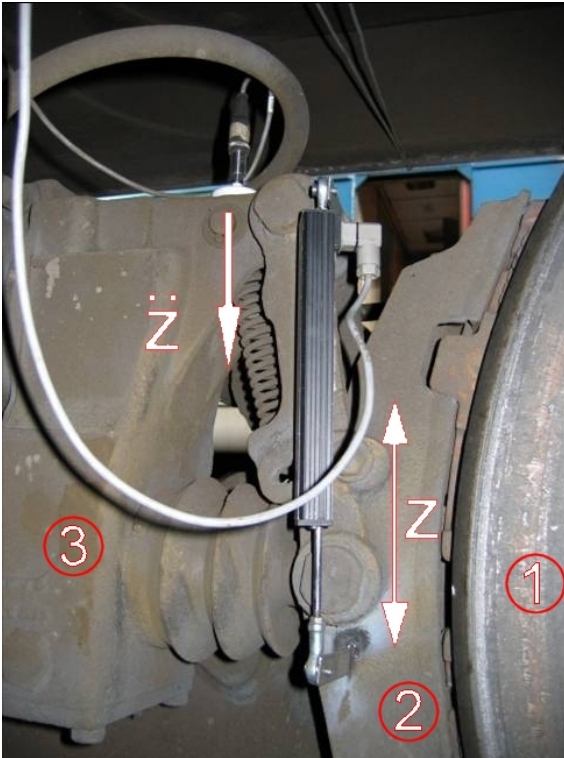
Fig. 3: Measurement points of vertical acceleration and displacement between BBU and brake shoe holder (1- wheel, 2 – shoe holder, 3 – BBU)
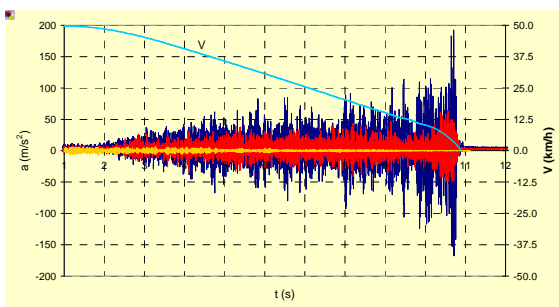
Fig. 4: BBU vibrations during different regimes of braking

In fig. 4 are shown typical vibrations during braking in the next cases:

1) emergency pneumatic braking (blue and red represents accelerations of two different BBUs), with max. cylinder pressure of 3,6 bar;

2) combined pneumatic and electro-dynamic braking (yellow), with max. air pressure of 0,5 bar.

Rapid braking with air brake only at low speeds produces strong self-excited vibrations, accompanied by characteristic sound. This vibrations are caused by high shoe pressure and increase of the friction coefficient of the P10 shoes just before stopping (Fig. 1).

Maximum measured BBU acceleration without use of the ED brake reached in one case 19g (blue line in fig. 4). In all cases it was not less than 5g, with eigenfrequency of about 70 Hz. Since the mass of BBU with brake shoes is 48 kg, repeated inertia and friction forces that acts in same direction are certainly enough, to cause screw breaks or support cracks appearance.

Relative accelerations between BBU and brake shoe were significantly lower. This implies that BBU and shoe vibrates almost as one body.

Several measurements show that while using electro-dynamic brake and air brake together, there are no critical dynamic loads that jeoperdise the strength of connecting plate of the BBU support, or screw connection (yellow line, Fig. 4).

3. Conclusions

Measurement results show that the most effecient measure to avoid dangerous screw and support breaks is regularly usage of combined ED and air brake. To avoid self-excited vibrations using air brake only, just before stopping the air pressure in the brake cylinder should be reduced.

Support was partially strengthend according to available free space.

Screw connection between support and BBU is very difficult to reach and tighten using regular torque wrench. Inadequate torque value enhances vibrations. Usage of the specially shaped torque wrench is necessary.

Comprehensive modification of the brake system is more expensive, but a possible alternative.

4. References

[1] G. Simić, V. Lučanin, D. Milković, Analysis of in-service conditions and strength of BBU support of EMU 412-416 (13.04-56-2007) (in Serbian), Faculty of Mechanical Engineering, Belgrade, Serbia.

NUMERICAL – EXPERIMENTAL IDENTIFICATION OF THE EFFORT STATE OF BANDS OF OPENCAST MINING MACHINES

Tadeusz Smolnicki, Mariusz Stańco, Damian Derlukiewicz [1],

[1] Wroclaw University of Technology, Faculty of Mechanical Engineering,
ul. Lukasiewicza 7/9, 50-371 Wroclaw, Poland

Corresponding author: tadeusz.smolnicki@pwr.wroc.pl

1. Introduction

The operating time of basic machines of the opencast mining usually amounts to several dozen years. At that time the machine is often modernized, equipped with new elements what over the course of time causes the change of loading of elements of the load-carrying structure. Bands on which booms are hung are one of the most responsible elements of the load-carrying system. Damaging this element can cause the disaster [1].

In case of rope bands a big safety factor usually exists, however when bands are made of metal sheets and joined with welding technology, are showing the great sensitivity to fatigue occurrences. At testing the exploitation strength an identification of loading the band from mass of the own machine is an essential problem what results from lack of possibilities of weighing individual elements of the machine without its disassembly. A self-propelled PGOT 5500 transporter is one of such machines exploited in Bełchatów lignite opencast mining. On picture 1. a machine was shown and with arrows object bands were marked.

Fig. 1: Self-propelled transporter – bands that demand the tension identification marked with arrows.

Bands are too responsible elements to use well-tried measurement methods as Strain-gauges drilled-hole method. The characteristic feature of bands is the occurrence of relatively straight, mutually orthogonal own forms. Using the method leaning against total applying the finite element method [2] and the measurement of free vibration frequencies [3] became essential.

2. Identification methodology

The base of the identification of force stretching the band – the average cross-sectional tension is the estimation of free vibration frequencies for a few first mods by the finite element method (fig. 2) and of characteristics free-vibration frequency – stretching the band for different states of fastening the band. In picture 3 courses for rotating and seizing pin joints were shown.

Fig. 2: Mode shape – 1st natural frequency.
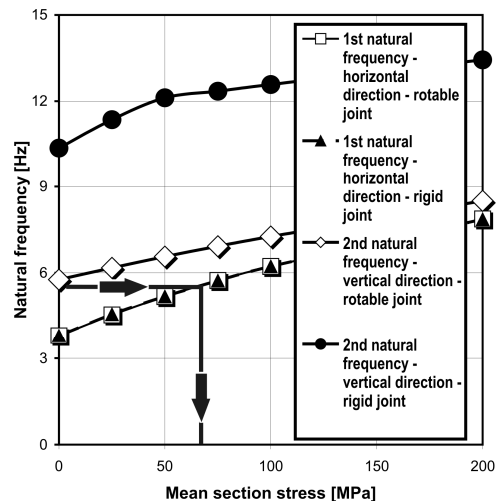
Fig. 3: Natural frequency – mean section stress diagram.

From numerical simulations a great sensitivity of the frequency of oscillation was stated in the plain of the turnover of bolts (vertical) from the state of the cinematic joint and practically negligible its influence on the frequency of oscillation in crosswise direction.

Through taking back measured frequencies to achieved results from FEM it is possible to estimate the tension of the band from the deadweight of the machine. At the small oscillation and loaded band, the appearing friction on bolts does not undergo the expansion and joints behave stiff, what allows for the identification of tension with the help of oscillation in the plain of the turnover of bolts.

3. Results

The method was used to bands arrowed in picture 1. Measurements were carried out in a few series, repeatable results were achieved. The instance of measured course of acceleration in horizontal direction for the band of counterweight boom and the estimated amplitude-frequency characteristics are shown on picture 4.
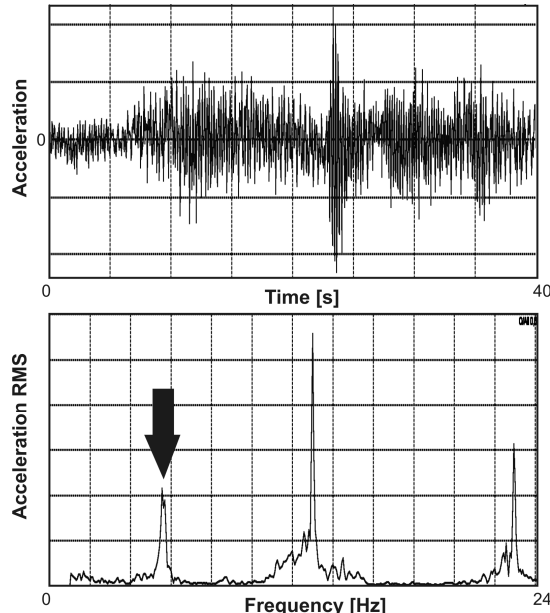
Fig. 4: Measured course of acceleration in horizontal direction (above) and estimated amplitude-frequency characteristic (beneath).

They stated that cross-sectional tension of the band of the counterweight boom from own mass amounted about 67 MPa. The estimated value enabled to conduct the full scope of strength and fatigue calculations including additional ingredients of the loading so like the wind, lowering base, inertial forces of mass

movements. The instances of results of equivalent stresses and stresses range are shown on fig. 5 and 6.
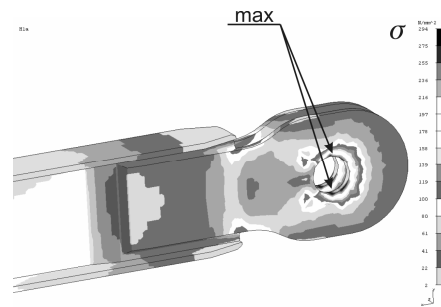
Fig. 5: Huber – von Misses stresses contour lines.
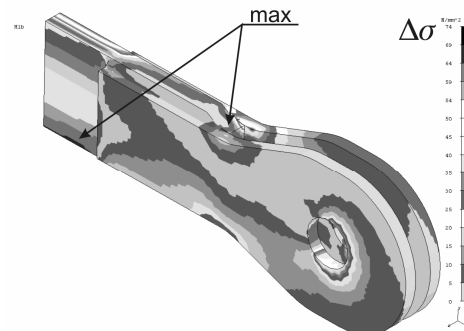
Fig. 6: Stresses range contour lines.

Results were being interpreted with the help of the DIN 22261 standard. They stated that obtained values were in a safe range.

4. Summary

Presented numerical-experimental methodology enables the identification of bands tension made of metal sheets on the physical object in field conditions in the simple and fast way. The conducted sensitivity analysis of free vibration frequencies to tension of the band and the way of supporting showed the good resolution of the method. Also a practical purpose was achieved – the answer to a question or the more further operation of the machine are not threatening with the disaster. The given method was applied with the success also for other machines.

5. References

[1] Czmochowski J.: Identyfikacja modeli modalnych maszyn urabiających w górnictwie węgla brunatnego. Oficyna Wydaw. PWroc., 2008. (in Polish)

[2] Rusiński E., Czmochowski J., Smolnicki T., Advanced Finite Element Method for Load-carrying Structures of Machines, Oficyna Wyd. PWr., Wrocław 2000 (in Polish)

IDENTIFICATION OF FATIGUE CRACK INITIATION ZONE OF FRICTION STIR-WELDED SAMPLES

Robert SOŁTYSIAK [1],

[1] University of Technology and Life Sciences, al. Prof. S. Kaliskiego 7, 85-789 Bydgoszcz, Poland.

Corresponding author: robsol@utp.edu.pl

1. Introduction

The progress in materials engineering and joining engineering results in the fact that new techniques of material joining are more and more widely used in engineering practice. One of the techniques is friction stir welding (FSW) method invented by The Welding Institute (TWI) in 1991 [1]. It is the best promising welding technique used to join various aluminum alloy components [2-3]. The aviation aluminum alloys, such as 2000 and 7000 series, which are used in aerospace industry to produce the components of airplane such as skeleton parts, bulkhead, and longeron and so forth [4-5], are considered to be very poorly weldable. The FSW method makes attempts at welding these kinds of aluminum.

However, the properties of innovatively welded joints can substantially differ from the properties of joints welded by traditional joining methods. Therefore, it is necessary to modify existing procedures or create new procedures for assessing fatigue life of the welded joints formed by using more and more modern metal joining technologies.

In the paper, results of identification of fatigue crack initiation zone of friction stir-welded samples of 2024 T3 aluminum alloys are reported. The paper also presents research results of the fatigue life of the samples made with use the FSW method in comparison with the fatigue life of the base material sample.

2. The research object

The Friction Stir Welding method was used for welding two 4,1 mm thick aluminum alloy 2024 T3 sheets (Fig. 1). The joint was made by the Polish Welding Centre of Excellence in Gliwice by using a numerically controlled friction welding machine with the tool shoulder diameter of 20 mm. The following parameters were used for the welding process: the tool rotational speed of 450 r/min and tool traverse speed of 160 mm/min.
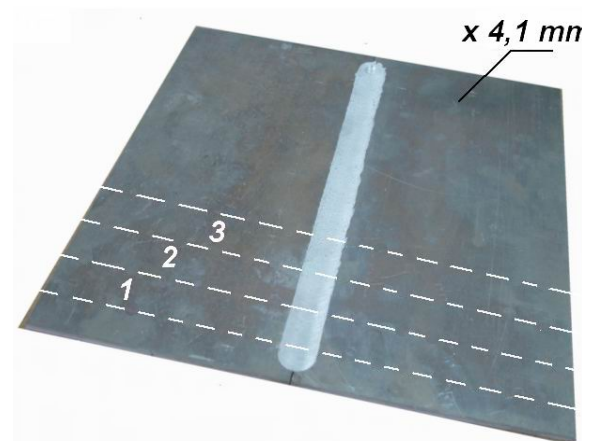
Fig. 1: The friction stir welded joint of aluminium 2024 T3 and the way of cutting samples no. 1, 2, 3.

The liquid-penetrant inspection was carried out on the friction stir welded sample. The sample was welded correctly, no defects were detected.

Four kinds of samples were used for investigation. Three of them were cut perpendicularly to the welding direction (Fig. 1). The first sample was 30,2 mm wide and the face and root of the weld remained intact. The second and third sample were 29,8 mm wide, but the face and the root of those samples were milled in order to remove the external geometrical notch, which can cause a strain concentration and consequently lead to the crack initiation. The milling was carried out on the area which was 40 mm long and 0,2 mm deep for the second sample and 0,7 mm deep for the third sample. The external machining was applied on the face as well as on the root of the joints using the plane milling cutter of diameter ø 20 mm. The fourth sample was made from base material. The measurements of third and fourth samples were the same. After milling the surfaces were polished.

3. The plan of experiment

The test was carried out during sinusoidal cyclic loading of max stress amplitude of 175 MPa (Fig. 2). The identification of fatigue crack initiation zone was carried out using the samples number 1, 2, 3. The fatigue life of these samples in comparison with the base material sample (no. 4) was also presented in this paper.
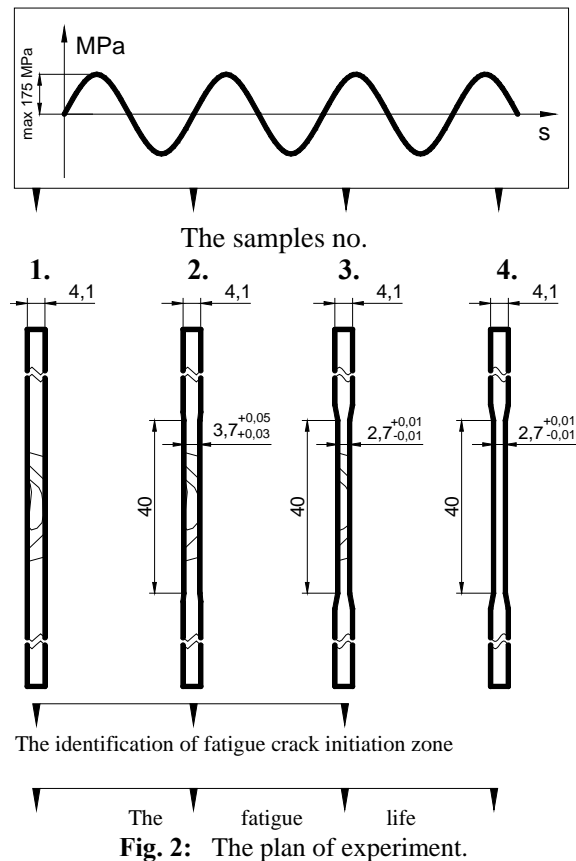
Fig. 2: The plan of experiment.
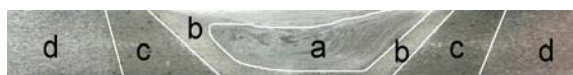
Fig. 3: Material macrostructures in a typical transversal section of an aluminum 2024 T3 welded joint: a – nugget, b - thermo-mechanically affected zone (TMAZ), c - heat affected zone (HAZ) and d – base material .

4. The macrostructure of FSW joint

The FSW joint macrostructures are different from macrostructures obtained by using a traditional welding method. We can distinguish not three but four individual zones in this type of joint (Fig. 3). Each of the zones may be characterized by different local material properties which, as a result, can cause the structural notches.

5. Conclusion

The results of the fatigue crack initiations zones identification and the fatigue life of FSW samples in comparison with the base material will be presented on 26th Symposium on Advances in Experimental Mechanics. The localization of the crack initiation zone will give the possibility of further investigation into procedures for assessing fatigue life in local approach. The results of local strain analysis with using local material properties of low strength zone of the FSW joint, the diagram of live strength and the knowledge of fatigue damage accumulating hypotheses are required to assess the fatigue life. When the results of fatigue life assessment are similar to the results of the experimental procedure, the proposed method may be used for other types of joints.

6. References

[1] Thomas W. M.: Friction stir butt welding. GB patent 9125978,6.12.1991. International patent application PCT/GB92/02203

[2] Fratini L., Zuccarello B.: An analysis of through-thickness residual stresses in aluminium FSW butt joints. International Journal Machine Tools & Manufacture 46 (2006) 611-619

[3] Shusheng Di, Xinqi Yang, Guohong Luan, Bo Jian: Comparative study on fatigue properties between AA2024-T4 friction stir welds and base materials. Materials Science and Engineering A 435–436 (2006) 389–395

[4] Boehm L.: New Engineering Processes in Aircraft Construction: Application of Laser-Beam and Friction Stir Welding. Glass Physics and Chemistry, Vol. 31, No. 1, 2005, pp. 27–29

[5] Strombeck A., Santos J. K., Torster F., Laureano P., Kocak M.: Fracture toughness behaviour of FSW joints on aluminum alloys. 1st Symposium on Friction Stir Welding, Thousand Oaks, California, USA 1999

PROBLEMS WITH ESTIMATION OF FATIGUE CRACK PROPAGATION LIFETIME IN OLD BRIDGE STEEL

Szata Mieczysław[1]), Pękalski Grzegorz[1]), Lesiuk Grzegorz[1])

[1]) Wrocław University of Technology, Faculty of Mechanical Engineering,
Smoluchowskiego 25 Str., 50370 Wrocław, Poland

Corresponding author: Mieczyslaw.Szata@pwr.wroc.pl

1. Introduction

Diagnostics and technical inspection of such objects as bridges constitutes an extremely important part of the engineering, particularly when the old structures are still in operation. In the USA alone, almost 120 thousands of bridges (about 20% of the total number) have exceeded 50th anniversary of their erection. Also in Wroclaw, Poland, there are many bridges remembering even the 19th century. Most often, the construction material used for their building was low-carbon steel, puddle at first, and later the cast one. In face of impossibility to substitute the objects with the new ones, it is necessary to take care for their operation safety. One of the main destruction causes in the old structures subjected to cyclic load conditions is uncontrolled fatigue crack propagation. Therefore, the new test methods enabling for quantitative evaluation of the sub-critical time of fatigue crack growth have to be sought for. However, in relation to the old steels, naturally predestined for structural and strength degrading processes, it can prove very difficult.

2. Structural degrading processes in the old steel

Phenomena and symptoms of structural degradation in the old steels have been presented and discussed in [1]. According to mentioned work, it can be stated that strength degradation processes in old steels consist mainly in: increase in hardness and material strength, drop in ductility and impact resistance, as well as drop in crack resistance. The above changes are well correlated with degradation processes characterised by the progressing decomposition of pearlite and bainite areas into ferrite and carbides, and progressing separation

processes (nitrides and carbides). Examples of such degraded structures can be seen in Fig. 1 and Fig. 2.
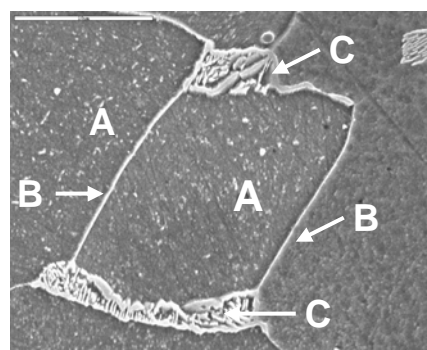
Fig.1. Exemplary pattern showing structural degrading symptoms (central Pomorski Bridge in Wroclaw) after 80 years of operation, magnification 4300x (SEM), Etched in 3%HNO$_3$.[2]

Letter A (Fig. 1) marks ferrite grains with numerous cementite and nitrides separations, B marks thick envelope of the Fe$_3$C, and C – partly degenerated perlit.
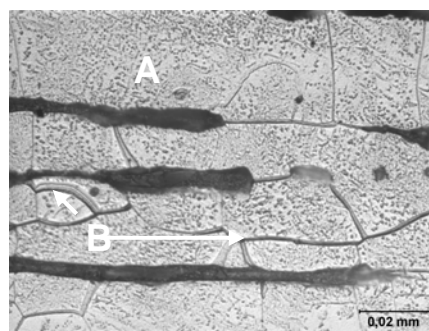
Fig.2. Exemplary pattern showing structural degrading symptoms (central Pomorski Bridge in Wroclaw) after over 120 years of operation, magnification 1000x (SEM), Etched in 3%HNO$_3$.[2]

Fig. 2, presents structure of ferrite grains with very big number of carbides and nitrides separations within the grains (A) and thick, continuous envelopes of Fe$_3$C at grain borders (B). Metallographic tests enable only

qualitative evaluation of the degrading advancement.

3. Modelling using fracture mechanics

In the fracture mechanics, numerous models of fatigue crack growth kinetics can be found. Unfortunately, many of them have limited scope of action, or are sensitive to the so basic quantity as the stress ratio R (F_{max}/F_{min}). Experience of the Authors indicate for the purposefulness of building (expanding) the model based at energy irreversibly dissipated in each load cycle. An example of such model could be:

$$\frac{da}{dN} = \frac{\alpha \Delta H}{\sigma_{plf} \varepsilon_{fc}} \quad (1)$$

In the model (1), σ_{plf} and ε_{fc} designate the cyclic yield point and critical cyclic value of deformation ε, respectively. ΔH is a new criterial quantity with the [J/m^2] dimension, representing the energy dissipated in each cycle of the loading spectrum. The basic advantage of that model is invariance of the diagram in relation to R ratio, and its linear character, which is illustrated at Fig. 3, by exemplary results for the 41Cr4 steel.
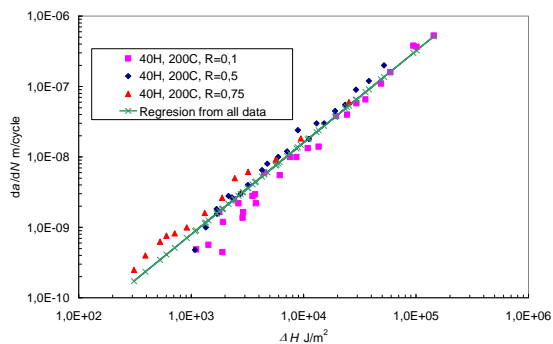
Fig.3. Kinetic fatigue fracture diagram for 40H (41Cr4 steel - heat treatment at 200°C) as a function of the energy parameter ΔH

Description of fatigue crack kinetics in the old bridge steels showing degradation symptoms (e.g. as presented in Fig 1 and 2) may prove difficult because of the material heterogeneity (large amount of impurities).

4. How to simplify the solution of kinetics equation?

While disregarding the influence of quantitative structure degrading on fatigue crack kinetics description, the simplified calculation procedures are still sought for, which could enable obtaining at least approximated value of the fatigue slot lifetime (though biased with tolerable error) in the engineering practice. Hopes for such description are aroused by the Method of Equivalent Surfaces presented in the work of [3]. The basis of this method is the hypothesis that flat cracks occurring in the homogeneous field of tensile stresses with convex contours *L* and identical surface areas *S* have the similar magnitudes of areas ΔS before a crack tip and the similar energies[3]. For the circular slot it assumes the form of:

$$N_{cr} = 16,051\alpha^{-1}\sigma_{plf}^2\sigma_{zw}^{-2}(1-R)^{-4}\left[\sqrt{\frac{S_{cr}}{S_{in}}} - 1 - 0,5\ln\frac{S_{cr}}{S_{in}}\right]^{-1} \quad (2)$$

Using the expression (2) and known initial quantities (S_{cr}, S_{in} – critical and initial slot surface, σ_{zw} – external load), the compatibility of exact solution results for ellipse and the approximated one (ellipse as a circle), for the ellipse semi-axes ratio grater than 0.3, has been shown in the [3] work (for the ratio equal 0,3, the concurrence is almost 95%). For smaller ratios the discrepancy proved to be significant.

5. References

[1] Pękalski G., Materials aspects of degradation of machines in opencast industry and theoretical description of relevant processes, Report SPR I-19, No 14/99, Wrocław 1999, (in Polish).

[2] Rabiega J.: Pękalski G., Materials testing the Pomorski bridges - South, Central and Nord on the Odra river in Wrocław, Report SPR No 9/2007, I-19, PWr, Wrocław 2007, (in Polish).

[3] Szata M., Description of crack propagation - theoretical approach and fitting accuracy to measurement results. Archives of Civil and Mechanical Engineering 2006 vol. 6, No 1, pp. 47-63,

BUCKET WHEEL EXCAVATOR RATING ON THE BASE OF EXPERTISE JUDMENT

Miloš Tanasijević, Dejan Ivezić[1)]

[1)] University of Belgrade, Faculty of Mining and Geology, Djusina 7, 11120 Belgrade 35, Serbia.

Corresponding author: tan@rgf.bg.ac.rs

1. Introduction

Rapid expansion of global demands for electricity power has caused, among other things, much greater exploitations of lignite on the open step mines. At the same time, there has been a necessity for development of giant machinery, primary bucket wheel excavators (BWE). Today, almost thirty BWEs are in service on the Serbian open step mines, Kolubara and Kostolac. They are of German production, and they were purchased from the producers like TAKRAF, O&K, KRUPP, during the past several decades. Today is half BWE in use 30 years and over. Due to the current economic crisis, and expressed the needs for rationalization costs, and on the other hand increasing need for energy, it is necessary to set the concept of assessment of the remaining capability of the machine, and defining their future. Is the machine writing-off or go to the revitalization and in what extent.

2. Existing methods for the evaluation of the remaining capability of the technical systems

The theory was developed two approaches to evaluation of the remaining capability of the technical systems, on the basis of technical measurements or on the basis of economical indicators. Significant technical measurement, often require stopping of machines and measure devices are very expensive. On the other hand, values of economic indicators are unobjective, considering that the Public Enterprise "Electric power industry of Serbia" commonly work in non market economy. Also, both approaches require a precise monitoring indicators of the excavators, indicators of the quality of maintenance, the cost of inputs and output of lignite exploitation and so on, which generally does not exist in Serbian lignite's open step mines. The problem of evaluation of the remaining capability of the BWE is an impressive, knowing that the BWE among most complex industrial machines. Same, from the standpoint of operate and from the standpoint of maintenance.

3. Evaluation of dependability on the basis of expert judgments

First of all, it is clear that the BWE should be viewed from the aspects of design, construction, maintenance and logistic during the period in operation and in periods of failure. Through ISO-IEC standards is introduced the dependability concept, which considers simultaneously reliability, maintainability and maintenance support. Apropos, dependability is introduced as overall indicator for quality of service for any technical system.

In this paper is presented a model [1] for dependability performance analysis of bucket wheel excavators. The model uses experts' judgment and estimations and thus prevents the problem of collecting data about BWE. At the end of, information about dependability indicators are often available only as experts' judgment and estimations. Fuzzy sets are used for introduction of these linguistically defined judgment and estimations in the explicit model for dependability determination of BWE`s components. Expertise judgment and estimations was realized with engineers employed in production and maintenance at open pit mine.

Bucket wheel excavator is a technical system with a complex hierarchical structure [2]. Therefore, it is necessary to make synthesis of information given in the fuzzy form from the level of components to subsystems, functional systems and whole bucket wheel excavator. This paper represents the utilization of evident reasoning theory (ER algorithm) [3] in these synthesis processes. The first was made on the decomposition excavators: systems, subsystems and components for which there are marks

dependability on the basis of fuzzy sets. For the gradual synthesis of dependability performance from the level of components to subsystems, systems and whole BWE evidential reasoning

theory is applied. The entire procedure of dependability evaluation on the base of ER algorithm, the results are given and received in the linguistic form.
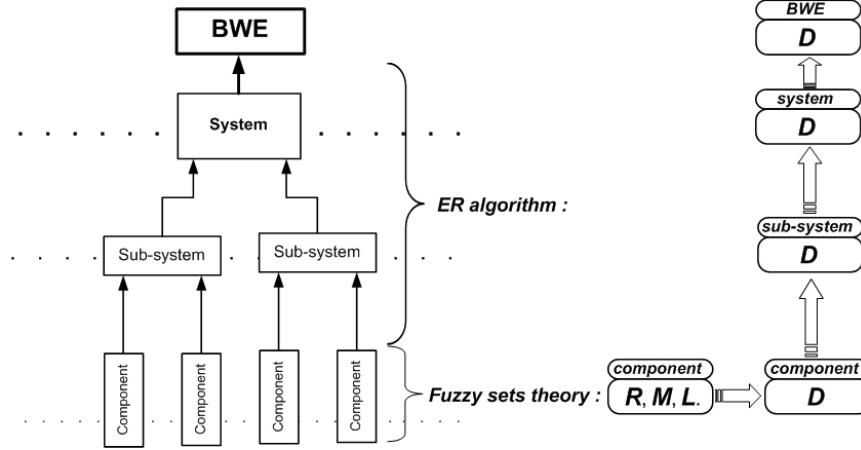
Fig. 1: Concept of BWE evaluation
(D – dependability, R – reliability, M – maintainability, L – maintenance support)

Dependability rating (D) received in final form, regardless of the level of hierarchical structure construction excavators (i):

$D_i = \{(\beta_{i1}, \text{"poor"}), (\beta_{i2}, \text{"average"}), (\beta_{i3}, \text{"good"}), (\beta_{i4}, \text{"excellent"})\}$

- where: $\beta_i = 0 \ldots 1$ and $\sum_{1}^{4} \beta = 1$.

This equation is accordance with the dependability fuzzy sets (Fig 2.).
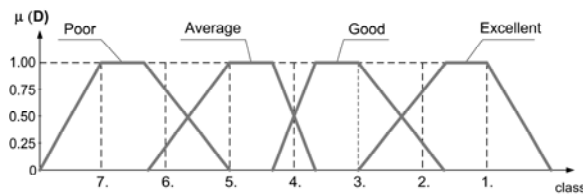
Fig. 2: Dependability fuzzy sets

4. Case study BWE SchRS 630

In the case study of this article, it is presented BWE SchRS 630, which operate in the Open Pit Mine Kolubara – Tamnava West Field. Based on the presented mathematical model is carried out experimental analysis of mechanical components of the excavators. The result marks dependability is provided for each component, subsystem, system, and

the entire BWE. Dependability evaluation of individual components, give a picture of the weak point of the excavators, and possible directions of revitalization. Overall rating

dependability of BWE, gives priority ranking excavators by introducing in the revitalization.

5. Conclusion

The importance of this research is reflected in the overall perception of reliability and quality of maintenance of such a complex mechanical system, as well as the experiment that took into account the expertise judgment employed engineers in the machine.

References

[1] Ivezić D., Tanasijević M., Ignjatović D., Fuzzy Approach to Dependability Performance Evaluation, Quality and Reliability Engineering International, Vol. 24 (2008) 779-792.

[2] Durst, W., Vogt, W., Schaufelradbagger, Trans Tech Publications, Clausthal, (1986).

[3] Wang J., Yang J.B., Sen P., Safety analyses and synthesis using fuzzy sets and evidential reasoning, Reliability Engineering and System Safety. Vol. 47-2 (1995) 103-118.

EXPERIMENTAL RESEARCH OF A COLLISION ENERGY ABSORBER OF A PASSENGER TRAIN

Jovan Tanasković [1)], Vojkan Lučanin [2)], Ivana Vasović [1)], Snežana Golubović [2)]

[1)] GOSA Institute, Milana Rakića Str. 35, 11000 Belgrade, Serbia

[2)] University of Belgrade, Faculty of Mechanical Engineering, Kraljice Marije Str. 16, 11000 Belgrade, Serbia

Corresponding author: jovant@eunet.rs

1. Introduction

The subject of this paper is research of the characteristics of shock absorbers of collision energy of passenger trains operating on the principle of tube compression into a special cone-like ring with a reduced diameter [1]. The absorber's role is to absorb as much of the collision kinetic energy as possible by controlled deformation, in order to protect the structure behind the absorption elements from deformation to the highest degree possible and thus protect the passengers and coach. In the moment of impact the kinetic energy is transferred to the ring that starts to compress the seamless tube. Thus energy absorption occurs by: *elastic-plastic deformation of the tube and friction between the ring and tube.* The total absorbed energy depends on the quality of the material (it should have a high plasticity), production quality and construction solution of the ring and tube. The purpose of this paper is to investigate the suitability and justifiability of the proposed construction of an absorber of collision energy of a passenger coach and determine solutions that are more efficient and suitable for applications in actual passenger coach constructions.

2. Experimental

Investigations of impact absorption used the following methods: quasi-static pressure loading (hydraulic press) and dynamic load (pneumatic hummer). Taking into account dimensions of the bumper and frontal part of the supporting vehicle structure, required amount of absorbed energy [2] and previous experience [3] stated above investigation was performed on the following elements: seamless tube-1 from low carbon steel (material P235T1)

and the cone-like ring-2 from quenched and tempered carbon steel (material C45E), Fig. 1.
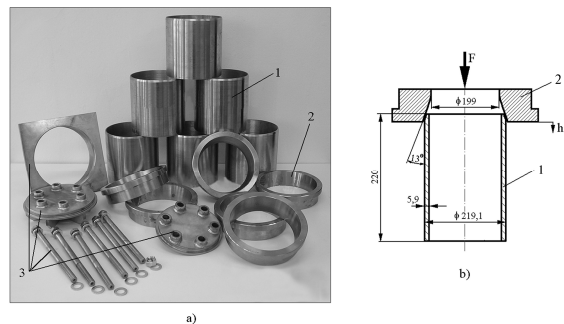
Fig. 1: Elements of tube shrinking absorber type samples

Position 3 on the Figure 1 shows elements for the fastening of a pre-deformed absorption pair. Figure 1b shows initial position of the absorption couple with characteristic dimensions. Measurement of the compression displacement was realized via two potentiometer movement indicators and measurement of the compression force was performed using a special indicator constructed on the base of measuring tapes connected into a full bridge.

Quasi-static investigations were performed in *two phases*. In the *first* – preforming phase, five sample pairs were compressed approximately 70mm. In this pre-deformed form (Figure 2a) absorption elements should be mounted on the front of the railway car structure.

a) Phase I - coupling   b) Phase II – absorption
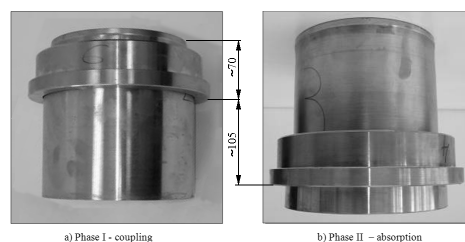
Fig. 2: Absorption couple

In the *second* experimental phase (phase of impact energy absorption), three samples were loaded statically on a press. For these samples, an additional stroke of approximately 105 mm was applied (Figure 2b). One sample was dynamically loaded on the hammer.

2.1 Experimental results

After the tests were completed, the recorded data was analyzed and force versus stroke diagrams was made [1]. Typical dependence of the compression force on the distance function obtained from investigations in the second phase of the experiment for three samples is presented in figure 3. The dependence is characterized by an approximately constant force value in the whole investigated region (for the distance of ≈105mm).
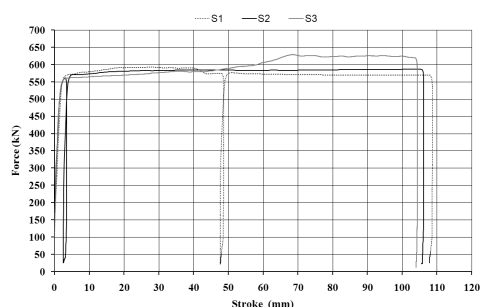
Fig. 3: Force versus stroke diagram – phase II

Figure 4 shows the dependence of the compression force versus displacement obtained by a dynamic test in the second impact energy absorption phase for a displacement of ≈ 20mm.
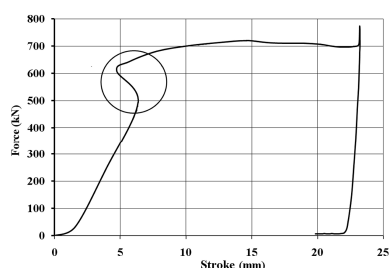
Fig. 4: Force versus stroke diagram – dynamic test

Investigation type	Average value	F_{max} (kN)	F_{av} (kN)	Stroke (mm)	W (kJ)
Quasi-static	x_{1-3}	603.08	585.86	105	61.52
Dynamic	x_4	719.96	562.12	20	11.24

Tab. 1: Characteristic parameters of phase II of the experiment

Table 1 contains parameters of significance for evaluating elements for energy absorption of the collision of passenger coaches obtained in the second phase of quasi-static and dynamic investigations.

3. Conclusion

For European railway passenger coaches, it is recommended to have a force of absorption elements between standard buffers and car structures between 1500 and 1750 kN (per end of coach) along with a maximum stroke of 135mm [2]. Having in mind that a somewhat lower force and thus energy values from the set ones were obtained in this work it was necessary to optimize some dimensions of elements. Prototype of new absorber with new dimensions was made (Figure 5).
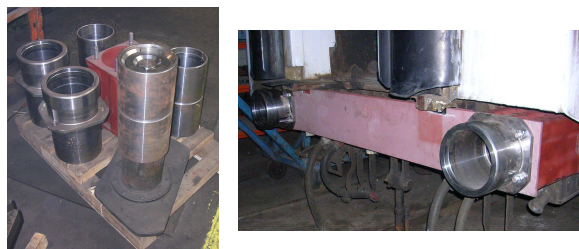
Fig. 5: Prototype of absorber

The final verification of tube shrinking absorber will be evaluated after conducting the crash test.

4. Acknowledgements

5. References

[1] Tanasković, J.: Research Of The Characteristics Of Collision Energy Absorber of Passanger Coaches, MSc Thesis (in Serbian), University of Belgrade Faculty of Mechanical Engineering, Belgrade, 2006.

[2] ORE B165, Dynamische festigkeit der Führerstandskabine gegenüber Frontalstossen, RP 8, Technische beschreibung des Fahrzeug-Designes, Utrecht 1991.

[3] Simić G., Lučanin V., Tanasković J., Radović N., Experimental research of characteristics of shock absorbers of impact energy of passenger coaches, Experimental Techniques, DOI: 10.1111/j.1747-1567.2008.00470.x

ON THE APPLICABILITY OF MORPHOMETRIC METHOD FOR EVALUATION OF THE WATERBORNE PARTICLES SIZE DISTRUBUTION

Srđan J. Tasić [1)], **Zorana Z. Golubović** [2)], **Dragan V. Petrović** [3)], **Zoran Đ. Golubović** [2)]

[1)] School of Applied Studies

[2)] University of Belgrade, Faculty of Mechanical Engineering

[3)] University of Belgrade, Faculty of Agriculture

Corresponding author: epetrodr@agrif.bg.ac.yu

1. Introduction

Filtration of process fluids represents an important step in a variety of technological processes. There are several types of filtration, and one of the most often used is mechanical filtration. In the filtration of this kind, substances are separated from each other by the application of adequate filtrational mediums and procedures. In this way, contaminants are restrained at the surface, or inside the volume of the filtrational media. Depending on the beginning and ending process conditions, filtration can consist of one or more filtration steps.

Among others, information related to the distribution of solid contaminants size distribution, which loads the process fluid, is crucial for constructing an efficient filter system [1]. Nowadays, these data are most commonly acquired by optical Particle Counter. However, other approaches are also available.

This paper presents the results of drinking water analysis based on two experimental methods: a common instrument known as the particles size counter and the morphometric method primarily specified for microbacterical analysis.

2. Experimental method

The idea of introducing an alternative method related to Particle Counter Analysis to commercial practice is based on the existing routine method primarily appropriate for bacteriological analysis: the morphometric method specified for measurement of microscopic objects (sizes of cells and their parts, for example). A sample of 1000ml is taken in regular time intervals from draining tap of filter housing. Concentration of the sample was done with filtration equipment produced by

Pall, using 0,47mm filter disc membranes whose absolute removal rating is 0,2 μm. Proximately before counting the particles, filter discs were flushed by redestilated water, which also represents necessary homogenisation of the sample.

The identical water sample was parallelly analysed by Liquid Particle Counter Liquilaz E20, an optical volumetric particle counter with sizing sensitivity range 2-125 μm. On the basis of both experiments, sizes of the contaminating solid particles are measured and the resulting distributions are calculated.

3. Numerical method

The normal probability density function (PDF in further text) has been successfully applied in describing the behaviour of relevant parameters in a variety of non-deterministic processes. This is a unimodal normally flattened (F=3) symmetrical function (S=0), where F and S are the skewness and flatness factors respectively. This is the most commonly used function in statistical modelling.

However, PDFs of real samples significantly deviate from this function very often. Among others, a possible approach for overcoming these situations is based on the hyperbolic function, introduced by Barndorf-Nielsen [2] to describe the asymmetric distributions of the wind-blown sand particle sizes.

The one-dimensional hyperbolic function can be represented in the form [3]:

$$f(x) = A(\alpha, \beta, \delta) \; e^{(-\alpha\sqrt{\delta^2 + (x-\mu)^2} + \beta(x-\mu))} \qquad (1)$$

The four arbitrary parameters: $\alpha > 0$, $|\beta| < \alpha$, $\delta > 0$ and $\mu \in (-\infty, \infty)$, that define its shape are evaluated numerically on the basis of the0 adequate empirical data set. A is the constant that enables the hyperbolic function (1) to

satisfy the standard condition of the theory of probability:

$$\int_{-\infty}^{\infty} f(x) \cdot dx = \int_{-\infty}^{\infty} PDF(x) \cdot dx = 1 \qquad (2)$$

It is defined as:

$$A(\alpha, \beta, \delta) = \frac{\sqrt{\alpha^2 - \beta^2}}{2 \cdot \alpha \cdot \delta \cdot K_1\left(\delta \cdot \sqrt{\alpha^2 - \beta^2}\right)} \quad , \qquad (3)$$

where K_1 is the Bessel function of the 3^{-rd} kind and 1^{-st} order.

4. Results and Discussion

Examination results of waterborne particle size distribution, accomplished by standard optical particle counter and morphometric method in the same sample of drinking water, are comparatively shown in fig. 1.
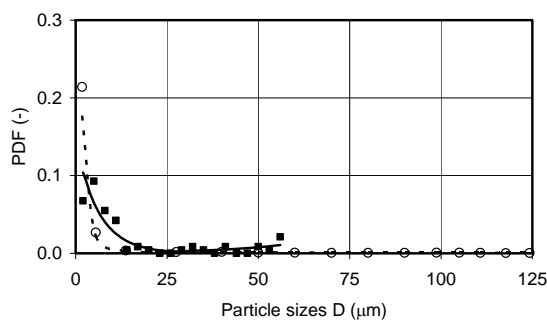
Legend:
- ■ morphometric method experimental data
- ○ particles size analysis experimental data
- ▬ fit of the data acquired by morphometric method
- - - - fit of the data acquired by particles size counter

Fig.1: Probability density functions of the waterborne particle size distribution, evaluated by particle size counter and by morphometric method.

	Particle sizes counter	Morphometric method
α	-0.3375519	-0.10442428
β	-0.349269878	-0.05298808
δ	5.051960988	0.00248212
μ	7.621563019	26.23557208
A	1.666789E-03	0.00229193

Tab.1: PDF hyperbolic function coefficients.

It can be concluded that concordance of data obtained by these two methods is not ideal, but their accordance is nevertheless satisfactory. The main problem originates from a limited sample of contaminated water analyzed by morphometric method. Consequently, large particles (over 60 μm

approximately) were not registered by this method, although they can easily be seen under the microscope because of large dimensions.

In both cases, measurement results shown in form of PDFs are successfully fitted by hyperbolic function (fig. 1), which coefficients are shown in table 1.

5. Conclusion

Comparison results of two experimental methods are presented in the paper: the optical particle counter method (commonly used for waterborn particles sizing and counting) and its possible competitor proposed by us - the morphometric method primarily specified for microbacterical analysis.

The general agreement between results ac–accomplished by these methods is encouraging, verifying in a way the applicability of morphometric method as a low cost alternative for Optical Particle Counter Analysis. However, further detailed research of massive water samples is still needed in order to resolve the problem completely.

This paper also confirms the fitting capability of hyperbolic function in describing the distribution of waterborn particles sizes, whose removal from drinking water represents one of the more important tasks.

6. References

[1] Golubović, Z., Šešlija, D., Milovanović, B., Majstorović, B., Vidović, M. (2007): The Challenges in Sterile Pressurised Air Preparation, BAM-CX/2007, Nr. 2310, Proceedings of the PAMM Conference PC 152-153 June, B.almadi, pp. 110-120.

[2] Barndorf-Nielsen, O. (1977): Exponentially decreasing distributions for the logarithm of particle size, Proc. R. Soc., London, A.353, pp. 401-419.

[3] Bhatia, J. C., Durst, F. (1988): LHPDF – A PC package for estimating parameters of *the log-hyperbolic distribution, moments and mean paramete*rs, Report LSTM 230/T/88.

ANALYSIS OF RESISTANCE FORCES ON INDIVIDUAL LOCOMOTIVE PARTS IN TRACK CURVATURE

Jovan Tepić[1)], Milan Kostelac[2)]

[1)] Faculty of Technical Sciences University of Novi Sad, Trg Dositeja Obradovića 6, 21000 Novi Sad, Serbia
[2)] Faculty of Mechanical Engineering and Naval Architecture University of Zagreb, I. Lučića 5, 10000 Zagreb, Croatia

Corresponding author: milan.kostelac@fsb.hr

1. Introduction

In order to evaluate the resistance in track curvature and wear of wheels and track, it is necessary to determine, in operating conditions, resistance force values on individual vehicle (locomotive) sections. Numerical, graphical or experimental methods can be used to solve this problem [1-2]. This work shows results of experimental analysis of the resistance force values in track curvature on individual parts of pulling vehicle – locomotive, on a scaled-down model in HO standard 1:87, with variable axle activity arrangement (*WA*). The experimental research was conducted with two identical four-axle locomotives (Fig. 1).

Fig. 1: Locomotive model

2. Measurements

This experiment proves the dependence of resistance force in track curvature W_R on track vehicle and path parameters: $W_R = f(R, v, WA)$, where:
W_R - resistance force in track curvature,
R - curvature radius,
v - motion velocity of locomotive model and
WA - axle activity arrangement.

Analysis was done on moving locomotive of constant mass with motion velocity v and constant power, whilst varying axle activity arrangement for different track curvature values. Locomotive parameters are velocity v

and number and arrangement of axle activity (axles can be driving – active A and free – passive P). Axle activity arrangement WA is: *AAAA, PAAA, APAA, AAPA, AAAP, APAP, PAPA, APPA* and *PAAP*.

Parameters of track path are radii: radius on the straight track $R000$ ($R = \infty$) and radii in curvature $R432$ ($R = 432$ mm), $R342$ ($R = 342$ mm) and $R250$ ($R = 250$ mm). The three radii of curvature were chosen in order to obtain more significant variation of experimental results.

Total resistance W is the sum of constant resistance force (resistance on the straight track) W_S, resistance of geometric and constructional characteristics of track path W_T and other resistance forces W_0. All the available methods of determining the resistance forces of track vehicle give total motion resistance W, but not the individual components W_S, W_T and W_0. Since the main goal of this experimental analysis is to determine the resistance components due to geometric and design characteristics of the track path W_T, an appropriate protocol for determining the individual resistance components is established in this work. This experiment used a model of a real engine in order to eliminate the effect of other resistance forces $W_0 = 0$ (e.g. wind power, effect of starting and accelerating the engine) and $W_T = W_R$. Therefore, the observed total resistance is a sum of constant resistance forces and resistance of geometric and constructional characteristics of track path (resistance in curvature) [3].

Measurement of track resistance W_T is in this case reduced to measuring the track resistance in curvature W_R on experimental track. Under presumption of the constant engine power, the resistance in curvature is determined by measuring the reduction in motion velocity of locomotive mode from entry to exit from the curvature.

3. Resistance values in curvature

Experimental values from measurements on straight path have shown that the locomotive travels uniformly for all combinations of axle activity arrangement *WA* and has constant velocity v = 0,652 m/s for 4, 3 and 2 active axles.

Each motion velocity has a corresponding resistance, calculated using the formula for constant resistance: $W_S = 4,6416\ v^4 - 8,328\ v^3 + 5,0963\ v^2 - 0,8906\ v + 0,1901$ [4].

During the motion through the curvature the velocity is reduced, as the vehicle is subjected to the constant as well as curvature resistance. The reduction in velocity is in fact the result of the resistance in curvature which can be calculated as the difference between the total resistance on straight path W_∞ and constant resistance W_S, i.e. $W_R = W_\infty - W_S$. The total resistance on the straight path W_∞ is calculated using the above expression for the motion velocity v. Constant resistance W_S is calculated from the same expression for relevant motion velocities at the end of curvature using corresponding radius R.

4. Resistance force in curvature on individual locomotive parts

Based on the theory of locomotive motion in curvature it is known that different vehicle parts have different axle load. In order to calculate the total resistance force on each axle, a linear equation for the defined activity arrangements has to be derived. For example, in the case *WA = PAAA* the sum of resistance forces in curvature for each axle is equal to the total resistance in curvature for the locomotive: $W_{1P} + W_{2A} + W_{3A} + W_{4A} = W_{PAAA}$.

Similar equations can be defined for each axle activity arrangement. Thus, the set of eight linear equations has been obtained. From the aforementioned set of equations the following results, given in Fig. 2 and Fig. 3 are obtained for different curvature radii.
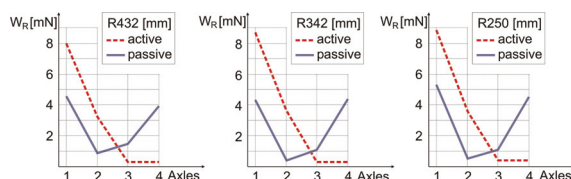
Fig. 2: Values of resistance forces in curvature per axle for *R*432, *R*342 and *R*250
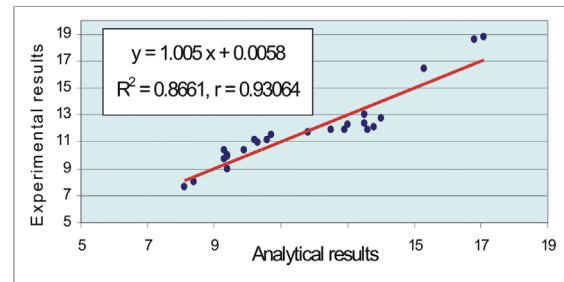
Fig. 3: Validation of experimental and analytical values of resulting resistance forces in curvature for *R*432, *R*342 and *R*250

5. Conclusions

Based on the experimental results and data analysis we can conclude:
- measurement results show that the resistance in curvature W_R increases with reduction of radius,
- the resistance force values are increasing with transfer of passive axle(s) towards the back of the vehicle,
- for *WA* combination with two passive axles, maximum value of resistance force is obtained when the passive pair of axles is closer to the back of the vehicle and
- the first undercarriage is the main bearer of the resistance force in curvature, accounting for over 64% of the total locomotiv resistance. This is confirmed in real working conditions by increased wear of the front undercarriage.

6. References

[1] H. Heumann, Grundzüge der Führung der Schinenfahrzeuge, Sonderdruck aus Elekrische Bahnen, Verlag Oldenbourg-München (1959).

[2] K. Sachs, Elekrische Triebfahrzeuge-Band 1, Zweite Aufgabe, Springer-Verlag Wien-New York (1973).

[3] J. Tepić, M. Kostelac, Application of gravitational method by determination of rail vehicles constant resistance, Transactions of FAMENA, Vol. 32, No. 2, Zagreb (2008) 60-70.

[4] J. Tepić, Istraživanje ponašanja vučne sile pri prolasku šinskih vozila kroz krivinu, Monografija, Beograd (2006).

EVOLUTION OF Cu-RICH PHASES DURING SOLUTION TREATMENT

Tillová Eva, Hurtalová Lenka, Chalupová Mária [1]

[1] University of Žilina, Faculty of Mechanical Engineering, Department of Material Engineering, Univerzitná 1, 010 26 Žilina, Slovakia.

Corresponding author: lenka.hurtalova@fstroj.uniza.sk

1. Introduction

Al-Si alloys are extensively used in the automotive industry due to their excellent castability, good mechanical properties, machinability and wear resistance. The addition of alloying elements such as Mg and Cu make these alloys heat treatable, further improving their mechanical properties and allowing their use in new, more demanding applications [1, 2]. The most common thermal treatments used with these alloys involve either age hardening the as-cast alloy or solution treatment followed by age hardening. For most applications, the solution treatment is usually adopted because it produce maximum tensile strength and hardness. During the solution treatment, the alloy is subjected to high temperatures for relatively long periods of time with two main objectives: to obtain maximum solubility and homogeneity of the alloying elements and impurities in the matrix and to modify the acicular morphology of the eutectic silicon to a less detrimental rounded one [3].

The solution temperature must be high enough and the treatment time long enough to allow maximum dissolution and homogenization of the alloying elements.

2. Experimental Results

As an experimental material was used recycled AlSi9Cu3 alloy with Al-10.7Si-2.4Cu-0.22Mn-0.9Fe-0.22Mg (wt.%). The melt was not modified or refined. Experimental cast samples were given a heat treatment - solution treatment for 2, 4, 8, 16 or 32 hours at three temperatures (505, 515 and 525°C); water quenching at 40°C and natural aging for 24 hours at room temperature. After heat treatment were samples subjected for mechanical test (strength tensile, ductility, hardness). The alloy and its heat treatment presented in this work is part of a larger project and the microstructural (Si morphology, DAS, Fe-rich phases) and mechanical property details of which have already been published [4, 5]. Present work is focused on study of the effect of solution heat treatment to the Cu-rich intermetallic phases.

Increasing the level of Cu improves the strength of the aluminium alloy through the formation of Cu based precipitate during heat treatment, the intermetallic phase that Cu form with Al during solidification according to the reaction: $L \rightarrow (Al + Al_2Cu + \beta\text{-}Al_5FeSi + Si)$ at 525°C. This reaction relates to the start of Al_2Cu precipitation towards the end of solidification and consequently may be nucleated on other interdendritic particles (Si, Fe-rich phases). The phase Al_2Cu solidifies in two forms: one massive or blocky (Al_2Cu) and the other a fine eutectic ((Al- Al_2Cu –Si) - Fig. 1a) formed which depends on the level of Cu, Fe and Sr in the alloy [3, 5].
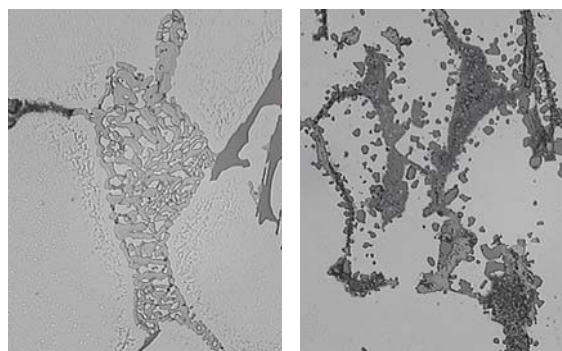
a) untreated, 1000 x   b) 515°C/4 hours, 1000 x
Fig. 1: Influence of heat treatment on morphology of Cu-rich phases (Al-Al$_2$Cu-Si), etch. HNO$_3$

After solution treatment by temperature 505°C Cu-rich phase disintegrated into smaller segments. This phase is gradually dissolved into the surrounding α-matrix with an increase in solution treatment time. By solution treatment by 515°C is this phase observed in the form coarsened globular particles and these occurs

along the black needles, probably Fe-rich Al_5FeSi phase (Fig. 1b).

Fig. 2 shows the average area of Al-Al_2Cu-Si phase obtained in solution heat treated samples. It is evident that heating at temperatures below the final solidification temperature (505°C, 515°C and 525°C) results in a dissolution of Al-Al_2Cu-Si phase. Dissolution is accelerated as soon as the holding time is increased to 4 hours, where the dissolution exhibits a relatively linear behaviour with holding time. Further heating does not bring about much change in the amount or average area of Cu-phases. Maximum surface of cooper intermetallic phases was observed by 525 °C with holding times 2 hours (9 995.5 μm^2). Minimum surface was observed by optimal temperature solution treatment 515°C (0.277 μm^2).
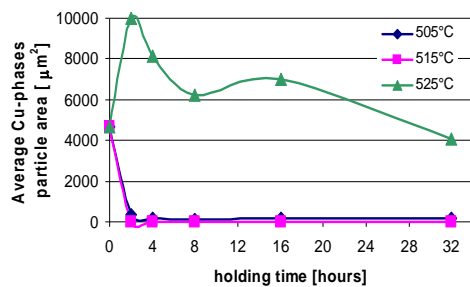
Fig. 2: Changes of average area Cu-rich phase's during the heat treatment

When the AlSi9Cu3 alloy is solution treated at temperature about the melting point of the eutectic (Al + Al_2Cu) phase, e.g. 525 - 540°C, the Cu- particles may undergo incipient melting even after periods as 4 hours as evidenced by the black spots (arrowed →) observed within the Al-Al_2Cu-Si particles (Fig. 3).

a) 525°C/2 hours   b) 525°C/32 hours
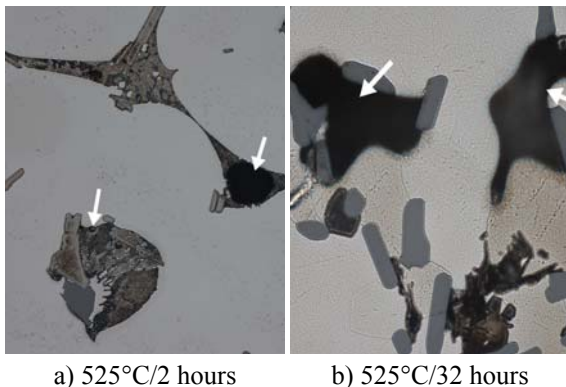
Fig. 3: Melting process of Al-Al_2Cu-Si particles, etch. Dix-Keller, 1 000 x

Melting process of Al-Al_2Cu-Si particles has 4 stages: after 2 - 4 hours is observed initiation of melting; after 8 hours showing massive Al_2Cu coexisting with Si and Fe-phase; next showing structureless phase – note the presence of the previously existing Al_2Cu eutectic at the outer fringes; finally showing the presence of cavities and structureless phase particles.

Heat treatment is one of the major factors used to enhance the mechanical properties of heat-treatable Al-Si alloys, through an optimization of both solution and aging heat treatments. The solution treatment homogenises the cast structure and minimizes segregation of alloying elements in the casting. Segregation of solute elements resulting from dendritic solidification may have an adverse effect on mechanical properties.

Fig. 4 shows the influence of heat treatment on the Brinell hardness. Hardness of solution treated test bars at 505 and 515°C are increased by increasing the solution temperature and time. Highest hardness was observed by temperature 515°C for times 2 hours (122 HBS). At 525°C, test bars show hardness reduction due to melting of the Al-Al_2Cu-Si phase.
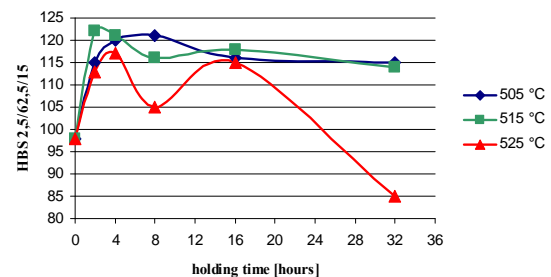
Fig. 4: Influence of solution treatment on hardness of recycled AlSi9Cu3 alloy

3. Acknowledgements

4. References

[1] F. H. Samuel, Journal of Materials Science, Vol. 33 (1998) 2283-2297.

[2] G. Nicoletto, R. Konečná et al., Materials Science Forum, Vol. 567-568 (2008), pp. 393-396.

[3] L. Lasa, J. M. Rodriguez-Ibabe, Journal of Materials Science, Vol. 39 (2004) 1343-1355.

[4] M. Panušková, E. Tillová, M. Chalupová, Problemy pročnosti/Strength of Materials, Vol. 391 (2008) 109-112.

[5] E. Tillová, M. Panušková, Mettalurgija, METABK 47 (3) 133-137 (2008) 1-4.

OPTIMAL SIZE DETERMINATION OF TACTILE SENSOR PLANTOGRAF V08 AND ITS ELECTRODES

Trinkl Aleš[1], Volf Jaromír[1], Novák Martin[2], Růžička Michal[1],

[1]   Czech University of Life Science in Prague, Technical Faculty, Department of Electrotechnics and Automatization. Kamýcká 129, 165 21 Prague 6, CZECH REPUBLIC.

[2]   Czech Technical University in Prague, Faculty of Mechanical Engineering, Department of Control and Instrumental Engineering. Technická 4, 166 07 Prague 6, CZECH REPUBLIC.

Corresponding author: volf@tf.czu.cz

1. Introduction

Plantograf V08 is a tactile transducer, which enables pick up tactile information of particular object and transfer this information to electrical signal. This sensor is focused for following applications: measurement of static and dynamic pressures distribution, human steps analysis, sitting position analysis, pressure distribution on foot flat and analysis of big joint status.

Plantograf V08 has to fulfil the following conditions: sensor can not change measured pressure distribution, has to measure static and dynamic load, has to have sufficient sensitivity and accuracy for given applications in each point of the sensor matrix.

The contribution is focused on description of the Plantograf V08 matrix construction, description of the electronic circuits which have the sensor matrix and optimal electrode size determination in the point where a thin film from a conductive silicon elastomer is used to transfer load to electrical signal.

2. Transducer description

Construction of the Plantograf V08 was designed with regards to minimisation of influence to the matrix measured points and maximisation of matrix point sensitivity. The matrix construction is described in a patent application [1].
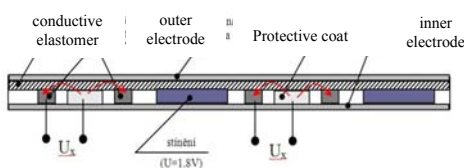
Fig. 1: Plantograf V08 Cross Section

A part of Plantograf V08 cross section is shown on the Fig.1. Both electrodes are corroded on one cuflex film placed on the bottom part of the sensor

matrix. Between electrodes are measured changes of elastomer resistance.

Every electrode is covered by the conductive elastomer in its whole surface. The electrodes with these conductive elastomers are protected by non-conductive flexible material which saves the elastomers from mechanical point of view.

Currents which flow in their sensor matrix and their directions are shown by indicators on the Fig. 1 and 2.

It means that current flow from the inner electrode through the conductive elastomer to the outer electrode.
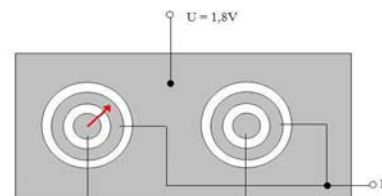
Fig. 2: Top View – Part of Plantograf V08 Sensor Matrix

3. Plantograf V08 electronic circuits

The previous Plantograf V05 construction had several drawbacks that we tried to remove with the new construction type. It had high current consumption causing heat-up and dependency of power consumption on applied load. Also the construction used high speed digital converters and the relatively complicated circuits. In the new version, all A/D converters were replaced by a simple RC circuit discharged over the sensor resistance. The connection operates as resistance to time converter. All function and control are integrated in a Xilinx Spartan 3 FPGA. These changes allowed miniaturizing the whole circuit and improving speed significantly. The estimated rate is currently approximately 1000 frames/s for online measurement and 5000 frames/s for offline

measurement where the data is stored to a memory card.

Fig. 3: Plantograf V08 – Sensor Matrix with Electronic Circuits

4. Determination of optimal electrode size

A basic task of measurement was determination of optimal electrode size which gives to the sensor matrix maximal measuring properties namely maximal measuring sensitivity.

A special modular system dedicated for tactile sensor measurement was used for measuring of the points placed on the sensor matrix. This system measures load of the matrix points in real time [2].

Simultaneously rate resistance is measured by means of SW and electronic circuits. Resistance can take values between 0 – 255.

The six different construction of the sensor matrix were measured during determination process. The sensor matrix had following size:
1. ØE=2mm, Ød=0,4mm, M=0,1mm – **LH**
2. ØE=2mm, Ød=0,1mm, M=0,1mm – **PH**
3. ØE=2,5mm, Ød=0,4mm, M=0,25mm – **LD**
4. ØE=2,5mm, Ød=0,1mm, M=0,25mm – **PD**
5. ØE 3,5mm, Ød=0,4mm, M=0,25mm, separated measuring points – **OB**
6. ØE 3,5mm, Ød=0,4mm, M=0,25mm, connected measuring points – **SB**

Construction sizes are described on the Fig.4.
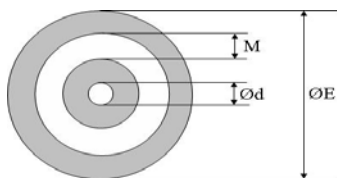
Fig. 4: Sizes of Measured Electrodes

Construction number 5 and 6 has got the same electrode size. Construction number 5 has got the conductive elastomer just in the measuring spots. Construction number 6 has got the conductive elastomer in its whole surface of the sensor matrix.

Every construction was measured in the following way:
- Tree points were measured on every construction

- Every point was measured tree times in range 0,5 – 9,5N (10 measurements) – loading
- Every point was measured tree times in range 0,5 – 9,5N (10 measurements) – unloading
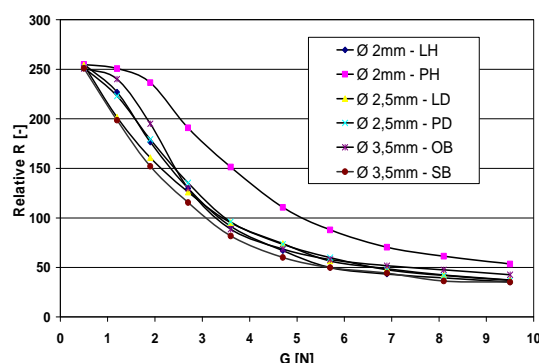
Fig. 5: Measured Values of Different Electrode Types
The average values from measurements are shown on the Fig.5.

5. Conclusion

The construction of the tactile transducer Plantograf V08 is the newest of the Plantograf Vxx line. It is designed to improve the features of the tactile sensors Plantograf V05 and Plantograf V07. The disadvantages of listed sensors were:
- Plantograf V05 – there occurred influence of the unloaded points which were placed in proximity of the loaded point.
- Plantograf V07 – difficult sensor matrix construction which needed precise production. Also there was a low sensitivity of the measuring points.

Measurement result shows that sensor sensitivity varies with used construction type of the sensor matrix. Construction type PH has got the lowest sensitivity Fig.1. Construction type SB has got the highest sensitivity.

Next measurement result says that the highest sensor size is used the highest sensitivity is reached. This construction size fulfils conditions which were designed for.

6. Acknowledgements

7. References

[1] Volf, J.; Novák, M.; Vlček, J.; Trinkl, A.: Zařízení na snímání taktilní informace, Patentová přihláška, duben 2009

[2] Trinkl, A.: Nová konstrukce taktilních snímačů – základní měření jednotlivých měřicích bodů snímací matice potřebné pro kalibraci snímače. Jemná mechanika a optika, 4., Praha 2008

POSSIBILITY OF LOAD SIMPLIFICATION FOR MULTIAXIAL FATIGUE TEST

Jakub Vágner [1)], Bohumil Culek jr. [2)], Bohumil Culek [3)],

[1)] Ing. Jakub Vágner, University of Pardubice, Jan Perner Transport Faculty,
Department of Transport Means and Diagnostics, Studentská 95, 532 10 Pardubice, Czech Republic,
tel.: +420 466 036 237, email: Jakub.Vagner@upce.cz

[2)] doc. Ing. Bohumil Culek, Ph.D., University of Pardubice, Jan Perner Transport Faculty,
Department of Transport Infrastructure, Studentská 95, 532 10 Pardubice, Czech Republic,
tel.: +420 466 036 398, email: Culek@upce.cz

[3)] prof. Ing. Bohumil Culek, CSc., University of Pardubice, Jan Perner Transport Faculty,
Department of Transport Means and Diagnostics, Studentská 95, 532 10 Pardubice, Czech Republic,
tel.: +420 466 036 187, email: Bohumil.Culek@upce.cz

Corresponding author: Jakub.Vagner@upce.cz

1. Introduction

A multi-axial loading is usually used for experimental fatigue tests of rail vehicle bogie frames. It requires using of many actuators in the same time. Therefore tests are expensive, time-consuming and depended on laboratory equipment. For this reason it is preferable to test only the most exposed construction parts, which allows use of less number of actuators in comparison with testing of whole construction. The aim of the work is to determine a possibility to find a solution for reduction of total number of actuators in a test of construction part. A procedure of transformation from triple-cylinder multi-axial test to double-cylinder or single-cylinder is described. The transformation is based on synthesis of theoretical (FEM) and experimental methods.

2. Specimen

Designed specimen meets following criterions:

- manufacturability and simplicity,
- possibility to use the triple- , double- and single-cylinder loading,
- possibility to determination of critical places,
- specimen is a part of rail vehicle bogie frame,
- critical places localization.

The construction detail (longitudinal and cross beam connection - Fig.1) was chosen from a few proposed construction details commonly used in rail vehicle bogie frame.

3. Fatigue critical places

The critical places were determined by FEM analysis (a curvature of the beams connection). The shape of the beams connection curvature was changed to decrease a total time of fatigue tests (Fig.2).

4. Load system

The load system of the specimen contains two forces (F_Z, F_Y) and one torque moment (M_X). Fastening tools were designed for fixation of the specimen to loading set (Fig.1).
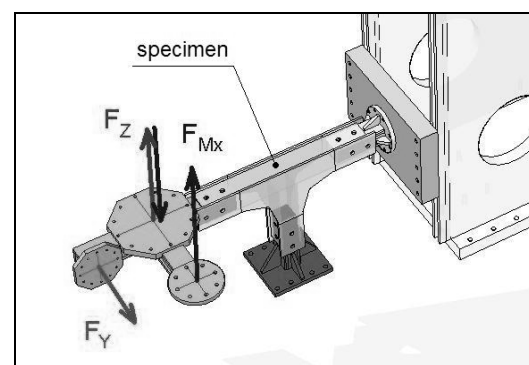
Fig. 1: Forces orientation

Each of three actuators is connected by two joints. By reason of load system stability are all forces directed in pulling (Fig.1). Only the force in Z direction can effect also in pushing. The system of actuators control allows application of three load forces together (dependent, independent) but also allows application of individual load force (described in Tab.1).

load	F_Z	F_Y	F_{MX}	F_Z F_Y F_{MX}
Z	$Z = F_Z$	stop	$Z = M_x/e$	$Z = F_Z - M_x/e$
Y	stop	$Y = F_Y$	stop	$Y = F_Y$
X	synch. with Z	stop	$X = M_x/e$	$X = M_x/e$

Tab. 1: The actuators control system

5. Load simplification

The aim of the work is to determine possible simplifications of the load system. The importance is to achieve comparative results in both cases (multi- and single-axial loading).

Example of simplification (from double-axial to single-axial loading):

1) propose multi-axial (double-axial) loading parameters,
2) FEM analysis (multi-axial and single-axial loading),
3) propose single-axial loading parameters,
4) experimental verification.

Crit. place [MPa]	$F_Z = 10$ kN $F_Y = 10$ kN	$F_Z = 10$ kN	$F_Z = 17$ kN
A	**248**	*138*	**249**
B	*70*	*138*	*249*

Tab. 2: Mechanical stress in critical places

The FEM results are presented on the Fig.2 and Fig.3 and Tab.2.
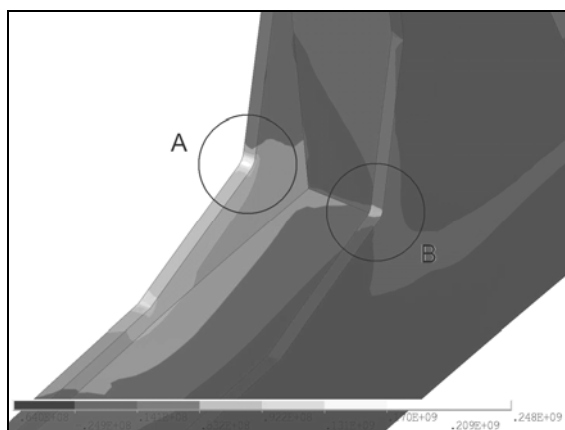
Fig. 2: FEM analysis results Fz=10 kN, F$_Y$=10 kN
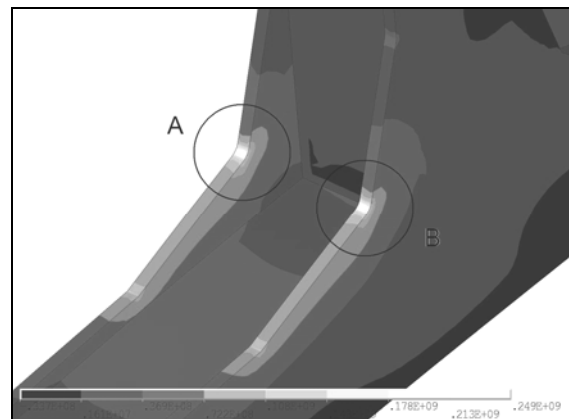
Fig. 3: FEM analyses results Fz=17 kN

6. Conclusion

In the paper is discussed experimental approach for determination of stresses by use of multi-axial load in comparison with single-axial load of tested specimen. The results show that the simplification is possible. The values of mechanical stresses (σ_l) in critical place **A** are *248 MPa* for multi-axial load and *249 MPa* for single-axial load. In both cases is the distribution of mechanical stresses different. Taking into account symmetry of the specimen is used simplification acceptable. The results are based on theoretical method (FEM). For this reason it is important to verify these theoretical results by experimental tests.

7. Acknowledgements

8. References

[1] VÁGNER, J.,CULEK, B. ml, CULEK, B. Simulace rozhodujících složek provozního namáhání částí kolejových vozidel na multiaxiálních zatěžovacích standech, Přehledová zpráva VCKV č. B5-01-2008, Pardubice 2008

THE INFLUENCE OF SUSPENSION DEGRADATION ON RELIABILITY OF WASHING MACHINE

Vasilije S. VASIĆ, Ph.d. student [1,2)], **Mihailo P. LAZAREVIĆ** [2)]

[1)] Gorenje d.d., R&D department of washing machines, Partizanska 12, 3503 Velenje, Slovenia.

[2)] University of Belgrade, Faculty of Mechanical Engineering, Kraljice Marije. 16, 11120 Beograd, Serbia.

Corresponding author: vasilije.vasic@amis.net (vaso.vasic@gorenje.si)

1. Introduction

The washing machine is considered as multibody dynamic system, which dynamic and reliability properties are strongly influenced by suspension system. The suspension system, usually made from coil springs and friction dampers, change their properties during the product life time due the ageing and/or (temperature) degradation. There exist real demand to determine in what extend is still acceptable their property degradation and in the same time washing machine operates in acceptable margins. Proposed analytical modelling is performed with alternative, robotical procedure.

2. Washing machine and modeling

There are two main approaches to achieve stability of washing machine at given operating process procedure (s.c. washing process) – geometry (e.g. mass and inertia) and suspension (springs, dampers). Fundamental task is to prevent excessive vibrations being transmitted to the housing of washing machine (**fig. 1a**), which could cause instability in form of walking and spinning. Engineers respond on this challenge with compromise solutions in terms of optimum vibration control, overall system performance, energy efficiency and cost. Evaluation of acceptable technical solution is possible already in conceptual phase of product design with analytical modelling and our multibody dynamic mechanical model with robotical approach - **fig. 1b**. Namely, robotical approach has proven itself as more suitable approach for the analytical modelling in case of evaluation multicomponent dynamic system for parametric modelling. In industrial environment

is very welcomed due its numerical simplicity and easily scanned, but also as tool for quality control or quality assurance. Analysis usually refers only to the nominal values, which are declared by producers and do not examine allowed deviations and possible degradations during exploitation (product lifetime).
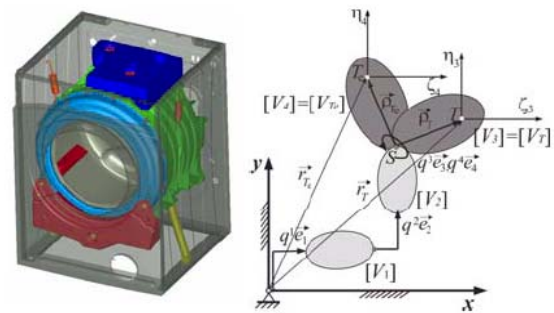
Fig. 1: Washing machine and multibody dynamic mechanical model (robotical approach)

In case of suspension system, main influential factors are besides geometry (e.g. angle of attachment) also degradation of damping due the wear out, environment influence (temperature) or even ageing.

2.1 Experimental results – friction dampers

The washing machine has different operating modes, which case different states of dynamic loads. The washing group (tub with drums and counterweights) – **fig.1a** is suspended by a pair of coil springs, which provide mechanical support nad vibration isolation at high frequency. The drum velocity during the working process passes through resonance of washing machine as it accelerates during the ramp-up to the spin cycle or stagnating from spin cycle to the steady state. To prevent unwanted and damaging vibratory motions which could occur during this process

phase, static vibration dampers are added to the suspension.

The most common used dampers in the washing machine are friction dampers and with damping force up to the 120 N. For the washing machine design engineers is well known, that they tend to change their properties due temperature and after certain number of process cycles.

For common friction dampers is experimentally evaluated ageing (cca. 10% of nominal value in 10 years with acceleration test) – **fig. 2** and correlation of damping properties to the temperature – **fig. 3**.
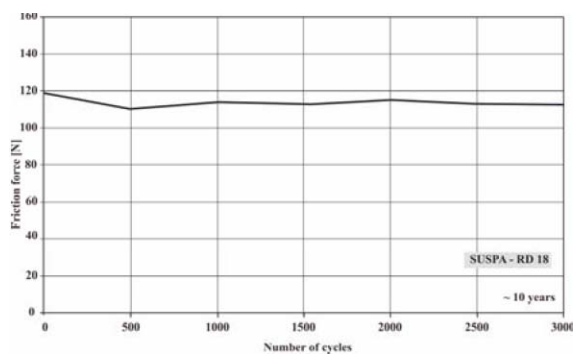
Fig. 2: Friction damper and operational time
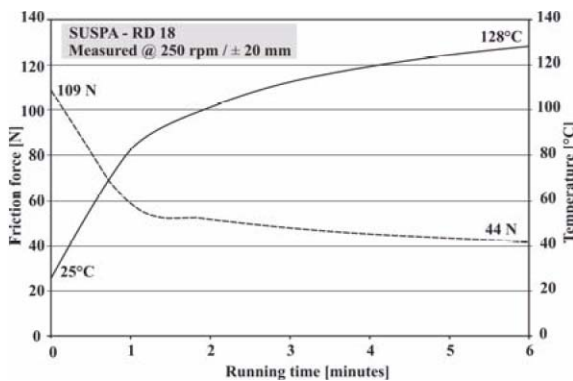
Fig. 3: Friction damper force related to temperature

2.2 Parametric multibody dynamic analysis

Parametric analysis has taken in account the end-values (boundary) property changes of dampers in validated model for motion and acceleration of washing group. Another parametric issue is drum agitation in terms of various and common drum's rotations. In many cases the amplitude of washing drum is in the margin of safety distance washing group/washing machine cabinet.

3. Conclusion

Mentioned approach is useful and handy in industrial environment to validate nominal values of suspension system and their possible (declared) deviation. To overcome negative phenomena, there are also presented some novelty technical solutions in area of springs and dampers. Generally, motion control and vibration control could not be treated as separate issues.

4. References

[1] M.P. Lazarević, V.S. Vasić: Mathematical modelling and simulation of a washing machine: a robotic approach, in: Proceedings of the Sixth International Conference on Computational Structures Technology, 02-05.09.2008, Athens, pp.115-122

[2] Vasic,V.S.,Lazarević, M.P.: Standard Industrial Guideline for Mechatronic Product Design, Faculty of Mechanical Engineering Transactions (2008) 36, Faculty of Mechanical Engineering, University Belgrade (Serbia), p. 103-108 (www.mas.bg.ac.yu/istrazivanje/biblioteka/publikacije/Transactions_FME/Volume%2036/3/02_MLazarevic.pdf)

[3] T. Dammann: Friction dampers RD 18 - Technical information, Suspa GmbH (March 2009)

[4] Yamada,Y.: Materials for springs, Springer-Verlag Berlin Heidelberg 2007

[5] Dixon,J.C.: The shock absorber handbook, John Wiley & Sons, 2007

[6] Harada, T., Kaneko,S., Honda,H., Watanabe, T., Fujita,E.: Development of efficient suspension damper for automatic washing machine, Nihon Kikai Gakkai Nenji Taikai Koen Ronbunshu (2002), vol.1, pp.165-166

[7] Jakšić , M. Boltežar, I. Simonovski and A. Kuhelj: Dynamic behaviour of the planar non-linear mechanical system — Part I: Theoretical modeling, J. of Sound and Vibr. 226(5) (1999), p.923-940

[8] Veternik,A.: Characterization of washing machine's dynamics behaviour, Diploma work, Faculty of mechanical engineering, University of Ljubljana; (2005)

COMPARISON OF LOCAL STRESSES AT SHRINKAGE AND GAS PORES IN CAST AL-SI ALLOYS

A. Vincenzi [1], G. Anzelotti [1], G. Nicoletto [1]

[1] University of Parma, Industrial Engineering Department, 43100 Parma, Italy.

Corresponding authors: gianni.nicoletto@unipr.it; vincenzi@ied.unipr.it

1. Introduction

Cast aluminum alloys are widely used in the automotive industry due to their excellent castability, corrosion resistance, and especially their high strength-to-weight ratio. Their application for cast components subjected to dynamic loading motivates continuing study of the fatigue behavior of cast Al-Si alloys. Casting pores are the most common defects and are almost inevitable with the casting technologies used in industry. Fatigue strength of cast aluminum heavily depends on pores formed during solidification because they favor fatigue crack initiation due to high local stress concentration, [1]. Different kinds of defects, classified as shrinkage and gas pores are shown in Fig. 1.
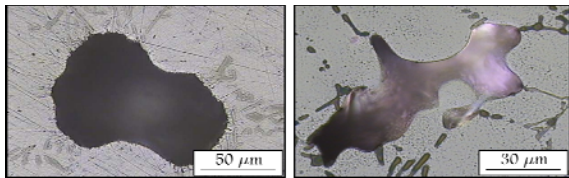
Fig. 1: Metallographic pictures of gas and shrinkage pores in an Al-Si alloys

The severity of pores in fatigue intuitively depends on size, morphology and density. However, there is no definite consensus of the most appropriate severity indicator because shrinkage pores are branched discontinuities while gas pore are roundish cavities.

Previous studies have been devoted to the quantification of pore severity in fatigue by theoretical and computational approaches. However, they have been essentially bi-dimensional in nature, i.e. based on metallographic images such as in Fig.1. It is believed that a more realistic assessment of the pore influence in fatigue can be obtained by determining the local mechanics at a realistic 3D pore. Recently X-ray computed tomography (XCT) has been applied to obtained real pore geometries in 3D, [2]. Typical XCT reconstructed gas and shrinkage pores are respectively shown in figure 2.

a)   b)
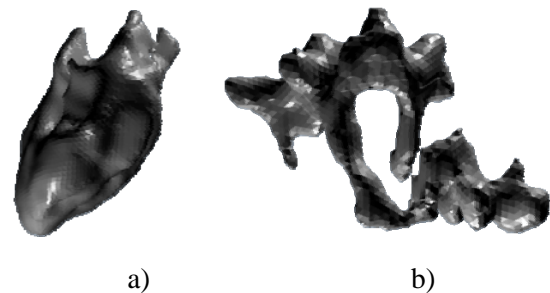
Fig. 2: XCT images of gas and shrinkage pores

This work is aimed at the study of the stress and strain concentration in the vicinity of realistic casting pores such as those of Fig. 2. The elastic-plastic finite element modelling of the mechanical response of a material with a three-dimensional pore was developed. Local stress concentration as a function of pore type and of load direction is determined and discussed.

2. FE Model Development

The finite element method was adopted to model a specimen consisting of a volume of elasto-plastic material containing a realistic pore obtained by XCT, see Fig. 3. The volume in the vicinity of the pore was finely meshed with solid elements, as shown in Fig. 3. A uniaxial tensile load was applied and the stresses and strains local to the pore determined. Different orientations of the pore with respect to the loading direction were investigated by rotation about two axes of the reference coordinate system. The assumed material parameters obtained with specific tensile tests are given in Tab. 1.

Tab. 1: Material model parameters of AlSi7Mg

E [MPa]	ν	R_s [MPa]	R_m [MPa]
75127	0.33	219	293

The applied nominal stress ranged from very low (i.e. elastic response) to a max load of 100 MPa (i.e. high cycle fatigue)

3. Elastic stress concentration

A typical stress distribution on the pore surface is shown in Fig. 3. The fine mesh allows to identify stress gradients on the pore surface and below the pore surface.
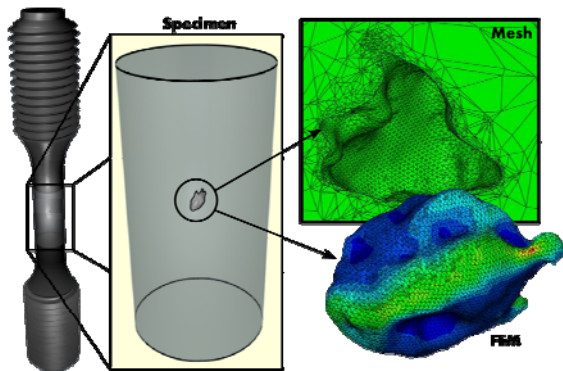
Fig. 3: Finite element analyses of a gas pore

The elastic stress concentration factor (K_t) defined as the ratio between the maximum Von Mises stress and the nominal stress was determined and plotted in Fig. 4 for different load directions. The average K_t is about 3 and the max K_t for the most unfavorable load direction is about 3.5.
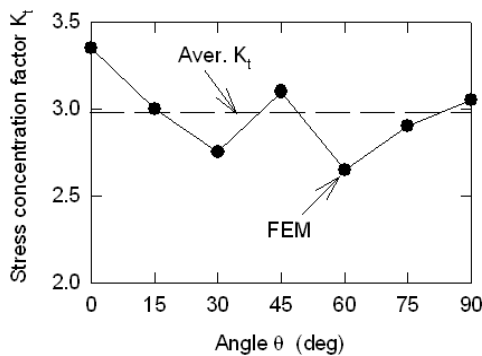
Fig. 4: Stress concentration factor for a gas pore stressed in different directions

Although not shown in detail here, gas and shrinkage pores have similar K_t because strecc concentration is mainly influenced by the local minimum radius of the pore surface, which is similar in the two cases. This result is consistent with [3] where it is stated that the shape of pores has a negligible effect on fatigue performance in cast aluminium alloys based on bi-dimensional FE investigation. The bi-dimensional FE approach however resulted in K_t that were considerably higher (almost twice)

than in the present 3D analysis. Results comparable to those of [3] (i.e. $K_t=6$) are obtained upon sectioning the present 3D pore and performing a 2D FE analysis (see Fig. 5).
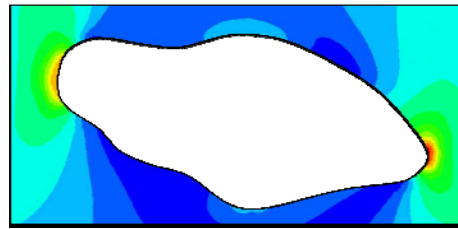
Fig. 5: Cross-section of a gas pore

4. Elastic-plastic analysis

The accumulated plastic strain as driving force for fatigue crack initiation around pores due to microplasticity was quantitatively determined by elastic-plastic FE analysis. The 3D investigation of the isolated pores demonstrated the validity of Neuber's rule, i.e. $(K_t)^2 = K_\varepsilon K_\sigma$ where K_ε and K_σ are the strain and stress concentration factors, respectively. Plasticity is found to develop at locations perpendicular to the load direction and with minimum curvature radius in the plane parallel to the load direction, see Fig. 6.
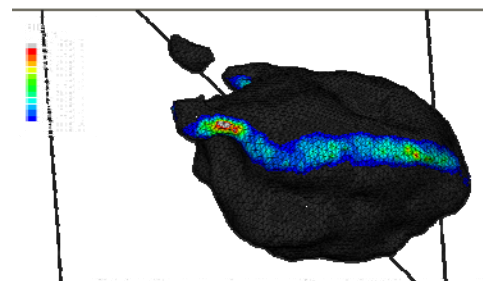
Fig. 6: Plastic strain on the inner pore surface

References

[1] J. Y. Buffiere et al., (2001), Materials Science and Engineering **A316**, 115–126.
[2] G. Anzelotti et al. (2009), Procs. DAS Symposium, Leoben, Austria
[3] Y. X. Gao et al. (2004), Fatigue Fract Engng Mater Struct, **27**, 559–570

MATHEMATICAL MODEL OF BLOOD FLOW THROUGH THE AORTIC VALVE

Zdravko Virag [1)], Fabijan Lulić [2)], Severino Krizmanić [1)]

[1)] University of Zagreb, Faculty of Mechanical Engineering and Naval Architecture, I. Lucica 5, 10000 Zagreb, Croatia.

[2)] Poliklinika Osiguranje Zagreb, Nemetova 2, 10000 Zagreb, Croatia.

Corresponding author: zdravko.virag@fsb.hr

1. Introduction

In lumped models of circulatory system the aortic flow is governed by unsteady Bernoulli equation. The aortic valve is usually considered as the idealized check valve. This means that the valve opens instantaneously for the positive flow and closes instantaneously preventing the negative (reverse) flow from arteries to the left ventricle. The invasive measurements show that during the valve closing phase the negative flow always occurs. It cannot be obtained by the idealized valve model and in this paper a model of the aortic valve that could predict negative aortic flow is proposed.

2. Mathematical model and numerical method

The characteristic opening and closing phases of the aortic valve are shown in fig. 1. Initially (at the beginning of systole) there is no blood flow through the aortic valve, and valve leaflets are at rest (panel A in fig. 1). When the left ventricle (LV) pressure exceeds the arterial pressure due to LV contraction, the unsteady Bernoulli equation holds

$$M \frac{\mathrm{d}Q}{\mathrm{d}t} = p_{\mathrm{lv}}^{M} - p_{\mathrm{sa}}^{M} - \frac{K\rho}{2A_{\mathrm{av}}^{2}} \left(Q - Q_{\mathrm{L}}\right)^{2}, \quad (1)$$

where Q is the absolute blood flow through the aortic root, M is the inertance coefficient, $\rho = 1050$ kg/m^3 is blood density, A_{av} is the aortic root area, p_{lv}^{M} and p_{sa}^{M} are measured left ventricle and arterial pressure, respectively, K is the minor loss coefficient and Q_{L} is the flow rate that defines the volume V_{L} swept by valve leaflets

$$\frac{\mathrm{d}V_{\mathrm{L}}}{\mathrm{d}t} = Q_{\mathrm{L}} \qquad (2)$$
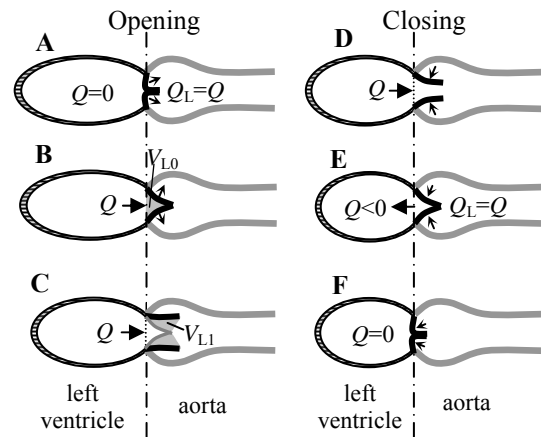
Fig. 1 Scheme of aortic valve opening (panels A to C) and closing (panels D to F)

During the first opening phase leaflets move into the arterial space with $Q_{\mathrm{L}} = Q$, but there is no orifice. The orifice occurs after the leaflets have swept a certain volume (see panel B in fig. 1) $V_{\mathrm{L0}} = \alpha A_{\mathrm{av}} \sqrt{4A_{\mathrm{av}}/\pi}$, where α is the model parameter. During the second opening phase the orifice increases from zero to the A_{av}, and leaflets sweep additional volume (see panel C in fig. 1) $V_{\mathrm{L1}} = \beta A_{\mathrm{av}} \sqrt{4A_{\mathrm{av}}/\pi}$, where β is the model parameter. In this phase $Q_{\mathrm{L}} = \left(1 - A/A_{\mathrm{av}}\right)Q$, where A is the orifice area which is related to V_{L} as $A = \left[(V_{\mathrm{L}} - V_{\mathrm{L0}})/V_{\mathrm{L1}}\right]^{2}$, see [1]. During these two phases inertance coefficient is defined as $M = \left(2 - A/A_{\mathrm{av}}\right)M_{0}$, where $M_{0} = \rho L/A_{\mathrm{av}}$ and L is the inertance length. After the flow has reached its maximum, the slow leaflets closing phase starts with $Q_{\mathrm{L}} = Q - Q_{\max}A/A_{\mathrm{av}}$. During this phase V_{L} decreases from $V_{\mathrm{L0}} + V_{\mathrm{L1}}$ to V_{L0} (see panels D and E in fig. 1) and at a certain moment Q becomes negative. For negative Q the

inertance coefficients is defined as $M = \delta M_0$, where δ is the model parameter. At the end of this phase (for $V_L = V_{L0}$, see panel E in fig. 1) leaflets coapt and equation (1) does not hold anymore. Measurements suggest that in the last rapid closing phase (after the leaflets coapt) the leaflets behave as a dumped oscillating system defined by

$$\frac{d^2Q}{dt^2} + 2\xi\frac{dQ}{dt} + (\omega^2 + \xi^2)Q = 0, \qquad (3)$$

where ξ and ω are constant parameters. During this phase $Q_L = Q$, and V_L should decrease from V_{L0} to zero. If we introduce another parameter $\gamma = \xi/\omega$, parameters ξ and ω are uniquely defined by V_{L0} (or α) and γ.

For the given measured left ventricle and arterial pressure and the set of model parameters: A_{av}, L, K, α, β, γ and δ, the set of equation (1) or (3) and (2) is solved numerically by fourth order Runge-Kutta method.

3. Results and conclusions

Proposed model has been applied to the measured data in man and pig. The measured left ventricle and arterial pressure are used as input, and the calculated aortic flow is compared with measured ones in figs. 2 and 3.
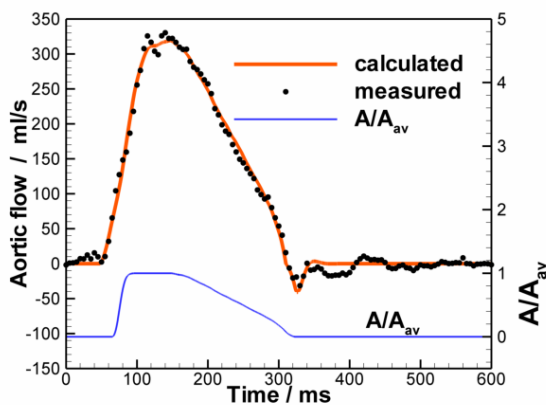
Fig. 2 Model results and measured data [2] in human (model data were A_{av}=2.9 cm^2, L=3 cm, K=1, α =0.15, β =0.4, γ =0.8, δ =10)
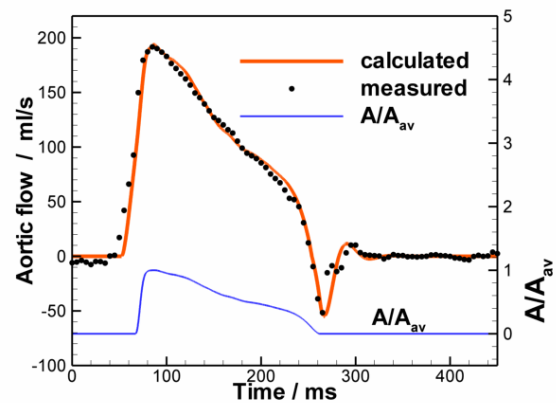
Fig. 3 Model results and measured data [3] in pig (model data were A_{av}=1.6 cm^2, L=1 cm, K=1, α =0. 5, β =0.6, γ =0.5, δ =3)

There is a very good agreement of the model results with the measured ones, with model parameters in physiological range.

Time varying aortic valve orifice A, shows two closing phases: a slow one followed by the rapid one, like in experimental observations. The model indicates that the leaflets coapt before the maximal back flow occurs.

4. Acknowledgements

The authors are greatly thankful to Patrick Segers and David Kass for generously providing the measured data.

5. References

[1] Z. Virag and F. Lulić, Modeling of aortic valve dynamics in a lumped parameter model of left ventricular-arterial coupling: Ann. Univ. Ferrara, Vol 54 (2008) 335-347.

[2] RP Kelly, CT Ting, TM Yang, CP Liu, WL Maughan, MS Chang and DA Kass, Effective arterial elastance as index of arterial vascular load in humans: Circulation, Vol 86 (1992) 513-521.

[3] P. Segers, N. Stergiopulos, N. Westerhof, P. Wouters, P. Kolh and P. Verdonck, Systemic and pulmonary hemodynamics assessed with a lumped-parameter heart-arterial interaction: J. of Eng. Math., Vol 47, 3-4 (2003) 185-199.

MATERIAL IDENTIFICATION BY THE TENSILE TEST

Karel Vítek [1],

[1] Department of Mechanics, Biomechanics and Mechatronics, Faculty of Mechanical Engineering,

CTU in Prague, Technicka 4, 16607 Prague, Czech Republic.

Corresponding author: karel.vitek@fs.cvut.cz

1. Introduction

The practical realization of the tensile test cannot provide the even load over the whole cross section - the partial force homogenous load. Thus, the evaluation of elasticity constant and other material properties can be determined with tensile test only with certain difficulties. The tensile specimen in the tensile machine is always loaded with tension and the same time with random unknown bending moment, which is unmeasured - see [1].

2. Regression Model of the Tensile Test

The Fig. 1 depicts the position of six strain gages (1 - 6) placed on the specimen. The gages are placed on boundary of the specimen cross section. The coordinates z,y are aligned with the direction of main central axis of the cross section. We suppose the second moments of the specimen cross section area to be J_y, J_z and also the components of the unknown bending moment to be M_y and M_z.
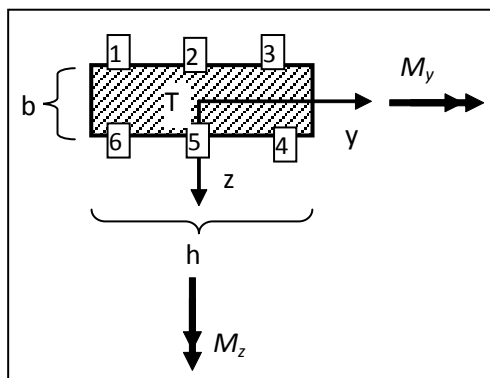
Fig. 1: Assembly of the specimen cross section boundary with the strain gauges 1 to 6. Load of the specimen with the unknown bending moment components M_y, M_z.

The dependence of a strain of the i-th strain gauge ε_i on the axis stress $\sigma = F/A$ and on the regression coefficient of the measured data set k_i can be described via equation (1). After substitution of the Hooke's law into equation

for the stress (2) under combination of bend and tension at the place of i-th strain gauge, we get a linear equation for three unknown variables. Two are the unknown bending moments M_y, M_z and third is the Young's modulus E

$$\varepsilon_i = k_i \frac{F}{A} \qquad (1)$$

$$\frac{M_z}{J_z} y_i - \frac{M_y}{J_y} z_i + \frac{F}{A} = \varepsilon_i E = k_i \frac{F}{A} E \qquad (2)$$

For modulus determination, it is sufficient to apply at least three strain gauges placed on the boundary of the sample cross section. The system of linear equations (3) can be composed for the data measured by these strain gauges, after these values are treated by linear regression according to equation (2).

$$\begin{bmatrix} \dots & \dots & \dots \\ +\dfrac{y_i}{J_z} & -\dfrac{z_i}{J_y} & -k_i\dfrac{F}{A} \\ \dots & \dots & \dots \end{bmatrix} \times \begin{Bmatrix} M_z \\ M_y \\ E \end{Bmatrix} = \begin{Bmatrix} \dots \\ -\dfrac{F}{A} \\ \dots \end{Bmatrix} \qquad (3)$$
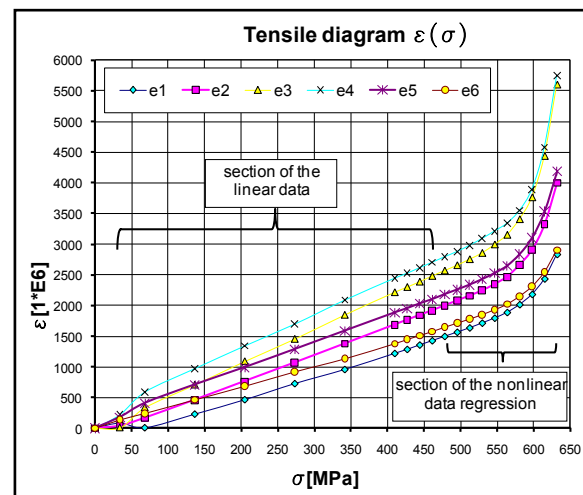
Fig. 2: Representative tensile diagram of the standardized tensile specimen from Fig. 1.

The measurement of the specimen tensile test with six strain gauges is depicted in Fig. 2. Axis of the stress σ stands for nominal axis stress, which is determined as a fraction of tension force F inflicted by tensile machine and the cross section surface A. This σ is not

equivalent to stress in the places, where the strain gauges measure its deformation values. By transformation of the linear computation model of the tensile test with use of equations (3) we receive unbiased linear regression of this linear data section of the tensile diagram. The function values are predetermined by Young's modulus E as shown in Fig. 3, which can be subsequently determined from the measured values. Each level of load, which is in reality decomposed into the tension and bending components, is represented in this final line by several deformation values of the measurement strain gauges. The linear area of deformation is smoothly followed by nonlinear deformation part in point ($\varepsilon_{lin}, \sigma_{lin}$).
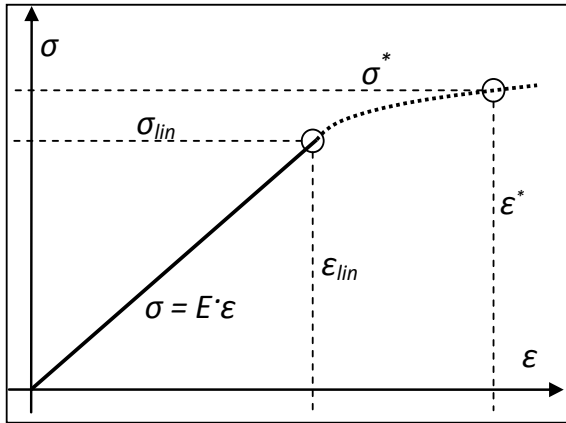
Fig. 3: The sequence regression principle

The nonlinear part of regression curve is depicted as $\sigma^*(\varepsilon^*)$. The range, where the strain stress relationship can be regressed linearly continues smoothly in point ($\varepsilon_{lin}, \sigma_{lin}$) into the nonlinear dependency $\sigma^*(\varepsilon^*)$, which respects only the assumption that the dependency is a smooth function. From the diagram depicted in Fig. 2, we can fit the nonlinear data section by polynomial regression functions $\varepsilon_i(\sigma)$ or $\sigma(\varepsilon)$ of the 4th order. This function (4) contains six parameters d_0 to d_5, which can be computed from the deformations measured by the gauges at certain nominal stress level. Normalized regression function for the $\sigma^*(\varepsilon)$ is also in the format of 4th order polynomial (5).

$$\varepsilon(z, y = d_0 + d_1 z + d_2 z^2 + d_3 y + d_4 y^2 + d_5 zy \qquad (4)$$

$$\sigma^*(\varepsilon) = c_0 + c_1 \varepsilon + c_2 \varepsilon^2 + c_3 \varepsilon^3 + c_4 \varepsilon^4 \qquad (5)$$

Distribution of the real axis stress load over the measured cross section $\sigma^*(z,y) = \sigma^*(\varepsilon(z,y), c_0, c_1, c_2, c_3, c_4)$ is then determined by the substitution of the equations (4) to (5), as the individual threads in the material have different deformation and the different deformation corresponds to different stress level. For the unknown coefficients c_0, c_1, c_2, c_3, c_4 there are several conditions to satisfy. First of all there are boundary conditions that the transition from linear area must be smooth – here formed as equations (6) and (7) and depicted in Fig. 3. Addition ally the force equilibrium condition (8) for the cross section area and moment equilibrium condition for the measured cross section must be fulfilled. The moment conditions (9, 10) are composed in the independent direction of coordinates z and y of the cross section.

$$\sigma^*(\varepsilon_{lin}) = c_0 + c_1 \cdot \varepsilon_{lin} + c_2 \cdot \varepsilon_{lin}^2 + c_3 \cdot \varepsilon_{lin}^3 + c_4 \cdot \varepsilon_{lin}^4 = E \cdot \varepsilon_{lin} \qquad (6)$$

$$\frac{d(\sigma^*(\varepsilon_{lin}))}{d\varepsilon_{lin}} = c_1 + 2 \cdot c_2 \cdot \varepsilon_{lin}^1 + 3 \cdot c_3 \cdot \varepsilon_{lin}^2 + 4 \cdot c_4 \cdot \varepsilon_{lin}^3 = E \qquad (7)$$

$$\iint_A \sigma^*(\varepsilon) \cdot dA = \sigma \cdot A = F \qquad (8)$$

$$\iint_A \sigma^*(\varepsilon) \cdot y \cdot dA = M_z \qquad (9)$$

$$\iint_A \sigma^*(\varepsilon) \cdot z \cdot dA = M_y \qquad (10)$$

In this system of equations, the known value is the stress on boundary of the linearized data part σ_{lin}, the next known variable is the Young's modulus E of this data part, the cross section A and the nominal stress σ – determined by the loading force F induced by the tensile machines. Additional requirement is to measure via experiment both moment components M_z, M_y, which must be measured.

3. Acknowledgements

4. References

[1] Vítek, K., Holý S.: Identification of the tensile material test, 37th International conference Experimental Stress Analysis, Frenštát pod Radhoštěm, 1999, pp. 213-216.

METHODS FOR ASSESSMENT OF CERAMIC AGEING

Miroslav Vokáč [1], Petr Bouška [1], Vladimír Hanykýř [2],Alexandra Kloužková [2]

1) Czech Technical University in Prague, Klokner Institute, Šolínova 7, 166 08 Praha 6 – Dejvice, Czech Republic
2) Institute of Chemical Technology Prague, Department of Glass and Ceramics, Technická 5, 166 28 Praha 6 – Dejvice, Czech Republic

Corresponding author: vokac.klok.cvut.cz

1. Introduction

Firing a ceramic raw material produces a relatively homogeneous composite with a complicated mineralogical composition.

The fired ceramic also contains an insufficiently stable phase and has relatively great open porosity, which makes it possible to bind a certain amount of water in its structure.

Long-term moisture action causes the water to bind with the ceramic material, with its different physical character.

This process leads to long-term volume changes in the ceramic material. The extent of these changes depends on the acting conditions, i.e., time, hygroscopic condition, raw material composition, and production technology.

A study of long-term volume changes in building materials made from porous ceramics has been carried out in the laboratories of the Klokner Institute and the Department of Glass and Ceramics. Several test specimens taken from various ceramic structures of known age and origin have been used in the analyses.

2. Porous structure of ceramics

The irreversible moisture expansion is related only to porous ceramics, e.g., fired clay ceramic, bricks, roof tiles, semivitreous porcelaine etc.

One the basic properties of ceramics are its porous structure. Porosity has an influence not only on changes in volume, but also on mechanical properties, resistance to climatic effects and thermal behaviour. Porosity can be described by liquid measurement, by mercury or by optical porosimetry.

3. Fundamentals of testing methods for determination of irreversible moisture expansion

The process of irreversible expansion could be accelerated by boiling in water, in steam or by high pressure steaming in autoclave. The determination of conventional values is based on these procedures.

Although this expansion is called irreversible, it could be removed by annealing at temperate above 600 °C, it means by re-firing of ceramic material. This property is utilised for determination of nature expansion of ceramic taken out from the structure.

4. Thermal dilatometric method

Dilatometric measurements are used to identify linear changes corresponding to the volume changes of ceramic bodies during firing or heating with a constant temperature rate. Dilatometric methods can be used for identifying certain minerals in ceramics or for a quantitative description of processes related to changes in the volume of the material. One of these processes is the ageing of porous ceramics made of natural raw materials.

The procedure utilized by the thermal dilatomer is based on accurate continuous measurement of specimen prolongation during a controlled increase in the temperature (from a value corresponding to laboratory conditions to a value of 650 °C).

Fig. 1: Thermal dilatometer for measuring of volume changes of ceramic material.

When the specimen is annealed first time the strain-temperature curve is obtained and, at the end of annealing, the ceramic body is like immediately after firing. After getting cool, the second annealing is done. The difference between the second and the first strain-temperature curve is due to an actual degree of rehydration and correspond to an actual irreversible moisture expansion of investigated specimen. Then, the treatment by boiling in water or in steam proceeds in order to accelerated rehydration process. After that, the third annealing is conducted. The difference between the second and the third strain-temperature curve is caused by the convention value of moisture expansion.
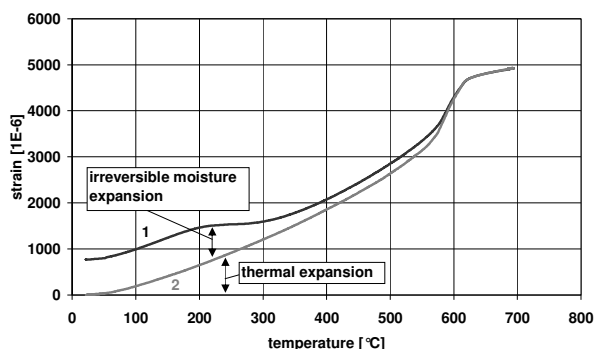
Fig. 2: Strain temperature relationships from thermal dilatometer, the first and the second annealing of the same sample.

5. Acknowledgement

6. References

[1] HANYKÝŘ, V., KUTZENDÖRFER, J., 2008. *Technologie keramiky.* Praha: Silikátový svaz. ISBN 978-80-86821-48-1.

[2] WILSON M. A., HOFF W. D., 2003. *Kinetics of moisture expansion in fired clay ceramics: a (time) ¼ law*. In: Physical Rewiew Letters, 90, 125503,(2003). ISSN: 0031-9007.

[3] VOKÁČ, M., BOUŠKA, P., HANYKÝŘ, V., 2007. *Dilatometric method for determination of irreversible moisture expansion.* In: XII. symposium SILICHEM 2007, Brno 19.-21.9.2007. Brno : VUT v Brně.

NANOINDENTATION OF OSTEOPOROTIC RAT BONES

Jana Vondrová[1], Jaroslav Lukeš[1],

[1] Czech Technical University in Prague, FME, Laboratory of Biomechanics, Technicka 4, 166 07 Prague, Czech Republic

Corresponding author: vondrova@biomed.fsid.cvut.cz

1. Introduction

Osteoporosis is a generalized systematic skeleton disease that is characterized by retrogression of the mechanical resistance of the bones. This retrogression is a consequence of quantity and quality changes in the bone mass, and it leads to an increased risk of bone fractures. Treatment for osteoporosis must correspond with the causative agent and with the state of the patient.

There is increasing demand for the evaluation of more bone parameters, especially in the area of mechanical stress distribution in the bone, so we have started to study the bone mechanical properties to various types of testing and these are three-point bending test, femoral neck fracture and finaly nanoindentation. The main benefit is that the mechanical properties of healthy and treated bones can be compared, and these findings can be confronted with medical tests.

2. Materials and Methods

In the study we used 16 rat femurs devided into two groups, group I – control, group II – castrated. The experiment was performed with Hysitron TriboLab nanoindentation system at the Faculty of Civil Engineering at CTU in Prague. It provides in-situ scanning of topography (SPM) and piezo automation with precision of the indent placement less then 1μm. The Berkovich tip works in closed environment on active antivibrating stage. Optic set up works with 1-10x zooming system with the zoom 5x as the default value.

Traditional trapezoidal shape of loading curve (15x10x15s; F_{max} = 7mN) was used for the indentation. The automation method was applied on each sample in two different zones. Grid of 3x3 indents in load control regime was used.

3. Experimental Results

The most common method for analyzing nanoindentation load-displacement data is that of Oliver and Pharr.

The hardness H and effective modulus E_{eff} are derived from

$$H = \frac{F_{max}}{A} \text{ and } E_{eff} = \frac{1}{\beta}\frac{\sqrt{\pi}}{2}\frac{S}{\sqrt{A}},$$

where F_{max} is the peak indentation load, A is the projected contact area, β is 1.034 for Berkovich indenter and S is the unloading stiffness.

The effective modulus is related to the specimen modulus through

$$\frac{1}{E_{eff}} = \frac{1-\nu^2}{E} + \frac{1-\nu_i^2}{E_i},$$

where E and ν are indentation modulus and Poisson's ratio (0.3 for bone) for the specimen, and E_i and ν_i are the same quantities for the indenter (1140 GPa and 0.07) [1].

As an example, the load-displacement data of the specimen no.2 are shown in fig. 1.
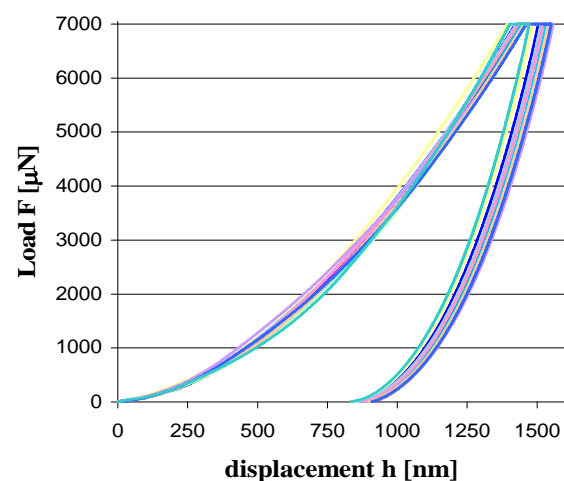
Fig. 1: Load-displacement data of the specimen no.2

The experimental results are shown in Tab. 1.

Sp. no.	H [GPa]	E_{eff} [GPa]	E [GPa]	Mean E [GPa]
1	0.19±0.05	3.64±0.51	3.32	
2	0.17±0.01	3.05±0.08	2.78	
3	0.18±0.01	3.54±0.15	3.23	
4	0.16±0.00	3.41±0.14	3.11	
5	1.07±0.11	26.90±3.53	24.53	3.11±0.16
6	0.17±0.01	3.54±0.15	3.23	
7	0.17±0.01	3.32±0.08	3.03	
8	0.16±0.01	3.37±0.09	3.07	
9	0.17±0.01	3.29±0.13	3.00	
10	0.15±0.01	3.30±0.15	3.01	
11	0.15±0.01	3.08±0.28	2.81	
12	0.16±0.01	3.38±0.10	3.08	
13	0.15±0.01	3.23±0.14	2.95	3.00±0.16
14	0.16±0.01	3.00±0.19	2.74	
15	0.17±0.02	3.49±0.21	3.18	
16	0.17±0.01	3.52±0.10	3.21	

Tab. 1: Values of the effective elastic modulus E_{eff}. hardness H and mean elastic modulus $E \pm$ SD

4. Conclusion

The measured data accord with the finding of the three-point bending test executed on the same specimens [2]. Just the specimen no.5 shows the excessive values. We did not find their cause, hence we excluded it from the calculation of the mean elastic modulus.

5. Acknowledgements

6. References

[1] Y. H. An, R. A. Draughn, Mechanical Testing of Bone and the Bone-Implant Interface, CRC Press LLC, Boca Raton, FL, 2000, 263.

[2] J. Vondrova, P. Ruzicka, R. Sedlacek, et al., The Effect of Alcohol Administration on the Bone Mechanical Properties. Proceedings of the 22nd DAS, Parma (2005), 106-107.

EXPERIMENTAL STRESS ANALYSIS AT A MODERNIZED PASSENGER COACH

Nicuşor Laurenţiu ZAHARIA

Romanian Railway Authority - AFER, 010719 Bucharest, 393 Calea Grivitei
Corresponding author: rentizaharia@yahoo.com

1. Introduction

This abstract present the experimental stress analysis at a modernized passenger coach. The life time of a railways rolling stock is around 30-40 years. It is necessary from time to time to bring up to date such product.

After such modification, tests are made in purpose to obtain a new certification from a Railway Commission.

The tests which are presented in this paper were performed at Romanian Railway Authority – AFER on Stress Analysis Bench Test (fig. 1).

Fig. 1: The coach on Stress Analysis Bench Test

The tests were carried out according to EN 12663.

2. Measurement points

The measurement points were located in the relevant areas (chassis and windows).

The measurements were performed in 66 points (figure 2). Hottinger LY11-10/120 strain gages were glued on the elements of the bogie with Hottinger Z70 adhesive.

The strain gages were connected at measuring devices with cables.

The measurements were performed with Hottinger Centipede 100 Multipoint Measuring Unit.

The measuring device Centipede 100 was connected to a laptop computer.

The acquisition software used was Catman 4.5 (an Hottinger product).

3. Tests

The following tests were performed in accordance with the above mentioned standard:
- 2000 kN compressive force at buffer level,
- vertical load.

The static tests permissible stress are shown in table 1:

Loads	Welding free area	Welding area
Horizontal [N/mm^2]	355	309
Vertical [N/mm^2]	237	215

Tab. 1: Permissible stress

4. Results

The measured stress was below the permissible stress for all measuring points except the following: at compressive force at buffer level, for strain gage V7.
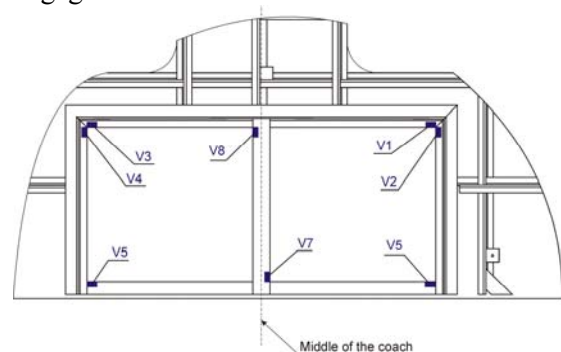
Fig. 2: Aspiration hole

In table 2 is presented the stress for V7 and V8 measuring points before reinforcing:

	Measuring point	
	V7	V8
Stress [N/mm^2]	-375	-312

Tab. 2: Results before reinforcing

The values from table 2 were calculated with Hooke's law.

Because the permissible stress of the static tests was exceeded, the commission formed from the manufacture people and the testing team decides to offer a modified design chassis longitudinal beam near the aspiration hole (fig. 3-6).

| a) Before | b) After |
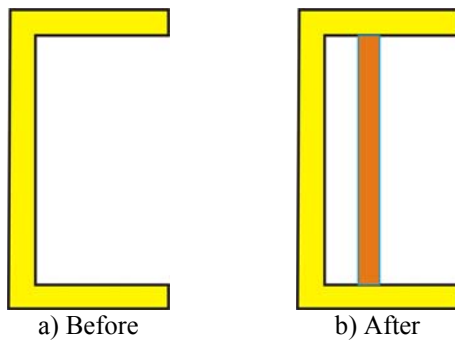
Fig. 3: Longitudinal beam
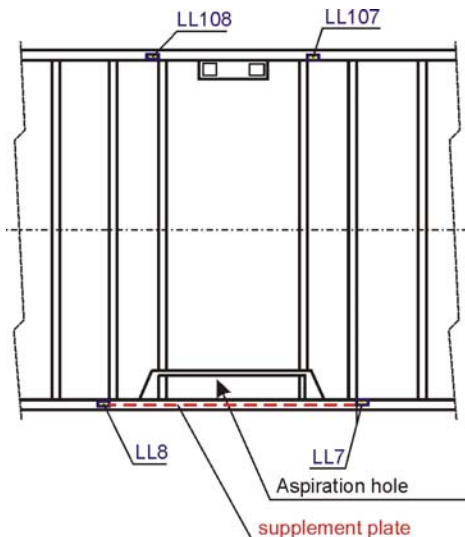
Fig. 4: Reinforced longitudinal beam

Fig. 5: Longitudinal beam (before reinforcing)

Fig. 6: Longitudinal beam (after reinforcing)

In table 3 is presented the stress for V7 and V8 measuring points after reinforcing:

	Measuring point	
	V7	V8
Stress [N/mm^2]	-260	-331

Tab. 3: Results after reinforcing

The values from table 3 were calculated with Hooke's law.

5. Conclusions

After the consolidation of the longitudinal beam, the results obtain at the repeated tests were smaller than permissible stress, so we can concluded that reinforcing solution was good.

After the tests the new certification from the Railway Commission was obtain.

6. References

[1] T. Ş. Mănescu, I. Copaci, S. Olaru, F. Creangă, Tensometria electrică în cercetarea experimentală, Editura Mirton, Timişoara, 2006

[2] I. Copaci, T. Ş. Mănescu, S. Olaru, F. Creangă, Rezistenţa la solicitari variabile care apar în exploatarea vehiculelor feroviare, Editura Mirton, Timişoara, 2005

[3] ***** EN 12663 *Structural requirements of railway vehicle bodies,* 2000

WEAR PROBABILITY TESTING
OF PLANETARY DRIVE SET PINIONS

Predrag Živković [1], Milosav Ognjanović[2]

1)   University of Pristina, Faculty of Technical Sciences, Kneza Miloša br.7, Kosovska Mitrovica, Serbia

2)   University of Belgrade, Faculty of Mechanical Engineering, Kraljice Marije 16, 11120 Belgrade

Corresponding author: jomine@sbb.co.yu

1. Introduction

The planetary gear set pinion has a small diameter so to the same torque it's exhibited to a very large force. A small number of teeth, and a small gear diameter also contributes to the stress on the teeth flanks. Favorable circumstance is that the load of gear is divided into the number of satellites, and the force in contacts is smaller in comparison with the same wheel size, which would be subject to the overall loads. This effect is lesser with unequality of distribution of load on the satellites and the fact that the central pinion is coupled with a variety of satellite gear flanks. It was studied with two stage planetary gear set (Fig.1).

Teeth flanks of central pinion are exposed to high stress. In addition, mesh frequency and the total number of pinion tooth contacts along service life is very high. During oppreating process, teeth of one of the gears are adapted to a flanks of another gear in mesh. In this case, planetary gear set pinion is adapted to three gear satelites, which significantly accelerates the wear. All this affects that flank failure of the central pinion is very specific. To the teeth of the pinion, are developed all types of teeth flank surface failure, and they are analyzed in [1,3].

2. Testing method and testing rig

For testing, closed system with power circulation was used (back to back system), and it is shown on Figure 2. This system provides a high degree of rationality in the long-term testing such as this. Two identical planetary gear drives are coupled so that the output couplings are inter-related. Input couplings that have the same speed of rotation are connected

in the closed back to back system. Side transmitters (Fig.2) for closing the flow of power (power circulation) are with transmission ratio 1:1. Load is realized through the realization of quasi-static load and elastic deformation of system before starting the test.
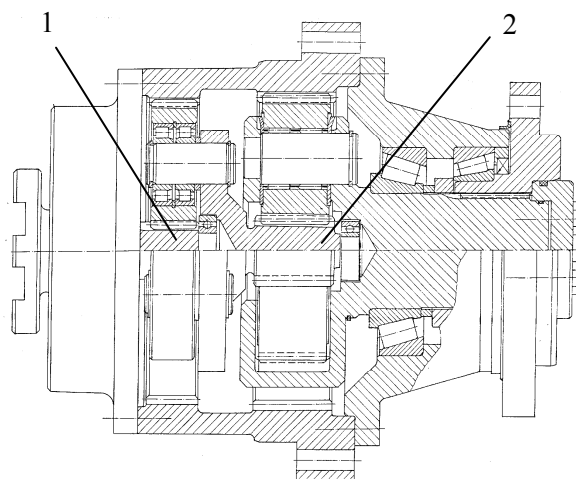
Fig. 1: Testing sample: two-stage planetary gear drive

Fig. 2: Testing of planetary gear drives in the back to back system (power circulation)

3. Test results and comments

For the critical state of wear thickness of the teeth flank surface layer was used $0.3m_n$, and the thickness corresponds to the failure probability, which tends to one. Bigining of teeth flank wear corresponds to the probability of failure which tends to zero. The results of testing and assumed failure probability flows are shown on Figure 3. For stress level σ_H=1421 N/mm^2, parametars of Wejbull's distrubution are η=2,5$\cdot$10^8 and β=1,5, and Weibull's distrubution function is:

$$P_R = 1 - e^{-\left(\frac{N}{2,5\cdot10^8}\right)^{1,5}}$$

For stress on teeth flanks σ_H=2412 N/mm^2, estimated parametars of Weibull's distibution are η =10^7 and β=2.

$$P_R = 1 - e^{-\left(\frac{N}{10^7}\right)^2}$$

On the basis of distributed probability of failure area waste of this probability is defined. It allows to determine the curve of distributed probability of failure for any level of stress, and also for any flank stress cycles number. Presented results coresponds to carbonised and grinded pinion teeth flanks. Those are indispensable for elementary reliability calculationion (estimation) in design process of gear drive units. This reliability is used as constraint for design parameters definition and for reliability balancing of all gear drive components.

4. Conclusion

Test methodology in the closed system of power circulation (back to back system) of planetary drive units is characterised by high level of rationality for long time testing. Testing process of the pinion takes place in real assembly and can be accelerated by increase of load and speed of rotation. Test results represent a good base for determining of elementary gear reliability which is indispensable for design parameters definition in the gear drive units design.
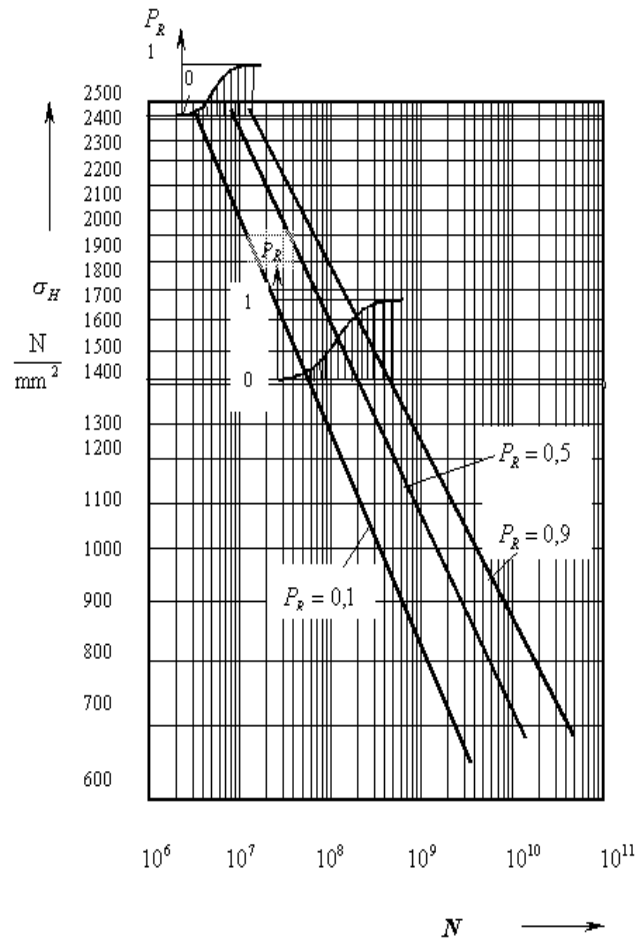
5. References

[1] Živković, P.: Investigation of efficiency and failures of planetary gear drive units (in Serbian), - PhD thesis, University of Belgrade, Faculty of Mechanical Engineering, Belgrade, 2006.

[2] Ognjanović M.: Progressive gear teeth wear and failure probability modeling, - Proceedings of the 5th International Conference on Tribology BALKANTRIB'05, Kragujevac 2005, pp 403-409

[3] Ognjanovic M, Živkovic P., Rosić B.: Methodology development of accelerated planetary gear drives testing (in Serbian), Source and Power transmission meeting-IPS-97, Podgorica – Bečići, 1997,pp 383-390

STRAIN ACCUMULATION PROCESS IN TIME-DEPENDENT MATERIALS EXPOSED TO CYCLIC LOADING

Barbara Zupančič, Anatolij Nikonov, Urška Florjančič, and Igor Emri,

University of Ljubljana, Faculty of Mechanical Engineering, Center for Experimental Mechanics, Aškerčeva 6, 1000 Ljubljana, Slovenia

Corresponding author: barbara.zupancic@fs.uni-lj.si

1. Introduction

Paper presents methodology for analyzing strain accumulation process in polymeric materials when exposed to periodical (cyclic) loading. Within each loading cycle material undergoes a combination of the creep and relaxation process. At certain conditions the retardation process between two loading cycles cannot be fully completed. Consequently strain starts to accumulate, which leads to hardening of the material and ultimately to the failure of polymeric product. We present mathematical methodology for predicting durability of such periodically loaded polymeric products, more specifically, for the case of the drive belts. Methodology includes numerical calculations of accumulated strain as a function of the number of loading cycles and function of loading angular velocity. Based on these calculations we can determine the critical angular velocity area of periodic loading where the strain accumulation is the most intensive, and may lead to material failure.

The strain response of the viscoelastic material exposed to the shear stress loading may be expressed as [1],

$$\gamma(t) = \tau(0)J(t) + \int_0^t J(t-s)\frac{\partial \tau(s)}{\partial s}ds. \qquad (1)$$

We take into consideration specific periodical loading conditions in terms of the shear stress. Evolution of the shear stress within one loading cycle is modeled as a tooth-like function [2]. Introducing this loading conditions and description of creep compliance function $J(t)$ in terms of discrete retardation spectrum,

$$J(t) = J_g + \sum_{i=1}^K L_i \left(1 - e^{-\frac{t}{\lambda_i}}\right),$$ into the Eq. (1), yields

the following expression for the cumulative accumulated strain,

$$\gamma(t, t \le N\xi) = \tau(0)J(t) + \tau_0 \sum_{n=1}^{n=N} \sum_{i=1}^K L_i \left[1 - \exp\left(-\frac{\pi}{\omega\lambda_i}\right)\right] \exp\left(-\frac{(\kappa+\pi)(2(N-n)+1)-\pi}{\omega\lambda_i}\right)$$

$$(2)$$

Eq. (2) describes the time-dependent evolution of the strain accumulation in the material as a function of the angular velocity, ω, geometry parameter $\kappa = \frac{l}{R}$, where l is the distance between the axes of the two pulleys, and R is the radius of the pulleys of the belt drive, and as a function of the number of cycles, N, to which the belt has been exposed to [2]. τ_0 presents the magnitude of the loading shear stress [2]. Analyzing strain accumulation in each consecutive cycle, we observe that at very small and very large operating angular velocities, ω, there will be no strain accumulation. It is therefore evident that accumulated strain must have an extreme at some critical angular velocity, $0 < \omega_{CR} << \infty$, which determines critical operating conditions, at which the strain accumulation process is the most intensive [2].

2. Analysis and Results

We have selected synthetic spectrum with "Gauss" distribution [3], to analyze the effect of the number of loading cycles, n, and loading angular velocity, ω, on the strain accumulation process during the cyclic loading, Fig. 1.
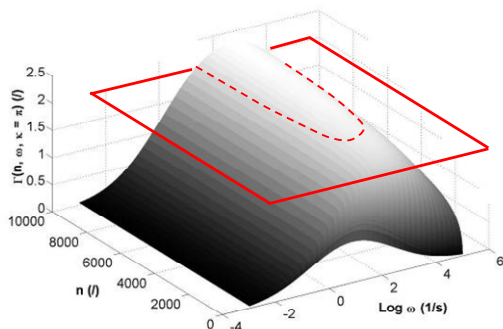
Fig. 1: 3D diagram of cumulative accumulated strain, $\Gamma(\omega, n, \kappa = \pi)$, as a function loading cycles, n, and angular velocity, ω.

If we define different upper limits of the accumulated strain, as shown with the cross-section plane in Fig. 1, and project the cross-section curve onto $n-\omega$ plane, we obtain different levels of critical angular velocity areas as shown in Fig. 2. Within the "critical area" we may expect the most intensive strain accumulation.
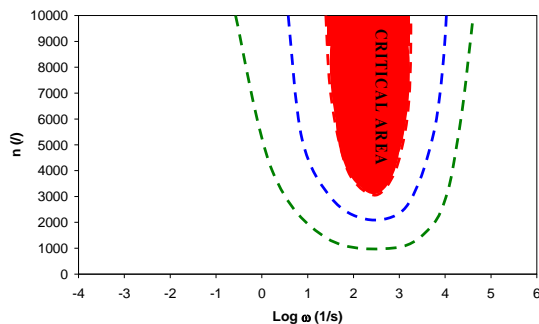
Fig. 2: Angular velocity area corresponding to three different vales of the cumulative accumulated strain.

Such diagrams may be used for predicting the expected life span of dynamically loaded polymeric products.

3. Conclusions

The strain accumulation process for the case of the drive belts was analyzed for material with the »Gauss« distribution of retardation spectra, which mimics well the behavior of real materials, as function of the loading angular velocity and the number of loading cycles. Based on these analyses we have proposed the methodology for predicting the durability (the life span) of dynamically loaded polymeric products.

4. References

[1] Tschoegl, N.W., The Phenomenological Theory of Linear Viscoelastic Behavior: An Introduction, 1989.

[2] Emri, I., Kramar, J., Hribar, A., Nikonov, A., Florjančič, U., *Mechanics of Time-Dependent Materials*, **10(3)**, 245-262, 2006.

[3] Emri, I.,von Bernstorff, B. S., Cvelbar, R., Nikonov, A., *Journal of Non-Newtonian Fluid Mechanics*, **129**, 75-84, 2005.

USING THE RESISTANCE CHANGE METHOD FOR INVESTIGATION OF BENDING EPOXY-CARBON COMPOSITE

Jacek Gadomski[1], Agnieszka Jarzębińska-Dziegciar[1], Paweł Pyrzanowski[1]

[1] Warsaw University of Technology, Faculty of Power and Aeronautical Engineering, Institute of Aeronautics and Applied Mechanics. Nowowiejska 24, 00-665 Warsaw, POLAND. Tel. +4822 234 53 16, corresponding author: jgadomski@meil.pw.edu.pl.

1. Introduction

Composite materials are very often used in complicated constructions but prediction of their work and damage is difficult till now.

In this paper authors used electrical resistance-based methods for investigation of work of carbon composites. The method is described in [1,2,3].

2. Specimens and Experimental Stand

Special specimens shown in Fig. 1 were made. The material used for a study was epoxy-carbon composite KDU-1002 with Epidian 53 resin with volume fraction of carbon 60%. 250 mm long, 25 mm wide, 2 mm thick laminate was manufactured using five layers of carbon tape. All fibers in the specimen were parallel.

Linear contacts were applied into specimens using special low resistance silver-based glue. In this test only contacts on both ends of the composite specimen (contacts 1-9, 2-8) and four contacts in the center of the specimen (contacts 4-6, 3-7) marked in Fig 1b) were used.
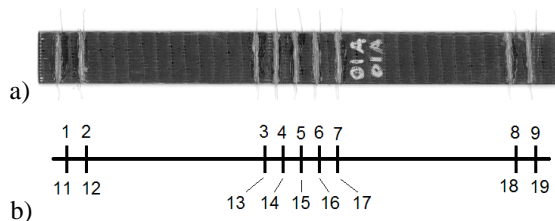
Fig. 1: View of the specimen: a) general view of structure; b) denomination of contacts.

For investigations the special experimental stand shown in fig. 2 was made.

The lever train with 4 guide rolls realizes pure bending of the specimen. The mechanism is driven by a cable, where one end of the cable is fixed to a screw actuator, the second end to a force gauge. The specimen was embedded with
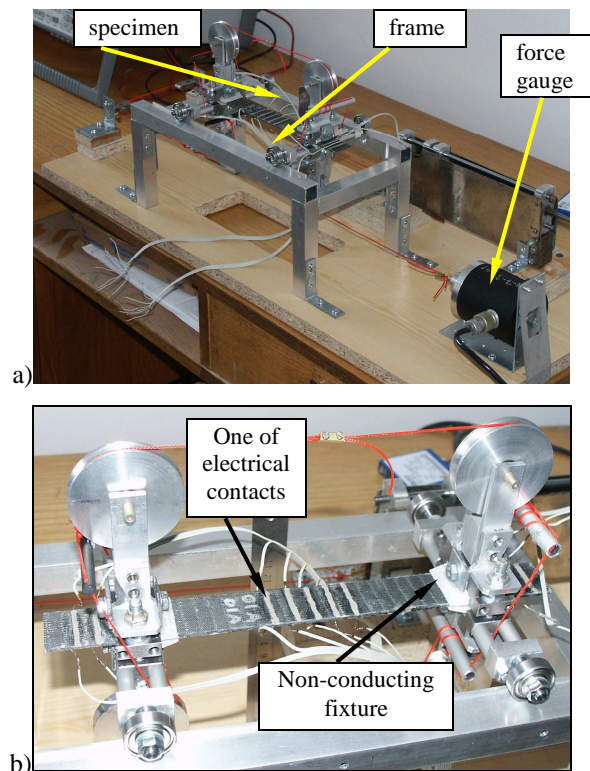
Fig. 2: Specimen on the stand: a) general view; b) magnification of the specimen

special clasps made from insulating glass-epoxy composite reducing stress concentration in the specimen.

For measurements a high-performance, 6½-digit digital multimeter Agilent 34401A was used. The measurement of resistance of the specimen was made by connecting a multimeter in 2-wires resistance measuring mode to selected contacts from bracket 1-19. The measurement of difference of potential was made in 4-wires resistance measuring mode by connecting constant current source to contacts 1-9. Potentials for various deflections were measured between two selected contacts from bracket 2-18.

3. Experimental Results

In fig. 3 relationship between the deflection and the load force for the specimen is presented.
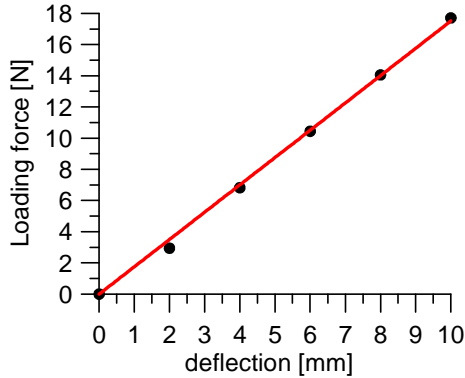
Fig. 3: Load force vs. deflection for the specimen.

Fig 4. shows the change of resistance for selected contacts for 2-wires method.
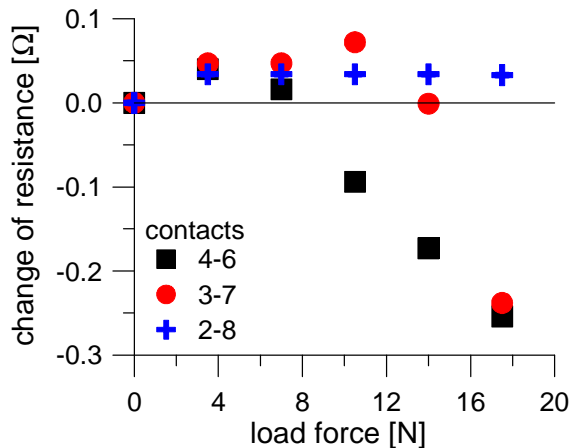
Fig. 4: Change of resistance vs. load force for the specimen – 2-wires method.

Fig 5. shows the change of resistance for selected contacts for 4-wires method.
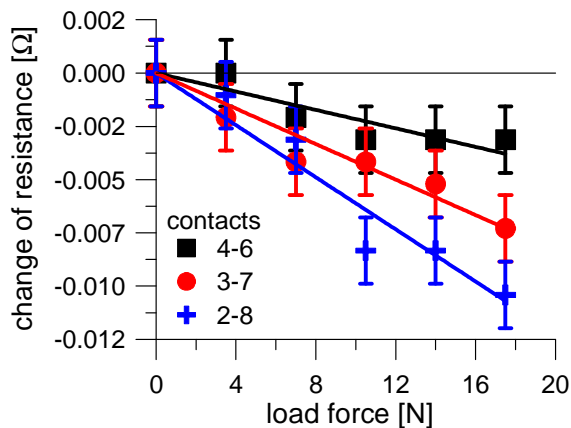
Fig. 5: Change of resistance vs. load force for the specimen – 4-wires method.

It is visible, that 2-wires method is worse than 4-wires method because of unknown additional resistance of contacts, significantly greater than resistance of composite. Results are unrepeatable, depending on factors difficult to determine.

4-wires method shows directly the resistance of composite, does not depend on other factors Results allow to determine resistivity of the specimen (data from the table in fig. 6)

Contacts	Distance [mm]	Resistivity [Ω/m]
4-6	20	1,25
3-7	40	1,38
2-8	210	1,48

Fig. 6: Resistivity of the specimen.

4. Summary

1. Results show that on the compressed side of the specimen resistance decreases together with increasing of load. This decrease depends on degree of reduction of fibers, what induces reduction of the way of current flow.

2. It is planned to examine more specimens and realization of static investigations until destruction of specimens and fatigue investigations under maximum loads equal to 90% damage load.

References

1. Jarzębińska-Dziegciar A., Pyrzanowski P. – Investigation of tension of carbon composites by usage the electrical resistance-based method, – Proc. of 24th Danubia-Adria Symposium on Experimental Methods in Solid Mechanics, Sibiu Romania, September 2007, 71-72.
2. Todoroki A., Tanaka M., Shimamura Y.: Measurement of orthotropic electric conductance of CFRP laminates and analysis of the effect on delamination monitoring with an electric resistance change method. – Compos. Sci. Technol. 62 (2002), 619-628.
3. Xiaa Z., Okabeb T., Parkc J.B., Curtina W.A., Takedac N. – Quantitative damage detection in CFRP composites: coupled mechanical and electrical models – Comp. Sci. Technol. 63 (2003), 1411–1422

LONG-TERM DEGRADATION OF POLYCARPOLACTONE TEMPLATES

Laszlo Olah [1), Ferenc Tuba [2), Lajos Borbas [3) , Brainslav Hadzima [3)

[1) Polymer Competence Center Leoben GmbH, Roseggerstr. 12, 8700 Leoben, Austria.

[2) Department of Polymer Engineering, BME, Muegyetm rkp. 1, 1111 Budapest, Hungary.

[3) Cooperative Research Center for Biomechanics, BME, Muegyetm rkp. 1, 1111 Budapest, Hungary.

[4) Department of Materials Engineering, FME University of Zilina, Slovak Republic

Corresponding author: olah@pccl.at

1. Introduction

Poly(ε-caprolactone) (PCL) is an often investigated and applied synthetic, degradable, biocompatible polymer because of its good biocompatibility, and its long degradation time (24-36 months), which is a results of the hydrolytic breakage of aliphatic ester linkages. Furthermore, polycaprolactone can be easily manufactured by conventional methods [1][2].

Numerous studies were aimed to reveal the degradation kinetics of PCL. One of the first publications over the deterioration of PCL was written by Pitt [3]. Llinear change was observed in semi-logarithmic plots of molecular weight versus time, until the number-average molecular weight (M_n) decreased to approximately 5000; regardless of the initial M_n.

The aim of the present study was to examine the time, temperature and molecular weight dependency of compressive mechanical properties of PCL and gain information for further applications.

2. Methods

2.1 Materials and processing methods

Various nominal number-avarage molecular weight (M_n) PCL samples (namely: CAPA 6250, M_n=2,5x10^4 Da and CAPA 6400, M_n=3,7x10^4 Da) were obtained from Solvay Caprolactones, Solvay Interox Ltd.

Phosphate buffered saline (PBS) was kindly supplied by Semmelweis University, 1st Department of Pathology and Experimental Cancer Research according to ISO 13781:1997 standard.

Polymers were dried before processing at 35°C over a day. Afterwards cylindrical samples (diameter: 6 mm, height: 7 mm) were hot pressed using a COLLIN P-200E-type compression moulding machine (at 120°C temperature and 50 bar pressure for 10 min, followed by cooling with water). Finally the samples were put in containers (volume: 5 cm^3), filled up with 4±0,5 cm^3 PBS and laid in a Heraus drier on 37±0,1°C respectively. At certain time intervals samples were removed, washed in distilled water and dried at 40°C under vacuum over 4 days.

2.2 Analytical procedures

The mechanical properties of dry specimens were measured at room temperature using a Zwick Z020 universal testing machine at a crosshead speed of 2 mm/min. The results were estimated according to ISO 604:2002 standard.

The thermal properties of samples were studied by a Perkin-Elmer DSC 7 equipped with a Perkin-Elmer Intercooler 2. Samples between 3 and 5 mg weight were measured at 10°C/min heating rate from -50°C to 100°C.

3. Results

In case of polymers, the length and the structure of molecular chains have crucial influence on the final properties. Most of the cases, the longer the polymer chains are, the better the mechanical properties. In our experiments, the lower molecular weight PCL was found superior compared to the higher

molecular weight one, because of the higher degree of cristallinity.

GPC measurements were carried out to measure the molecular weight as a function of the degradation time, and the degradation-rate was found similar in both cases (Fig. 1.) It suggests that the molecular weight has no crucial on the degradation kinetic, which could enable engineers to vary the life-time of implants by changing the molecular weight.
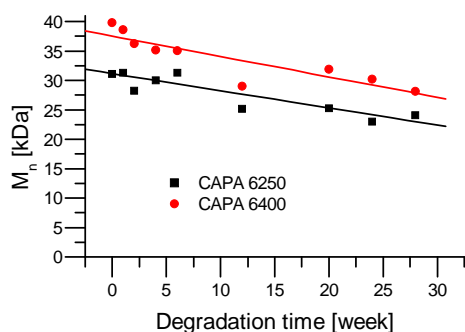
Fig. 1: Number average molecular weight of polycaprolactone as a function of degradation time

Since PCL is a hydrolytically degradable material, loss of mechanical properties was observed. The molecular weight was found having crucial influence on the decrement of compressive modulus as a function of degradation time (Fig. 2). The lower mechanical weight sample lost 30% of its modulus, while the deterioration of higher molecular weight samples was less than 15%.
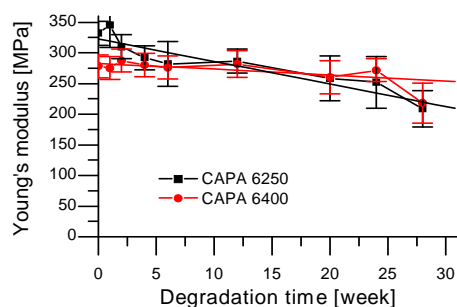
Fig. 2: Compressive modulus of polycaprolactone as a function of degradation time

As it can be seen on Fig. 3 one of the reasons of declining properties was the change of morphology and crystalline structure. The decrease of enthalpy of melting, temperature of melting-peak and area of peak was also noticed. It means that either the amount or the quality of crystalline lamellas decayed which are the signs of degradation and of the wider molecular weight distribution.

Fig. 3: Calorimetric melt curves of CAPA 6250

4. Acknowledgements

5. References

[1] Hutmacher, D.W. Scaffolds in tissue engineering bone and cartilage, Biomaterials, 21, 2000. pp. 2529-2543.

[2] Nair, L.S., Laurencin, C.T. Biodegradable polymers as biomaterials, Prog. Polym. Sci., 32, 2007. pp. 762-798.

[3] Pitt, C.G., Chasalow, F.I., Hibionada, Y.M., Klimas, D.M. and Schindler, A.: Aliphatic polyesters. I. The degradation of poly(ε-caprolactone) in vivo, Journal of Applied Polymer Science, Vol. 26, No. 11, pp. 3779-3787, 1981.

SEMI-INDUSTRIAL APPROACH FOR WEAR-MEASUREMENT OF INJECTION MOULDS

Laszlo Olah [1], Walter Friesenbichler [2]

[1] Polymer Competence Center Leoben GmbH, Roseggerstrasse 12, 8700 Leoben, Austria.

[2] University of Leoben, Institute of Plastics Processing, Franz-Josef-Str. 18, 8700 Leoben, Austria.

Corresponding author: olah@pccl.at

1. Introduction

Wear phenomenon in plastics processing has been a significant issue since the first phenol based product was produced in the beginning of 20th century. However the wear related problems have become more pronounced, since the customers need lighter and smaller products, which have typically very small wall-thicknesses (resulted in high production rates and pressure), and are made of highly filled or reinforced materials, which can further induce the wear phenomenon. In addition, the tolerances are very tight; for example in the automotive industry, where practically no deformation or surface error can be tolerated.

To overcome this issue, we have further improved our wear-testing device, which is now capable to measure the wear of plastic mould steels in situ. This is the following step to give real-life time prediction of injection moulds.

2. Experimental Results

2.1 Experimental materials

For the experiments, M200 steel (EN/DIN designation 1.2312) was chosen as sample material produced by Böhler Edelstahl GmbH, Kapfenberg, Austria. Four types of polyamide 66-based compounds were used, because these engineering plastics are of great importance in plastic industry, but they are well known for their abrasiveness. The four compounds were Ultramid A3W (non-filled polyamide 66), Ultramid A3WG3 (15w% of glass fiber), Ultramid A3WG6 (30w% of glass fiber) and Ultramid A3WG10 (50w% of glass fiber).

2.2 Experimental methods

For wear experiment, an injection mould has been designed, into which the steel specimens could have been inserted and replaced after each test-run. The design of the product is shown on Fig. 1.
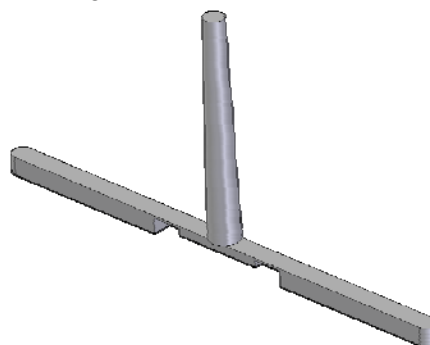
Fig. 1: Product made of various polyamides by injection moulding.

Two wear specimens that have 40°C temperature (just like normal injection moulds) form a rectangular gap of 0.5 mm, in which high local shear stresses and shear rates are produced just as at gates in real-injection moulds. Certain amounts of polymer melt are injected through the gap, and induce the abrasion on the surface of both specimens.

For the experiments, BA 1000/200 CDK-SE Unilog TC 40 type injection molding machine with a 30 mm standard screw was used. A constant melt flow-rate ($45cm^3/s$) was applied during each experiment. The gravimetric wear-loss was analyzed by analytical balance, which had an accuracy of ±0.01mg. The worn-surface morphology was studied by optical microscope. At each serial two specimens were studied, and in each case the average is shown on the plots.

2.3 Experimental results

The worn surface is shown on Figure 2. On the left, the specimen was eroded by non-filled polyamide, and the right specimen was deteriorated by polyamide compound, which contained 50 weight percent of glass fiber. In each case the photographs were taken after the first 2000 shots.

Fig. 2: Surface morphology after 2000 shots of polyamide compounds: non-filled (left); 50w% glass fiber (right).

The non-filled polymer induced a slight change of morphology, and at the same time the filled polyamide compounds induced significant amount of wear. Similar observations of surface morphology could be introduced that we showed last year as a result of enhanced model wear-tests.

The unexpected result of the experiment was that during the first 250-500 shots the wear-loss is majorly governed by the surface quality (hardness, roughness, carbide size etc) and the glass-fiber content has minor influence. For example, the non-filled polymer induced a very strong erosion of the surface, and reduced the surface roughness (Fig. 3).
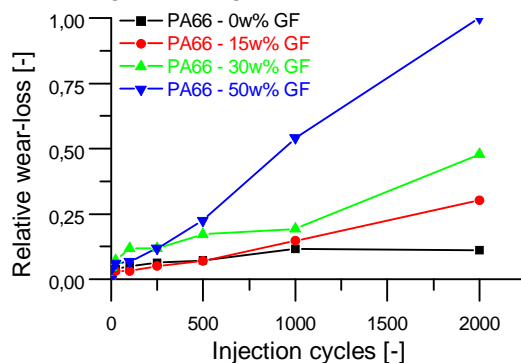
Fig. 3: Wear-loss induced by various PA66 compounds as a function of injection shots.

After the first 500 shots the wear-loss became linear function of injection shots. The slope of the curve was highly dependent on the glass-fiber-content of the compounds, and an exponential relationship was found (Fig. 4).
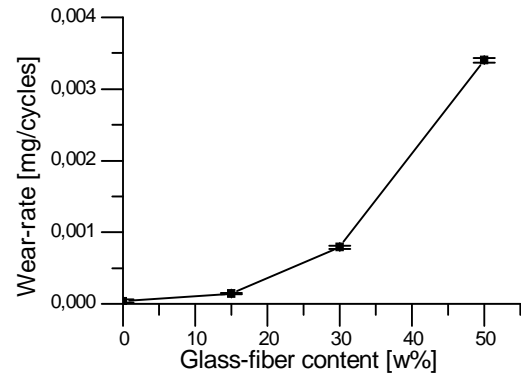
Fig. 4: Wear-rate as a function of glass fiber content of the compounds.

These results are the first steps to predict the real-life-time of injection moulds, and help the mould designers to understand more in details of wear mechanisms occurring during plastics processing of highly filled polymer compounds.

3. Acknowledgements

4. References

[1] Mennig, G.: Wear in Plastics Processing – How to Understand, Protect and Avoid. Hanser Publishers Munich-Vienna-New York, 1995.

[2] Friesenbichler W., G. Langecker, D. Caliskanoglu: Abrasive/corrosive wear on plastic mould steels, measured under practical conditions. Proceedings of the 7th International Tooling Conference, Torino, 2006

TRIBOLOGICAL INVESTIGATION OF ELASTOMERIC MATERIALS USED IN SEAL COMPONENTSTLE

I. Gódor[1], A. Javidi[1], B. Strohhäussl[2], F. Summer[2] and H. Krampl[2],

[1] University of Leoben, Chair of Mechanical Engineering, Franz-Josef-Str. 18, 8700 Leoben, Austria.

[2] Polymer Competence Center Leoben GmbH, Roseggerstraße 12, 8700 Leoben, Austria

Corresponding author: istvan.godor@unileoben.ac.at

1. Introduction

The lifetime of elastomeric materials used in seal components can be divided into three phases based on their functional behavior. These phases are known as run-in phase, operating phase and breakdown phase. There are many parameters, which influence these phases such as normal load (contact pressure), sliding speed, temperature, micro topography of friction surface and lubricant (state of lubrication). The goal of this work is to gain better understanding how these parameters affect the tribological behavior of the elastomeric materials used in seal components.

2. Material and experimental set-up

The investigated material TPE was developed by the company SKF-Economos. A Pin-on-Plate test configuration was developed due to identify the behavior of tribological system. The tribological investigations were carried out using two different methods. The test methods were accomplished by means of Plint TE77 tribometer for high frequency and AMB tribometer for low frequency friction test. Fig. 1 shows Plint TE77 tribometer.
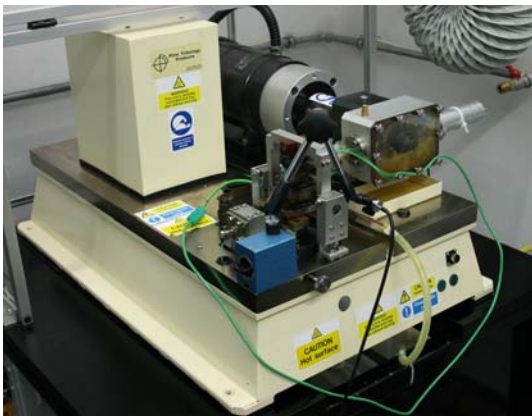
Fig. 1: Plint TE77 tribometer

High frequency tribological tests were conducted on a Plint TE77 tribometer with reciprocating configuration, which includes a control unit incorporating COMPEND acquisition software. Fig. 2 illustrates an image of the reciprocating test system of the TE77 tribometer.
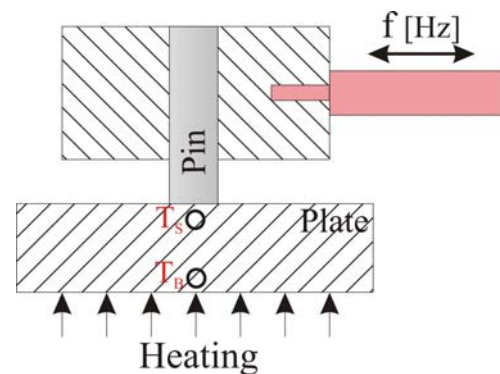
Fig. 2: General scheme of the reciprocating motion Plint TE77 tribometer

The specimen temperature T_B was measured at the bottom of steel specimen, while the contact-near-temperature T_S is measured at a hole drilled in the steel specimen close to the contact surface between Pin and Plate. In order to evaluate the contact-near-temperature caused by a different combination of parameters, finite element analyses using the ABAQUS® were carried out in this study (Fig. 3).
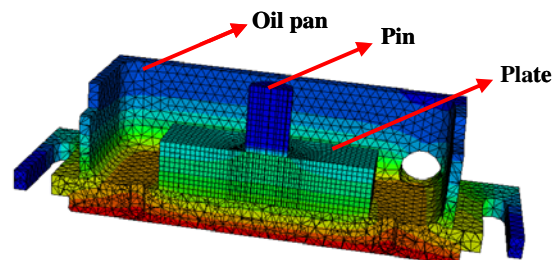
Fig. 3: Evaluation of contact-near-temperature using finite element analysis

TE77 tribometer provides sequence control of load, frequency and temperature in addition to the data of the reciprocating test system of the TE77 tribometer. The reciprocating friction tests consisted of many steps that combined different values of normal load, friction frequency and temperature. Fig. 4 shows a typical plot of measured data.
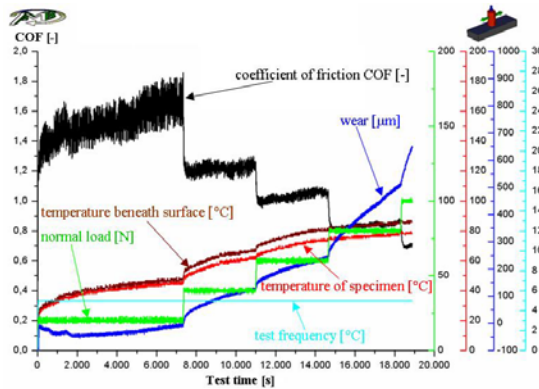
Fig. 4: Typical plot measured by TE77 tribometer

In order to study the tribological behavior of TPEs at low frequencies, a linear tribometer was designed and constructed at Chair of Mechanical Engineering (AMB). Friction tests were conducted using a reciprocating wear machine where the TPE pin was subjected to a constant load and slides on a reciprocating bed, which was driven by a spring as an elastic member (Fig. 5).

Fig. 5: Linear tribometer AMB

TPEs show the stick-slip effect at slow sliding speeds. During the stick stage, there is no relative motion between the two contact surfaces and during slip the relative velocity increases from zero to a maximum and then decreases to zero to enter the stick stage again. It is undesirable in precision movements and quiet operations. Sometimes the severe vibration can even cause damage and failure of machine components [1-2].

The pin-on-plate tests using by AMB were carried out at different normal load and different roughness of counterbody. The duration of each friction test was extended to 24 hours Fig. 6 illustrates a typical plot measured by AMB.
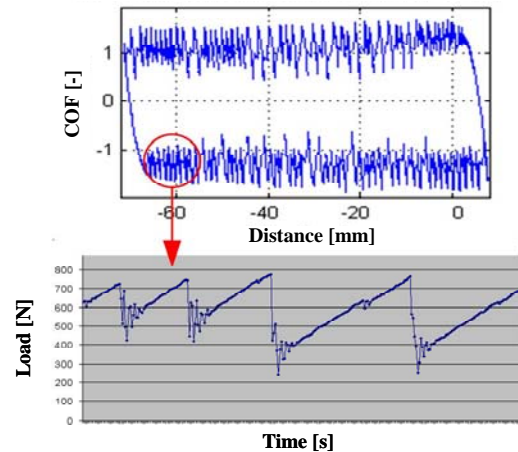
Fig. 6: Typical plot measured by AMB

It has been observed that the amplitude of the stick-slip decreases when Load and surface roughness increase.

3. Acknowledgements

4. References

[1] C. Gao, D. Kuhlmann-Wilsdorf and D.D. Makel, Fundamentals of stick-slip. Wear 162–164 (1993) 1139–1149.

[2] P. Diss and M. Brendlé, A general approach to discontinuous transfer films: influence of sliding speed and stick-slip phenomena. Wear 203-204 (1997) 564-572.

COMPARATIVE STUDIES OF HARDENED SURFACE LAYERS UNDER CONTACT STRESS

A. Trausmuth [1), I. Godor[1), M. Stoschka[1),

[1) Chair of Mechanical Engineering, University of Leoben, Franz-Josef-Str. 18, 8700 Leoben, Austria.

Corresponding author: andreas.trausmuth@unileoben.ac.at

1. Introduction

For many complex stressed components such as gears, camshafts or rail wheels the contact loading plays a major role. Constantly increasing requirements with respect to the load-carrying capacity in contact call for an accurate knowledge of the fatigue and damage processes under contact loading as a necessary prerequisite for further optimization. The present work examines experimentally the local influences and differences of case hardened and plasma nitrided layers on their load carrying capacity under rolling contact fatigue (RCF). In order to model experimentally the characteristic point and line contact conditions, the experiments were performed on a Ball-on-Rod (BoR) test rig as well as on a two-disc rolling contact fatigue test rig (2-RCF).

2. Experiments

To evaluate the selected materials under contact stress for different types of contact, the boundary conditions of the experiments have been varied across a large range of contact pressure and slip onditions.

		BoR		
	Slip S [%]	0		
	p_{max} [GPa]	5,2	5,9	6,3
number of specimen	31CrMoV9 EHT 0,37mm	15	15	10
	R 935 EHT 0,3mm	15	15	10
	20MnCr5 EHT 0,5mm	6	12	10
	20MnCr5 EHT 1,6mm	-	-	-

2-RCF								
0			10			22		
0,7	0,9	1,1	0,7	0,9	1,1	0,7	0,9	1,1
2	3	2	2	2	1	2	2	-
2	3	2	-	-	-	-	-	-
-	-	-	-	-	-	-	-	-
2	3	2	2	2	1	2	2	-

Table 1: test program: number of experiments investigated

2.1 Tribological testing method

The BoR-test, in Figure 1, consists in rolling three pre-stressed balls having an aperture of $^1/_2$" across a rod-shaped specimen (Material *M50*). Due to the presence of point contacts and the possibility of multiple rolling cycles, this test rig is generally used for highest contact pressures (up to to *7 GPa*) and for highest test frequencies (up to *120 Hz*). One disadvantage is the undefined slip during free rolling of the balls along the rod.
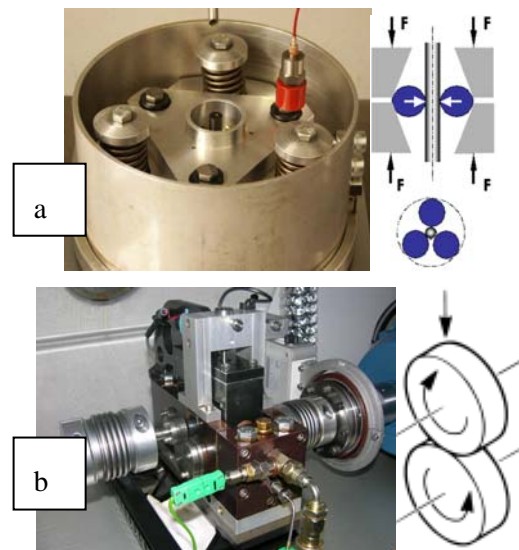
Figure 1: RCF test stand. a) Ball-on-Rod test rig (NTN Technical Center),
b) two-disc test rig TE 74 (Phoenix Tribology)

The line contact occurring in the two-disc test rig TE 74, Figure 1 is of some more practical relevance. The test stand provides medium contact pressure (up to *2 GPa*), test frequencies (up to *40 Hz*) and a very broad slip range adjustable from zero to hundred percent. The adjustable oil volume and variable oil temperature (max. *200 °C*) allows to adjust the test situation to practical situations such as they occur in gears. For the experiments of the present study, the engine oil Shell Rimula *SAE 10W 40* was applied by central lubrication.

Both test stands, BoR and 2-RCF, have a vibration control whereby the occurring raise of vibration amplitude from the global failure can be used as a standard shut down criterion.

3. Results

3.1 Point contact (BoR)

The plasma nitrided material *31CrMoV9* and *R935* was tested up to 10^9 cycles in contact low cycle fatigue. The experiments were made on three different stress levels with a test frequency of *150 Hz*, with maximal nominal contact pressure *5,2 GPa*, *5,9 GPa* and *6,3 GPa*.
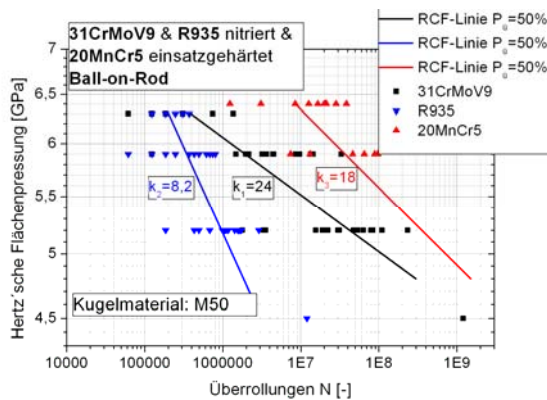
Figure 2: contact low cycle fatigue line of BoR-experiments

Figure 2 shows that the inclinations of the contact S/N curves are markedly different for the two materials. The material *R935* has a high notch sensitivity. Due to the different inclinations of the S/N curves, the load-carrying capacity of the nitrided steel *31CrMoV9* is higher in the lower contact low cycle fatigue regime. The material *20MnCr5* shows a higher contact fatigue lifetime.

3.2 Line contact (2-RCF)

Damage evolution can be subdivided roughly into three stages (Fig. 3.3 a). The duration and evolution of each stage depends on the load as well as on the material.

The transitions between these stages are easily recognized from the test readouts early and will be called characteristic damage or rather characteristic wear. Fig. 3.3 a show the allocation of these characteristic transitions.

Fig. 3.3 b shows the results of the 2-RCF analysis without slip.
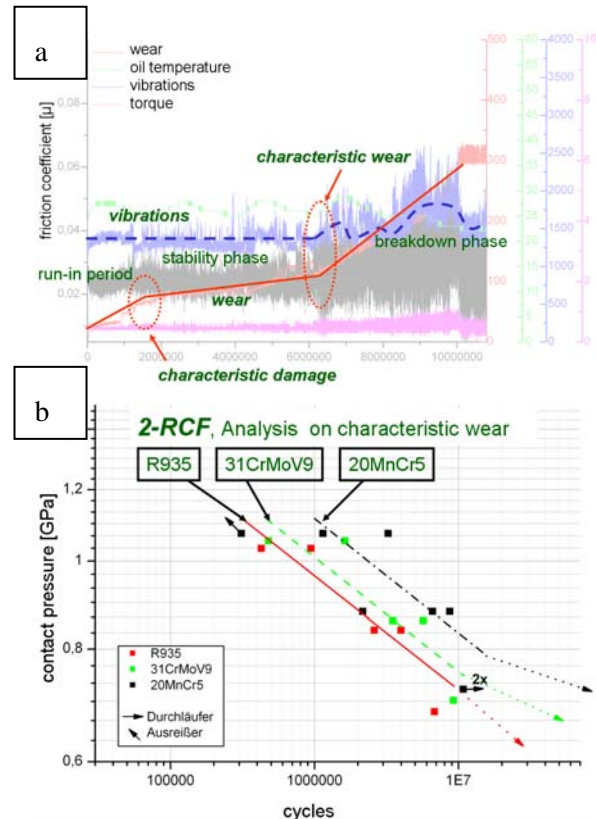
Figure 2: interpretation oF 2-RCF-low cycle fatigue line. a) test readout, definition of characteristic wear and characteristic damage, b) 2-RCF-low cycle fatigue without slip using characteristic wear

According to this approach the contact low cycle fatigue line represents the beginning of the breakdown phase, characterized by a marked increase of wear.

4. References

[1] Trausmuth A.: Verhalten von Plasma-nitrierschichten unter Kontaktbeanspruchung. Diplomarbeit, Montanuniversität Leoben, 2008.

[2] Bader M.: Beitrag zur Charakterisierung der Wälzbeanspruchung von Gradientenschichten. Diss. TU Freiberg, 2002.

[3] Trausmuth A., Gódor I., Stoschka M., Leitner H.: Verhalten von gehärteten Randschichten unter Kontaktbeanspruchung, Symposium 2008 der Österreichischen Tribologischen Gesellschaft, S81-93, ISBN 978-3-901657-30-6 (B,V)

ANALYSIS OF WARM PRE-STRESSING EFFECT FOR RPV ASSESSMENT

Szabolcs SZÁVAI [1)], Róbert BELEZNAI [2)]

[1)] Bay Zoltán Foundation for Applied Research, Institute for Logistics and Production Systems, H-3519, Miskolc-Tapolca, Iglói 2., Hungary

Corresponding author: szabolcs.szavai@bay-logi.hu

1. Introduction

The presented research work is connected to a running project NESC-VII, which is a European cooperative action in support of Warm Pre-Stressing (WPS) use in the Reactor Pressure Vessel (RPV) integrity assessment. WPS is a phenomenon which justifies, that crack does not propagate during unloading cycle in case of PTS. BZF takes part in the modelling work, where the WPS effects on J-integral should be determined. In the first stage of the project a preliminary calculation has been performed. An overview is given about finite element calculation of pre-cracked Charpy-like 3PB specimen, which has been performed to analyze the effect of WPS on fracture toughness value of RPV steel for two load cases (**L**oad-**U**nload-**C**ool-**F**racture and LCUF). Besides the calculation, material tests were also performed in different temperatures.
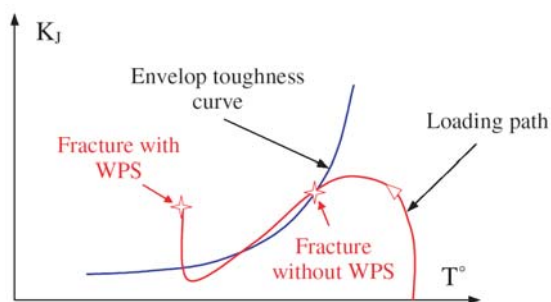
Fig. 1: WPS phenomenon

2. Material properties

Analyses on the specimen under WPS condition have been performed on a 18MND5 (A533B) ferritic steel. The material has been manufactured according to the RCC-M specifications by Creusot Loire Industrie in 1995. The material properties are provided by AREVA NP, France, [1]. True strain-stress curves from -150°C to 20°C are available for the calculation. These curves have been extrapolated to large strains thanks to a Hollomon's type relation, e.g.:

$$\sigma = K(\varepsilon^p)^n \qquad (1)$$

(σ is the stress, ε^p the plastic strain, K and n two coefficients). The Young modulus values of 18MND5 ferritic steel were also temperature dependent.

3. Finite element model of 3PB specimen

Pre-cracked Charpy-like 3PB specimen geometry without side-grooving was chosen for the analysis. The specimen contained a crack with a ratio, a/W=0.34 (a - crack length, W – with of the specimen).
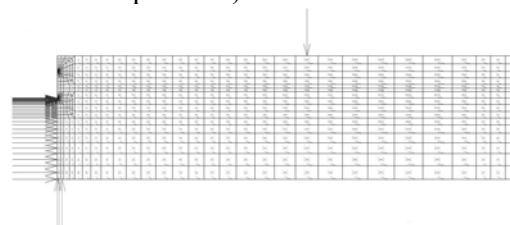
Fig. 2: Mesh of the large scale Charpy-like 3PB specimen

The mesh of the half part of the specimen with is presented in the Fig.2. For the analysis plain strain condition was applied. J-integral was calculated based on virtual crack extension (VCE) method, which is implemented into the software and with the help of analytical formulas based on Load – Load line displacement (LLD) curve (worked out in the VOCALIST project, [2]).

WPS thermal conditions were that the initial temperature was T=20°C, after the temperature was decreased to T=-150°C. In the first case the specimen was unloaded before the cooling. In the second case the specimen was cooled at first under constant load and after it was unloaded. Both case was followed by again an Load-Unload cycle at constant T=-150°C temperature.

4. Results

J-integral was plotted in time during the WPS loading cycles. Result of finite element calculation and analytical solution were compared for both case (Fig. 3-4). In case of LCU preloading the residual J-value calculated by FEM is much higher, than in LUC case. The results show that the VOCALIST method is not applicable for non proportional load.
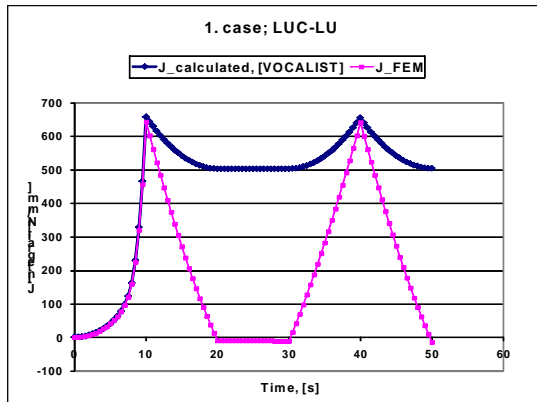
Fig. 3. J-integral curves under WPS condition in case of LUC-LU cycle
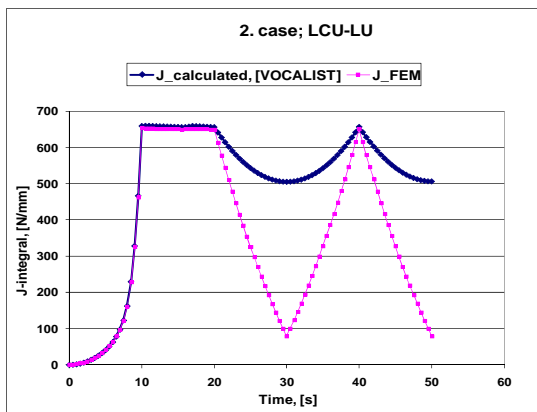
Fig. 4. J-integral curves under WPS condition in case of LCU-LU cycle

5. Experimental tests

The WPS effect can arise from several facts such as blunting of the crack tip, residual stresses or that the preliminary high-level loading performed changes in the crystalline structure of the material. Due to preload the initial homogenous, isotropic texture will become anisotropic structure, which can have higher fracture toughness.
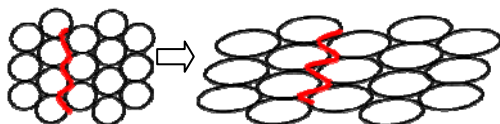
Fig. 5. Grain texture pre-deformation

For analysing the effect of the grain texture predeformation, mechanical tests were performed at different levels of pre-stressing.

S235-JR plate was the base material of the investigation. The transient temperature of the steel is about -20-0°C so the preload was done at room temperature. WPS effect was tested during LCUF cycle. 3PB specimens were used. The pre-load was 90% of the fracture toughness at 20°C. The specimens were cooled to -40°C under constant load. However K_I was significantly higher that the K_{IC} at -40°C, no fracture occurred during the cooling. During the reloading at low temperature higher fracture toughness was measured than without pre-loading so the WPS has been demonstrated.

To analyse the effect of pre-deformation a series of test have been started with different axial pre-load level. The first test was performed on 90 per cent of ultimate tensile stress pre-stressing level, specimens have much more lower fracture toughness at T=-40°C, than without pre-stressing. However the first result was negative further measurements will be carried out on lower axial pre-loading level.

6. Conclusions

An overview is given in the present paper about finite element calculation of pre-cracked Charpy-like 3PB specimen, which has been performed to analyze the effect of WPS on fracture toughness value of reactor pressure vessel steel. Two different loadcase were applied in the calculation, and it can be stated, that Vocalist methode nor applicable for WPS analysis, because in the unloading cycle the methode does not describe J-integral well. From the calculated J-integral can be seen that the residual J is significant in case of LCU-LU cycle. However, the mechanism of the WPS is already an open issue. That is why; further investigations are required.

7. References

[1] [1] NESC VII project: presentation of data necessary for the feasibility test pre definition, AREVA NP, France, 2008.
[2] [2] Validation of constraint based assessment methodology in structural integrity, VOCALIST project report, 2004.

INVESTIGATION OF THE TOOTH ROOT LOAD CARRYING CAPACITY OF A HYPOID GEAR

Philip Herics, Christoph Haberer, Wilfried Eichlseder

Montanuniversität Leoben, Chair of Mechanical Engineering, Franz-Josef-Str. 18, 8700 Leoben, Austria.

Corresponding author: philip.herics@stud.unileoben.ac.at

1. Introduction

The development of modern automotive drive trains is governed by the competing demands of constantly increasing transmitted power as well as weight and cost reduction. For the evaluation of the load carrying capacity of hypoid wheels a new test procedure is developed. With the unique servo-hydraulic test procedure it is possible to test the load carrying capacity of the tooth in single contact engagement.

2. Hypoid Wheel Test Procedure

With a unique servo-hydraulic test procedure (Figure 1), accomplished on an Instron Structural Testing system (IST) controlled by a FASTRACK 8800, it is possible to test the load carrying capacity of the hypoid gear tooth root in single contact engagement against one pinion tooth up to 4000 Nm. For this purpose the neighboring teeth of the hypoid wheel are removed to ensure a contact overlap with a value of 1. The advantage of single contact engagement testing is that the pulsating load is located on one tooth flank (single contact) and the estimation of the load carrying capacity of a single tooth root is possible [1].
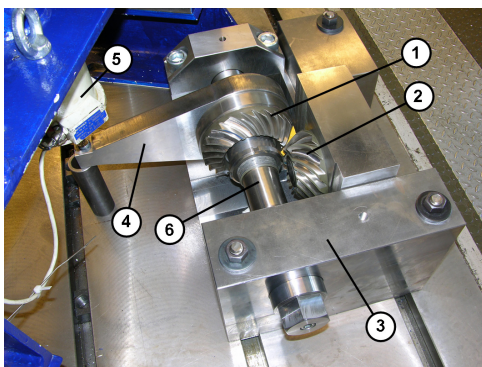
Fig. 1: Servo hydraulic test procedure for hypoid gears

Via a servo-hydraulic actuator with a maximum load of 50 kN equipped with a load cell **5** (Figure 1) a pulsating force is applied to a lever arm **4**. The testing torque is transfused from the shaft on the hypoid gear wheel **1** via three bolts with a diameter of 10mm on the backside of the hypoid wheel. The testing torque on the hypoid wheel **1** is used for life fatigue description. The counterpart of the wheel – the pinion **2** – is fixed to a stiff clamping device. The shaft **6** is supported by the massive device. The displacement measurement is achieved by a Linear Variable Differential Transformer (LVDT) system integrated into the servo actuator. Especially for hypoid gears the development of a test rig is challenging because the epicyclical shape of the tooth flanks and the characteristic stiffness of the contact pairs cannot be respected by a pressure head design.

The characteristics of the servo-hydraulic test are:

- test closed to the real component and the application

- concentrated force on one tooth flank

- differences in load, lubrication and stiffness unlike the real roll off situation

- comparative study on the damage mechanisms

Of course the single engagement tests differ from the real engagement situation. The following listing guides to the real meshing process.

- During the meshing process between two teeth inner dynamics occur due to differences in the stiffness of the contact partners and meshing interferences. Component tests on a servo-hydraulic test bench in single contact use sinus loads, which forces the tooth gradually, no

additional dynamic forces occur. The influence of inner dynamics is described in several standards with a dynamic factor taking the increase of loading into account.

- The stiffness of the test procedure is much higher than in the real gear box.

- In real application and loaded roll-off tests the weakest tooth of a gear pair limits the lifetime of the entire system. Additional statistical influences on the fatigue results by testing arbitrary tooth pairs and not the weakest tooth on the servo-hydraulic test bench come from single contact testing.

- Differences in the mean stress in the tooth root due to the loading on the forward tooth, which provokes a pressure loading in the tooth root lead to 10% lower tooth root fatigue strength testing on the servo-hydraulic test bench.

- The lubrication conditions in single contact testing are totally different than in the roll-off situation. Through the high pressure forces between two tooth flanks in single contact and microslip movement, fretting fatigue and wear occurs. To avoid crack initiation on the tooth flank, the flanks were covered with a thin MoS_2 lubrication film.

Taking the listed differences into account the results of single contact testing can be transferred to the real meshing situation between to gears in engagement.

3. Fracture Analysis

The fatigue failure of a hypoid gear tooth root caused by cyclic loading starts with the crack initiation directly at the surface. In the next step a fatigue crack growth occur and discharge in the forced rupture. The fatigue fracture surface looks very fine-grained depending on the velocity of the fracture progress.
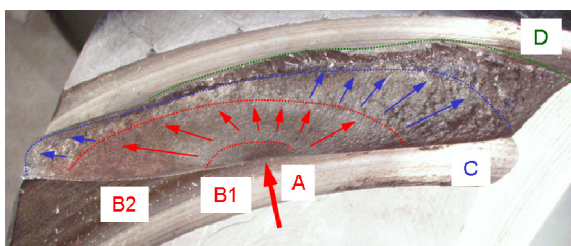
Fig. 2: Tooth root fracture analysis

Figure 2 shows the fracture surface of a hypoid gear wheel, where the initial crack was induced in the tooth root at about half of the tooth length directly at the surface. The fine-grained initial crack area **A** (Figure 3) is marked with an arrow. Consequently this results in a slow stable crack growth with a main direction of propagation along the length and smaller propagation into depth direction.
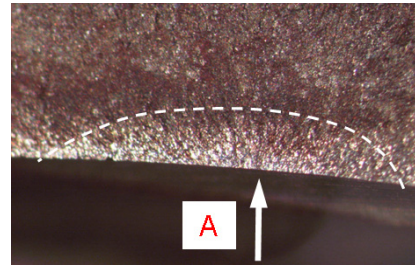
Fig. 3: Half-elliptical crack initiation area

The result is a half elliptical fine-crystalline fracture surface **B1** (Figure 2). The stable crack growth is accelerated in depth and length direction and it leads to a rougher fracture surface **B2**. Within the area **C** the crack growth gets increasingly unstable and finally leads to the forced rupture **D**.

4. Conclusions

With the unique servo-hydraulic test procedure it is possible to test the load carrying capacity of the tooth in single contact engagement. The fracture analysis shows the initial crack in the tooth root directly at the surface. For a comparative study of different materials or heat treatments the test procedure is very useful.

5. Acknowledgements

6. References

[1] C. Haberer, H. Leitner, W. Eichlseder, A. Dietrich: Fatigue Life Behavior of a Hypoid Gear Tooth Root Taking the Influences of Orbital Forging into Account. SAE World Congress, Paper No. 2009-01-0812, 20.-23. April, Detroit, 2009

COMPARISON OF GEAR TOOTH ROOT STRESSES BY ANALYTICAL, NUMERICAL AND EXPERIMENTAL EVALUATION

Martin Leitner, Christoph Haberer, Wilfried Eichlseder

Montanuniversität Leoben, Chair of Mechanical Engineering, Franz-Josef-Str. 18, 8700 Leoben, Austria.

Corresponding author: martin.leitner@stud.unileoben.ac.at

1. Introduction

The knowledge of the local stresses in the tooth root is very important for the evaluation of the load carrying capacity of gear wheels. The equations and its related coefficients in DIN 3990 Part 3 Method B [1] do not provide a reliable solution to the wide variety of non-standard gear tooth profiles. So it is necessary to evaluate these tooth stresses by finite element simulations or strain gauge measurements. Thus the differences of the stress values between these methods have to be known.

2. Evaluation of the gear tooth root stresses

2.1 Analytical Evaluation according to the DIN 3990 Part 3 Method B standard

The calculation in this standard is based on the maximum gear tooth root stress σ_F in the critical cross section (fig. 1).
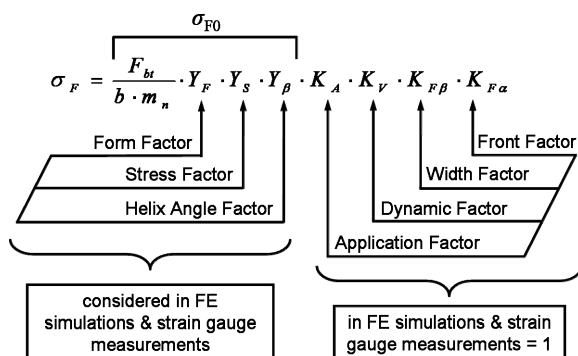
Fig. 1: Calculation of the maximum stress in the tooth root via DIN 3990 Part 3 Method B

To ensure the comparability of the results it is necessary to calculate the nominal tooth root stress σ_{F0}. The Form Factor Y_F regards the influence of the tooth shape to the nominal bending stress for a force attack in the outside single engaging point. By the Stress Factor Y_S a conversion of the nominal bending stress to a

local tooth root stress is achieved. The Helix Angle Factor Y_β accounts the difference of the tooth root stress between the helical gear and the equivalent spur gear which is the base of the calculation.

$$Y_F = \frac{6 \cdot \frac{h_{Fe}}{m_n} \cdot \cos(\alpha_{Fe})}{\left(\frac{s_{Fn}}{m_n}\right)^2 \cdot \cos(\alpha_n)}$$

$$Y_S = \left(1,2 + 0,13 \cdot \frac{s_{Fn}}{h_{Fe}}\right) \cdot \left(\frac{s_{Fn}}{2 \cdot \rho_{Fn}}\right)^{\frac{1}{(1,21+2,3 \cdot h_{Fe}/s_{Fn})}}$$

$$Y_\beta = 1 - \varepsilon_\beta \cdot \frac{\beta}{120°}$$
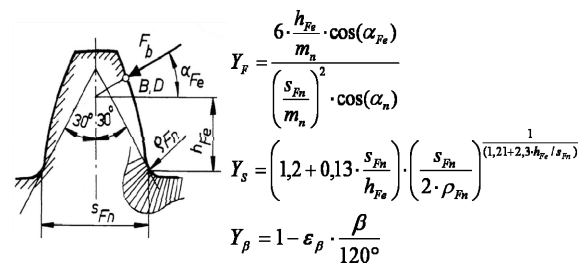
Fig. 2: Definition of the critical cross section and the position of the force attack point [1]

Fig. 2 depicts one gear tooth with the attendant definitions of the critical cross section and the force attack point.

2.2 Numerical Evaluation by finite element simulations

The first step in the simulation chain is the generation of the tooth shape by the software package KISSsoft. Afterwards the finite element pre-processing – in particular the assembling of the 2D- and 3D-FE model – the solution and post-processing by the software Abaqus 6.7 CAE was accomplished. One of the 3D-FE simulation outputs is displayed in fig. 3.
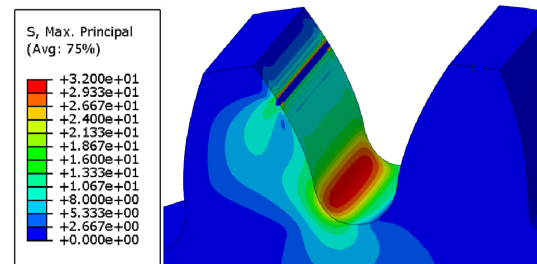
Fig. 3: 3D-FE simulation result pictured with the maximum principal normal stress (F_{bt} = 5 kN)

Obviously the maximum principal normal stress in the tooth root is not constant along the width of the spur gear.

For detailed consideration, a three-dimensional diagram with the software package MATLAB 6 was created (fig. 4).
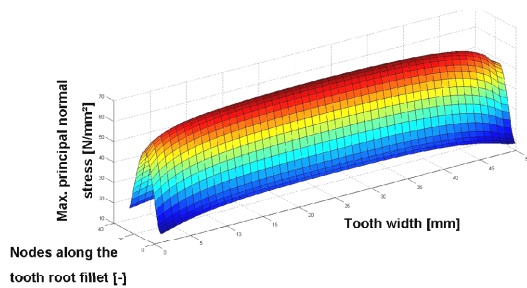
Fig. 4: Position dependent maximum principal normal stress

With the help of the 3D diagram (fig. 4) it was possible to evaluate the value and the exact position of the highest maximum principal normal stress in the tooth root fillet.

2.3   Experimental Evaluation by strain gauge measurements in the tooth fillet

For this investigation it was necessary to design a preferably stiff and easy to handle test rig. Fig. 5 shows the 3D-drawing and the spur gear, which is assembled with six strain gauges along the tooth root width.
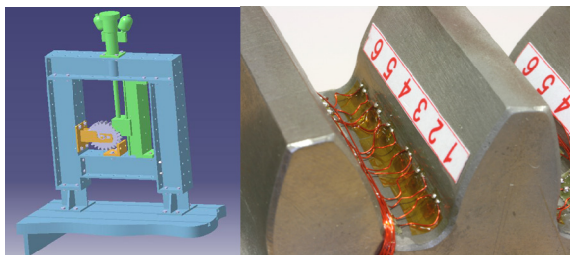
Fig. 5: Test rig and the assembled tooth root

As it is only possible to measure the strain in the tooth root, it was necessary to evaluate the stress. From the stress condition in the tooth root the equation for the conversion is

$$\sigma = \frac{E \cdot \varepsilon \cdot (1 - x \cdot \nu)}{1 - \nu^2} \quad \text{with} \quad 0 \le x \le \nu \quad (1)$$

$x = 0$ …plane strain condition

$x = \nu$ …plane stress condition

Whereas E [N/mm²] is the Young's modulus, ε [−] the measured strain in the tooth root and ν [−] the Poisson's ratio.

According to former strain gauge trials, in the literature was found that

$x = 0{,}05$ [2]

This indicates that there is almost none deformation along the transverse direction (along the width of the gear) in the tooth root.

3. Comparison of the Results

In this work two spur-toothed gears (z=16 and z=24, m_n=10mm, b=50mm) were tested. A confrontation of the analytical (DIN), experimental (SG) and numerical (3D and 2D) stress results σ_{F0} in N/mm² is shown in tab. 1. The difference $\Delta\sigma$ is referenced to the analytically calculated stresses according to DIN 3990 Part 3 Method B.

	DIN	SG	3D	2D
z=16	33,3	33,3	31,7	30,6
$\Delta\sigma$	-	0,0 %	-4,8 %	-8,1 %
z=24	30,9	30,5	30,0	28,1
$\Delta\sigma$	-	-1,3 %	-2,9 %	-9,1 %

Tab. 1: Comparison of the maximum stress values σ_{F0} in the tooth root (F_{bt} = 5 kN)

4. Conclusions

The comparison of the tooth root stresses delivers a good compliance with a small difference up to approximately 10 %. The results of the DIN standard are like expected on the conservative safe aspect. The highest stress values appear in the range near the half width because in this place, opposite to the front surface, the deformations are disabled. In DIN 3990 Part 3 Method B the maximum stress is assumed in the 30° tangent which is confirmed by the finite element simulation.

5. Acknowledgements

6. References

[1] DIN 3990-1987: Tragfähigkeitsberechnung von Stirnrädern Teil 3: Berechnung der Zahnfußtragfähigkeit. Beuth V. Berlin,1987

[2] M. Hirt, Messtechnische Briefe, 10. Jg. (1974), Heft 2

EFFECTS OF ANISOTROPY AND EFFECTIVE STRAIN ON THE FATIGUE PROPERTIES OF A TITANIUM ALLOY

Wen Tan[1], Michael Stoschka[2], Martin Riedler[3], Wilfried Eichlseder[2]

[1] University of Leoben, CD-Laboratory for Fatigue Analysis, Franz-Josef-Str. 18, 8700 Leoben, Austria.

[2] University of Leoben, Chair of Mechanical Engineering, Franz-Josef-Str. 18, 8700 Leoben, Austria.

[3] Böhler Schmiedetechnik GmbH & Co KG, Mariazellerstraße 25, 8605 Kapfenberg Austria.

Corresponding author: wen.tan@unileoben.ac.at

1. Introduction

For the development of components computational lifetime calculation becomes more and more important to fulfil the interacting requirements of lightweight design and cost efficiency. Especially in aerospace industry, where typically Ti-alloys are used for high performance lightweight structure components, it becomes an important factor to consider the manufacturing process and linking the local lifetime the customer demands.

2. Methodical approach

The investigated material is an $(\alpha+\beta)$-Ti-6Al-4V-alloy. Specimens for static and dynamic tests are taken out of forged and post heat-treated ingots to set up different microstructures, see [1]. The high cycle fatigue and tensile tests were executed at a servo-hydraulic test rig. Due to the process variation, a wide number of different microstructures, ranging from lamellar to bimodal textures with different a-content and a-contiguity, has been observed [2]. First results regarding the effect of anisotropy and effective strain are shown in this paper.

3. Influence of anisotropy

The specimens for the material tests were manufactured out of forged V-Shapes, as shown in Fig. 1. The effect of anisotropy is characterised by different specimen orientations. Further on, the investigated specimens are turned clockwise through $45°$.
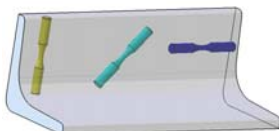
Fig. 1: Different specimen position for anisotropy

3.1 Static test

To describe the influence of the anisotropy on the static material properties tensile tests were carried out. As shown in Tab. 1 the vertical orientated specimen show only minor higher static strength values, while the ultimate strain values are smaller.

Specimen	Young's Modulus [GPa]	Tensile strength [MPa]	Yield strength [MPa]	Uniform Strain [%]	Ultimate Strain [%]
horizontal	**122**	**978**	**926**	**8,9**	**19,5**
vertical	**118**	**989**	**937**	**7,0**	**16,6**

Tab. 1: Static properties dependent of anisotropy

3.2 Cyclic test

Tensile/compression tests were carried out with a stress ratio of $R=0$. Contrary to the static tests which show only a minor difference in yield strength, the cyclic tests show an extended lifetime of about two for the horizontal orientated specimens especially significant in the high-cycle-fatigue range; see Fig. 2.
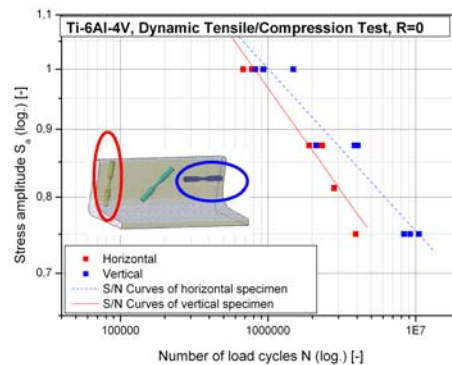
Fig. 2: S/N-curves for anisotropy

4. Influence of effective strain

The effect of effective strain is characterised by evaluating different specimen positions taken out of the V-shape. Low effective strain appears at only at the corner, whereat high effective strain is given in the mid-positions.
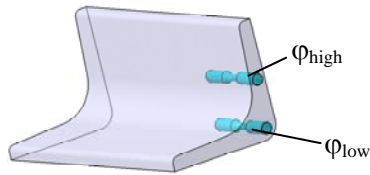
Fig. 3: Specimen position for effective strain

4.1 Static test

The specimens with high effective strain show higher values in static strength as well as a reduced ductility; see Tab. 2.

Specimen	Young's Modulus [GPa]	Tensile strength [MPa]	Yield strength [MPa]	Uniform Strain [%]	Ultimate Strain [%]
high eff. str.	118	989	937	7,0	16,6
low eff. str.	110	957	878	9,4	20,2

Tab. 2: specific values for effective strain

4.2 Cyclic test

Cyclic tensile/compression tests to characterise effective strain influence at tumescent stress level were carried out. The results of the S/N-tests show an slightly improved material behaviour for the specimens with high effective strain; see Fig 5.
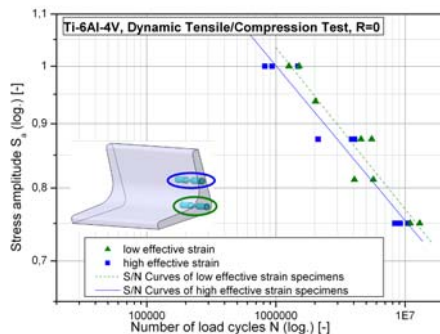
Fig. 4: S/N-curves for effective strain

5. Microstructure

Fig. 5 shows typically microstructures of metallographic sections taken out of horizontal and vertical orientated specimens. The differences in lifetime can be linked to the microstructural properties based on α-contiguity, size of the α-prime particles and size of the β-lamellae distance.
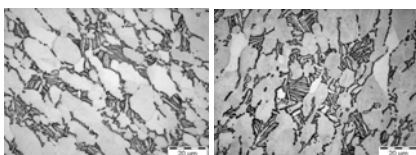
Fig. 5: Microstructure of horizontal (left) and vertical (right) orientated specimens

The preferred manufacturing orientation in the V-Shape can be determined from the anisotropy test specimens which exhibits considerable lifetime values, especially for the high-cycle-fatigue region. The light optical investigation metallographic sections taken out of the effective strain specimen show no major influence on the microstructural α-grains and their contiguity.

Because of standard evaluation methods like intersection counting of the primary a-grains do not map the $(\alpha+\beta)$-microstructure in a sufficient way; additional methods will be developed further on in the research project [3].

6. Conclusion

The results in the S/N tests show a significant difference in the high-cycle-fatigue lifetime values due to the manufacturing process. These differences are also recognisable in the varying microstructure.

In the future work a model should be established to describe the fatigue life in dependence of the $(\alpha+\beta)$-microstructure, to support the local consideration of microstructural aspects in lifetime calculation.

7. Acknowledgements

8. References

[1] M. Riedler, M. Stockinger, M. Stoschka and W. Eichlseder, Fatigue Analysis of Forged Aerospace Components based on Microstructural Parameters. Key Engineering Materials, Vol. 348-349 (2007) 185-188.

[2] W. Tan, M. Stoschka, M. Riedler and W. Eichlseder, Contribution to the influences of the microstructure on the fatigue behaviour of Ti-6Al-4V Alloy, 25th Danubia Adria Symposium S 257-258.

[3] M. Stoschka, M. Stockinger, H. Leitner, M. Riedler, Assessment of lifetime calculation of forged IN718 aerospace components based on a multi-parametric microstructural evaluation, Superalloys 2008, pp573-582.

EXPERIMENTAL METHODS TO INVESTIGATE THE RUNNING-IN PROPERTIES OF SOFT COATINGS

Florian Grün[1], István Gódor[2], Wilfried Eichlseder[1,2]

[1] University of Leoben, CD-Laboratory for Fatigue Analysis, Franz-Josef-Str. 18, 8700 Leoben, Austria

[2] University of Leoben, Chair of Mechanical Engineering, Franz-Josef-Str. 18, 8700 Leoben, Austria

Corresponding author: florian.gruen@unileoben.ac.at

1. Introduction

Soft coatings improve the running-in behaviour and the sliding properties of lubricated tribosystems. In the context of this study, an experimental methodology to elucidate the sliding properties is presented and it is benchmarked using a polymer based coating applied on a tribomaterial sliding against a steel counterpart.

2. Test methodology

Since polymeric overlays are applied in large-area contact systems, we designed a test methodology using a large-area system. The ring on disc test configuration used here has been described in detail in previous studies [1]. A rotating disc consisting of the coated tribomaterial is rubbed against a static steel ring. The set-up, the geometry and the surface finish are depicted in Fig. 1. Splash lubrication was used using fully formulated engine oil. Temperatures (T_1 and T_2) and the Coefficient of Friction (*COF*) were measured. Several test strategies have been developed to visualize the selected system properties. Within these tests the speed was kept constant and the loading was changed in predefined steps/periods. After the test the sliding surfaces were analysed using laser confocal microscopy (Olympus LEXT).
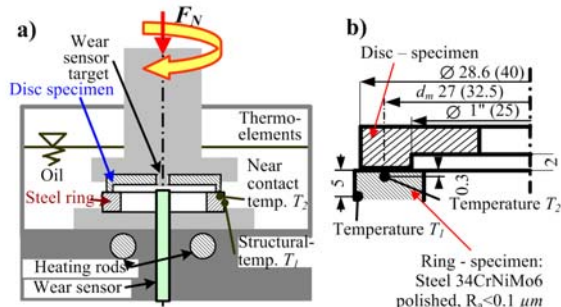
Fig. 1: a) Test configuration – Ring on Disc [1], b) Detail [2]

3. Benchmark of test methodology

Fig. 2 depicts the tribometric results of a step test in which the loading was increased monotonously in steps of 1.8 MPa every 24 h. With a sliding speed of 2.5 m/s one step corresponds to a sliding distance of more than 200 kilometres. The overall test duration was 3 days. The results show running-in during the first loading step. During this running-in process the measured COF and temperatures decline. This indicates the adaptation of the system to the corresponding tribological loading. Each increase in loading results in a recurrence of the running-in processes. At the fourth step the loading limit of the system is exceeded and the system fails due to seizure.
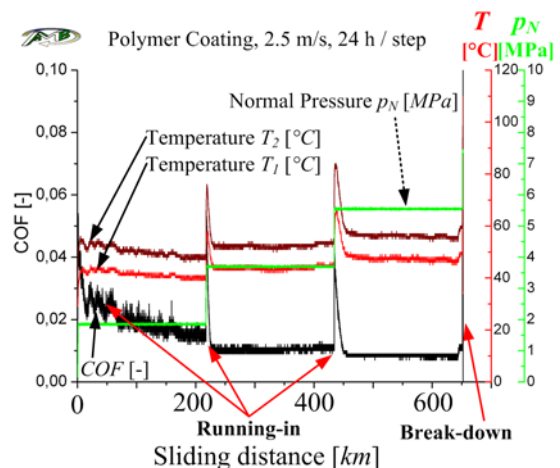
Fig. 2: Step test (monotonic) – repeated running-in processes until system failure

To clarify the conditions which require a re-adaptation of the surface structure, we designed a test strategy in which the loading is alternated in several periods. One period consists of 1 h high loading (3.6 MPa) followed by 3 h low loading (1.8 MPa). The results are shown in Fig. 3. Running-in can be observed during the first loading step of 1.8 MPa and at the first loading step of 3.6 MPa. The consecutive 3 h time steps of low load don't lead to a repeated

demand of the system for re-running-in. In further experiments we also increased the duration of the low load steps to 24 h. We didn't detect repeated running-in either.
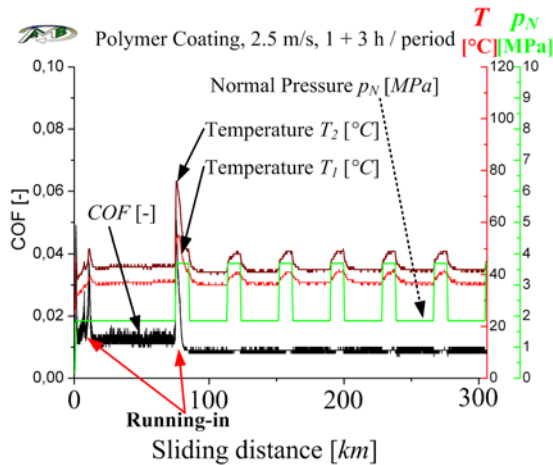
Fig. 3: Step test (periodic) – single running-in event

Fig. 4 depicts LEXT images of a sample at different stages of its lifetime. The test parameters differ from the tests shown previously. A borehole of 0.6 mm in diameter, which was drilled in the surface before the test, guarantees to analyse always the same area. Fig. 4(a) shows the surface in its pretest condition. The topography shows high roughness. The difference in height between the topography peaks and valleys is about 10 μm. During running-in the peaks are worn to form plateaus which inherently bear the tribological loading, Fig. 4(b).
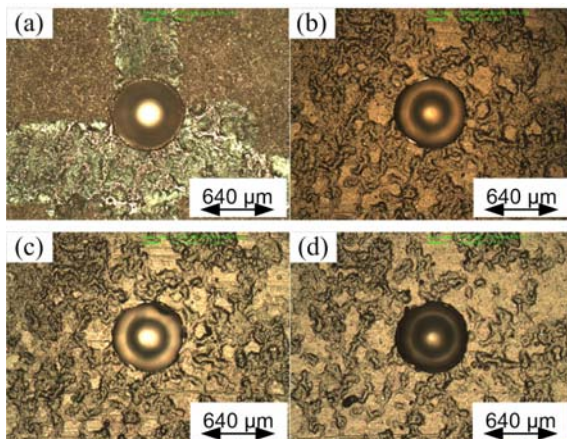
Fig. 4: LEXT images of sliding surfaces [3], a) new, b) after running-in, c) first loading step, d) second loading step

The depressions between the plateaus act as reservoirs for the lubricant which is released when necessary. Additional loading resumes the mild wear processes whereby the size of the formed plateaus increases, Fig. 4(c) and Fig. 4(d).

4. Conclusion

The results pinpoint the suitability of the methodology to visualize the running-in processes due to precise COF and temperature measurements under large area contact conditions. Several described test strategies allow for visualizing the conditions which are necessary to cause running-in. In this study of a polymeric overlay the increase in load beyond previous load levels is identified as prerequisite for a re-running-in. During the running-in the surface topography changes and a plateau type structure is formed, which facilitates smooth sliding.

5. Acknowledgements

6. References

[1] F. Grün, I. Gódor, W. Eichlseder. Schadensorientierte Prüfmethoden und abgeleitete Funktionsmodelle für Gleitwerkstoffe, Trib. und Schmierungs., 54 (2007) 5, pp. 26-30.

[2] F. Gruen, I. Godor, W. Eichlseder. Test methods to characterise differently designed tribomaterials, Tribotest, 2008, 14, 159-176. DOI: 10.1002/tt.57.

[3] F. Grün, I. Gódor, W. Gärtner and W. Eichlseder, Influence of overlays on the tribological behavior of journal bearing materials, World Tribology Congress, 2009, submitted

Author Index